



Measurement of the Standard Model W^+W^- production cross-section using the ATLAS experiment on the LHC

Martin Zeman

► To cite this version:

Martin Zeman. Measurement of the Standard Model W^+W^- production cross-section using the ATLAS experiment on the LHC. High Energy Physics - Experiment [hep-ex]. Université Paris Sud - Paris XI; České vysoké učení technické (Prague), 2014. English. NNT : 2014PA112263 . tel-01141822

HAL Id: tel-01141822

<https://theses.hal.science/tel-01141822>

Submitted on 13 Apr 2015

HAL is a multi-disciplinary open access archive for the deposit and dissemination of scientific research documents, whether they are published or not. The documents may come from teaching and research institutions in France or abroad, or from public or private research centers.

L'archive ouverte pluridisciplinaire **HAL**, est destinée au dépôt et à la diffusion de documents scientifiques de niveau recherche, publiés ou non, émanant des établissements d'enseignement et de recherche français ou étrangers, des laboratoires publics ou privés.



UNIVERSITÉ PARIS-SUD
CZECH TECHNICAL UNIVERSITY (PRAGUE)

ÉCOLE DOCTORALE 517 :
PARTICULES, NOYAUX ET COSMOS

Laboratoires :
CEA Saclay, DSM/Irfu/SPP
CERN, ATLAS Collaboration

THÈSE DE DOCTORAT

PHYSIQUE

par

Martin ZEMAN

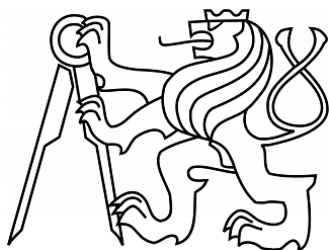
Measurement of the Standard Model W^+W^- production cross-section using the ATLAS experiment on the LHC

Date de soutenance : 02/10/14

Composition du jury :

Directeur de thèse : M. Christophe Royon
Co-directeur de thèse : M. Václav Vrba
Présidents du jury : M. Igor Jex
M. Etienne Augé
Examineurs : M. Vojtěch Petráček
M. Gregory Soyez
M. Jiří Chýla
M. Josef Žáček
M. Jaromír Kukal

Rapporteurs : M. Alexander Kupčo
M. Dmytro Volynskyy



A DOCTORAL THESIS SUBMITTED TO
Czech Technical University in Prague
Université Paris-Sud

PRESENTED BY

M. Martin ZEMAN

FOR THE DEGREE OF

Doctor of Philosophy abbreviated **Ph.D.**

IN THE FIELDS OF

Application of natural sciences
Particles, nuclei and cosmos

ON THE SUBJECT OF

**Measurement of the Standard Model W^+W^- production
cross-section using the ATLAS experiment on the LHC**

EXAMINED BY THE JURY

M.	Václav	VRBA	Supervisor
M.	Christophe	ROYON	Supervisor
M.	Alexander	KUPČO	Referee
M.	Dmytro	VOLYANSKY	Referee
M.	Igor	JEX	Chairman
M.	Etienne	AUGÉ	Chairman
M.	Vojtěch	PETRÁČEK	Examiner
M.	Gregory	SOYEZ	Examiner
M.	Jiří	CHÝLA	Examiner
M.	Josef	ŽÁČEK	Examiner
M.	Jaromír	KUKAL	Examiner



Thèse préparée au
Commissariat à l'énergie atomique
CEA de Saclay
DSM/Irfu/SPP, bât. 141
91 191 Gif-sur-Yvette CEDEX

MEASUREMENT OF THE STANDARD MODEL W^+W^- PRODUCTION CROSS-SECTION USING THE ATLAS EXPERIMENT ON THE LHC

DOCTORAL THESIS

CANDIDATE: Ing. Martin ZEMAN

STUDY PROGRAMME: Application of natural sciences, Nuclear engineering
Particles, nuclei and cosmos

INSTITUTES: Czech Technical University in Prague
Faculty of Nuclear Science and Physical Engineering
Université Paris-Sud
Particles, nuclei and cosmos (École Doctorale 517)
Institute of Physics at the Academy of Sciences of the Czech Republic
Commissariat à l'énergie atomique, Saclay (CEA)
Organisation européenne pour la recherche nucléaire (CERN)

SUPERVISORS: prom. fyz. Václav VRBA, CSc.
prof. Christophe ROYON

THESIS EXTENT:

Number of pages: 344
Number of figures: 154
Number of tables: 97
Number of equations: 235

Abstract

Measurements of di-boson production cross-sections are an important part of the physics programme at the CERN Large Hadron Collider. These physics analyses provide the opportunity to probe the electroweak sector of the Standard Model at the TeV scale and could also indicate the existence of new particles or probe beyond the Standard Model physics. The excellent performance of the LHC through years 2011 and 2012 allowed for very competitive measurements. This thesis provides a comprehensive overview of the experimental considerations and methods used in the measurement of the W^+W^- production cross-section in proton-proton collisions at $\sqrt{s} = 7$ TeV and 8 TeV.

The treatise covers the material in great detail, starting with the introduction of the theoretical framework of the Standard Model and follows with an extensive discussion of the methods implemented in recording and reconstructing physics events in an experiment of this magnitude. The associated online and offline software tools are included in the discussion. The relevant experiments are covered, including a very detailed section about the ATLAS detector.

The final chapter of this thesis contains a detailed description of the analysis of the W-pair production in the leptonic decay channels using the datasets recorded by the ATLAS experiment during 2011 and 2012 (Run I). The analyses use 4.60 fb^{-1} recorded at $\sqrt{s} = 7$ TeV and 20.28 fb^{-1} recorded at 8 TeV. The experimentally measured cross section for the production of W bosons at the ATLAS experiment is consistently enhanced compared to the predictions of the Standard Model at centre-of-mass energies of 7 TeV and 8 TeV. The thesis concludes with the presentation of differential cross-section measurement results.

Acknowledgments

I would like to thank to my supervisors Václav Vrba for providing me with the opportunity to participate in the ATLAS experiment at CERN and Christophe Royon who introduced me to the possibility of applying for a joint PhD between Université Paris-Sud XI in France and the Czech Technical University in Prague. My sincere thanks also belong to Jiří Popule for his organisational support, as without his help I might have drowned in paperwork.

I would also like to give thanks to all my colleagues from the Academy of Sciences of the Czech Republic, namely Oldřich Kepka who came up with the idea of working in collaboration on the WW cross-section measurement and Jiří Hejbal for his work on the project. Many thanks also belong to my colleagues from CERN and CEA Saclay, especially Yusheng Wu, Dimitra Tsionou, Phillip Sommer, Jun Gao and Karen Chen who worked very hard on the analysis for over two years to get the results out even after many setbacks that required a change of strategy and complete reimplementation. I am also especially grateful to my friends Pavel Jež, Jakub Cuth, Petr Kulháněk and Matthias Schott for helping with proofreading of this thesis.

Also a thank you:

- ▶ to my long-term friends Pavel, Tomáš, Martin, Marek, Lída, Jan, Adéla, Šárka, Hana, Michal and Saša for being my friends even at times when I myself was not very friendly,
- ▶ to one of my oldest friends, Eduard, who taught me what losing everything really means,
- ▶ to my fiends from CERN: Michal, Jakub, Jan, Tomáš, Ondřej, Vojtěch and Mito with his family for always welcoming me with open arms even though that wherever I go, rain soon follows,
- ▶ to all my friends from “between the worlds” for the shared love of science-fiction, fantasy and cyberpunk, be it Dune, Star Wars, A Song of Ice and Fire, Planescape or Sprawl,
- ▶ to my would be femme fatale Lucie for teaching me a crucial lesson about love and trust,
- ▶ and finally to my family, who managed not to disown me through this difficult period. Instead, they have always supported me without asking anything in return.

In conclusion, I probably cannot name all the wonderful people I have had the pleasure to meet over the years at CERN. I wish you all a rich and full life of success and happiness, wherever you are. Live long and prosper.

Statement of originality

To the best of my knowledge and belief all of the material presented in this thesis is of my own original work with the use of referenced sources.

Prague, July 20, 2014

Martin ZEMAN



Titre de la thèse :

Mesure de la section efficace de production du Modèle standard des W^+W^- bosons à l'expérience ATLAS

CANDIDAT: Ing. Martin ZEMAN

SPECIALITÉ: Application des sciences naturelles – génie nucléaire
Particles, nuclei and cosmos

INSTITUTS: Université technique de Prague
Faculté des sciences physiques et de l'atome
Université Paris-Sud
Particles, nuclei and cosmos (École Doctorale 517)
Institute of Physics at the Academy of Sciences of the Czech Republic
Commissariat à l'énergie atomique, Saclay (CEA)
Organisation européenne pour la recherche nucléaire (CERN)

SUPERVISEURS: prom. fyz. Václav VRBA, CSc.
prof. Christophe ROYON

Déclaration d'originalité

Au meilleur de ma connaissance tout le matériel présenté dans cette thèse est de mon propre travail originaux avec l'utilisation de sources référencées.

Prague, 20 juillet 2014

Martin ZEMAN



Název disertační práce:

Měření účinného průřezu W^+W^- bosonů ve Standardním modelu na experimentu ATLAS

UCHAZEČ: Ing. Martin ZEMAN

STUDIJNÍ OBOR: Aplikace přírodních věd – Jaderné inženýrství
Particles, nuclei and cosmos

INSTITUTE: České vysoké učení technické v Praze
Fakulta jaderná a fyzikálně inženýrská
Université Paris-Sud
Particles, nuclei and cosmos (École Doctorale 517)
Fyzikální ústav Akademie věd ČR, v. v. i. (FZÚ)
Commissariat à l'énergie atomique, Saclay (CEA)
Organisation européenne pour la recherche nucléaire (CERN)

VEDOUCÍ PRÁCE: prom. fyz. Václav VRBA, CSc.
prof. Christophe ROYON

Prohlášení

Prohlašuji, že jsem svou disertační práci vypracoval samostatně a použil jsem pouze podklady (literaturu, projekty, software etc.) uvedené v příloženém seznamu.

V Praze, 20. července 2014

Martin ZEMAN



Front matter	i
Table of Contents	vii
List of Figures	xii
List of Tables	xvi
Introduction	xix
Notation	xx
1 Theoretical framework	1
1.1 Symmetries and conservation laws	2
1.1.1 Lagrangian formalism	3
1.1.2 Noether's theorem for fields	3
1.1.3 Poincaré group	4
1.1.4 Scalar representation	5
1.1.5 Spinor representation	5
1.1.6 Particle classification according to spin-statistics relationship	5
1.1.7 Principle of gauge invariance	7
1.1.8 Note on particle interactions and perturbation theory	9
1.1.9 Experimental considerations	10
1.2 Quark model	11
1.2.1 Experimental evidence	12
1.2.2 Gauge invariance of quantum chromodynamics	13
1.2.3 Strong coupling	15
1.3 Electroweak sector	16
1.3.1 Weak interactions and symmetries	16
1.3.2 Principles of electroweak unification	17
1.3.3 Particle classification according to particle family	19
1.3.4 Vector boson production	19
1.4 Construction of the Standard Model	21
1.4.1 Particle classification according to fundamental interaction	21
1.4.2 Integrity of the Standard Model	22
1.5 Basics of statistical inference	23
1.5.1 Random variable	24
1.5.2 Parameter estimation	25
1.6 References	26

2	Experimental background	29
2.1	Particle accelerators	30
2.1.1	Accelerator geometry	31
2.1.2	Accelerator kinematics	32
2.1.3	Accelerator dynamics	34
2.1.4	Luminosity and interaction rate	40
2.2	Large Hadron Collider	43
2.2.1	Current performance	45
2.2.2	Performance goals	45
2.2.3	Injection chain	47
2.2.4	Lattice layout	48
2.3	Detector systems	51
2.3.1	Large hybrid detector systems	51
2.3.2	Measurement nomenclature	52
2.4	Experiments at the LHC	54
2.4.1	General purpose experiments: ATLAS and CMS	54
2.4.2	CMS (Compact Muon Solenoid)	54
2.4.3	ALICE (A Large Ion Collider Experiment)	55
2.4.4	LHCb (Large Hadron Collider beauty)	57
2.4.5	TOTEM (TOTAl Elastic and diffractive cross section Measurement)	57
2.4.6	LHCf (Large Hadron Collider forward)	59
2.4.7	MoEDAL (Monopole and Exotics Detector at the LHC)	59
2.5	The ATLAS Experiment	59
2.5.1	General layout	60
2.5.2	ATLAS coordinate system	60
2.5.3	Magnet system	61
2.5.4	Inner Detector	63
2.5.5	Calorimetry	70
2.5.6	Muon spectrometer	77
2.5.7	Forward detectors	80
2.6	Experimental conditions	80
2.6.1	Calibration and alignment	80
2.6.2	Delivered luminosity	82
2.6.3	Pile-up	85
2.7	References	87
3	Computational and reconstruction tools	92
3.1	Trigger and data acquisition	93
3.1.1	Level 1 Trigger flow	95
3.1.2	High-level trigger and data acquisition system	97
3.1.3	Streaming	97
3.1.4	Trigger menu	98
3.1.5	Monitoring	100

3.1.6	Operational performance	101
3.2	Data representation and distribution	101
3.2.1	Data quality	102
3.2.2	Analysis paths	103
3.2.3	Event data model	104
3.2.4	Operational model	105
3.2.5	Analysis software	107
3.2.6	Analysis work-flow	108
3.3	Physics objects reconstruction	108
3.3.1	Tracking	109
3.3.2	Vertexing	113
3.3.3	Muon reconstruction	115
3.3.4	Electron reconstruction	123
3.3.5	Jet reconstruction	129
3.3.6	Missing transverse energy reconstruction	136
3.4	Implementation	138
3.4.1	Development goals	139
3.4.2	Implementation of analysis objects	142
3.5	References	146
4	Measurement of the Standard Model WW cross-section	155
4.1	Analysis overview	158
4.1.1	Cross-section extraction	159
4.1.2	Efficiencies and weights	161
4.2	Event selection	162
4.2.1	Differences between the 7 TeV and 8 TeV analysis	167
4.2.2	Final selection	167
4.2.3	Event selection cut-flow	170
4.3	Signal and background modelling	172
4.3.1	Signal samples	172
4.3.2	Background samples	174
4.3.3	Pileup re-weighting	176
4.3.4	PDF re-weighting	180
4.4	Trigger decision	180
4.4.1	Trigger matching	183
4.4.2	Trigger efficiency	185
4.5	Object definitions	186
4.5.1	Muon definition	186
4.5.2	Electron definition	193
4.5.3	Jet definition	198
4.5.4	Missing transverse energy definition	199
4.5.5	Stream overlap removal	202
4.5.6	Object overlap removal	202

4.6	Datasets	203
4.6.1	Derived datasets	203
4.6.2	Data cleaning	204
4.7	Acceptance	205
4.7.1	Cut optimization	206
4.7.2	Selection acceptance	212
4.7.3	Jet veto uncertainties	212
4.7.4	Fiducial region	215
4.8	Systematic uncertainties	216
4.8.1	Lepton systematics	217
4.8.2	Jet systematics	222
4.8.3	Missing transverse energy systematics	224
4.8.4	Missing transverse momentum systematics	224
4.9	Background estimates	226
4.9.1	Simultaneous fit method	226
4.9.2	Z+jets background: Transfer factor method	228
4.9.3	Top background: Jet veto survival probability	229
4.9.4	Top background: Transfer factor method	232
4.9.5	W+jets and multijet background: Matrix method	234
4.9.6	Other diboson production	237
4.10	Cross-section results	238
4.10.1	Candidates and backgrounds	238
4.10.2	Cross-section extraction	244
4.10.3	Cross-section uncertainties	245
4.11	Unfolding	246
4.11.1	Efficiency and background	250
4.11.2	Unfolding methodology	250
4.11.3	Implementation	252
4.11.4	Unfolded distributions	254
4.12	References	257
5	Discussion and conclusions	267
	Appendices	273
A	Monte Carlo samples	273
A.1	Analysis at 7 TeV	273
A.2	Analysis at 8 TeV	277
B	Systematics cut-flow progression	281
	Glossary	293
	Acronyms	310

Symbols	313
Bibliography	314
Index	340

LIST OF FIGURES

1.1	Discovery of J/ψ and Z, W bosons	11
1.2	Quark combinations	12
2.1	Geometric arrangement of particle accelerators	31
2.2	Schematic drawing of a symmetric focusing-defocusing (FODO) cell	36
2.3	Betatron oscillations	36
2.4	Betatron oscillation amplitude and phase	37
2.5	Beam size	38
2.6	Emittance of a particle ensemble	39
2.7	Schematic illustration of the hourglass effect	39
2.8	Relative beam sizes around IP1 (ATLAS) in collision	40
2.9	Crossing angle at the interaction point	42
2.10	Delivered luminosity in ATLAS versus time for 2010, 2011, 2012	44
2.11	Peak luminosity versus time	44
2.12	Number of colliding bunches versus time	44
2.13	LHC injection chain	46
2.14	Schematic drawing of the LHC layout	46
2.15	Bunch filling scheme of the LHC	48
2.16	Triple bunch splitting in the PS	49
2.17	Schematic of the cross over between inner and outer beam pipe in the LHC	49
2.18	Cross section of LHC cryodipole and a simulation of the magnetic flux	50
2.19	Schematic of impact parameters	54
2.20	ATLAS experiment schematics	56
2.21	CMS experiment schematic	56
2.22	ALICE experiment schematic	58
2.23	LHCb experiment schematic	58
2.24	ATLAS coordinate system	61
2.25	ATLAS magnet system	62
2.26	Pixel Detector	64
2.27	Schematic drawing of the structural elements of the ATLAS Inner Detector (barrel)	65
2.28	Schematic drawing of the structural elements of the ATLAS Inner Detector (end-cap)	65
2.29	Quarter-section of the ATLAS inner detector	66
2.30	Schematic drawing of the ATLAS pixel detector	67
2.31	ATLAS pixel module	69
2.32	Schematic principle of silicon detectors	69
2.33	Schematic drawing of the ATLAS SCT modules	70
2.34	ATLAS calorimeter system	71
2.35	ATLAS calorimeter barrel module	73

2.36	Cumulative amount of material in the ATLAS calorimeter system	73
2.37	Schematic drawing of the ATLAS HCAL modules	74
2.38	Schematic drawing of the calorimeter end-cap cryostat	76
2.39	Schematic drawing of the transition region between the barrel and end-cap cryostats	76
2.40	Schematic drawing of the ATLAS Muon Spectrometer	78
2.41	Schematic drawing of the ATLAS Muon Spectrometer	79
2.42	Placement of ATLAS forward detectors along the beam-line	81
2.43	Detector misalignment	81
2.44	Horizontal beam profile	83
2.45	The maximum mean number of events per beam crossing versus day	86
2.46	High pileup event display	86
2.47	Mean number of interactions per bunch crossing for the 2011 and 2012 data	87
2.48	The maximum mean number of interactions per bunch crossing versus day	87
3.1	ATLAS TDAQ system	94
3.2	ATLAS L1 Trigger block diagram	95
3.3	Schema of the L1 muon trigger	96
3.4	Schema of the L1 electron, photon and tau lepton trigger	96
3.5	Trigger efficiencies with variable thresholds and hadronic leakage veto	99
3.6	Trigger monitoring flowchart	100
3.7	Event Filter stream recording rates	102
3.8	WLCG Tier-1 and Tier-2 sites	106
3.9	ATLAS Run-I Analysis Model	108
3.10	ATLAS event cross section	109
3.11	High pileup event display	110
3.12	High pileup event display	111
3.13	Track ambiguity solving process	112
3.14	Tracking efficiency	113
3.15	Vertex reconstruction efficiency at 7 TeV	115
3.16	Efficiency to reconstruct and then select the PV at 8 TeV	115
3.17	Vertexing resolution in 7 TeV	116
3.18	Vertexing resolution in 7 TeV	116
3.19	Muon reconstruction types in ATLAS	118
3.20	Di-muon invariant mass for isolated combined muons with $p_T > 25$ GeV	120
3.21	MC resolution corrections for ID and MS for the STACO (Chain 1) reconstruction.	120
3.22	MC scale corrections for ID and MS for the STACO (Chain 1) reconstruction.	120
3.23	Muon track and calorimeter isolation	122
3.24	Muon calorimeter isolation correction	122
3.25	Electron energy scale correction factor	125
3.26	Electron energy smearing correction factor	125
3.27	Illustration of isolation computation	128
3.28	Evolution of corrected calorimeter isolation	128
3.29	Implementation of the isolation correction	128

3.30	Reconstruction using the anti- k_T algorithm	130
3.31	Overview of the ATLAS jet reconstruction	131
3.32	Overview of the ATLAS jet calibration scheme	131
3.33	Comparison of jet response between 2011 and 2012	133
3.34	Average energy of jets as a function of pseudorapidity	134
3.35	Comparison of jet energy scale as a function of pseudorapidity in 2011 and 2012	134
3.36	SFrame flow chart	140
3.37	ElectroweakBosons framework	140
3.38	The AnalysisBase hierarchy	143
3.39	Class inheritance graph for implemented physics objects	145
3.40	Implementation of the Store class	146
4.1	Standard Model tree-level leading-order Feynman diagrams for diboson production	157
4.2	Standard Model Feynman diagrams for WW production through the $q\bar{q}$ initial state	158
4.3	Standard Model Feynman diagrams for WW through gluon-gluon fusion	158
4.4	Standard Model proton-(anti)proton cross sections as a function of collider energy	160
4.5	Kinematic distributions of the selected events at 8 TeV after preselection stages (1)	164
4.6	Kinematic distributions of the selected events at 8 TeV after preselection stages (2)	165
4.7	Kinematic distributions of the selected events at 8 TeV after preselection stages (3)	166
4.12	Azimuthal angle between missing transverse energy and momentum	169
4.13	Jet multiplicity distribution before the jet veto	170
4.14	Invariant mass distribution at 8 TeV after various stages of the cut flow	171
4.15	Standard Model Feynman diagrams for Z + jets and $t\bar{t}$ backgrounds	176
4.16	Distribution of the average number of reconstructed vertices as function of the average number of interactions per bunch crossing	178
4.17	Pile-up re-weighting procedure schematically	178
4.18	Effect of PDF re-weighting on Z + jets samples on $ \eta $ distributions (before)	179
4.19	Effect of PDF re-weighting on Z + jets samples on $ \eta $ distributions (after)	179
4.20	Kinematic distributions of the selected events at 8 TeV at final cut stage (1)	181
4.21	Kinematic distributions of the selected events at 8 TeV at final cut stage (2)	182
4.22	Comparison of L2StarB di-electron trigger performance	184
4.23	Trigger efficiencies at 7 TeV	188
4.24	Single-lepton and di-lepton trigger comparison in e^+e^- channel	189
4.25	Single-lepton and di-lepton trigger comparison in $\mu^+\mu^-$ channel	189
4.26	Single-lepton and di-lepton trigger comparison in $e^\pm\mu^\mp$ channel	189
4.27	Reconstruction efficiency for STACO combined only muons at 7 TeV	192
4.28	Muon reconstruction efficiency for STACO combined muons at 8 TeV	192
4.29	Muon isolation efficiency for STACO muons at 7 TeV	193
4.30	Muon isolation efficiency for STACO muons at 8 TeV	193
4.31	Electron reconstruction efficiency for 2011 and 2012 dataset	196
4.32	Electron identification efficiency for 2011 and 2012 dataset	197
4.33	Comparison of electron likelihood identification efficiency	197
4.36	Comparison of relative missing transverse energy	200

4.37	Distribution of the azimuthal angle between missing energy and missing momentum	202
4.38	Vertexing resolution in 7 TeV	206
4.39	Comparison of $\vec{E}_T(\text{RefFinal})$ in the same flavour channels	210
4.40	Comparison of $\vec{E}_{T,\text{Rel}}(\text{RefFinal})$ in the same flavour channels	210
4.41	Comparison of \vec{p}_T in the same flavour channels.	211
4.42	Comparison of $p_T(\ell\ell)$ in the same flavour channels.	211
4.43	The 2D significance plots in same flavour channel for optimization grid scan on cut variable pairs.	213
4.44	The 2D significance plots in the combined flavour channel for optimization grid scan on cut variable pairs.	213
4.45	Effect of muon smearing and scale systematic uncertainties	221
4.46	Effect of electron smearing and scale systematic uncertainties	221
4.47	Effect of jet smearing and scale systematic uncertainty on jet p_T multiplicity	223
4.48	Effect of jet smearing and scale systematic uncertainty on missing transverse energy	224
4.49	Pileup systematic uncertainty as a function of leading p_T distribution	225
4.50	Missing transverse energy systematic uncertainties on scale and resolution	225
4.53	Final kinematic distributions of the WW candidates at 8 TeV at final cut stage (1)	242
4.54	Final kinematic distributions of the WW candidates at 8 TeV at final cut stage (2)	243
4.55	Schematic of the unfolding method	253
4.56	Unfolding ingredients at 7 TeV	255
4.57	Unfolding results at 7 TeV	255
4.58	Unfolding ingredients at 8 TeV	256
4.59	Unfolding results at 8 TeV	256
4.60	Unfolding closure test	257
4.61	Resolution of the leading lepton p_T at 8 TeV	257
5.1	Comparison between the theoretical WW cross sections and the measurement	270
5.2	Unfolded distributions of leading lepton p_T	271
B.1	Pseudorapidity	304

LIST OF TABLES

1.1	The quark family	13
1.2	Lepton and quark doublets	18
1.3	The lepton family	19
1.4	The boson mediators	20
1.5	Branching ratios of W^+ decay modes	20
1.6	Fundamental interactions	21
1.7	Elementary particles in the Standard Model	22
2.1	Centre of mass energy for different types of collisions	34
2.2	Accelerators active after the year 2000	35
2.3	LHC Parameters in 2011 and 2012 compared to nominal	47
2.4	Parameters of the CERN injection chain	48
2.5	ATLAS Inner Detector parameters	66
2.6	ATLAS calorimeter system parameters	75
2.7	ATLAS Muon Spectrometer parameters	78
2.8	Summary of van der Meer scans performed at ATLAS interaction point	83
2.9	Characteristics of detectors used for luminosity measurement	84
2.10	Systematic uncertainties on luminosity scale	85
3.1	ATLAS data quality status flags	103
3.2	Data formats and sizes	105
3.3	Sorting of muon quality levels in the STACO collection	121
4.1	Object overlap removal considered in each analysis	163
4.3	Summary of observed data events and expected signal and background contributions at 8 TeV	172
4.4	Theoretical uncertainties on the signal cross-section	173
4.5	Summary of possible contributions to the WW final state at 8 TeV	174
4.6	WW signal production processes for signal modelling in the 7 TeV analysis	175
4.7	WW signal production processes for signal modelling in the 8 TeV analysis	175
4.8	Trigger chains used in 7 TeV analysis	183
4.9	Trigger chains used in 8 TeV analysis	183
4.10	Muon tag and probe definition for 7 TeV trigger efficiency measurement	186
4.11	Electron tag and probe definition for 7 TeV trigger efficiency measurement	187
4.12	Muon definition used in 7 TeV analysis	190
4.13	Muon definition used in 8 TeV analysis	190
4.14	Electron definition used in 7 TeV analysis	195
4.15	Electron definition used in 8 TeV analysis	195
4.16	Electron isolation scale factors	198

4.17	Summary of correction applied to nominal objects	201
4.18	Analysis dataset versions	204
4.21	Cut optimization and signal significance in e^+e^- channel	209
4.22	Cut optimization and signal significance in $\mu^+\mu^-$ channel	209
4.23	Cut optimization and signal significance in $e^\pm\mu^\mp$ channel	209
4.24	Jet veto scale factor and predicted acceptance	214
4.25	The uncertainties in jet veto contributions	215
4.27	Uncertainty sources and associated relative uncertainties for WW signal acceptance	218
4.28	Cut progression of systematic uncertainties on the signal samples	219
4.29	Cut progression of jet energy scale components systematics on the signal samples	220
4.31	Jet energy scale uncertainty components for signal samples	223
4.34	Z + jets background yields in the signal region	229
4.35	Systematic sources of the transfer factor method for Z + jets background	230
4.36	Statistical and total systematic uncertainties of the transfer factor for Z + jets back- ground estimation	230
4.37	Summary of observed events in top JVSP estimation method	231
4.38	Results of jet veto efficiencies used in top JVSP estimation method	232
4.40	Top background yields in the signal region	234
4.41	Systematic sources of the transfer factor method for top background	235
4.42	Statistical and total systematic uncertainties of the transfer factor for top background estimation	235
4.43	Other diboson background estimates	237
4.44	Cut progression of systematic uncertainties on “other diboson” background pro- cesses for combined channel	239
4.45	Cut progression of jet energy scale components systematics on “other diboson” background processes for combined channel	240
4.46	Systematic uncertainties for the combined “other diboson” background processes	241
4.47	Summary of observed events and expected signal and background contributions .	243
4.48	Measured fiducial WW cross sections	245
4.49	Measured total WW cross sections	245
4.50	Relative systematic uncertainties on the fiducial WW production cross-section for each channel	247
4.51	Relative systematic uncertainties on the total WW production cross-section for each channel	248
4.52	Unfolding summary at 7 TeV	258
4.53	Unfolding summary at 8 TeV	259
A.1	WW signal production processes for signal modelling for the 7 TeV analysis . . .	273
A.2	Samples used to model Z + jets backgrounds for the 7 TeV analysis	274
A.3	Samples used to model top backgrounds for the 7 TeV analysis	275
A.4	Samples used to model W + jets backgrounds for the 7 TeV analysis	275
A.5	Samples used to model heavy-flavour W + jets and Z + jets backgrounds for the 7 TeV analysis	276

A.6	Samples used to model the di-boson backgrounds WZ , ZZ , $W\gamma$, $W\gamma^*$ for the 7 TeV analysis	276
A.7	WW signal production processes for signal modelling in the 8 TeV analysis	277
A.8	Processes used to model top backgrounds for the 8 TeV analysis	277
A.9	Samples used to model Z + jets backgrounds for the 8 TeV analysis	278
A.10	Samples used to model W + jets backgrounds for the 8 TeV analysis	279
A.11	Samples used to model heavy-flavour W + jets backgrounds for the 7 TeV analysis	279
A.12	Processes used to model the di-boson backgrounds WZ , ZZ , $W\gamma$, $W\gamma^*$ for the 8 TeV analysis	280
B.1	Systematic uncertainties including stat. errors	282
B.2	Jet energy scale components systematics including stat. errors	283
B.3	Cut progression of systematic uncertainties on the signal samples for e^+e^- channel	284
B.4	Cut progression of jet energy scale components systematics on the signal samples for e^+e^- channel	285
B.5	Cut progression of systematic uncertainties on the signal samples for $\mu^+\mu^-$ channel	286
B.6	Cut progression of jet energy scale components systematics on the signal samples for $\mu^+\mu^-$ channel	287
B.7	Cut progression of systematic uncertainties on the signal samples for $e^\pm\mu^\mp$ channel	288
B.8	Cut progression of jet energy scale components systematics on the signal samples for $e^\pm\mu^\mp$ channel	289
B.9	Cut progression of systematic uncertainties on the signal samples for $\ell^+\ell^-$ channel	290
B.10	Cut progression of jet energy scale components systematics on the signal samples for $\ell^+\ell^-$ channel	291

“Do not trust elementary particles, they make everything up.”

PARTICLE PHYSICS is an academic field at the very frontier of science. It is particularly interesting to theorists and experimentalists alike, as it is directly linked to cosmology and pushes for advances in electrical engineering, accelerator and detector design and computing. Being one of the fortunate few who have the privilege to work on such “cutting edge” experiments, the main purpose of my thesis is to provide a comprehensive overview of the methods and strategies employed in physics analyses and to report the results of WW cross-section measurement I have been working on for over two years. That is why a substantial portion of the text is oriented on information collection and references. The structure of the text adopts the following outline:

Chapter 1: Theoretical framework aims to present the basic principles of the Standard Model, its mathematical formulation and testable predictions. The first section discusses the historical development that led to the development of the Standard Model and continues with its formal definition. Finally, we also introduce important concepts from statistics that are used in the analysis presented here.

Chapter 2: Experimental background describes the physical and engineering principles behind particle accelerators and detectors. The main focus is given to the Large Hadron Collider at CERN and the ATLAS experiment with all its subsystems, since these are referred to in the following chapters.

Chapter 3: Computational and reconstruction tools summarizes the ATLAS online and offline software and my personal contributions to its development.

Chapter 4: Measurement of the Standard Model WW cross-section presents my own work on the W pair production cross-section measurement using the ATLAS detector. The chapter fully describes the definition of physics objects, event selection and background estimation methods and concludes with providing the cross-section extraction and differential cross-section distributions.

Chapter 5: Discussion and conclusions summarises the whole thesis and discusses results from the previous chapter.

As this work is a natural extension of my master thesis [Zem10], some content has been based on it, although completely rewritten, corrected and updated.

Natural units

The two fundamental constants of special relativity and quantum mechanics are the speed of light in vacuum c and the reduced Planck constant \hbar , sometimes referred to as the Dirac constant:

$$\hbar \equiv \frac{h}{2\pi} = 1.054\,571\,726(47) \times 10^{-34} \text{ J s}$$

$$c = 299\,792\,458 \text{ m s}^{-1}$$

High-energy physics uses the system of *natural units* defined such that $c = \hbar = 1$. The main advantage of this approach is that many equations take a more “simple” form. The natural unit of charge is defined using the elementary charge $e \equiv 1.602\,176\,565(35) \times 10^{-19} \text{ C}$ and energy is given in *electronvolts* (eV), which correspond to the energy of a particle with charge e accelerated by an electric field of 1 V (the rest mass of proton corresponds roughly to 1 GeV).

Consequently, the values of mass (m), momentum (mc) and energy (mc^2) are now represented in terms of GeV while length (\hbar/mc) and time (\hbar/mc^2) in GeV^{-1} . The following conversion factors are useful when relating experimental observables [Par13]:

$$(\hbar c) = 197.33 \text{ GeV am}$$

$$(\hbar c)^2 = 0.39 \text{ GeV}^2 \text{ mb}$$

Mathematical symbols

The following mathematical symbols are used throughout the text:

- ▶ Δx denotes a finite forward difference: $\Delta x \equiv f(x + h) - f(x)$,
- ▶ ∂x denotes the partial derivative while dx denotes the total differential,
- ▶ δx denotes variation used in variational calculus,
- ▶ ϵ_{ijk} denotes the totally antisymmetric Levi-Civita tensor:

$$\epsilon_{123} = \epsilon_{231} = \epsilon_{312} = +1$$

$$\epsilon_{213} = \epsilon_{132} = \epsilon_{321} = -1$$

- ▶ The Poisson brackets are defined for two functions of phase-space variables $a(q_k, p_k), b(q_k, p_k)$:

$$\{a, b\} = \frac{\partial a}{\partial q_k} \cdot \frac{\partial b}{\partial p_k} - \frac{\partial a}{\partial p_k} \cdot \frac{\partial b}{\partial q_k}$$

- ▶ Commutator ($-$) and anti-commutator ($+$) of two elements a and b of an associative algebra are defined as:

$$[a, b]_- = ab - ba \quad [a, b]_+ = ab + ba$$

Vector notation and Minkowski metric

Vectors are written as boldface such as in the case of Cartesian three vectors $\mathbf{x} = (x_1, x_2, x_3) = (x, y, z)$ or general N element vectors: $\boldsymbol{\theta} = (\theta_1, \theta_2, \dots, \theta_N)$ with Latin indices running $1, 2, \dots, n$.

In relativistic physics, coordinates of time and space are treated equally. The relativistic four-vectors are denoted with an *italic* type with Greek letter indices running over 0, 1, 2, 3. The space-time point (or an *event*) and the four-gradient are denoted as:

$$x^\mu \equiv (x^0, x^1, x^2, x^3)^T = (t, x, y, z)^T = (t, \mathbf{x})^T \quad \text{in Minkowski space, and}$$

$$\partial_\mu \equiv \frac{\partial}{\partial x^\mu} = \left(\frac{\partial}{\partial x^0}, \frac{\partial}{\partial x^1}, \frac{\partial}{\partial x^2}, \frac{\partial}{\partial x^3} \right) = \left(\frac{\partial}{\partial t}, \frac{\partial}{\partial x}, \frac{\partial}{\partial y}, \frac{\partial}{\partial z} \right) = \left(\frac{\partial}{\partial t}, \nabla \right)$$

where x^μ is naturally raised and ∂_μ is naturally lowered. The metric tensor is defined as:

$$g^{\mu\nu} \equiv g_{\mu\nu} \equiv \text{diag}(1, -1, -1, -1),$$

and thus the covariant vectors are:

$$x_\mu = g_{\mu\nu} x^\nu = (t, -x, -y, -z) \quad \text{and} \quad \partial^\mu \equiv \frac{\partial}{\partial x_\mu} = \left(\frac{\partial}{\partial t}, -\frac{\partial}{\partial x}, -\frac{\partial}{\partial y}, -\frac{\partial}{\partial z} \right)$$

Other four-vectors are defined as:

$$\begin{aligned} p^\mu &\equiv (E, p_x, p_y, p_z)^T = (E, \mathbf{p})^T && \text{as the four-momentum} \\ k^\mu &\equiv (\omega, k_x, k_y, k_z)^T = (\omega, \mathbf{k})^T && \text{as the wave four-vector} \\ A^\mu &\equiv (\phi, A_x, A_y, A_z)^T = (\phi, \mathbf{A})^T && \text{as the field four-vector} \end{aligned}$$

By Einstein's summation convention repeated indices are summed over (notation of a sum is ignored):

$$\mathbf{a} \cdot \mathbf{b} = a_1 b_1 + a_2 b_2 + \dots + a_N b_N = \sum_{k=1}^N a_k b_k = a_k b_k$$

With the notation introduced above, the familiar physics concepts obtain the following form:

$$\begin{aligned} \text{Invariant interval:} \quad ds^2 &\equiv dx_\mu dx^\mu = dt^2 - d\mathbf{x}^2 = dt^2 - dx^2 - dy^2 - dz^2 \\ \text{Classical electromagnetism:} \quad \mathbf{j} \cdot \mathbf{A} &\equiv j_\mu A^\mu = \rho\phi - \mathbf{j} \cdot \mathbf{A} \\ \text{Continuity equation:} \quad \partial_\mu j^\mu &= 0 \quad \Leftrightarrow \quad \frac{\partial \rho}{\partial t} + \nabla \cdot \mathbf{j} = 0 \\ \text{D'Alembert operator:} \quad \partial_\mu \partial^\mu f &= \square f = \frac{\partial^2 f}{\partial t^2} - \triangle f \end{aligned}$$

Using both the three-vectors and four-vectors in a single equation will be clearly distinguished:

$$\begin{aligned} E^2 - \mathbf{p} \cdot \mathbf{p} &= E^2 - p_1 p_1 - p_2 p_2 - p_3 p_3 = E^2 - \sum_{k=1}^3 p_k p_k = \\ &= E^2 - p_k p_k = p_0 p_0 - p_k p_k = p_\mu p^\mu = p^\mu p_\mu = |p|^2 \end{aligned}$$

Quantum mechanics

When talking about quantum mechanics, we adopt the *Dirac bra-ket notation*. The system is represented by a complex Hilbert space \mathcal{H} . Each dynamic variable is assigned a linear self-adjoint operator on \mathcal{H} : $A \mapsto \hat{A}$. Operators on a space \mathcal{V} are denoted using boldface with hat: $\hat{\mathbf{A}} : \mathcal{V} \mapsto \mathcal{V}$.

Square integrable functions $\alpha : \mathbb{C}^n \rightarrow \mathbb{C}^n$ on Hilbert space $\alpha \in \mathcal{H}$ are called *ket vectors*. Functionals $\beta : \mathbb{C}^n \rightarrow \mathbb{C}^n$ on dual space $\beta \in \mathcal{H}^\dagger \{ \langle \phi_1 |, \dots, \langle \phi | \}$ are called *bra vectors*. The inner product of $|\psi\rangle \in \alpha$ and $\langle \phi | \in \beta$ is called the *braket*: $\langle \phi | \psi \rangle$. The exact form of state vectors and operators is a matter of choice and depends on physicist's preference:

$$\begin{array}{lll} \text{in } \mathbb{C}^n : & |\mathbf{a}\rangle = (a_1, a_2, \dots, a_n) & |\mathbf{b}\rangle = (b_1, b_2, \dots, b_n) \\ \text{in } l^2 : & |\mathbf{a}\rangle = \{a_k\}_{k=1}^\infty & |\mathbf{b}\rangle = \{b_k\}_{k=1}^\infty \\ \text{in } L^2 : & |\mathbf{a}\rangle = a_x = a(x) & |\mathbf{b}\rangle = b_x = b(x) \end{array}$$

with the scalar products given

$$\begin{array}{ll} \text{in } \mathbb{C}^n : & \langle \mathbf{a} | \mathbf{b} \rangle = a_1^* b_1 + a_2^* b_2 + \dots + a_n^* b_n = a_n^* b_n \\ \text{in } l^2 : & \langle \mathbf{a} | \mathbf{b} \rangle = a_1^* b_1 + a_2^* b_2 + \dots + a_n^* b_n + \dots = \sum_{k=1}^\infty a_k^* b_k = a_n^* b_n \\ \text{in } L^2 : & \langle \mathbf{a} | \mathbf{b} \rangle = \int_{-\infty}^\infty a(x)^* b(x) dx \end{array}$$

One such choice of representation on $L^2(\mathbb{R}^3)$ uses superposition of complex wave functions that are exponentially proportional to the particle energy E and momentum \mathbf{p} :

$$\psi(t, \mathbf{x}) = A(E, \mathbf{p}) e^{i(Et - \mathbf{p} \cdot \mathbf{x})} = A(\omega, \mathbf{k}) e^{i(\omega t - \mathbf{k} \cdot \mathbf{x})} \quad (1)$$

where A is the amplitude. This representation is called Schrödinger's wave mechanics and describes the system by differential equations. Another choice for non-commutative objects can be infinite sequences on l^2 space using infinite matrices as operators (i.e. Heisenberg's matrix mechanics).

Mandelstam variables

It is useful to describe particle interactions using physical invariants. In the simplest case of two particle interaction, the Lorentz-invariant *Mandelstam variables* are defined as

$$\begin{aligned} s &= (p_A^\mu + p_B^\mu)^2 = (p_C^\mu + p_D^\mu)^2 \\ t &= (p_A^\mu - p_C^\mu)^2 = (p_B^\mu - p_D^\mu)^2 \\ u &= (p_A^\mu - p_D^\mu)^2 = (p_B^\mu - p_C^\mu)^2 \\ s + t + u &= m_1^2 + m_2^2 + m_3^2 + m_4^2 \end{aligned}$$

where p^μ is the four-momentum and m is the invariant mass. Indices 1 and 2 represent the incoming particles and indices 3 and 4 represent the outgoing particles. We should also note, that \sqrt{s} corresponds to the energy in the centre-of-mass frame.

Main matter

THEORETICAL FRAMEWORK

Contents

1.1	Symmetries and conservation laws	2
1.1.1	Lagrangian formalism	3
1.1.2	Noether's theorem for fields	3
1.1.3	Poincaré group	4
1.1.4	Scalar representation	5
1.1.5	Spinor representation	5
1.1.6	Particle classification according to spin-statistics relationship	5
1.1.7	Principle of gauge invariance	7
1.1.8	Note on particle interactions and perturbation theory	9
1.1.9	Experimental considerations	10
1.2	Quark model	11
1.2.1	Experimental evidence	12
1.2.2	Gauge invariance of quantum chromodynamics	13
1.2.3	Strong coupling	15
1.3	Electroweak sector	16
1.3.1	Weak interactions and symmetries	16
1.3.2	Principles of electroweak unification	17
1.3.3	Particle classification according to particle family	19
1.3.4	Vector boson production	19
1.4	Construction of the Standard Model	21
1.4.1	Particle classification according to fundamental interaction	21
1.4.2	Integrity of the Standard Model	22
1.5	Basics of statistical inference	23
1.5.1	Random variable	24
1.5.2	Parameter estimation	25
1.6	References	26

THE STANDARD MODEL of particle physics is an effective theory for subatomic scales that includes three of the four known fundamental interactions: electromagnetic, weak and strong. It postulates that all matter in the Universe can be built from 12 fundamental fermions and 12 anti-fermions respectively, interactions amongst which are mediated by 4 *gauge bosons*. All [Standard Model](#) particles appear as point-like down to the very limit of our experiments: 1×10^{-18} m. The [Standard Model](#) is built as a quantum field theory with an internal symmetry group $SU(3)_C \otimes SU(2)_L \otimes U(1)_Y$.

The predictive power of quantum field theories has been demonstrated in many experiments. In 2008 the Harvard group measured the magnitude of electron magnetic dipole moment. The difference between the measured value and theoretical value from [QED](#) was less than 0.28 parts per trillion (10^{-12}) [[HFG08](#)]. The electroweak theory has been verified down to a few parts in a thousand and perturbative [QCD](#) to the order of a few percent. Altogether the precision of [Standard Model](#) predictions is extraordinary, making it one of the most successful theories mankind has come up with so far.

The existence of *weak boson W* and *weak boson Z* was predicted using the electroweak theory developed by [Sheldon L. Glashow](#) [[Gla61](#)], [Steven Weinberg](#) [[Wei67](#)] and [Abdus Salam](#) [[Sal68](#)] and experimentally verified at [CERN](#) in 1981 on the UA1 and UA2 experiments at the *Super Proton Synchrotron* (SPS). Their masses were found to be compatible with the [Standard Model](#) prediction. Followed by the discoveries of the top quark in 1995, the τ neutrino in 2000 the model has already sustained its validity for more than 50 years. Most importantly, the [Standard Model](#) also predicted the mechanism of spontaneous symmetry breaking and the existence of the *Higgs boson H*. In 2012, the *Higgs boson* was discovered by the [ATLAS Collaboration](#) [[ATL12](#)] and [CMS Collaboration](#) [[CMS12](#)].

Despite its success, the [Standard Model](#) is not a complete theory of fundamental interactions as it does not incorporate gravitation described through the means of the general theory of relativity (curved space-time). Consequently, the model does not account for the expansion of the universe, does not predict the existence of dark matter or dark energy or explain the fine-tuning of fundamental physical constants. Neutrino masses and oscillations are not incorporated into the [Standard Model](#) either.

The objective of this chapter is to provide a qualitative description of the theoretical framework behind the [Standard Model](#) and define the terminology used throughout the thesis.

1.1 Symmetries and conservation laws

The notion of symmetry plays an important role in physics. The concept started in the 19th with the classification of crystals through the identification of symmetries in their basic patterns. We can conceptualize the idea of a symmetry by picturing a spherically symmetrical ball, which will under the effect of spatial rotation stay the same, i.e. remain invariant to the rotational transformation.

[Pierre Curie](#) [[Cur94](#)] has extended the understanding of symmetries by connecting it with the behaviour of physical systems. This is known as the *Curie principle* which states that there is a causal relationship between the symmetry of the cause and that of the effect. The effect of symmetry

on the dynamics of a physical system was formalized by [Emmy Noether \[Noe18\]](#), who showed that every continuous symmetry in a physical system leads to a conservation law of a certain quantity. This quantity is defined by the symmetry and is conserved only if the action on the system is invariant under that symmetry. This framework has proven to be an effective tool, as the underlying symmetries of a physical system can be used to derive physical laws.

1.1.1 Lagrangian formalism

The description of physical systems through the formalism of *Lagrangian functions* \mathcal{L} provides a compact approach that allows direct investigation of underlying symmetries. The classical *Lagrangian* function $L(t, \mathbf{q}, \dot{\mathbf{q}})$ is a functional of generalised coordinates in time $q_k = q_k(t)$, which is by definition non-relativistic. In relativistic field theories the *Lagrangian* function L is redefined as a spatial integral of *Lagrangian* density \mathcal{L} , which is a function of event x^μ , one or more fields $\varphi_k(x_\mu)$ and all their derivatives $\partial_\mu \varphi_k(x^\mu) = \left(\frac{\partial \varphi_k}{\partial t}, \frac{\partial \varphi_k}{\partial \mathbf{x}} \right)$:

$$L = \int_V \mathcal{L}(\varphi_k, \partial_\mu \varphi_k) d^3x .$$

With the variation defined as a virtual displacement of fields: $\delta \varphi_k = \varphi_{k,\text{virt}}(x^\mu) - \varphi_{k,\text{real}}(x^\mu)$ the action S can be expressed as:

$$S = \int_{t_1}^{t_2} L dt = \int_{t_1}^{t_2} \left(\int_V \mathcal{L} d^3x \right) dt = \int_\Omega \mathcal{L}(\varphi_k, \partial_\mu \varphi_k) d^4x \quad (1.1)$$

such that the integral over the four space-time coordinates preserves the relativistic invariance. [[Pic07](#), p. 42]

Following from the principle of least action, if the variation of action satisfies $\delta S = 0$ we obtain the Euler-Lagrange equations of motion for a field [[PS95](#), pp. 15–16]:

$$\boxed{\partial_\mu \left(\frac{\partial \mathcal{L}}{\partial(\partial_\mu \varphi_k)} \right) - \frac{\partial \mathcal{L}}{\partial \varphi_k} = 0} \quad (1.2)$$

which unwound for a field in Cartesian coordinates gives:

$$\frac{\partial}{\partial t} \left(\frac{\partial \mathcal{L}}{\partial(\partial \varphi / \partial t)} \right) + \frac{\partial}{\partial x} \left(\frac{\partial \mathcal{L}}{\partial(\partial \varphi / \partial x)} \right) + \frac{\partial}{\partial y} \left(\frac{\partial \mathcal{L}}{\partial(\partial \varphi / \partial y)} \right) + \frac{\partial}{\partial z} \left(\frac{\partial \mathcal{L}}{\partial(\partial \varphi / \partial z)} \right) - \frac{\partial \mathcal{L}}{\partial \varphi} = 0$$

1.1.2 Noether's theorem for fields

Suppose that we know Lagrangian density $\mathcal{L}(\varphi, \partial_\mu \varphi)$ that is invariant under some set of continuous transformations:

$$\varphi_k(x^\mu) \mapsto \varphi'_k(x^\mu) = \varphi_k(x^\mu) + \epsilon \delta \varphi_k(x^\mu), \quad \epsilon \rightarrow 0. \quad (1.3)$$

In order to find the quantity that is conserved in the transformation we require that the variation

of both the original and the transformed action is zero:

$$\delta S = \delta \int_{\Omega} \mathcal{L}(\varphi_k, \partial_\nu \varphi_k) d^4x = \delta \int_{\Omega} \mathcal{L}(\varphi'_k, \partial_\nu \varphi'_k) d^4x' = 0,$$

and we find that:

$$\delta \mathcal{L} = 0 = \sum_k \left\{ \left[\frac{\partial \mathcal{L}}{\partial \varphi_k} - \partial^\mu \left(\frac{\partial \mathcal{L}}{\partial (\partial^\mu \varphi_k)} \right) \right] \delta \varphi_k + \partial_\mu \left[\frac{\partial \mathcal{L}}{\partial (\partial_\mu \varphi)} \delta \varphi_k \right] \right\} \quad (1.4)$$

If the fields satisfy the Euler-Lagrange equations (1.2), then the first term is zero and the rest can be interpreted as a continuity equation of some four-current j^μ :

$$\partial_\mu j^\mu = 0 \quad \text{for} \quad j^\mu = \sum_k \frac{\partial \mathcal{L}}{\partial (\partial^\mu \varphi_k)} \delta \varphi_k \quad (1.5)$$

which is generally referred to as the *Noether's current*. This allows us to define a conserved quantity:

$$Q \equiv \int_V j^0(t, \mathbf{x}) d^3\mathbf{x} \quad (1.6)$$

by simply integrating the density over space. The condition $\partial_\mu j^\mu = 0$ guarantees that Q is a constant of motion: $dQ/dt = 0$. [Pic07, p. 42].

The derived quantity is a direct result of the Noether's theorem. For every continuous single-parameter transformation group that leaves equations of motion invariant there is a corresponding Noether's current $\partial_\mu j^\mu = 0$ and, consequently, a conserved quantity. In other words for every continuous symmetry in nature there is a conservation law of certain quantity (energy, momentum, angular momentum, electric charge etc.). This quantity is defined by the symmetry and is conserved only if the action is invariant under that symmetry [Pic07, p. 41]. For the full derivation of the theorem see the textbook by Michael E. Peskin and Dan V. Schroeder [PS95], pp. 17–18.

1.1.3 Poincaré group

If the laws of physics are invariant under a specific transformation, then in accordance with Noether's theorem, each of these invariances leads to a conserved quantity. If a **Lagrangian** of the system is explicitly independent of time t , then, the conserved quantity is defined as *energy*. Likewise, invariance to spatial translation in space leads a conserved quantity defined as *momentum*, and invariance to spatial rotation defines the *angular momentum*. Each of these quantities has a clear physical interpretation from classical mechanics and places important constraints on the evolution of a system.

For Minkowski space-time, the coordinate translations $(\delta t, \delta x, \delta y, \delta z)$, rotations R_z, R_x, R_y and Lorentz boost $\Lambda_{tx}, \Lambda_{ty}, \Lambda_{tz}$ form the **Poincaré group of transformations**, which is a ten dimensional Lie group. A physical law invariant under these transformation can be expressed in terms of representations of a symmetric group. The conservation laws arising from invariances with respect to the Poincaré group provide an excellent tool to describe the dynamics of elementary particles.

1.1.4 Scalar representation

The representation of a real scalar field is the simplest possible quantum field which corresponds to spin $s = 0$. In order to write a [Lagrangian](#) for the field, we have to arrange the derivatives of the field $\varphi(x^\mu)$ such that the result is a scalar:

$$\mathcal{L}_S = (\partial_\mu \varphi(x^\mu))^\dagger \partial_\mu \varphi(x^\mu) \quad (1.7)$$

This Lagrangian density leads to a simple wave equation: $2(\partial_\mu \partial^\mu \varphi) = 0$, hence we introduce a factor $\frac{1}{2}$ into [eq. \(1.7\)](#) as a convention. One can then try and guess the Lagrangian density that would lead to the correct wave equation as shown for example in [\[Kan93, pp. 19–20\]](#):

$$\mathcal{L}_{KG} = \frac{1}{2} (\partial_\mu \varphi(x^\mu))^\dagger (\partial_\mu \varphi(x^\mu)) + \frac{1}{2} m^2 \varphi(x^\mu) \varphi(x^\mu)^\dagger \iff (\partial^\mu \partial_\mu - m^2) \varphi(x^\mu) = 0 \quad (1.8)$$

which is of course the Klein-Gordon equation describing a complex scalar field $\varphi(x^\mu)$ corresponding to the behaviour of a free particle. All we added to [eq. \(1.7\)](#) was another quadratic term $\alpha \varphi^2$, where α corresponds to the particle mass squared. The field $\varphi(x^\mu)$ represents a particle of mass m with spin $s = 0$. Both the field $\varphi(x^\mu)$ and its complex conjugate $\varphi(x^\mu)^\dagger$ satisfy the [eq. \(1.8\)](#) which means that particles with $s = 0$ are their own anti-particles. [\[Pic07, p. 42\]](#) In addition, the state of the particle in the rest frame does not change with the application of boosts: $\Lambda_{tx}, \Lambda_{ty}, \Lambda_{tz}$. This property is important, as it allows us to classify particles according to spin and justifies our choice of spin as the dimension of the representation.

1.1.5 Spinor representation

The structure of the Lorentz group leads to two possible choices of representation corresponding to spin $s = \frac{1}{2}$ referred to as *spinors*. Both options exhibit different behaviour with respect to parity (a phenomenon referred to as *chirality*), which requires that we define a right-handed ϕ_R and a left-handed ϕ_L component of the field. In case the system is invariant to parity transformations, the two objects are combined into a so called *bi-spinor* ϕ .

The Lagrangian for a free particle describes a field of a single fermion with mass m . Using [eq. \(1.2\)](#) it yields the famous Dirac equation:

$$\mathcal{L}_{\text{Dirac}} = \bar{\psi}(x^\mu) (\gamma^\mu \partial_\mu - m) \psi(x^\mu) \iff (\gamma^\mu \partial_\mu - m) \psi(x^\mu) = 0 \quad (1.9)$$

where $\bar{\psi}$ denotes Dirac adjoint: $\bar{\psi} = \psi^\dagger \gamma^0$, the matrix γ^0 is included to ensure proper behaviour in Lorentz transformations. [\[Pic07, p. 42\]](#)

1.1.6 Particle classification according to spin-statistics relationship

It is clear that the best option for classifying particles is in terms of their discrete physical properties. The classification based on spin follows the reasoning behind the *exclusion principle* proposed by [W. Pauli \[Pau25\]](#). In quantum systems, particles propagate as probabilistic wave functions. Suppose we only have two particles in a state $|\psi\rangle = |a_1, a_2\rangle$ and we want to switch their position using a Hermitian exchange operator $\hat{\mathbf{E}}_{21}$. Switching two particles and then switching them back is equal to

not switching them at all, thus: $\hat{E}_{21}^2 = \hat{1}$. The operator eigenvalues can only be $\lambda = \pm 1$ and that there are only two possible states this operator can project:

$$|a_1, a_2\rangle = \hat{E}|a_1, a_2\rangle = \pm|a_1, a_2\rangle \quad (1.10)$$

We call this property wave function symmetry (+1) or antisymmetry (−1). If wave function is symmetrical, then

$$|a_1, a_2\rangle = |a_2, a_1\rangle \quad \text{therefore} \quad a_1 = a_2 = a \quad (1.11)$$

and both wave functions describe the same state, i.e. particles 1 and 2 can occupy the same quantum state. Antisymmetrical wave function means that

$$|a_1, a_2\rangle = -|a_2, a_1\rangle \quad \text{which is never satisfied for} \quad a_1 = a_2 = a \quad (1.12)$$

thus no two particles can occupy the same quantum state simultaneously. With this we have established, that there are two types of particles according to wave function symmetry. The concept was eventually expanded based on observation in experiments by [Walther Gerlach and Otto Stern \[GS22\]](#). Elementary particles can be classified into two categories based on spin (in units of \hbar):

Bosons are particles with integer spin ($0, \hbar, 2\hbar, \dots$) named after Satyendra Nath Bose who derived the properties of their statistical behaviour with Albert Einstein. Their wave-function is *symmetrical*: $|\psi_{12}\rangle = |\psi_{21}\rangle$, therefore Pauli exclusion principle *does not apply*. Bosons can create a Bose-Einstein condensate, because they always attempt to occupy the least energetic state. The *Bose-Einstein statistics* can be derived from the partition sum of occupation numbers $N_k = \{0, 1, 2 \dots n\}$ [Per00, p. 309]:

$$\bar{N}_k = \frac{1}{\exp\left(\frac{1}{kT}(E_k - \mu)\right) - 1} \quad (1.13)$$

The equation of motion for a free particle with spin $s = 0$ particle is given by the scalar representation in [eq. \(1.8\)](#).

Fermions are particles with half-integer spin: ($\frac{1}{2}\hbar, \frac{3}{2}\hbar, \dots$) named after Enrico Fermi who derived the properties of their statistical behaviour with Paul A. M. Dirac. Their wave-function is *anti-symmetrical*: $|\psi_{12}\rangle = -|\psi_{21}\rangle$, therefore Pauli exclusion principle *applies*. No two identical fermions may occupy the same quantum state simultaneously. The *Fermi-Dirac statistics* can be derived from the partition sum of occupation numbers $N_k = \{0, 1\}$ [Per00, p. 310]:

$$\bar{N}_k = \frac{1}{\exp\left(\frac{1}{kT}(E_k - \mu)\right) + 1} \quad (1.14)$$

The spin- $\frac{1}{2}$ fields are represented by spinors as described above. The equations of motion is given in [eq. \(1.9\)](#).

The Pauli's exclusion principle describes a fundamental property of nature that allows electron shells to be built up in the vicinity of atomic nuclei and, consequently, allows for the existence

of chemical elements (classified by the Mendeleev periodic table). It should be noted here, that both Fermi-Dirac and Bose-Einstein statistics lead Maxwell-Boltzmann statistics in classical limit, provided the density and momentum of the particles is low enough.

1.1.7 Principle of gauge invariance

Now we have to establish the link between free particles and interactions using the notion of symmetry. The simplest example can be illustrated on electromagnetic fields. First, consider the evolution for a free particle with spin $\frac{1}{2}$ given by its wave function ψ of a corresponding \mathcal{L} from eq. (1.9). If we study its symmetries we find that it is invariant under global transformation of the field phase U_θ , i.e. rotation of the field in a complex plane:

$$\psi(x^\mu) \xrightarrow{U(1)} \psi'(x^\mu) = e^{i\theta} \psi(x^\mu) \quad (1.15)$$

$$\bar{\psi}(x^\mu) \xrightarrow{U(1)} \bar{\psi}'(x^\mu) = e^{-i\theta} \bar{\psi}(x^\mu) \quad (1.16)$$

where θ is an arbitrary real constant everywhere in space-time. The \mathcal{L} remains invariant and the Noether's current is: $j^\mu = \bar{\psi} \gamma^\mu \psi$ [MLM02, pp. 33–37] [Pic07, p. 2] This transformation is referred to as $U(1)$. It is unitary $U_\theta^\dagger U_\theta = 1$ and Abelian $U_{\theta_1} U_{\theta_2} = U_{\theta_2} U_{\theta_1}$ and by definition global (since θ is not a function of space-time coordinates x^μ).

However, global phase transformations cannot be considered as observables since the information about field phase would need to propagate faster than light. Consequently, the phase of $\psi(x)$ is without any physical meaning. We can redefine the problem and require that the symmetry is a function of space-time $\theta = \theta(x^\mu)$ (i.e. making it *local*), but the Lagrangian is no longer invariant under such transformation:

$$\begin{aligned} \mathcal{L} \mapsto \mathcal{L}' &= \bar{\psi}' (\gamma^\mu \partial_\mu - m_0) \psi' = \\ &= e^{-i\theta(x^\mu)} \bar{\psi} (\gamma^\mu \partial_\mu - m_0) e^{i\theta(x^\mu)} \psi = \\ &= \bar{\psi} (\gamma^\mu \partial_\mu - m_0 c) \psi + \bar{\psi} \gamma^\mu \psi \partial_\mu \theta(x^\mu) \\ &= \mathcal{L} + j^\mu(x^\mu) \partial_\mu \theta(x^\mu) \end{aligned} \quad (1.17)$$

Only when θ does not depend on space-time $\partial_\mu \theta(x^\mu) = 0$ is \mathcal{L} invariant. The term j^μ is a vector current carried away by this phase rotation [MLM02, p. 38]. The *gauge principle* is the requirement, that invariance to such phase transformation should hold locally. This is only possible if we modify the **Lagrangian** by introducing a gauge field A^μ transforming in such a way that it cancels out the vector current term in eq. (1.17):

$$\mathcal{L} \mapsto \mathcal{L}_{\text{new}} \equiv \mathcal{L}_{\text{Dirac}} + g j_\mu A^\mu, \quad (1.18)$$

where the constant g is a dimensionless measure of the strength of the interaction – formally referred to as the *coupling constant*. One can then show the invariance of \mathcal{L}_{new} with respect to $U(1)_{\text{local}}$ transformation:

$$\mathcal{L}'_{\text{new}} = \mathcal{L}'_{\text{Dirac}} + g \bar{\psi} \gamma^\mu \psi A'_\mu = \mathcal{L}_{\text{Dirac}} + \bar{\psi} \gamma^\mu \psi \partial_\mu \theta(x^\mu) + g \bar{\psi} \gamma^\mu \psi A'_\mu$$

and provided that A'_μ transforms like:

$$A'_\mu(x^\mu) = A_\mu(x^\mu) - \frac{1}{g} \partial_\mu \theta(x^\mu) \quad (1.19)$$

we preserve the invariance of the **Lagrangian**:

$$\mathcal{L}'_{\text{new}} = \mathcal{L}_{\text{Dirac}} + g \bar{\psi} \gamma^\mu \psi A_\mu = \mathcal{L}_{\text{new}} \quad (1.20)$$

The new **Lagrangian** \mathcal{L}_{new} is made invariant with respect to the $U(1)_{\text{local}}$ transformation by introducing a spin 1 gauge boson field A^μ . First we introduce the following substitution for the derivative:

$$\partial_\mu \mapsto D_\mu \equiv \partial_\mu - i \frac{g}{1} A_\mu(x^\mu) \quad (1.21)$$

The newly introduced D_μ is referred to as *covariant derivative*, which is defined as a derivative that transforms in such a way that Dirac equation remains unchanged [MLM02, p. 38]: The modified **Lagrangian** will look very similar, only now the interaction term is included in D_μ :

$$\mathcal{L} = \bar{\psi}(x^\mu) (i \gamma^\mu D_\mu - m_0) \psi(x^\mu) = \quad (1.22)$$

$$= \bar{\psi}(x^\mu) (i \gamma^\mu \partial_\mu - m_0) \psi(x^\mu) + g \bar{\psi} \gamma_\mu \psi A_\mu(x^\mu). \quad (1.23)$$

Here, the covariant derivative D_μ is called the *minimal coupling* as it describes interaction between gauge bosons and particles. In case of a theory of electromagnetism, the coupling constant can be identified with the electric charge $g \equiv e$, which is the quantity preserved by the invariance with respect to local gauge transformation $U(1)_{\text{local}}$ [MLM02, pp. 37–38].

Starting from the components of a classical field theory:

$$\mathcal{L}_{\text{elmag}} = \mathcal{L}_{\text{particle}} + \mathcal{L}_{\text{interaction}} + \mathcal{L}_{\text{field}} = \mathcal{L}_{\text{particle}} - e j_\mu A^\mu - \frac{1}{4\mu_0} F_{\mu\nu} F^{\mu\nu} \quad (1.24)$$

the full electromagnetic \mathcal{L} can be obtained by including the particle term from the Dirac equation eq. (1.9) [MLM02, p. 39]:

$$\mathcal{L}_{\text{QED}} = \bar{\psi}(x^\mu) (i \gamma^\mu \partial_\mu - m_0 c) \psi(x^\mu) - \frac{1}{4\mu_0} F_{\mu\nu} F^{\mu\nu} - e j_\mu A^\mu = \quad (1.25)$$

$$= \bar{\psi}(x^\mu) (i \gamma^\mu D_\mu - m_0 c) \psi(x^\mu) - \frac{1}{4\mu_0} F_{\mu\nu} F^{\mu\nu} \quad (1.26)$$

where the electromagnetic field A^μ is gauge invariant as it is defined to satisfy the Lorentz gauge invariance $\partial_\mu A^\mu = 0$. The symmetry holds only if we introduce the electromagnetic field into the **Lagrangian**.

This **Lagrangian** describes a quantum field of electromagnetic interactions, the theoretical framework is called *quantum electrodynamics* (QED). Maxwell in his unification of electricity and magnetism predicted the existence of electromagnetic waves which in QED rise as a gauge boson mediator (quantum of light) which is identified with the *photon* γ . This symmetry is also connected with a conservation law, in this case it is the conservation of electric charge e . The theory describes the *electromagnetic interaction* through the means of the **Lagrangian** eq. (1.26) which leads directly

to the Maxwell equations:

$$\partial_\mu F^{\mu\nu} = j^\nu = e\bar{\psi}\gamma^\nu\psi \quad (1.27)$$

where j^ν is the electromagnetic current. [Pic07, p. 2]

The *quantum electrodynamics* (QED) created by R. Feynman [Fey49] [Fey50], Julian Schwinger [Sch48] and S. Tomonaga [Tom49] was the first quantum field theory that provided a consistent relativistic quantum mechanical description of electromagnetism. The principle of gauge invariance has become such a powerful tool to understand electromagnetism and proved useful in describing the strong and weak interactions as well.

1.1.8 Note on particle interactions and perturbation theory

Field interactions in quantum field theory are represented by Feynman diagrams using the formalism of a perturbation theory. In quantum field theories, all the forces of nature are described in terms of particle exchange. In QED, all electromagnetic phenomena can be described as an exchange of electromagnetic field quanta – photons. Let us consider a simplified example: when an electron emits a photon it recoils in order to conserve momentum. Adhering to the concept, we arrive at the inescapable conclusion that producing a new particle out of “thin air” would violate the conservation of energy. Consider, however, the Heisenberg’s uncertainty principle. Emitting a zero mass particle with momentum p is allowed provided that the borrowed energy that produced the particle $\Delta E = cp$ is given back within time $\Delta t \approx \frac{\hbar}{cp}$. Consequently, the exchange particle can only go as far as $\Delta x \approx c\Delta t \approx \frac{\hbar}{p}$ which is basically one wavelength away from the source. [HM85, pp. 7–11] Such a particle cannot be considered measurable, as it cannot “live” without the presence of independent charges. This is the reason the exchange particles are commonly referred to as *virtual*.

In perturbation theory, the interaction between particles is introduced through a perturbation of the system. Consequently, the unperturbed solutions of the free particle equations are no longer valid. Instead, the goal is to find the expression for the scattering amplitude between the initial state (before the interaction occurs) and final state (after the interaction occurs). The Feynman diagrams represent the terms in the perturbation series for the amplitude. The diagrams are built out of propagators, vertices and external points, all of which are associated with an analytic expression. Particles are noted with arrows going forwards in time, antiparticles as arrows going backwards in time. Multiple vertices might be connected by a bosonic or fermionic propagator. This way quantum field theories make the connection with experimental observables like the *cross-section* σ or decay rate. See the excellent introduction into the subject by Francis Halzen and Alan D. Martin [HM85] (chapter 3) or the rigorous approach by Michael E. Peskin and Dan V. Schroeder [PS95]. An excellent discussion can also be found in the recently published textbook by Tom Lancaster and Stephen J. Blundell [LB14].

In QED, an electron is not just a single free particle. All electrically charged particles emit a cloud of virtual photons around them. A virtual photon can subsequently annihilate into a pair of virtual charged particles (for example electron-positron pairs in the vacuum). An electron surrounded by a cloud of these electron-positron pairs will repel the electrons and thus the positrons will be preferentially closer the electron. When probing this structure from distance the surrounding positrons will screen the electron which will affect the measured charge. A high-energy probe

that manages to get closer and closer to the original electron will see less and less effects from the virtual particles, so that the effective charge will increase. This property has important physical implications for the perturbative expansion of QED. See re-normalization in [HM85], chapter 7 and also figure 1.5.

1.1.9 Experimental considerations

Theories meets with experiments by providing verifiable predictions, usually in terms of a hypothesis or measurable quantities. By design, quantum field theories can predict either the existence of a new elementary particle or a new interaction vertex of known particles. As noted above, the formalism of quantum field theories can be used to compute two quantities that can be statistically analysed: interaction **cross-sections** and particle *decay widths*. **Cross-section** expresses the likelihood that any particular final state particle b_i will come from interaction of particles a_i :

$$\sigma(a_1 a_2 \rightarrow b_1 b_2 \dots b_n) = \frac{\text{Transition rate} \cdot \text{Number of final states}}{\text{Initial flux}}. \quad (1.28)$$

Because the differential cross section $\frac{d\sigma}{d\Omega}$ for particles outgoing in solid angle Ω is related to the machine **luminosity** \mathfrak{L} (see section 2.1.4):

$$\frac{d\sigma}{d\Omega} = \frac{1}{\mathfrak{L}} \frac{d^2 N}{dt d\Omega} \quad (1.29)$$

where $\frac{d^2 N}{dt d\Omega}$ is the number of particles outgoing per unit time in solid angle, it allows for comparison between two different experiments with different beam parameters. The relationship between **cross-sections** and the scattering matrix is discussed in detail in [PS95, pp. 99–107].

In order to obtain the cross section from experimental data, we have to identify the particles produced in the experiment. **Chapter 2** provides an extensive overview of how the detector can determine the mass, momentum and charge of the final state particles. In case the former particle is unstable the only way to identify it is through its decay products and that is where decay width comes in:

$$\Gamma(a_1 \rightarrow b_1 b_2 \dots b_n) = \frac{\text{Number of decays per unit time}}{\text{Number of } a_i \text{ particles present}} \quad (1.30)$$

The decay width is related to the particle's lifetime as a reciprocal sum of all its decay rates: $\tau = \Gamma_{\text{TOT}}^{-1}$ [PS95, p. 101]. The last missing piece of the puzzle is the mass of the unstable particle, which can be determined from the invariant mass of its products. Plotting the cross section as a function of mass the unstable particle will show as a *resonance* given by the relativistic Breit-Wigner formula

$$\sigma \approx \frac{1}{p^2 - m^2 + im\Gamma} \quad (1.31)$$

where p is the four momentum of the unstable particle and m is its mass. This is the common way used in experiments to discover unstable particles predicted by the theory. Of course certain quality cut criteria are in place in order to avoid misinterpreting a random fluctuation as a new particle [PS95, p. 101].

Figure 1.1a shows evidence for the J/Ψ particle, and fig. 1.1b for the **W boson**. When looking for a new particle, experimentalists identify the decay products of the particle in question and plot

their invariant masses in a histogram. If there is a peak (i.e. a resonance), it is possible they are originating from a new particle as can be seen in these figures.

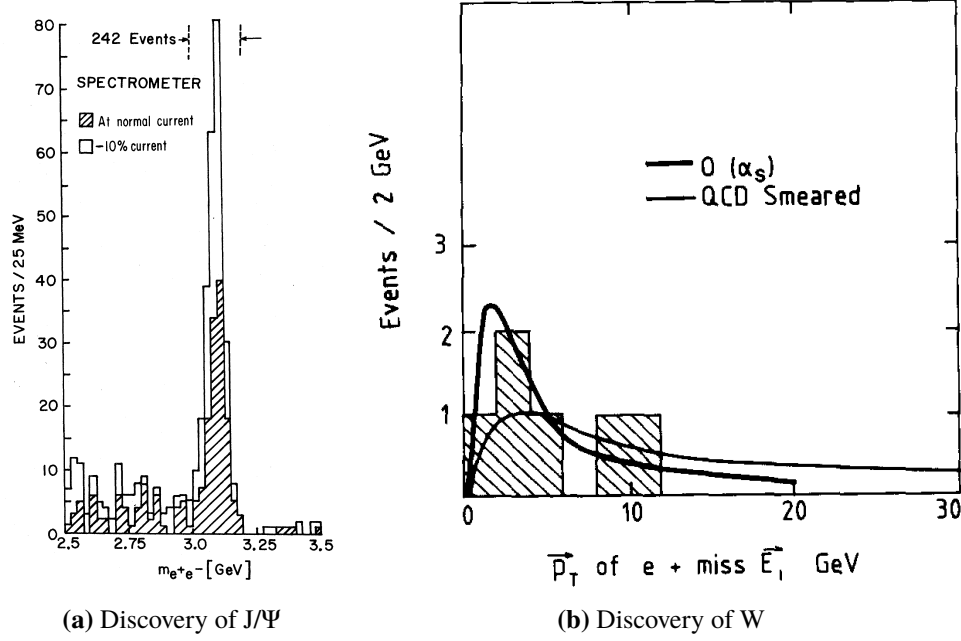


Figure 1.1: Discovery plots of J/Ψ and W bosons. The particle shows as a resonance peak at given mass provided the experiment can provide sufficient collision energy. In case of the J/Ψ , the decay products are an electron pair, the W decays into a charged lepton and a complement neutrino. Figures from [Aub+74] and [UA183].

1.2 Quark model

One of the many achievements of the [Standard Model](#) was the successful development of a classification scheme for *hadrons*. [Murray Gell-Mann \[Gel64\]](#) and [George Zweig \[Zwe64a\] \[Zwe64b\]](#) independently postulated that the systematics of hadrons can be accounted for by assembling them from elementary particles with fractional charge, see [table 1.1](#). Gell-Mann called these particles *quarks*: namely *up* quark u , *down* quark d and *strange* quark s [MLM02, p. 89]. The model allows only the following two combinations of quarks [Per00, pp. 23–26]:

- *Baryons* (from Greek $\beta\alpha\rho\nu\varsigma$ meaning “heavy”) that are a combination of 3 quarks. Typical baryons are *nucleons*, particles of atomic nuclei – *protons* (uud) and *neutrons* (udd). The common baryons made from u , d and s quarks can be represented by the group:

$$3 \otimes 3 \otimes 3 = 10 \oplus 8 \oplus 8 \oplus 1 \quad (1.32)$$

- *Mesons* (from Greek $\mu\epsilon\sigma\omicron\varsigma$ meaning “middle”) are particles made from a combination of quark q and anti-quark \bar{q} . Taking only four of the constituents quarks u , d , s and c , the combinations can be represented by 16-plet based on decomposition:

$$4 \otimes \bar{4} = 15 \oplus 1 \quad (1.33)$$

Typical mesons are pions like π^+ ($u \bar{d}$) or kaons like K^+ ($u \bar{s}$). Given the addition of spin from the constituent quarks, mesons are considered as pseudoscalar bosons ($s = 0$) or vector bosons ($s = 1$).

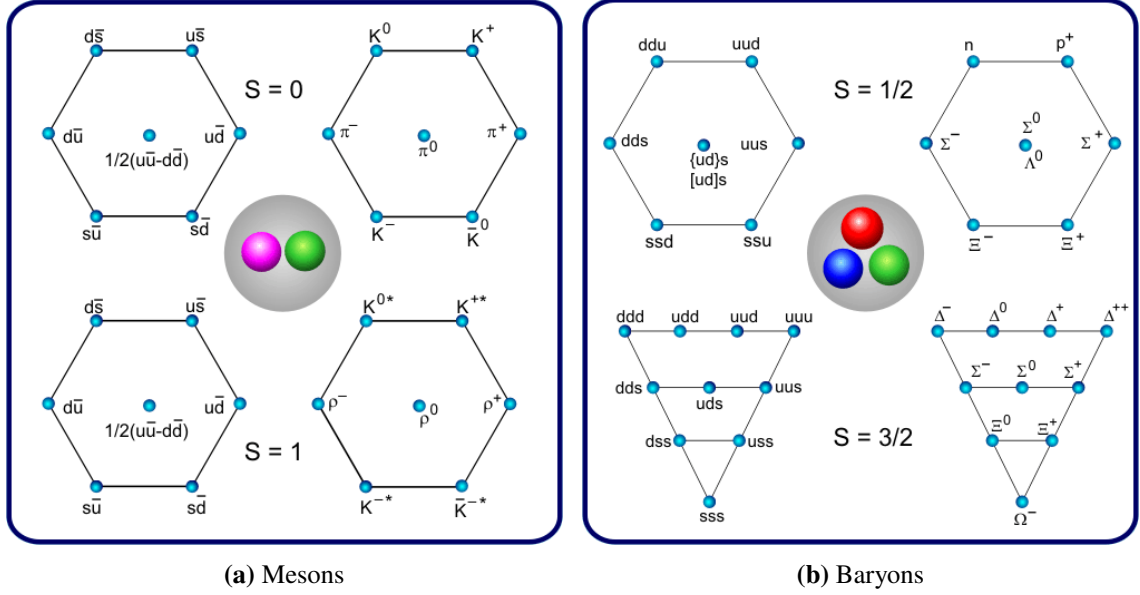


Figure 1.2: Quark combinations. Figure from [Kul14].

1.2.1 Experimental evidence

Electrons make ideal probes to look inside composite particles like *hadrons* because they do not interact strongly. The *deep inelastic scattering* experiments performed at the SLAC in 1968 showed that the proton contained much smaller, point-like objects and was therefore not an elementary particle [Per00, pp. 156–160]. These mass centres were referred to as *partons* which were introduced through the mathematical concept of structure functions. At the time, physicists were reluctant to identify partons with quarks, since there were still inconsistencies in the treatment of specific particles like Δ^{++} resonance with experimentally measured spin $\frac{3}{2}$ (uuu). Such a particle cannot exist unless quarks have another degree of freedom which is intrinsic to the strong interaction and has not been observed outside hadrons.

To solve this problem, O. Greenberg [Gre64] introduced the idea of *colour charge* that would allow such combinations as Δ^{++} to occur. Generally speaking, this new property follows a basic RGB model: three identical quarks of three different “colours” would make a “white” baryon combination that was not in conflict with Pauli’s principle. Antiquarks would have *anticolour*, thus allowed “white” combinations would be:

$$\text{baryons} = q^R + q^G + q^B = \text{“white”} \quad (1.34)$$

$$\text{mesons} = q^R + \bar{q}^R = \text{“white”} \quad (1.35)$$

implying that only “white” combinations of quarks are directly observable.

The physical property of colour charge allowed for a new classification hadrons, for example when a new quark was discovered in quarkonia studies at Brookhaven. The new meson discovered

by J. Aubert et al. [Aub+74] was referred to as J, while the team at SLAC led by J. Augustin et al. [Aug+74] called the particle ψ , leading to particle name J/ψ ($c\bar{c}$). This was supplemented with the evidence for existence of another two quarks. The discovery was made at FNAL in 1977 by a team led by Leon M Lederman [Led79]. They discovered a new particle they called Y, which was made from a bound state of *beauty* (*bottom*) quark and antiquark ($b\bar{b}$). The sixth quark referred to *truth* (*top*) was discovered much later also at FNAL by the CDF Collaboration [CDF95] in 1995, mainly because its energy was much higher than expected.

In summary, there is irrefutable evidence for a total six kinds of quarks. In the SM, the quarks arranged in doublets corresponding to three particle generations. There are three generations of quarks and every quark can exist in three colours, for a summary see table 1.1. [Per00, pp. 95–101]

Quark symbol	Isospin I	El. charge e	Mass $m[\text{MeV}]$	Generation	Anti-quark symbol
u	$+\frac{1}{2}$	$+\frac{2}{3}$	1.50 to 3	1	\bar{u}
d	$-\frac{1}{2}$	$-\frac{1}{3}$	3 to 7	1	\bar{d}
c	$+\frac{1}{2}$	$+\frac{2}{3}$	1250 ± 90	2	\bar{c}
s	$-\frac{1}{2}$	$-\frac{1}{3}$	95 ± 5	2	\bar{s}
t	$+\frac{1}{2}$	$+\frac{2}{3}$	$172\,000 \pm 2700$	3	\bar{t}
b	$-\frac{1}{2}$	$-\frac{1}{3}$	4200 ± 70	3	\bar{b}

Table 1.1: The quark family with all generations. Masses m increase with generation, lifetime τ decreases. Data from [Par13].

1.2.2 Gauge invariance of quantum chromodynamics

As shown in section 1.1.7, interactions between electrons (or positrons) and photons can be expressed in terms of gauge theory with a $U(1)$ internal symmetry. Since quarks assemble by colour, the representation takes form of 3×3 matrices that allow us to arbitrarily mix the quarks by acting on a three vector of quark wave functions [MLM02, pp. 89,92]:

$$\mathbf{q} = \begin{pmatrix} q^R \\ q^G \\ q^B \end{pmatrix} \quad (1.36)$$

M. Y. Han and Y. Nambu [HN65] and O. Greenberg [Gre64] independently proposed that the non-Abelian group represented by the 3×3 matrices is $SU(3)_C$ and, as it was later shown, this indeed is the local internal symmetry corresponding to the gauge field of QCD. The Dirac Lagrangian for free particle is modified to accommodate the $SU(3)_C$ states of freedom [MLM02, p. 92]:

$$\mathcal{L}_{\text{QCD}} = \bar{\mathbf{q}}(\not{\partial} - m_0)\mathbf{q} . \quad (1.37)$$

The procedure is now very similar to section 1.1.7. Firstly, physics should be invariant with respect to a change in colour charge, i.e. no matter how we iterate the bases. Secondly, physics must

be local, thus the transform is defined as:

$$\mathbf{q} \mapsto \mathbf{q}' = U(x^\mu) \mathbf{q}(x^\mu) = e^{-i\omega^a(x^\mu)\text{Tr}(T^a)} \mathbf{q}(x^\mu) \quad (1.38)$$

where T^a are $\text{SU}(3)_C$ generators which obey the following commutation relations:

$$[T^k, T^l]_- = i f^{klm} T^m. \quad (1.39)$$

and the structure constants f^{abc} form a totally antisymmetric tensor:

$$\begin{aligned} f^{123} &= 2, \\ f^{147} &= -f^{156} = f^{246} = f^{257} = f^{345} = -f^{367} = 1, \\ f^{458} &= f^{678} = \sqrt{3}. \end{aligned}$$

In accord with the QED case, the goal is to keep the Dirac equation unchanged by the transformation eq. (1.38). The invariance of the **Lagrangian** can be ensured by introducing the gauge field G^μ provided the field holds:

$$G_\mu \rightarrow G'_\mu = U G_\mu U^\dagger - \frac{i}{g_s} (\partial_\mu U) U^\dagger, \quad (1.40)$$

where g_s is the coupling constant and G_μ is the gauge field added in to cancel the terms created by the former derivative. The covariant derivative is given by [MLM02, p. 92]:

$$D_\mu \mapsto D'_\mu = U(x^\mu) D_\mu \quad \text{is given by} \quad D_\mu = \partial_\mu - i \frac{g_s}{\hbar} G_\mu. \quad (1.41)$$

However, in QED electron acts on a electric charge which is a simple scalar. In QCD the coupling constant g_s acts on the vector fields $G_\mu = G_\mu^a T^a$ [MLM02, pp. 92–93]. By definition, the $SU(N)$ group of $N \times N$ unitary matrices. Thus for $\text{SU}(3)$ we have $\det U \stackrel{!}{=} 1 = e^{-i\omega^a \text{Tr}(T^a)}$ and we obtain $N^2 - 1 = 3^2 - 1 = 8$ gluons represented by the following 8 generators of $\text{SU}(3)$ group called *Gell-Mann matrices* that have been chosen as an analogue to the Pauli matrices $T^a = \frac{1}{2} \lambda^a$ [MLM02, pp. 270–271]:

$$\begin{aligned} \lambda^1 &= \begin{pmatrix} 0 & 1 & 0 \\ 1 & 0 & 0 \\ 0 & 0 & 0 \end{pmatrix}, & \lambda^2 &= \begin{pmatrix} 0 & -i & 0 \\ i & 0 & 0 \\ 0 & 0 & 0 \end{pmatrix}, & \lambda^3 &= \begin{pmatrix} 1 & 0 & 0 \\ 0 & -1 & 0 \\ 0 & 0 & 0 \end{pmatrix}, \\ \lambda^4 &= \begin{pmatrix} 0 & 0 & 1 \\ 0 & 0 & 0 \\ 1 & 0 & 0 \end{pmatrix}, & \lambda^5 &= \begin{pmatrix} 0 & 0 & -i \\ 0 & 0 & 0 \\ i & 0 & 0 \end{pmatrix}, & \lambda^6 &= \begin{pmatrix} 0 & 0 & 0 \\ 0 & 0 & 1 \\ 0 & 1 & 0 \end{pmatrix}, \\ \lambda^7 &= \begin{pmatrix} 0 & 0 & 0 \\ 0 & 0 & -i \\ 0 & i & 0 \end{pmatrix}, & \lambda^8 &= \frac{1}{\sqrt{3}} \begin{pmatrix} 1 & 0 & 0 \\ 0 & 1 & 0 \\ 0 & 0 & -2 \end{pmatrix}, & \text{thus } G_\mu &= \frac{1}{2} \lambda^a G_\mu^a. \end{aligned}$$

The field term of the **Lagrangian** is given similarly to QED by a gauge invariant field strength

tensor for each gluon field:

$$G_{\mu\nu}^i = \partial_\mu G_\nu^i - \partial_\nu G_\mu^i - g_s f^{ijk} G_\mu^j G_\nu^k, \quad (1.42)$$

and the gauge invariant QCD Lagrangian is:

$$\mathcal{L}_{\text{QCD}} = \bar{\mathbf{q}}[i\hbar\gamma^\mu\partial_\mu - m_0c]\mathbf{q} - \frac{1}{4}G_{\mu\nu}^i G^{i\mu\nu} \quad (1.43)$$

where \mathbf{q} is the quark field, $\bar{\mathbf{q}}$ is the anti-quark field and index i in the field tensor $G^{i\mu\nu}$ stands for summation over $i = 1, 2, \dots, 8$ gluon fields $G^{\mu\nu}$ [MLM02, p. 92]. The newly introduced vector fields $G_\mu = G_\mu^a T^a$ are referred to as *gluons* (from English *glue*). The **Lagrangian** is local gauge invariant under **SU(3)** transformation provided the gluons are massless and their mass term vanishes.

1.2.3 Strong coupling

The **QCD** field tensor given by eq. (1.42) contains gluon self-interactions and that gluons mediate colour charge. One can infer from the Heisenberg uncertainty principle, that in order to emit a virtual particle of non-zero mass would cost an amount of energy $\Delta E > m_0c^2$ and that energy has to be given back in time less than $\Delta t \approx \frac{\hbar}{\Delta E}$. This effectively means that it is forbidden to fly distance longer than $c\Delta t \approx \frac{\hbar c}{\Delta E} < \frac{\hbar c}{m_0c^2}$, thus maximum distance such force can be carried is $d_{\text{max}} \approx \frac{\hbar}{m_0c}$. This property is sometimes described as *virtual particles going off the mass shell*.

In analogy with **QED**, the strong coupling constant α_s can be defined with respect to a given energy scale. Given a dimensionless observable which depends only on the energy scale Q , the perturbation series to calculate α_s leads to ultraviolet (UV, i.e. high energy) divergences. To resolve the issue, one can introduce an arbitrary energy scale called the *renormalisation scale* at which the divergences are removed. The processes to renormalise the coupling is to make it dependent on the energy scale Q at which one observes the coupling. The dependence of a coupling g on the energy-scale Q is known as *running* of the coupling:

$$\alpha_s \equiv \frac{g_s^2(Q^2)}{4\pi} \approx \frac{1}{\beta_0 \ln\left(\frac{Q^2}{\Lambda_{\text{QCD}}^2}\right)} \quad (1.44)$$

where Λ_{QCD} is the scale at which the effective coupling becomes large and β_0 is the constant proposed by **H. Politzer** [Pol73], **David Gross and Frank Wilczek** [GW73] in 1973. For values of Q^2 much larger than Λ_{QCD}^2 the effective coupling is small and the perturbative theory provides a good description of the underlying physics. The theory behind running couplings is referred to as the *renormalization group*. From this equation it is clear, that with increasing Q^2 , the coupling becomes small for short distances or high energies. This leads to two important properties that are unique to **QCD**:

- **Asymptotic freedom:** At shorter distances quarks move relatively freely. When the distances grow larger, gluons act more and more strongly to pull the quark back, similarly to pulling a spring. [Per00, p. 185]
- **Colour confinement:** Quarks can not be observed as free particles because they are confined inside hadrons. Similarly, there are no free gluons. An attempt to separate a quark from the

hadron results in gradual increase of the binding energy until there is enough to create a quark anti-quark pair which then recombines, creating another hadron. When this happens as a result of a collision in an accelerator, the process creates jets of particles along the quark's path, see [section 3.3.5](#). [Per00, pp. 178–180] [PS95, p. 425].

To summarise, QCD is a $SU(3)_C$ gauge theory of strong interaction which describes the dynamics of quarks and gluons. The strong nuclear force is mediated by the gluons, which are electrically neutral spin $s = 1$ particles. The term *parton* remains in use to date as a collective term for the constituents of hadrons (quarks, antiquarks, and gluons). For more information on QCD see the comprehensive overview provided by Michael E. Peskin and Dan V. Schroeder [PS95], pp. 533, 545–594

1.3 Electroweak sector

In the previous section it has been shown that the principle of gauge invariance provides powerful means to build a successful theory explaining the behaviour of elementary particles. One is able to determine the QCD and QED Lagrangians and the corresponding gauge fields. Another piece of the puzzle lies in the integration of weak interactions into the theory.

1.3.1 Weak interactions and symmetries

Weak interactions are one of the four fundamental forces in nature alongside the electromagnetic and strong forces discussed earlier in this chapter. In the [Standard Model](#) the weak forces are mediated through W and Z bosons. A qualitative description of weak forces usually starts with the discussion of *particle decay*. Through experimental means it has become evident that most particles have finite (and some indeed very short) lifetime and decay into particles with lower mass. Since particle lifetimes differ significantly across the board and the decay products vary, it has become increasingly pressing to find any conservation laws that apply. A symmetry with respect to $U(1)$ implies conservation of electric charge and hence conservation of *particle number*: $N_{\text{particles}} = N_{\text{matter}} - N_{\text{antimatter}}$. A virtual photon transition is a good example of this:

$$\gamma \rightarrow e^+ + e^- \quad (1.45)$$

However, for some known decays the conservation of energy or momentum did not seem to apply. A famous example of this is the β decay, which is a decay of neutrons inside atomic nuclei [Per00, p. 197]:

$$n \rightarrow p + e^- + ? \quad (1.46)$$

where the missing energy was attributed to some undetectable particle predicted by Wolfgang Pauli in 1931 and named later by Enrico Fermi as the *neutrino* ν . In case of the beta decay the missing particle proved to be an electron antineutrino $\bar{\nu}_e$. Since we are not able to see neutrinos directly (in a detector) they must interact very weakly or almost not at all and for this reason the interaction was called *weak*.

Obtaining direct evidence for the existence of neutrinos requires building very specific instruments since they rarely interact with the material. In general-purpose detectors neutrinos can only

be accounted for by measuring the missing energy or momentum in the collision products, see [section 2.3](#). Experiments dedicated to neutrino physics are designed to detect the Cherenkov radiation produced by electrons interacting with the neutrino inside the detector's substantive volume (e.g. Super-Kamiokande). Studying the behaviour of weak interactions is important especially because it does not seem to follow the symmetries that electromagnetic or strong interaction do obey.

In 1957 Chien-Shiung Wu conducted an experiment, where she was observing Cobalt 60 decay products in strong magnetic field at cryogenic temperatures. The experiment showed that a number of beta rays (e^-) detected by the experiment was different based on the orientation of the magnetic field. Consequently, parity in such interaction is not conserved, right and left are fundamentally different [Per00, pp. 81–82]. In light of this discovery, a new property has been established for particles called *helicity* which is the sign of the projection of particle spin \mathbf{S} or total angular momentum \mathbf{J} on the direction of its momentum. [Per00, pp. 19–20].

Since right-handed neutrinos were never detected, it has been concluded that all neutrinos are left-handed. However right-handed anti-neutrinos do exist, therefore neutrino helicity is symmetrical to $\hat{\mathbf{C}}\hat{\mathbf{P}}$, not just parity. No left-handed anti-neutrino was observed, thus we are left with two candidates for fundamental global symmetry: time and $\hat{\mathbf{C}}\hat{\mathbf{P}}$. The CPLEAR experiment at CERN later confirmed that T reversal is also not a fundamental symmetry and $\hat{\mathbf{C}}\hat{\mathbf{P}}$ followed it in 1964 in hands of James Cronin and Val Logsdon Fitch [MLM02, p. 9].

Based on the discovery of $\hat{\mathbf{C}}\hat{\mathbf{P}}$ violation Makoto Kobayashi and Toshihide Maskawa generalised former work of Nicola Cabibbo into the Cabibbo–Kobayashi–Maskawa matrix that describes the probability of transition from one quark to another under the weak interaction and predicted that there are at least three different generations of particles. This was confirmed by discovering of J/Ψ and Υ bound states [Aub+74] [Led79].

To summarize, the fundamental properties of weak interactions are:

- **Short distance:** weak force is extremely short distance: $G_f^{1/2} = 6.70 \times 10^{-18}$ m. Enrico Fermi tried to explain this with something analogous to QED, but with short ranged mediator. Because the range is limited by: $\Delta x \approx c\Delta t \approx \frac{\hbar}{p}$ it would require for that particle to have substantial mass $m_0 \approx 100$ GeV.
- **Helicity selective:** weak interaction only acts on left-handed particles and right-handed anti-particles.

1.3.2 Principles of electroweak unification

Following the principle of gauge invariance, it is possible to construct the theory based on the same principles. We know from experiments that all fermions have three generations. We have already discussed one family of particles: quarks in [section 1.2](#). The other family, *leptons* (from Greek $\lambda\epsilon\pi\tau\acute{o}\varsigma$, leptos, meaning “thin”), was constructed by regrouping particles that did not fit into the quark model. To unify electromagnetic and weak interactions we must bring neutrinos into the picture as well [Per00, p. 19].

If we arrange all fermions by flavour so that each of the three generations is represented in a pair of particles, we obtain the so called *weak doublets*. For leptons, one element of the doublet is a charged particle with non-zero mass refereed to as *charged lepton* and the other is neutral, nearly massless neutrino which bears corresponding designation. Electromagnetic interaction affects only

particles with non-zero electric charge and weak interaction acts on the entire left-handed (LH) doublet. All known leptons exist also as antiparticles, however neutrinos have only one helicity $H = -1$ and thus all doublets of anti-fermions are right-handed (RH). Quarks are arranged in a similar way.

Family	Flavour			e	Y [-]
leptons	$\begin{pmatrix} \nu_e \\ e \end{pmatrix}_L$	$\begin{pmatrix} \nu_\mu \\ \mu \end{pmatrix}_L$	$\begin{pmatrix} \nu_\tau \\ \tau \end{pmatrix}_L$	$\begin{pmatrix} 0 \\ -1 \end{pmatrix}$	$-\frac{1}{2}$
quarks	$\begin{pmatrix} u \\ d \end{pmatrix}_L$	$\begin{pmatrix} c \\ s \end{pmatrix}_L$	$\begin{pmatrix} t \\ b \end{pmatrix}_L$	$\begin{pmatrix} +\frac{2}{3} \\ -\frac{1}{3} \end{pmatrix}$	$\frac{1}{6}$

Table 1.2: Lepton and quark doublets arranged by generation (columns of two doublets) [Per00].

Because weak interaction act on a particle doublet we need something to act on the doublets that is built like a 2×2 matrix:

$$\frac{1}{2}\sigma_1 = \frac{1}{2} \begin{pmatrix} 0 & 1 \\ 1 & 0 \end{pmatrix}, \quad (1.47)$$

$$\frac{1}{2}\sigma_2 = \frac{1}{2} \begin{pmatrix} 0 & -i \\ i & 0 \end{pmatrix}. \quad (1.48)$$

where the structure of the matrices noticeably resembles $SU(2)$: σ_1 and σ_2 are 2×2 matrices, unitary with $\det \sigma_k = 1$. However $SU(2)$ has three generators, the third one being [MLM02, pp. 56–58]:

$$\frac{1}{2}\sigma_3 = \frac{1}{2} \begin{pmatrix} 1 & 0 \\ 0 & -1 \end{pmatrix}. \quad (1.49)$$

Consequently, we have 3 matrices, but only two weak interacting charged currents have been observed in β decay. Another problem is that the third matrix seems to be wrong if we used all of them to distribute electric charge. We can however fix this when we try to add what we already know from QED to combine $SU(2) \otimes U(1)$ and if we introduce the idea of *hypercharge* Y : The resulting group is:

$$G \equiv SU(2)_L \otimes U(1)_Y \quad (1.50)$$

where L refers to left-handed fields and Y is the *hypercharge*. Group $SU(2)$ has three generators, $U(1)$ has one generator that is in fact just a phase, so all together we have 4 gauge bosons. Two of them: W^+ , W^- do the charged current weak interaction and we are left with two other mediators. [MLM02, pp. 59–60]

From $U(1)$ we know that one of the two missing is a photon and using hypercharge Y we can adjust the matrices so that electric charge for leptons comes out correctly:

$$\frac{1}{2}\sigma_3 + Y = \frac{1}{2} \begin{pmatrix} \frac{1}{2} + Y & 0 \\ 0 & -\frac{1}{2} + Y \end{pmatrix}. \quad (1.51)$$

As for values of hypercharge Y , for leptons we need $Y = -\frac{1}{2}$ so that electric charges of the doublets come out correctly as $Q = I_3 + Y = 0$ or $Q = -1$. For quarks, we need $Y = \frac{1}{6}$ so that quark electric

Lepton symbol	Spin $s[\hbar]$	El. charge $ Q_e[e] $	Lifetime $t_l[s]$	Mass $m[\frac{\text{MeV}}{c^2}]$	Generation	Year of discovery	Anti-lepton symbol
e^-	$\pm\frac{1}{2}$	1	∞	0.511	1	1897	e^+
ν_e	$\pm\frac{1}{2}$	0	2.2×10^{-6}	< 0.000002	1	1956	$\bar{\nu}_e$
μ^-	$\pm\frac{1}{2}$	1	290.6×10^{-15}	105.66	2	1937	μ^+
ν_μ	$\pm\frac{1}{2}$	0	—	< 0.19	2	1962	$\bar{\nu}_\mu$
τ^-	$\pm\frac{1}{2}$	1	—	1777	3	1975	τ^+
ν_τ	$\pm\frac{1}{2}$	0	—	< 18.2	3	1995	$\bar{\nu}_\tau$

Table 1.3: The lepton family with all generations. Masses m increase with generation, lifetime τ decreases. Data from [Per00, p. 22], [Par12].

charges are $Q = +\frac{2}{3}$ and $Q = -\frac{1}{3}$. [MLM02, p. 58]

The last missing boson corresponds to the third generator and it was not identified until 1973 when Gargamelle found a *neutral current weak interaction* in the reaction $\nu_\mu + e^- \rightarrow \nu_\mu + e^-$. That is a new type of interaction mediated by a neutral boson which was named Z^0 . The masses of weak gauge bosons were predicted to $m_W \approx 80 \text{ GeV}$, $m_Z \approx 90 \text{ GeV}$. Precise measurements of W and Z bosons were eventually done at SppS and on CERN LEP in e^+e^- collisions by Carlo Rubbia and Simon van der Meer, see [UA183] [UA283].

The idea to intertwine electromagnetic and weak interactions in a single $SU(2)_L \otimes U(1)_Y$ gauge invariant framework was coined by S. L. Glashow, S. Weinberg and A. Salam in 1960s. Abelian theories describe symmetries formed by commutative groups $U(1)$ as in the example of QED. Yang and Mills introduced in 1954 the non-Abelian gauge transformations of groups $SU(N)$ and it has been shown that QED can be generalised. A compact summary of electroweak Lagrangian terms version can be found in [MLM02, pp. 59–61].

1.3.3 Particle classification according to particle family

Leptons are elementary particles with half-integer spin and are therefore fermions (Fermi-Dirac statistics). All leptons are subject to electroweak interactions, obey the conservation of lepton number L and their baryon number $B = 0$.

Quarks are also fermions but they combine to create other particles. Because of confinement, quarks are inseparable constituents of *hadrons*. All quarks are subject to electromagnetic, weak and strong interactions, obey the conservation of baryon number B and their lepton number $L = 0$.

Exchange particles act as force carriers in particle interactions. Each interaction has its own virtual exchange boson and fermions are surrounded by a cloud of these virtual particles creating an interaction field (see table 1.4).

1.3.4 Vector boson production

Since this thesis reports on the measurement of W pair cross-section, let us now focus on the W production mechanisms. W bosons decay into two fermions. The quark decay is referred to as

Mediated interaction	Mediator	Spin/Parity	Mass m [MeV]
electromagnetic	γ – photon	1^-	$m_\gamma = 0$
weak	W^+, W^-, Z^0 – vector bosons	$1^-, 1^+$	$m_W = 80.2, m_Z = 91.2$
strong	G – 8 gluons	1^-	$m_G = 0$
gravitational	g – graviton (?)	2^+	$m_g = ?$

Table 1.4: The boson mediators [Per00, p. 10].

hadronic, as the quarks immediately enter a bound state as discussed in section 1.2. The leptonic decay products consists of a charged lepton and a corresponding (anti)-neutrino. The *branching ratio* (BR) between the decay channels can be calculated from the decay widths:

$$\Gamma_{\text{tot}} = \Gamma(W^+ \rightarrow e^+ \nu_e) \left[3 + 3 \sum_{n=1}^2 \sum_{m=1}^3 |V_{nm}|^2 \right] \quad (1.52)$$

where the first term in square brackets corresponds to the three lepton families, and the second term is multiplied by 3 due to account for the three possible quark colours. The first sum runs only over the first two generations, because the W mass is insufficient to produce the massive top quark. The $|V_{nm}|$ represents element of the CKM matrix. If we exploit its unitarity we can express:

$$\sum_{n=1}^2 \sum_{m=1}^3 |V_{nm}|^2 = \sum_{n=1}^2 [V V^\dagger]_{nn} = 2 \quad (1.53)$$

which allows us to simply compute the *branching ratios* $R_i = \Gamma_i / \Gamma_{\text{tot}}$ without actually knowing the value of $\Gamma(W^+ \rightarrow e^+ \nu_e)$ decay width, see table 1.5. Now the possible WW decay channels are:

- **Fully hadronic** when both W bosons decay into quark pairs. This channel is clearly characterized by four light jets and two b-jets.
- **Lepton and a jet** when one W decays into leptons and the other decays into a quark pair. These events are characterised by an isolated lepton (electron or muon), *missing transverse energy* \cancel{E}_T from the escaped neutrino and by two light jets and two b-jets.
- **Dilepton** when both W bosons decay into lepton pairs. This channel yields to high- p_T isolated leptons (electrons or muons) and a large *missing transverse energy* from the two neutrinos.

Decay mode	Expected	Measured
$e^+ \nu_e$	11.11 %	$(10.75 \pm 0.13) \%$
$\mu^+ \nu_\mu$	11.11 %	$(10.57 \pm 0.15) \%$
$\tau^+ \nu_\tau$	11.11 %	$(11.25 \pm 0.20) \%$
hadrons	66.77 %	$(67.60 \pm 0.27) \%$

Table 1.5: Branching ratios of W^+ decay modes. Data from [Par12]

1.4 Construction of the Standard Model

The [Standard Model](#) of particle physics is constructed as a $SU(3)_C \otimes SU(2)_L \otimes U(1)_Y$ gauge theory that describes the strong, weak and electromagnetic interactions. It was formulated in 1970s and it is the best theory we have to date because it accounts for nearly all experimental data from particle physics. Theoretical framework is built by relativistic quantum field theories that are capable of extremely precise predictions. Electroweak theory has been verified down to a few parts in a thousand and perturbative QCD to a few percent. All particles predicted by the [Standard Model](#) have been discovered.

Standard Model postulates that all matter in the Universe can be built from 24 fundamental building blocks (*fermions*): six *quarks*, six *leptons* and their respective anti-particles. These particles interact with each other in three distinctive types of interactions mediated by 12 characteristic *gauge bosons* [Per00, pp. 7–12].

1.4.1 Particle classification according to fundamental interaction

Electromagnetic interactions repels electrically like-charged particles and accounts for all electromagnetic phenomena. It is mediated by a massless gauge boson – γ photon.

Weak interactions affect all left-handed fermions and right-handed anti-fermions as well as W and Z bosons (it does not affect gluons or photons). It is capable of violating parity symmetry and changing flavour through the means of particle decay. It is mediated by massive charged current W^+ , W^- and neutral current Z^0 bosons

Strong interactions bound all the atomic nuclei together. The strong force binds the quarks in neutrons and protons, and the neutrons and protons within nuclei. It is the strongest of all interactions and is colour charge selective: it affects only gluons, quarks and their products.

Gravitational interactions occur between all with non-zero energy. It is not incorporated into the Standard Model because there is currently no evidence for gravitational gauge bosons. Instead the interaction is described by general theory of relativity using curved spacetime. Amongst all interactions it is thoroughly dominant on macro-scale level as a long-range attractive force.

interactions	Electromagnetic	Weak	Strong	Gravitational
internal symmetry	$U(1)_Y$	$SU(2)_L$	$SU(3)_C$	–
gauge boson	photon γ	W^+ , W^- , Z^0	8 gluons G	graviton (?)
range	∞	10^{-18} m	$\leq 10^{-15}$ m	∞
source	electric charge	weak charge	colour charge	mass
coupling constant α	$\frac{Q_e}{4\pi\hbar\epsilon_0 c} = \frac{1}{137}$	$\frac{G(Mc^2)^2}{\hbar^2 c^2} \approx 10^{-5}$	≤ 1	$\frac{G_N M^2}{4\pi\hbar c} \approx 10^{-40}$
typical cross-section σ	10^{-33} m ²	10^{-39} m ²	10^{-30} m ²	–
typical lifetime τ	10^{-20} s	10^{-10} s	10^{-23} s	–

Table 1.6: Fundamental interactions. Data from [Per00, p. 52]

The Standard Model describes all these interactions (with the exception of gravity) in a single mainframe. All elementary particles summarised in [table 1.7](#).

mass →	$\approx 2.3 \text{ MeV}/c^2$	$\approx 1.275 \text{ GeV}/c^2$	$\approx 173.07 \text{ GeV}/c^2$	0	$\approx 126 \text{ GeV}/c^2$
charge →	$2/3$	$2/3$	$2/3$	0	0
spin →	$1/2$	$1/2$	$1/2$	1	0
	u up	c charm	t top	g gluon	H Higgs boson
QUARKS	$\approx 4.8 \text{ MeV}/c^2$ $-1/3$ $1/2$ d down	$\approx 95 \text{ MeV}/c^2$ $-1/3$ $1/2$ s strange	$\approx 4.18 \text{ GeV}/c^2$ $-1/3$ $1/2$ b bottom	0 0 1 γ photon	
	$0.511 \text{ MeV}/c^2$ -1 $1/2$ e electron	$105.7 \text{ MeV}/c^2$ -1 $1/2$ μ muon	$1.777 \text{ GeV}/c^2$ -1 $1/2$ τ tau	91.2 GeV/c ² 0 1 Z Z boson	
LEPTONS	$< 2.2 \text{ eV}/c^2$ 0 $1/2$ ν_e electron neutrino	$< 0.17 \text{ MeV}/c^2$ 0 $1/2$ ν_μ muon neutrino	$< 15.5 \text{ MeV}/c^2$ 0 $1/2$ ν_τ tau neutrino	$80.4 \text{ GeV}/c^2$ ± 1 1 W W boson	GAUGE BOSONS

Table 1.7: Summary of Standard Model fundamental particles. Figure from Wikipedia.

1.4.2 Integrity of the Standard Model

It has been shown how the procedure of gauge invariance can be used to reveal interaction fields and what symmetries the Standard Model uses to represent these interactions. Another integral part the Standard Model is the mechanism of *spontaneous symmetry breaking* (SSB). The reason behind this connection is the pattern of masses observed for leptons and weak interacting gauge bosons. The different transformation properties of left and right handed doublets disallow for any mass terms in the Lagrangian, because their presence breaks the gauge invariance.

In principle, SSB adds specific terms to the **SM** Lagrangian that have all required gauge symmetries but can evolve into a specific stable state where some internal symmetry is broken. For each breaking we obtain a mass term and at least one massive scalar boson we call *Higgs*. In case of the Standard Model the breaking is $SU(3) \otimes SU(2) \otimes U(1) \rightarrow SU(3) \otimes U(1)$ and the Lagrangian is left with exactly three mass terms for W and Z bosons and no mass term for the photon. Masses of fermions are obtained through Yukawa mechanism which ensures the Higgs couples correctly to LH and RH doublets. Because of this the Higgs boson is a necessary integral part of the model for it to work correctly at higher energies [MLM02, pp. 61–65].

The **Standard Model** has been examined by numerous experimental tests. The experimentally observed particles it has predicted and indicated the experiments that discovered them. From the more recent experiments, the Large Electron–Positron Collider at CERN largely contributed to experimental verification by precisely measuring specific values like the mass of the **Z** and **W** bosons.

For some of its internal problems the Standard Model is not regarded as a complete theoretical framework. There are new theories like *supersymmetries* (SUSY) and other unification theories that provide an extension to the Standard Model. SUSY introduce superpartners to all elementary particles to answer the problem of mass, see [MLM02, pp. 147–190]. Attempts also exist to answer the question about SM choice of group representation for example by unifying the electro-weak theory with quantum chromodynamics in a single field as $SU(5)$, $SU(10)$ etc., the resulting model is called the *Grand Unification Theory*.

Another problem is gravitation and cosmology. *String theories* propose a mechanism to intertwine quantum field theory with general relativity. This should bring us a unified theory for all fundamental interactions and explain the origin of dark matter and dark energy which causes problems in modern cosmologies where the difference between theoretical prediction and experiment is of the order of 10^{120} .

1.5 Basics of statistical inference

Generally, experimental measurements in particle physics do not provide a single sharp value that could be used to dismiss a given hypothesis. A certain degree of randomness is always involved, mainly due to the fact that quantum theory is inherently non-deterministic. Coincidentally, any measurement in any sort of experiment always comes with random measurement errors. In principle, it would be possible to eliminate these experimental limitations, provided there were no engineering and cost limitations.

In mathematics we express randomness with the concept of *probability*. Probability \mathcal{P} is defined as a real mapping that for arbitrary sets of random events lies on the interval $\mathcal{P} \in \langle 0, 1 \rangle$. Sum of all probabilities over all possible results is equal to 1 (certainty). One can then define joint probability $\mathcal{P}(A, B)$ and conditional probability $\mathcal{P}(A|B)$ and from it derive the Bayes theorem. Very comprehensive introduction to statistics by Glen Cowan [Cow98], for technical reference see [Par12, pp. 386–402]

In statistics two interpretations of probability are widely used [Cow98, pp. 1–2]. Consider the *sample space* S with subsets denoted A and B :

- a) **Laplace model** which interprets sets A and B as outcomes of a repeatable experiment. The probability $P(A)$ resp. $P(B)$ is given as the frequency of this outcome, hence this approach is also referred to as *frequentist statistics*:

$$P(A) = \lim_{N \rightarrow \infty} \frac{N(\text{outcome is } A)}{N} \quad (1.54)$$

$$P(B) = \lim_{N \rightarrow \infty} \frac{N(\text{outcome is } B)}{N} \quad (1.55)$$

- b) **Kolmogorov model** where sets A and B are hypotheses, i.e. statements that are true or untrue. The probability $P(A)$ resp. $P(B)$ represents the degree of belief that hypothesis A resp. B is true. This approach is referred to as *subjective probability*.

1.5.1 Random variable

The frequentist interpretation implied in eq. (1.55) describes the probability of outcome A as a relative frequency of outcomes belonging to set A . Repeating the experiment will give outcomes from A with probability $P(A)$. Consider a simplified example in flipping a coin. The probability of obtaining heads while flipping twice is the same as probability for flipping two coins. These events can be described in terms of a *random variable*, provided we take a step back from physical reality and talk only about numerical values attributed to the individual outcomes. [Cow98, p. 7]

A random variable X is a numerical assessment of individual outcomes from an arbitrary set of events that attributes a number and individual probability to each outcome. Values attributed to X can be:

a) **discrete** $x_i \in X$, where $i = 1, 2, \dots$, then random variable is:

$$P_X(x_i) = p_i \quad (1.56)$$

$$\sum_i P(x_i) = 1 \quad (1.57)$$

b) **continuous** x defined by the *probability density* (PDF) function $F : \mathbb{R} \rightarrow \langle 0, 1 \rangle$:

$$P_X(\text{that value } x \text{ can be found in } [x, x + dx]) = f(x) dx \quad (1.58)$$

$$\text{and } \int_{-\infty}^{\infty} f(x) dx = 1, \text{ } x \text{ must found somewhere} \quad (1.59)$$

Probability density functions or *cumulative distribution function* (CDF) $F(x) = \int_{-\infty}^x f(a) da$ or $F(x) = \sum_{x_i \leq x} p(x_i)$ give a complete description of random variable distribution. These distributions are different for each random variable and from experiment to experiment but fall into a limited number of basic patters which can be described analytically. A comprehensive overview of analytical PDFs is provided in [Par12, p. 257] and [Cow98, pp. 26–37]. Since functions of random variables are also random variables, we can define joint PDF $f(x, y)$ and conditional PDF as one can do for probability $f(x|y) = f(x, y)/f(y)$.

The main goal of statistical analysis is to find a sufficient way of characterising a particular distribution. These characteristics are referred to as *random variable moments*, more commonly referred to as simply the “width” or “shape”. The first raw moment is called *expected value* given as:

$$E(X) = \int_{-\infty}^{+\infty} x f(x) dx \quad \text{or} \quad E(X) = \sum_i x_i P_X(x_i) \quad (1.60)$$

Another important characteristic is the first central moment or *variance* $D(X)$:

$$D(X) = E([X - E(X)]^2) = \sigma(X)^2 \quad (1.61)$$

$$\text{where } E(X^2) = \int_{-\infty}^{+\infty} x^2 f(x) dx \quad \text{or} \quad E(X^2) = \sum_i x_i^2 P_X(x_i) \quad (1.62)$$

where $\sigma(X)$ is the *standard deviation* σ defined as its square root. Other higher order moments can be defined such as *skewness* (third central moment) or *kurtosis* (fourth central moment), see [Par12, p. 386].

1.5.2 Parameter estimation

The validity of a given statistical model is verified from the experimental data. One starts with a general model to describe the observations, but the actual parameters θ_i of the PDFs are often unknown. Parameter *estimators* denoted $\hat{\theta}_i$ are functions of the dataset used to guess the probable value of some PDF parameter θ_i [Cow98, p. 64].

Suppose we have a set of N independent unbiased measurements x_i of some unknown quantity μ . The most common is the *arithmetic mean* estimator:

$$\hat{\mu} = \frac{1}{N} \sum_{i=1}^N x_i \quad (1.63)$$

which for $N \rightarrow \infty$ gives unbiased expected value: $\hat{\mu} \rightarrow \mu$. Variance can be estimated by the *variance estimator*:

$$\hat{\sigma}^2 = \frac{1}{N-1} \sum_{i=1}^N (x_i - \mu)^2 \quad (1.64)$$

which for $N \rightarrow \infty$ gives unbiased variance: $\hat{\sigma}^2 \rightarrow \sigma^2$.

Both $\hat{\mu}$ and $\hat{\sigma}^2$ have their own variance (error of estimation and error of this error). If x_i have different known variances σ_i^2 , weighted average must be used to obtain a more efficient estimator.

1.5.2.1 Maximum likelihood estimation

By definition, probability distributions can be used to predict unknown outcomes based on known parameters of the distribution. The concept of *likelihood* inverts the problem, it allows us to estimate unknown distribution parameters from the known outcomes of the experiment. The *maximum likelihood* estimation is one of the most generally used of parameter estimation as it allows to estimate parameters even if there is no apriori knowledge about the distribution.

Suppose we have a set of N independent measurements x_i described by a joint PDF $f(x_i, \theta_o)$ where θ_i is a set of M unknown parameters from an identical distribution. Because the measurements x_i are independent, then their joint PDF factorises and the likelihood function is:

$$L(\theta_i) = \prod_{i=1}^N f(x_i, \theta_i) \quad (1.65)$$

The method of maximum likelihood finds estimators $\hat{\theta}_i$ to be those values of θ_i that maximise the likelihood $L(\theta_i)$: $\hat{\theta}_i = \arg \max_{\theta_i} L(\theta_i)$

Since it is usually easier to work with *log-likelihood* $\ln(L)$, the maximum likelihood estimate can be found by solving *M likelihood equations*:

$$\frac{\partial \ln(L)}{\partial \theta_i} = 0 \quad (1.66)$$

whose solutions are the parameters of the given PDF. [Par12, p. 393]. Other estimation methods exist: the common *least square method* which coincides with maximum likelihood in special cases or Bayesian estimation which requires apriori knowledge of the measured PDF [Par12, pp. 393–401]. The maximum likelihood estimation is used to extrapolate the WW [cross-section](#), see [section 4.10](#).

1.6 References

- [HFG08] D. Hanneke, S. Fogwell, and G. Gabrielse. “New Measurement of the Electron Magnetic Moment and the Fine Structure Constant”. In: *Physical Review Letters* 100.12 (Mar. 2008), p. 120801. ISSN: 0031-9007. DOI: [10.1103/PhysRevLett.100.120801](https://doi.org/10.1103/PhysRevLett.100.120801). arXiv: [0801.1134](https://arxiv.org/abs/0801.1134) (cit. on p. 2).
- [Gla61] Sheldon L. Glashow. “Partial-symmetries of weak interactions”. In: *Nuclear Physics* 22.4 (Feb. 1961), pp. 579–588. ISSN: 00295582. DOI: [10.1016/0029-5582\(61\)90469-2](https://doi.org/10.1016/0029-5582(61)90469-2) (cit. on p. 2).
- [Wei67] Steven Weinberg. “A Model of Leptons”. In: *Physical Review Letters* 19.21 (Nov. 1967), pp. 1264–1266. ISSN: 0031-9007. DOI: [10.1103/PhysRevLett.19.1264](https://doi.org/10.1103/PhysRevLett.19.1264) (cit. on p. 2).
- [Sal68] Abdus Salam. “Weak and Electromagnetic Interactions”. In: *Conf.Proc.* C680519 (1968), pp. 367–377 (cit. on p. 2).
- [ATL12] ATLAS Collaboration. “Observation of a new particle in the search for the Standard Model Higgs boson with the ATLAS detector at the LHC”. In: *Physics Letters B* 716.1 (Sept. 2012), pp. 1–29. ISSN: 03702693. DOI: [10.1016/j.physletb.2012.08.020](https://doi.org/10.1016/j.physletb.2012.08.020). arXiv: [1207.7214](https://arxiv.org/abs/1207.7214) (cit. on p. 2).
- [CMS12] CMS Collaboration. “Observation of a new boson at a mass of 125 GeV with the CMS experiment at the LHC”. In: *Physics Letters B* 716.1 (Sept. 2012), pp. 30–61. ISSN: 03702693. DOI: [10.1016/j.physletb.2012.08.021](https://doi.org/10.1016/j.physletb.2012.08.021). arXiv: [1207.7235](https://arxiv.org/abs/1207.7235) (cit. on p. 2).
- [Cur94] Pierre Curie. “Sur la symétrie dans les phénomènes physiques, symétrie d’un champ électrique et d’un champ magnétique”. fr. In: *Journal de Physique Théorique et Appliquée* 3.1 (1894), pp. 393–415. DOI: [10.1051/jphystap:018940030039300](https://doi.org/10.1051/jphystap:018940030039300) (cit. on p. 2).
- [Noe18] Emmy Noether. “Invariante Variationsprobleme”. In: *Gött. Nachr.* (1918), pp. 235–257 (cit. on p. 3).
- [Pic07] Antonio Pich. “The Standard Model of Electroweak Interactions”. In: (May 2007), p. 50. arXiv: [0705.4264](https://arxiv.org/abs/0705.4264) (cit. on pp. 3–5, 7, 9).
- [PS95] Michael E. Peskin and Dan V. Schroeder. *An Introduction To Quantum Field Theory*. Westview Press; First Edition edition, 1995, p. 864. ISBN: 0201503972 (cit. on pp. 3, 4, 9, 10, 16).
- [Kan93] Gordon Kane. *Modern Elementary Particle Physics: Updated Edition*. Upd Sub (A. Westview Press, 1993, p. 352. ISBN: 0201624605 (cit. on p. 5).
- [Pau25] W. Pauli. “Über den Zusammenhang des Abschlusses der Elektronengruppen im Atom mit der Komplexstruktur der Spektren”. In: *Zeitschrift für Physik* 31.1 (Feb. 1925), pp. 765–783. ISSN: 0044-3328. DOI: [10.1007/BF02980631](https://doi.org/10.1007/BF02980631) (cit. on p. 5).
- [GS22] Walther Gerlach and Otto Stern. “Das magnetische Moment des Silberatoms”. In: *Zeitschrift für Physik* 9.1 (Dec. 1922), pp. 353–355. ISSN: 1434-6001. DOI: [10.1007/BF01326984](https://doi.org/10.1007/BF01326984) (cit. on p. 6).

- [Per00] Donald H. Perkins. *Introduction to High Energy Physics*. 4th. Cambridge University Press, 2000, p. 426. ISBN: 0521621968 (cit. on pp. 6, 11–13, 15–21).
- [MLM02] T. Morii, C. S. Lim, and S. N. Mukherjee. *The Physics of the Standard Model and Beyond*. World Scientific Pub Co Inc, 2002, p. 312. ISBN: 9810245718 (cit. on pp. 7, 8, 11, 13–15, 17–19, 22, 23).
- [Fey49] R. Feynman. “Space-Time Approach to Quantum Electrodynamics”. In: *Physical Review* 76.6 (Sept. 1949), pp. 769–789. ISSN: 0031-899X. DOI: [10.1103/PhysRev.76.769](https://doi.org/10.1103/PhysRev.76.769) (cit. on p. 9).
- [Fey50] R. Feynman. “Mathematical Formulation of the Quantum Theory of Electromagnetic Interaction”. In: *Physical Review* 80.3 (Nov. 1950), pp. 440–457. ISSN: 0031-899X. DOI: [10.1103/PhysRev.80.440](https://doi.org/10.1103/PhysRev.80.440) (cit. on p. 9).
- [Sch48] Julian Schwinger. “On Quantum-Electrodynamics and the Magnetic Moment of the Electron”. In: *Physical Review* 73.4 (Feb. 1948), pp. 416–417. ISSN: 0031-899X. DOI: [10.1103/PhysRev.73.416](https://doi.org/10.1103/PhysRev.73.416) (cit. on p. 9).
- [Tom49] S. Tomonaga. “On a Relativistically Invariant Formulation of the Quantum Theory of Wave Fields”. In: *Progress of Theoretical Physics* 1.2 (Feb. 1949), pp. 27–42. ISSN: 0033-068X. DOI: [10.1143/PTP.1.27](https://doi.org/10.1143/PTP.1.27) (cit. on p. 9).
- [HM85] Francis Halzen and Alan D. Martin. *Quarks and Leptons: An Introductory Course in Modern Particle Physics*. 1985. DOI: [10.1119/1.14146](https://doi.org/10.1119/1.14146) (cit. on pp. 9, 10).
- [LB14] Tom Lancaster and Stephen J. Blundell. *Quantum Field Theory for the Gifted Amateur*. 2014. ISBN: 0191510939 (cit. on p. 9).
- [Aub+74] J. Aubert, U. Becker, P. Biggs, J. Burger, M. Chen, G. Everhart, P. Goldhagen, J. Leong, T. McCorriston, T. Rhoades, M. Rohde, Samuel Ting, Sau Wu, and Y. Lee. “Experimental Observation of a Heavy Particle J”. In: *Physical Review Letters* 33.23 (Dec. 1974), pp. 1404–1406. ISSN: 0031-9007. DOI: [10.1103/PhysRevLett.33.1404](https://doi.org/10.1103/PhysRevLett.33.1404) (cit. on pp. 11, 13, 17).
- [UA183] UA1 Collaboration. “Experimental observation of isolated large transverse energy electrons with associated missing energy at”. In: *Physics Letters B* 122.1 (Feb. 1983), pp. 103–116. ISSN: 03702693. DOI: [10.1016/0370-2693\(83\)91177-2](https://doi.org/10.1016/0370-2693(83)91177-2) (cit. on pp. 11, 19).
- [Gel64] Murray Gell-Mann. “A schematic model of baryons and mesons”. In: *Physics Letters* 8.3 (Feb. 1964), pp. 214–215. ISSN: 00319163. DOI: [10.1016/S0031-9163\(64\)92001-3](https://doi.org/10.1016/S0031-9163(64)92001-3) (cit. on p. 11).
- [Zwe64a] George Zweig. “An SU_3 model for strong interaction symmetry and its breaking”. In: (Jan. 1964) (cit. on p. 11).
- [Zwe64b] George Zweig. “An SU_3 model for strong interaction symmetry and its breaking”. In: (Feb. 1964) (cit. on p. 11).
- [Kul14] Petr Kulhánek. *Aldebaran Group for Astrophysics webpage*. 2014. Available at: <http://www.aldebaran.cz/>, visited on 07/20/2014 (cit. on p. 12).

- [Gre64] O. Greenberg. “Spin and Unitary-Spin Independence in a Paraquark Model of Baryons and Mesons”. In: *Physical Review Letters* 13.20 (Nov. 1964), pp. 598–602. ISSN: 0031-9007. DOI: [10.1103/PhysRevLett.13.598](https://doi.org/10.1103/PhysRevLett.13.598) (cit. on pp. 12, 13).
- [Aug+74] J. Augustin, A. Boyarski, M. Breidenbach, F. Bulos, J. Dakin, G. Feldman, G. Fischer, D. Fryberger, G. Hanson, B. Jean-Marie, R. Larsen, V. Lüth, H. Lynch, D. Lyon, C. Morehouse, J. Paterson, M. Perl, B. Richter, P. Rapidis, R. Schwitters, W. Tanenbaum, F. Vannucci, G. Abrams, D. Briggs, W. Chinowsky, C. Friedberg, G. Goldhaber, R. Hollebeek, J. Kadyk, B. Lulu, F. Pierre, G. Trilling, J. Whitaker, J. Wiss, and J. Zipse. “Discovery of a Narrow Resonance in e^+e^- Annihilation”. In: *Physical Review Letters* 33.23 (Dec. 1974), pp. 1406–1408. ISSN: 0031-9007. DOI: [10.1103/PhysRevLett.33.1406](https://doi.org/10.1103/PhysRevLett.33.1406) (cit. on p. 13).
- [Led79] Leon M Lederman. “Resonant and Continuum Dilepton Production”. en. In: *Physica Scripta* 20.2 (Aug. 1979), pp. 227–234. ISSN: 0031-8949. DOI: [10.1088/0031-8949/20/2/016](https://doi.org/10.1088/0031-8949/20/2/016) (cit. on pp. 13, 17).
- [CDF95] CDF Collaboration. “Observation of Top Quark Production in $p\bar{p}$ Collisions with the Collider Detector at Fermilab”. In: *Physical Review Letters* 74.14 (Apr. 1995), pp. 2626–2631. ISSN: 0031-9007. DOI: [10.1103/PhysRevLett.74.2626](https://doi.org/10.1103/PhysRevLett.74.2626) (cit. on p. 13).
- [Par13] Particle Data Group. “Review of Particle Physics”. In: *Physical Review D* (2013) (cit. on p. 13).
- [HN65] M. Y. Han and Y. Nambu. “Three-Triplet Model with Double SU(3) Symmetry”. In: *Physical Review* 139.4B (Aug. 1965), B1006–B1010. ISSN: 0031-899X. DOI: [10.1103/PhysRev.139.B1006](https://doi.org/10.1103/PhysRev.139.B1006) (cit. on p. 13).
- [Pol73] H. Politzer. “Reliable Perturbative Results for Strong Interactions?” In: *Physical Review Letters* 30.26 (June 1973), pp. 1346–1349. ISSN: 0031-9007. DOI: [10.1103/PhysRevLett.30.1346](https://doi.org/10.1103/PhysRevLett.30.1346) (cit. on p. 15).
- [GW73] David Gross and Frank Wilczek. “Ultraviolet Behavior of Non-Abelian Gauge Theories”. In: *Physical Review Letters* 30.26 (June 1973), pp. 1343–1346. ISSN: 0031-9007. DOI: [10.1103/PhysRevLett.30.1343](https://doi.org/10.1103/PhysRevLett.30.1343) (cit. on p. 15).
- [UA283] UA2 Collaboration. “Observation of single isolated electrons of high transverse momentum in events with missing transverse energy at the CERN p collider”. In: *Physics Letters B* 122.5-6 (Mar. 1983), pp. 476–485. ISSN: 03702693. DOI: [10.1016/0370-2693\(83\)91605-2](https://doi.org/10.1016/0370-2693(83)91605-2) (cit. on p. 19).
- [Par12] Particle Data Group. “Review of Particle Physics”. In: *Physical Review D* 86.1 (July 2012), p. 010001. ISSN: 1550-7998. DOI: [10.1103/PhysRevD.86.010001](https://doi.org/10.1103/PhysRevD.86.010001) (cit. on pp. 19, 20, 23–25).
- [Cow98] Glen Cowan. *Statistical Data Analysis*. Cowan1998: Oxford University Press, 1998, p. 216. ISBN: 0198501552 (cit. on pp. 23–25).

EXPERIMENTAL BACKGROUND

Contents

2.1	Particle accelerators	30
2.1.1	Accelerator geometry	31
2.1.2	Accelerator kinematics	32
2.1.3	Accelerator dynamics	34
2.1.4	Luminosity and interaction rate	40
2.2	Large Hadron Collider	43
2.2.1	Current performance	45
2.2.2	Performance goals	45
2.2.3	Injection chain	47
2.2.4	Lattice layout	48
2.3	Detector systems	51
2.3.1	Large hybrid detector systems	51
2.3.2	Measurement nomenclature	52
2.4	Experiments at the LHC	54
2.4.1	General purpose experiments: ATLAS and CMS	54
2.4.2	CMS (Compact Muon Solenoid)	54
2.4.3	ALICE (A Large Ion Collider Experiment)	55
2.4.4	LHCb (Large Hadron Collider beauty)	57
2.4.5	TOTEM (TOTal Elastic and diffractive cross section Measurement)	57
2.4.6	LHCf (Large Hadron Collider forward)	59
2.4.7	MoEDAL (Monopole and Exotics Detector at the LHC)	59
2.5	The ATLAS Experiment	59
2.5.1	General layout	60
2.5.2	ATLAS coordinate system	60
2.5.3	Magnet system	61
2.5.4	Inner Detector	63
2.5.5	Calorimetry	70
2.5.6	Muon spectrometer	77
2.5.7	Forward detectors	80
2.6	Experimental conditions	80
2.6.1	Calibration and alignment	80
2.6.2	Delivered luminosity	82
2.6.3	Pile-up	85
2.7	References	87

TESTING THEORETICAL PREDICTIONS in the field of particle physics requires building extraordinary scientific instruments. We have shown in [chapter 1](#) that the [Standard Model](#) has been built to explain the characteristics and behaviour of elementary particles. The goal of *theoretical physics* is to provide a testable hypothesis that explains the behaviour we observe in nature which is then tested by independent repeatable experiments.

Our objective here is the study of the fundamental constituents of matter at a scale of 10^{-18} m and below. The attainable resolution is fundamentally limited by the characteristics of what we implement as the *probe*. Light microscopes cannot probe deeper than the scale limit given by the Rayleigh criterion. Our ability to probe objects on smaller scales comes, at least conceptually, from the fact that particles behave as waves. As implied by the wave-particle duality of quantum mechanics, the frequency of the wave scales with its energy. Higher frequency equals shorter wavelength and thus better resolution: $E = \hbar\omega = \frac{2\pi\hbar}{\lambda}$. More importantly, high-energy collisions produce secondary particles from the kinetic energy of the incident particles. It is for this reason that there is a certain overlap between the term particle physics and *high energy physics*.

High energy particles do exist in nature and have been observed in cosmic rays. In fact, observations of cosmic rays directly led to the discovery of muon and positron. However the event rate of high-energy cosmic rays colliding with a fixed target is too small for us to be able to investigate processes with small production [cross-sections](#). Instead, we have to build machines that will allow us to collide particles at high energies and observe the results directly. Niels Bohr stated the simple truth about these experiments in his speech on February 5, 1960:

“It may perhaps seem odd that apparatus as big and as complex as our gigantic proton synchrotron is needed for the investigation of the smallest objects we know about. However, just as the wave features of light propagation make huge telescopes necessary for the measurement of small angles between rays from distant stars, so the very character of the laws governing the properties of the many new elementary particles which have been discovered in recent years, and especially their transmutations in violent collisions, can only be studied using atomic particles accelerated to immense energies.”

In this chapter we are going to provide detailed description of the experimental apparatus used to produce and record data used in the analysis described in [chapter 4](#). We describe the production and measurement of particle collisions in separate sections and we dedicate individual sections to the description of the [Large Hadron Collider \(LHC\)](#) and the [ATLAS experiment \(A Toroidal LHC ApparatuS\)](#).

2.1 Particle accelerators

All accelerator machines work on the same basic principle: they use electro-magnetic fields to accelerate particles to high energies and to contain them in well defined stream along the *design path* until they hit their target. This is the reason why particle physics is sometimes referred to as [High-energy physics \(HEP\)](#). Accelerator physics and engineering is an independent field with many excellent books and lectures covering the subject, for example the book by [Klaus Wille and Jason McFall \[WM01\]](#), overview in [[Par12](#), ch. 27], [[Bai07](#)] and the classic by [E.D. Courant and H.S. Snyder \[CS00\]](#).

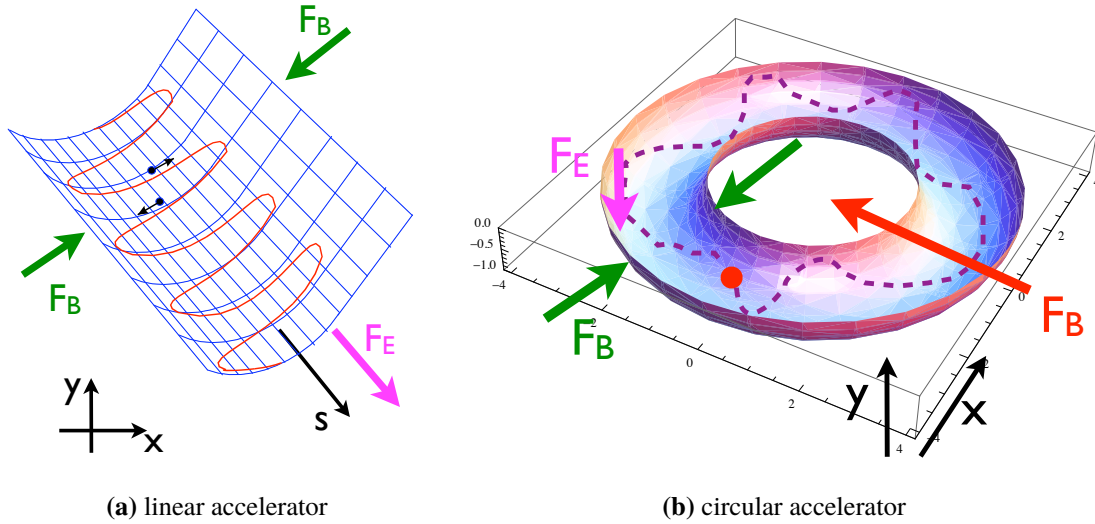


Figure 2.1: Geometric arrangement of particle accelerators. Figures from [Gil13, p. 9].

Probe particles have to satisfy two criteria: they have to be charged and they have to remain stable until they collide. Electrons, protons or heavy ions are ideal probe candidates, although recent discoveries in particle physics have sparked initiative in design of “Higgs factory” accelerators that would collide muons [Fer14]. There is also recent interest in obtaining experimental evidence for the creation of electron-positron pairs in collision of two photons which could be observed in future photon-photon colliders. [Pik+14]

Looking back at the design implemented by John Douglas Cockcroft and Ernest Thomas Sinton Walton [CW32] in 1932, the simplest solution for an accelerator machine is a direct current (DC) voltage multiplier or a Van de Graaf accelerator. The main problem with both of these designs is that they are limited by the potential difference that can be held between the charged surfaces. Realistically, this provides the maximum accelerating voltage of the order of $\approx 10 \text{ MV m}^{-1}$ [Per00, p. 341] meaning the particles are accelerated to energies of the order of MeV. To avoid these issues, Rolf Wideröe has come up in 1928 Rolf Wideröe [Wid28] with a design that uses high frequency (RF) alternating current (AC) sources to carefully time a bunch of particles to get a succession of accelerating kicks from a series of accelerating elements with relatively small potential differences. [Per00, p. 338].

2.1.1 Accelerator geometry

Particle accelerators produce and accelerate streams of particles in a well confined space within a collection referred to as the *beam*. The *bending force* acting on the beam is given by the Lorentz force in eq. (2.1) is produced by the magnetic dipoles, the *focusing force* is enforced by magnetic multi-poles (quadrupoles). The accelerating elements can be arranged in two ways:

Linear accelerator (*linac*, see fig. 2.1a) is made out of a series of oscillating electric potential that accelerate particles along a linear beam line. The final beam energy depends on the accelerator total length and voltage per cavity. Most linacs typically produce fields of a few MeV per metre. [Per00, p. 338]. Given their limitations, linear accelerators are mostly used as a part of synchrotron injection system. The 3.20 km long linear accelerator at SLAC is

the largest linac in the world producing electron and positron beams with peak energies of about 50 GeV [SLA]. Linacs have many practical applications in electrical engineering and radiation. A simple linear accelerator is present in every CRT screen or lamp electrode.

Circular accelerator is a design descended from the *cyclotron*, where particle are accelerated along a spiral path inside a static magnetic field. Modern-day circular accelerators are almost exclusively *synchrotrons* (see fig. 2.1b) where the beam pipes are shaped in a torus. This allows for repeated acceleration of particles as they circulate along the beam line with revolution frequency f_{rev} . In order to exceed the rest mass of most particles, one has to arrange that both magnetic field \mathbf{B} and the revolution frequency f_{rev} increase in synchronisation with particle velocity v as they accelerate, hence the name *synchrotron*. The final beam energy depends on the ring radius and peak strength of the magnetic field. Using superconducting magnets is possible to surpass TeV scale [Per00, p. 339].

The term *storage ring* is sometimes used to describe a circular accelerator that can contain the particle beam for a significant time (hours in general). The storage ring mainly consists of dipole magnets that provide beam confinement in the desired volume and higher order multi-poles (quadrupoles) which are used to correct for instabilities [Per00, p. 341]. Linacs are generally built in a straight line which means bending particle trajectory is not required, instead *collimators* are employed to shape the beam.

Construction and maintenance modern-day particle accelerators requires a large of collaboration of scientists, years of research and development with generous funding. The construction of LHC took more than 10 years with the collaborative support from CERN, United States, Japan, Russia, Canada and India.

2.1.2 Accelerator kinematics

The particle beam is constrained in a vacuum pipe that passes through a succession of electromagnets and accelerating cavities called *lattice*. A charged particle moving through a magnetic field experiences a *bending force* given by the equation for the Lorentz force

$$\mathbf{F} = e \cdot (\mathbf{E} + \mathbf{v} \times \mathbf{B}), \quad (2.1)$$

where \mathbf{F} [N] is the force, \mathbf{E} [$\frac{V}{m}$] is the electric field that accelerates or decelerates the particles, \mathbf{B} [T] is the magnetic field that confines the particles, e [C] is the electric charge of the particle, \mathbf{v} [ms^{-1}] is the instantaneous velocity of the particle and \times signifies the vector product [Hol14]. The equation can be derived from the classical electromagnetic Lagrangian eq. (1.26) using Euler-Lagrange equation eq. (1.2). [Per00, p. 339]:

The momentum of an accelerated proton in a synchrotron depends on the ring curvature radius r_c [m] and value of magnetic field B [T]:

$$p = 0.299 \cdot B \cdot r_c \quad (2.2)$$

The probe energy is the most important parameter in particle physics. It follows from special relativity that the energy of a particle at rest is given by its rest mass and the energy of a moving

particle is given by boosting $E = \gamma E_0 = \gamma m_0$ where γ is the Lorentz factor as defined as:

$$\gamma = \frac{1}{\sqrt{1 - \beta^2}} \quad (2.3)$$

where $\beta \equiv v/c$ signifies the actual velocity of the moving particle in fractions of c . For particles accelerated to relativistic speeds, the γ factor becomes very large and $\beta \rightarrow 1$. One can trivially show from:

$$p^2 = E^2 - m_0^2 \quad (2.4)$$

that for a large Lorentz factor the kinetic energy term grows $E \gg E_0$ so that we can approximate $E \approx p$ even for massive particles. This approximation gives less than 1 % error for electrons with energies over 3.20 MeV and protons over 5.80 GeV. It follows that the energy and momentum of a high energy particle is numerically approximately equal [Nav14] [Bai07, p. 18].

Once the particles are accelerated to the nominal energy, the beam is aimed at a target to produce collisions. Collider experiments can have two different forms:

Fixed target experiments collide the beam with a stationary target. To express the centre-of-mass energy at collision, we compute the squared four-momentum of some incident particle with rest mass m_1 , energy E_1 and momentum \mathbf{p}_1 hitting a fixed target particle with mass m_2 , energy E_2 and momentum \mathbf{p}_2 :

$$p_\mu p^\mu = (E_1 + E_2)^2 - (\mathbf{p}_1 + \mathbf{p}_2)^2 = m_1^2 + m_2^2 + 2E_1 E_2 - 2\mathbf{p}_1 \mathbf{p}_2 \quad (2.5)$$

where we substituted $E^2 - \mathbf{p}^2 = m_0^2$ with rest masses of particles 1 and 2. In the rest frame of the target particle the momentum is zero $\mathbf{p}_2 = 0$ and the rest energy is simply $E_2 = m_2$. Now, if the target and the beam particles have identical rest masses $m_0 \equiv m_1 \equiv m_2$, then the centre-of-mass energy becomes:

$$E_{\text{CM}}^2 = p_\mu p^\mu = 2m_0^2 + 2m_0 E_1 \quad (2.6)$$

From this we conclude that for fixed target experiments with high energy beam $E_1 \gg m_0$ the collision energy rises only as a square root of beam energy E_1 [Per00, pp. 6,343] [CER06, p. 361]

$$E_{\text{CM}} \approx \sqrt{E_1} \quad (2.7)$$

The centre-of-mass energy squared is sometimes denoted $s \equiv E_{\text{CM}}^2$.

Colliding beam experiments or simply *colliders* use two counter-rotating beams that collide at given interaction points. Head on collisions of two particles with energies E_1, E_2 and momenta $\mathbf{p}_1, \mathbf{p}_2$ give the total centre-of-mass energy

$$E_{\text{CM}}^2 = (E_1 + E_2)^2 - (\mathbf{p}_1 + \mathbf{p}_2)^2 \quad (2.8)$$

The collision point is in the laboratory rest frame. Assuming both particles have identical

masses, their momenta are exactly opposite $\mathbf{p}_1 = -\mathbf{p}_2$ and the centre-of-mass energy becomes

$$s = E_{\text{CM}}^2 = (E_1 + E_2)^2 \quad (2.9)$$

Obviously, this is a critical advantage over fixed target experiment. The energy of colliding beams in the centre-of-mass frame rises linearly with the sum of the two energies

$$E_{\text{CM}} \approx E_1 + E_2 \quad (2.10)$$

Colliding beam accelerators produce collisions with the highest reachable energies [Per00, pp. 7, 343] [HM06]. Table 2.1 shows a comparison of energies computed for fixed target collisions and colliding beams.

Collision	Collision	E_{CM} colliding beams	E_{CM} fixed target
Proton-Proton	7000 on 7000	14 000	114.60
Electron-Electron	100 on 100	200	0.32
Electron-Proton	30 on 920	235	7.50

Table 2.1: Centre of mass energy for different types of collisions. Energies are in GeV. For fixed target we assume the sum of both energies for the moving particle (i.e. 14 000 GeV, 200 GeV and either electron or positron at 950 GeV) Data from [HM06, p. 362].

2.1.3 Accelerator dynamics

After specifying the accelerator layout and desired kinematic properties, the designer has to consider the beam dynamics and the time varying phenomena affecting the motion of particles inside the beam. The focusing properties of the machine are commonly referred to as *beam optics*. Transverse and longitudinal effects are considered individually. The goal here is to keep the large number of particles exactly distributed in timed bunches and focused close to the accelerator design path. For this purpose, the lattice is populated with higher order multi-pole magnet systems:

- *focusing quadrupoles* providing convergent lensing
- *defocusing quadrupoles* providing divergent lensing and,
- *drift spaces* along which no transformation is applied, see fig. 2.2.

In the transverse direction, the motion of the particle along the design path is characterised by displacement $x(s)$ and $y(s)$ from the design path along the x and y axes, see fig. 2.3a. In the ideal case the equations of motion can be approximated by equation of a harmonic oscillator with no damping as shown in [Hol14, p. 32] [Bai07, p. 27]

$$\frac{dx}{dt} + K_x x = 0, \quad (2.11)$$

$$\frac{dy}{dt} + K_y y = 0, \quad (2.12)$$

Accelerator	Nominal energy [GeV]	Location
Proton synchrotrons:		
PS	28	CERN, CH
BNL AGS	32	DESY, DE
KEK	12	DESY, DE
Serpukhov	76	Protvino, RU
SPS	450	CERN, CH
Tevatron II	1000	FNAL, US
Electron accelerators:		
SLAC Linac	25–50	SLAC, US
DESY Synchrotron	7	DESY, DE
Colliding beam machines:		
PETRA	22 + 22	DESY, DE
PEP	18 + 18	SLAC, US
CESR	8 + 8	Cornell, US
TRISTAN	30 + 30	Tsukuba, JP
SLC	50 + 50	SLAC, US
LEP I	50 + 50	CERN, CH
LEP II	100 + 100	CERN, CH
SppS	310 + 310	CERN, CH
Tevatron I	1000 + 1000	FNAL, FR
HERA	30e + 820p	DESY, DE
LHC	7000 + 7000	CERN, CH

Table 2.2: Accelerators active after the year 2000. Data from [Per00, p. 345].

where K is a restoring force constant independent of s . From classical mechanics the solution of a simple harmonic oscillator is given by harmonic functions:

$$x = A \cos(\omega t + \phi) \quad (2.13)$$

where A is the amplitude of the oscillation, ω is the frequency and ϕ is the phase shift. In [eq. \(2.12\)](#) the oscillations are defined with respect to the design path s . Naively, we replace $t = s/v$ and we can write the solution as:

$$x = A \cos(\omega s v^{-1} + \phi) \quad (2.14)$$

$$\frac{dx}{ds} = A \omega v^{-1} \cos(\omega s v^{-1} + \phi). \quad (2.15)$$

We can plot the oscillations in the $(x, dx/ds)$ phase space as shown in [fig. 2.3b](#). The motion of each particle describes an ellipse in the $(x, dx/ds)$ phase space defined by A in x and $A\omega$ in dx/ds . In reality however, the situation is more complicated. The beam consists of a large number of particles, each with its own betatron oscillations, its own amplitude and phase, their confined path is not ideally circular and is affected by the accelerator lattice, since the focus elements are also not distributed uniformly. To generalize [eq. \(2.12\)](#) we make the focusing strength a function of

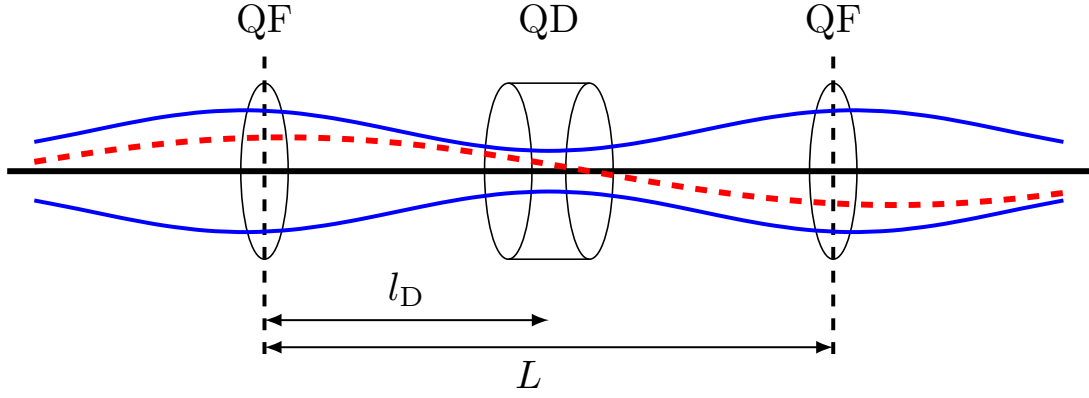


Figure 2.2: Schematic drawing of a symmetric focusing-defocusing (FODO) cell. The lattice consists of a focusing (QF) and defocusing lens (QD) in alternating order with drift spaces in between. Figure based on [Hol13] [CER06, p. 41].

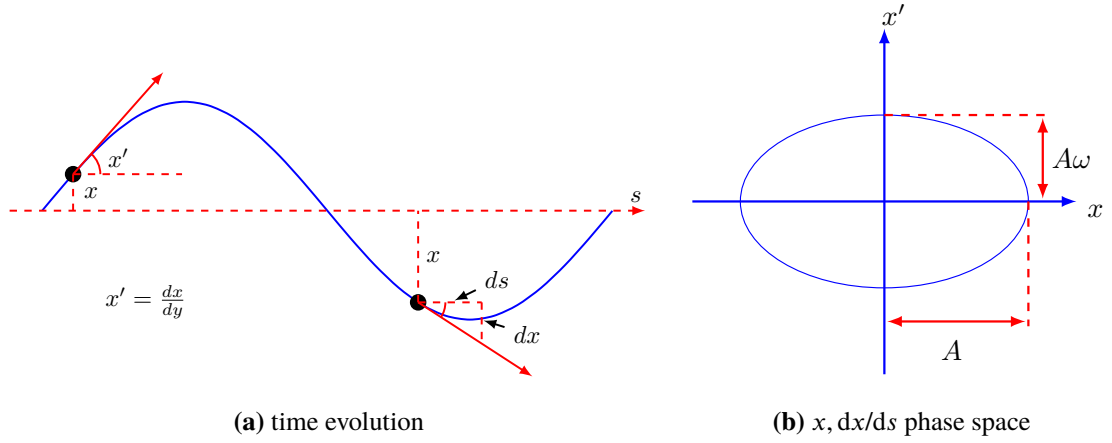


Figure 2.3: Betatron oscillations. Figures based on [Bai07, pp. 27, 28].

the design path s :

$$\frac{dx}{ds} + K_x x = 0, \quad \text{where} \quad K_x \equiv \frac{e}{p} \frac{\partial^2 B}{\partial x^2} + \frac{1}{r^2} \quad (2.16)$$

$$\frac{dy}{ds} + K_y y = 0, \quad \text{where} \quad K_y \equiv -\frac{e}{p} \frac{\partial^2 B}{\partial y^2}. \quad (2.17)$$

This equation is known as Hill's equation. The solution is discussed in [Par12, p. 313] [Hol14, p. 36] [Let13, p. 6] [Bai07, p. 38]. In the special linear case for multiple revolutions of the reference particle the solution is the following harmonic function:

$$x(s) = \sqrt{\beta(s)} \sqrt{\epsilon} \cos(\psi(s) + \phi). \quad (2.18)$$

The amplitude of the oscillation is given by the amplitude modulation function $\beta(s)$ and the transversal beam emittance constant ϵ , and the phase is given by the phase advance $\psi(s)$ for a particular particle trajectory. Emittance is a critical beam parameter which is defined through the invariance of a single particle under the transformation through the storage ring. The implications

of such invariance for an ensemble of particles is discussed in [section 2.1.3.2](#). The amplitude modulation function $\beta(s)$ is determined from the accelerator magnet arrangement and must be deduced or determined numerically for a given lattice configuration. Like the lattice itself, it has to satisfy periodicity condition

$$\beta(s + L) = \beta(s) \quad (2.19)$$

where L is an arbitrary length corresponding to a repeating element in the storage ring. [\[Hol14, p. 36\]](#) One can show that the phase shift and the oscillation amplitude are inversely proportional to one another: $d\psi/ds \sim 1/\beta(s)$ [\[Par12, p. 313\]](#). Assume now that the particle is confined in a parabolic potential, if the parabola arms are more open then the betatron oscillation amplitude is larger so the phase advances more slowly. If they are more closed the amplitude is smaller while the phase advances more rapidly. [Figure 2.4](#) depicts the situation more clearly.

It is also possible to reimplement the solution in [eq. \(2.18\)](#) for a situation specific to circular accelerators. Here we introduce the so called *Twiss parameters* $\alpha, \beta, \gamma, \phi$ that provide a convenient description of particle trajectories using periodic parameters instead of a solution for a single focusing element. It is not our goal here to provide the complete derivation of these parameters but rather to outline the meaning behind critical beam parameters like emittance since these are important for the definition of [luminosity](#) and interaction rate. A more general derivation including the interdependence of Twiss parameters can be found in [\[Hol14, p. 38\]](#) [\[CER06, p. 37\]](#) [\[Par12, p. 313\]](#) and [\[CS00\]](#).

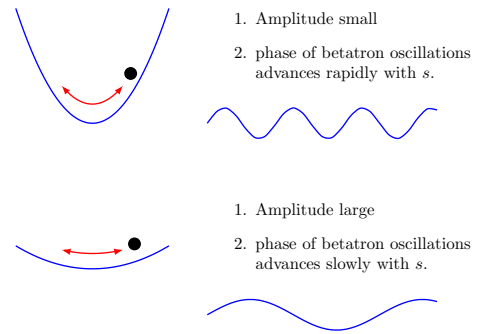


Figure 2.4: Betatron oscillation amplitude and phase [Figure based on \[Bai07, p. 38\]](#).

2.1.3.1 Additional corrections

There are a multitude of additional effects on the accelerator performance which go beyond the scope of this thesis. We can give a short example of gravitational effects, since particles being accelerated along the lattice are not exempt from the effects of gravity. One can easily show that in order for a proton to fall a distance equal to the beam pipe radius:

$$r = \frac{1}{2}gt^2 \quad \Rightarrow \quad t = \sqrt{\frac{2r}{g}} \quad (2.20)$$

it takes just 71.39 ms for it to fall the distance of the inner radius of the LHC beam pipe $r = 25$ mm [\[CER08, p. 56\]](#). Given the revolution frequency this corresponds to roughly 800 laps in the LHC. Gravitational corrections to the design path must be applied to keep the beams contained. [\[VC\]](#)

There is also room for very surprising effects. For example, in 1995, an effect on the LEP dipoles caused by rail road trains in the Geneva region has been observed. It was shown that the cause was a parasitic flow of electricity along the LEP ground cable and perturb the dipole field even though the accelerator was more than 100 m underground. [\[Bra+97\]](#)

2.1.3.2 Emittance of a particle ensemble

The emittance parameter introduced in eq. (2.18) provides a good description of the beam dimension. A single observation of a single particle at a fixed position in s yields only a single data point in the $(x, dx/ds)$ phase space. For a fixed position the amplitude function is constant $\beta(s) = \beta$ so one does obtain the phase space ellipse only by subsequently measuring the particle over many turnarounds at the fixed position, see fig. 2.6.

Populating the phase space with many non-interacting particles measured at the same position fills the phase space plot with many distributed data points. The area within the contour contains a certain percentage of the data points, i.e. particles. and is proportional to the emittance of the beam which is conserved whatever the magnetic focusing or bending operation. This reasoning follows directly from Liouville's theorem [CER06, p. 2].

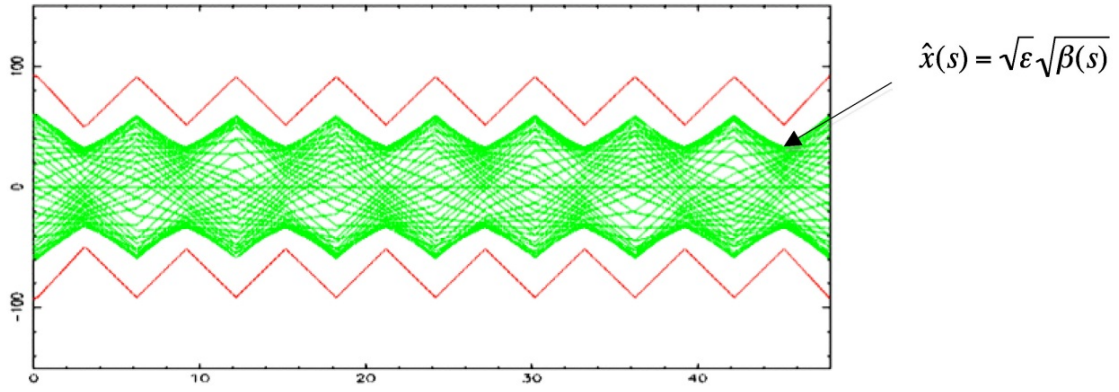


Figure 2.5: The overlapping trajectories of many single particles define the beam cross-section. Figure from [Hol14, p. 39].

From the solution of the equations of motion (2.18) the maximum amplitude follows from $\cos(\psi(s) + \phi) = 1$:

$$\max(x(s)) = \sqrt{\epsilon} \sqrt{\beta(s)} \quad (2.21)$$

which gives us a measure of the beam dimension. Assuming the transverse particle density distribution inside the beam is Gaussian, we can represent the complete beam using a single reference particle contained within one standard deviation σ of the beam. We can then simply obtain the beam size of 1σ from the *normalized transverse beam emittance* ϵ and the amplitude constant β [Hol14, p. 39]:

$$\sigma = \sqrt{\epsilon} \sqrt{\beta} \quad (2.22)$$

A low emittance beam is a beam where particles have nearly the same momenta and are clustered close together. Keeping the emittance as small as possible increases the probability of interaction in the collision thus increasing the *luminosity* (see section 2.1.4). [Par12, p. 314] From the phase space perspective, the beam dimension is simply given as the projection of the phase space ellipse onto the x axis. Emittance can also be measured in longitudinal direction where it describes the bunch spacing.

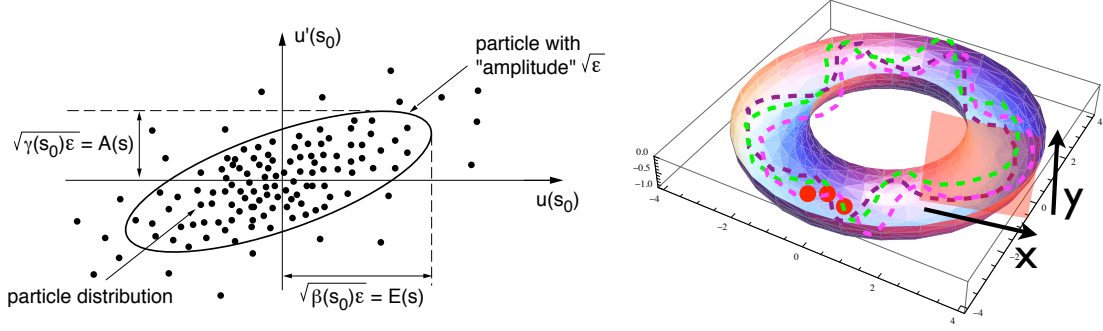


Figure 2.6: Emittance of a particle ensemble. The u variable corresponds to x used in the text, s_0 denotes the position on the accelerator where the beam is the widest. Figures from [Gil13, p. 45].

2.1.3.3 Betatron function at the interaction point

Amplitude modulation function $\beta(s)$ as defined in eq. (2.18) evolves with the reference frame position on the accelerator. For physics, it is however most interesting to know the value of $\beta(s)$ in the neighbourhood of the *interaction point* (IP) where the beam optics are designed to produce the narrowest possible focus. This value is usually referred to as β^* . Due to imperfections in the beam optics design the minimum of the low- β region might not be exactly at the *interaction point*. The value of the $\beta(s)$ functions varies with distance s to the minimum given by:

$$\beta(s) = \beta^* \left(1 + \frac{s^2}{\beta^*} \right) \quad (2.23)$$

This is important because the beam size is thus dependent on the distance from the *interaction point* $\sigma(s) = \sqrt{\beta(s)}\epsilon$ which leads to a reduction of collision rate and consequently *luminosity*. This situation is referred to as *hourglass effect* because of the shape of the amplitude function. [HM06, p. 369]

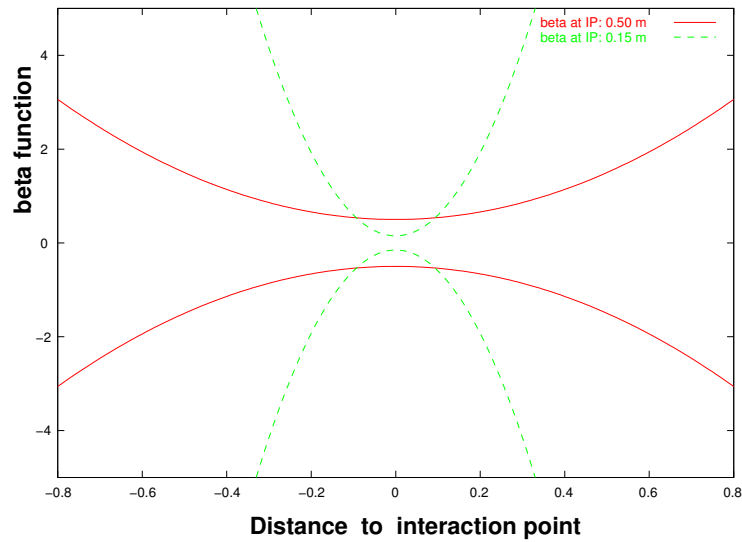


Figure 2.7: Schematic illustration of the hourglass effect. $\beta(s)$ is plotted for two different values of β^* . Figure from [HM06, p. 369].

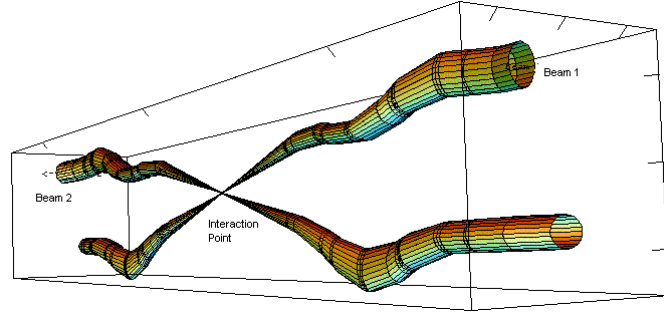


Figure 2.8: Relative beam sizes around IP1 (ATLAS) in collision. Figure from [CER13].

2.1.4 Luminosity and interaction rate

Luminosity is a critical parameter of an accelerator. It is a measure of the number of collisions produced per surface area and per second. The number of events N_{tot} produced by the accelerator is a product of the total probability of interaction expressed in terms of the total interaction **cross-section** σ_{tot} [m²] together with the time integral over the instantaneous **luminosity** [m⁻² s⁻¹] [Par13, p. 28.1]

$$N_{\text{tot}} = \sigma_{\text{tot}} \int \mathfrak{L}(t) dt. \quad (2.24)$$

To obtain a differential form, we define the collision rate $R(t)$ simply as the number of collisions over time $R(t) \equiv dN_{\text{tot}}/dt$ [Hz] and obtain [CER08, p. 3]:

$$R(t) = \mathfrak{L}(t) \cdot \sigma_{\text{tot}}. \quad (2.25)$$

By the nature of our experiment, the products of elastic scattering escape undetected and so we express the probability of interaction only by the inelastic pp **cross-section** σ_{inel} . If two bunches containing N_1 and N_2 particles collide head-on with a frequency f_{rev} [Hz], the instantaneous **luminosity** at the **interaction point** is defined as [ATL13, p. 7]

$$\mathfrak{L} \equiv f_{\text{rev}} \cdot N_b \cdot N_1 \cdot N_2 \cdot \int \hat{\rho}_1(x, y) \hat{\rho}_2(x, y) dx dy \quad (2.26)$$

where $\hat{\rho}_{1,2}(x, y)$ is the normalized particle density function in the transverse $(x - y)$ plane of beam 1 and beam 2. Frequency f_{rev} is usually referred to as the *revolution frequency* and N_b is the number of bunches.

Assuming that the particle densities for each beam can be factorized into independent horizontal and vertical components we can separate the previous equation into:

$$\mathfrak{L} = f_{\text{rev}} \cdot N_b \cdot N_1 \cdot N_2 \cdot \Omega(\hat{\rho}_1(x), \hat{\rho}_2(x)) \Omega(\hat{\rho}_1(y), \hat{\rho}_2(y)) \quad (2.27)$$

where the components

$$\Omega(\hat{\rho}_1(x), \hat{\rho}_2(x)) \equiv \int \hat{\rho}_1(x) \hat{\rho}_2(x) dx \quad (2.28)$$

$$\Omega(\hat{\rho}_1(y), \hat{\rho}_2(y)) \equiv \int \hat{\rho}_1(y) \hat{\rho}_2(y) dy \quad (2.29)$$

are the beam-overlap integrals in each direction. In his paper [vMee68] in 1968, Simon van der Meer has proposed a method of measuring the beam-overlap by sweeping the beams across each other in each direction. One of the two beams is displaced with respect to the other one and the resulting rate of events produced by beam-beam interaction is counted by the detector, from which we can calculate:

$$\Omega(\hat{\rho}_1(x), \hat{\rho}_2(x)) = \frac{\mathfrak{L}_x(0)}{\int \mathfrak{L}(\Delta_x) d\Delta_x} \quad (2.30)$$

where $\mathfrak{L}_x(x)$ is the **luminosity** measured during the horizontal scan at a separation Δ_x . $\mathfrak{L}_x(0)$ represents the maximum at zero beam separation in a given direction. This method is usually referred to as **van der Meer (VMS) scan**. Furthermore, we define the characteristic beam profile parameters Σ_x, Σ_y as the inverse of the beam overlap:

$$\Sigma_x \equiv \frac{1}{\sqrt{2\pi}} \frac{\int \mathfrak{L}(\Delta_x) d\Delta_x}{\mathfrak{L}_x(0)} \quad (2.31)$$

and analogically for Σ_y . This allows us to rewrite eq. (2.27) into a form

$$\mathfrak{L}(t) = f_{\text{rev}} \frac{N_b \cdot N_1 \cdot N_2}{2\pi \cdot \Sigma_x \Sigma_y} \quad (2.32)$$

which corresponds to the simplified definition of **luminosity** $\mathfrak{L}(t) = f_{\text{rev}} \cdot N_b \cdot N_1 \cdot N_2 / A$ as shown for example in [Per00, p. 344], where $A [\text{cm}^2]$ is the cross-sectional area of the beams assuming perfect overlap. This equation allows us to calculate instantaneous **luminosity** for two oppositely directed beams at a given time directly from the beam parameters.

Assuming that the bunches have identical Gaussian transverse profile and that the particle distributions are not altered during the bunch crossing, the number of counted events will have a Gaussian distribution with maximum at *zero beam displacement* and parameters Σ_x and Σ_y will coincide with the standard deviation σ_x and σ_y as shown in [CER06, p. 364]:

$$\mathfrak{L}(t) = f_{\text{rev}} \frac{N_b \cdot N_1 \cdot N_2}{2\pi \cdot 2\sigma_x \sigma_y} \quad (2.33)$$

This is the commonly used expression for the luminosity of two beams with identical Gaussian transverse profiles $\sigma_x = \sigma_{x,1} = \sigma_{x,2}$. Real accelerator machines however introduce additional engineering complications like the hourglass effect we introduced in section 2.1.3.3 and the beam crossing angle which we discuss in the following section.

2.1.4.1 Luminosity and beam parameters

Luminosity can also be expressed in terms of beam emittance ϵ and amplitude functions $\beta(s)$ [Par12, p. 314]

$$\mathfrak{L} = F f_{\text{rev}} \frac{N_b N_1 N_2 \gamma}{4\pi \sqrt{\epsilon_x \beta_x^* \epsilon_y \beta_y^*}} \quad (2.34)$$

where γ is the relativistic factor. Here, we also introduce the geometric luminosity reduction factor F that is defined as the projection of the beam transverse profile given the beam crossing angle.

Non-zero beam crossing will reduce $F < 1$ thus reducing the total integrated luminosity even though the angle is very small. In fact, the angle is so small, that in a tight bunch spacing it might lead to long distance interactions between the beams. The situation is depicted in fig. 2.9.

The reduction factor F can be calculated from the geometry of the collision as shown in [HM06, p. 366]. The crossing-angle is represented as two separate rotations $\theta_c/2$ and $-\theta_c/2$ in the (x, s) plane. After transforming the coordinates once obtains the expression for the luminosity like in eq. (2.34) with the reduction defined as:

$$F \equiv \frac{1}{1 + \left(\frac{\sigma_s \theta_c}{\sigma_x} \right)^2} \quad (2.35)$$

where θ_c is the full crossing angle, σ_x and σ_s the beam transverse and longitudinal profiles at the interaction point . [CER08, p. 3]:

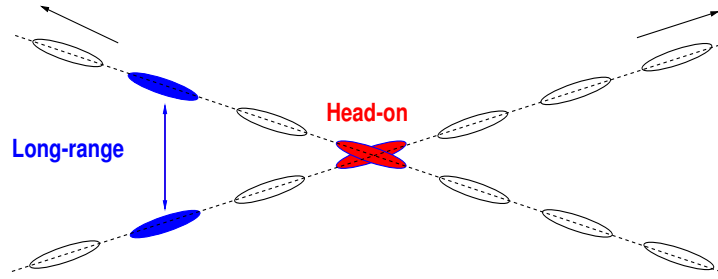


Figure 2.9: Crossing angle at the interaction point . Figure from [HM06, p. 389].

2.1.4.2 Integrated luminosity

Since instantaneous luminosity is a function of time, we define the total integrated luminosity that corresponds the total collected data size:

$$L \equiv \int_0^T \mathfrak{L} dt \quad (2.36)$$

which relates directly to the total number of observed events:

$$L \cdot \sigma_{\text{tot}} = N_{\text{tot}} \quad (2.37)$$

The integrated luminosity is expressed in inverse cross-section units, most commonly inverse nanobarn nb^{-1} , inverse picobarn $\text{pb}^{-1} = 1 \times 10^3 \text{ nb}^{-1}$, inverse femtobarn $\text{fb}^{-1} = 1 \times 10^3 \text{ pb}^{-1}$. The time integral is computed over a certain time period when the machine was running (days, months, years). Thus, integrated luminosity can be viewed as an indication of the collider productivity. [HM06, p. 371] For example, if the machine runs for 10 hours at $\mathfrak{L} = 10^{34} \text{ m}^{-2} \text{ s}^{-1} = 1 \mu\text{b}^{-1} \text{ s}^{-1}$ then it will produce a total of $L = 3600 \mu\text{b}^{-1} = 3.60 \text{ nb}^{-1}$. The expected number of events can now be obtained simply by multiplying with the production cross-section. The cumulative luminosity delivered to ATLAS is shown in fig. 2.10 as a function of time. Figure 2.11 (resp. fig. 2.12) shows the peak instantaneous luminosity (resp. the number of colliding bunches) as a function of time.

2.1.4.3 Luminosity lifetime

Throughout the run the **luminosity** decreases due to the degradation of the beam. The main cause is the loss of the number of particles from collisions. The total number of particles in the beam changes over-time with the decay constant λ as:

$$\frac{dN_p}{dt} = -\lambda N_p \quad (2.38)$$

This is an ordinary exponential decay with the solution:

$$N_p(t) = N_p \exp\left(-\frac{t}{\tau}\right) \quad (2.39)$$

where $N_p(t)$ is the number of particles at any given time. Here, the **luminosity** decay time given by:

$$\tau \equiv \frac{N_0}{\mathfrak{L}_0 \cdot \sigma_{\text{tot}} \cdot N_{\text{IP}}} \quad (2.40)$$

where \mathfrak{L}_0 is the initial beam luminosity, σ_{tot} is the total cross section and N_{IP} is the number of interaction points. Consequently, the **luminosity** decays as:

$$\mathfrak{L} = \frac{\mathfrak{L}_0}{(1 + t/\tau)^2} \quad (2.41)$$

Assuming the nominal **LHC** luminosity $\mathfrak{L} = 10^{34} \text{ cm}^{-2} \text{ s}^{-1}$ and the total cross-section $\sigma_{\text{tot}} = 10^{25} \text{ cm}^{-2}$ at 14 TeV including proton-proton and proton-gas interactions, the decay time for the beam is $\tau = 44.85 \text{ h}$ [CER08, p. 6]. A host of additional effect contribute to the the luminosity loss and their importance is discussed in [CER08]

Each experiment measures its delivered **luminosity** independently with a variety of detector systems. This commonly yields an observed number of interaction per *bunch crossing* (BC) from which the delivered **luminosity** is calculated, see section 2.6.2.

2.2 Large Hadron Collider

The *Large Hadron Collider* (LHC) [CER13] is currently the world's largest and most powerful two-ring hadron collider installed in the existing 26.66 km tunnel built by the *European Organization for Nuclear Research* (CERN) formerly for the **LEP** machine between 1984 and 1989 on the outskirts of Geneva. The tunnel is made of eight arcs and is situated between 45 m and 170 m underground with 1.4% inclination towards lake Léman. The tunnel is surrounded by molasse rock and limestone which provides excellent shielding from cosmic rays or any other outside interference. [CER08, p. 1] Due to its length and location, it crosses the Swiss and French border twice.

The project was approved by the **CERN** Council in December 1994, the finalized technical design report [CER04] was published in 2003. The decision to build the **LHC** at **CERN** was strongly influenced by the possibility to re-use the **LEP** tunnel and the accelerator injection chain (see section 2.2.3). The machine first launched on September 10, 2008. Unfortunately due to a serious technical fault the machine had to be repaired to be relaunched in November 2009.

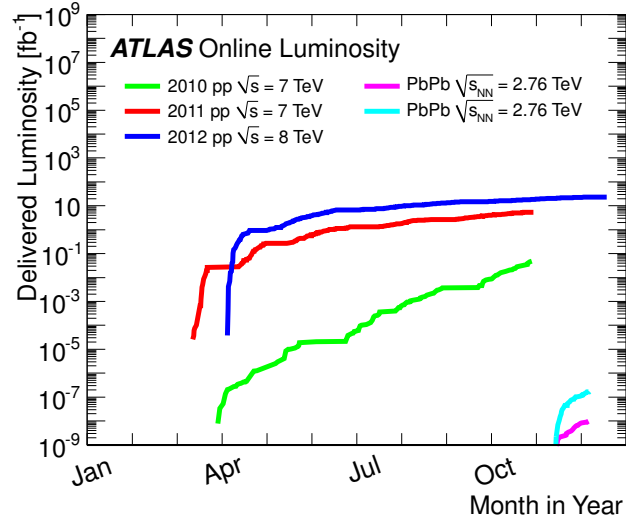


Figure 2.10: Cumulative luminosity versus day delivered in *ATLAS* during stable beams for $p - p$ and $Pb - Pb$ collisions is shown for 2010 (green for $p - p$, magenta for $Pb - Pb$), 2011 (red for $p - p$, turquoise for $Pb - Pb$) and 2012 (blue) schedule. Figure from [ATL14d].

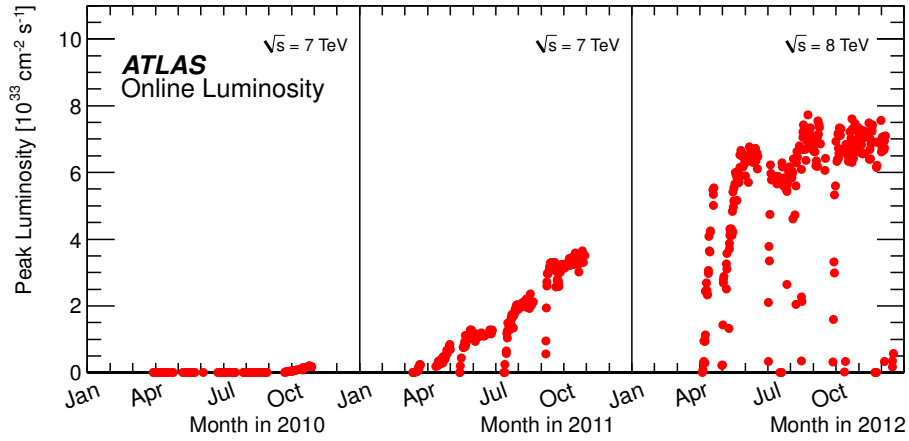


Figure 2.11: Peak instantaneous luminosity delivered in *ATLAS* per day versus time during the $p - p$ runs of 2010, 2011 and 2012. The on-line luminosity measurement is used for this plot. Figure from [ATL14d].

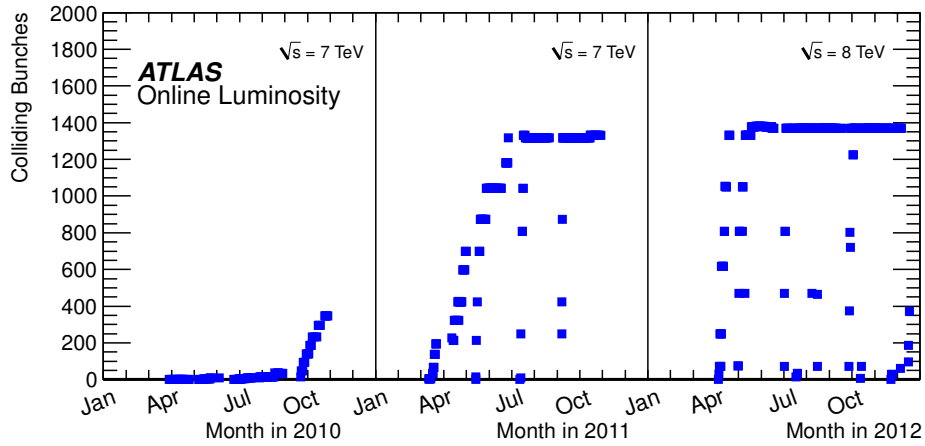


Figure 2.12: Number of colliding bunches in *ATLAS* versus time during the $p - p$ runs of 2010, 2011 and 2012. Figure from [ATL14d].

2.2.1 Current performance

At the time of writing this thesis the LHC has delivered an integrated luminosity of 5.46 fb^{-1} in 2011 and 22.80 fb^{-1} in 2012. The machine also ran over the course of 2010 and produced 45.00 pb^{-1} , but this period was mainly dedicated to commissioning of the machine [Lam13] [ATL14d]. The current beam status can be monitored here: [CER14a].

The LHC has two high-luminosity experiments: ATLAS at IP 1 (see section 2.5) and CMS at IP 5 (see section 2.4), both aiming at peak luminosity $\mathfrak{L} = 10^{34} \text{ cm}^{-2} \text{ s}^{-1}$. There are also two low-luminosity experiments described in section 2.4: LHCb and TOTEM and one LHC experiment, ALICE, dedicated to the study of heavy ion collisions. [CER08, p. 3]

2.2.2 Performance goals

The LHC was designed on principles linked only to the latest technology and engineering process (like superconductivity). The goal of the LHC is to probe the physics beyond the Standard Model using proton collisions with a centre-of-mass energy up to 14 TeV and heavy ion collisions (e.g. Pb) up to 2300 TeV. Assuming two identical beam profiles, the maximum nominal machine luminosity is

$$\mathfrak{L}(t) = F \frac{N_p^2 N_b f_{\text{rev}}}{4\pi\epsilon_N \beta^*} = 10^{34} \text{ cm}^{-2} \text{ s}^{-1}. \quad (2.42)$$

At peak conditions the LHC is expected to deliver $\approx 100 \text{ fb}^{-1}$ on a yearly basis. The first inverse femtobarn was delivered by May 2011 and in April 2012 the LHC achieved 8 TeV with an instantaneous luminosity over $6 \times 10^{33} \text{ cm}^{-2} \text{ s}^{-2}$, see fig. 2.11 [ATL14d]. By comparison, the Tevatron produced 1 fb^{-1} by 2005 after running for about 4 years and by the end of March 2011 delivered a total of 10.50 fb^{-1} per experiment [Pap11].

The parameters of the LHC and their corresponding values for Run-1 in 2011, 2012 in comparison with the nominal values are given in table 2.3. The energy, β^* function and the crossing angle are all controlled by the LHC directly, however the emittance and peak energy depend on the entire accelerator chain. The LHC ring is designed to store 2808 bunches per beam separated by 25 ns, each bunch containing about 1.10×10^{11} protons (this is usually referred to as *bunch intensity*). The main limitations to the machine performance are [CER08, pp. 4-7]:

- ▶ beam-beam interaction limit and beam instabilities that limit the maximum particle density per bunch,
- ▶ limitations of the mechanical aperture,
- ▶ maximum dipole field strength and field quality (nominal field strength above 8 T) at a current of around 11 850 A,
- ▶ quench protection limits ,
- ▶ maximum heat load on the cryogenic system,
- ▶ stored energy containment and
- ▶ luminosity lifetime as discussed in section 2.1.4.3.

The longest stable beam so far was achieved during the 2012 period. Fill 2692 on June 2, 2012 lasted for 22.80 hours [ATL14b].

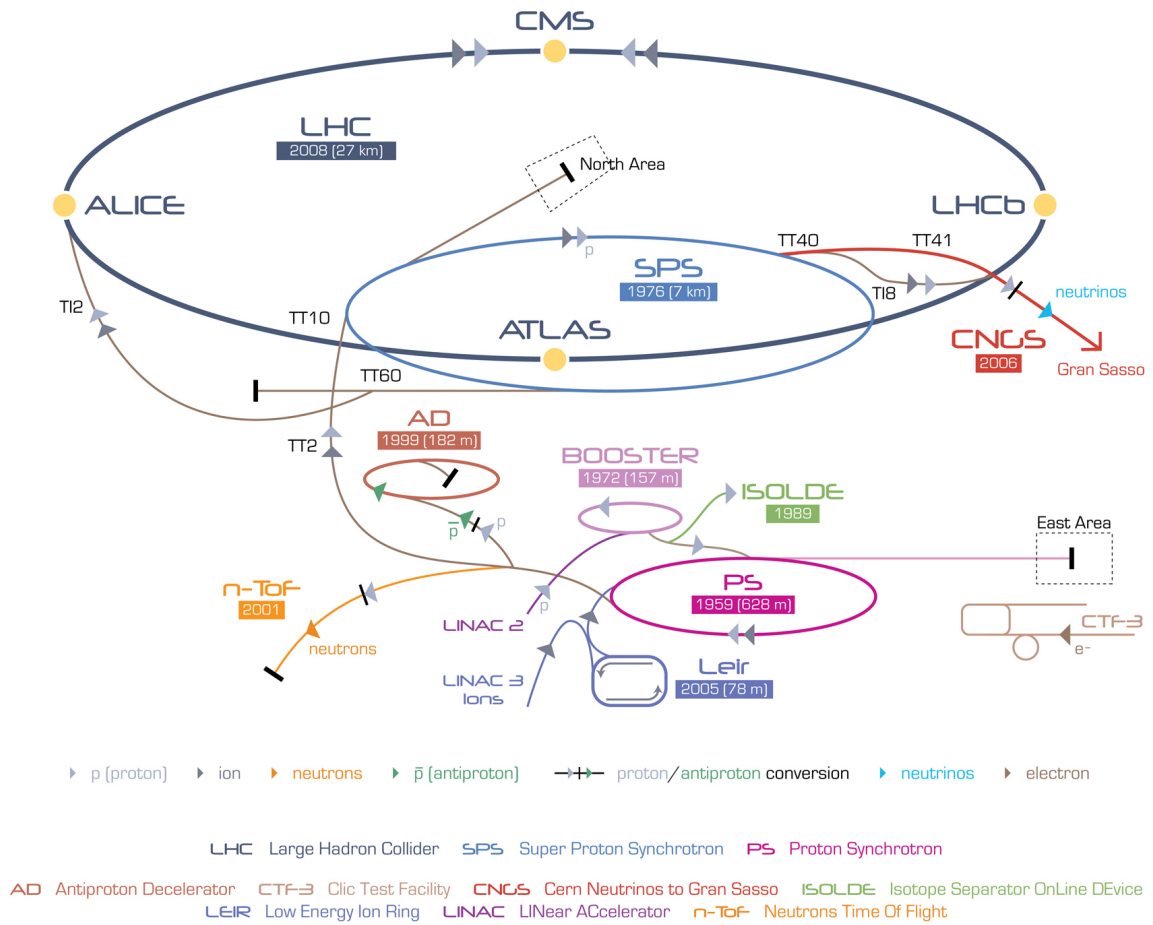


Figure 2.13: LHC injection chain. Figure from [CER13].



Figure 2.14: Schematic of the LHC layout with marked insertion regions, sectors and octants. Figure from [CER13].

Symbol	Meaning	Units	Nominal	Run-1 2011	Run-1 2012
E	Beam energy for protons	TeV	7.0	3.5	4.0
N_p	Number of particles per bunch	–	1.15×10^{11}	1.50×10^{11}	1.70×10^{11}
N_b	Number of bunches per beam	–	2808	1331	1380
τ_b	Bunch spacing	ns	25	50	50
ϵ_n	Normalized 1σ emittance $\equiv \gamma\epsilon$	μmrad	3.75	2.5	2.5
β^*	Beta function at IP 1 and 5	m	0.55	1.0	0.6
θ_c	Crossing angle through IP 1 and 5	μrad	285	240	290
\mathcal{L}_{max}	Peak instantaneous luminosity	$\text{cm}^{-2} \text{s}^{-1}$	10^{34}	3.60×10^{33}	7.73×10^{33}
L	Integrated luminosity delivered at IP 1	fb^{-1}	$\approx 100/\text{yr}$	5.46	22.80

Table 2.3: LHC Parameters in Run-1 (2011 and 2012) compared to the nominal parameters. Not all bunches contributed to the delivered luminosity. The 2011 part of Run-1 was mostly dedicated to exploring the machine limits with the main goal of 2012 was the production of enough statistics to search for the Higgs boson. Data from [Bai14, p. 567], corrections from [Lam13] [ATL14b] [CER14b].

2.2.3 Injection chain

LHC is only the latest addition to the CERN accelerator complex. The whole injection chain starts with a duoplasmatron source. This is essentially a chamber filled with hydrogen gas where hydrogen atoms are stripped of their electrons by applying an electric field. The resulting ions (i.e. protons) are injected into Linac2, where they are accelerated to 50 MeV. The chain continues with the

1. Proton Synchrotron Booster (PSB) which accelerates to 1.40 GeV,
2. Proton Synchrotron (PS) accelerating to 26 GeV,
3. Super Proton Synchrotron going up to 450 GeV and finally enters the LHC.

The circumference ratios are 1/11 PS/SPS and 7/27 for SPS/LHC. These accelerators were upgraded after the LHC proposal to meet the new technical requirements. [Bai14] The total energy stored in the final beam can be calculated the parameters in table 2.3. For the nominal parameters this yields:

$$E_S = N_p \cdot N_b \cdot E_{\text{beam}} \cdot e \quad [\text{J}, -, -, \text{eV}, \text{J eV}^{-1}] \quad (2.43)$$

$$E_S = 2808 \cdot 1.15 \times 10^{19} \cdot 7 \times 10^{12} \text{ eV} \cdot 1.60 \times 10^{-19} \text{ J eV}^{-1} = 362 \text{ MJ} \quad (2.44)$$

which corresponds to approx. 0.58 A. Assuming beam parameters for Run-1 2012 period the stored beam energy is less than half the nominal: ≈ 140 MJ. In addition to this, the total energy stored in the LHC magnet system is approximately 600 MJ. This energy is safely disposed at the end of each run, also in case of emergency the beam abort facilities are used. [CER08, p. 5]

Figure 2.13 shows the full injection chain, the parameters are summarized in table 2.4. Filling the LHC requires 12 cycles of the SPS, each SPS fill requires 3 to 4 cycles of the PS synchrotrons. The PS and SPS cycling times are 21.60 s and 3.60 s respectively, which yields a total LHC filling time of about 4 minutes per beam. Given other engineering limits and evaluation time, the maximum time to ramp up beam energy from 450 GeV to 7 TeV is approximately 20 minutes. [CER08, p. 7] The nominal bunch filling scheme for 25 ns bunch spacing is shown in fig. 2.15. The first bunches in each beam collide in Interaction points 1 and 5. [Her06, p. 393]

The accelerator chain is responsible for the production of LHC bunch trains. Six PSB bunches are captured in PS and then split in three by simultaneous application of high-frequency waveforms.

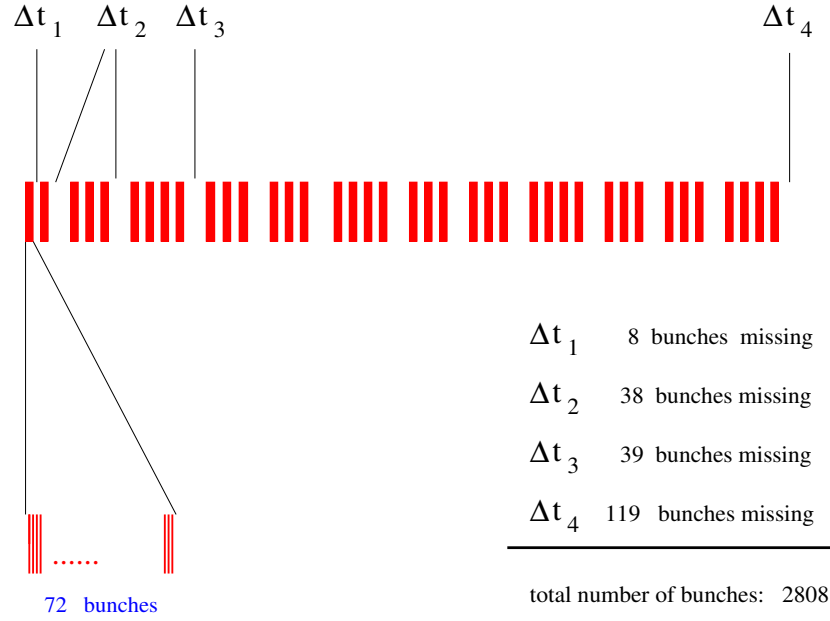


Figure 2.15: Bunch filling scheme of the LHC. Figure from [Her06, p. 393]. Corresponding figure can be also found in [CER08, p. 141].

Machine	Nominal E	β	N_p	N_B	Scheme
Linac2	50 MeV	0.31	1×10^{13}	1	Fill each ring of PSB
PSB	1.40 GeV	0.92	1.38×10^{12}	1	Two-turn injection into PSB
PS	25 GeV	1.00	1.15×10^{11}	72	Six injections, each bunch split by three
SPS	450 GeV	1.00	1.15×10^{11}	288	Four PS batches of 72
LHC	14 TeV	1.00	1.15×10^{11}	2818	12 SPS cycles, 234 334 334 334

Table 2.4: Parameters of the CERN injection chain for nominal LHC beams and no losses. Data from [Bai14], where numbers for 10% loss estimation are also provided.

This way the single bunch is transformed into two in the higher-frequency system as shown with real data in fig. 2.16. Given the scheme, the implications for the separate machines are given in table 2.4. [Bai14, p. 570]

2.2.4 Lattice layout

As a colliding beam accelerator, the LHC has two beams that travel in separate beam pipes in clockwise and counter-clockwise direction. The layout follows the tunnel geometry as it was designed for LEP. The machine is divided into eight sectors, each sector is defined by an Interaction point at each end. Octants start in the middle of a sector and end in the middle of the following sector. They cross over at the insertion regions indicated in fig. 2.17. The two high-luminosity Interaction points (ATLAS and CMS) are located at the opposite side of the ring.

Two more experimental stations are located at IP 2 and IP 8, which also include the injection systems for Beam 1 and Beam 2 respectively. The remaining four sections do not have beam crossings as they are used for cleaning and beam abort [CER08, p. 7]. The particles also lose ≈ 7 keV of energy per cycle due to synchrotron radiation, which is compensated by the magnet system as well.

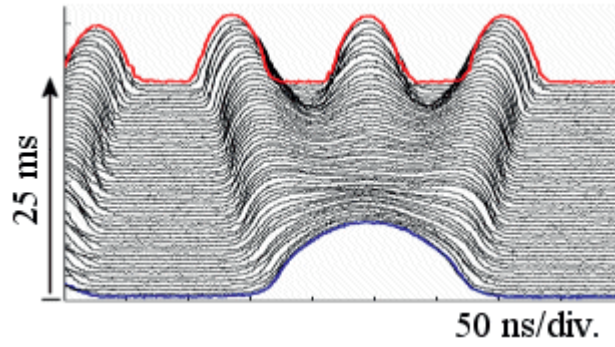


Figure 2.16: Triple bunch splitting in the PS. Figure from [Bai14, p. 571]

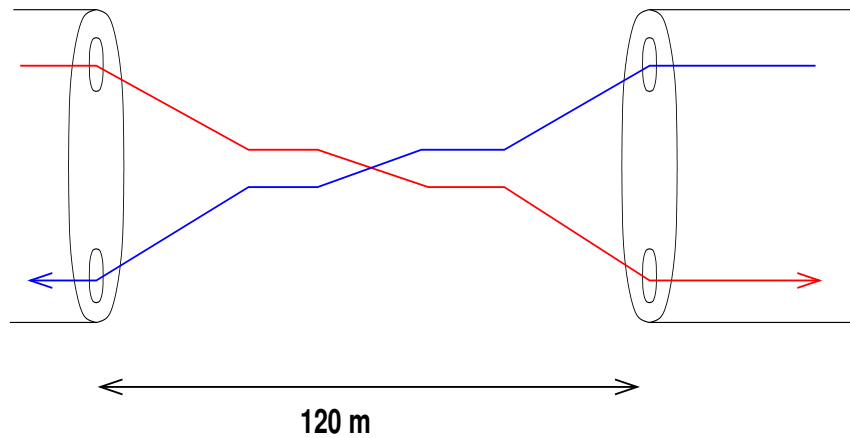


Figure 2.17: Schematic of the cross over between inner and outer beam pipe in the LHC. Figure from [Her06, p. 388].

The LHC lattice has evolved over several versions. The whole ring is effectively a polygon that consists of 1232 dipole segments. Each dipole segment is 14.30 m long and weights ≈ 35 tonnes, the cross-section is shown in fig. 2.18 along with magnetic flow simulation. The internal arrangement incorporates a twin-bore magnet (US patent 5374913 A) each having beam pipes within. The design provides opposite magnetic fields to each beam pipe while being placed in the same cryostat. Additionally, 392 quadrupole and other multipole magnets have been installed for beam optics.

Superconducting coils are used to achieve the required field strengths. The magnets have to be cooled down to 1.90 K by the cryogenic system using liquid nitrogen and liquid helium. Helium is an excellent coolant. At this temperatures it behaves as a super-fluid, with extremely low viscosity and very high thermal conductivity. There are 90 tonnes of liquid helium at 1.90 K in the system. The dipole cold mass is contained within the shrinking cylinder as shown in fig. 2.18. [CER08, p. 23]

Running at nominal performance the average power requirements of the LHC reach 120 MW, 27.50 MW goes to the cryogenic system and ≈ 22 MW to all LHC experiments. LHC accounts for more than two thirds of the power consumption of the entire CERN laboratory which is approx. 130 GWh in total, assuming 720 operational hours per month. [CER13, energy consumption]

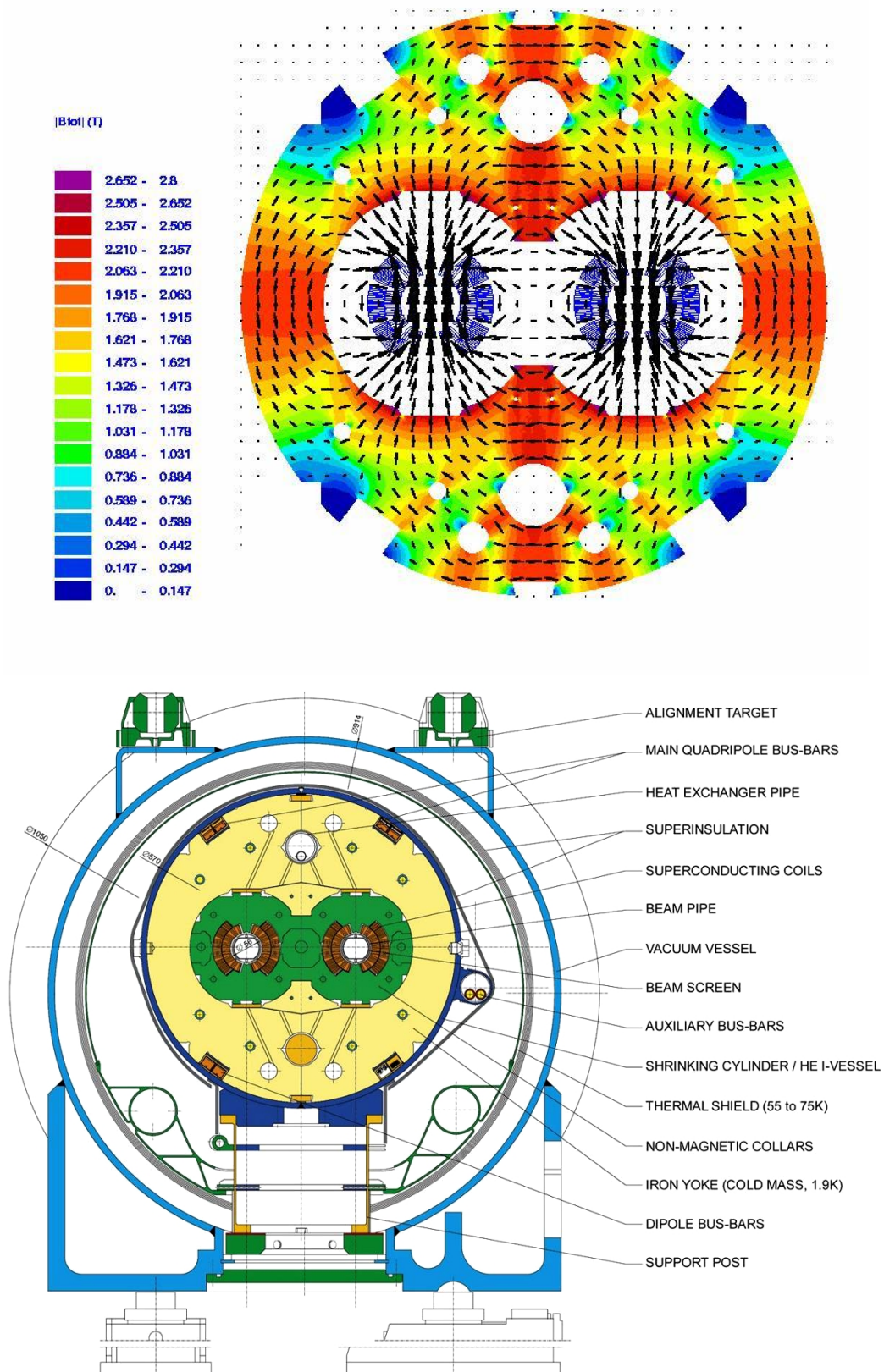


Figure 2.18: Detail of LHC cryodipole cross-section and a simulation of the magnetic flux. Each beam has the same charge, so in order to make them run in opposite directions inversely oriented magnetic field for the other pipe is used. Pipes share the same mechanical structure. Figures from [CER04, p. 172] and [CER08, p. 23].

2.3 Detector systems

Observation and measurement of particles occurs through their interaction with surrounding matter. Particles travelling through the detector deposit energy to the medium which leads to some macroscopic observable effect through excitation or ionisation of other particles inside the medium. Visual observation, as it is familiar to us, is also an observation of interaction, as photons are scattered from objects and then “detected” using photosensitive ganglion cells in the retina of a human eye.

Virtually any detector works as a transducer. It converts one form of energy into another form of energy to produce a signal, in this case the interactions with the detector medium are converted into an electric current. Particles are identified based on the difference in mass, electric charge and their kinematic properties. However, only five of the [Standard Model](#) particles can be observed directly: e^\pm , μ^\pm and γ , concerning the rest we need to understand that:

- ▶ Quarks are always confined to a bound state which allows us to detect them only through interaction of stable or semi-stable hadrons: π^\pm , K^\pm , K^0 (mesons) and n , p (baryons).
- ▶ Hadrons made from quarks have short decay lengths but they can reach the innermost layers of the detector, so they can be identified by their short tracks.
- ▶ Lifetime of higher generation particles (e.g. τ leptons) is too short for them to even reach the detector.
- ▶ Heavier bound states of quarks (like bottomonia or charmonia) decay quickly and we are able to identify them only through their decay products following tracks in some pattern
- ▶ Neutrinos or are not observable directly. They require dedicated approach using large volume detectors like the Super-Kamiokande.

Historically, there have been numerous designs of particle detectors. *Bubble chambers* were instrumental to the discovery of the existence of positrons and *cloud chambers* provided experimental evidence for the existence of muons. *Cherenkov radiation counters* are used to date to detect the Cherenkov radiation emitted by the products of the collision with an incoming neutrino. Solid-state semi-conductor micro-detectors, calorimeter systems and scintillation detectors are used in combination in all modern day experiments. See [\[Per00, pp. 349–376\]](#) for a comprehensive introduction into the basic principles of particle detectors and their historical context.

Colliding beam experiments, such as those on the [LHC](#), produce secondary particles at the [IP](#) which then fly out in all directions. A layered detector system with cylindrical geometry built around the interaction point is practically the only solution in this case since we cannot surround the [IP](#) with a sphere because of beam pipes, accessibility for maintenance etc. On the other hand, fixed target experiments only require one arm of detectors which are placed beyond the target medium.

2.3.1 Large hybrid detector systems

In modern particle physics experiments, the key requirement on the detector system is its ability to identify different kinds of particles simultaneously. The solution to this challenge is to create a scientific instrument composed of many different kinds of detectors, where each system contributes to the measurement. The detectors are usually arranged in layers, starting from the high granularity systems (like semi-conductor trackers) to the most voluminous like calorimeters and muon chambers.

[Per00, p. 374]. Current beam energies, interaction rates and precision requirements set stringent standards for the design of particle detectors. Experiments constructed for the LHC are the most advanced and most complicated particle detectors ever built.

The detector system is arranged such that its active material provides maximum coverage around the Interaction point as is practically possible. The size of the entire array can reach tens of meters in all directions. For example, the ATLAS detector is 25 m in diameter making it the largest hybrid detector built to date. Given the fact that relativistic particles travel the distance of one meter in approx $c^{-1} = 3.33 \text{ ns m}^{-1}$, the time resolution of the whole system must be in the order of nanoseconds. More complications to the design of hybrid detector system arise from the placement interconnections and readout electronics which are required for each of the detector subsystems. Consider also, that the entire aperture needs to be radiation resistant.

2.3.2 Measurement nomenclature

Throughout this thesis we are going to be describing measurements performed by ATLAS, which is a cylindrical hybrid detector system. Physicists seamlessly transform between Cartesian, cylindrical and spherical coordinates but when describing particle kinematics a Lorentz invariant coordinate system is preferable. For this reason physicists prefer to use a coordinate called *pseudorapidity* η instead of polar angle θ [ATL08c, p. 1]:

$$\eta = -\ln \tan \left(\frac{\theta}{2} \right) \quad (2.45)$$

which goes to infinity for very small θ . The Lorentz boost invariance is important in particle physics since one can rarely expect that the interaction happens exactly at the origin of the coordinate system. By relativistically translating the origin, one can get the coordinates of the centre-of-mass frame.

In terms of particle momenta, *pseudorapidity* is closely related to *rapidity* y and is in fact used as its close approximation:

$$\eta = \frac{1}{2} \ln \left(\frac{|\mathbf{p}| + p_z}{|\mathbf{p}| - p_z} \right) \text{ and } y = \frac{1}{2} \ln \left(\frac{E + p_z}{E - p_z} \right) \quad (2.46)$$

where p_z is the momentum component parallel to the beam axis. *Pseudorapidity* however, depends only on the polar angle of the particle trajectory and does not account for the object's energy. That is why computing *rapidity* directly is often desirable when describing the kinematics of heavier objects like jets. We also define the *pseudorapidity*-azimuthal angle distance between two particles:

$$\Delta R = \sqrt{\Delta \eta^2 + \Delta \phi^2} \quad (2.47)$$

which is particularly useful when determining track isolation for example.

Because of the geometry of the detector and the nature of the experiment an unknown portion of the secondary particles escapes. Hence any constraints on the conservation of momentum or energy can be set in the plane perpendicular to the beam axis, i.e. (x-y). We introduce *transverse momentum* p_T and *transverse energy* E_T and the relationships between a transverse variables and detector coordinates are:

$$p_T = \sqrt{p_x^2 + p_y^2} = |p| \sin(\theta) \quad (2.48)$$

$$p_x = p_T \cdot \cos(\phi) \quad \text{and} \quad p_y = p_T \cdot \sin(\phi) \quad (2.49)$$

It should be noted that particle kinematics are measured with maximum resolution in the transverse plane, where the particle crosses most of the detector material.

In order to detect particles from invisible or semi-invisible final states (like W decay) we also employ a quantity called *missing transverse energy*. This net energy arises from the presence of undetected particles that contribute to the total of energy inside the detector. For the reasons mentioned above, the conservation of momentum can only be reliably constrained in the transverse plane, as the p_T of the initial state is in ideal case zero:

$$\mathbf{E}_T \equiv - \sum_i \left(\sqrt{p_x^2 + p_y^2} \right) \quad (2.50)$$

where the sum runs over all visible final state particles. [Par13, p. 425]

Now consider a situation, where we would be trying to measure a parent particle of mass m that decays into two particles from which one is invisible (like a neutrino). For these semi-invisible final states we define a quantity called *transverse mass* m_T that puts a maximum constraint on the parent particle in terms of its mass:

$$m_T^2 \equiv (E_{T1} + E_{T2})^2 - (p_{T1} + p_{T2})^2 \quad (2.51)$$

where we identify the invisible particle with *missing transverse energy*:

$$p_{T1} \equiv \mathbf{E}_T \quad (2.52)$$

and for massless daughters ($m_1 = m_2 = 0$) we get an upper limit of mass $m = \max(m_T)$ [Par12, p. 425]

$$m_T^2 = 2|p_{T1}||p_{T2}| (1 - \cos \phi_{12}) \quad (2.53)$$

The transverse direction is again preferable due to resolution limitations in the longitudinal directions since the z component of a neutrino is effectively unknown. This quantity was successfully used at *Tevatron* to measure the W mass, since neutrino masses are experimentally known to be nearly zero

Additional parameters contribute to the description of particle trajectory helix. The *transverse impact parameter* d_0 is defined as the shortest distance between the nominal *IP* and the particle trajectory helix in $(x - y)$ or $(R - \phi)$ plane. The *longitudinal impact parameter* z_0 is defined as the shortest distance between the trajectory and the beam pipe in the z direction (beam axis). The d_0 parameter may be signed to preserve information about the direction. In that case d_0 is defined as positive if the azimuthal coordinate:

$$\phi - \phi_0 = \frac{\pi}{2} + n \cdot 2 \cdot \pi \quad (2.54)$$

where $n \in \mathbb{Z}_0$. The following diagram shows the parameters split into transverse plane $(x - y)$ (on the left) and longitudinal view $(r - z)$ (on the right) [ATL14a, Trk::Perigee]:

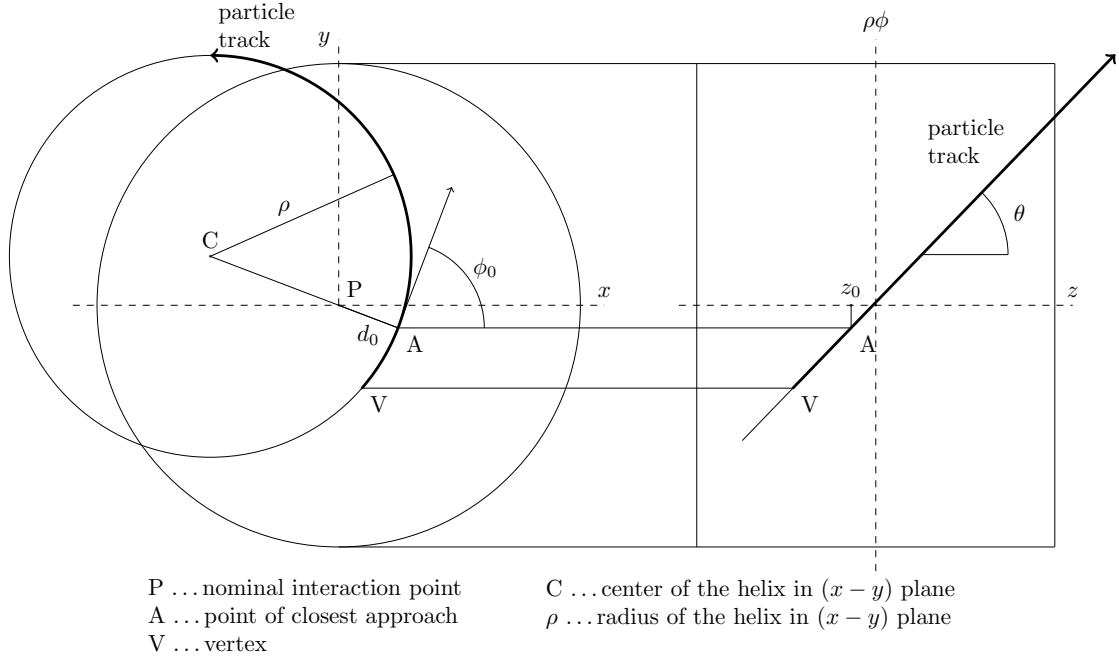


Figure 2.19: Schematic drawing of transverse d_0 and longitudinal z_0 impact parameters. Figure based on [ATLAS Doxygen](#) documentation for class [\[ATL14a, Trk::Perigee\]](#).

2.4 Experiments at the LHC

In total there are seven experiments at the [LHC](#), four of these occupy [Interaction points](#) 1, 2, 5 and 8 as indicated in the [fig. 2.14](#) in [section 2.2](#). There are also non-LHC experiments at [CERN](#), like ISOLDE, CLOUD etc. [\[CER\]](#), however only [LHC](#) experiments are relevant for this thesis. [CERN](#) is not directly involved in running and maintaining the experiments. Each experiment has its own international collaboration, funded independently from [CERN](#). [CERN](#) is effectively a member of each experiment, and contributes to their budget. [\[CER\]](#).

2.4.1 General purpose experiments: ATLAS and CMS

Two of the [LHC](#) experiments are designed to record similar measurements, and the rest are specialized in certain fields of physics. The general purpose experiments: [ATLAS](#) and [CMS](#) differ in technical solution and design in the interest of validating results. The main difference between [ATLAS](#) and [CMS](#) is in the magnet system and calorimeter design. Both experiments are shown schematically in [figs. 2.20](#) and [2.21](#).

Mirroring experiments in their entirety is the only way that particle physics can reduce systematic uncertainties and random errors and provide independent verification (or falsification) of discoveries as is required by the scientific method. We shall start with their individual description here. The main focus of this thesis is on the [ATLAS](#) experiment to which we dedicate a full [section 2.5](#).

2.4.2 CMS (Compact Muon Solenoid)

The second largest general-purpose detector on [LHC](#) is installed at Point 5, Cessy, France. It is called “compact” because it is approximately four times smaller than [ATLAS](#) but weights twice as

much. **CMS** has similar physics goals as **ATLAS**, but uses different technological approach and detector design to accomplish them. Both **ATLAS** and **CMS** simultaneously released publications showing the experimental evidence for the existence of the Higgs boson [ATL12] [CMS12]. The physics program now focuses on measuring its properties while also probing for new physics at TeV scale like SUSY and providing further validation of the **Standard Model**, see [CMS06, pp. 5–6] for original **CMS** physics goals.

The **CMS** aperture diameter is 21.60 m long, 15 m in diameter and its total mass is approximately 12 500 tonnes. According to [CMS06, p. 6] the technical requirements for the detector instrumentation are:

- ▶ high performance muon detection in the region $|\eta| < 2.4$ and ability to determine unambiguously the charge of muons,
- ▶ central tracking system with high momentum resolution for charged particles,
- ▶ hadron calorimeter with large hermetic coverage over $|\eta| < 5$ designed to entirely surround collisions and prevent electrically charged particles from escaping (with the exception of muons).

The muon system is built around a solenoid magnet in the form of a cylindrical coil 13 m long with an inner diameter of 5.90 m, making it the largest superconducting magnet ever built. Operating at temperature of 4 K it produces an axial magnetic field of ≈ 4 T at an electric current of nearly 20 kA. The whole **CMS** detector system requires about 10 MW power supply to run and about 1200 m³ of water per hour for cooling*.

The tracker is composed of approx. 250 m² of segmented silicon sensors. Electromagnetic calorimeter is made of lead tungstate (PbWO₄) crystals and the hadron calorimeter is made from brass and steel (which mostly contributes to detector's weight). The whole structure is supported by 0.40 mm thick structures made from carbon-fibre and glass fibre (in the barrel). For the high performance muon detection **CMS** uses three types of detectors: drift tubes, cathode strip chambers and resistive plate chambers.

CMS engineers took a different approach when constructing the detector. Instead of building it underground like other **LHC** experiments did, it was constructed on the surface in 15 separate sections that were then lowered into the cave where it was reassembled. This allowed them to work in parallel and save time [CMS10]. As of May 2014, over 3000 scientists and engineers from 172 institutes in 40 countries are involved in the experiment [CMS10].

2.4.3 ALICE (A Large Ion Collider Experiment)

ALICE is the only **LHC** experiment optimised and dedicated to the study of heavy ion collisions. Experiments at **CERN SPS** in 1980s and their continuation on Relativistic Heavy Ion Collider (RHIC) in Brookhaven National Laboratory provided some evidence that at a centre-of-mass energy per nucleon pair of 5.50 TeV quarks are no longer confined inside hadrons. Protons and neutrons 'melt', freeing the quarks from their gluon bonds creating a state of matter called *Quark-Gluon Plasma*, which probably existed just after the Big Bang when the Universe was still extremely hot. Today such a state of matter is probably present around the vicinity of quasar cores. The **ALICE**

*The *jet d'eau* (water jet) in Geneva pumps 1800 m³ per hour

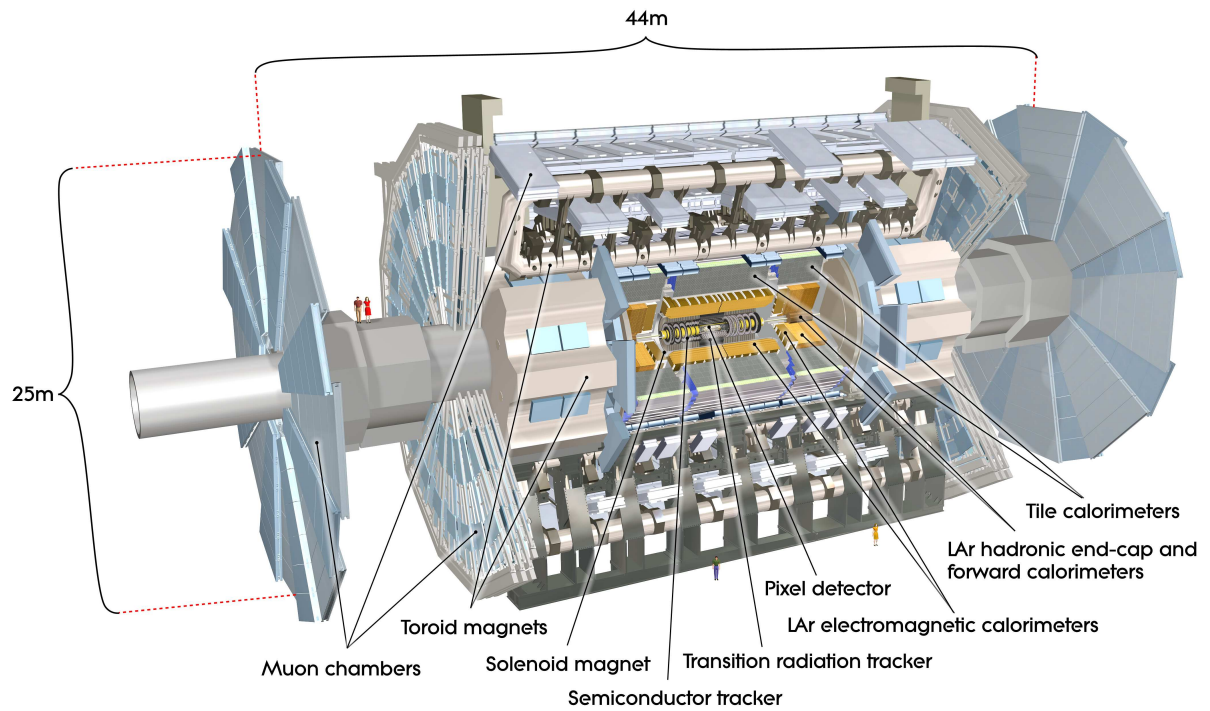


Figure 2.20: Schematic view of the [ATLAS](#) experiment. Figure from [\[ATL08c, p. 4\]](#) [\[ATL10b\]](#).

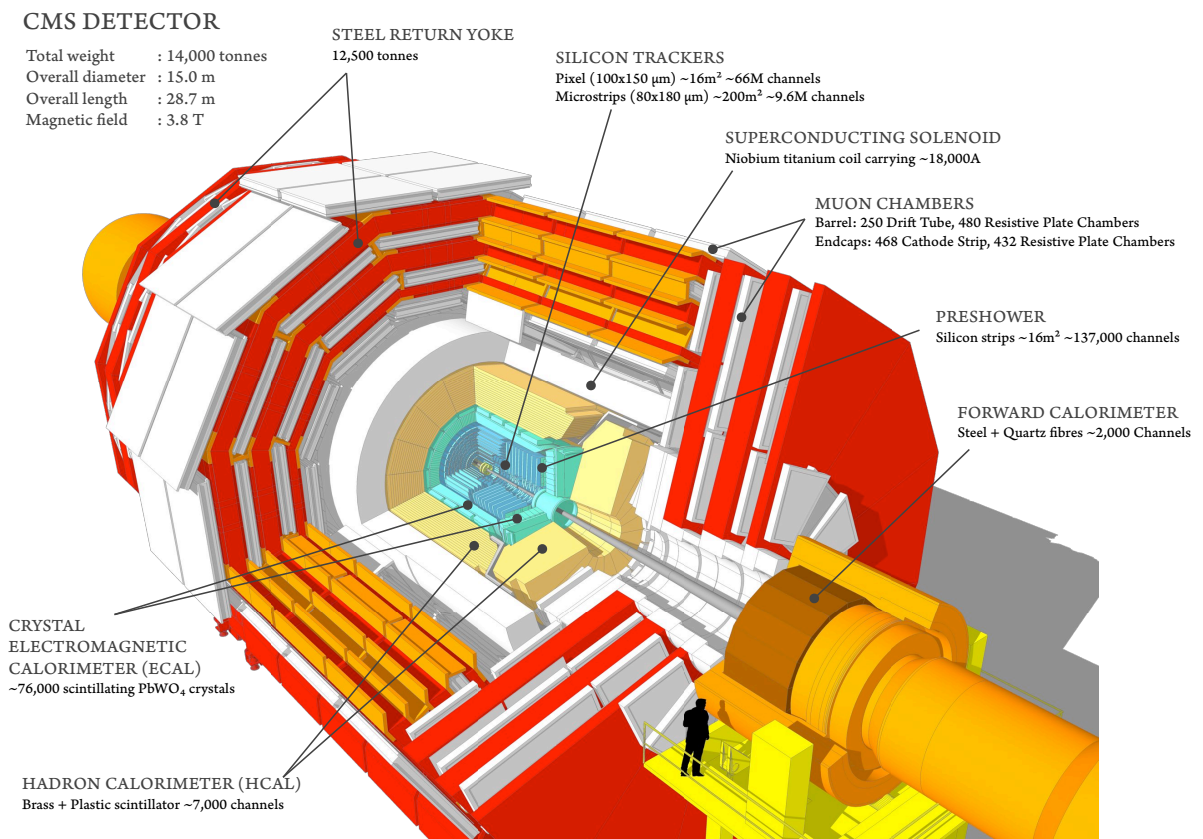


Figure 2.21: Schematic view of the [CMS](#) experiment. Figure from [\[SM13, p. 3\]](#).

collaboration aims to study the quark-gluon plasma phase-transitions leading to re-hadronisation as it expands and cools. This means one could observe how QGP progressively creates the particles that constitute ordinary matter [ALI10].

The experimental set-up is schematically shown in fig. 2.22. It is 26 m long, 16 m in diameter and weights 10 000 tonnes. ALICE is designed to measure a large set of observables over as much of phase space as possible. The central barrel provides a pseudorapidity coverage $|\eta| < 0.9$ and complete azimuthal coverage of collisions. Its main parts are the Silicon detectors (ITS), a large time projection chamber (TPC) and a transition radiation detector (TRD) and a time-of-flight array (TOF). Hadron ring-imaging Cherenkov counters (HMPID) and photon detection crystals (PHOS) are placed in the outer shells. The single arm segment is a muon spectrometer with its own magnet ($2.5 < |\eta| < 4.0$ coverage). The experiment is hosted at CERN Point 2 near St. Genis-Pouilly, France. The ALICE collaboration consists of more than 1000 scientists from 120 institutes in 32 countries [April 2010] [ALI09] [ALI10].

2.4.4 LHCb (Large Hadron Collider beauty)

In contrast with the other LHC experiments, LHCb is a single arm forward detector dedicated to the study of heavy flavour physics. The aim of the experiment is to record precision measurements of $\hat{C}\hat{P}$ violations to provide deeper understanding of the matter anti-matter asymmetry of our Universe. Phenomena that indicate $\hat{C}\hat{P}$ violation can occur in rare decays of charm and beauty hadrons. Rather than flying out from the IP in all directions, these hadrons stay within the forward kinematic region (i.e. travel along the beam pipe). Thus, the whole experiment is arranged along the beam pipe in a single arm as shown in fig. 2.23. The detector is 10 m high, 13 m wide and weights 5600 tonnes and is located at Ferney-Voltaire in France (Point 4). The collaboration has 670 scientists from 65 different universities and laboratories located in 16 countries as of May 2014. [LHC14]

2.4.5 TOTEM (TOTAl Elastic and diffractive cross section Measurement)

This experiment focuses on physics that is not accessible to the general-purpose detectors: total cross section, elastic scattering and diffraction dissociation. In the case of elastic and (most) diffractive events, intact protons need to be detected at large $|\eta|$ and it is therefore necessary to use specialised detectors. All of TOTEM's sub-detectors (Roman Pots (RPS) and two particle telescopes) have high acceptance for particles produced in this region. The experiment is therefore capable of bringing in some unique observations the other detectors can't easily do.

The experimental apparatus consists of:

- ▶ eight *Roman pots* placed in pairs at four locations near the collision point of the CMS experiment. They will detect protons scattered at very small angles in elastic or quasi-elastic reactions.
- ▶ A forward inelastic detector covering about 4 pseudorapidity units in the forward cones (from $|\eta| = 3$ up to $|\eta| = 7$) with full azimuthal acceptance. [TOT10].

TOTEM measurements are important to determine the overall rate of inelastic collisions. It is located at Cessy, France, near the CMS experiment. The TOTEM collaboration consists of 50 scientists from 9 institutes in 7 countries [April 2010].

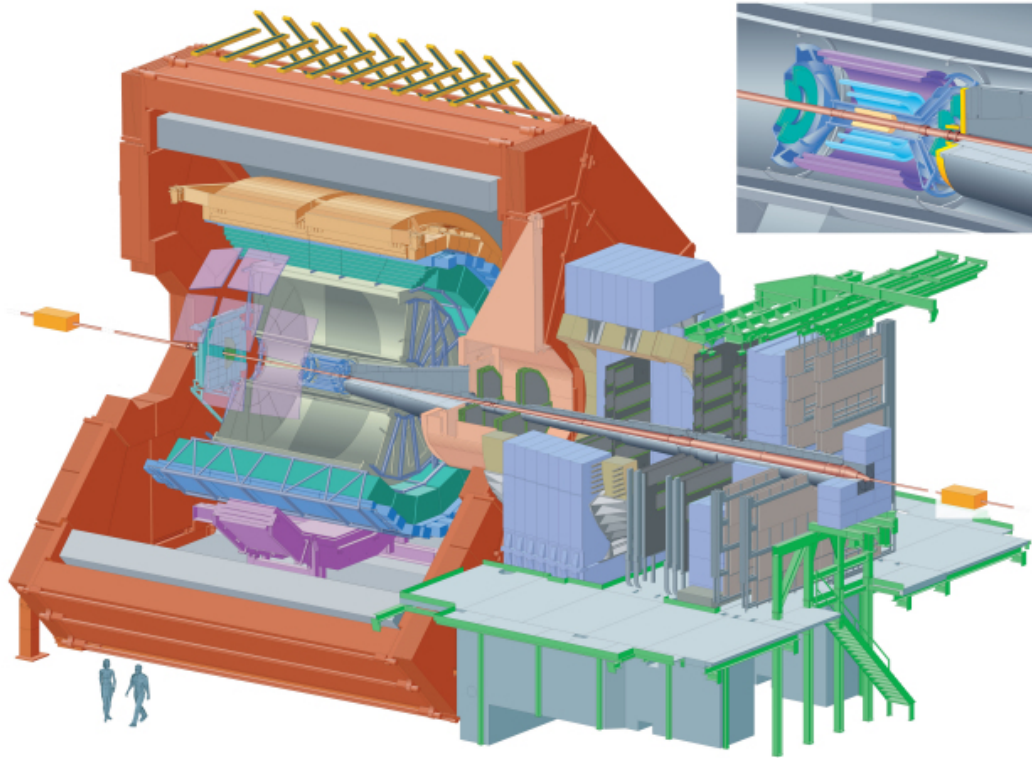


Figure 2.22: Schematic of the ALICE experiment. Figure from [ALI10].

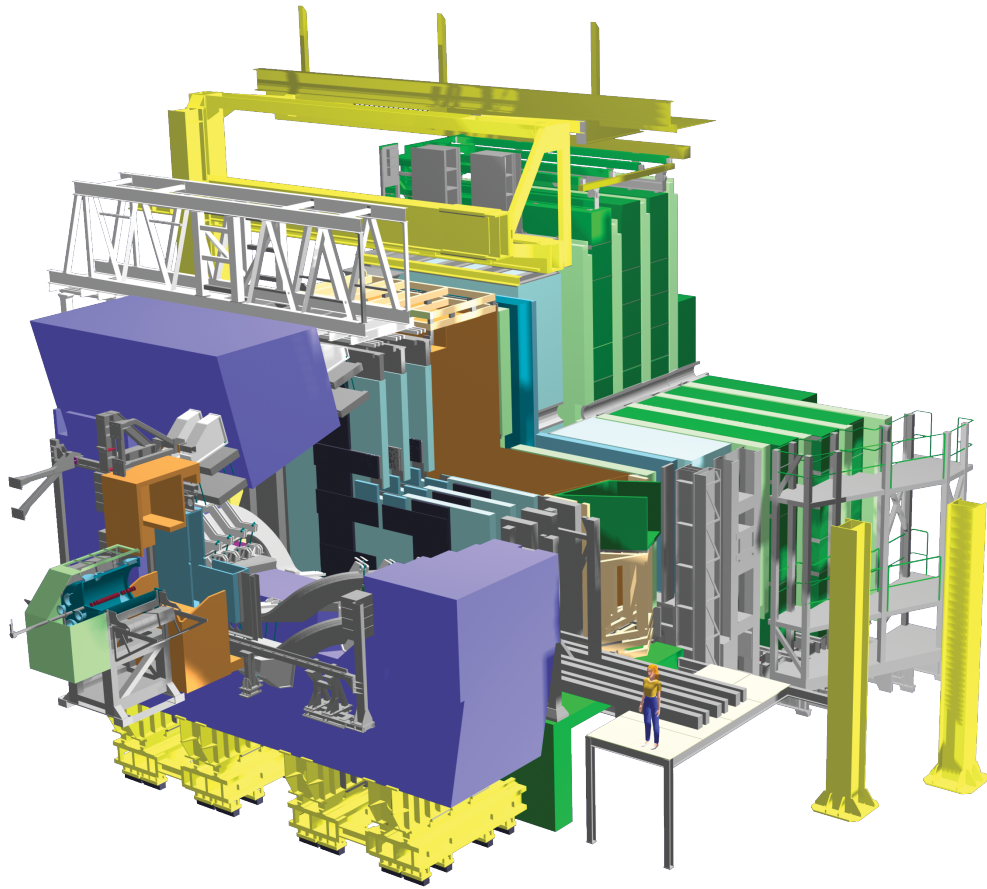


Figure 2.23: Schematic of the LHCb experiment. Figure from [LHC14].

2.4.6 LHCf (Large Hadron Collider forward)

LHCf is a LHC experiment designed to detect forward particles coming from the collisions at large $|\eta|$ to simulate the production of cosmic ray showers in laboratory conditions. The goal is to provide important clues to experiments studying high-energy cosmic rays, which is possible given the LHC energy. The experiment consists of two different 40 kg calorimeters, each 30 cm long, 80 cm high, 10 cm wide placed approximately 140 m away from Point 1 site. Currently 62 scientists from 13 institutes in 6 countries are involved [April 2010] [LHC10, About].

2.4.7 MoEDAL (Monopole and Exotics Detector at the LHC)

The goal of seventh LHC experiment is the search for the magnetic monopole and other highly ionizing massive particles, making it the only experiment dedicated solely to beyond the Standard Model physics including SUSY and extra dimensions. The MoEDAL Collaboration has built a detector around the same interaction point as the LHCb experiment. The array is composed of 400 modules with a total area of 250 m². The MoEDAL experiment is the most recent addition to the LHC family, it was approved in 2010 [MoE14].

2.5 The ATLAS Experiment

ATLAS [ATL10b] is a hybrid particle detector and the largest of the LHC experiments. It was designed as a general purpose experiment to probe the widest possible range of physics: from soft QCD to electroweak precision experiments, Higgs boson searches and other interesting phenomena at TeV scale, including beyond the Standard Model physics. The experimental conditions at LHC pose a challenge to detector design as it requires fast radiation resistive sensors with fine granularity, largest possible geometrical acceptance and efficient particle identification.

Constructing and maintaining this complex state-of-the-art detector requires the participation of a large and skilled workforce. The ATLAS collaboration has more than 3000 scientific authors from 174 institutes located in 39 countries. The leadership and administration is distributed amongst various governance bodies: the collaboration board, executive board, the spokesperson, resource review board etc. Each detector subsystem has its own management team as do the physics analysis teams. The conveners are elected from relevant institutions. [ATL11a, pp. 6a–8a]

Since the discovery of the Higgs boson [ATL12], the scientific programme now focuses on measuring its physical properties. Key components of the physics programme also include Standard Model measurements, electroweak boson production or dedicated top quark studies. In addition, the search continues for experimental evidence of new physics, for example:

- ▶ direct observation of CP violation,
- ▶ decays of supersymmetric particles (squarks, sleptons, gluinos),
- ▶ new gauge bosons (W' , Z'),
- ▶ quark compositeness,
- ▶ exotic matter: dark matter, black holes, extra dimensions etc.

2.5.1 General layout

The experiment was designed and constructed over the course of 20 years and has been in operation since the successful launch of the LHC in 2009. The whole detector has a diameter of approx. 25 m, is more than 45 m long and weighs around 7000 tonnes. It has been installed at the Large Hadron Collider Interaction Point 1 in the UX15 cavern located at CERN Meyrin site in Switzerland. The cavern floor is 92 m underground to provide adequate shielding from background radiation like cosmic rays. [ATL11a, p. 1a]

The layout has a forward-backward symmetric cylindrical geometry with coverage up to $|\eta| < 4.9$. The dominant feature of the experiment is its enormous magnet system that consists of a central solenoid, *barrel region* and *end-cap region* toroids (hence the name “toroidal apparatus”) providing a magnetic field of 2 T, resp. 4 T. The detector subsystems are structured in layers. Going from the centre outwards we encounter:

- ▶ **Inner Detector (ID)** providing precision measurement of particle trajectories and momenta,
- ▶ **Calorimeter system** (ECAL and HCAL) which measures their energies and detects missing transverse energy from neutrinos or generally SUSY particles like neutralinos, if they exist,
- ▶ **Muon Spectrometer (MS)** which identifies and measures muons punching through the detector mass and complements the trigger system.
- ▶ **Magnet System** that bends charged particle trajectories allowing momentum measurement.

For a schematic illustration of ATLAS, see fig. 2.20. In this section we are going to describe the key components of each of the subsystems. The ATLAS Collaboration provides full documentation on the design and performance of each subsystem in the form of technical design reports: [ATL94] [ATL99b] [ATL99a] [ATL08b] [ATL08c].

2.5.2 ATLAS coordinate system

The trajectories of particles produced at the interaction point need to be parametrized. For this we need to define a coordinate system. ATLAS defines its coordinate systems as follows [ATL08c, p. 1]:

Cartesian: Right-handed coordinate system with the nominal Interaction point at its origin. The z-axis is defined by the beam direction, positive z-axis is defined counter-clockwise on the LHC ring (towards Point 8). The detector has two sides: side A which has positive z and side C which has negative z coordinate.

The (x-y) plane is transverse to the beam direction. Positive x-axis is defined from the interaction points towards the centre of the LHC ring, positive y-axis points from the cavern upwards to the surface.

Cylindrical: Cylindrical coordinates are a generalization of polar coordinates used in two dimensions. We introduce the plane normal along the beam axis z and the azimuthal angle ϕ defined around it. The Cartesian coordinates in the transverse plane are simply a projection of the radial distance while the longitudinal direction stays the same: $x = R \cos(\phi)$, $y = R \sin(\phi)$, $z = z$ [Wei].

Spherical: The polar angle θ is the angle from the beam axis in a sense of positive z , i.e. it points anti-clockwise on the LHC ring. As was mentioned in section 2.3.2, using pseudorapidity instead of polar angle is preferred.

For clarity, the coordinate system is illustrated in fig. 2.24.

2.5.3 Magnet system

One of the main features of ATLAS is its unique magnet system [ATL10a]. The magnetic field is a necessary component to allow measurement of charged particle momenta. In total, there are four large superconducting magnets producing magnetic field 2–4 T (which outperforms even state-of-the-art magnetic resonance imaging machines).

The *central solenoid* envelopes the Inner Detector in axial magnetic field of 2 T at the nominal current 7.73 kA. The structure was carefully optimised to keep material thickness as low as possible, the whole coil contributes only ≈ 0.66 radiation lengths X_0 . The coil is 2.40 m in diameter, 5.30 m long and weighs 5 tonnes. It is made of 9 km of superconducting wire wound in 1154 turns. The operating temperature is 4.50 K achieved with liquid helium as coolant. The cooling process takes less than a day and charging takes approximately 30 minutes. The total energy stored in the magnet reaches over 38 MJ. [ATL08c, p. 20] [ATL11a, 2b]

The *barrel toroid* consists of 8 flat air-core coils surrounding the calorimeters. At each side, both end-cap toroids are arranged in a shape of a torus, see section 2.5.3. Each coil is mounted

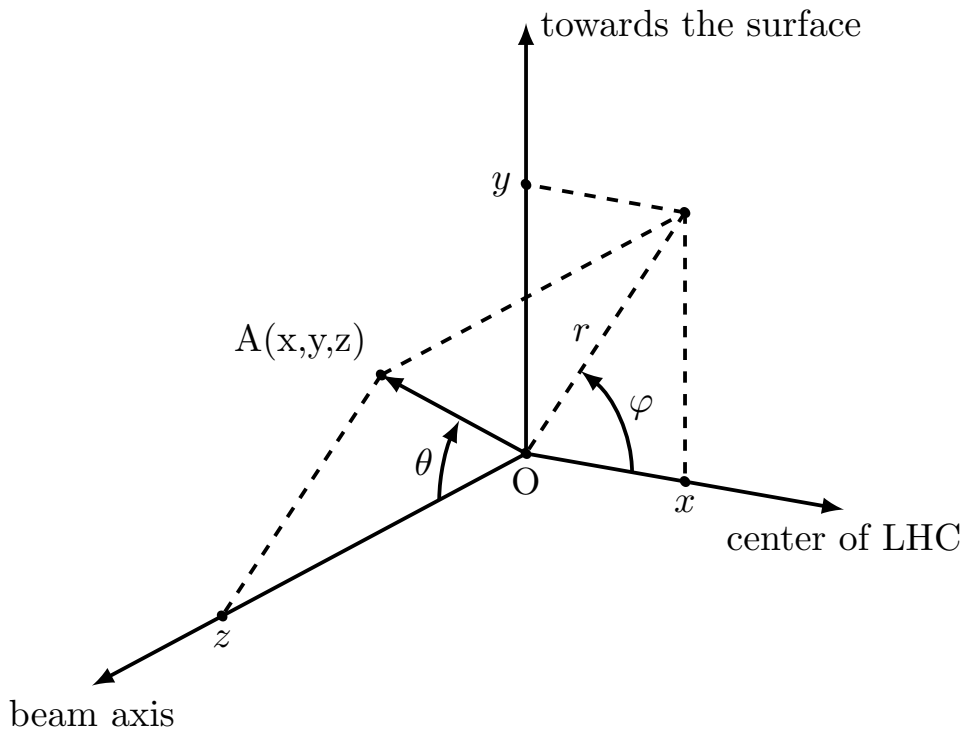


Figure 2.24: Definition of the ATLAS coordinate system which is used to describe position of any point $A(x, y, z)$ in it.

to eight outer rings. The magnet system is 25.30 m long, with an outer diameter of 20.10 m and weighs 830 tonnes. The coils are made from a total of 100 km of superconducting wire that operates at a 20.50 kA nominal current and a temperature of 4.70 K. [ATL08c, p. 21] [ATL11a, 2b]

The *end-cap toroids* are placed on the outer side of the detector in both directions and twisted by 22.50° to ensure ideal overlap in the transverse plane. The coils are 5.00 m long, with an outer diameter of 10.70 m and weighs 240 tonnes, otherwise they are nearly identical to the *barrel* toroids.

The entire system provides a magnetic field over a volume of approximately $12\,000\text{ m}^3$ contained within the cylindrical space defined by the coils. An axial magnetic field of $\approx 2\text{ T}$ is provided for the inner detector and a toroidal field of $\approx 0.50\text{ T}$ and $\approx 1\text{ T}$ for the muon system *barrel* and *end-caps*. The total energy stored in all magnets is $\approx 1.60\text{ MJ}$. [ATL08c, pp. 20–37].

Note on momentum measurement in a uniform magnetic field

The *Inner Detector* as well as the *Muon Spectrometer* measures the tracks and momenta of charged particles. The trajectory of a charged particle in a uniform magnetic field is a helix and the relationship between the curvature and magnetic field is given in eq. (2.2) [Par13, 32.11]. If we consider a simplified example where particle tracks are circular, we can use the description of circular motion to demonstrate how the particle momentum is measured.

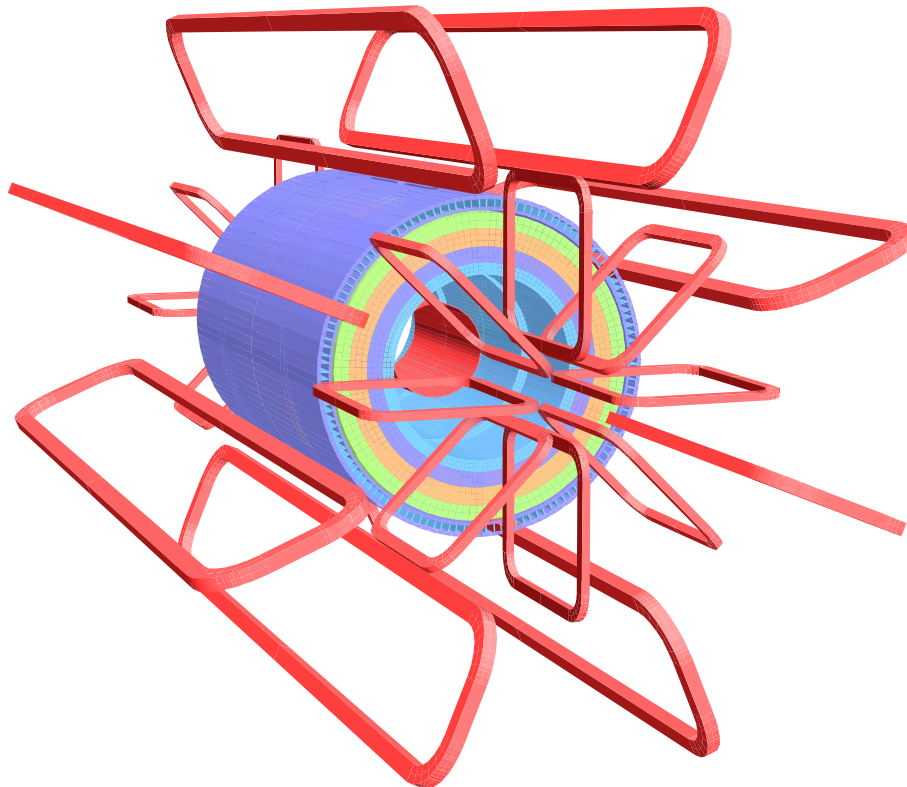


Figure 2.25: Schematic of the ATLAS magnet system. There are a total of eight *barrel* and *end-cap* toroid coils (shown in red) and the central solenoid placed on the inside of the calorimeter volume. (see section 2.5.5 for more information about the calorimeter system). Figure from [ATL08c, p. 20]

Suppose the magnetic field \mathbf{B} [T] goes in z direction, then the force \mathbf{F} [N] required to keep the particle moving on a circular path of radius R [m] is given by the centripetal force:

$$\mathbf{F} = m \cdot \mathbf{a} \quad \text{where} \quad \mathbf{a} = \omega^2 R = \frac{\mathbf{v}^2}{R} \quad \text{thus} \quad \mathbf{F} = m \cdot \frac{\mathbf{v}^2}{R} \quad (2.55)$$

where \mathbf{v} [m s^{-1}] is the particle velocity and ω [rad] is its angular velocity.

The force acting on a particle in a field is given by the Lorentz force, see eq. (2.1). Consider that the track is perpendicular to the magnetic field \mathbf{B} and that electric field $\mathbf{E} = 0$. Since the field was the cause of the change in particle trajectory, we equate the cause and

$$e \cdot v \cdot B = m \cdot v^2 \cdot R^{-1} \quad \text{which simplifies to:} \quad p = e \cdot R \cdot B \quad (2.56)$$

The elementary electric charge for charged particles e is known, the value of the magnetic field B is given by the detector's magnet system and the radius R can be calculated from the track. However the actual direction is given by the Lorentz angle with respect to the existing electric field and the real calculation is more complex. [ATL10b] [ATL08a]

2.5.4 Inner Detector

Let us first focus on the experiment's tracking system. At nominal conditions, the LHC will produce about 1000 particles from the collision at the IP every 25 ns [ATL08c, p. 5]. This places enormous demands on required tracking and vertexing resolutions and timing. In ATLAS, the solution to this problem lies in using high-resolution semiconductor-based detectors made from layers of silicon pixel sensors and pairs of silicon micro-strips with increasing granularity around towards the vertex region. Continuous tracking detectors made of multiple layers of gaseous straw tubes with the capability to generate and detect transition radiation are placed at outer radii.

The combination of semiconductor sensors and straw tubes proved cost-effective and also offers independent methods of measurement. The entire array is referred to as the **Inner Detector** and is 6.20 m long with outer radius 2.10 m. Moving inside out these subsystems are referred to as the *Pixel Detector* (PIX), the *Semiconductor Tracker* (SCT), and the *Transition Radiation Tracker* (TRT), the layout is illustrated in fig. 2.26. Figures 2.27 and 2.27 show the placement of structural elements and examples of particle tracks. [ATL08c, pp. 5–7]

To maximize geometrical acceptance each subsystem is arranged in two regions:

- **barrel** where the active surface is arranged in concentric layers with increasing radii parallel to the beam axis,
- **end-cap** further away from the IP in the longitudinal direction, where the disks (or wheels) are placed perpendicular to the beam axis.

This arrangement maximises the active surface of the detector within $|\eta| < 2.5$. The entire tracker system is enveloped in the *Central Solenoid* (± 3513 mm and radius of 1150 mm) and submerged in a 2 T magnetic field (see section 2.5.3). The ID sensor elements detect charged particles by measuring the liberated charge carriers inside the material at discrete space points. Neutral particles do not leave a track and as such are not detected by the ID.

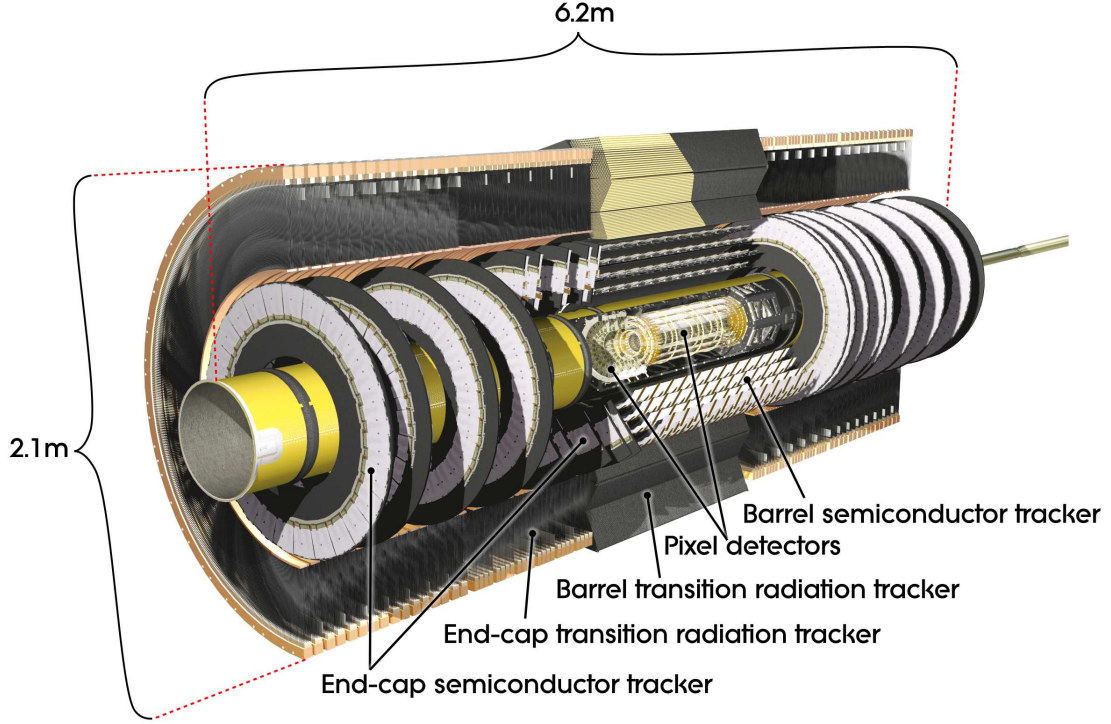


Figure 2.26: Schematic view of the [ATLAS ID](#). Figure from [ATL08c, p. 6] [ATL10b].

All sub-detectors are designed for high-precision measurement of charged particle trajectories. Furthermore the [Pixel Detector](#) contributes to accurate vertexing and measurement of impact parameters, the [SCT](#) to precise measurement of momentum and the [TRT](#) introduces a pattern recognition system allowing for electron identification complementary to the calorimeter system. The nominal resolution is $\sigma_{p_T}/p_T = 0.05\% p_T \oplus 1\%$, where \oplus represents summing in quadrature. The minimal p_T threshold is 0.40 GeV (but can go lower to about 0.10 GeV if required for low- p_T tracking) [ATL08c, pp. 53–54]

2.5.4.1 Pixel Detector

The [Pixel Detector](#) [ATL08a] [Hug06] [Mos11] is a high-granularity high-precision semiconductor tracker installed at the very heart of [ATLAS](#). The detector is designed so that it provides at least three measured points for track reconstruction within $|\eta| < 2.50$. The innermost layer (sometimes referred to as the [b-layer](#)) is situated just 5 cm from the beam pipe. This close proximity allows the detection of short-track particles such as B hadrons and τ^\pm leptons by providing the resolution necessary for precise measurement of impact parameters. These particles decay before reaching the detector and the secondary vertex has to be reconstructed from their decay products.

The pixel detector is a ≈ 1.30 m long cylindrical structure with ≈ 25 cm in diameter. It is made up of 1744 modules spread over three [barrel](#) layers (containing 1456 modules) and three [end-cap](#) disks on each side (288 modules) and covering an area of 1.70 m^2 in total. The [barrel](#) layers have a radius of 50.50 mm, 88.50 mm and 122.50 mm. Each is made of identical staves arranged like fan blades with an inclination angle of 20° . This way the modules are overlapping each other to provide hermetic coverage. There are 22, 38 and 52 staves in the respective layers, each stave is composed

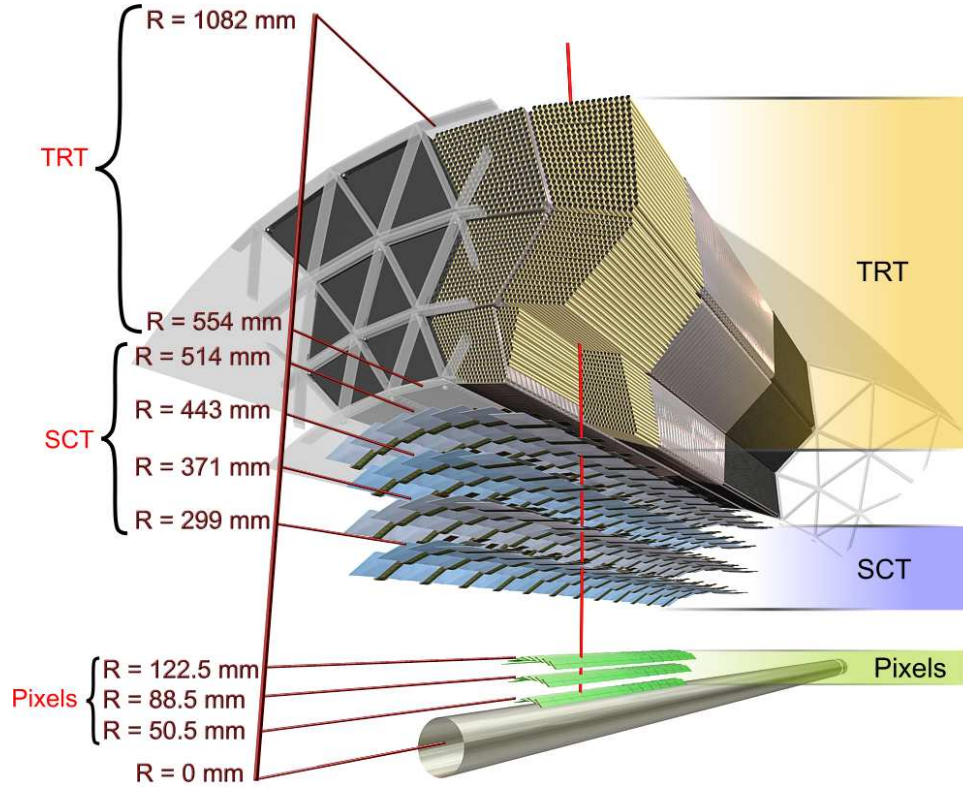


Figure 2.27: Schematic drawing of the structural elements of the **ATLAS ID** in the transverse direction showing the **barrel** region. The detector material is traversed by a charged track with $p_T = 10$ GeV which is shown as the red line. The track traverses successively the beam-pipe, all three cylindrical **PIX** layers in the barrel region (module element $50 \mu\text{m} \times 400 \mu\text{m}$), four **SCT** barrel layers (module element $80 \mu\text{m}$) and ≈ 36 straws of **TRT** (4 mm in diameter). The figure also shows the radial distance of each barrel layer from the beam pipe. Figure from [ATL08c, p. 55] [ATL10b].

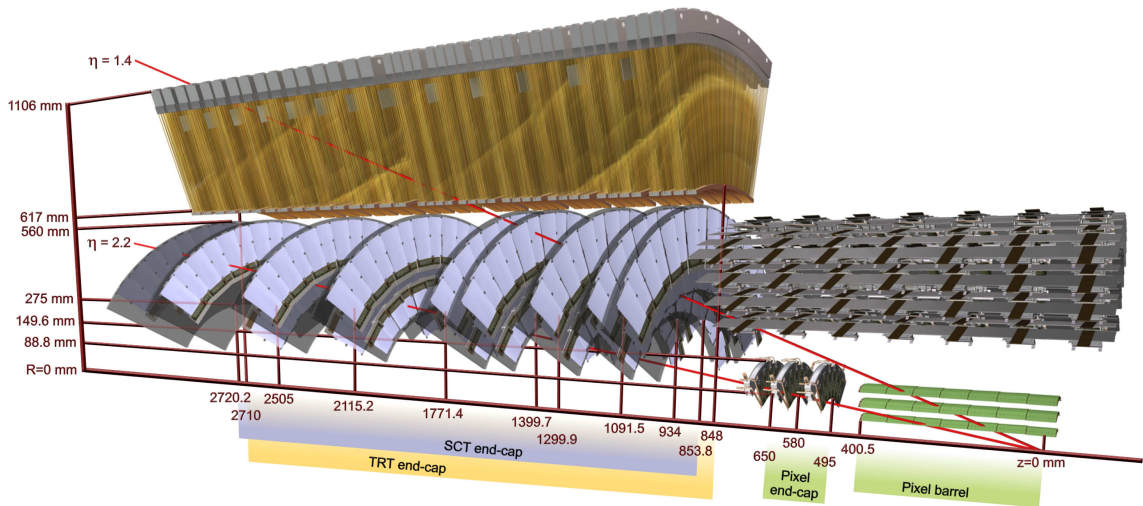


Figure 2.28: Schematic drawing of the structural elements of the **ATLAS ID** in the longitudinal direction shows mainly the **end-cap** region. The detector material is traversed by two charged tracks with $p_T = 10$ GeV and large pseudorapidity ($|\eta| = 1.4$ and 2.2). The first track traverses the beam pipe, then all three cylindrical pixel layers in the barrel region (module element $50 \mu\text{m} \times 400 \mu\text{m}$), four **SCT end-cap** disks (module element $80 \mu\text{m}$) and ≈ 40 straws of **TRT** (4 mm in diameter). The second track has a larger $|\eta|$ which causes it to traverse only the first **PIX** layer, two **PIX end-caps** and the last four **end-caps SCT** (and no **TRT**). The figure also shows the radial distance of each barrel layer from the beam pipe. Figure from [ATL08c, p. 56] [ATL10b].

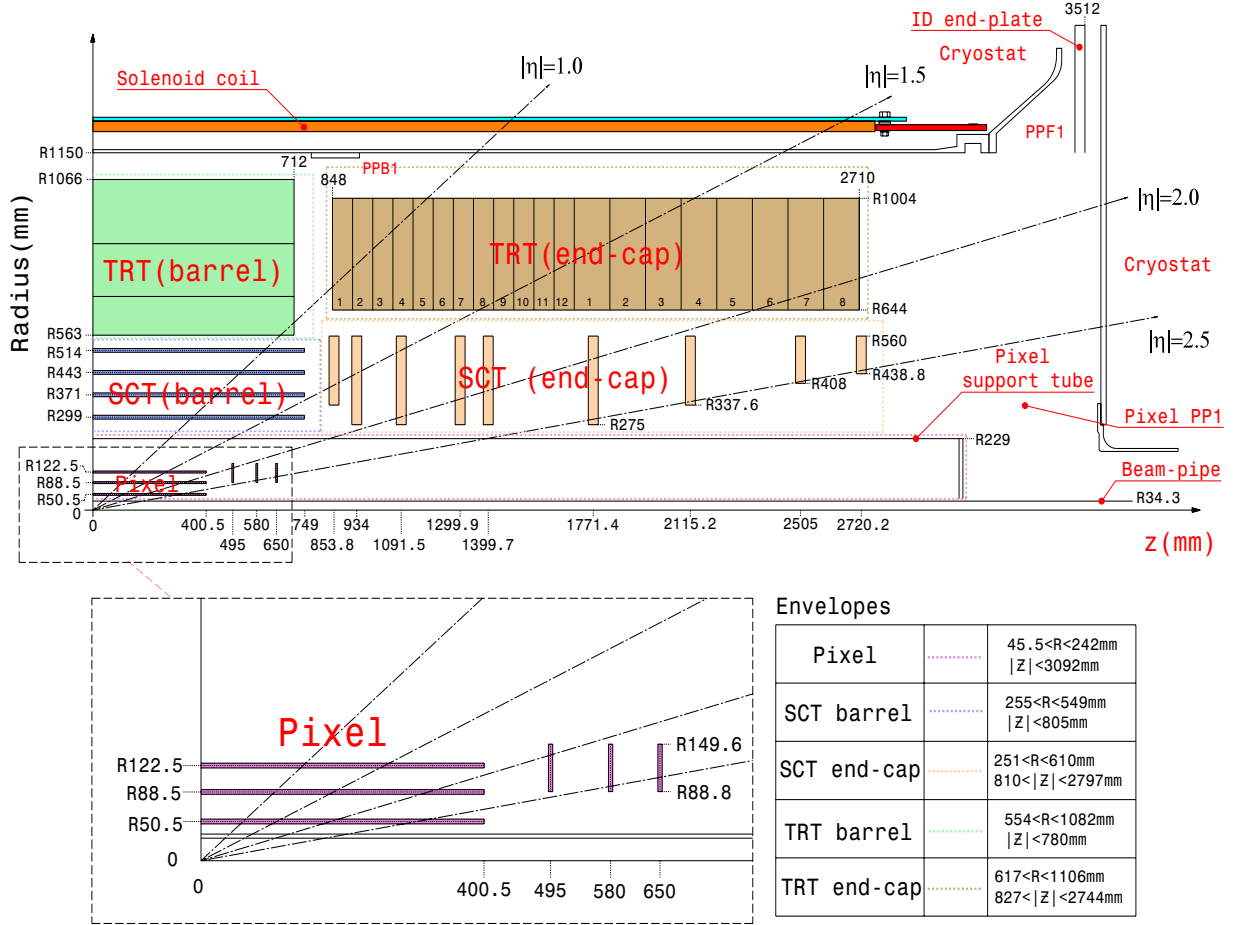


Figure 2.29: Plan view of a quarter-section of the ATLAS ID showing dimensions of all major detector elements. The Pixel Detector is zoomed in at the lower left. Dimensions of the subsystem envelopes are given on the bottom right. The labels PP1, PPB1 and PPF1 indicate support services. Figure from [54][ATL08c].

System	Position	Radial extension [mm]	Intrinsic accuracy [μm^2]	η coverage [-]
Pixels	layer-0	$50.5 < R < 122.5$	$10 (R - \phi), 115 (z)$	± 2.50
	layer-1 and layer-2		$10 (R - \phi), 115 (z)$	± 2.50
	3 end-cap discs	$88.8 < R < 149.6$	$10 (R - \phi), 115 (R)$	± 2.50
SCT	4 barrel layers	$299 < R < 514$	$17 (R - \phi), 580 (z)$	± 1.50
	18 end-cap discs	$251 < R < 560$	$17 (R - \phi), 580 (R)$	± 2.50
TRT	axial barrel straws	$563 < R < 1066$	130 per straw	± 1.00
	radial forward straws	$644 < R < 1004$		± 2.00

Table 2.5: Parameters of the ID subsystems. The Pixel Detector covers an area of 1.70 m^2 , SCT covers 60 m^2 and the total volume of the TRT is 16 m^3 . *Intrinsic accuracy* means that the accuracy specifications are met by the nominal physical and mechanical precision of the machine, geometry and scales, but independent of installation. The values are nominal from the ATLAS 1994 technical proposal but the actual resolution is dependent on beam luminosity. Data from [ATL94], corrections and actualisations from [ATL11a] [ATL08c, pp. 7,57] [Mos11]

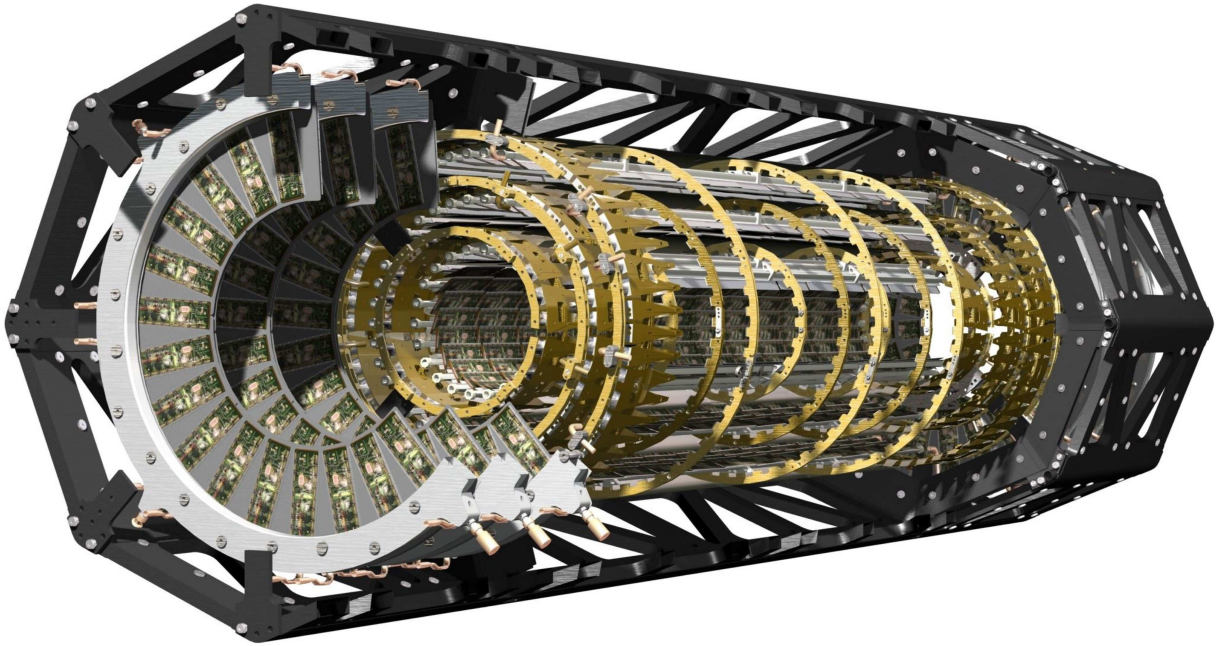


Figure 2.30: Schematic drawing of the [ATLAS Pixel](#). The figure shows the module placement atop the three [barrel](#) layers and three [end-cap](#) wheels within the octagonal support frame. Figure from [\[ATL08c, p. 86\]](#) [\[ATL10b\]](#).

of 13 pixel modules. Each [end-cap](#) disk is made of 8 pixel disk sectors with 6 modules per sector (3 on front, 3 at the back). A schematic cut-away view of the whole structure is shown on [fig. 2.30](#) [\[ATL08c, pp. 57,60–63\]](#)

The pixel module has outer dimensions of 63.40×24.40 mm and consists of 16 front-end (FE) read out chips and one Module Control Chip (MCC) that routes the 40 MHz clock and commands to each FE. Each module has over 47 000 pixels, and there are 1744 modules in the [barrel](#) region only. In total the [Pixel](#) detector has over 80 million channels which is over 80% of the readout channels of the whole [ATLAS](#). [\[Mos11, p. 61\]](#) [\[ATL08a\]](#). [\[ATL11a, p. 1b\]](#)

All pixel sensors are structurally identical, the finest structures are called pixel cells or simply “pixels” and about 90% have dimensions of 50×400 μm^2 and have a thickness of 250 μm . The size of the remaining cells is 50×600 μm^2 as these cover the gaps between neighbouring FE chips. Every pixel is bump-bonded to read-out electronics on the module. Apart from the connecting cables, [barrel](#) and [end-cap](#) modules are identical. [\[ATL08c, p. 57\]](#) A single sensor cell can only record that a particle has passed through it but not where inside the volume it passed. When a charged particle traverses the cell it liberates charge carriers (electrons and holes) along the way which produces the signal. The principle is roughly outlined in [fig. 2.32](#).

The intrinsic accuracy is 10 μm in the transverse plane and 115 μm in the longitudinal direction. For a summary see [table 2.5](#). Performance studies using test beams have later shown the actual accuracy of 14×115 μm^2 . The sensors are a major heat source and require cooling, ideally at temperatures -5°C to -10°C to maintain manageable signal to noise ratio. The chosen coolant is octafluoropropane (C_3F_8), since it is non-flammable, non-conductive, chemically inert and radiation-stable [\[ATL08c, p. 98\]](#). The operating voltage is 150 V which needs to be gradually increased to an estimated 600 V due to radiation damage caused by the close proximity of the detector to the [IP](#). Estimates show that after 7 years in operation, the expected 1 MeV neutron

equivalent fluence could reach $13.50 \times 10^{14} \text{ cm}^{-2}$ in the B-Layer, which roughly translates into 790 kGy of ionising radiation [ATL08c, p. 17]. The total power consumption ranges somewhere around 15 kW. [ATL11a, p. 1b]

2.5.4.2 Semiconductor Tracker (SCT)

Tracking at larger radii is handled by the SCT subsystem. This level is designed very similarly to the Pixel Detector. It uses the same method of detection, very similar materials. The barrel region contains eight strip layers mounted at $R = 300, 373, 447, \text{ and } 520 \text{ mm}$ and 9 end-cap disks installed between 839 to 2735 mm in z . The main difference between SCT and PIX is in the implementation of the modules as they are required to cover a much larger area for reasonable cost.

The detector is designed to record at least four hits for each track passing through it. In the barrel region, the SCT uses small-angle ring-chained strips mounted parallel to the beam axis. Each strip is 6.40 cm long with an inter-strip distance of $80 \mu\text{m}$. In the end-cap region the strip are running radially at an angle of 40 mrad . The strips provide precise measurements in $(R - \phi)$ but less precise measurements in the longitudinal direction. The intrinsic accuracy in $R - \phi$ is $17 \mu\text{m}$, however the accuracy in z is intrinsically $580 \mu\text{m}$ which is more than five times worse than for the pixels [ATL08c, p. 6] [ATL10b] The entire sub-detector consists of 4088 two-sided modules covering the area of 60 m^2 . The total number of readout channels ranges to approximately 6.30 million. [ATL11a, p. 1b]

2.5.4.3 Transition Radiation Tracker (TRT)

The outer level of the tracking system uses a different design than SCT and PIX. It takes advantage of transition radiation (hence the name) which is generated by relativistic charged particles traversing the boundary between two media with different dielectric constants (like solid metal and gas). The detector is composed of approx. 400 000 drift tubes arranged in layers with a 2 mm radius and a wall thickness of $35 \mu\text{m}$. The TRT is designed to operate at room temperature. [ATL08c, pp. 68–69]

The TRT only provides $R - \phi$ information and $|\eta| < 2.0$ coverage (which has been decreased since the original TDR [ATL94]). Its intrinsic accuracy is about an order lower: $130 \mu\text{m}$ per straw. However, a continuous tracking detector compensates for this disadvantage by providing a much higher number of measurements. On average 36 hits inside TRT are expected for a single track with $p_T > 0.50 \text{ GeV}$ within the geometrical acceptance. [ATL08c, pp. 6,59]

The gas mixture is made of non-flammable Xe(70%) CO_2 (27%) O_2 (3%) and its total volume inside the straws reaches 3 m^3 . As the particle passes through the straws it ionises the oxygen inside and the resulting electric field makes the ionised electrons drift creating electrical current. TRT uses an internal calibration in order to meet the stringent requirements on tracking resolution. The goal of this calibration is to estimate the distance of closest approach of a charged particle to each wire in the TRT. This distance is usually referred to as the *drift circle*.

The TRT is also the key system in the Inner Detector because of its ability to identify electrons. Because of their small mass, electrons at relativistic velocities emit more transition radiation than heavier particles like charged pions. The mean rate of energy loss is given by the Bethe-Bloch equation, which can be found in: [Par13, p. 31.2.3] or [Per00, p. 349]. Radiative losses described by the equation are however relevant only for muons and pions since electrons collide with other

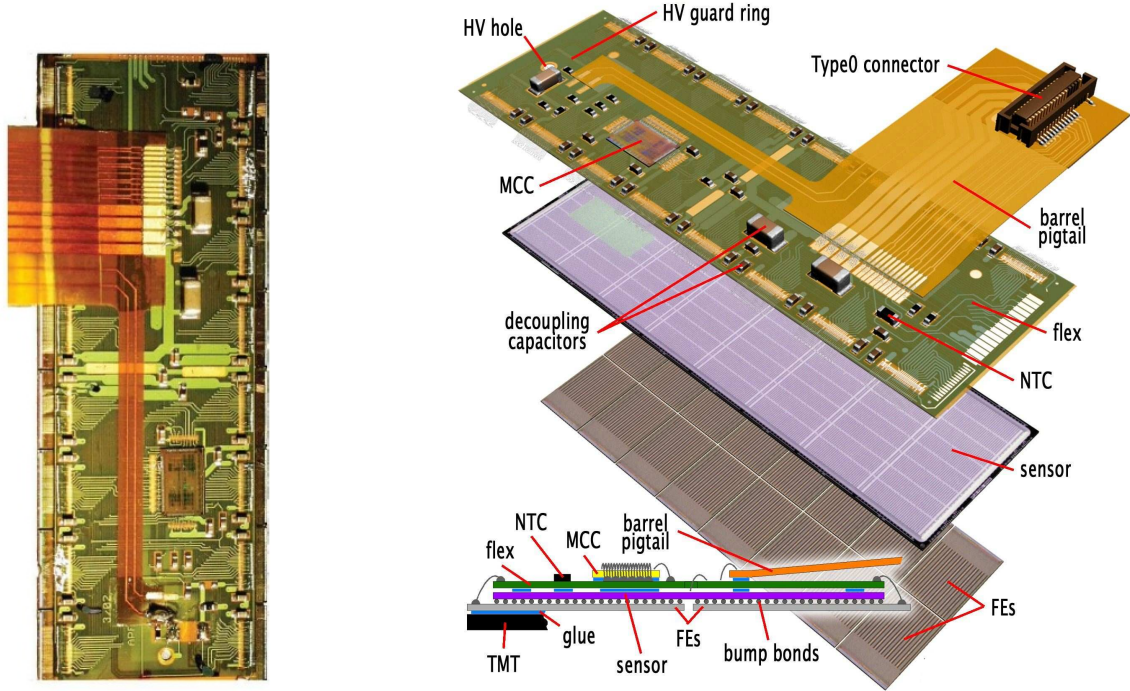


Figure 2.31: Photograph (left) and schematic view (right) of the [ATLAS barrel](#) pixel module illustrating the placement of the module-control chip (MCC), front-end (FE) chips, NTC thermistors, high-voltage (HV) elements and the signal connector. The active region of $63.40 \times 24.40 \mu\text{m}$ contains more than 46 000 pixel cells. Figures and data from [\[ATL08c, p. 61\]](#).

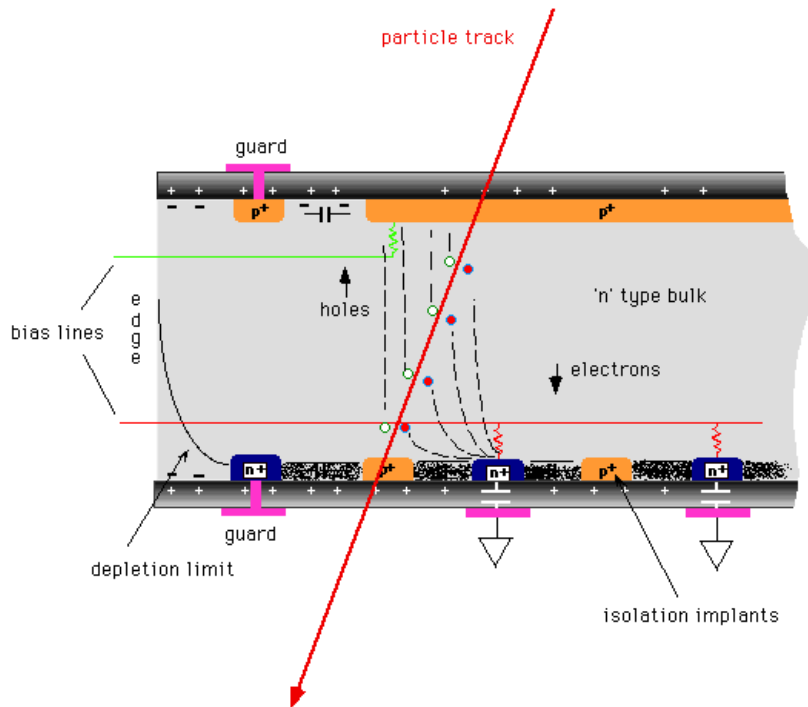


Figure 2.32: Schematic principle of silicon detectors shown on a [SCT](#) silicon strip. The bulk of the detector is depleted by a bias voltage applied across the wafer. When a charged particle passes through the detector it liberates charge carriers producing an electric field. Separated by the field, the holes drift to the back plane, the electrons to the readout strips. This current is the source of the signal that is then amplified and used to mark a hit in the detector. Figure and caption from [\[Par97, ATLAS - Silicon Detectors\]](#).

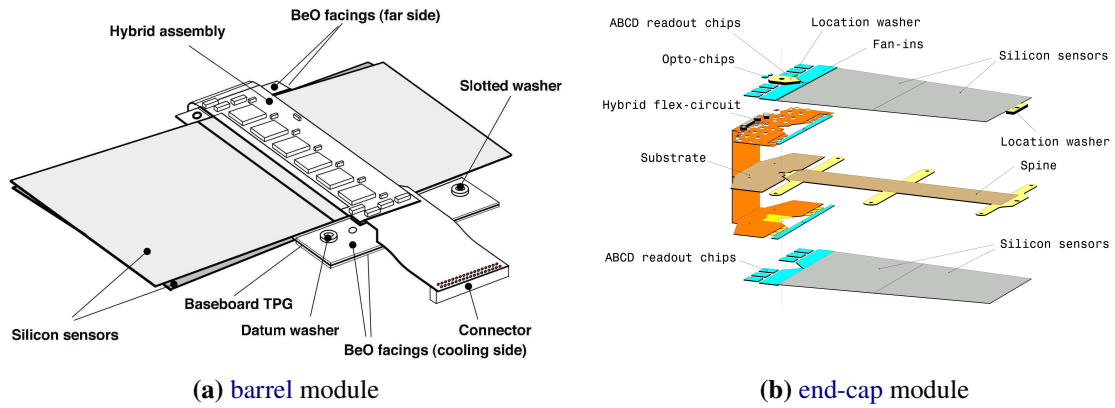


Figure 2.33: Schematic drawing of the ATLAS SCT modules. The barrel module is shown on the left and an exploded view of the end-cap module is shown on the right. Both schematics show the high thermal conductivity spine denoted TPG that links between the coolant and the sensors. Figure from [ATL08c, pp. 65,67].

electrons making the incident particles indistinguishable and lose a majority of their energy via bremsstrahlung. This difference is the basis of their identification. [Par13, sec. 31]

2.5.5 Calorimetry

Calorimeters in particle physics are detectors that serve as a partially active medium which measures the energy and position by means of absorption. The incident particle interacts in the large volume of the detector generating secondary particles and those generate tertiary particles and so on. We refer to this cascade as a particle *shower*. The majority of the incident particle energy dissipates as ionisation or excitation of the medium, which is why these instruments are called *calorimeters*, they measure the total deposited energy in the material. [Par13, sec. 32.9] [Per00, p. 368].

Large hybrid detectors generally employ two types of calorimeters: one for electromagnetic showers caused by electrons and photons and another one which absorbs showers caused by inelastic collisions of hadrons with the nuclei in the material. Both systems are installed in ATLAS and are referred to as the *Electromagnetic Calorimeter (ECAL)* and the *Hadron Calorimeter (HCAL)*: The main tasks of the calorimeter system is to measure:

- Energies and directions** of incident particles to reconstruct their kinematic properties and separate photons and electrons from hadrons.
- Missing energy** (E_T in transverse plane) as it indicates the presence of weakly interacting particles (neutrinos). The total momentum in the collision is conserved because the colliding protons have equal and oppositely directed momenta, hence the total momentum of all collision products must be zero. Any missing contributions from invisible particles can be identified in this manner.

Calorimeters in ATLAS cover larger pseudorapidity range than the Inner Detector going up to $|\eta| < 4.9$ which means they significantly contribute to the overall reconstruction of the event. Calorimeters are also responsible for the containment of electromagnetic and hadronic showers [ATL08c, pp. 7–10]. The calorimeter system is shown schematically in fig. 2.34 and the pseudorapidity coverage is shown in detail in table 2.6.

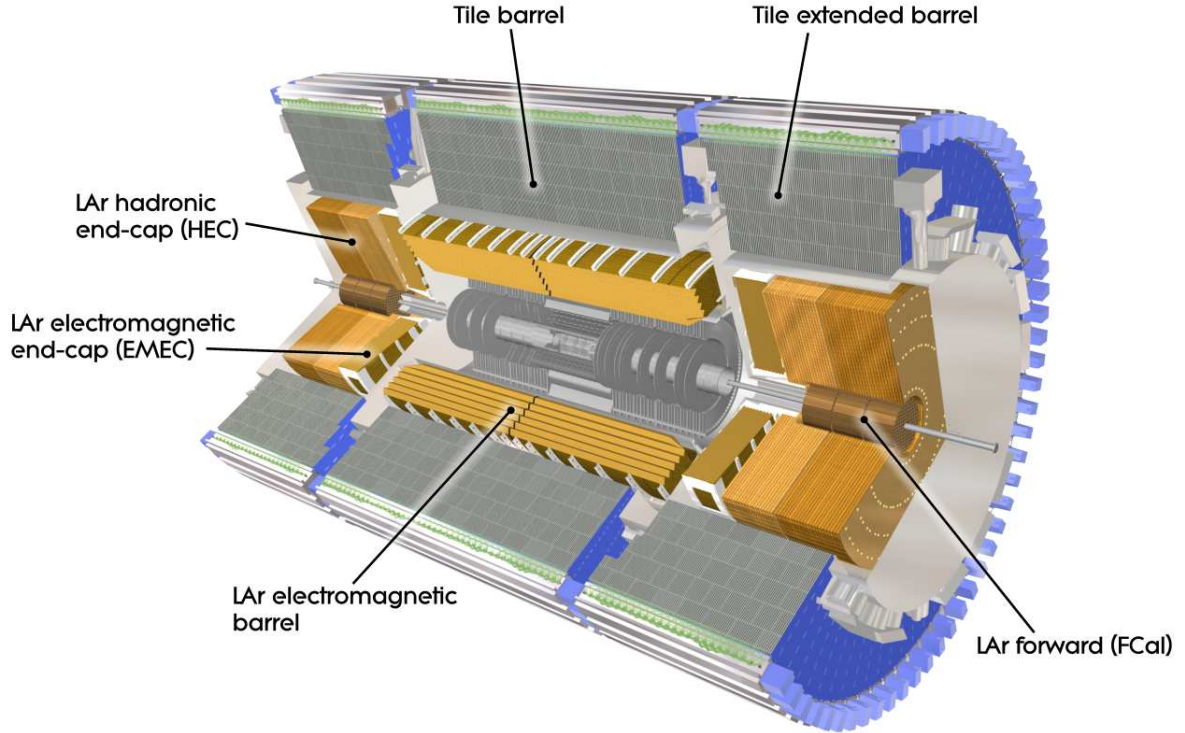


Figure 2.34: Schematic drawing of the ATLAS calorimeter system. Figure from [ATL08c, p. 8] [ATL10b].

2.5.5.1 Electromagnetic calorimeter

Electromagnetic showers are caused by a combination of two phenomena: *bremsstrahlung* and pair production. A parent electron radiates a photon as it passes through the material. This photon then converts to $e^+ e^-$ pairs which in turn radiate and subsequently produce more pairs and so on. The shower propagates through the detector until the energy of the parent E_0 reduces to certain depth D . When $E_0/2^D$ becomes less than what is required for ionisation of neighbouring particle shower abruptly stops. This way the initial energies of parents transform into the rest masses of numerous low energy electrons and positron resulting in a macroscopically observable effect. For more information see [Per00, pp. 368–371].

Electromagnetic shower calorimeters are designed to absorb secondary electrons or photons and produce signals proportional to their energies. The total thickness of the ECAL is larger than 22 radiation lengths in the barrel and larger than 24 in the end-caps (called EMEC). Passing the whole calorimeter translates to roughly 10 interaction lengths giving us a high resolution for energetic jets while also reducing the punch-through to levels manageable by the MS. Figure 2.36 shows the interaction length dependence on pseudorapidity. Hermetic coverage in the largest possible $|\eta|$ range is required for precise missing transverse energy measurements. [ATL08c, p. 8].

The ECAL is divided into a barrel part ($|\eta| < 1.475$) and two end-caps ($1.375 < |\eta| < 3.2$) located at a radius $2.8 < R < 4\text{m}$. The barrel is 6.40 m long and 53 cm thick, weights about 114 tonnes and has about 110 000 read-out channels. It is made of high-granularity liquid argon and lead modules arranged in three layers. The modules are shaped in the form of an accordion to maximize the absorber surface and ensuring that all particles pass through roughly the same amount

of material. Figure 2.35 shows a sketch of a **barrel** module giving granularity for each layer. The three longitudinal layers have **radiation lengths** of $m_T \approx 4.3, 16, 2$.

Each **end-cap** is mechanically divided into two coaxial wheels covering the region ($1.375 < |\eta| < 2.5$) and ($2.5 < |\eta| < 3.2$) respectively, each approx. 63 cm thick and weighing 27 tonnes [ATL08c, pp. 8,114–116]. Each of the three sections have their own cryostat and the operating temperature for the LAr is -183°C . [ATL11a, 1a]

The absorber plates are immersed in *liquid argon* and placed approximately 4 mm apart. Liquid argon is mainly used because it is a high density insulator able to withstand high voltage. A copper grid immersed between the absorber layers acts as an electrode. The whole system is put in a constant 2000 V electric field. When the shower particles produced in the lead plates ionise the argon the electrons drift under the effect of the field to the read-out electrodes. The signal amplitude at the electrode is proportional to the number of electrons reaching the electrode. The nominal resolution is $\sigma_E/E = 10\% \sqrt{E} \oplus 0.7\%$, where \oplus represents summing in quadrature.

2.5.5.2 Hadronic calorimeters

The hadron shower calorimeters are designed to measure hadrons produced in high energy collisions like π^\pm , K^\pm , K^0 , also protons and neutrons [Per00, p. 371]. Similarly to electromagnetic showers, interactions of high energy hadrons within the absorber plates transform the incident energy into many secondary low energy hadrons. Shower particles passing through the scintillating tiles produce light proportional to the incident energy which specifies our read-out signal. Following a standard design, this calorimeter is usually placed behind the electromagnetic calorimeter because hadrons require denser absorbing material (usually copper or steel). For more information see [ATL08c, pp. 120–134].

The **ATLAS HCal** is composed of three separate systems:

Hadronic tile calorimeter (TileCal) is placed directly outside the **ECAL** and is separated into a large **barrel** in the range $|\eta| < 1.0$ and two extended barrel cylinders on either side ranging $0.8 < |\eta| < 1.7$. The absorber plates are made from steel interleaved with scintillating sheets serving as the active material. It is made out of three layers placed perpendicular to the beam with thickness with the total thickness of 7.4 interaction lengths. The scintillator light passes through wavelength shifting fibres attached to the scintillator tile into a read-out photomultiplier. The entire TileCal is composed of 64 wedge-shaped modules each 5.60 m long and weighing 20 tonnes [ATL11a]. The module is shown schematically in figure 2.37a. [ATL08c, p. 10]

LAr Hadronic End-cap Calorimeter (HEC) consists of two wheels located directly behind the **ECAL end-caps** on each side of the detector and inhabits the same cryostat as the **ECAL**. It extends **pseudorapidity** range of $1.5 < |\eta| < 3.2$ overlapping with the forward calorimeter. The detector is designed in a very similar fashion to **ECAL**, but uses 25 mm and 50 mm thick copper absorber plates instead of lead. The plates are interleaved with 8.50 mm LAr gaps. Each wheel is composed of 32 identical wedge-shaped modules, see figure 2.37b. The inner resp. outer radius is 2.03 m resp. 0.48 m [ATL08c, p. 10].

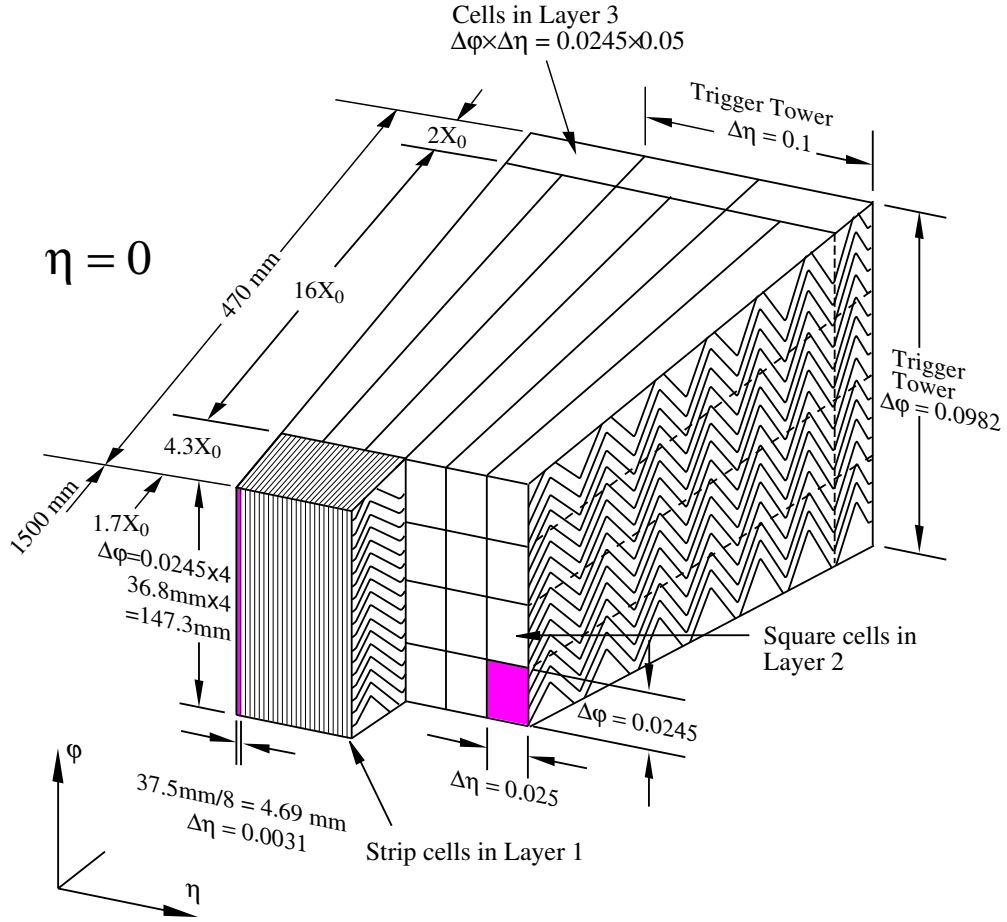


Figure 2.35: Schematic drawing of the accordion shaped barrel modules in the ATLAS ECAL. The figure shows the granularity in $\eta - \phi$ for each layer and the trigger tower. Figure from [ATL08c, p. 114].

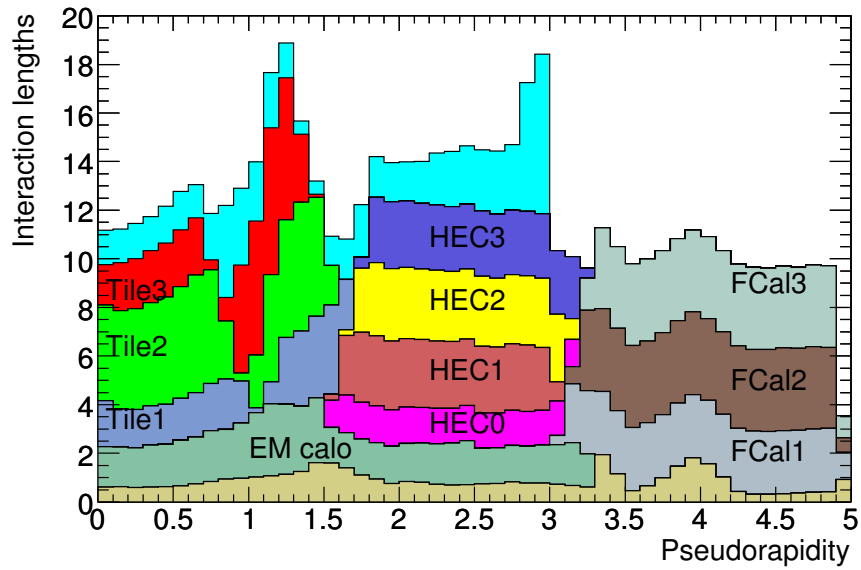


Figure 2.36: Cumulative amount of material in the ATLAS calorimeter system expressed in terms of interaction length as a function of pseudorapidity. Peaks indicate overlaps between the subsystems. Figure from [ATL08c, p. 112].

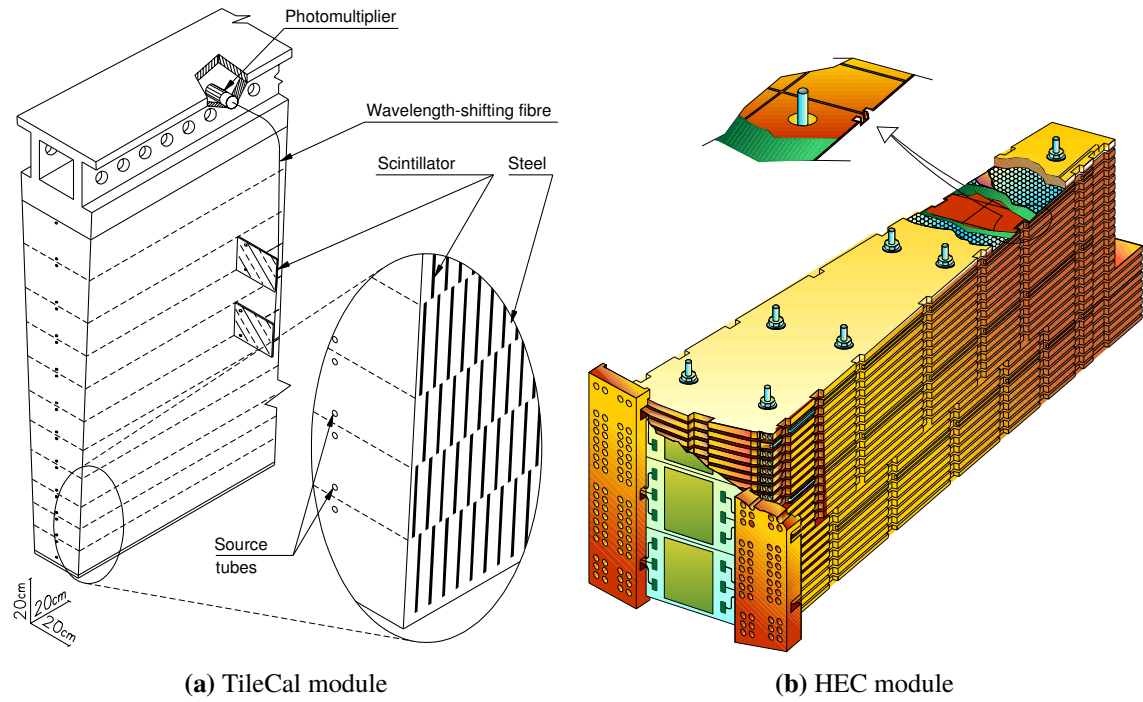


Figure 2.37: Schematic drawing of the [ATLAS](#) TileCal and HEC modules. Figures from [[ATL08c](#), pp. 122,128].

LAr forward (FCal) provides hadronic as well as electromagnetic measurements and covers the high [pseudorapidity](#) range $3.1 < |\eta| < 4.9$. It is approx. 10 interaction lengths deep and uses LAr technology with copper and tungsten absorber plates which are optimized for hadronic interactions. [[ATL08c](#), p. 10]

Figure 2.38 shows a schematic of the calorimeter [end-cap](#) clearly indicating the described detector systems. The nominal resolution of the [HCAL](#) is $\sigma_E/E = 50\% \sqrt{E} \oplus 3\%$, where \oplus represents summing in quadrature. The resolution is worse in the forward direction: $\sigma_E/E = 100\% \sqrt{E} \oplus 10\%$. [[ATL08c](#), p. 5]

Note on instrumentation: service gap

Because of the complexity of the experiment the number of service connections required to keep all detector systems operational is significant. Since cables and connections are inactive material they create gaps in the detector. The largest of such gap regions is referred to as the *crack region* situated between the [barrel](#) and [end-cap](#) parts of the calorimeter system. Figures 2.38 and 2.39 illustrate the problem. To remedy this, there is a number of smaller detector systems placed alongside the connections like the *gap scintillators* and *plug tile calorimeter*. However due to the reduced acceptance most analyses introduce cuts that remove this [pseudorapidity](#) range of these detectors from the analysis. For example, for electrons, it is a standard procedure to leave out the $1.37 \leq |\eta| \leq 1.52$ range entirely.

EM Calorimeter	barrel	end-cap	
Coverage	$ \eta < 1.475$	$1.375 < \eta < 3.2$	
Longitudinal segmentation	3 layers	3 layers	$1.5 < \eta < 2.5$
		2 layers	$1.375 < \eta < 1.5$
			$2.5 < \eta < 3.2$
Granularity ($\Delta\eta \times \Delta\phi$)			
- Layer 1	0.003×0.1	0.025×0.1	$1.375 < \eta < 1.5$
		0.003×0.1	$1.5 < \eta < 1.8$
		0.004×0.1	$1.8 < \eta < 2.0$
		0.006×0.1	$2.0 < \eta < 2.5$
		0.1×0.1	$2.5 < \eta < 3.2$
- Layer 2	0.025×0.025	0.025×0.025	$1.375 < \eta < 2.5$
		0.1×0.1	$2.5 < \eta < 3.2$
- Layer 3	0.05×0.025	0.05×0.025	$1.5 < \eta < 2.5$
Presampler	barrel	end-cap	
Coverage	$ \eta < 1.52$	$1.5 < \eta < 1.8$	
Longitudinal segmentation	1 layer	1 layer	
Granularity ($\Delta\eta \times \Delta\phi$)	0.025×0.1	0.025×0.1	
Hadronic tile	barrel	end-cap	
Coverage	$ \eta < 1.0$	$0.8 < \eta < 1.7$	
Longitudinal segmentation	3 layers	3 layers	
Granularity ($\Delta\eta \times \Delta\phi$)			
- Layer 1 and 2	0.1×0.1	0.1×0.1	
- Layer 3	0.2×0.1	0.2×0.1	
Hadronic LAr	barrel	end-cap	
Coverage		$1.5 < \eta < 3.2$	
Longitudinal segmentation		4 layers	
Granularity ($\Delta\eta \times \Delta\phi$)			
		0.1×0.1	$1.5 < \eta < 2.5$
		0.2×0.2	$2.5 < \eta < 3.2$
LAr forward calorimeter	forward		
Coverage	$3.1 < \eta < 4.9$		
Longitudinal segmentation	3 layers		
Granularity ($\Delta\eta \times \Delta\phi$)	$\approx 0.2 \times 0.2$		

Table 2.6: Parameters of the [ATLAS](#) calorimeter system giving pseudorapidity coverage, granularity and longitudinal segmentation for each subsystem. Data from [\[ATL08c, p. 9\]](#).

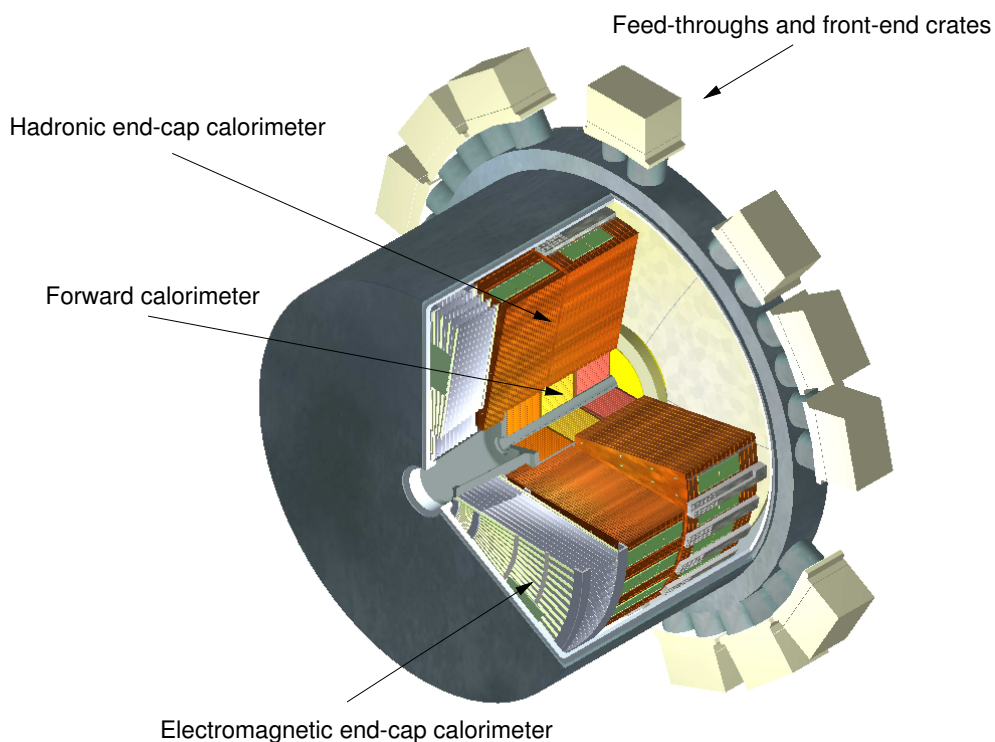


Figure 2.38: Schematic drawing of the calorimeter **end-cap** cryostat showing the position of HEC, FCal and **ECAL end-caps** systems. The figure also shows the **end-cap** region separated from the barrel by an instrumentation gap for cables and feed-throughs. Figure from [ATL08c, p. 135].

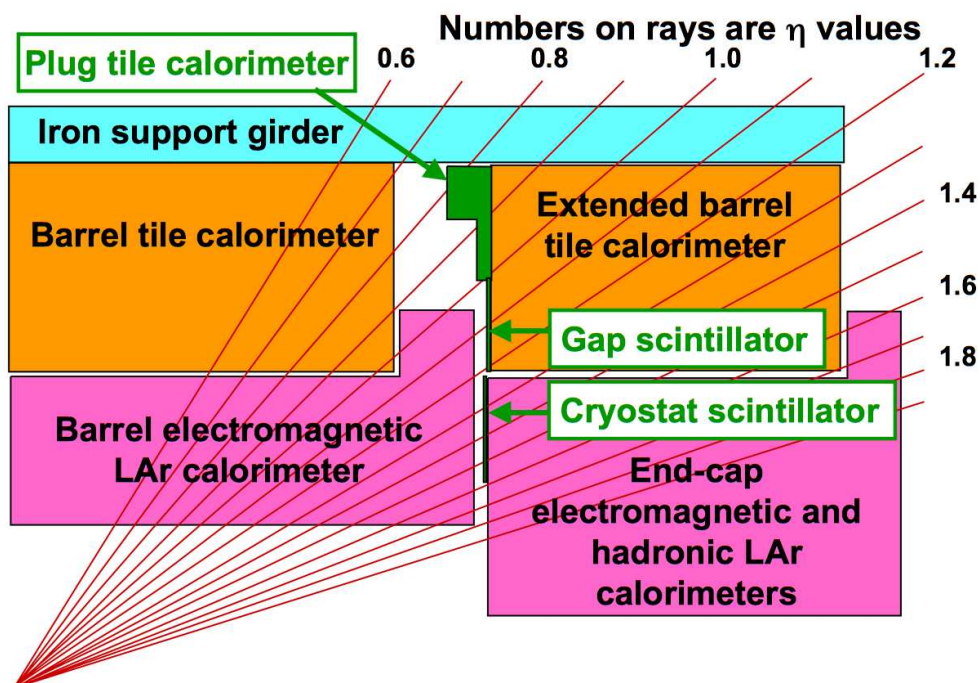


Figure 2.39: Schematic drawing of the longitudinal cross-section of the transition region between the barrel and **end-cap** cryostats. Additional scintillator elements are installed to provide correction for the inactive material. However most physics analyses introduce cuts to remove the region from the selection phase space. Figure from [ATL08c, p. 137].

2.5.6 Muon spectrometer

Relativistic muons have much lower energy loss rates than that the mean value given by the Bethe-Bloch equation [Par13, p. 31.2.3], muons lose only about 1 MeV per millimetre even in a medium like steel. Such particles classified as *minimum ionising particles* (MIPs). Combined with their relatively long lifetime, this is the reason why muon detection systems are placed on the outside layers of the detector.

In ATLAS four different methods of muon detection are implemented. Two of them (CSC and MDT) are designed for precision measurement and the other two (RPC and TGC) are designed for triggering. A short summary is given in table 2.7. The nominal resolution of MS is $\sigma_{p_T}/p_T = 10\%$ up to 1 TeV. All muon detectors are placed on the outside of the calorimeter system. We are going to provide a description of all systems in detail.

2.5.6.1 Monitored Drift Tubes

Monitored Drift Tubes (MDT)s provide precision track measurement over the largest η -range ($|\eta| < 2.7$). The sensors consist of gas-filled aluminium tubes 3 cm in diameter, with high-voltage wires running down through them. The tubes are filled with non-flammable gas composed of 91% Ar and 3% CO₂ pressurized to 3 bars. Because of the high potential difference between the wire and the tube wall, the traversing muon ionizes the gas atoms that in turn drift along the potential caused by the wire resulting in an electric current. With careful timing calibration, muon positions can be measured with an accuracy of $< 50 \mu\text{m}$. The curvature of the muon path determines its momentum and sign of charge. The tubes are mounted perpendicular to the beam axis.

2.5.6.2 Cathode Strip Chambers

Cathode Strip Chambers (CSC)s are used at large pseudorapidities $2.0 < |\eta| < 2.7$ where high incident rate is expected. It is a multi-wire proportional chamber with segmented cathode plates oriented perpendicularly. The chamber is filled with a mixture of 80% Ar, 20% CO₂.

2.5.6.3 Resistive Plate Chambers

The main function of RPC is to provide trigger capabilities and complement the other systems. These RPC stations are installed in the pseudorapidity range $|\eta| < 1.05$ on both sides of an MDT. The gas mixture is composed of 94.7% C₂H₂F₄, 5% C₄H₁₀ and 0.3% SF₆.

2.5.6.4 Thin Gap Chambers

The end-cap region $1.05 < |\eta| < 2.7$ of the muon trigger system is covered by *Thin Gap Chambers* (TGC)s. Similarly to RPC, they contribute to the measurement of the azimuthal angle ϕ and muon triggering. The TGC are multi-wire proportional chambers wire-to-cathode distance of 1.40 mm. The principle of detection is the same as for CSC but their main advantage lies in very high time resolution due to small wire-to-wire distance which is important in the end-cap region. The cells are filled with a mixture of 55% CO₂ and 45% n-C₅H₁₂ (n-pentane). All TGCs provide approx. 400 000 readout channels. [ATL08c, pp. 198–200] [ATL11a, 1a]

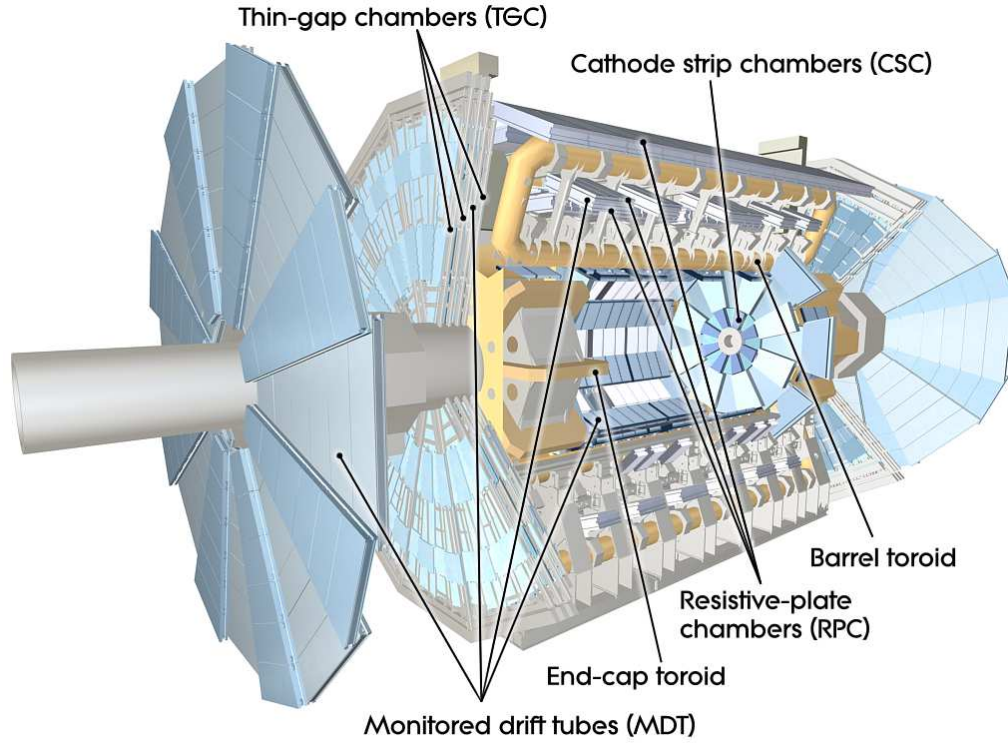


Figure 2.40: Schematic drawing of the [ATLAS Muon Spectrometer](#) showing each of the subsystems. Figure from [ATL08c, p. 11] [ATL10b].

Monitored drift tubes	MDT
Coverage	$ \eta < 2.7$ (innermost layer $ \eta < 2.0$)
Number of chambers	1088 (1150)
Number of channels	339 000 (354 000)
Function	precision tracking
Cathode strip cambers	CSC
Coverage	$2.0 < \eta < 2.7$
Number of chambers	32
Number of channels	31 000
Function	precision tracking
Resistive plate chambers	RPC
Coverage	$ \eta < 1.05$
Number of chambers	544 (606)
Number of channels	359 000 (373 000)
Function	triggering, second coordinate
Thin gap chambers	TGC
Coverage	$1.05 < \eta < 2.7$ (2.4 for triggering)
Number of chambers	3588
Number of channels	318 000
Function	triggering, second coordinate

Table 2.7: The [ATLAS Muon Spectrometer](#) parameters. Data from [ATL08c, p. 12].

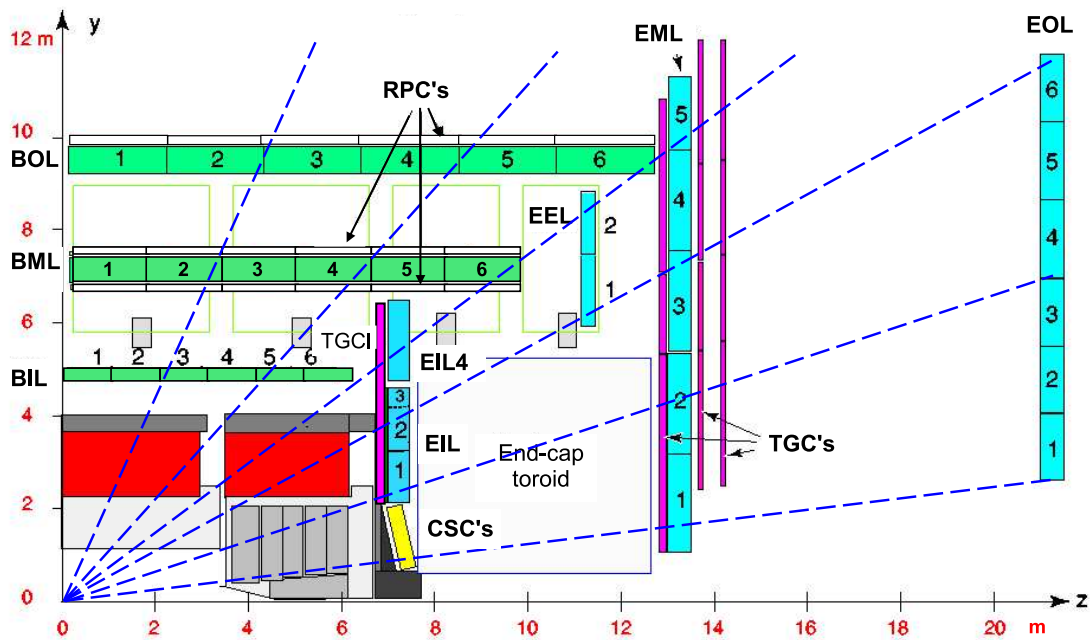
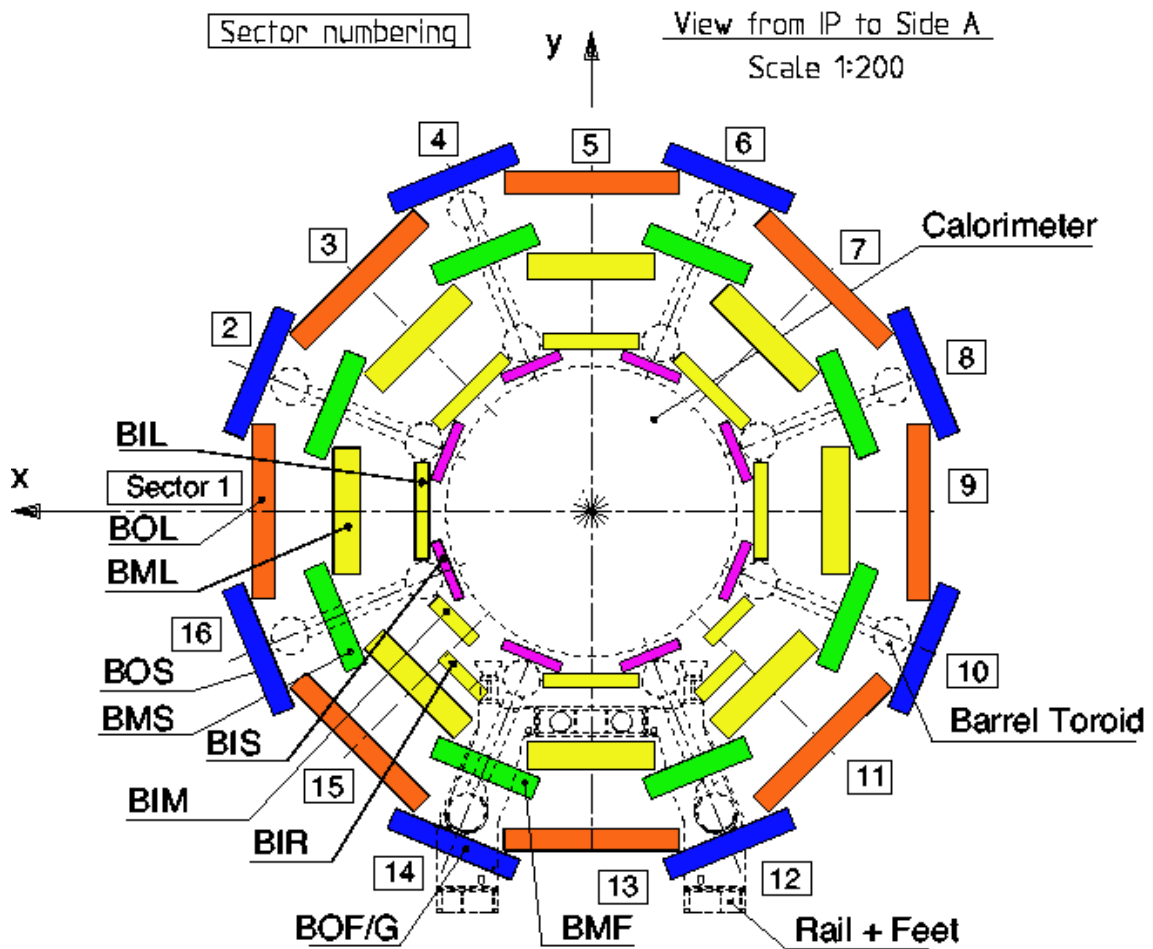


Figure 2.41: Schematic drawing of the ATLAS Muon Spectrometer. Figures from [ATL08c, pp. 122,128].

2.5.7 Forward detectors

Detectors placed in areas of large [pseudorapidity](#) are referred to as forward detectors [[ATL08c](#), p. 14]. In [ATLAS](#) their main function is to measure [luminosity](#) delivered in [ATLAS](#). The following three detector systems are installed at various distances along the beam pipe (see [fig. 2.42](#)):

[LUCID \(Luminosity measurement using Cherenkov Integrating Detector\)](#) is made out of an array of Cherenkov tubes made from aluminium and filled with C_4F_{10} surrounding the beam pipe at distance ± 17 m (in both directions) from the [Interaction point](#). Its main and key function is the measurement of [luminosity](#) using the products of inelastic pp scattering escaping at large [pseudorapidities](#). By design the detector provides both the measurement of integrated luminosity as well as online monitoring of instantaneous luminosity. The goal of its design is to measure [luminosity](#) with an uncertainty lower than 5 %. [[ATL08c](#), p. 206]

The detector works on the principle of detecting Cherenkov radiation. When a charged particle passes through the gas, it emits Cherenkov photons. This radiation produces 60–70 photo-electrons in the gas and an additional ≈ 40 electrons in the quartz window separating the gas tubes from the read-out photomultiplier (PMTs). The PMT threshold is roughly equivalent to ≈ 15 photo-electrons. [[ATL13](#), p. 4]

[ALFA \(Absolute Luminosity For ATLAS\)](#) is installed inside specialized retractable devices called *Roman pots* mounted at ± 240 m from the [Interaction point](#). The Roman pots are special devices mounted inside the accelerator. In its retracted position the Roman pot leaves the full aperture of the vacuum chamber free for the beam. This is important at injection when the beam lacks focus. When the beam become stable and reach nominal energy, the Roman pot is allowed to move closer to the beam axis until it approaches as close as 1 mm to the beam. In this position ALFA can measure particles emitted at very large η .

[ZDC \(Zero-Degree Calorimeter\)](#) was designed mainly to complement the measurement of heavy ion collisions inside [ATLAS](#) by measuring neutrons escaping at [pseudorapidities](#) $|\eta| \geq 8.2$. The calorimeter is made of alternating quartz rods and tungsten plates. It is located at ± 140 m from the [Interaction point](#).

2.6 Experimental conditions

The goal of this section is to examine the technological limitations of the experiment. The following concepts have important and significant effects on the way physics analyses on the [LHC](#) can be performed.

2.6.1 Calibration and alignment

The geometrical precision of a particle detector is determined by its design but also partly by the assembly. It is of course impossible to arrange the detector identically to the blueprint, there are always microscopic shifts in position of detector modules caused by the manufacturing process

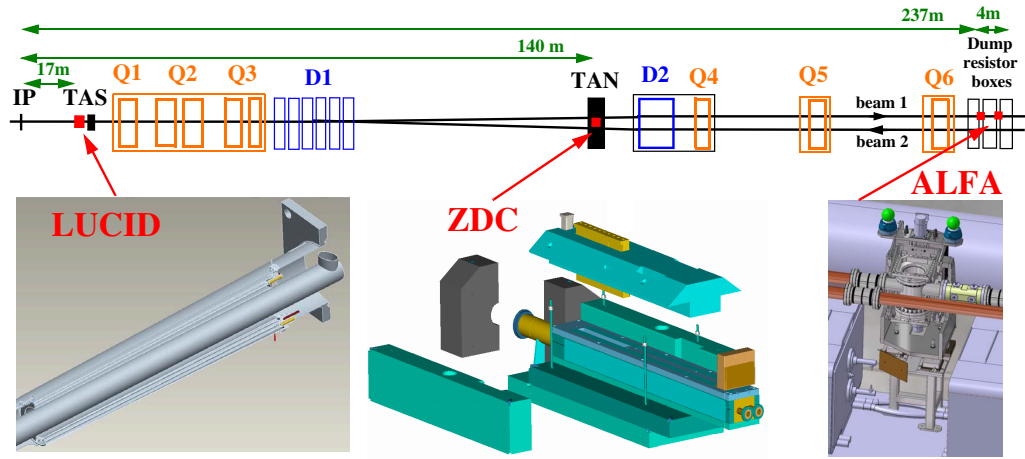


Figure 2.42: Placement of *ATLAS* forward detectors along the beam-line. Figure from [ATL08c, p. 207].

or even entire detector elements could have been moved during construction and installation. Sometimes even an entire detector subsystem is shifted because of the construction of surrounding systems. The assembly tolerance levels for accepted modules in the *ID* is given in [ATL08c, pp. 57, 66].

Generally, the condition where for engineering reasons the modelled detector geometry is different from reality is referred to as *mis-alignment*. This problem is not just restricted to shifts from nominal positions. Material deformations are also present, caused by temperature gradients, tensions caused by the forces produced from the magnet system or simply the effect of gravity. These conditions are strictly monitored.

Mis-alignment directly affects the performance of tracking and vertexing algorithms and all subsequent physics reconstruction that relies on them (like *flavour tagging*). To ensure that *mis-alignment* of detector modules does not impact the tracking uncertainties by more than 20 % above the intrinsic resolution, the actual module positions must be determined within approx. $7\text{ }\mu\text{m}$ for *Pixel*, $12\text{ }\mu\text{m}$ for *SCT* and $30\text{ }\mu\text{m}$ for *TRT* in the $(R - \phi)$ plane. For a precision measurement of the mass of the *W* boson, the module position have to be exactly determined within a level of $1\text{ }\mu\text{m}$ or better. [ATL08c, p. 299] A lepton from *W* decay typically carries a transverse momentum of $p_T \approx 40\text{ GeV}$, resulting in a sagitta of approximately 1 mm as the lepton traverses the *ID* cavity. To get a systematic alignment uncertainty below 0.10 % of the sagitta in the *ID*, the uncertainty in module position must go beyond $\approx 1\text{ }\mu\text{m}$. [ATL08c, p. 28] The expected nominal precision of *ATLAS* subsystem was given in the previous section.

To illustrate the effect, fig. 2.43 shows schematically the effect of *misaligned* modules. The filled black rectangle represents the actual position of the three modules. The dashed

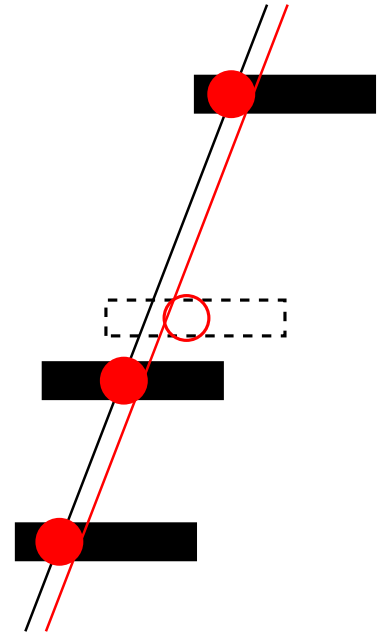


Figure 2.43: Detector misalignment and its effect on track reconstruction. Based on a figure by Grant Gorfine.

rectangle represents the nominal position of the middle module which is actually *misaligned*. The solid black line represents the real particle track with full red dots as hit in modules. The empty red circle is where the reconstruction algorithm expects the hit was made based on the knowledge of the perfect detector geometry. The result is the fitted track showed as a red line which is clearly different from the real trajectory of the particle. The procedure that determines accurately the actual positions of detector elements and sets the corrective constants is called *alignment*. This task is enormously complex since there are 6 degrees of freedom for every module if treated as a rigid body. Different techniques are used for alignment involving Monte Carlo simulations, cosmic-ray data and combined test-beam (CTB). All these approaches are based on the minimisation of hit residual from high- p_T tracks. The residual is defined as the measured hit position minus the expected hit position from the track extrapolation. Testing the detector with millions of tracks is required to reach the required precision. More information on alignment of the inner detector in [ATL08c, pp. 299–302].

2.6.2 Delivered luminosity

The determination of delivered *luminosity* is a critical ingredient in physics analyses. *Luminosity* measured at the experiment (per second, per run, per period) is proportional to the number of events observed for a specific process given its *cross-section*. Any uncertainty on the total integrated *luminosity* directly propagates into the uncertainty of the whole measurement, it is therefore absolutely essential that these uncertainties are estimated very carefully. The different methods and algorithms are discussed in great detail in ATLAS *luminosity* public documentation [ATL14d] [ATL13] [ATL11b] [ATL11c] [ATL11d].

Expressing \mathfrak{L} from eq. (2.25), the *luminosity* is proportional to the interaction rate and inversely proportional to the *cross-section-NoValue-*. The delivered luminosity inside ATLAS is given by the rate of inelastic collisions R_{inel} over the pp inelastic *cross-section* σ_{inel} :

$$\mathfrak{L} = \frac{R_{\text{inel}}}{\sigma_{\text{inel}}}. \quad (2.57)$$

In analogy to eq. (2.34) the *luminosity* of a storage ring operating with a revolution frequency f_{rev} and N_b bunch pairs colliding at the IP can be written as [ATL13, p. 2]

$$\mathfrak{L} = \langle \mu \rangle \frac{N_b f_{\text{rev}}}{\sigma_{\text{inel}}}, \quad (2.58)$$

where instead of providing the beam profiles and number of particles for each of the colliding bunches we have introduced the *mean number of interactions per bunch crossing* $\langle \mu \rangle$. Since the accelerator revolution frequency f_{rev} and the number of bunch pairs is known from external measurements of the accelerator parameters, the goal is to measure $\langle \mu \rangle$ and σ_{inel} to obtain the delivered *luminosity*.

The total inelastic *cross-section* and consequently the *mean number of interactions per bunch crossing* degrades with the efficiency ϵ_{alg} of a particular *luminosity* reconstruction algorithm on a particular detector:

$$\sigma_{\text{vis}} = \epsilon_{\text{alg}} \cdot \sigma_{\text{inel}}, \quad (2.59)$$

$$\langle \mu \rangle_{\text{vis}} = \epsilon_{\text{alg}} \cdot \langle \mu \rangle. \quad (2.60)$$

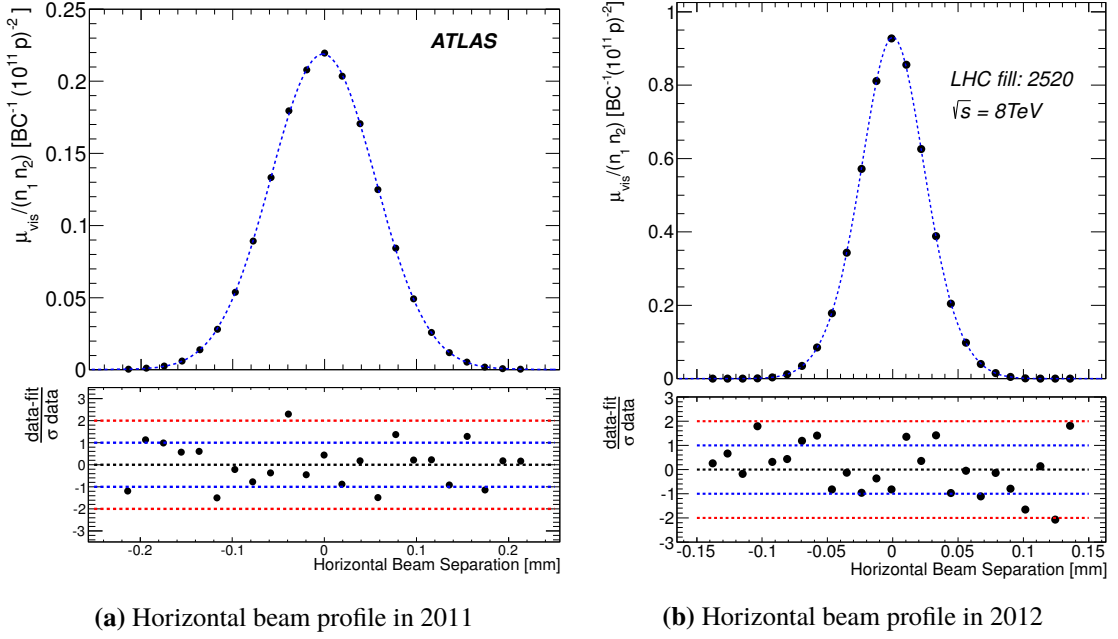


Figure 2.44: Horizontal beam profile showing the specific interaction rate versus the nominal beam separation. Figures from [ATL13] [Lum12]

where $\langle \mu \rangle_{\text{vis}}$ is an experimentally observable quantity and σ_{vis} for a particular detector is fixed. For the determination of **luminosity** these efficiencies cancel out, as is obvious from eq. (2.58).

This effectively means, that in order to use $\langle \mu \rangle$ as a **luminosity** monitor, we simply have to determine the visible **cross-section** for each detector and each algorithm. The calibration of σ_{vis} is performed using **van der Meer scan** that allow us to determine the absolute beam **luminosity** from the direct measurement of beam parameters, see section 2.1.4. Combining the scan with the knowledge of bunch population provides a direct determination of the **luminosity**. Comparing this **luminosity** delivered in the **VMS** scan to the the visible interaction rate $\langle \mu \rangle_{\text{vis}}$ yields the visible **cross-section** σ_{vis} . The summary of **VMS** scans performed at IP 1 is given in table 2.8, the scans performed on May 15, 2011 were used to determine the **luminosity** uncertainties on 7 TeV analyses. The profile of scan VII is given in fig. 2.44. [ATL13, p. 7]

Scan number	I	II–III	IV–V	VII–IX	I–III
LHC Fill Number	1059	1089	1386	1783	2520
Date	Apr 26, 2010	May 9, 2010	Oct 1, 2010	May 15, 2011	April 16, 2012
No. of colliding bunches N_b	1	1	6	14	35
Total bunches per beam	2	2	19	38	48
Typical bunch intensity [10^{11}]	0.10	0.20	0.90	0.80	0.60
Typical β^* at IP [m]	2	2	3.50	1.50	0.60
Approx. transverse beam size [μm]	45	45	57	40	18
Nominal half crossing angle [μrad]	0	0	± 100	± 120	± 145
Typical luminosity per bunch [$\mu\text{b s}^{-1}$]	4.50×10^{-3}	1.80×10^{-2}	0.22	0.38	0.81
$\langle \mu \rangle$ [interactions/BC]	0.03	0.11	1.30	2.30	5.20

Table 2.8: Summary of the main characteristics of **van der Meer scan** scans performed at **ATLAS** interaction point in 2010 and 2011. H indicates a horizontal scan, V indicates a vertical scan. Data from [ATL13] [Lum12].

The systematic uncertainty of the **luminosity** measurement is reduced using multiple algorithms

and different detection methods. Generally speaking, the methods of **luminosity** measurement can be classified into three categories: *event counting*, *hit counting*, *particle counting*. The majority of algorithms in **ATLAS** use event counting, where each particular **BC** is required to pass a set of criteria designed to detect the presence of at least one inelastic pp collision which allows us to express $\langle\mu\rangle \approx N_{\text{pass}}/N_{\text{BC}}$. [ATL13, pp. 2–3] However in the case of higher $\langle\mu\rangle$, the condition referred to as *pile-up* (PU) (see section 2.6.3), this relationship is no longer linear and Poisson statistics must be used. The linearity of event counting algorithms is cross-checked using hit counting algorithms at high values of $\langle\mu\rangle$. Here, instead of counting **bunch crossings** with more than one interaction, we count the number of readout channels above a given threshold. See the description of **EVENTOR** and **EVENTAND** algorithms in [ATL13, pp. 5–6].

Detector	Pseudorapidity coverage	# of readout channels
Pixel Detector	$ \eta < 2.5$	8×10^7
Semiconductor Tracker	$ \eta < 2.5$	6.30×10^6
Transition Radiation Tracker	$ \eta < 2.0$	3×10^5
Minimum Bias Trigger Scintillators (MBTS)	$2.09 < \eta < 3.84$	32
LAr:EMEC	$2.5 < \eta < 3.2$	3×10^4
LAr:FCal	$3.1 < \eta < 4.9$	5632
Beam Conditions Monitor (BCM)	$ \eta = 4.2$	8
LUCID	$5.6 < \eta < 6.0$	32
ZDC	$ \eta > 8.3$	16

Table 2.9: Comparison of relevant characteristics of detector used for **luminosity** measurement. Data from [ATL11b, p. 3].

There are two fast detectors in **ATLAS** that are capable of making precise **luminosity** measurement for each bunch crossing. The first is Cherenkov forward detector **LUCID** which we described in section 2.5.7 and the second is dedicated **Inner Detector** monitoring system **BCM** (Beam Conditions Monitor) which consists of four small diamond sensors arranged around the beam pipe at $z = \pm 184$ cm from the **IP**. The list of contributing detectors is given in table 2.9 [ATL13, pp. 3–4] [ATL13, p. 26]. The total **luminosity** uncertainty on the results in this thesis is 1.80 % (2.80 %) for 7 TeV (8 TeV) analysis. Table 2.10 shows the summary of systematic uncertainties on the **luminosity** measurement:

- Bunch population product can vary by 10–20 % between collisions and is determined by an external analysis on the accelerator.
- Calibration uncertainties of the **VMS** scan come from beam position jitter, consistency of visible **cross-section**, beam-beam effects, emittance growth etc.
- “Afterglow” corresponds to any residual activity at the **Interaction point** after the collision.
- **BCM** stability uncertainty comes from the tuning of **BCM** thresholds throughout the data taking period.
- Long-term stability evaluates the time dependency of each algorithm (over time, the detector response and sensitivity may change)

See [ATL13] for a detailed discussion of systematic uncertainties on **luminosity**. It should be noted here that our understanding of the beam parameters and our detector improve over time which

leads to reduction of systematic uncertainties. This can be already seen by comparing results from [ATL13] and [ATL11c].

Uncertainty source	2010	2011	2012
Bunch population product $N_1 N_2$	3.10 %	0.50 %	0.38 %
Calibration uncertainties	1.50 %	1.40 %	3.25 %
Afterglow correction	–	0.20 %	0.20 %
BCM stability	–	0.20 %	–
Long-term stability	0.50 %	0.70 %	1.00 %
$\langle\mu\rangle$ dependence	0.50 %	0.50 %	1.00 %
Total uncertainty	3.50 %	1.80 %	3.57 %

Table 2.10: Sources of relative systematic uncertainties $\delta\mathcal{L}/\mathcal{L}$ on the calibrated luminosity scale coming from the VMS scan. The reduction in bunch population uncertainty comes from the better understanding of the bunch population products. Data from [ATL13].

2.6.3 Pile-up

The LHC was designed to be a discovery machine, it's main goal is to generate largest possible statistics of inelastic pp collisions at high energies. This high occupancy environment is particularly challenging to precision analyses. Depending on the length of the read-out window of the particular sub-detector, overlapping signals from multiple interactions or neighbouring bunch crossings can be present when the detector is read out. This phenomenon is referred to as **pile-up**. This is usually divided into:

- a) **in-time pile-up** which results from multiple interactions in the same bunch crossing, and
- b) **out-of-time pile-up** refers to overlapping of the read-out window with interactions from adjacent bunch crossings.

Assuming the number of pp interactions per bunch crossing follows a Poisson distribution, we define μ is the mean value. During a fill μ decreases with decreasing beam intensity and increasing emittance. The number of interactions per bunch crossing also varies between bunches, thus the number of interactions averaged over all bunch crossings and averaged over the data analysed is referred to as **mean number of interactions per bunch crossing**. In data, $\langle\mu\rangle$ is calculated using the formula eq. (2.58), as discussed in the section above. The **mean number of interactions per bunch crossing** for 7 TeV and 8 TeV is shown in fig. 2.47. During 2011 the proton bunches were typically separated by 50 ns, which is still twice the nominal LHC spacing. [Was12]

As shown in fig. 2.45, $\langle\mu\rangle$ has increased to more than 15 by the end of 2011 and certain runs had up to 23 interactions per bunch crossing, reaching the design value of the LHC. By 2012 the peak number of interactions by far exceeded 30 (see fig. 2.48), which is beyond the design specifications of the ATLAS Inner Detector. However, to date, no indication of detector saturation has been observed [Was12, p. 17]. However, under these conditions, a precise **pile-up** modelling is required, otherwise it would inevitably lead to a global increase of systematic uncertainties. As we mentioned in section 2.6.2, the relationship between event count and delivered **luminosity** is not linear in the presence of high **pile-up** which is why it also directly affects the **luminosity** uncertainty,

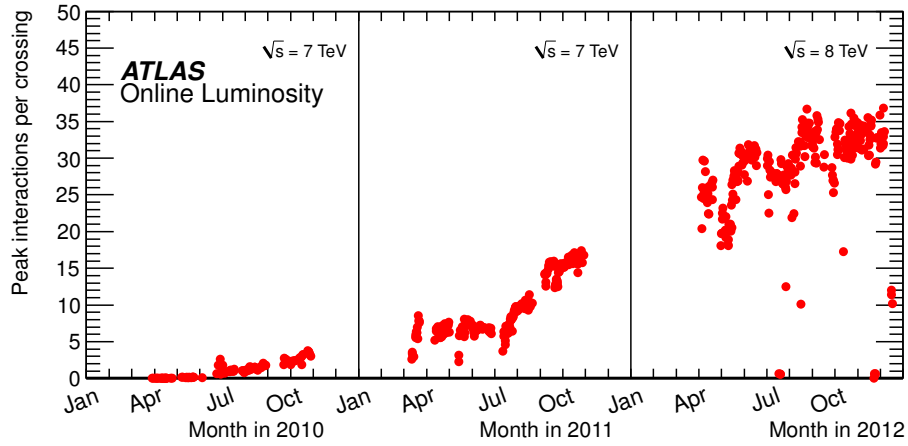


Figure 2.45: The maximum mean number of events per beam crossing versus day during the pp runs of 2010, 2011 and 2012. The plot shows the average value for all bunch crossings in a lumi-block. The online luminosity measurement is used for this calculation. Only the maximum value during stable beam periods is shown. Figure from [ATL14d].

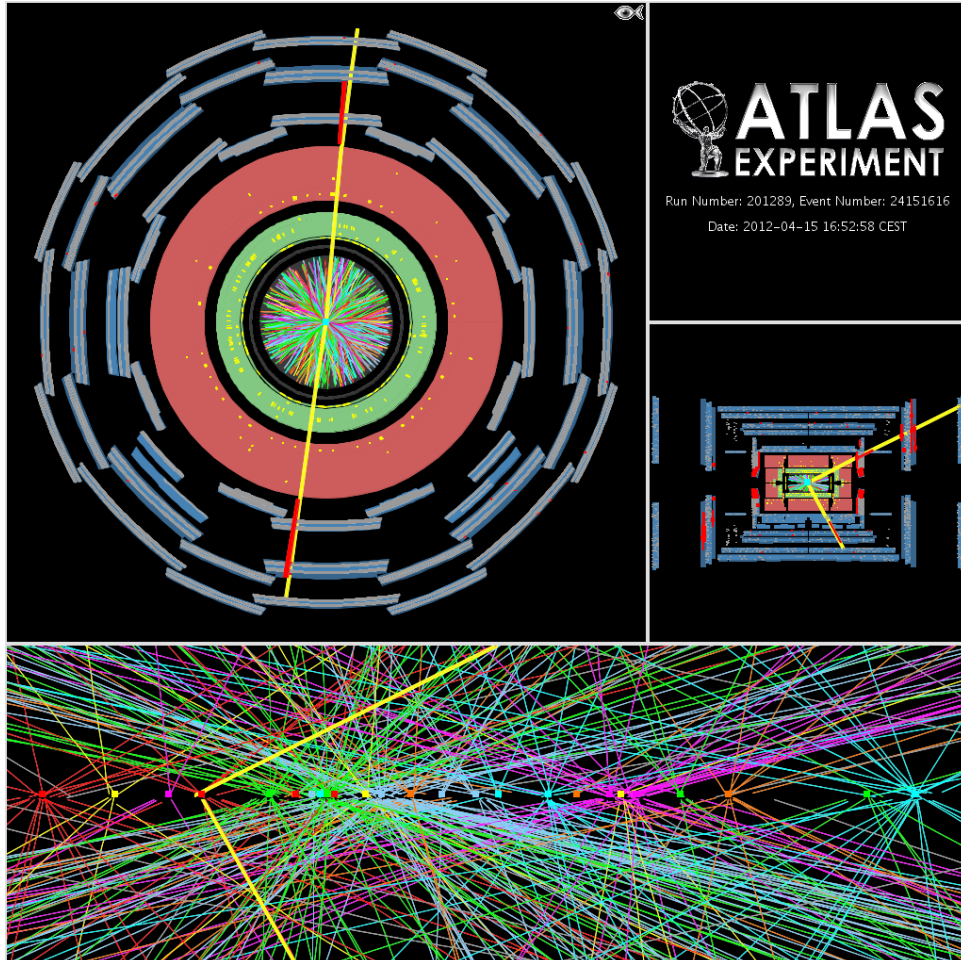


Figure 2.46: Event display of a candidate Z event with 25 reconstructed vertices. This event was recorded on April 15, 2012 and demonstrates the high pileup environment in 2012 running ($\beta^* = 0.60$ m). For this display the track p_T threshold is 0.40 GeV and all tracks are required to have at least 3 Pixel and 6 SCT hits. The vertices shown are reconstructed using tracks with p_T greater than 0.40 GeV, but with tighter requirements on the number of hits on the tracks than in the 2011 reconstruction. Figure from [ATL14c].

see table 2.10. To achieve the necessary performance, **pile-up** robust requirements on reconstructed objects have to be applied. We will describe the effect of increased **pile-up** on the physics object reconstruction in the subsequent chapter.

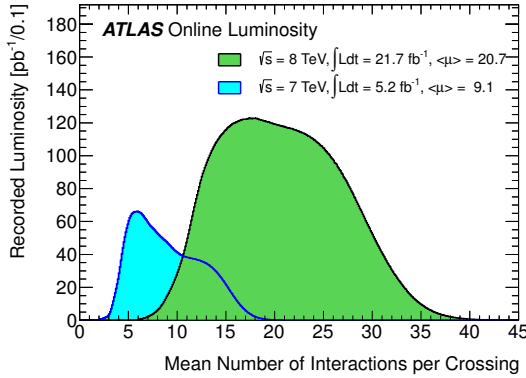


Figure 2.47: Mean number of interactions per bunch crossing for the 2011 and 2012 data. The integrated luminosities and the mean number of interactions per bunch crossing values are given within the figure. The mean number of interactions per bunch crossing corresponds to the mean of the Poisson distribution of the number of interactions per beam crossing calculated for each bunch. Figure from [ATL14d].

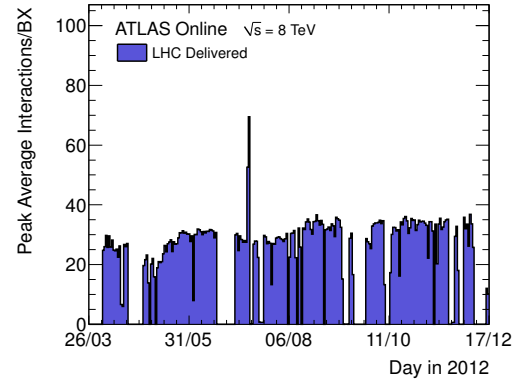


Figure 2.48: The maximum mean number of interactions per bunch crossing versus day. The plot shows the average value for all bunch crossings in a given *lumi-block* (LB). The on-line luminosity measurement is used for this calculation. Only the maximum value during stable beam periods is shown. The spikes during summer months were caused by test runs. Figure from [ATL14d].

2.7 References

- [WM01] Klaus Wille and Jason McFall. *The Physics of Particle Accelerators: An Introduction*. 2001. ISBN: 978-0198505495 (cit. on p. 30).
- [Par12] Particle Data Group. “Review of Particle Physics”. In: *Physical Review D* 86.1 (July 2012), p. 010001. ISSN: 1550-7998. DOI: [10.1103/PhysRevD.86.010001](https://doi.org/10.1103/PhysRevD.86.010001) (cit. on pp. 30, 36–38, 41, 53).
- [Bai07] S Baird. “Accelerators for pedestrians”. In: (Feb. 2007) (cit. on pp. 30, 33, 34, 36, 37).
- [CS00] E.D. Courant and H.S. Snyder. “Theory of the Alternating-Gradient Synchrotron”. In: *Annals of Physics* 281.1-2 (Apr. 2000), pp. 360–408. ISSN: 00034916. DOI: [10.1006/aphy.2000.6012](https://doi.org/10.1006/aphy.2000.6012) (cit. on pp. 30, 37).
- [Fer14] Fermi National Accelerator Laboratory. *Muon Accelerator Program (MAP) homepage*. 2014. Available at: <http://map.fnal.gov/>, visited on 05/19/2014 (cit. on p. 31).
- [Pik+14] O. J. Pike, F. Mackenroth, E. G. Hill, and S. J. Rose. “A photon–photon collider in a vacuum hohlraum”. In: *Nature Photonics* advance on (May 2014). ISSN: 1749-4885. DOI: [10.1038/nphoton.2014.95](https://doi.org/10.1038/nphoton.2014.95) (cit. on p. 31).
- [CW32] John Douglas Cockcroft and Ernest Thomas Sinton Walton. “Artificial Production of Fast Protons”. In: *Nature* 129 (1932), pp. 242, 649 (cit. on p. 31).

- [Per00] Donald H. Perkins. *Introduction to High Energy Physics*. 4th. Cambridge University Press, 2000, p. 426. ISBN: 0521621968 (cit. on pp. 31–35, 41, 51, 52, 68, 70–72).
- [Wid28] Rolf Wideröe. “Über ein neues Prinzip zur Herstellung hoher Spannungen”. In: *Archiv für Elektrotechnik* 21.4 (July 1928), pp. 387–406. ISSN: 0003-9039. DOI: [10.1007/BF01656341](https://doi.org/10.1007/BF01656341) (cit. on p. 31).
- [Gil13] Simone Gilardoni. “Introduction to Accelerators (1/2)”. In: *Italian Teachers Programme* (Sept. 2013) (cit. on pp. 31, 39).
- [SLA] SLAC. *The Stanford Linear Accelerator Center*. Available at: <http://www.slac.stanford.edu/gen/grad/GradHandbook/slac.html>, visited on 05/23/2014 (cit. on p. 32).
- [Hol14] B. J. Holzer. “Introduction to Transverse Beam Dynamics”. In: (Apr. 2014), p. 19. DOI: [10.5170/CERN-2013-007.27](https://doi.org/10.5170/CERN-2013-007.27). arXiv: [1404.0923](https://arxiv.org/abs/1404.0923) (cit. on pp. 32, 34, 36–38).
- [Nav14] Rod Nave. *HyperPhysics*. 2014. Available at: <http://hyperphysics.phy-astr.gsu.edu/hbase/hph.html>, visited on 05/19/2014 (cit. on p. 33).
- [CER06] CERN. “CAS - CERN Accelerator School: Intermediate Course on Accelerator Physics - CERN Document Server”. In: (2006). DOI: [10.5170/CERN-2006-002](https://doi.org/10.5170/CERN-2006-002) (cit. on pp. 33, 36–38, 41).
- [HM06] Werner Herr and B Muratori. “Concept of luminosity”. In: (2006). DOI: [10.5170/CERN-2006-002.361](https://doi.org/10.5170/CERN-2006-002.361) (cit. on pp. 34, 39, 42).
- [Hol13] Bernhard J. Holzer. “Beam optics and lattice design for particle accelerators”. In: (Mar. 2013), p. 36. DOI: [10.5170/CERN-2013-001.171](https://doi.org/10.5170/CERN-2013-001.171). arXiv: [1303.6514](https://arxiv.org/abs/1303.6514) (cit. on p. 36).
- [Let13] Alan Letchford. “Beam dynamics in linacs”. In: (2013). DOI: [10.5170/CERN-2013-001.1](https://doi.org/10.5170/CERN-2013-001.1) (cit. on p. 36).
- [CER08] CERN. “LHC Machine”. en. In: *Journal of Instrumentation* 3.08 (Aug. 2008), S08001–S08001. ISSN: 1748-0221. DOI: [10.1088/1748-0221/3/08/S08001](https://doi.org/10.1088/1748-0221/3/08/S08001) (cit. on pp. 37, 40, 42, 43, 45, 47–50).
- [VC] Xabier Cid Vidal and Ramon Cid. *Taking a closer look at LHC*. Available at: <http://www.lhc-closer.es/>, visited on 05/19/2014 (cit. on p. 37).
- [Bra+97] Enrico Bravin, Peter Galbraith, M A Geitz, Bernd Dehning, G Brun, A Drees, K N Henriksen, M Koratzinos, and G Mugnai. “The Influence of Train Leakage Currents on the LEP Dipole Field”. In: *Nucl. Instrum. Methods Phys. Res., A* 417 (Sept. 1997), pp. 9–15 (cit. on p. 37).
- [CER13] CERN. *LHC Machine Outreach*. 2013. Available at: <http://lhc-machine-outreach.web.cern.ch/>, visited on 05/19/2014 (cit. on pp. 40, 43, 46, 49).
- [Par13] Particle Data Group. “Review of Particle Physics”. In: *Physical Review D* (2013) (cit. on pp. 40, 53, 62, 68, 70, 77).
- [ATL13] ATLAS Collaboration. “Improved luminosity determination in pp collisions at $\sqrt{s} = 7$ TeV using the ATLAS detector at the LHC”. In: (Feb. 2013), p. 27. arXiv: [1302.4393](https://arxiv.org/abs/1302.4393) (cit. on pp. 40, 80, 82–85).

- [vMee68] S van der Meer. “Calibration of the effective beam height in the ISR”. In: (1968) (cit. on p. 41).
- [ATL14d] ATLAS Collaboration. *Luminosity Public Results*. 2014. Available at: <https://twiki.cern.ch/twiki/bin/view/AtlasPublic/LuminosityPublicResults>, visited on 05/06/2014 (cit. on pp. 44, 45, 82, 86, 87).
- [CER04] CERN. “LHC Design Report”. In: (2004). DOI: [10.5170/CERN-2004-003-V-1](https://doi.org/10.5170/CERN-2004-003-V-1) (cit. on pp. 43, 50).
- [Lam13] Mike Lamont. “Status of the LHC”. en. In: *Journal of Physics: Conference Series* 455.1 (Aug. 2013), p. 012001. ISSN: 1742-6596. DOI: [10.1088/1742-6596/455/1/012001](https://doi.org/10.1088/1742-6596/455/1/012001) (cit. on pp. 45, 47).
- [CER14a] CERN. *LHC Online Status Display*. 2014. Available at: <http://op-webtools.web.cern.ch/op-webtools/vistar/vistars.php?usr=LHC1>, visited on 05/24/2014 (cit. on p. 45).
- [Pap11] Vaia Papadimitriou. “Luminosity determination at the Tevatron”. In: (June 2011). arXiv: [1106.5182](https://arxiv.org/abs/1106.5182) (cit. on p. 45).
- [ATL14b] ATLAS Collaboration. *ATLAS Data Summary*. 2014. Available at: <https://atlas.web.cern.ch/Atlas/GROUPS/DATAPREPARATION/DataSummary/2012/records.html>, visited on 05/25/2014 (cit. on pp. 45, 47).
- [Bai14] R Bailey. “An Application for Research: the Large Hadron Collider”. In: (Apr. 2014), p. 10. DOI: [10.5170/CERN-2013-007.565](https://doi.org/10.5170/CERN-2013-007.565). arXiv: [1404.0966](https://arxiv.org/abs/1404.0966) (cit. on pp. 47–49).
- [CER14b] CERN. *LHC Performance and Statistics*. 2014. Available at: <http://lh-statistics.web.cern.ch/LHC-Statistics/>, visited on 05/22/2014 (cit. on p. 47).
- [Her06] Werner Herr. “Beam-beam interactions”. In: (2006). DOI: [10.5170/CERN-2006-002.379](https://doi.org/10.5170/CERN-2006-002.379) (cit. on pp. 47–49).
- [ATL08c] ATLAS Collaboration. “The ATLAS Experiment at the CERN Large Hadron Collider”. In: *Journal of Instrumentation* 3.08 (Aug. 2008), S08003–S08003. ISSN: 1748-0221. DOI: [10.1088/1748-0221/3/08/S08003](https://doi.org/10.1088/1748-0221/3/08/S08003) (cit. on pp. 52, 56, 60–82).
- [ATL14a] ATLAS Collaboration. *ATLAS Computing TWiki*. 2014. Available at: <https://twiki.cern.ch/twiki/bin/view/AtlasComputing>, visited on 05/07/2014 (cit. on pp. 53, 54).
- [CER] CERN. *CERN Public Website*. Available at: <http://www.cern.ch/>, visited on 05/27/2014 (cit. on p. 54).
- [ATL12] ATLAS Collaboration. “Observation of a new particle in the search for the Standard Model Higgs boson with the ATLAS detector at the LHC”. In: *Physics Letters B* 716.1 (Sept. 2012), pp. 1–29. ISSN: 03702693. DOI: [10.1016/j.physletb.2012.08.020](https://doi.org/10.1016/j.physletb.2012.08.020). arXiv: [1207.7214](https://arxiv.org/abs/1207.7214) (cit. on pp. 55, 59).
- [CMS12] CMS Collaboration. “Observation of a new boson at a mass of 125 GeV with the CMS experiment at the LHC”. In: *Physics Letters B* 716.1 (Sept. 2012), pp. 30–61. ISSN: 03702693. DOI: [10.1016/j.physletb.2012.08.021](https://doi.org/10.1016/j.physletb.2012.08.021). arXiv: [1207.7235](https://arxiv.org/abs/1207.7235) (cit. on p. 55).
- [CMS06] CMS Collaboration. *CMS Technical Design Report (post 2005)*. Technical Design Report CMS. Geneva: CERN, 2006 (cit. on p. 55).

- [CMS10] CMS Collaboration. *CMS Public Website*. <<http://cms.web.cern.ch/cms/>>. Apr. 2010. Available at: <http://cms.web.cern.ch>, visited on 05/07/2014 (cit. on p. 55).
- [ATL10b] ATLAS Collaboration. *ATLAS Public Website*. <<http://www.atlas.ch>>. May 2010. Available at: <http://www.atlas.ch>, visited on 05/06/2014 (cit. on pp. 56, 59, 63–65, 67, 68, 71, 78).
- [SM13] Tai Sakuma and Thomas McCauley. “Detector and event visualization with SketchUp at the CMS experiment”. In: (Oct. 2013) (cit. on p. 56).
- [ALI10] ALICE Collaboration. *ALICE Public Website*. <<http://aliceinfo.cern.ch/Public/>>. Apr. 2010. Available at: <http://aliceinfo.cern.ch/Public/>, visited on 05/07/2014 (cit. on pp. 57, 58).
- [ALI09] ALICE Collaboration. *ALICE Technical Design Reports*. Mar. 2009 (cit. on p. 57).
- [LHC14] LHCb Collaboration. *LHCb Public Website*. <<http://lhcb-public.web.cern.ch/lhcb-public/>>. Apr. 2014. Available at: <http://lhcb-public.web.cern.ch/>, visited on 05/07/2014 (cit. on pp. 57, 58).
- [TOT10] TOTEM Collaboration. *TOTEM Public website*. <<http://totem-experiment.web.cern.ch/totem-experiment/>>. Apr. 2010. Available at: <http://totem-experiment.web.cern.ch/totem-experiment/>, visited on 05/07/2014 (cit. on p. 57).
- [LHC10] LHCf Collaboration. *LHCf Public Website*. <<http://www.stelab.nagoya-u.ac.jp/LHCf/>>. Apr. 2010. Available at: <http://www.stelab.nagoya-u.ac.jp/LHCf/>, visited on 05/07/2014 (cit. on p. 59).
- [MoE14] MoEDAL Collaboration. *The Monopole & Exotics Detector at the LHC*. 2014. Available at: <http://moedal.web.cern.ch>, visited on 07/18/2014 (cit. on p. 59).
- [ATL11a] ATLAS Collaboration. *ATLAS Fact Sheets*. 2011. Available at: http://www.atlas.ch/fact_sheets.html, visited on 11/08/2013 (cit. on pp. 59–62, 66–68, 72, 77).
- [ATL94] ATLAS Collaboration. *ATLAS Technical Proposal for a General-purpose Pp Experiment at the Large Hadron Collider at CERN*. Ed. by LHC Experiment Committee. Geneva: CERN, Dec. 1994, p. 272. ISBN: 9290830670, 9789290830672 (cit. on pp. 60, 66, 68).
- [ATL99b] ATLAS Collaboration. *ATLAS detector and physics performance: Technical Design Report, 2*. Technical Design Report ATLAS. Geneva: CERN, 1999 (cit. on p. 60).
- [ATL99a] ATLAS Collaboration. *ATLAS detector and physics performance: Technical Design Report, 1*. Technical Design Report ATLAS. Geneva: CERN, 1999 (cit. on p. 60).
- [ATL08b] ATLAS Collaboration. “Expected Performance of the ATLAS Experiment - Detector, Trigger and Physics”. In: (Dec. 2008). arXiv: 0901.0512 (cit. on p. 60).
- [Wei] Eric W. Weisstein. *Wolfram MathWorld: The Web’s Most Extensive Mathematics Resource*. en. Available at: <http://mathworld.wolfram.com/>, visited on 05/08/2014 (cit. on p. 60).

- [ATL10a] ATLAS Collaboration. *ATLAS Magnet System*. <<http://atlas-magnet.web.cern.ch/atlas-magnet/>>. 2010. Available at: <http://atlas-magnet.web.cern.ch/atlas-magnet/>, visited on 05/07/2014 (cit. on p. 61).
- [ATL08a] ATLAS Collaboration. *ATLAS Pixel Detector group homepage*. <http://atlas.web.cern.ch/Atlas/GROUPS/INNER_DETECTOR/PIXELS/pixel.html>. 2008. Available at: http://atlas.web.cern.ch/Atlas/GROUPS/INNER_DETECTOR/PIXELS/pixel.html, visited on 05/07/2014 (cit. on pp. 63, 64, 67).
- [Mos11] J. Moss. “Commissioning and operation of the ATLAS pixel detector”. In: *Nuclear Instruments and Methods in Physics Research Section A: Accelerators, Spectrometers, Detectors and Associated Equipment* 650.1 (Sept. 2011), pp. 1–5. ISSN: 01689002. DOI: [10.1016/j.nima.2010.11.190](https://doi.org/10.1016/j.nima.2010.11.190) (cit. on pp. 64, 66, 67).
- [Hug06] F. Hugging. “The ATLAS pixel detector”. In: *IEEE Transactions on Nuclear Science* 53.3 (June 2006), pp. 1732–1736. ISSN: 0018-9499. DOI: [10.1109/TNS.2006.871506](https://doi.org/10.1109/TNS.2006.871506). arXiv: [0401068](https://arxiv.org/abs/0401068) [physics] (cit. on p. 64).
- [Par97] Particle Physics Department at the Rutherford Appleton Laboratory. *Technology for Particle Physics*. 1997. Available at: http://hepwww.rl.ac.uk/OpenDays97/Atlas_SCT_sidetector.htm, visited on 05/09/2014 (cit. on p. 69).
- [ATL11b] ATLAS Collaboration. “Luminosity determination in pp collisions at $\sqrt{s} = 7$ TeV using the ATLAS detector at the LHC”. In: *The European Physical Journal C* 71.4 (Apr. 2011), p. 1630. ISSN: 1434-6044. DOI: [10.1140/epjc/s10052-011-1630-5](https://doi.org/10.1140/epjc/s10052-011-1630-5). arXiv: [1101.2185](https://arxiv.org/abs/1101.2185) (cit. on pp. 82, 84).
- [ATL11c] ATLAS Collaboration. “Luminosity Determination in pp Collisions at $\sqrt{s} = 7$ TeV using the ATLAS Detector in 2011”. In: (Aug. 2011) (cit. on pp. 82, 85).
- [ATL11d] ATLAS Collaboration. “Updated Luminosity Determination in pp Collisions at $\sqrt{s} = 7$ TeV using the ATLAS Detector”. In: (Mar. 2011) (cit. on p. 82).
- [Lum12] The Luminosity Group. “Preliminary Luminosity Determination in pp Collisions at $\sqrt{s} = 8$ TeV using the ATLAS Detector in 2012”. In: (Nov. 2012) (cit. on p. 83).
- [Was12] Christoph Wasicki. “Track and vertex reconstruction of the ATLAS Inner Detector in the high multiplicity LHC environment”. In: *Journal of Physics: Conference Series* 396.2 (Dec. 2012), p. 022056. ISSN: 1742-6588. DOI: [10.1088/1742-6596/396/2/022056](https://doi.org/10.1088/1742-6596/396/2/022056) (cit. on p. 85).
- [ATL14c] ATLAS Collaboration. *ATLAS Public Event Displays*. Available from: <<https://twiki.cern.ch/twiki/bin/view/Atlas/EventDisplayPublicResults>>. May 2014. Available at: <https://twiki.cern.ch/twiki/bin/view/AtlasPublic/EventDisplayPublicResults>, visited on 06/03/2014 (cit. on p. 86).

3

COMPUTATIONAL AND RECONSTRUCTION TOOLS

Contents

3.1	Trigger and data acquisition	93
3.1.1	Level 1 Trigger flow	95
3.1.2	High-level trigger and data acquisition system	97
3.1.3	Streaming	97
3.1.4	Trigger menu	98
3.1.5	Monitoring	100
3.1.6	Operational performance	101
3.2	Data representation and distribution	101
3.2.1	Data quality	102
3.2.2	Analysis paths	103
3.2.3	Event data model	104
3.2.4	Operational model	105
3.2.5	Analysis software	107
3.2.6	Analysis work-flow	108
3.3	Physics objects reconstruction	108
3.3.1	Tracking	109
3.3.2	Vertexing	113
3.3.3	Muon reconstruction	115
3.3.4	Electron reconstruction	123
3.3.5	Jet reconstruction	129
3.3.6	Missing transverse energy reconstruction	136
3.4	Implementation	138
3.4.1	Development goals	139
3.4.2	Implementation of analysis objects	142
3.5	References	146

PHYSICS ANALYSIS is, generally speaking, a discipline of mathematically processing and studying the data recorded from reproducible experiments, in order to obtain a physical result comparable with theoretical predictions. As we have shown in the previous chapter, experiments in the field of particle physics require the involvement of a large number of scientists and engineers, going to thousands for the largest of these experiments. With experiments of this scale and with the statistics the LHC is able to produce, the experimental data take the form of a large dataset. The data is represented by simple event-by-event table, where the physical quantities recorded by the detector are stored.

Analysing large volumes of data naturally requires the usage of computers. The computational software allows particle physicists to employ familiar mathematical objects, like state vectors, Lorentz vectors and eventually histograms to be compared with theoretically predicted distributions for a given physical quantity. Collaboration software also provide tools for statistical or mathematical analysis and interactive graphical representations of the dataset.

3.1 Trigger and data acquisition

Trigger and data acquisition system (TDAQ) [ATL14c] is a term used to collectively describe the data collection and filtering system. At nominal conditions the LHC bunch crossing rate is 40 MHz (25 ns bunch spacing) which yields about a billion collisions per second. A single bunch crossing is considered as an *event*.

Without any selection, 40 million events produced every second and recorded by ≈ 100 million read-out channels in the ATLAS detector alone would produce up to 1 PB s^{-1} . Such data intake is beyond any technological solution currently available. The trigger systems are designed to reduce the amount of recorded data while ensuring that minimum number of interesting physics events are lost. The algorithm is based on only a subset of the detector information to make the decision fast enough [ATL08b, p. 64]. Events recorded with the minimum possible selection are referred to as *minimum-bias events*, but a majority of them contain no interesting high- p_T physics objects and as such can be safely discarded. The goal is to reduce the event rate from 40 MHz to a few hundred Hz, i.e. the trigger rejection factor must be of $\mathcal{O}(10^5)$.

The TDAQ in ATLAS is designed as a three-level system to reduce the data rate in successive steps, the hierarchy is outlined in fig. 3.1. The figure shows the design values as well as the peak values reached during 2012 data taking. The levels are defined as follows [Ask+08]:

Level-1 Trigger (L1) is a hardware-based system which uses a reduced granularity information from the calorimeter and the muon system to search for signatures of high- p_T muons, electrons, photons, jets and τ leptons. There is no tracking information from the ID because the simultaneous readout is not fast enough. Only events accepted at this level are used to seed the subsequent levels. Even this coarse event selection provides us with $\mathcal{O}(10^3)$ rejection factor, which reduces the data rate to approximately 75 kHz at nominal conditions (≈ 65 kHz at peak 2012 conditions). This is the peak frequency at which this level can operate, limited by the bandwidth of the readout system. In principle, it is possible to upgrade the system to increase the readout frequency up to 100 kHz [ATL08b, pp. 14,218]. Level 1 is designed for minimum possible processing time.

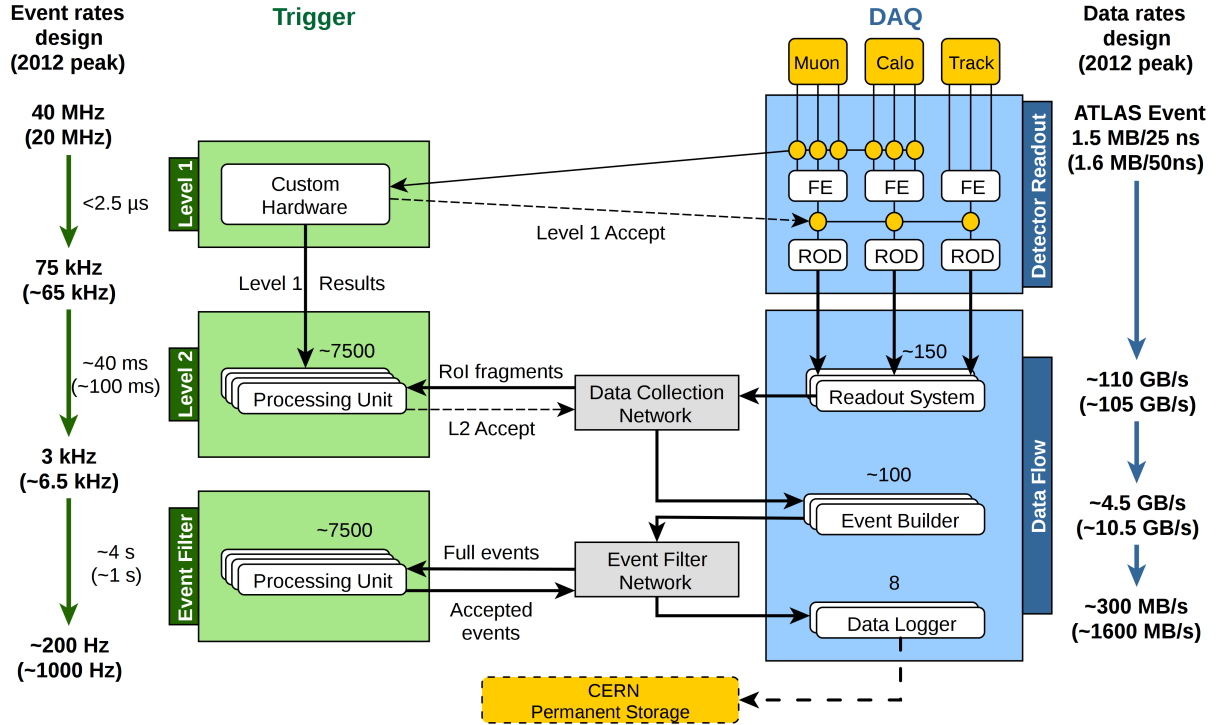


Figure 3.1: Outline of the **ATLAS TDAQ** system. The trigger path is shown on the left, the data path on the right. The data is pushed from the three main parts of **ATLAS**: **Inner Detector** (track), the calorimeter (calo) and the **Muon Spectrometer** (Muon) through the front-end chips (FE) and the readout-drivers (ROD) where the first trigger selection is applied. Only calorimeter and muon chamber information is used for **L1** decision, as the tracking information readout is not fast enough. The chain then follows the trigger flow (see text). The nominal rates are shown for each level with the 2012 peak values in comparison (in parentheses). Figure from [Col13]. The corresponding figure with 2011 values can be found in [Neg12, p. 2].

High Level Trigger (HLT) which consists of Level-2 (L2) trigger and the *Event Filter (EF)*.

The Level-2 trigger accesses only a small percentage of the event data available through the so-called *region-of-interest (RoI)*. These regions are created by a dedicated hardware component from the information provided by the **L1** trigger firing in the presence of a triggering object. The **HLT** algorithms have access to full event information within the **RoI**: coordinates, energy, type of signature and additionally tracks from the **Inner Detector** with full granularity. The L2 reduces the data rate by an order of magnitude to 3 kHz (≈ 6 kHz at peak 2012 conditions) with a latency of 40 ms. After passing the **EF**, the final rate is reduced by almost another order of magnitude to ≈ 400 Hz (≈ 1000 Hz) and an average processing time of about 4 s [Neg12, p. 2]. Both levels are implemented as a distributed software system with ≈ 500 (L2) and ≈ 1700 (EF) dual CPUs on a high performance network [ATL11a, 4a].

In the last data taking period, the **ATLAS TDAQ** system was successfully operated well beyond the design parameters. The adaptation and performance of the trigger systems at 2011 and 2012 run conditions are discussed in [Neg12]. The modular design allowed the system to expanded to operate at more than five times the nominal bandwidth. Given the trigger reduction the estimated amount of recorded data at 2012 conditions is ≈ 10 PB per year for **ATLAS** only. For more information see [ATL08b, pp. 14,218–256]

3.1.1 Level 1 Trigger flow

The trigger decision is processed in the *Central Trigger Processor (CTP)* using the inputs from the dedicated muon triggering chambers (*RPC* and *TGC*) and coarse information from the calorimeter trigger system. The *L1* block diagram is shown in fig. 3.2. The *CTP* translates the trigger decision into control and timing signals and distributes to the detector subsystems which in turn push the recorded data from the front-end electronics into the detector specific read-out drivers (*RODs*). [Neg12, p. 2] It also introduces *dead time* during which the detector readout system is busy recording the data from the sub-detectors and cannot accept another event. Performance and timing are critical in a trigger system. The average processing time in *Level-1 Trigger* is lower than $2.50\ \mu\text{s}$. [Neg12, p. 2]

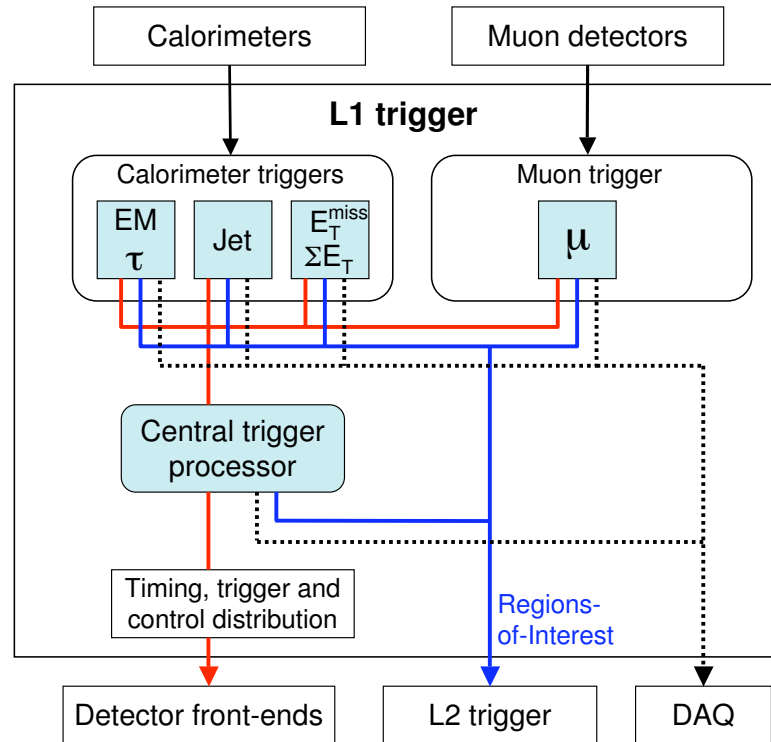


Figure 3.2: Block diagram of the *L1* trigger. The overall *L1* decision is made by the *CTP* from from calorimeter and muon trigger input. The paths to the detector front-ends (red), *L2* trigger (blue), and data acquisition system (black) are shown from left to right. Figure from [ATL08b, p. 220].

The muon *L1* triggers is based on *RPC* in the *barrel* region and *TGC* in the *end-caps* of the *Muon Spectrometer*. The chambers are arranged in three planes in the *barrel* and the *end-caps*, as shown in fig. 3.3. The trigger searches for detector hits consistent with the presence of high- p_T muons originating in the *IP*. The coincidence of hits in the different trigger stations is called a *road*, which tracks the path of a muon from the *IP* through the detector. The width of the road is a function of the desired cut on p_T : the smaller the road, the higher the cut on p_T , as shown in fig. 3.3. The decision is made based on the muon candidate multiplicity at a certain p_T threshold. The logic provides programmable p_T thresholds that are indicated in the trigger name: *L1_MUX*, where *X* is the threshold. The low- p_T trigger threshold ranges between $\approx 6\text{--}9\text{ GeV}$ and the high- $p_T \approx 9\text{--}35\text{ GeV}$. Any double-counted candidates are removed. [ATL08b, pp. 220,230]

The calorimeter data is grouped into so-called *trigger towers* with reduced granularity and then processed. The tower granularity is $\eta \times \phi = 0.1 \times 0.1$ in the *barrel* region, but varies in size in the forward regions. The data are processed by two independent subsystems: the *cluster processor* (CP) and the *jet-energy processor* (JEP), collectively referred to as (L1Calo). The cluster processor then searches for localized high *transverse energy* deposits typical for electrons, photons and tau leptons. The procedure is shown schematically in fig. 3.4. Jet candidates are identified by their deposit in a larger volume using JEP as is the triggering on missing energy. [ATL08b, pp. 224–227]

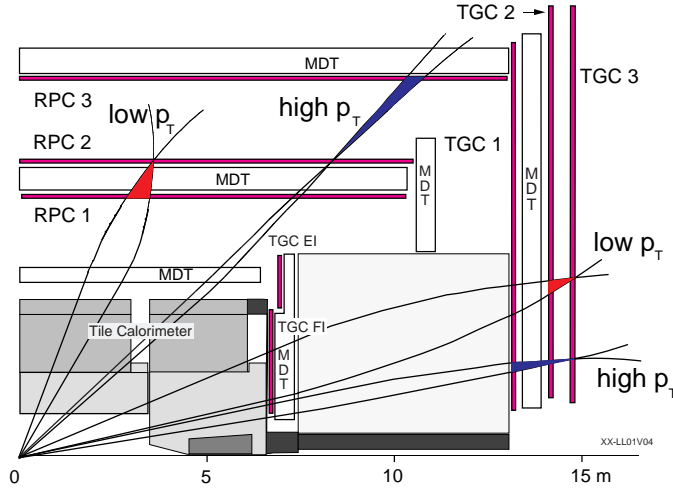
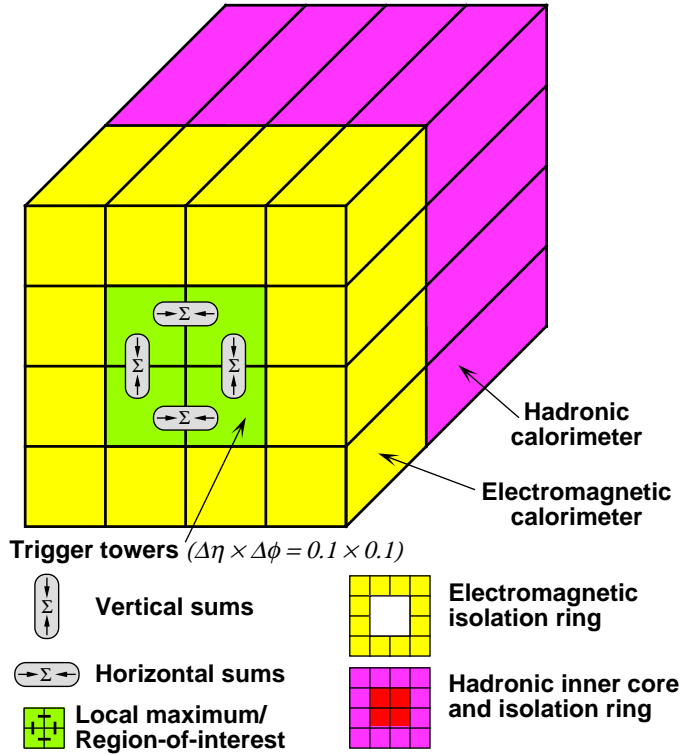


Figure 3.3: Schematic of the L1 muon trigger. When a muon generates a hit the algorithm tracks the path of a muon from the IP through the detector within a *road* whose centre is defined by the line of conjunction of the hit in the pivot plane with the IP. The width of the road is a function of the desired cut on p_T . The system is designed for three low- p_T and three high- p_T thresholds. The algorithm is performed in both the η and the ϕ projections to reduce accidental triggers from low-energy particles in the cavern. [ATL08b, p. 231] Figure from [ATL12g].

Figure 3.4: Building blocks of the L1 calorimeter *cluster processor* trigger algorithm for electrons, photons and tau leptons. The electron/photon trigger identifies clusters of 2×2 ECAL trigger towers (yellow) in which at least one of the four possible two-tower sums 1×2 (vertical) or 2×1 (horizontal) exceeds a pre-defined threshold. A hadron veto with 1 GeV threshold was additionally introduced in the mid-2011 to account for η dependent inefficiencies, see section 3.1.4. The τ algorithm uses the same basic elements in ECAL and sums them with HCAL (magenta) towers directly behind and compares the total with a pre-defined threshold. [ATL08b, p. 225]. Figure from [ATL11e] [ATL08b, p. 226].



3.1.2 High-level trigger and data acquisition system

The components of the [HLT](#) provide a direct interface between the detector read-out and the central mass storage facility (Tier0, see [section 3.2.4](#)). We shall briefly describe them here:

Read-out system receives and buffers the event data fragments pushed from the detector subsystems for each event accepted by the [L1](#). The event is then forwarded on request to the subsequent stages of the [DAQ/HLT](#) system.

L2 consists of the *RoI builder* (RoIB) and multiple processing and supervising units. The L2 has access to only a small subset of the event data produced by the detector. The amount of data fetched in an [RoI](#) ranges between 2–6 % of the total event size, depending on the nature of the event.

Event-builder which assembles the event fragments accepted by L2 and builds them into complete events with a single formatted data structure before passing them to the [EF](#).

Event Filter is effectively the last level of the trigger. The [EF](#) has access the full event information with full granularity and additionally uses reconstruction algorithms that are the same or similar to those used in the offline reconstruction (see [section 3.3](#)). In addition, the [EF](#) classifies the selected events into pre-determined set of event streams, see below.

Configuration, control, monitoring are [DAQ](#) services designed to configure trigger thresholds and monitor data quality online. Controllers are a fundamental aspect of the [HLT](#), issuing commands to the whole system and providing diagnostic access and error recovery.

The systems are interconnected via Gigabit Ethernet, a full block diagram of the [TDAQ](#) is given in [[ATL08b](#), p. 219]. See also [[ATL08b](#), pp. 242–250] for technical details. The trigger systems are constantly monitored using online algorithms and control scripts. Since the system is not yet fully automated, a human element is required to monitor the data intake constantly, while a team support experts ensures the correct functionality of the control scripts. The goal is to eventually fully automate this procedure so that a minimum number of personal are required for online monitoring.

3.1.3 Streaming

The [trigger](#) algorithm output is organized into streams. Each stream is designed for a different purpose. Physics analysis streams clearly require full detector data, while monitoring and calibration streams focus on a specific data subset or detector region.

There are `physics`, `calibration`, `Express` and `Debug` streams. The `physics` stream is used to feed physics analyses and as such contains only complete events processed through the [TDAQ](#) system with no errors. Any events with procedural failures are saved as a part of the `DEBUG` stream for later investigation. The `Express` and `calibration` streams save only a subset of events (typically $\approx 10\%$) for data quality monitoring or sub-detector performance studies respectively.

The `physics` stream is important for the analysis presented in this thesis. There are a total of five physics streams: `Egamma`, `Muons`, `JetTauEtmiss`, `Bphys` and `Minbias` where each stream corresponds to a physics signature: electrons/photons, muons, hadronic and tau jets and

[missing transverse energy](#), B-physics and minimum-bias events, respectively. The streams are inclusive, which means that some events can be duplicated across streams if the event is passed by triggers assigned to different streams. Physics objects recorded in the stream are reconstructed at the central mass storage facility, see [section 3.3](#). MC simulation does not produce streams as there is no runtime triggering. [\[ATL14r\]](#)

3.1.4 Trigger menu

The composition of a particular stream may change over time as triggers are added, removed or modified. The global configuration of trigger algorithms is referred to as the *trigger menu*. It defines *trigger chains* as cascades of [L1](#) and [HLT](#) algorithms for a specific physics signature. One of the advantages of this arrangement, it that the features extracted by [L1](#) can be shared by providing similar trigger chains with the same cache, thus reducing the processing time.

The trigger menu is composed from the following classes of trigger chains [\[ATL14o\]](#):

Single object triggers: are used for final states with at least one characteristic physics object, e.g. a single muon trigger with a nominal threshold at 6 GeV (in p_T or E_T) is referred to in the trigger menu as `mu6`.

Multiple object triggers: select final states with two or more characteristic objects of the same type. For example, a di-muon trigger for selecting $J/\psi \rightarrow \mu^- \mu^+$ decays is looking for two low- p_T muons in the event. Triggers requiring a multiplicity of two or more objects are indicated in the trigger menu by pre-pending the required multiplicity to the trigger name, e.g. `2mu6`, `5j30` etc.

Combined triggers: select final states with two or more characteristic objects of different types. For example, a trigger chain requiring 12 GeV electron and a 8 GeV muon would be denoted as `e12_mu8`. By analogy, a 13 GeV muon plus 20 GeV E_T trigger for selecting $W \rightarrow \mu \nu$ decays would be denoted `mu13_xe20`.

Topological triggers: are used for final states that require selections based on information from two or more [RoI](#). For example the $J/\psi \rightarrow \mu^- \mu^+$ trigger combines tracks from two muon [RoI](#).

As is indicated in the above description, the energy threshold is chosen differently for each physics object specifically and this is indicated in the trigger nomenclature. When referring to a particular trigger, the prefix `L1`, `L2`, `EF` indicates the corresponding trigger level (see above [sections 3.1.1](#) and [3.1.2](#)). Thus, a [L1](#) trigger item with a 6 GeV threshold is referred to as `L1_MU6`, while the same item for `L2` is denoted `L2_MU6`.

The trigger rates within the menu can be adjusted by changing the triggering thresholds and by applying additional selection cuts. Based on the selectivity of the cut, the triggers are arranged into categories `loose`, `medium` and `tight` which is added as a suffix to the trigger name, e.g. `e10_medium`. Any additional trigger requirements are indicated by adding a letter to the trigger name:

- v ...indicates a *variable threshold* which was introduced from September 2011 to correct for dead-material effects causing non-uniform [trigger](#) efficiencies with respect to calorimeter η .

Thresholds are increased by 1–2 GeV in the high efficiency regions following the coarse L1 granularity of $\Delta\eta = 0.4$. [But12, p. 5] The exact values of η -dependent thresholds for the main L1 seed triggers are shown in [ATL12f, p. 6], the effect is shown in fig. 3.5.

- h ...indicates a hadronic layer leakage veto (also called *hadronic core isolation*) at L1 on energy deposited in the hadronic layers of the calorimeter. The trigger selects the event provided that $E_{\text{had}} < 1$ GeV within a region of $\eta \times \phi = 0.2 \times 0.2$ behind the cluster. Consequently, this is also applied at EF level.
- i ...indicates *isolation*, which is a measure of the amount of energy in the vicinity of the signature. The isolation criterion looks for an amount of *transverse energy* deposited in the calorimeter within a ΔR of a lepton. The muon track isolation variable is defined as the $\sum p_T$ of tracks having $p_T > 1$ GeV found in the Inner Detector in a cone of $\Delta R < 0.2$ around the muon candidate, after subtracting the p_T of the muon [ATL12g, p. 18]. The tracking isolation applied to electron requires the *transverse energy* inside a cone of $\Delta R < 0.2$ to be less than 10 % of the the electron energy, i.e.: $\sum_{\Delta R < 0.2} p_T < 0.1 \cdot E_T(e^\pm)$

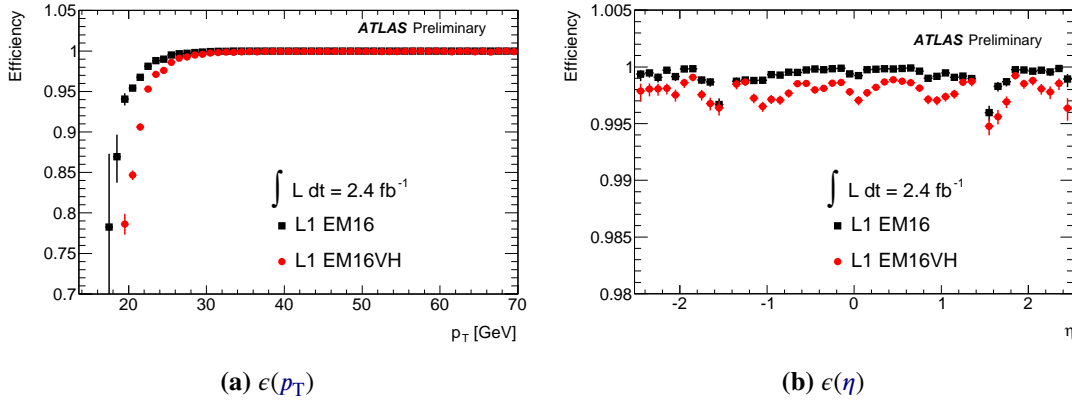


Figure 3.5: Comparison of trigger efficiencies with variable thresholds and hadronic leakage veto (VH) shown as function of electron E_T (left) and η (right) for L1EM16 and L1EM16VH triggers. Efficiencies are derived from $Z \rightarrow e^+e^-$ events using tag-and-probe method. The offline electron is required to satisfy medium++ identification criteria. The efficiency as a function of pseudorapidity (right) is shown for electrons at the trigger plateau $E_T > 25$ GeV. The E_T threshold at which the trigger reaches full efficiency is not significantly altered by the introduction of variable threshold and hadronic leakage veto trigger requirements while the right plot shows the new VH trigger to be less dependent on η than the non-VH trigger (sic.). Figures from [But12, p. 6] [ATL12f, p. 7].

Hence, the single electron trigger EF_e24vhi_medium1 used in the 2012 menu is an EF level electron trigger with variable E_T threshold to improve efficiency in sub-optimal η bins. Additionally, the included hadronic core isolation and tracking isolation requirements are included. Particle identification criteria are also included in the trigger name. The electron identifications loose1, medium1 and tight1 were implemented to correspond to the “plus-plus” category of offline electrons, see section 3.3.4.2. The trigger nomenclature is summarized in the online documentation [ATL14o] [ATL12h]. Approximately 500 triggers are currently defined in the trigger menus. [ATL14r]. The full 2010 menu is shown in [ATL11e] and the 2011 menu is discussed in [IP11]. Currently, the detailed information regarding 2012 menu is only available in the internal online documentation [ATL14j] [ATL14p].

Any trigger can be re-optimized to the available bandwidth using trigger *prescale* factors (or

simply [prescales](#)). Pre-scaling a trigger by a factor X means that the given trigger chain will only accept every X th event passing the trigger requirements. Application of [prescales](#) is an important compensation of [luminosity](#) decay (see [section 2.1.4.3](#)). As the luminosity drops during an [LHC](#) fill, the [prescales](#) on triggers are adjusted to maximize the available bandwidth for the [physics](#) streams. Calibration and monitoring rate is kept constant throughout the run. Pre-scales can be changed at any point during the run and will take effect at the beginning of a new [lumi-block](#). Setting $X = 0$ will disable the specific chain completely. [[ATL10a](#)]

3.1.5 Monitoring

The data quality monitoring procedures ensure that the collisions produced by [LHC](#) are successfully recorded by [ATLAS](#). In order to ensure that all the hardware and software components are functioning properly, specific tools for *online* and *offline* monitoring have been developed. The online monitoring allows the experts in the [ATLAS](#) control to monitor data taking throughout the [LHC](#) fill. Offline monitoring experts investigate the contents of the [Express](#) stream and review the data quality assessment a few hours after the run and follow-up on any suspected problems. The monitoring work flow is neatly summarized in [[BC13](#)], we show one of the flow charts here in [fig. 3.6](#).

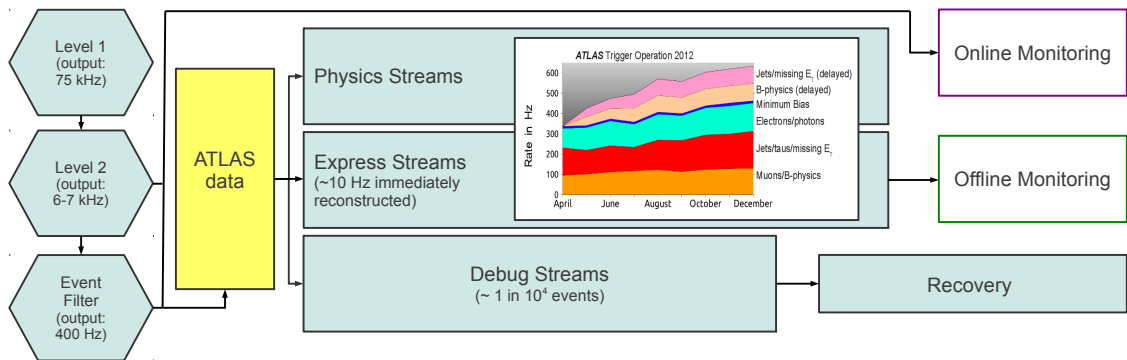


Figure 3.6: [ATLAS](#) trigger monitoring flowchart. The separate function of the offline and online monitoring are explained in the text. Figure from [[BC13](#)].

The offline data quality evaluation runs at the same time with the full reconstruction on the [EXPRESS](#) stream. The stream samples approx 1in10 recorded events so that it can be processed at the [CERN Tier0](#) machines in a few hours after the run. The processed output usually takes form of a large number of histograms of rate measurements, trigger efficiencies and kinematic distributions which is subsequently fed into the [DQMF](#). The [DQMF](#) is an application with web-based interface designed for efficient performance assessment of the data quality both in the online and offline regime. Its variety of functions is explained in [[CG10](#), pp. 2–3].

Many of the data quality checks set automated threshold alarm levels on the histograms or investigate shape differences using a goodness-of-fit test. In 2011 data-taking at 7 TeV only 3 % of all data were declared unrecoverable due to an issue in the trigger system whereas in 2012 this has been reduced below 1 %. [[Oli13](#), p. 1] Any data flagged with detector or trigger issues is marked in the so-called [GoodRunsList \(GRL\)](#), which are then used at the analysis stage to ensure that the data is physics-ready.

I have worked as a data quality monitoring expert for B-physics and Muons [HLT](#) slices over the

period of 3 years. The task mainly consists of monitoring and data quality assessment using the [DQMF](#) tool, mid-level reconstruction validation and debugging, reprocessing the debug stream and providing support to the online monitoring shifters in the [ATLAS](#) Control Room. The summary of shifter's tasks and responsibilities is given in the internal online documentation [[ATLi](#)].

3.1.6 Operational performance

Throughout 2011 the *Data acquisition* (DAQ) recorded 4.64 fb^{-1} collisions at $\sqrt{s} = 7 \text{ TeV}$ with an overall efficiency of 94.90 %. The LHC provided ≈ 1550 hours of stable beam at 50 ns bunch spacing giving an input rate of 20 MHz with an average of 17 primary vertices per single *bunch crossing* (see [fig. 2.47](#)). The maximum output rate was limited to $\approx 65 \text{ kHz}$ to prevent excessive dead time. The stream output rate is shown in [fig. 3.7a](#). One of the main challenges of this period was the fast-paced evolution of trigger requirements. [[Neg12](#), p. 3] Analysers have to pay special attention to use correct triggers in each data taking period, see [section 3.1](#). The output size is about 1.30 MB per event. Throughout the year, the HLT computing resources increased by $\approx 50 \%$ which allowed the TDAQ to run at 95 % efficiency [[Col13](#)].

In 2012, the trigger menu had to adjusted in response to the challenging *pile-up* conditions which increases the computational complexity of reconstruction algorithms. The LHC operated with the same bunch spacing of 50 ns. Given the increased *luminosity*, the *mean number of interactions per bunch crossing* has increased to an average of 37 (*ibid.*). As shown in [[Neg12](#), p. 4] and [[Col13](#)], both the HLT processing and time and resulting event size are $\langle \mu \rangle$ dependent. The event size has increased up to 1.70 MB. An overall 1800 hours of stable beams were the stream output rate is shown in [fig. 3.7b](#). Thanks to the impressive effort of the run control and online data quality monitoring teams the TDAQ was operated well beyond its nominal parameters and recorded more than twice the data in 2011 at with less than 5 % inefficiency from dead-time, run stops and ramp-up [[Col13](#)].

3.2 Data representation and distribution

When referring to [ATLAS](#) data, we usually mean the raw data output after the *Event Filter*. With data rate of 1600 MB s^{-1} (700 MB s^{-1}) (see [fig. 3.1](#)) collected over 1800 hours (1550 hours) in 2012 (2011) [[Col13](#)] requires more than $\approx 10 \text{ PB}$ ($\approx 3.60 \text{ PB}$) of storage for the raw data alone, not accounting for reconstruction, reprocessing and any derived formats. This data must be stored in an robust, reliable and efficient way allowing simultaneous access to the users. The large number of physicists collaborating on the experiment also make it essentially impossible to deploy a completely unified analysis software that would fulfil the individual needs of every group or even every individual physicist. This leads to an inevitable conclusion, that [ATLAS](#) computing model needs to employ:

- ▶ performance-critical design,
- ▶ open-source object-oriented analysis framework,
- ▶ distributed computing.

The [ATLAS](#) computing model, as it was originally proposed in 1996 [[ATL96](#)], did predict the computing requirements to a certain degree. Ultimately, in agreement with Moore's law, there has

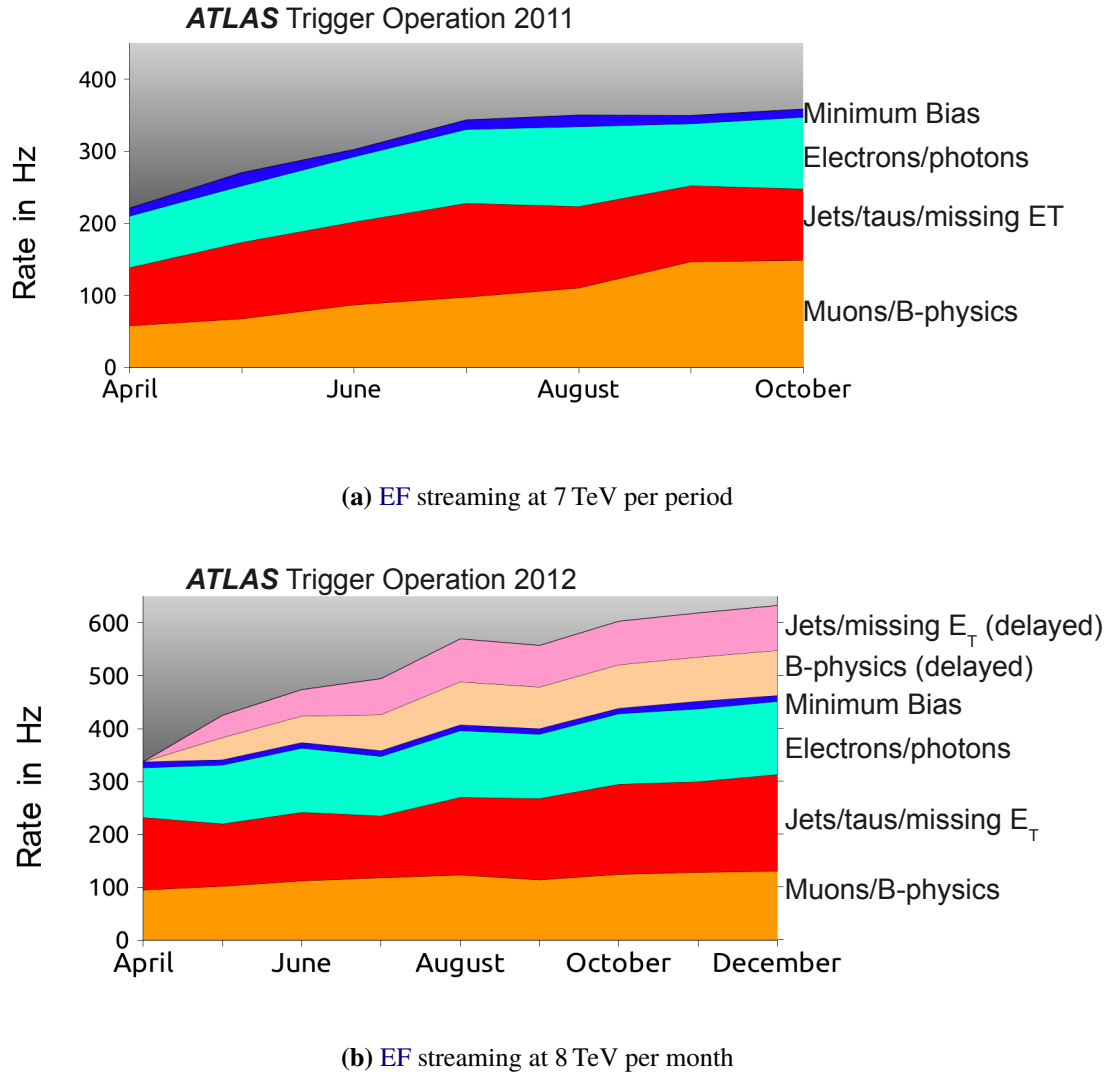


Figure 3.7: Event Filter stream recording rates per month. The yield is averaged over the periods (7 TeV) or months (8 TeV) for which the LHC declared stable beams. Runs with special conditions such as VMS scans or ALFA runs are not included. Figures from [ATL14q].

been enormous development in the computing power and available disk storage which led to the general review of the ATLAS computing model submitted in the computing technical design report [ATL05] in 2005. The ATLAS computing model is a rapidly evolving field, it is not my goal here to provide its extensive historical description but rather a general outline of the model used until 2013, which is relevant for the software framework developed as means of analysis presented in this thesis. Updated guidelines are available in the internal documentation [ATLj].

3.2.1 Data quality

Monitoring of data quality is essential to maintain consistent physics object reconstruction across the large dataset. The data quality (DQ) monitoring information is concentrated into DQ status flags that reflect the overall status of relevant ATLAS subsystems. The flags are assigned per lumi-block, which is a fundamental unit of time in luminosity measurement and corresponds to roughly 1 minute. There are three kinds of DQ status flags:

- *Detector subsystem* flags which determine the status of [ATLAS](#) subsystems (assigned by sub-detector or by task).
- *Trigger* flags which monitor failed events in [TDAQ](#) (assigned per [L1](#) systems and [HLT](#) slices)
- *Combined performance* flags assigned by performance groups who determine a combination of [DQ](#) flags under which good physics object can be consistently defined.

These monitoring tasks can be also classified in terms of *online* (during the [LHC](#) fill) or *offline* monitoring (e.g. accessing processed event through `Express` stream). The [DQ](#) flags are stored in the conditions database with any of the 5 possible following values, as shown in [table 3.1](#).






	Value	Meaning	Comment
	-1	disabled	relevant system disabled
	0	undefined	not enough statistics (very short runs) or problems with DQMF
	1	bad	not good for physics
	2	flawed	use with caution, later reclassified as red or green
	3	good	good for physics

Table 3.1: Summary of data quality status flags used in [ATLAS Data Quality Monitoring Framework \(DQMF\)](#). The flags are listed in order of “badness”, as clearly a disabled system or undefined state of the detector cannot be used for physics.

The final output is a list of [lumi-blocks](#) correctly flagged for physics use. This list is commonly referred to as `GoodRunsList`. A [GRL](#) configuration is defined by a query of detector and combined performance [DQ](#) flags in a given run range. Removing [lumi-block](#) leads to a reduction of total integrated [luminosity](#) available for physics analyses. The actual integrated [luminosity](#) for a given [GRL](#) can be obtained using the `iLumiCalc` service, which is a standard [ATLAS](#) tool for luminosity calculations. Note that the definition of a [GRL](#) depends on the analysed final state. Analysis-specific [GRL](#) may apply additional criteria like a specific trigger configuration. [[ATL12b](#)]

3.2.2 Analysis paths

Physics analyses employ [Monte Carlo \(MC\)](#) models to describe the signal and background composition observed in experimental data. In [ATLAS](#) nomenclature, the term “data” is exclusively used when referring to the data reconstructed from [ATLAS](#), while the term “MC” is used when referring to any simulated sample.

In case of [MC](#), the whole simulation procedure has to proceed through a series of steps. At the *generation* stage, events corresponding to a specific physics process are produced through many possible [MC](#) generators ([MC@NLO](#), [POWHEG](#) and others, see the glossary). The *simulation* step models the passage of particles through matter as corresponds to the digital model of [ATLAS](#) detector geometry. This step is handled by the Geant4 software tool-kit, which is a powerful tool that simulates a wide range of processes with energies well into to the TeV, also accounting for [mis-alignment](#), magnetic field inhomogeneities and other detector distortions. Detailed description of Geant4 is outside the scope of this thesis, see [[Ago+03](#)] [[Gea](#)]. The simulated events are then *digitized*, introducing detector effects and noise such that the output of the digitization resembles the format of real events coming out of the detector.

Reconstruction algorithms are applied as a last step such that it proceeds the same way on the detector data or digitized MC. [ATLj] The detector-specific reconstruction algorithms start from reconstruct tracks and vertices, and then proceed to physics objects like candidate electrons, muons, and hadronic jets, as described in section 3.3. Because of the overlap between the term “simulated” events and the simulation step of the full chain, in ATLAS we refer to simulated events processed through the full chain as MC events. An alternative approach using ATLAS Fast Simulation (ATLFAST) II [RPF98] [She] provides a fast simulation of the detector and its parts. It is not used for the analysis presented in chapter 4.

3.2.3 Event data model

The full chain steps discussed above correspond to the derived data formats. In the ATLAS event data model, the MC events or the raw data for each stream are represented in a unified hierarchy of file/data types [ATL14i] [ATL05, pp. 7–8]:

Raw data are the direct output of Event Filter, sometimes referred to as *byte-stream* to indicate the persistent flow through the trigger system. At peak 2012 this format reaches ≈ 1.60 MB per event at 1000 Hz. The format is a direct input of reconstruction step in the full chain and is stored only until the reconstruction is finished (for discussion of *delayed streams*, see [ATL13g]).

Simulated event data refers to the wide range of data types from generator events (e.g. Pythia, Herwig) to simulated hits (Geant4). In most case, EVGEN format is a direct MC generator output in HepMC event record [Dob+]. HITS format is the output from Geant4.

Raw Data Objects (RDO) which is a C++ object representation of the byte-stream information. RDO files can get over 2 MB per event because in addition to the digitized records they also contain MC truth.

Event Summary Data (ESD) is the full output of the detector reconstruction stored in organized containers (POOL format, see below), it contains reconstruction details such as tracks and their hits, calorimeter clusters etc. to allow particle identification, track re-fitting, jet calibration etc. Access to ESD is generally unnecessary for most physics and performance applications other than re-calibration and re-reconstruction. The nominal size is 1 MB per event. ESD are deleted after roughly 4 weeks due to space limitations.

Analysis Object Data (AOD) is a reduced summary of the reconstructed event derived from ESD, format remains the same. AOD contains sufficient information for common physics analyses using reconstructed physics objects: electrons, muons, jets, etc. Nominal size is over 100 kB per event and is intended to be the starting point for most physics analyses.

Derived Physics Data (D3PD) are derived from one of the formats above (usually AOD) either by implementing a specific selection (*skimming*), reducing the event summary (*slimming*) or both (*thinning*), while providing some additional user-provided data. Averages 10 kB per event, varies by physics channels and applied thinning.

Tag data (TAG) are database or [ROOT](#) files containing event-level meta-data allowing simple and efficient way to search for events in a given analysis.

The *Pool Of persistent Objects for LHC (POOL)* format is incorporated into the Persistency Framework [[CERb](#)] which is a collaborative project between the [CERN](#) IT Department and three [LHC](#) experiments: [ATLAS](#), [CMS](#) and [LHCb](#). It provides an event-based store for C++ objects using a mixture of streaming, meta-data and relational technologies (databases). [ROOT](#) format, on the other hand, is completely stand-alone event-by-event table commonly referred to as *N-tuple (NTUP)*. The summary of data formats is given in [table 3.2](#).

Item	Abbr.	Origin	Specification	kB/event
Raw data	RAW	data	output of event filter (HLT)	≈ 1000
Generated events	EVNT	MC	evgen HepMC	≈ 100
Simulated events	HITS	MC	simulation POOL output	≈ 1000
Raw Data Objects	RDO	MC ,data	digitisation output POOL files	≈ 3700
Event Summary Data	ESD	MC ,data	full reconstruction output	≈ 3700
Analysis Object Data	AOD	MC ,data	derived from ESD for analysis	≈ 550
Derived Physics Data	D3PD	MC ,data	skimmed / slimmed / thinned AOD or ESD	varies ($\mathcal{O}(10)$)
Tag data	TAG	MC ,data	event-level meta-data	1

Table 3.2: [ATLAS](#) data formats and nominal event sizes. Data from [[ATL05](#), p. 7], updated from [[ATL141](#)] [[Bir+14](#), p. 20].

3.2.4 Operational model

[CERN](#) has adopted the distributed computing approach to data analysis, as it is effectively the only solution when dealing with a large dataset and a large number of users requiring uninterrupted and simultaneous access to it. Well-designed distributed systems have other advantageous properties:

- the computational entities are autonomous with distributed access to data,
- user interface is independent of the local site implementation and topology,
- the reliability of the entire system is impervious to failures of individual computers.

The global computing infrastructure for [LHC](#) experiments is provided by the *Worldwide LHC Computing Grid (WLCG)* project [[Sch+05](#)] [[WLC](#)]: an international collaboration of more than 150 computing centres in nearly 40 countries which makes it the largest computing grid in the world to date. The mission of the [WLCG](#) project is to provide global computing resources to store, distribute and analyse the data produced by the [LHC](#) experiments (currently almost 100 PB on disk for [ATLAS](#) alone [[CER14](#), p. 8]).

Managing the availability of data produced in one physical location and required in another location is the main challenge of this approach. The general philosophy of distributed computing network is that the user's job follows the data, not vice versa, thus minimising the necessity to transfer large datasets between sites. User analysis is currently the most resource-intensive activity on the grid in terms of the number of submitted jobs and the volume of data processed approaching 1 EB [[CER14](#), p. 8]. [WLCG](#) currently employs more 100,000 processors from more than 150 sites. The sites are structured in layers, or *tiers*, dedicated to specific services: [[ATL05](#), pp. 5,141] [[WLC](#)]:

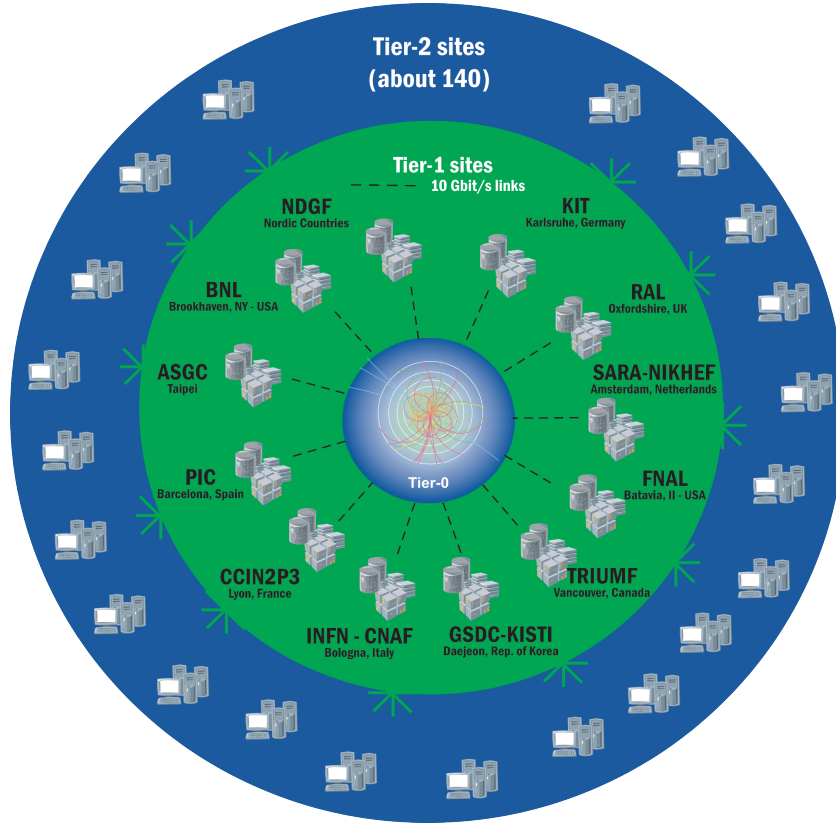


Figure 3.8: WLCG Tier-1 and Tier-2 sites. Figure from [WLC].

Tier-0 includes the CERN Data Centre in Geneva, Switzerland and the Wigner Research Centre for Physics in Budapest, Hungary connected by 100 Gbit s^{-1} links. The main task of Tier-0s is the safe-keeping and distribution of raw data as CERN provides only about 20 % of the necessary computing power for event processing. The data are archived on CERN Advanced STORage manager (CASTOR) [CERa] and first-pass calibration/alignment and reconstruction procedures are conducted within 48 hours.

Tier-1 involves twelve large computing centres with mass storage capacity and uninterrupted access. These sites are mainly responsible for safe-keeping of a proportional share of raw and reconstructed data, large scale reprocessing, distribution to Tier-2 sites as well as scheduled large scale tasks for physics and detector groups. Tier-1 sites are listed in fig. 3.8.

Tier-2 sites are typically provided by universities and other scientific institutes able to store data and provide adequate computing power for simulation and group analysis. Derived datasets are distributed Tier-2s.

Tier-3 are sites designed to provide access to the distributed computing resources and provide local storage for user data. It can consist of local computing clusters or individual user machines, there is no formal relationship between WLCG and Tier-3 resources.

It should be noted that the specific usage of tiers differs between experiments and adapts to the needs of the collaborators.

3.2.5 Analysis software

[ATLAS](#) software code base is written mainly in the C++, Fortran, and Python languages and is organised in over 2000 software packages (more than 6 million lines in total). The code is maintained by more than 400 developers and used by more than 2500 physicists. [Ryb13, p. 1] External dependencies include an additional 100 software packages including HepMC, Geant4 and [MC](#) generators mentioned above and [ROOT](#) (see below). The high number of individual packages sharing a common architecture allows the framework to suit individual needs of physicists while keeping these development contained using versioning. The underlying architecture is inherited from the Gaudi project developed for [LHCb](#) [[ATL14a](#)] [[ATL05](#), p. 27].

From the perspective of the analyser, the software for *numerical computing* and processing of [ATLAS](#) datasets can be categorized in two ways. One can take the fully-integrated approach using *Athena framework* or a stand-alone using [ROOT](#):

[Athena](#) is the object-oriented control framework that links the simulation, reconstruction and physics packages to the common data model. It contains the majority of software packages mentioned above: generators, simulation tool-kits (G4ATLAS), analysis tools, atlas-specific enhancements and [HLT](#) control, many of them implement [ROOT](#) at some level. The framework and algorithm code is based on C++ and *Fortran*. The hard coded parts are controlled via configuration inputs written in *Python* and *BASH*. Configuring and building [Athena](#) releases is managed by centrally deployed *Configuration Management Tool* (CMT). The whole framework runs exclusively on the [CERN](#) Linux distribution Scientific Linux (currently SLC6) which is a modification of Red Hat with physics related software pre-installed [[ATL05](#)]. It is in principle possible, with deep limitations, to make [Athena](#) work on other Linux distributions or Mac OS X.

[ROOT](#) [[ROOa](#)] [[ROOb](#)] is a stand-alone object-oriented framework written in C++. It is developed at [CERN](#) for data processing and physics analysis by an independent team. [ROOT](#) provides computation and physics-specific classes that allow the user to visualise data, plot and fit histograms and use a variety of computational procedures similarly to MATLAB, Mathematica or other commercial software. [ROOT](#) classes are connected and compatible with [Athena](#). [ROOT](#) was used extensively in the analysis presented in this thesis.

Using the framework requires moderate understanding of all listed programming languages and a very good understanding of [Athena](#) architecture itself. Tutorials are available in [ATLAS](#) online documentation [[ATL14a](#)] as well as other information about configuration and object hierarchy. [Athena](#) is constantly under development, latest release relevant for the analysis presented in this thesis is 17.1.4.8.

It should be noted, that majority of [ATLAS](#) software is platform dependent and as such the adoption of a suitable integrated development environment rests with the user. To bridge the gap between the fully-integrated and the stand-alone approach, the *RootCore package* [[ATL1](#)] was developed. It essentially helps users to build several [Athena](#) packages outside of [Athena](#). Other [CERN](#) analysis tools include *event viewers* (*Atlantis* [[ATLa](#)], *Virtual Point 1* [[ATLc](#)]) which are used for graphical visualisation of analysed events, even providing interactive 3D visualisation.

Additional development tools include: `a4` [EW] and *SFrame framework* [KHB], which are mainly designed to help with the most common tasks when handling ATLAS-produced datasets in AOD and D3PD format respectively.

3.2.6 Analysis work-flow

All of the full chain steps listed above are implemented as part of *Athena*. The stand-alone analysis approach is thus only effective if the user finds himself at the end of the full chain, working with D3PD. In analogy to the previous categories, there are also two kinds of derived formats:

- DESD, and DAOD which are stored in pool format. The stored information is accessible via *Athena* or using at least a partially-integrated framework like `a4`.
- D3PDs are derived from pool format and stored as a ROOT n-tuple, where information is accessible using *Athena* and ROOT. See [ATLe] for explanation of different kinds of D3PD.

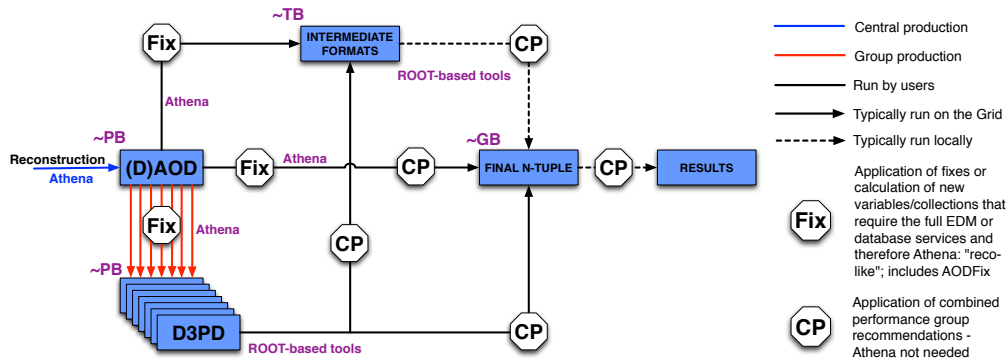


Figure 3.9: The ATLAS Run-I Analysis Model from AOD onwards. Users either analyse the (D)AOD directly in *Athena* or convert the (D)AOD into a ROOT NTUP format or D3PD. Figure from [Lay+13, p. 2].

As it stands, when using the analysis work-flow used from 2010 to 2014 most users opted for the stand-alone approach as it is much easier to implement. The D3PD are provided centrally for large analysis groups. The work-flow is shown schematically in fig. 3.9. Very often these $\mathcal{O}(\text{PB})$ size formats were reduced to intermediate formats of $\mathcal{O}(\text{TB})$ in size using some form of thinning. The notable problem with this model arises when any of the higher-level data are reprocessed (for example to implement bug fixes). Any user at the end of the chain has to wait until all re-processed data are processed and converted to D3PD, a procedure that can take months given the full dataset and a reasonable set of MC samples. The limitations of this analysis model are extensively discussed in [Lay+13]. In preparation for LHC Run-II, the new work-flow will introduce a new format xAOD to streamline the processing and harmonize the definition of physics objects [ATL14n].

3.3 Physics objects reconstruction

The definition and reconstruction of physics objects from the detector signals is a critical component of our physics analysis. In this section we aim to give an overview on how the objects are defined and reconstructed. All relevant detector components have been described in chapter 2, section 2.5.

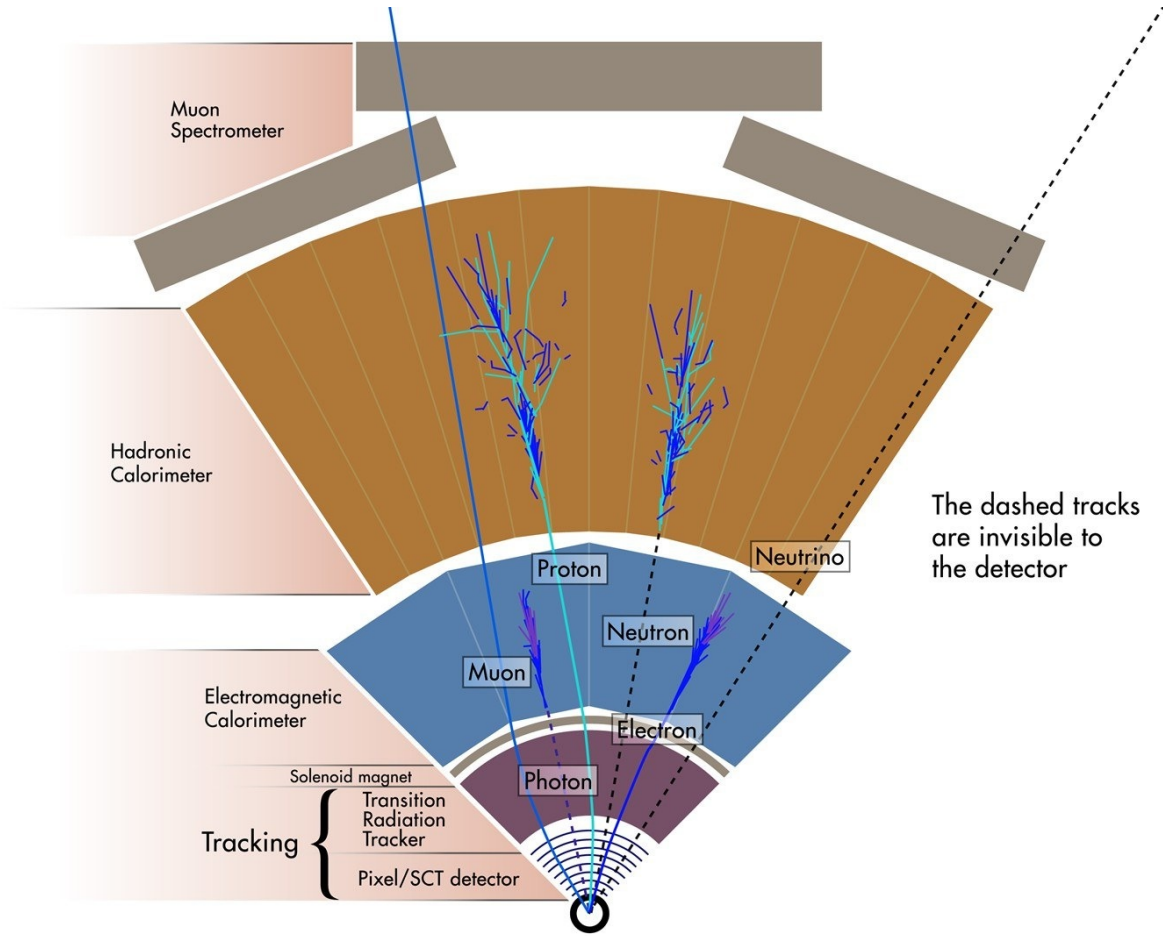


Figure 3.10: ATLAS event cross section. Selective particle identification in the ATLAS detector. Figure from [ATL10b].

3.3.1 Tracking

Detector tracks are reconstructed trajectories that correspond exclusively to charged particles recorded by the detector's tracking system. As we discussed in section 2.5.3, the trackers are submerged in the magnetic field which allows us to determine the particle momenta from the parameters of the reconstructed track helix. In ATLAS, the charged particle tracks within $|\eta| < 2.5$ and with transverse momenta $p_T > 0.40$ GeV (but as low as 0.10 GeV for specific studies or minimum-bias measurement) are recorded in the Inner Detector. Tracks are the most elementary and essential physics objects as they are used in vertexing and reconstruction of electrons and muons. In the previous chapter, figs. 2.27 and 2.28 show the ID traversed by 10 GeV tracks in the barrel and end-cap regions.

The tracks are reconstructed by a sequence of algorithms collectively referred to as ATLAS NEWT (New Tracking) which has been introduced in 2007 as a common model to ensure maintainability and long and reliable usage, full details are provided here [Cor+07]. The reconstruction sequence is organized in three stages:

Pre-processing stage, where the raw data recorded by Pixel and SCT in the form of *clusters* are converted into three dimensional representations of the silicon signals called *space-points*.

For **Pixel** this is a simple task, because the modules provide a two-dimensional measurement in $(\phi - z)$ in three layers at three radii. The **clusters** recorded on **SCT** strips, however, cannot be directly transformed into a three-dimensional representation since the measurement is not constrained along the strip. To work around the problem, the algorithm was designed to utilize the knowledge of cluster information from opposite sides of the **SCT** module. Coupled with the knowledge of beam spot this is used to define the **SCT** space-point. [Cor+07, p. 12] Next, the **TRT** raw data are converted into calibrated **drift circles** to be used at a later stage of track association.

Track-finding stage where different tracking algorithms are applied to sequentially fit track segments to the defined space-points. The NEWT model uses two track finding sequences: *inside-out* and a consecutive *outside-in*. The inside-out sequence starts from the layers closest to the **IP** and moving outwards progresses through the space-points using a combinatorial Kalman filter. The algorithm can be divided to two steps:

1. *Track seed finding* where track seeds are formed from the combination of space-points in the **Pixel** layers and the first **SCT** layer.
2. *Track candidate creation* where the track seeds become track candidates after they are extended throughout the rest of the **SCT**.

At this point the space-point objects are dissolved. The track segment extension now proceeds through each silicon layer by minimizing the χ^2 of the track. It progressively updates the track information and covariance matrices thus predicting precisely the track representation on the next measurement surface. Since a charged particle generally produces more than one hit per event, the prediction gives the most likely extension of the trajectory. A hit is a measurement point assigned to a track. If no **clusters** are found, the algorithm proceeds to the next layer. Outliers are identified by their large χ^2 contribution and subsequently removed. [Cor+07, p. 15]

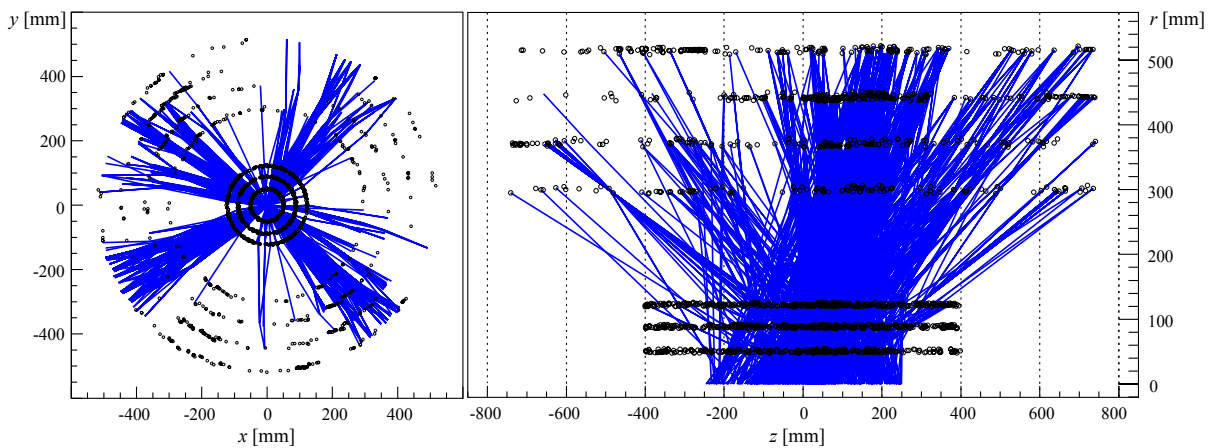


Figure 3.11: Track seeds consisting of two, resp. three objects in the **ATLAS ID** (barrel region) for a simulated $t\bar{t}$ event reconstructed with no vertex constraints. The space-point seeds that build the three objects are spread over a large z -range which in turn leads to a large number of the track candidates for further processing. Figure from [Cor+07, p. 15].

An example of track finding performed for a simulated $t\bar{t}$ event is given in [figs. 3.11](#) and [3.12](#).

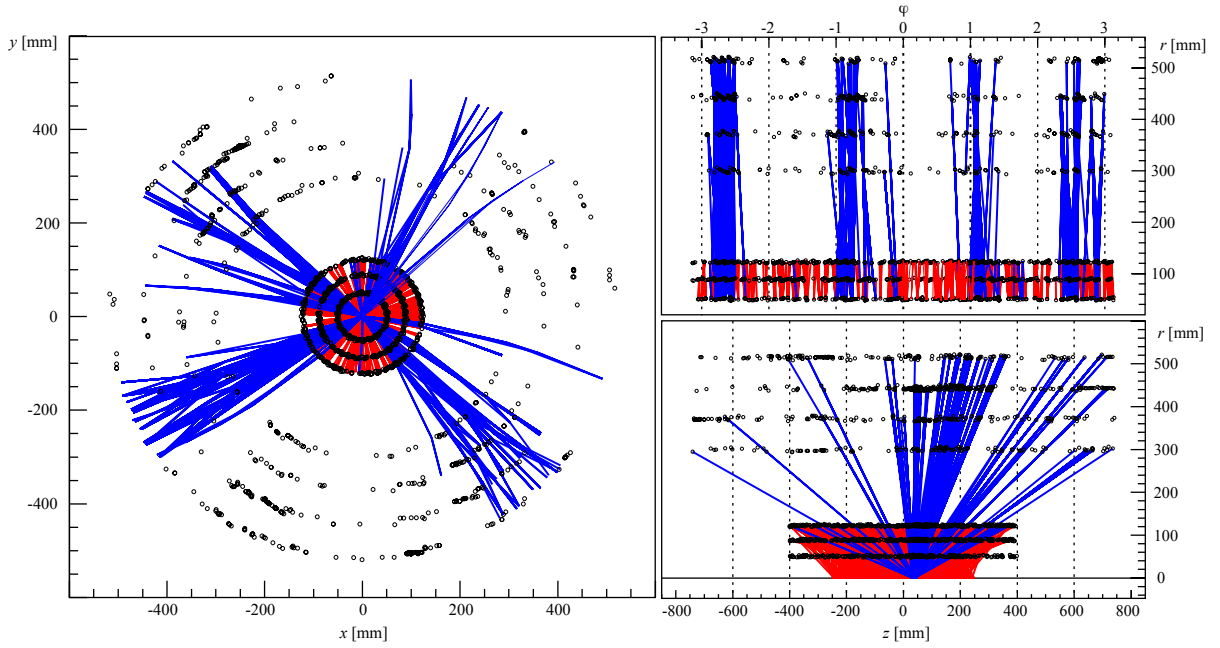


Figure 3.12: Track seeds consisting of two, resp. three objects in the *ATLAS ID* (barrel region) for a simulated $t\bar{t}$ event reconstructed with the z -vertex constraint seed search. The seeds consisting of two space-points are used to determine z -coordinates of the predicted vertex positions. Only *vertices* within a defined range around the interaction point are used to constrain further seeds with three or more space-points. For convenience, only seeds that are entirely in the barrel region are drawn. Figure from [Cor+07, p. 14].

As one can see from the figures, the number of reconstructed tracks is very high. Any outliers and ambiguities need to be removed and fake track rejected. An individual track scoring is applied using quality cuts based on the number of associated clusters, limits on the number of holes per track etc. A hole is non-existing but expected measurement point given the track trajectory. A track passing through an inactive module does not count towards the number of holes. An example of ambiguity solving for *SCT barrel* is given in fig. 3.13. The selected candidates are then extended into the *TRT* to associate the *drift circle* information. The finalized tracks are then refitted with the full information available from all three detectors and compared to the silicon track candidates. Bad fits are again labelled as outliers. [ATL08b, p. 298]

Post-processing stage where track candidates are extended into *TRT* by searching the volume for compatible measurements. The inside-out algorithm is used as a baseline, designed for efficient reconstruction of particles with $p_T > 400$ MeV and mean lifetime $\tau > 3 \times 10^{-11}$ s directly produced in the pp collision or coming from subsequent decays of particles with lifetime shorter than 3×10^{-11} s [Was12, p. 4].

The outside-in track reconstruction is an alternative that does not rely on a track seed found in *Pixel* or the *SCT*. Tracks coming from secondary *vertices* further inside the *ID* volume or from photon conversion may not produce sufficient silicon hits to be accepted as a seed in the inside-out method. The outside-in algorithm starts from local pattern recognition inside the *TRT* volume, we provide a simplified explanation in figure [Cor+07, p. 17]. Additional processing stages are implemented to deal with bremsstrahlung kink corrections.

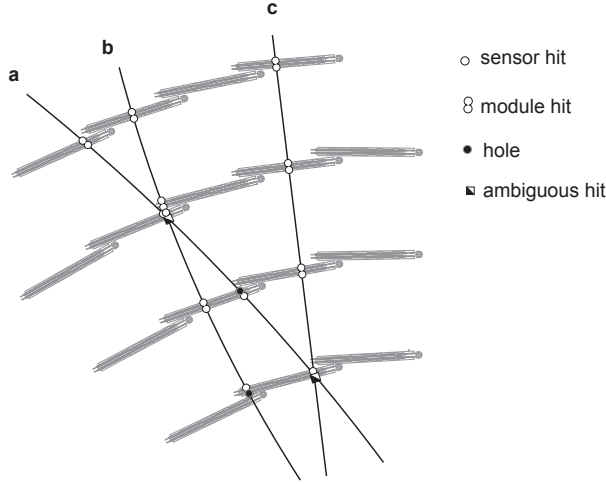


Figure 3.13: Simplified model of the track ambiguity solving process, illustrated for the SCT barrel. Tracks **a**, **b**, and **c** have been found through the seeded track finding, but share several hits. The χ^2/N_{dof} may not be appropriate to distinguish a true from a fake track, therefore dedicated track scoring that is optimised for each sub-detector used. In the shown example, e.g. a module hit representing measurements on both sides of the SCT silicon detector are scored relatively higher than two single hits without associated backside module. Hits in a overlap region as for track **b** are in particular high scored, while holes on track, i.e. an expected hit that has not been found, lead to a penalty in the track score. Figure from [Cor+07, p. 16].

The fit returns a finalised track state vector with the following coordinates:

$$(3.1) \quad \mathbf{T} = \begin{pmatrix} r_0 \\ z_0 \\ \theta \\ \phi \\ q/p \end{pmatrix} \quad \text{where} \quad \begin{array}{lll} r_0 & \dots & \text{minimum radial distance from the beam pipe} \\ z_0 & \dots & \text{distance parallel to beam pipe as defined in section 2.3.2} \\ \theta & \dots & \text{azimuthal angle as defined in section 2.3.2} \\ \phi & \dots & \text{polar angle as defined in section 2.3.2} \\ q/p & \dots & \text{charge over momentum of the track} \end{array}$$

The coordinates of the particle helix are given for the point closest to the beam. In this minimal representation the tracks are passed further, given the high track multiplicity. The innate ID uncertainty on the measurement of charged track momentum is $0.05\% p_T \oplus 1\%$, as shown in section 2.5.4. The uncertainty is dominated by mis-alignment (see section 2.6.1) and magnet bending power uncertainties (see [ATL08b, p. 29]).

In a high pile-up environment the pattern recognition algorithms could be confused by the high detector occupancy which could potentially lead to an increase of fake tracks (i.e. tracks not matching to a primary or secondary particle). As shown in [AEH10] [Was12], the algorithms can be made sufficiently pileup robust by tightening the track quality requirements like the minimum number of silicon hits. A set of *robust* requirements can be defined as follows:

- at least 9 hits in silicon detectors (Pixel + SCT),
- exactly zero holes in the Pixel detector.

The exact track quality criteria used in our analysis are given in chapter 4. The track reconstruction efficiency is determined using precise modelling of the individual detector response in MC simulation. The efficiency is defined as the fraction of matched reconstructed tracks over primary particles within the ID kinematic and geometric acceptance: $p_T > 400 \text{ MeV}$ and $|\eta| < 2.5$. The efficiency estimated for muons (resp. electrons) with $p_T > 1 \text{ GeV}$ is better than 95 % (resp. 80 %) in the ID barrel region. The efficiency drops below 60 % at large η for electrons reconstructed from low momentum tracks due to the large amount of material in the ID, see figures in [ATL08a, p. 26].

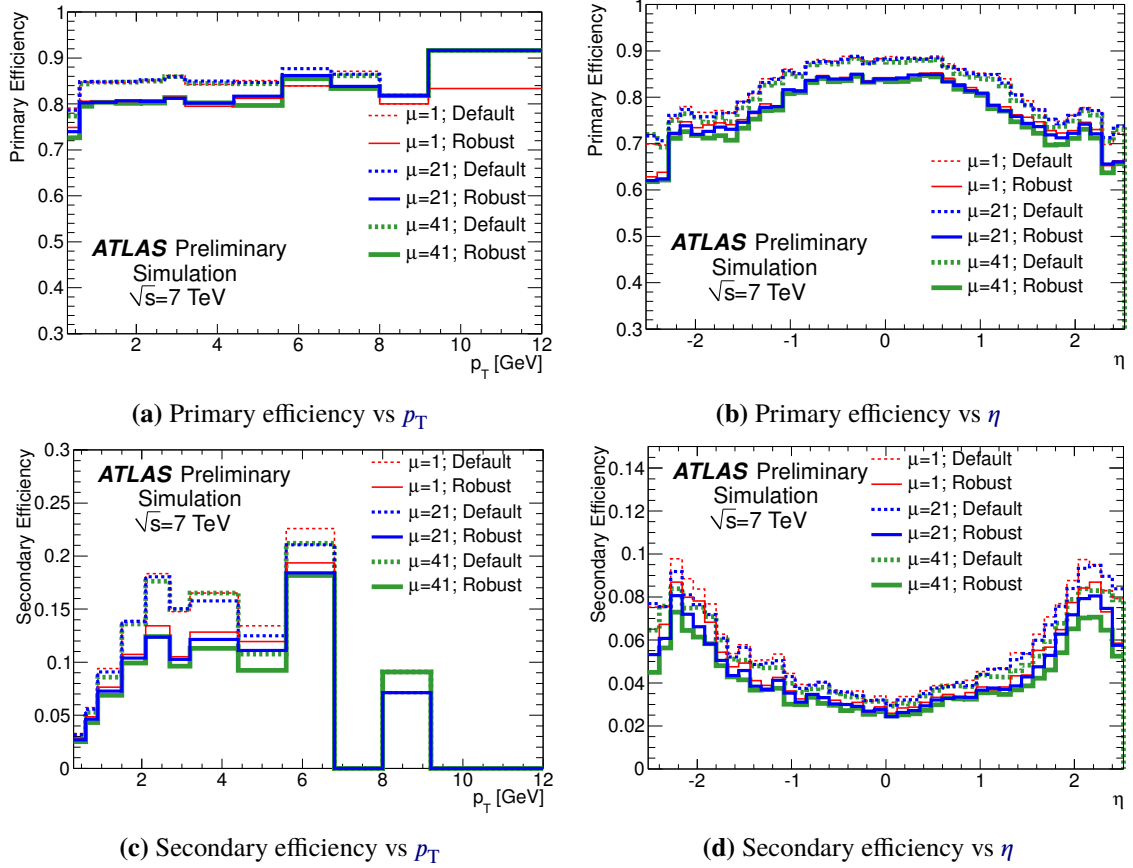


Figure 3.14: Primary and secondary tracking efficiencies in a minimum bias MC sample. Different histograms colours correspond to different $\langle\mu\rangle$. The distributions are shown for tracks passing default (dashed) and robust (solid) requirements. Statistical uncertainties are not shown, but they are significant, especially for the low multiplicity of secondary particles at high- p_T . Figures from [Was12, p. 5].

Figures 3.14a and 3.14b show the track reconstruction efficiency as a function of p_T and η between samples containing no pile-up ($\mu = 1$) and samples with high pile-up. In both cases the overall efficiency is reduced by $\approx 5\%$ given the tighter hit requirements but remains stable with increasing pile-up. The efficiency for secondary tracks also remains stable while losing 1–2 % due to robust requirements, see figs. 3.14c and 3.14d. [Was12, p. 5]

3.3.2 Vertexing

Reconstruction of the interaction vertex is based on the reconstructed tracks as discussed in the previous section. The *primary vertex* (PV) corresponds to the origin of a hard collision in the Interaction point. Then, a *secondary vertex* (SV) is reconstructed from tracks of charged particles produced in every decay of primary particles. The reconstruction of primary vertices is done in two steps:

1. The primary vertex finding algorithm first associates the reconstructed tracks with vertex candidates,
2. the vertex fitting algorithm then reconstructs the vertex position for a given set of tracks, calculates its corresponding error matrix, and refits the associated tracks.

The association and fitting algorithms are collectively referred to as *iterative vertex finding*, the detailed implementation is given in [ATL10c]. The algorithm works as follows:

- Select reconstructed tracks compatible with the vertex. The selection is based on the number of silicon hits and track impact parameters d_0 and z_0 [ATL10c] within the Inner Detector kinematic acceptance $|\eta| < 2.5$ and $p_T > 400$ MeV (although $p_T > 150$ MeV was used in initial studies). At least 2 tracks are required for each vertex candidate. [Was12, p. 7]
- Construct a vertex seed by looking for a global maximum in the distribution of associated track z coordinates. The beam spot position is used as a three-dimensional constraint.
- Determine vertex position using a robust χ^2 fitting algorithm. This procedure is referred to as *adaptive vertex fitting*. Outliers are down-weighted.
- Remove tracks incompatible with the vertex by more than 7σ and seed a new vertex. Repeat until all tracks are associated to vertices.

After all vertices are reconstructed, the primary vertex is selected. For a given bunch crossing, the PV in the event is selected by requiring the vertex to be reconstructed with at least 3 good tracks and that their total $\sum p_T^2$ is the largest of all vertices in the event. The increase in the required number of associated tracks is to ensure the vertex corresponds to a hard-scattering pp collision. Vertexing performance studies have been performed for low-multiplicity data in [ATL10c] and for high-multiplicity in [Pag+12a] [Pag+12b]. The resolution is determined for 7 TeV and 8 TeV data using a data driven method by randomly splitting the reconstructed vertices in two, each conserving approximately half the original number of tracks (*split-vertex technique*). The distance between the pairs is used to estimate the combined intrinsic vertex resolution from the distribution of the pull. [ATL10c, p. 3]

The vertex resolution in x and z is shown in figs. 3.17 and 3.18. The data is was recorded in specialized minimum-bias runs at $\sqrt{s} = 7$ TeV and later at 8 TeV with $\langle\mu\rangle$ less than 0.1. The resolution is shown as a function of number of tracks and a sum of their transverse momenta and both figures show a comparison with a minimum-bias MC, which shows excellent agreement. The measurement error decreases with increasing values of N_{trk} and $\sqrt{\sum p_T^2}$. For events with 50 or more tracks or $\sqrt{\sum p_T^2} > 10$ GeV the resolution has been measured to be about $30\mu\text{m}$ in the transverse plane and about $50\mu\text{m}$ in the longitudinal direction [Mel+11] [Pag+12a]:

	σ_x, σ_y	σ_z
7 TeV for $\sqrt{\sum p_T^2} > 10$ GeV	$\approx 20\mu\text{m}$	$\approx 40\mu\text{m}$
8 TeV for $\sqrt{\sum p_T^2} > 10$ GeV	$\approx 10\mu\text{m}$	$\approx 40\mu\text{m}$

The vertex reconstruction efficiency is shown for a minimum bias sample at 7 TeV in fig. 3.15 with the same track-to-particle matching used to calculate the tracking efficiency in the previous section. With the increasing number of fake tracks in high pile-up environment, the probability to reconstruct a fake vertex increases. In simulation, vertices are considered as fake when it is reconstructed mainly from fake tracks. The vertex reconstruction efficiency clearly follows this trend, as it drops by $\approx 20\%$ when reaching $\langle\mu\rangle = 40$. Selecting the robust tracks with at least 9 hits in the silicon detectors (Pixel + SCT) and exactly zero holes in the Pixels reduces the efficiency

at low $\langle\mu\rangle$ by 5 %, but shows slight improvement beyond $\langle\mu\rangle = 35$. [Was12, p. 7] The result of applying even harder requirements is shown in fig. 3.16 for 8 TeV data. It shows the efficiency of primary vertex reconstruction as a function of the mean number of interactions per bunch crossing for three different physics signatures and the corresponding efficiencies of the same process if requiring two leptons with $p_T > 10$ GeV. This is especially relevant for the analysis presented in this thesis, as the measured final state includes two high- p_T leptons.

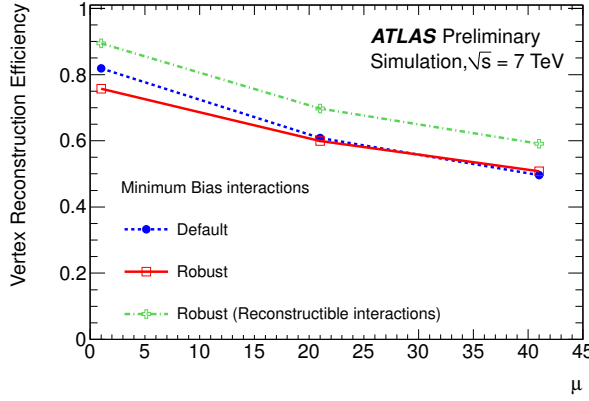


Figure 3.15: Vertex reconstruction efficiency at 7 TeV as a function of mean number of interactions per bunch crossing in a minimum-bias Monte Carlo simulation inside the Inner Detector acceptance. The default track selection (blue, dashed) and robust track requirements (red, solid) are shown separately. The vertex reconstruction efficiency with the robust track requirements is shown for reconstructible interactions (green, dot-dashed), defined as having at least two stable charged primary particles with $|\eta| < 2.5$ and $p_T > 400$ MeV. Figure from [Was12, p. 8].

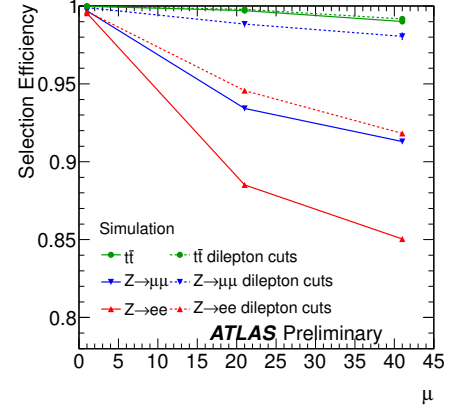


Figure 3.16: Efficiency to reconstruct and then select the primary vertex from the hard-scatter interaction at 8 TeV as a function of the mean number of interactions per bunch crossing for three distinct physics signatures. The points are calculated using the Monte Carlo simulation with or without an event selection requiring two generated electrons or muons with $p_T > 10$ GeV. Figure from [Pag+12a, p. 1].

3.3.3 Muon reconstruction

The final state muons produced at the LHC range from low-momentum muon emerging from b-jets to high-momentum isolated muons produced in W/Z decays. The reconstruction strategy takes advantage of the combination of independent measurements performed by the primary detector system, the Muon Spectrometer, and the Inner Detector. The ID measurement provides precise measurements within $|\eta| < 2.5$ at low and intermediate momenta, the MS takes over beyond ≈ 30 GeV and up to $|\eta| < 2.7$. [ATL08b, pp. 313, 315].

Currently, there are two main muon reconstruction algorithms implemented for ATLAS: the STACO algorithm (sometimes referred to as Chain 1) described in [Nic+10] [Has+07] and MUID algorithm (Chain 2) [Ada+03]. The algorithms differ in track reconstruction and measurement combination, but their performance is comparable. The analysis presented in this thesis uses the STACO algorithm so we shall focus mainly on describing the details of its implementation. It should be noted that currently an enhanced algorithm called Chain 3 is in development and will be a common requirement in future analyses.

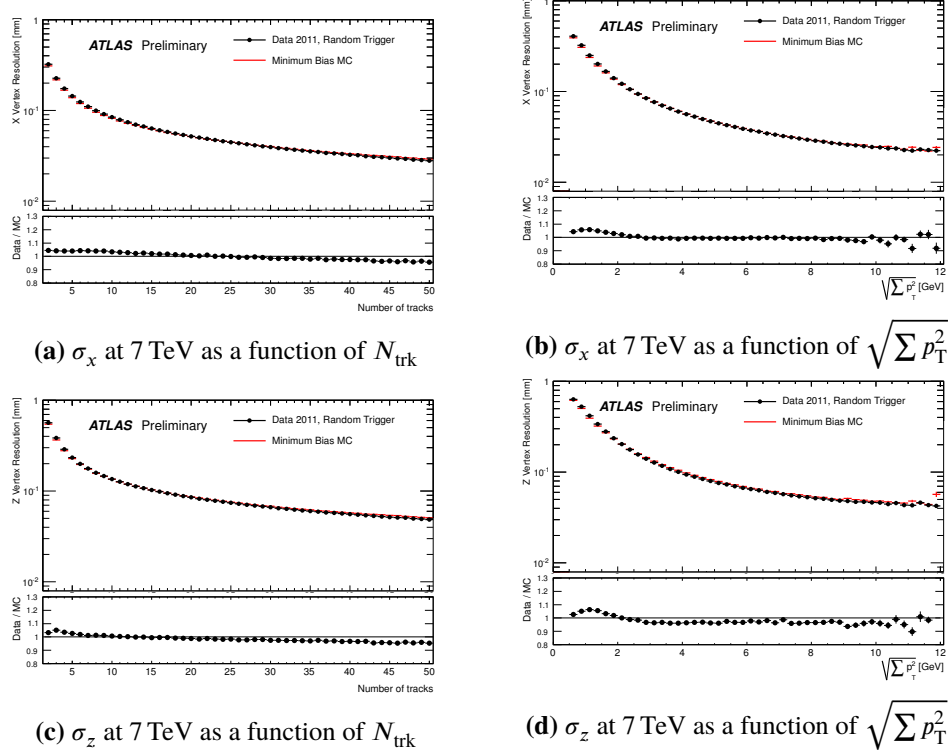


Figure 3.17: Vertex position resolution in x (resp. z) for 7 TeV data (black) and MC (red) shown as a function of the number of tracks in the vertex fit and as function of the square root of the sum of the squared momenta of these tracks. Data were collected using a 5 Hz random trigger EF_RD0_FILLED_NOALG. Figures from [Mel+11] [ATL14h].

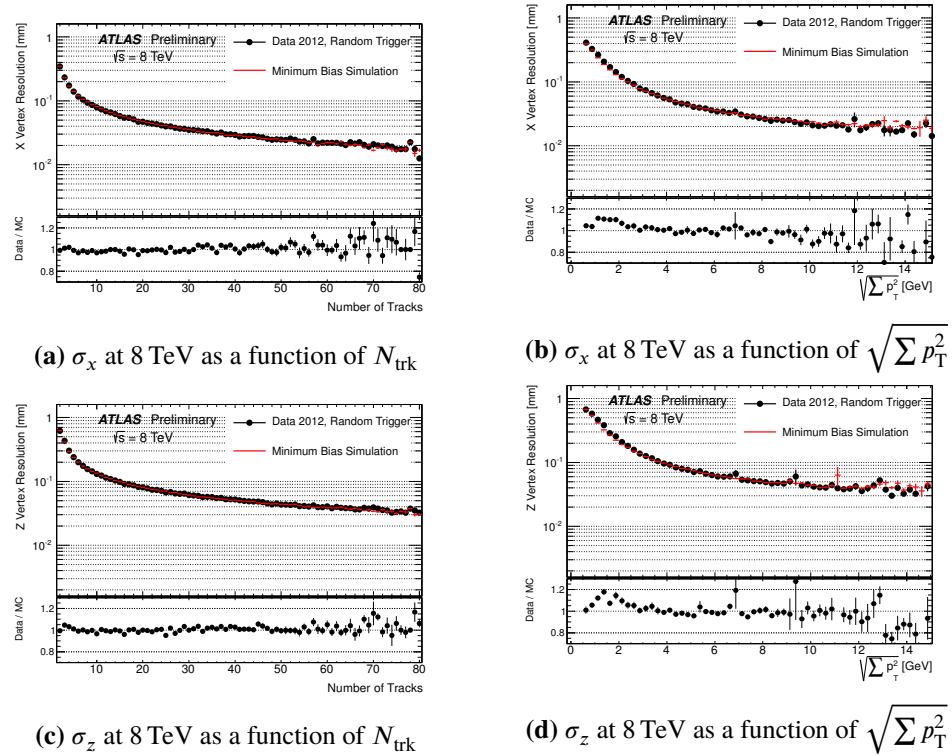


Figure 3.18: Vertex position resolution in x (resp. z) for 8 TeV data (black) and MC (red) shown as a function of the number of tracks in the vertex fit and as function of the square root of the sum of the squared momenta of these tracks. Data have been collected by a minimum bias trigger during a dedicated fill with an mean number of interactions per bunch crossing of about 0.01. Figures from [Pag+12a] [ATL14h].

The muon track reconstruction starts with the pre-processing of raw data to form **drift circles** in the **MDT** or clusters in the **CSC** and the trigger chambers (**RPC** and **TGC**). Pattern recognition is used to search for tracks segments. In **MS**, a track segment is defined as a single straight line in a single **MDT** or **CSC** station. The search for segments is seeded with the evidence of activity in the trigger chambers in a window of $\eta \times \phi = 0.4 \times 0.4$. Measurements from different stations are then combined to form a track candidate, starting from the outer and middle stations and extrapolating back. The final fitting procedure takes into account the full hit information, geometrical description of the traversed material and magnetic field inhomogeneities. [ATL08b, pp. 315–316]

The muon reconstruction and identification efficiencies are measured using a **tag-and-probe** method in $Z \rightarrow \mu^+ \mu^-$ samples. See section 4.5.1 in chapter 4 for the full discussion.

3.3.3.1 Muon identification

By design, **ATLAS** recognizes four types of muons, the categories are labelled according to the reconstruction method. The principle is schematically shown in fig. 3.19 [ATL13e, p. 2]:

Standalone muons (SA) (referred to as **MUONBOY** in the **STACO** collection) are reconstructed solely from the measurement in the **MS**. The **pseudorapidity** range $|\eta| < 2.7$ is defined by the **MS** acceptance (see section 2.5.6). The recorded track is propagated back through the detector to the **IP**. The energy loss caused by the calorimeter and **ID** material is estimated by an algorithm, which uses either the parametrised expected energy loss or the measured calorimeter energy. [ATL08b, p. 316] The advantage of **standalone** algorithms is that they have a slightly higher **pseudorapidity** coverage, but very low momentum muons might not reach the outermost stations. [ATL08a, p. 166]

Segment-tagged muons (ST) (also called **MUTAG** in the **STACO** collection) are reconstructed from the track segment in the **ID**: **PIX** + **SCT** + **TRT** in the **pseudorapidity** range $|\eta| < 2.5$. This **ID** segment is extrapolated to the inner muon stations and associated to a reconstructed muon segments in **MS** or used to select muon **drift circles** in a cone of ≈ 100 mrad from which the segment is reconstructed. This method is an important extension to the **standalone** measurement mainly because the middle stations are missing in the **barrel/end-cap** transition region $1.1 < |\eta| < 1.7$ and muons with momenta below 6 GeV do not always reach the **MS** layer. [ATL08b, p. 316] The **MUTAG** algorithm tags muons by minimizing the χ^2 difference between a nearby track segment and its prediction from an extrapolated track. The alternative **MUGIRL** algorithm is a part of the **MUID** family and uses an artificial neural network rather than the χ^2 approach and redoes the segment finding for all **ID** segments in the region around the track. [ATL08a, p. 166]

Calo-tagged muons are reconstructed from an energy deposit in the calorimeter. This method is used mainly for specialized analyses requiring deeper understanding of low- p_T muons. The average muon energy deposit in the calorimeter is small compared to low- p_T hadrons and electrons. However, muons traverse the full volume of the calorimeter, producing the characteristic ionizing signature through to outermost layers. [ATL08a, p. 163]

Combined muons (CB) (often referred to as **STACOMUONS** in the **STACO** collection) are reconstructed from combination of full **ID** tracks matched to **MS** tracks. Both of the muon combination

algorithms, **STACO** and **MUID**, pair the **MS** with **ID** tracks by minimizing the χ^2 defined as the difference between the outer and the inner track vectors \mathbf{T} weighted by their combined covariance matrix \mathbf{C} :

$$\chi^2_{\text{match}} = (\mathbf{T}_{\text{MS}} - \mathbf{T}_{\text{ID}})^\top (\mathbf{C}_{\text{MS}} + \mathbf{C}_{\text{ID}})^{-1} (\mathbf{T}_{\text{MS}} - \mathbf{T}_{\text{ID}}) \quad (3.2)$$

STACO then does a statistical combination of the inner and outer track to obtain the combined track vector

$$\mathbf{T}_{\text{CB}} = (\mathbf{C}_{\text{MS}}^{-1} + \mathbf{C}_{\text{ID}}^{-1})^{-1} (\mathbf{C}_{\text{MS}}^{-1} \mathbf{T}_{\text{MS}} + \mathbf{C}_{\text{ID}}^{-1} \mathbf{T}_{\text{ID}}) \quad (3.3)$$

and **MUID** does a partial inside-out refit as mentioned above. [ATL08a, p. 166] This combination significantly improves the momentum resolution for track with $p_T < 100$ GeV and effectively suppresses fake muon produced in pion or kaon decays-in-flight. The MuTAG algorithm mentioned above is designed to complement the **STACO** combined muon reconstruction and as such uses only the track segments not used to reconstruct a combined muon. MuGIRL, on the other hand, considers all of the **ID** segments, so the **MUID** and **STACO** families overlap. [ATL08b, p. 316]

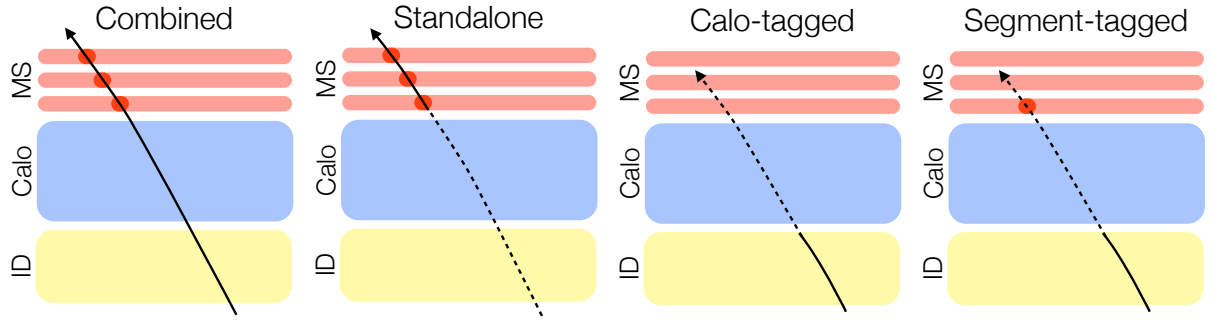


Figure 3.19: Muon reconstruction types in **ATLAS**. Courtesy of Lynn Marx [Mar13].

3.3.3.2 Muon momentum scale and resolution

The muon momentum scale $s(p_T)$ and resolution $\sigma(p_T)$ are important parameters for data analyses with high- p_T muon final states. These two parameters effectively quantify how well the detector measures the momentum of any given muon to account for the limited accuracy and calibration of the detector. All muons coming measured by the detector are subject to these uncertainties, collectively referred to as “detector smearing”. In order to improve the data/MC agreement, all simulated muons should be affected by the same uncertainties as are the muons observed in data. Hence, we are required to smear and/or scale the MC muon momentum using random numbers according to a specific parametrisation.

The first estimation of the muon momentum resolution was presented in [ATL11c] in 2010 on 40 pb^{-1} at 7 TeV with preliminary calibration and alignment constants. The momentum resolution is extracted from the width of the di-muon mass distributions in $Z \rightarrow \mu^+\mu^-$ decays and from comparisons of the independent measurements coming from **ID** or **MS**. Since this study, the parametrization has been altered only slightly, mainly due to the very large statistics collected in

2012 dataset. Generally speaking, the muon resolution is a quadratic sum of two terms:

$$\frac{\sigma(p_T)}{p_T} = a \oplus b \cdot p_T \quad (3.4)$$

where the a parameter represents the effect of multiple scattering that is independent of p_T and the b parameter is linearly proportional to p_T and corresponds to the spatial detector resolution (which also includes detector mis-alignment). The correction is applied to these terms separately and if we also include momentum re-scaling, denoted s , we obtain the following equation that allows us to derive the corrected muon momentum p_T^{corr} from the simulated p_T^{MC} :

$$p_{T,\text{det}}^{\text{corr}} = p_{T,\text{det}}^{\text{MC}} \cdot s_{\text{det}}(\eta) \left(1 + \Delta a_{\text{det}}(\eta) \mathcal{N}(0, 1) + \Delta b_{\text{det}}(\eta) \mathcal{N}(0, 1) p_{T,\text{det}}^{\text{MC}} \right), \quad (3.5)$$

where $\text{det} = \text{MS}$ or ID because each sub-detector has its own momentum resolution. $\mathcal{N}(0, 1)$ is a standard normal distribution. The effect of the correction is shown in fig. 3.20 that shows the Z mass and the data/MC agreement before (left) and after (right) smearing and scaling the simulated muons.

As is indicated in the equation, all the correction factors $s_{\text{det}}(\eta)$, $\Delta a_{\text{det}}(\eta)$ and $\Delta b_{\text{det}}(\eta)$ are pseudorapidity dependent. For the 8 TeV analysis, the factors are derived in 16 different pseudorapidity regions of the detector. The main motivation for this correction is to obtain an improved agreement to the p_T measured in data. The values of smearing, resp. scaling parameters are given in figures 3.21, resp. 3.22 derived from $Z \rightarrow \mu^+ \mu^-$ data for STACO reconstruction. The systematic uncertainty on the smearing is estimated by varying the Z boson mass windows in the template fit. The dependence of the muon momentum scale on the muon momentum and charge dependent effects on the scale corrections are covered by the present systematic uncertainty. For more details see [ATL13e] (8 TeV) and [ATL11d] (7 TeV).

3.3.3.3 Muon isolation correction

Isolation is a powerful criterion for rejecting non-prompt muons. We look for activity inside a cone around the muon track of $\Delta R = \sqrt{\Delta\eta^2 + \Delta\phi^2}$ smaller than a given area A [ATL11d, p. 8]. In high pile-up environment it is necessary to separate the isolation criteria for the tracker and the calorimeter, because the calorimeter correction is highly pile-up dependent:

- **Calorimeter based isolation:** $\sum_{\Delta R < A} E_T^{\text{corr}}(i)/p_T^{\text{corr}}(\mu)$, where E_T is the total transverse energy deposited in the calorimeter cells in the cone around the muon, excluding the muon itself. The calorimeter isolation energy is corrected for the muon energy loss.
- **Track based isolation:** $\sum_{\Delta R < A} p_T(i)/p_T^{\text{corr}}(\mu)$, where the sum extends over all charged particle tracks within the cone, excluding the track of the muon itself. Tracks must come from the PV and quality cuts apply.

The choice of isolation criteria depends on the analysis but most commonly $A = 0.3(0.4)$ is chosen as it fully contains the muon. The data/MC comparison of the track and calorimeter isolation distributions for the probe muon at $\sqrt{s} = 7$ TeV are shown in fig. 3.23. The agreement between data and MC is excellent, which leads to a reliable prediction of isolation efficiency. Muon isolation corrections are implemented to help recover the calorimeter isolation efficiency. The

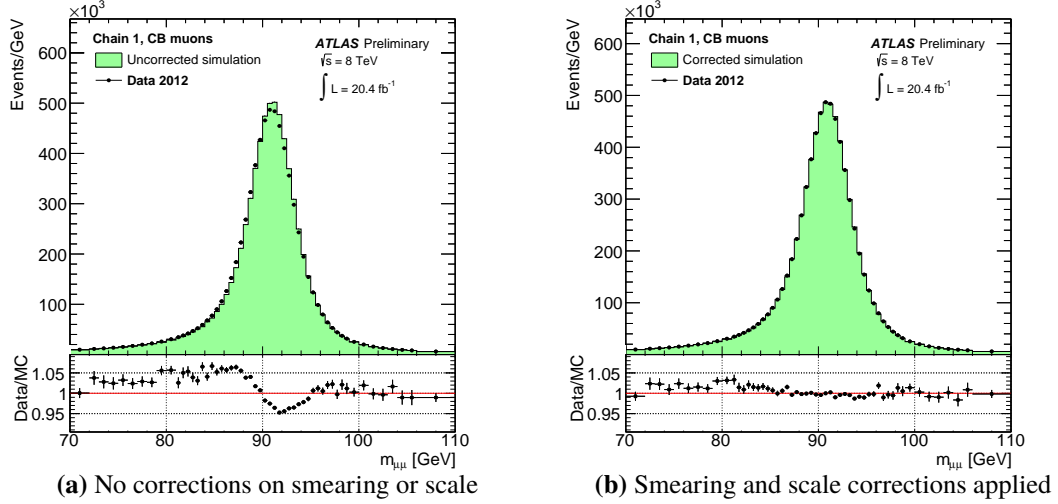


Figure 3.20: Di-muon invariant mass for STACO (Chain 1) isolated combined muons with $p_T > 25$ GeV. The plots show the di-muon invariant mass at $\sqrt{s} = 8$ TeV, the MC consists of POWHEG simulation of $Z \rightarrow \mu^+\mu^-$ process plus additionally background events. The left plot shows the distribution with no corrections applied. The corrections applied to the right plot have been derived from the full 2012 dataset. Figures from [ATL13e, p. 8].

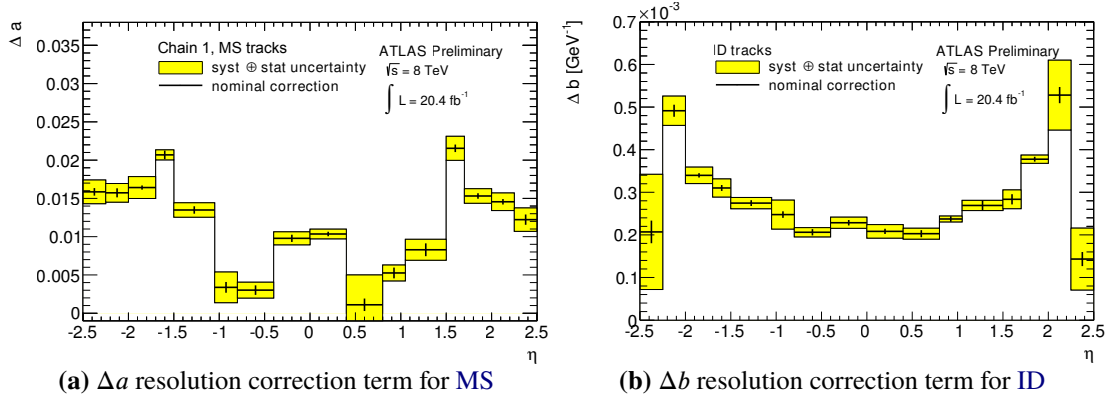


Figure 3.21: MC resolution corrections for ID and MS, derived from $Z \rightarrow \mu^+\mu^-$ data for the STACO (Chain 1) reconstruction. The systematic uncertainty on the correction is shown in yellow. The main systematic uncertainty comes from the extraction of the corrections from a template fit with a varied window around the Z boson mass. Figures from [ATL13e, p. 9].

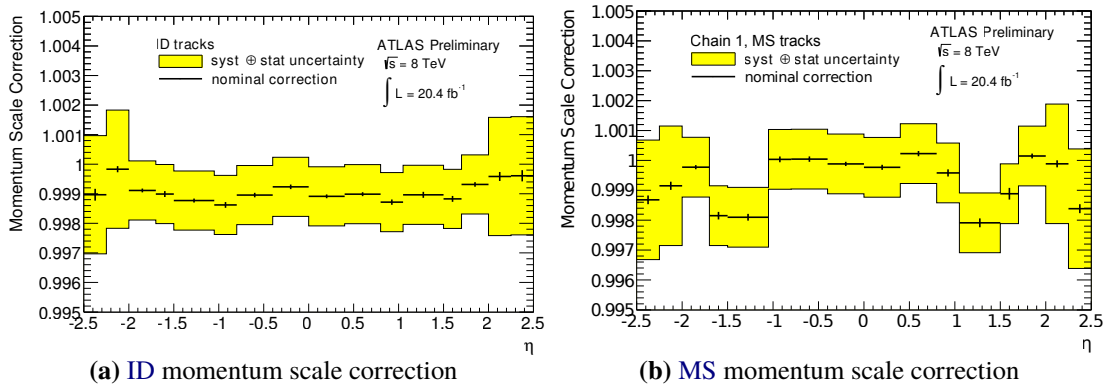


Figure 3.22: MC scale corrections for ID and MS, derived from $Z \rightarrow \mu^+\mu^-$ data for the STACO (Chain 1) reconstruction. The systematic uncertainty on the correction is shown in yellow. The main systematic uncertainties of 0.10 % and 0.20 % were introduced to cover a possible momentum dependence of the correction (the larger uncertainty is applied to the forward region of the detector). Figures from [ATL13e, p. 9].

correction is calculated using [tag-and-probe](#) on $Z \rightarrow \mu^+\mu^-$ with di-muon *invariant mass* m window within 10 GeV of the Z peak. High- p_T leptons ($p_T > 25$ GeV) are used to reduce background contamination. [\[ATL14k\]](#).

The median calorimeter isolation distribution (available as `ETCONEXX` variable in [D3PD](#)) is fitted as a quadratic function of the number of primary [vertices](#):

$$\sum_{\Delta R < N} E_T^{\text{corr}}(i) = \sum_{\Delta R < N} E_T(i) - a(\eta)N_{\text{vtx}}^2(\eta) - b(\eta)N_{\text{vtx}}(\eta) - c(\eta) \quad (3.6)$$

where $a(\eta)$, $b(\eta)$ and $c(\eta)$ are functions of [pseudorapidity](#) fitted in bins of [pseudorapidity](#) (separating [barrel](#) and [end-caps](#)) against the number of primary [vertices](#) N_{vtx} [\[ATL13c, p. 18\]](#).

The results of the fit for 2011 and 2012 dataset are shown in [fig. 3.24](#) for two cone sizes. The difference between the $\sqrt{s} = 7$ TeV and 8 TeV isolation corrections are due to the improvements in the noise suppression applied to calorimeter cells, hence the isolation correction is smaller in 2012 than it was in 2011. The performance package `MuonIsolationCorrection` is used to correct the median variable. Details on implementation in [\[ATL14k\]](#).

The performance package `MuonIsolationCorrection` is used to correct the median variable. The recommended version for $\sqrt{s} = 7$ TeV was `MuonIsolationCorrection-00-08` and `MuonIsolationCorrection-01-01` version was recommended for 8 TeV analyses. [\[ATL14b\]](#)

3.3.3.4 Muon quality

Muons are assigned different quality levels based on a set of criteria. The ranking is algorithm dependent, we shall discuss only flag definition for the [STACO](#) collection here. We define three quality flags (or “words”): `LOOSE`, `MEDIUM` and `TIGHT`, each corresponding to the particular muon type. [Combined](#) muons are always of `TIGHT` quality, whereas the [segment-tagged](#) muons can be classified into all three depending on the quality of the reconstructed segments. The latest classification scheme from the performance package `MuonUtils-00-07-50` is given in [table 3.3](#). In our analysis we use exclusively [combined](#) muons for the signal region. The full documentation is available here [\[ATL14m\]](#).

Muon author	Quality flag
STACOMUON candidate	TIGHT
MUTAG candidate with at least 3 TGC hits in tagging segments	TIGHT
MUTAG candidate with at least 2 tagging segments	TIGHT
MUTAG candidate with only 1 tagging segment in end-cap region $ \eta > 1.05$ and no TGC hits in tagging segments	LOOSE
MUTAG candidate not belonging to the preceding categories	MEDIUM
MUONBOY candidate	MEDIUM

Table 3.3: Sorting of muon quality levels in the [STACO](#) collection

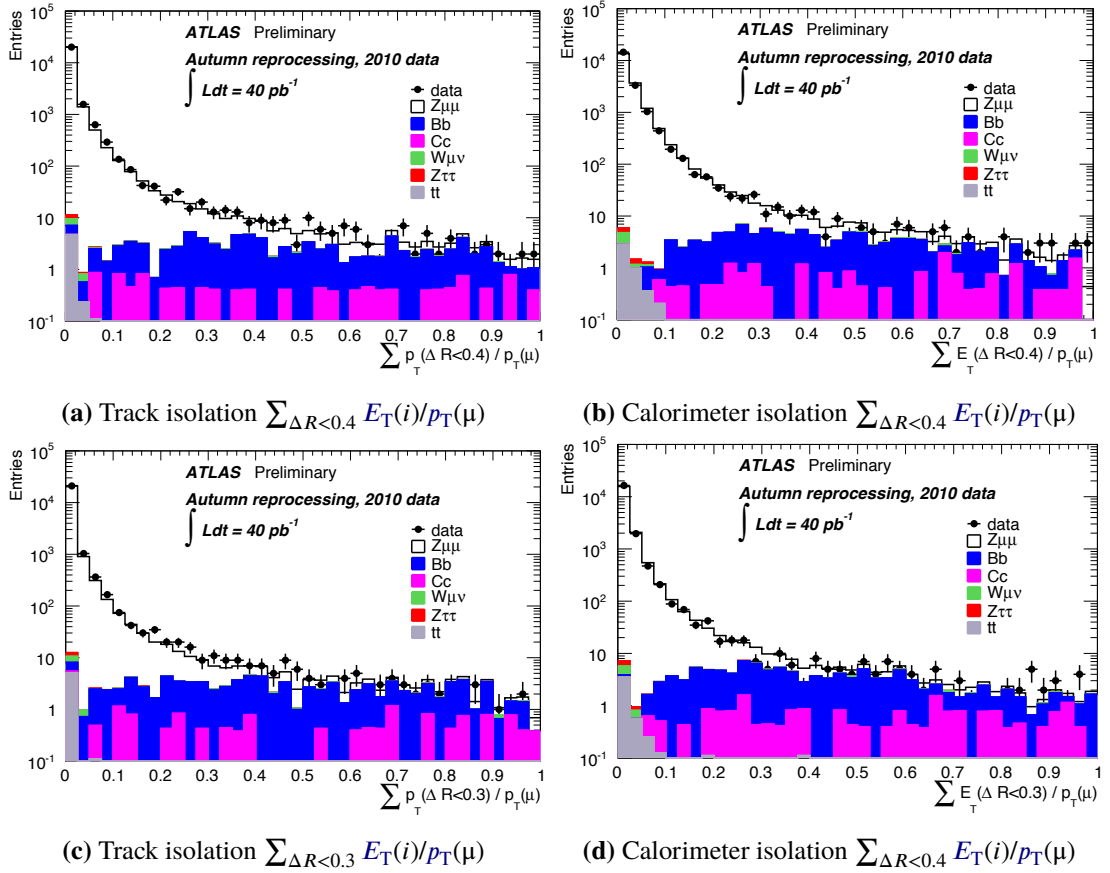


Figure 3.23: Muon track and calorimeter isolation distributions for the probe muon at $\sqrt{s} = 7$ TeV. The figure compares the measured isolation variables with the MC prediction. The excellent data/MC agreement provides a reliable prediction of the isolation efficiency used in physics analyses. The isolation correction was applied. Figures from [ATL11d, p. 16].

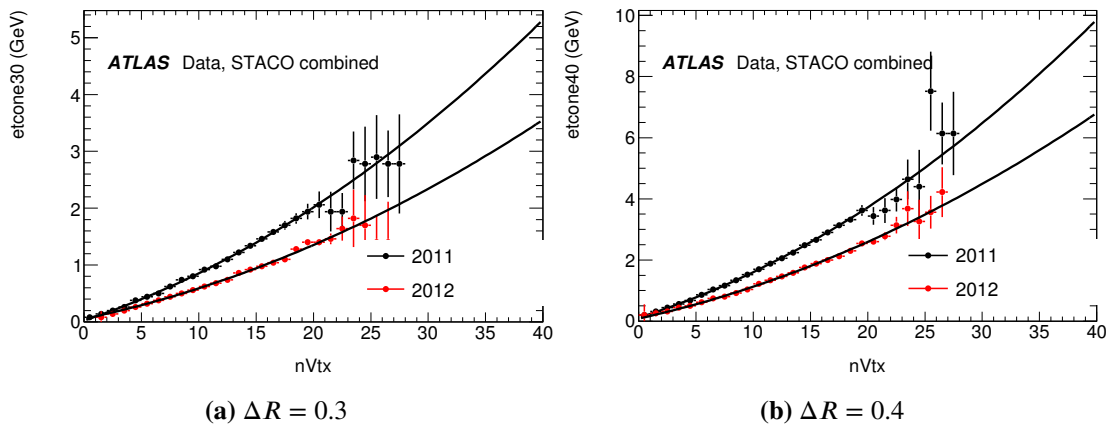


Figure 3.24: Muon calorimeter isolation correction. Quadratic fits of the median calorimeter isolation $\sum_{\Delta R < 0.3} E_T^{\text{corr}}(i)/p_T^{\text{corr}}(\mu)$ (ETCONE30 variable in D3PD) is shown at $\sqrt{s} = 8$ TeV. The difference in slope between the datasets is due to the noise suppression applied to the calorimeter to address the high pile-up which leads to a smaller correction. Figures from [ATL14k] (sic.).

3.3.4 Electron reconstruction

Electrons in [ATLAS](#) are reconstructed from a combination of energy deposits (clusters) in the calorimeter which are then associated to tracks of charged particles measured in the [ID](#). There are two types of clustering algorithms:

Sliding window algorithm starts by dividing the calorimeter into units in $(\eta - \phi)$ space referred to as *towers*. Each tower is defined as a fixed size rectangle $\eta \times \phi = 0.025 \times 0.025$ (corresponding to the granularity of the [ECAL](#) middle layer) summed over all calorimeter layers. The algorithm then sums all cells within a window and searches for a local energy maximum above a certain threshold (normally 3 GeV). The window size varies between 3×7 ($\eta - \phi = 0.075 \times 0.175$) and 5×5 ($\eta - \phi = 0.125 \times 0.125$) for the middle layer in the [barrel](#) and the [end-caps](#). The choice of window size optimizes between the conflicting requirements of maximising the collection of the clustered energy and preventing the degradation of resolution by minimising noise and [pile-up](#). The advantage of the fixed cluster size is that it allows a precise energy calibration. It should be noted here, that the window size may not fully cover the electron or photon energy deposit and in that case some energy will *leak* (see leakage correction in [section 3.3.4.4](#)). [[ATL08b](#), p. 322]

Topological clustering starts with a seed cell and iteratively adds the neighbouring cell to the cluster if the energy in the new cell is above a threshold defined as a function of the expected noise. *Topological clusters* are seeded by cells with large signal to noise ratio and then grow iteratively by adding the neighbouring cells provided the energy deposit recorded in these cells is greater than 2 standard deviations above the calorimeter noise level. The nominal energy deposit to build a seed is 4 standard deviations above the noise level. The algorithm finishes by including all direct neighbour cells on the outer perimeter [[Lam+08](#), pp. 4,9]. This algorithm is efficient at suppressing noise in clusters and is recommended to be used for 8 TeV run conditions as it is more [pile-up](#) robust (output variables are denoted `TOPOETCONEXX`)

Physics at the [LHC](#) is expected to produce electrons with p_T in range between a few GeV to a few TeV. This requires a powerful and efficient electron identification system that could cover such a wide spectrum. Electron reconstruction is easily contaminated by hadronic jets and photon conversions. Electrons travelling from the [Interaction point](#) lose on average between 20–50 % of their energy (depending on η) by the time they leave the [SCT](#) and about 10–50 % of photons convert into electron-positron pairs. The [TRT](#) plays an important role in electron identification by cross-checking and complementing calorimeter-seeded reconstruction and identification, especially at energies below 25 GeV [[ATL08b](#), p. 310]. Any candidate that matches a photon conversion reconstructed in the [Inner Detector](#) is flagged. Electron and photon candidates are separated by requiring the electrons to have an associated track while having no associated conversion. Photons are defined as having no matched tracks or being matched to a reconstructed conversion. [[ATL08b](#), p. 326]

For the 8 TeV dataset, the electron reconstruction algorithm has been modified. The main goal was to improve reconstruction efficiency for electrons that undergo significant energy loss in the detector. This is achieved with an electron recovery procedure executed around each electromagnetic energy cluster passing very loose shower shape requirements. Furthermore, the track-to-cluster

matching procedure was improved to favour the primary electron track in case of cascades due to *bremsstrahlung* [ATL14f, p. 5]. The reconstruction efficiencies are discussed in section 4.5.2.1 in chapter 4.

The electron reconstruction and identification efficiencies are measured using a *tag-and-probe* method in $Z \rightarrow e^+e^-$ samples. Section 4.5.2 in chapter 4 gives the full discussion these efficiencies. The lack of special treatment for *bremsstrahlung* effects in the electron reconstruction method used for 2010 and 2011 dataset results in inefficiencies of the electron trajectory reconstruction with strong dependence on the electron *pseudorapidity*. The radiative losses (and the resulting change in the track curvature) are approximated as a weighted sum of Gaussian function using the *Gaussian Sum Filter algorithm* (GSF) which performs a refit of the track. Electrons reconstructed this way are referred to as GSF electrons. This reconstruction approach is not used in this thesis, see [ATL12c] for more details.

3.3.4.1 Electron energy scale and resolution

The *Electromagnetic Calorimeter* energy scale and resolution was derived from $Z \rightarrow e^+e^-$ and $J/\psi \rightarrow e^+e^-$ events using *tag-and-probe* for both central and forward regions. Low- E_T electron are produced from J/ψ , high- E_T isolated electron come from the Z decay. Electrons are required to be within the geometric acceptance of the calorimeter $|\eta| < 2.47$ in the *barrel*, excluding the transition region $1.37 < |\eta| < 1.52$, and $2.5 < |\eta| < 4.9$ for the *end-caps*. The energy scale in a given region i is parametrised by:

$$E_{\text{meas}} = E_{\text{true}}(1 + \alpha_i) \quad (3.7)$$

where E_{true} is the true electron energy, E_{meas} is the energy measured by the calorimeter and α_i is the residual miscalibration. The α energy-scale correction factors are determined by minimizing the negative log-likelihood quantifying the compatibility of an event with the Z line shape. [ATL11b, p. 8] The resulting correction is produced separately in different bins of η . The correction validity range is $10 < p_T < 1000$ GeV up to $|\eta| < 4.9$.

The fractional electron energy resolution in the calorimeter is parametrised as

$$\frac{\sigma_E}{E} = \frac{a(\eta)}{\sqrt{E}} \oplus \frac{b(\eta)}{E} \oplus c(\eta) \quad (3.8)$$

where $a(\eta)$ is the sampling term, $b(\eta)$ is the noise term and c is the constant term. All parameters are η -dependent, the sampling term is dominant across the full *pseudorapidity* range but is well described, within a 10% uncertainty, by the MC simulation. The noise term is significant only at low energies but its contribution cancels out, since the noise description is directly plugged into the simulation from data. The relevant contribution to resolution mismodelling is attributed to the constant term $c(\eta)$ which corresponds to the experimental resolution of the detector. The resolutions are derived from fits of the invariant mass distributions using a Breit-Wigner convolved with CB. Smearing the simulated energy reproduces reasonably the invariant mass distribution in $J/\psi \rightarrow e^+e^-$ and $Z \rightarrow e^+e^-$ events, see fig. 3.26 [ATL14d] [ATL11b, pp. 12–13]

Different source of systematic uncertainties are included in the correction, accounting for energy deposited in extra material, the pre-sampler detector energy scale, calorimeter electronic calibration, cross-talk and *pile-up* effects. The dominant uncertainties are the ones associated to the uncertainty

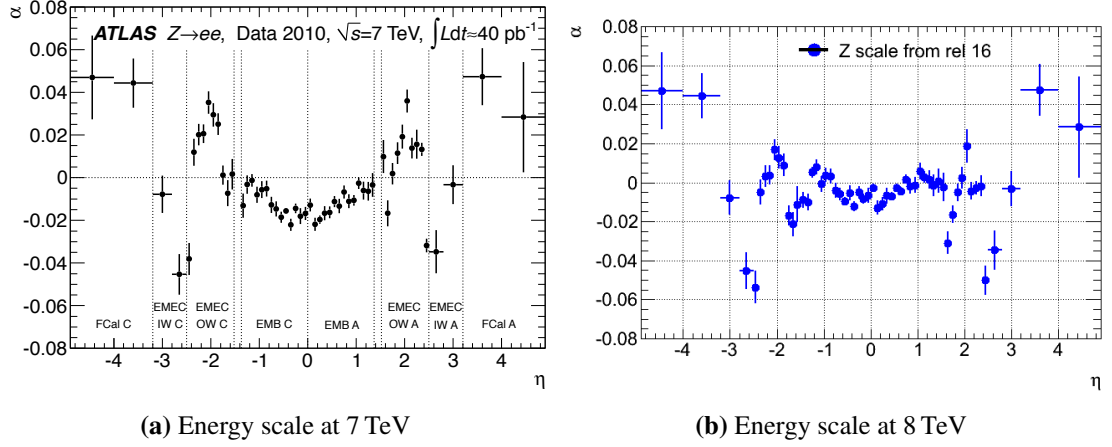


Figure 3.25: Electron energy scale correction factor α derived from fits of $Z \rightarrow e^+e^-$ shown as a function of pseudorapidity for $\sqrt{s} = 7$ TeV (left) and 8 TeV (right). The shown uncertainties are statistical only. The boundaries of different detector sections are indicated by dotted lines in the left figure. Figures from [ATL11b, p. 10] [ATL14d].

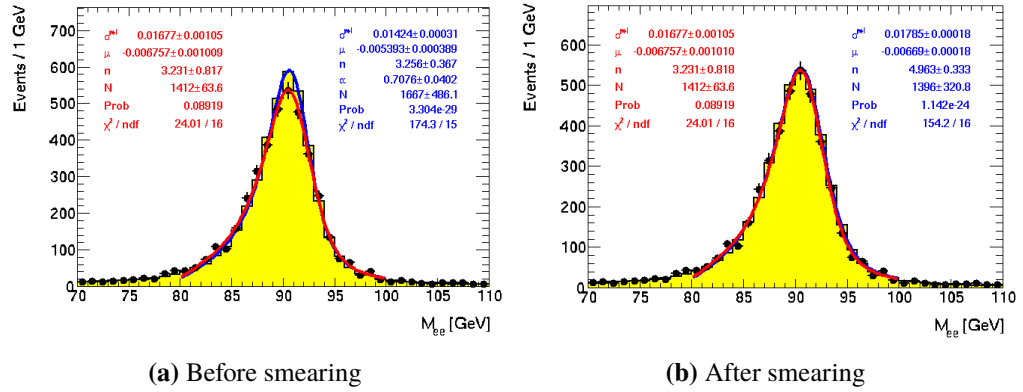


Figure 3.26: Electron smearing calibration for 7 TeV analyses (Release 16) derived from the fit to the Z invariant mass. Figures from [ATL14d] (sic.).

on the knowledge of additional material in front of the calorimeter and on the pre-sampler energy scale. The overall systematic on the electron energy scale varies from 0.30–1.60 % at 7 TeV. For forward electrons, the uncertainties grow to 2–3 %. Pseudorapidity and E_T dependence shown in [ATL13f].

3.3.4.2 Electron identification

After reconstruction, procedural electron identification gives a clear discrimination between real electrons and all possible backgrounds. The standard electron identification for isolated high- p_T electrons is based on cuts on the electromagnetic shower shapes, the information from the reconstructed track, transition radiation and track-to-cluster matching. [ATL13f]. The operating points as defined [ATL08b, p. 327] have been largely modified or discontinued. The 2012 menu for 8 TeV and high pile-up has been re-optimized to use variables that are more pile-up robust. We provide a comprehensive list of the major quality criteria, the full implementation details can be found in [ATLf]:

- LOOSE++ level introduces cuts on shower shape in the first and middle layers of the ECAL

and cuts on longitudinal hadronic leakage for both $\sqrt{s} = 7$ TeV and 8 TeV. It further requires track quality hits in the **Pixel** and the **SCT**: more than one pixel hits or a pixel outlier and more than 7 silicon hits or outliers in total. The track-to-cluster matching criteria are also very loose: $|\Delta\eta| < 0.015$. The **LOOSE++** efficiency is 95 % estimated from $Z \rightarrow e^+e^-$ **tag-and-probe** studies. For $\sqrt{s} = 8$ TeV run conditions dataset, the shower shape cuts were loosened to recover efficiency at high **pile-up**, this reduced the rejection of the **LOOSE++** operating point by 20%.

- **MEDIUM++** menu includes all **LOOSE++** cuts. The shower shape cuts are tightened as well as the track-cluster matching $|\Delta\eta| < 0.005$ which now also includes a cut on $d_0 < 5$ mm. Track quality requirements are also stricter, adding a requirement of at least one hit or outlier in the **b-layer** for $|\eta| < 2.01$ and stricter pixel hit requirements. For 2012, the shower shape cuts were again loosened and track quality cuts were changed as well. The rejection with respect to 7 TeV dataset has dropped and is η dependent. Efficiency of the **MEDIUM++** operating is around ≈ 85 % estimated from $Z \rightarrow e^+e^-$ with a small dependence on **mean number of interactions per bunch crossing**.
- **TIGHT++** has the same or tighter cuts with respect to **MEDIUM++** operating point. The track quality requirement are stricter ($d_0 < 1$ mm) and new cuts on cluster-track energy-momentum ratio E/p , $\Delta\phi$ and photon conversions are introduced. For 8 TeV dataset the **b-layer** requirements are extended over the full **pseudorapidity** range. The rejection is 10–15 % worse with respect to 2011. **TIGHT++** efficiency is ≈ 78 %.

3.3.4.3 Electron likelihood identification

The cut-based particle identification can be improved by implementing a multivariate analysis technique (MVA) on a multitude of input parameters. We construct a likelihood function that makes use of signal and background discriminating variables and calculate an overall probability that a given event or object is signal or background. These probabilities are combined into a discriminant:

$$\frac{\mathfrak{L}_{\text{sig}}}{\mathfrak{L}_{\text{sig}} + \mathfrak{L}_{\text{bkg}}} \quad \text{where} \quad \mathfrak{L}_{\text{sig}}(\mathbf{x}) = \prod_{i=1}^n P_{i,\text{sig}}(x_i) \quad (3.9)$$

and depending on the cut value we get different operating points with specific signal efficiency and background rejection. All input variables are represented by a vector \mathbf{x} and $P_{i,\text{sig}}(x_i)$ is the value of the signal probability density function of the i -th variable evaluated at x_i . The same is defined for backgrounds.

The discriminant offers five new operating points with different background rejection: **VERY LOOSE**, **LOOSE**, **MEDIUM**, **TIGHT** and **VERY TIGHT**. Compared to the 2012 cut-based menus, the likelihood identification has improved rejection of light-flavour jets and photon conversions as shown in the supporting note [Ali+13, p. 28]. The analysis at 8 TeV presented in this thesis uses likelihood identification for precisely this reason. The final reconstruction and identification efficiencies at 8 TeV are shown in [fig. 4.33](#).

3.3.4.4 Electron isolation correction

Similarly to muons (see [section 3.3.3.3](#)), electron isolation cuts are implemented in addition to the identification criteria in order to further reject fake electrons produced in hadron decays. Since various analyses have different needs, these cuts are not introduced on the reconstruction level as object quality flags but are defined by analysis groups themselves. Again, we define two kinds of isolation using a cone ΔR around the object:

- Calorimeter based isolation: $\sum_{\Delta R < N} E_T^{\text{corr}}(i)/p_T^{\text{corr}}(\mu)$, where E_T is the total transverse energy deposited in the calorimeter cells in a cone of ΔR around the electron. A rectangle of electromagnetic calorimeter cells (corresponding to $\Delta\eta \times \Delta\phi = 5 \times 7$ cells in the middle layer) centred on the e_{gamma} candidate is removed in order to subtract the e_{gamma} energy itself.

In the nominal approach, all cells from the [ECAL](#) and [HCAL](#) are used except the crack scintillators (in the TileGap3 layer) and no noise suppression is applied. These are referred to as “standard `etcone`” variables. The [pile-up](#) conditions in 2012 required a different strategy because of the increase in calorimeter noise. The final isolation variable is built by summing the transverse energy of [topo-clusters](#) (see electron topological clustering algorithm described above) with positive energy inside the isolation cone. [Figure 3.27](#) shows the difference between the cell and topological cluster approach ([topo-clusters](#) shown in orange). For more detailed discussion on the recommended variables see [\[ATL14e\]](#) and [\[LdV12\]](#).

- Track based isolation: $\sum_{\Delta R < N} p_T(i)/p_T^{\text{corr}}(\mu)$, where the sum extends over all charged particle tracks within a cone excluding the track of the electron itself. To make this kind of isolation energy [pile-up](#) robust, tracking quality cuts (at least 4 silicon hits) and impact parameter cuts are applied to ensure the track originated in the [PV](#). [\[ATL13f\]](#)

From the description above, it is obvious that are two main issues that affect electron isolation:

Leakage: The central core of the isolation cone may not fully cover the electron or photon energy deposit in the calorimeter. This in effect means that some this energy will leak outside and cause the isolation energy to grow as a function of electron/photon E_T . This is obvious from the [fig. 3.27](#), where a fraction of the energy leaks outside the boundary rectangle.

The “leakage correction” is determined in bins of [pseudorapidity](#) and p_T for simulated electrons and photons. For each given [pseudorapidity](#) bin out of 10, the distribution is fitted with [Crystal Ball](#) function $f(x; \alpha, \beta, \mu, \sigma)$ in 48 bins of p_T from 20 GeV to 500 GeV (i.e., bin width is 10 GeV). An example of the fit for $250 \leq p_T < 260$ GeV and $0.8 \leq |\eta| < 1.15$ is shown in [fig. 3.29](#). The evolution of the [Crystal Ball](#) mean μ in each p_T bin is then fitted with a linear function:

$$-c_{p_T} = ap_T + b \text{ and the correction is applied as } \frac{\text{EtconeXX}}{\text{topoEtconeXX}} + c_{p_T}. \quad (3.10)$$

Unlike muons, the fit is linear for the sake of simplicity, however in some cases quadratic correction could perhaps give a better approximation in future implementations. Further discussion of the fit in [\[LdV12\]](#). No corrections are determined in the transition regions

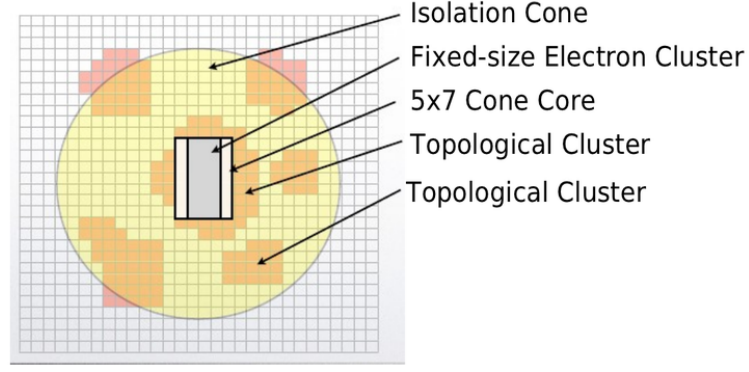


Figure 3.27: Illustration of isolation computation. The grid represents the electromagnetic calorimeter middle-cell granularity. The e_{γ} candidate energy is mostly contained in the central white rectangle which has a standardized area $\Delta\eta \times \Delta\phi = 5 \times 7$. A yellow cone of size $\Delta R = 0.4$ is drawn around the candidate. The Et_{coneXX} variables (with no noise suppression) use all cells within this, while in the $topoEt_{coneXX}$ variables (with a topological noise suppression) use cells belonging to *topo-clusters* shown as orange areas. Figure from [ATL14e] or [LdV12].

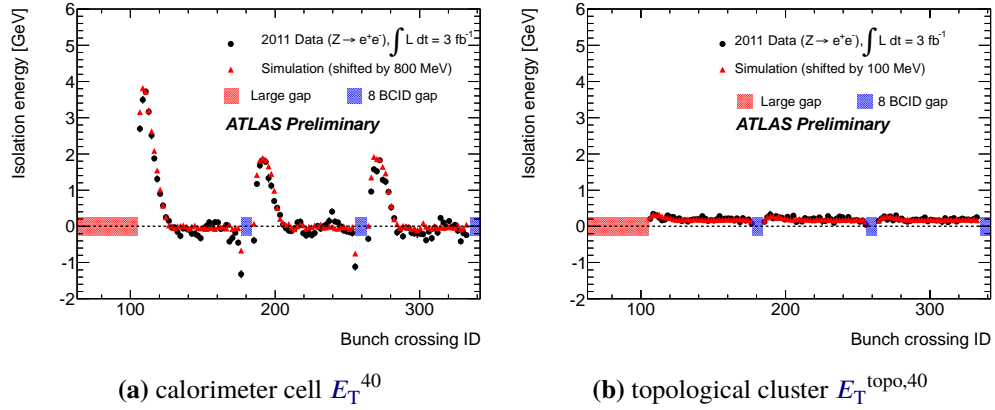


Figure 3.28: Evolution of corrected calorimeter isolation *Crystal Ball function* (CB) μ_{CB} for electromagnetic and hadronic calorimeter cells E_T^{40} (left) and for topological cluster transverse energies $E_T^{topo,40}$ (right) as a function of the bunch train position (BCID). This clearly shows that the isolation energy based on *topo-clusters* (right) is insensitive to *pile-up* since the mean value is constant with respect to the proton bunch train position. This robustness comes from consistently using *topo-clusters* for both raw isolation and ambient energy density corrections. Only the first three sub-trains of the first train are shown. The MC BCID have been shifted by 104 to match the data configuration. Figures from [ATLd] [LdV12, p. 9].

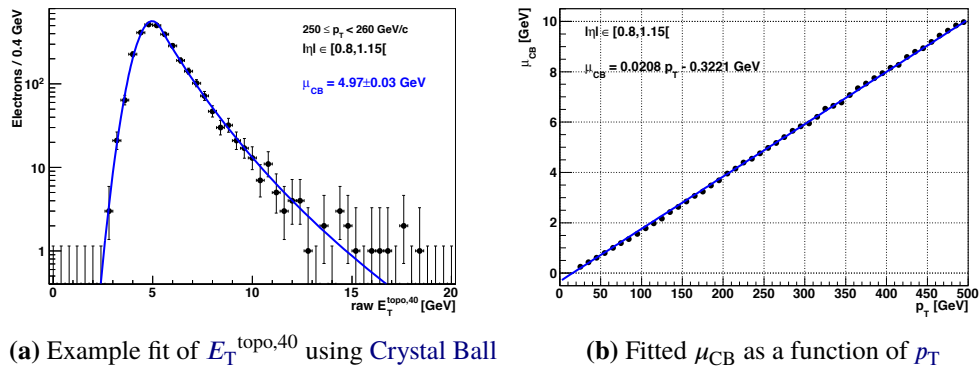


Figure 3.29: The two figures show the implementation of the isolation correction. Figure 3.29a show the distribution of the raw isolation energy $E_T^{topo,40}$ for simulated electrons in a given *pseudorapidity* and p_T bins. The right plot 3.29b shows the evolution of the raw $E_T^{topo,40}$ *Crystal Ball* mean as a function of p_T . The result of a linear fit is also given. The given leakage correction to be applied on an electron of a specific p_T is simply the opposite of this relation. Figure from [LdV12].

($|\eta| \in [1.37, 1.52]$) and at the edge of the **end-caps** ($|\eta| \in [2.37, 2.47]$). The current release for 2012 dataset (Rel 17.2) recalculates the leakage correction for both electrons and photons and cover a p_T range from 7–3000 GeV [ATL12a].

Pile-up: The amount of activity in the current event (both from “underlying events” and “in-time pileup”) as well as previous events (“out-of-time pileup”) contributes to the deposited energy measured in the isolation cone. One would expect that a parametrized correction on the isolation against the number of primary **vertices** would make isolation independent on N_{PV} on average. However, the EGAMMA performance group has shown that this discriminant is not optimal, since N_{PV} contains no information about the local activity in the cone around the object or the signal-to-noise ration of the given event. It also does not address “out-of-time pileup” at all.

Instead, the electron isolation is corrected on an event-by-event basis using ambient energy density (ED) normalized to the area of arbitrary cone sizes (20, 30, 40). The algorithm uses the jet clustering algorithm k_t with p_T threshold lowered to 0 in order to reconstruct positive topological clusters. We then calculate the median of the energy distribution over the jet area $p_T^{\text{jet}}/A^{\text{jet}}$ in broad **pseudorapidity** bins (two bins for 2011) to build the energy density. The correction is then given in the “granularity units” for the area of electron cluster:

$$c = -\rho_{UE} \cdot (\pi R^2 - 5 \times 7 \times 0.025 \times \pi/128) \quad (3.11)$$

Because this method uses the calorimeter energy of the current event it intrinsically removes the underlying event in addition to pileup. [ATL12a] The **pile-up** robustness of topological clusters is obvious from fig. 3.28 where the effect of “in-time” and “out-of-time” pileup is nearly removed thanks to the ED correction. It should be noted that the topological cluster variable was not available until 2012 data taking.

The package `egammaAnalysisUtils-00-04-55` integrates several tools that are used for correcting these effects. The recommended corrections for out-of-core signal energy leakage and ambient energy density pileup corrections are applied using the `GetPtEDCorrectedTopoIsolation` method of the `CaloIsolationCorrections` tool. Detailed information on different implementations of isolation and the corrections are provided in [ATL14e] [ATL12a] [LdV12].

3.3.5 Jet reconstruction

In **high-energy physics**, the term *jet* is synonymous with a collimated spray of energetic hadrons produced from the collision. Jets (or lack thereof) are a key ingredient for many physics analyses, especially on the **LHC** where jet energy measurements are the dominant source of systematic uncertainties.

In **ATLAS**, jets are measured as groups of topologically-related energy deposits in the calorimeters (*calorimeter jets*) associated to tracks of charged particles measured in the **ID** (*track jets*). Jet reconstruction algorithms used in **ATLAS** implement some sort of sequential recombination to build jets. The k_T [Ell93], Cambridge/Aachen [Dok+97] [WW99] and **anti- k_t** [CSS08] algorithms belong

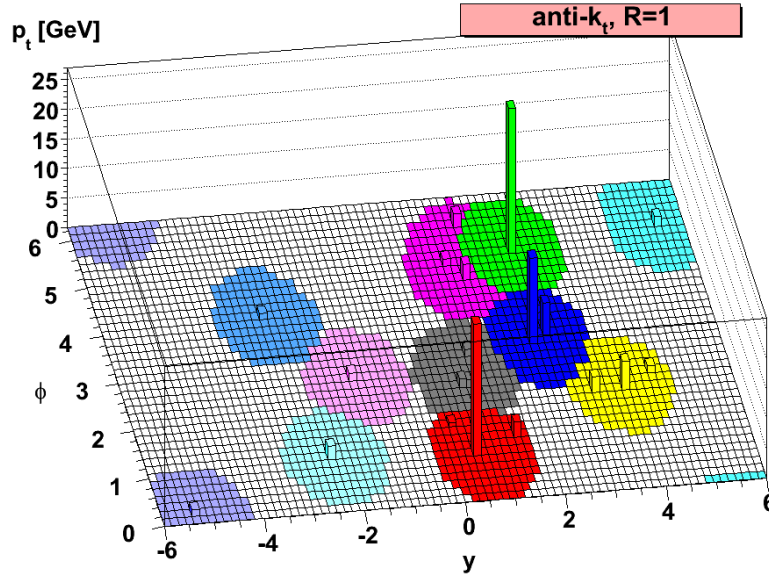


Figure 3.30: Reconstruction using the $\text{anti-}k_t$ algorithm. A sample parton-level event generated with [Herwig](#), together with many random soft particles clustered with $\text{anti-}k_t$ algorithm at $R = 1$. The figure illustrates the active areas resulting in hard jets. Figure from [CSS08, p. 4].

into this group. Their performance, sensitivity and optimization is a subject of high importance and considerable debate. In this thesis we are going to focus solely on jets reconstructed with $\text{anti-}k_t$ algorithm with distance parameter of $R = 0.4$ (*AntiKt4EM*, *AntiKt4LC*, where EM/LC refers to the energy scale calibration, see [section 3.3.5.2](#)), as this is relevant to the analysis presented in [chapter 4](#). For detailed description of large- R jets and different clustering algorithms see [ATL12d], [ATL13b, p. 1]

The $\text{anti-}k_t$ algorithm starts from the energy deposits of electromagnetic and hadronic showers in the calorimeters. The jets discussed in this thesis were reconstructed from the [topo-clusters](#) with a positive energy. [Topo-clusters](#) are build from topologically connected calorimeter cells that contain activity above a certain noise level, we have already discussed this in [section 3.3.4](#). We introduce distance d_{ij} between jet entities i and j defined as:

$$d_{ij} = \min(k_{Ti}^{2p}, k_{Tj}^{2p}) \frac{\Delta_{ij}^2}{R^2} \quad (3.12)$$

where $\Delta_{ij}^2 = (y_i - y_j)^2 + (\phi_i - \phi_j)^2$ and k_T , y_i and ϕ_i are the [transverse momentum](#), [rapidity](#) and azimuthal angle of entity i . R is the radius parameter, which for the algorithms used in this thesis is fixed to $R = 0.4$. Parameter p is the relative power, different algorithms correspond to different values of p . The k_T algorithm corresponds to $p = 1$, $\text{anti-}k_t$ to $p = -1$ and $p = 0$ corresponds to Cambridge/Aachen. The clustering algorithm then proceeds by sorting through the distances d_{ij} between entities in R . If the minimum distance coincides with the distance between entity and the beam:

$$d_{iB} = k_{Ti}^{2p} \quad (3.13)$$

we call the entity a jet. [CSS08, pp. 1–2]

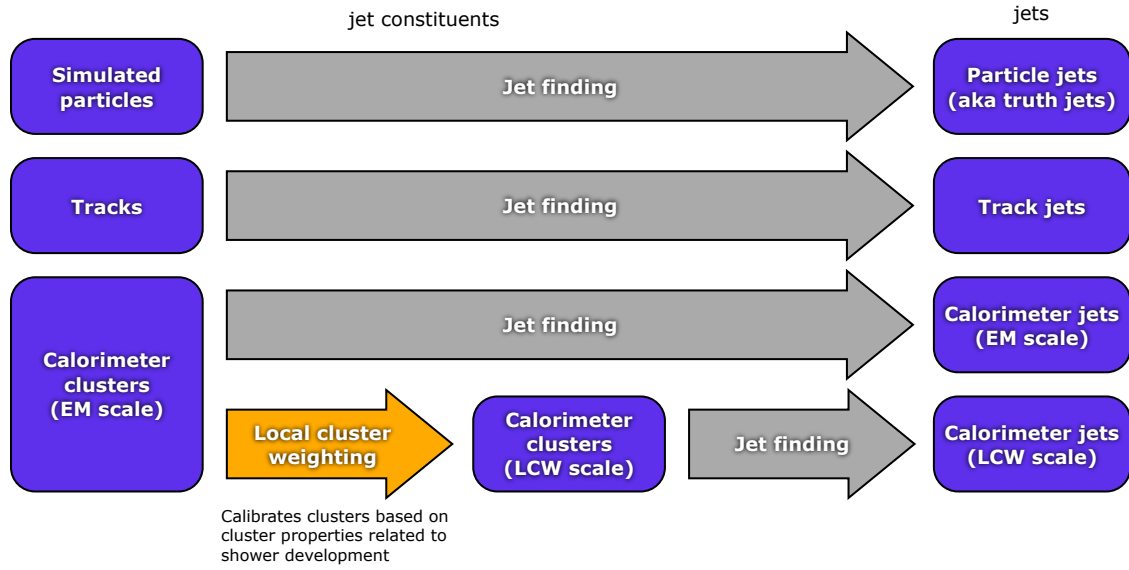


Figure 3.31: Overview of the ATLAS jet reconstruction. After the jet finding, the jet four momentum is defined as the four momentum sum of its constituents. Figure from [ATL13b, p. 3].

3.3.5.1 Jet calibration

The calorimeter provides only a partial measurement of the total energy deposited by hadrons mainly for the following reasons [ATL13a, p. 5]:

- ▶ Uninstrumented or inactive regions (dead material) of the detector measure no energy,
- ▶ Leakage of energy outside the calorimeters (punch-through),
- ▶ Incomplete reconstruction of the jet cone, where not all particles inside the jet are included in the reconstructed jet,
- ▶ Calorimeter noise thresholds and particle reconstruction inefficiency results in signal losses.

The corrections are estimated using a combination of two techniques. The *in-situ* techniques use the transverse momentum balance between a jet and a reference object (e.g. a photon or a Z boson) $\langle p_T^{\text{jet}}/p_T^{\text{ref}} \rangle$. In a large dataset the jet energy calibration can be determined from the ratio between jet energy measured with the ATLAS calorimeter and the true energy corresponding to simulated jets after full ATLAS simulation (see section 3.2.2). These reference jets, normally referred to as *truth jets*, are produced in MC simulations from simulated stable particles using the same jet reconstruction algorithm. [ATL13b, pp. 3–5]

The calibration procedure outlined in fig. 3.32. [ATL13a, p. 5] consists of four steps:

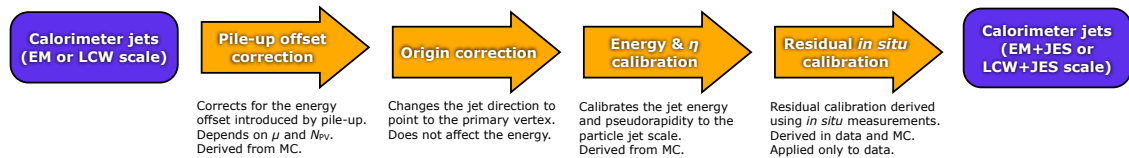


Figure 3.32: Overview of the ATLAS jet calibration scheme. The pile-up, absolute JES and the residual *in-situ* corrections calibrate the scale of the jet, while the origin and the η corrections affect the direction of the jet. Figure from [ATL13b, p. 3].

Pile-up offset correction subtracts the average additional energy due to multiple pp interactions from the energy measured in the calorimeters. The effects of **pile-up** on the *jet energy scale* (JES) are caused by both additional proton collisions in a recorded event (in-time **pile-up** approximated by N_{PV}) and by past and future collisions influencing the measurement of the energy deposited in the current **BC** (out-of-time **pile-up** approximated by $\langle\mu\rangle$) [ATL13b, p. 4]:

$$E_{\text{T}}^{\text{corrected}} = E_{\text{T}}^{\text{uncorrected}} - \mathcal{S}(\eta, N_{\text{PV}}, \tau_{\text{BC}}) \quad (3.14)$$

where $\mathcal{S}(\eta, N_{\text{PV}}, \tau_{\text{BC}})$ is the jet energy offset (shift) as a function of **pseudorapidity**, number of **PV** and bunch spacing. The correction constants are obtained by computing the difference between the statistical average of calorimeter tower **transverse energy** at $N_{\text{PV}} = 1, 2 \dots N$ and the average energy for events where $N_{\text{PV}}^{\text{ref}} = 1$:

$$\mathcal{S}_{\text{tower}}(\eta, N_{\text{PV}}) = \langle E_{\text{T}}^{\text{tower}}(\eta, N_{\text{PV}}) \rangle - \langle E_{\text{T}}^{\text{tower}}(\eta, N_{\text{PV}}^{\text{ref}}) \rangle \quad (3.15)$$

The values are computed for all **primary vertex** multiplicities separately. It has been shown in jet performance studies that applying the **pile-up** offset correction is critical for a successful calibration of jets the high occupancy conditions in 2012 data taking. [SBS14, p. 5]

Origin correction compensates for the displacement of the **primary vertex**. The jet direction is recomputed such that the jet originates from the hard-scattering vertex instead of the geometrical centre of the detector. Does not affect jet energy. [ATL13a, p. 12]

Jet energy and direction correction applies constants derived from the comparison of the kinematic observables of reconstructed jets and those from truth jets in **MC** simulation. We will discuss these correction in more detail in the following section.

Residual in-situ calibration accounts for remaining discrepancies by balancing jet p_{T} with respect to reference jet measured in data and **MC**. The correction is derived from the double ratio:

$$\frac{\langle p_{\text{T}}^{\text{jet}}/p_{\text{T}}^{\text{ref}} \rangle_{\text{data}}}{\langle p_{\text{T}}^{\text{jet}}/p_{\text{T}}^{\text{ref}} \rangle_{\text{MC}}} \quad (3.16)$$

derived from a variety of in-situ methods and applied to data. The correction also accounts for p_{T} and **pseudorapidity** dependence by exploiting the p_{T} balance in simulated dijet events using jets measured in central and forward regions of the detector (dijet η -intercalibration), see [ATL13b, p. 5].

3.3.5.2 Jet energy scale and resolution

Hadronic jets reconstructed in the calorimeter with energy $E_{\text{meas}}^{\text{jet}}$ do not correspond to the energy of final state at the particle level. The goal of jet energy calibration is to correctly relate the calorimeter response to the true jet energy independent of **pile-up**. The jet response is defined simply as:

$$R(\eta) = \frac{E_{\text{jet}}^{\text{truth}}(\eta)}{E_{\text{jet}}^{\text{reco}}(\eta)}. \quad (3.17)$$

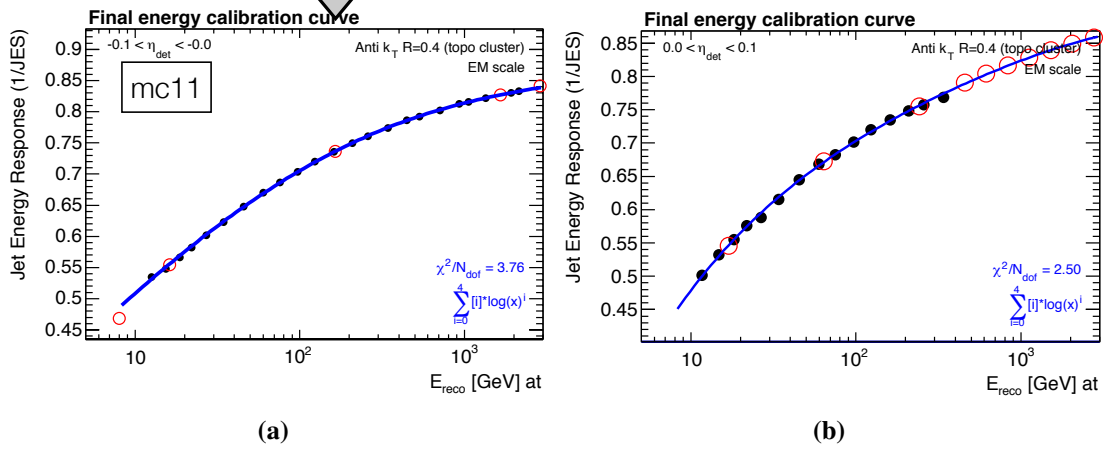


Figure 3.33: Comparison of jet response between 2011 and 2012. The 2012 method was modified to account for of [pile-up](#) on the measurement of low-energy jets. Figure from [SBS14, pp. 3,11] (sic.).

The factor is derived as a function of reconstructed jet η and p_T using MC truth jets. In the simplest calibration scheme (EM+JES or [AntiKt4EM](#) in the case of our analysis) the jet calibration is derived as a simple correction relating the [Electromagnetic Calorimeter](#) response to the true jet energy:

$$E_{\text{calib}}^{\text{jet}} = E_{\text{meas}}^{\text{jet}} / f_{\text{calib}} \left(E_{\text{meas}}^{\text{jet}} \right) \quad \text{where} \quad E_{\text{meas}}^{\text{jet}} = E_{\text{EM}}^{\text{jet}} - C(N_{\text{PV}}) \quad (3.18)$$

The $E_{\text{EM}}^{\text{jet}}$ is the calorimeter energy measured at the electromagnetic scale, $E_{\text{calib}}^{\text{jet}}$ is the calibrated jet energy, f_{calib} is the calibration function evaluated in small [pseudorapidity](#) regions and $C(N_{\text{PV}})$ is the correction for additional energy coming from multiple pp interactions. [ATL13a, p. 6]

The [local cluster weighting \(LCW\)](#) is an alternative calibration method that applies corrections to calorimeter [topo-clusters](#) independent of any jet context. The corrections are based on the difference in response from electromagnetic and hadronic [topo-clusters](#) using the following observables: [ATL13a, p. 61]:

1. [Topo-cluster](#) cell energy density.
2. Cluster isolation characterising the activity around the cluster. The variable is defined as the ratio of the number of un-clustered cells neighbouring the given [topo-cluster](#).
3. Longitudinal depth of the cluster barycentre in the calorimeter. It is defined as the distance along the shower axis to the shower centre.
4. Energy fraction deposited in different calorimeter layers.

The energy corrections are derived from single charged and neutral pion MC simulations. [ATL13a, p. 6] The hadronic energy correction weights are calculated from the true energy deposits given by MC and multiplied by a weight [ATL13a, p. 61]

$$w_{\text{HAD}} \cdot p + w_{\text{EM}} \cdot (1 - p) \quad (3.19)$$

where p is the probability of the [topo-cluster](#) to be determined as hadronic. This weighting takes into account the different nature of hadronic and electromagnetic showers. The comparison of the EM scale and [LCW](#) scale correction is shown in [fig. 3.34](#), the correction for [LCW](#) scale are clearly much smaller.

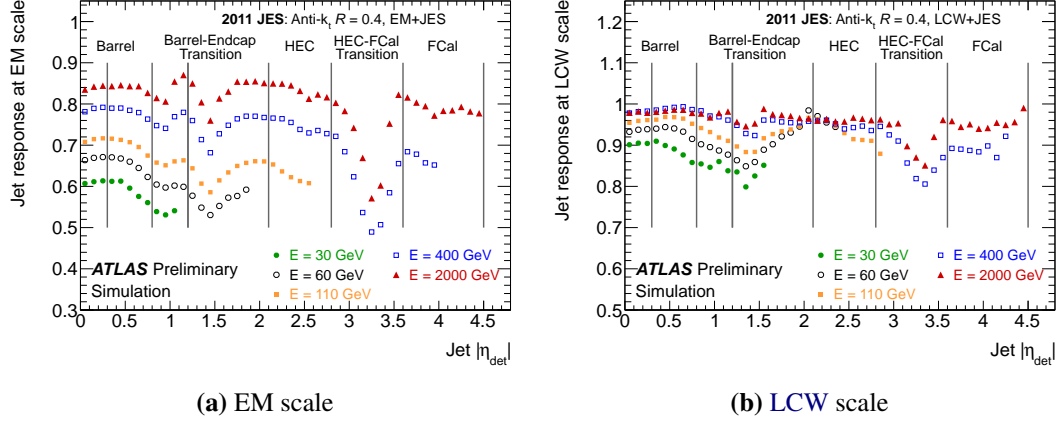


Figure 3.34: Average energy of jets formed from topological clusters calibrated at the EM (left) or the LCW scale (right) with respect to the truth jet energy in MC simulation ($E_{\text{EM}}^{\text{jet}}/E_{\text{truth}}^{\text{jet}}$) or ($E_{\text{LCW}}^{\text{jet}}/E_{\text{truth}}^{\text{jet}}$) as a function of the jet $|\eta|$ before applying the correction for the event vertex shown separately for various truth jet energies. Also indicated are the different calorimeter regions. The inverse of the response shown in each bin is equal to the average jet energy scale correction. This result is based on PYTHIA inclusive jet sample. Figure from [ATL13b].

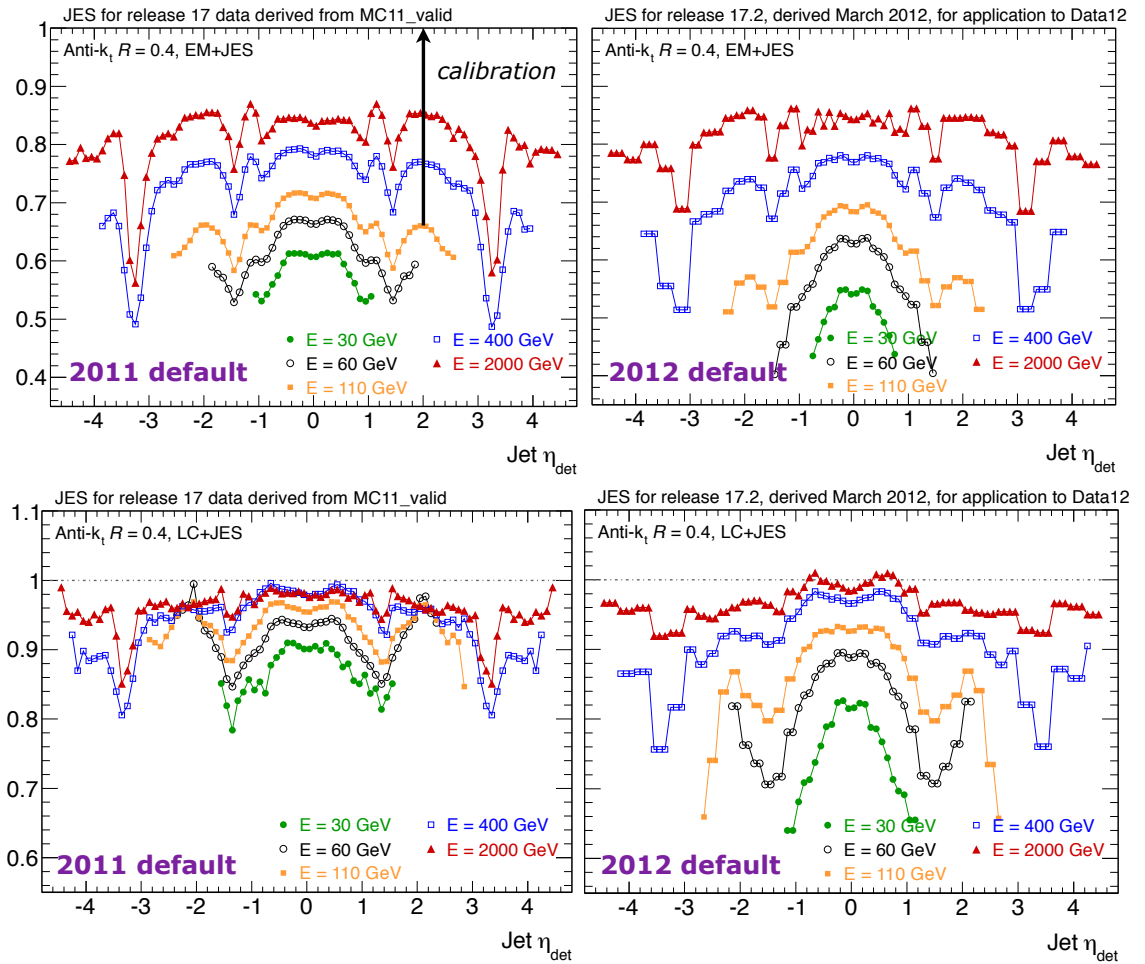


Figure 3.35: Comparison of jet energy scale as a function of pseudorapidity in 2011 (left) and 2012 (right) in both row. The top row shows the default EM scale, the bottom row shows the LCW scale. Although the LCW calibration shows a significant improvement with respect to the EM scale in 2011, in 2012 the correction gets significantly large due to the full pile-up offset removal. Figures from [LG, pp. 6–7] (sic.).

There are two main types of **JES** uncertainty: uncertainties that affect reference p_T of recoil and uncertainties that come from **MC** modeling and kinematic cuts. The **JES** uncertainties are contained using a full treatment of bin-to-bin correlations for systematic uncertainties. This is achieved by splitting of the nuisance parameters coming from the various in-situ techniques. The full set of baseline uncertainties contains over 60 nuisance parameters, but was not yet finalized at the time of writing this thesis. For the analysis presented in [chapter 4](#), we use a reduced set of 14 nuisance parameters for the $\sqrt{s} = 8$ TeV analysis on the 2012. The reduced set is divided into [\[ATL14i\]](#):

- ▶ 6 parameters from the reduction of the **in-situ analyses** nuisance parameters (originally ≈ 50) corresponding to **Z** + jet, **γ** + jet and multi-jet balance (labelled `Effective_NP*` in the implementation).
- ▶ 2 parameters from **η -intercalibration (modelling and statistics)**.
- ▶ 1 parameter from the behaviour of high- p_T jets in propagation of single hadron uncertainties to jet.
- ▶ 1 nuisance parameter from **MC** non-closure relative to MC12a. This term needs to be applied if the **MC** samples used in the analysis are not MC12a or MC12b, as these were the baseline samples with which the calibrations were derived.
- ▶ 4 nuisance parameters from **pile-up** (3 of which are $\langle\mu\rangle$ or N_{PV} dependent).

Additional nuisance parameters related to flavour and topology uncertainties:

- ▶ 1 nuisance parameter from the sample's flavour composition.
- ▶ 1 nuisance parameter from the sample's flavour response uncertainty.
- ▶ 1 nuisance parameter from b-jets. This has to be applied to b-jets only, and it is an alternative to the flavour composition and response uncertainties for those jets.
- ▶ 1 nuisance parameter for punch-through jets.

In case of the 2011 dataset we estimate only the total jet energy scale systematic uncertainty for the 7 TeV analysis, as this was the recommended procedure at the time, since the decorrelated uncertainty estimation was not finalized. It is entirely out of the scope of this thesis to describe each of the in-situ studies in detail, more details are provided in talks and documented code linked in [\[ATL14i\]](#) and [\[ATLg\]](#). All **jet energy scale** systematic uncertainties are propagated through the analysis presented in this thesis. In order to maintain the high degree of uncertainty separation we evaluate the uncertainties using the full information on correlations, see [section 4.8](#).

The 2011 uncertainties for **anti- k_t** ($R = 0.4$) are below 3 % in the range $60 \leq p_T \leq 1000$ GeV and can be reduced below 2.50 % if the **LCW** scale is used. The uncertainty is the largest for low- p_T jets in the forward region, where it amounts to 6 % [\[ATL13b, pp. 24–30\]](#). In 2012, the high **pile-up** environment the uncertainty is estimated in $p_T \in 25, 40, 60, 80, 100$ GeV and $\eta \in 0.0, 0.5, 1.0, 2.0, 3.0, 4.0$ bins. The total uncertainty increased to nearly 5 % (4 %) in the central region at EM (**LCW**) scale. [\[ATLh\]](#) It should be noted here, that the calibration constants are calculated down to 10 GeV at EM (**LCW**) scale, which corresponds to about 20 (15) GeV, and the in-situ measurements only go down to 17 GeV.

An additional uncertainty is estimated by degrading the **jet energy resolution (JER)** in **MC**. The “truth resolution” derives from the width of the distribution of jet response $R(\eta)$ (3.17). The

resolution function is parametrized similarly (3.8) as:

$$\frac{\sigma_E}{E} = \sqrt{\frac{a^2(\eta)}{E} + \frac{b^2(\eta)}{E^2} + c^2(\eta)} \quad (3.20)$$

where a is the Gaussian sampling term, b is the noise term and c is the constant term. [ATL08b] The results of the fit are shown in [Sac+]. To evaluate JER systematics in the analysis, each jet energy is smeared by a random factor pulled from $\mathcal{N}(1, \sigma_{\text{smear}})$ where:

$$\sigma_{\text{smear}} = \sqrt{(\sigma_{\text{truth}} + \Delta_{\text{Data-MC}})^2 - \sigma_{\text{truth}}^2} \quad (3.21)$$

Effectively, a random energy that corresponds to a resolution smearing of 10 % is added to each jet (20 % at LCW +JES at high η). The resulting shift of the ratio is evaluated and added in quadrature to the overall systematic uncertainty. [Sac+]

3.3.5.3 Jet quality

Jets are classified into three categories, the good, the bad and the ugly:

- **Good:** jets to be used in physics analysis
- **Bad:** jets which need to be removed, since they are either from background events or caused by detector effects.
- **Ugly:** Jets in problematic calorimeter regions that are not well measured.

Consequently, good jets are defined simply as those jets which are neither bad, nor ugly. Cleaning of jets is applied to both data and MC and is critical to analyses dependent on E_T . A recommended strategy is to drop the event if a bad high- p_T jet is present.

Bad jets are recognized as jets not associated to real energy deposits in the calorimeters. They arise from various sources, ranging from hardware problems, LHC beam conditions, and cosmic-ray showers. The cleaning is made using a combination of jet variables like energy fraction in the ECAL, maximum energy fraction in one calorimeter layer, measured and predicted shape and calorimeter response etc. The removal cuts are provided at 4 working points (BadLooseMinus, BadLoose, BadMedium, BadTight), unless an analysis uses a trigger based on high- p_T jets and high E_T events, the looser cleaning criteria are sufficient. See [ATLk] [ATL14g] for more details.

3.3.6 Missing transverse energy reconstruction

As we discussed in section 2.5.5, the presence of missing energy indicates the presence of invisible particles (like neutrinos coming from W decay). In our experiment, this missing energy is defined in the transverse plane, where it is useful for physics analyses. The momentum imbalance is calculated from a negative vector sum of the momenta of all reconstructed particles in the pp collision:

$$\vec{E}_T = - \sum_i \vec{p}_T(i) \quad (3.22)$$

The symbol E_T indicates its magnitude. [ATL13d, p. 1] In ATLAS the missing transverse energy is reconstructed from deposits in the calorimeters and muons reconstructed by the Muon Spectrometer

(including low- p_T segment-tagged muons):

$$\cancel{E}_{x(y)} = \cancel{E}_{x(y)}^{\text{calo}} + \cancel{E}_{x(y)}^{\text{MS}} \quad (3.23)$$

Leftover tracks are added to the $\cancel{E}_{x(y)}^{\text{calo}}$ to recover contributions from low- p_T particles not reconstructed by the calorimeter. The calculation of the calorimeter term $\cancel{E}_{x(y)}^{\text{calo}}$ uses reconstructed and calibrated physics objects: electrons, photons, hadronically decaying τ^\pm -leptons, jets and finally muons. The $x(y)$ term is simply a sum of these components:

$$\cancel{E}_{x(y)} = \cancel{E}_{x(y)}^{e^\pm} + \cancel{E}_{x(y)}^\gamma + \cancel{E}_{x(y)}^{\tau^\pm} + \cancel{E}_{x(y)}^{\text{jets}} + \cancel{E}_{x(y)}^{\text{SoftTerm}} + \cancel{E}_{x(y)}^{\mu^\pm, \text{calo}} \quad (3.24)$$

where each term is calculated as a negative sum of the corresponding calibrated reconstructed objects projected onto $x(y)$ directions [ATL12e, p. 4]:

$$\cancel{E}_{x(y)}^{\text{term}} = - \sum_i^{N_{\text{term}}} E_i \sin(\theta_i) \cos(\phi_i), \quad (3.25)$$

This procedure is commonly referred to as the METReFFinal algorithm. The terms for individual objects are defined as [ATL12e, p. 4] [ATL13d, p. 4]:

- ▶ $\cancel{E}_{x(y)}^{e^\pm}, \cancel{E}_{x(y)}^\gamma, \cancel{E}_{x(y)}^{\tau^\pm}$ correspond to objects reconstructed from cells in clusters associated to electrons and photons, all with calibrated $p_T > 10$ GeV. The electrons are calibrated with the standard ATLAS calibration [ATL11b], photons are calibrated at the electromagnetic scale (EM). The τ -jets are calibrated with the LCW and the tau energy scale (TES) correction is applied. Tau leptons are not considered in the missing transverse energy modelling for the analysis presented in this thesis, see [13b] [13a] for more details concerning the treatment of τ leptons.
- ▶ $\cancel{E}_{x(y)}^{\text{jets}}$ is reconstructed from cells and clusters associated to jets with calibrated $p_T > 20$ GeV. The jets are reconstructed using the anti- k_t algorithm with distance parameter $R = 0.4$. Each jet is corrected for the pile-up and is subsequently calibrated with the LCW +JES scheme.
- ▶ $\cancel{E}_{x(y)}^{\text{SoftTerm}}$ is calculated from soft jets plus clusters and tracks not associated with any objects. The clusters are calibrated using the LCW method, overlapping tracks and clusters are removed. In previous implementations, e.g. [ATL12e] for the 2011 dataset, these contributions were calculated separately denoted as $\cancel{E}_{x(y)}^{\text{SoftJets}}$ and $\cancel{E}_{x(y)}^{\text{CellOut}}$.
- ▶ $\cancel{E}_{x(y)}^{\text{MS}}$ is calculated from the momenta of selected muons:

$$\cancel{E}_{x(y)} = - \sum_{\text{muons}} p_{x(y)}^{\mu^\pm}. \quad (3.26)$$

This includes combined muons in the region $|\eta| < 2.5$ to reduce the contributions from fake muons as well as standalone muons reconstructed in the MS ($|\eta| < 2.7$), especially in the $2.5 < |\eta| < 2.7$ range, where the Inner Detector tracks are not available. Any muons which are fake, badly measured or simply not reconstructed can produce a source of fake \cancel{E}_T .

- ▶ $\cancel{E}_{x(y)}^{\mu^\pm, \text{calo}}$ is the contribution originating from energy lost by muons in the calorimeter. For an isolated muon, the term is omitted as the combined measurements by the ID and MS, which

already considers the energy loss in the calorimeter. For non-isolated muons, the energy deposited in the calorimeter cannot be unambiguously assigned to particles within the jet. Instead, the **MS** is used to determine the energy loss and the energy is added back to the calorimeter term. [ATL12e, p. 4]

Finally, the total transverse component is built from the total $x(y)$ terms:

$$\mathcal{E}_T = \sqrt{\mathcal{E}_x^2 + \mathcal{E}_y^2}. \quad (3.27)$$

It is useful to describe \mathcal{E}_T using its magnitude \mathcal{E}_T and the azimuthal angle to preserve information about the x, y components [ATL12e, p. 3]:

$$\phi = \arctan\left(\frac{\mathcal{E}_x}{\mathcal{E}_y}\right) \quad (3.28)$$

3.3.6.1 Missing energy scale and resolution

The \mathcal{E}_T calculated by the `METReffinal` algorithm uses calorimeter energy deposits associated with high- p_T objects such as electrons, photons, muons and jets. The transverse energy of the objects is then used as a replacement for the original cell energy, since the objects have a more accurate calibration than the bare calorimeter cell calibration. The scale and resolution uncertainties on electrons, muons and jets have therefore a direct impact on the \mathcal{E}_T and need to be propagated correctly, see section 4.8.3. Apart from the $\mathcal{E}_{x(y)}^{\text{SoftTerm}}$ which accounts for energy not associated to any objects, no additional treatment is required here. We should emphasize here, that precise measurement of the **missing transverse energy** is fundamental to our analysis.

The uncertainties are studied using the `MISSINGETUTILITY-01-02-04` tool, that handles the specific object uncertainties as well as \mathcal{E}_T soft scale and resolution systematic terms.

3.4 Implementation

The analysis presented in this thesis was implemented in C++ and **ROOT** using the stand-alone approach. The full code was integrated within `ElectroweakBosons` software package [ATLb], which is a C++ framework based on **ROOT**, `RootCore` and `SFrame` (see section 3.2). It has been originally developed by the **CERN** Analysis Team (CAT) as working environment for di-boson analyses. Let us start with discussing the external dependencies in more detail:

SFrame is also a C++ package independent of **Athena**. The main goal of `SFrame` is to provide a general **HEP** stand-alone analysis framework based solely on **ROOT** trees. Given a standard work-flow, an analysis in particle physics is performed in *cycles*, where each cycle corresponds to a new treatment of the dataset. `SFrame` follows this cycle-based philosophy by splitting an analysis in several cycles as indicated in fig. 3.36. Each cycle works with I/O **ROOT** trees and control histograms in user-specified format. The goal and implementation of all analysis cycles is fully in the hands of the user. The cycles are steered using templated XML configuration files where the user provides the meta-data describing the cycle, e.g. integrated

luminosity, the input ROOT trees, output format and any cycle-dependent settings. `SFrame` is currently developed by Attila Krasznahorkay, David Berge and Johannes Haller. [KHB]

SMultiFrame is an `SFrame` extension developed by Massimiliano Bellomo that allow multiple derived classes to be run sequentially inside one `SFrame` cycle. This feature is referred to as *multi-tool functionality* in the documentation [ATLb].

RootCore is a package manager to handle external dependencies like ROOT-based detector performance packages. [ATLJ]

3.4.1 Development goals

One of the main challenges in developing a common framework for user analysis is the constant evolution of physics performance packages and very user-dependent requirements and coding styles. Many of the discrepancies manifested during 2011 analysis at $\sqrt{s} = 7$ TeV. This eventually led me to reimplement the common framework with the following goals:

- ▶ streamline the implementation and class hierarchy, clearly separate the user code for physics objects from `RootCore` tools and data management
- ▶ make the code more robust, improve performance when running with multiple instances,
- ▶ improve code readability, simplify code extensibility for new users,
- ▶ maintain collaboration and support new users with new ideas.

This is something I have intensively worked over the period of 2 years. The code is available as a `ElectroweakBosons-14-00-00` branch of the framework. For the purpose of the analyses presented in this chapter, the $\sqrt{s} = 7$ TeV analysis still used the original `ElectroweakBosons` while the 8 TeV data were analysed using the re-implemented version. As a direct result of my contribution to the development of this framework the following major tasks for the analysis team fell under my responsibility:

- ▶ the production of `Derived Physics Data`,
- ▶ full event selection implemented with all systematic uncertainties,
- ▶ production of `N-tuple` format for unfolding,
- ▶ plotting of all the kinematic and final selection histograms.

Currently, the branch 14-00-00 supports 4 other analyses and more than 10 users in total. Other main developers are Jakub Cuth, Oldřich Kepka and Valerie Lang. The code is available from `ATLAS` SVN and is documented using Doxygen. The original release of `ElectroweakBosons` is also used to date, mainly for legacy analyses on the 2011 dataset. It is maintained by Massimiliano Bellomo.

3.4.1.1 Structure of the code

The framework is organized into a small number of simple `SFrame` packages connected to external performance tools enveloped by `RootCore`. For the purpose of the framework, these `SFrame` packages are referred to as *analysis tools*. The tools relevant for this thesis are:

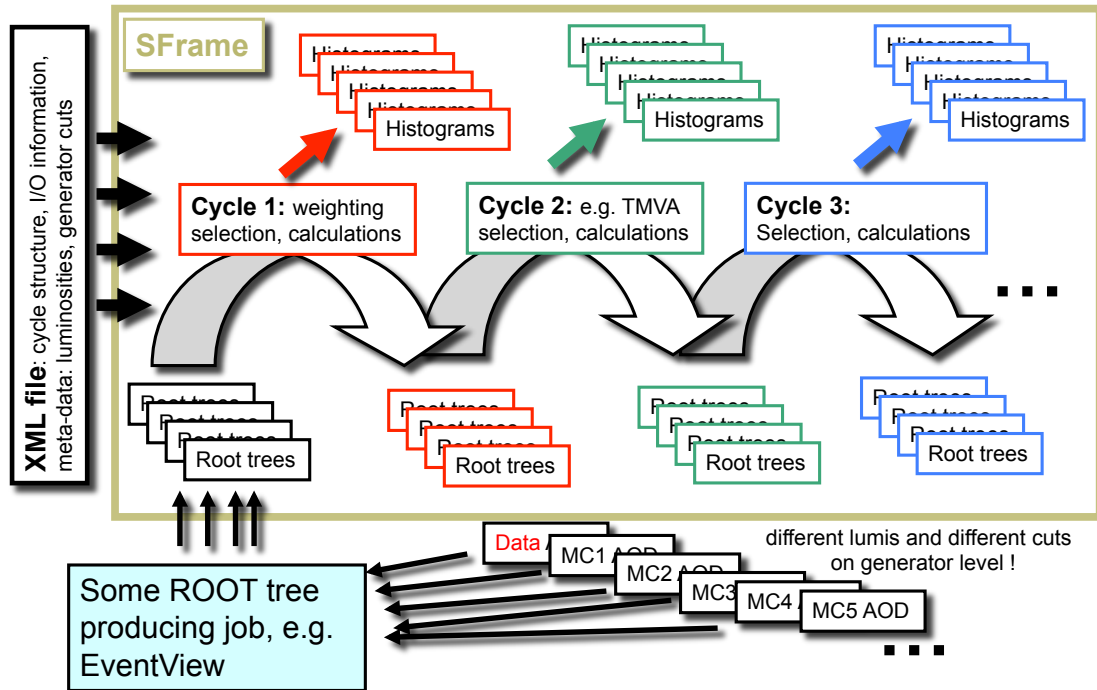


Figure 3.36: *SFrame* flow chart indicating the idea of an *analysis cycle*. The figure shows a generic analysis running in three cycles: first with standard selection, re-weighting and calculations. The output of this cycle is then fed into cycle 2, that uses event-by-event TMVA methods on the pre-selected dataset to extract the desired physics which is fed into cycle 3 to finalize the results. Courtesy of Massimiliano Bellomo.

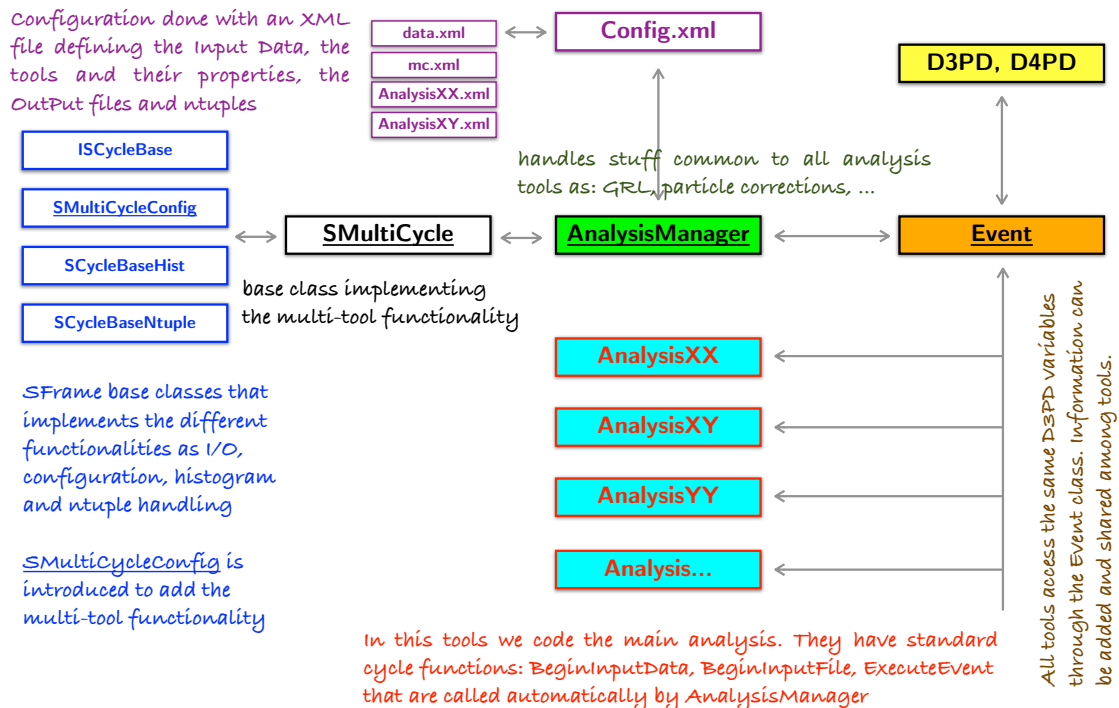


Figure 3.37: Structure of the *ElectroweakBosons* framework. The main analysis cycle *AnalysisManager* sequentially executes a configurable number of analysis tools through *SMultiCycle*. Data access to the *D3PD* branches is provided via *Event* singleton within the event loop. User-provided settings are passed from XML configuration files. Courtesy of Massimiliano Bellomo.

- **AnalysisBase**: the core software package which implements the main analysis cycle **AnalysisManager**. This cycle sequentially executes a configurable number of analysis tools through **SMultiFrame**. It also provides a static instance of **AnalysisConfig** class designed to contain all configurable properties processed from the user-provided XML configuration files.
- **AnalysisToolBase**: the base analysis tool class from which all user analysis tools are derived. Common histogramming, cut-flow and control functions are implemented at this level.
- **AnalysisWW**: houses the WW analysis code including object definitions, event cleaning, reconstruction and fiducial selection, including also **N-tuple** and histogram making.
- **Skimmer**: analysis tool designed for **D3PD** production based on the variables common to all analysis tools (via **EventBase** class, see below).

The class hierarchy is shown in [fig. 3.38](#). [Figure 3.37](#) clearly explains the functions and relationships between the cycle manager, analysis tools and **SFrame**. The **AnalysisBase** class provides all the basic functionalities through dedicated classes:

Event entries are read in an event-loop through class **Event** which provides data access by (re)connecting the variable pointers to the corresponding entry in the **N-tuple**. The class is implemented as a singleton design pattern (static instance).

Listing 3.1: **EventBase.h**

```

14 class EventBase : public TObject
15 {
16 public:

31     UInt_t   RunNumber; ///< Keep this first in the header file as is determines
                        order in the output n-tuples
32     UInt_t   lbn;
33     Float_t   averageIntPerXing;
34     UInt_t   EventNumber;
35     UInt_t   coreFlags;
36     Bool_t   streamDecision_Muons;
37     Bool_t   streamDecision_Egamma;
38     Bool_t   streamDecision_JetTauEtmiss;

```

Analysis objects provide data encapsulation for physics objects (Muon, Electron, Jet) relative to the reconstruction algorithm. Thus, for example, **MuonStaco** encapsulates the relevant **D3PD** variables **mu_staco_pt**, **mu_staco_E** etc. Creating an instance of **Muon** will instantiate the correct algorithm **MuonStaco**, **MuonMuid**, **MuonChain3** based on the settings provided in the user configuration file.

Base classes provide access **D3PD** variables through **Event** for a given reconstruction algorithm specified by the user in the configuration file. Assuming that object **Muon * mu** is defined for index = 0, the key difference lies of course in the convenience in data handling:

Toolboxes handle relevant **RootCore** tools for the given physics object. For example **Muon-**

```

1 double pt = ev->mu_staco_pt->at(0);
2
3 double pt = mu->pt;

```

Toolbox provides access to centrally provided muon performance tools like MuonIsolationCorrection.

Listing 3.2: MuonToolbox.h

```

1260 MuonSmear::SmearingClass          * smearTool;
1261 CorrectCaloIso                    * caloisoTool;
1262 Analysis::AnalysisMuonConfigurableScaleFactors * muSFTool;
1263 MuonIsolationSF                    * isolationTool;
1264 MuonTriggerMatching                * triggerMatchingTool;

```

Stores are templated data and memory management classes designed to handle the storage and retrieval of analysis objects in memory. The implementation follows from the graph in fig. 3.40.

Listing 3.3: Muon.h

```

196 typedef Store<Muon> MuonStore;

```

Listing 3.4: Electron.h

```

221 typedef Store<Electron> ElectronStore;

```

3.4.2 Implementation of analysis objects

The common [ROOT N-tuple](#) does not represent reconstructed physics objects in any object-oriented way. The format is essentially a large event-by-event table filled with a very long list of variables represented by numerical types or vectors (or a matrix if the variable is represented in more dimensions). This simple structure is of course very convenient for simple tasks, as it requires no deep understanding of data encapsulation or polymorphism.

In [ElectroweakBosons](#), the parent class that provides access to the [D3PD](#) variables (or their pointers) is referred to as [EventBase](#). The [STACO](#) muon variables defined in the [D3PD](#) look like this:

Listing 3.5: Event.h

```

1260 Int_t          mu_staco_n;
1261 std::vector<float> *mu_staco_E;
1262 std::vector<float> *mu_staco_pt;
1263 std::vector<float> *mu_staco_m;
1264 std::vector<float> *mu_staco_eta;
1265 std::vector<float> *mu_staco_phi;

```

Similar variables are defined for other objects (electron, photons, jets etc.) and for each reconstruction algorithm ([MUID](#) muons, [STACO](#) muons, default electron, [GSF](#) electrons etc.). The list

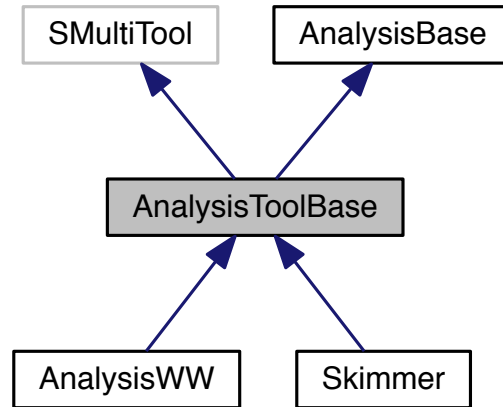


Figure 3.38: The AnalysisBase hierarchy

of variables is quite extensive. We should make it clear at this point, that essentially, the code is designed just for computing, getting and saving numbers in a variety of formats. The framework itself is indeed rather simple.

The goal of my implementation is to provide the user with access to data that are conveniently encapsulated. Each physics object is represented by a class that provides access to data, computation methods and corrections provided by external performance packages. In terms of common analysis needs, an analysis object can be represented just by 4 parameters:

- ▶ Index which corresponds to the integer **D3PD** index, i.e. the index of the object from all the objects of this type in the measured event. The `index` is linked directly through `Event` class.
- ▶ Smearing setting that corresponds to application of smearing as we discussed in [section 3.3](#)
- ▶ Scale setting that corresponds to momentum/energy scale as we discussed in [section 3.3](#)
- ▶ Factor setting which specifies what kind of systematic effects are to applied on object reconstruction efficiencies.

Each physics object is represented by a class that provides access to data, computation methods and corrections provided by external performance packages.

Listing 3.6: Muon.h

```

22 class Muon
23     : public Lepton
24 {
25 public:
26
109 bool   ObjectQuality      ();
110 bool   ObjectQuality      (Recommendation recommendation);
111 bool   TriggerMatching    ();
112 bool   TriggerMatching    (string const & triggerChain);
113 void   KinematicCorrection ();
114 void   UseToolbox         (string Systematics, bool doSystematics = false)
    ;
115 float  IsolationCorrection (int conesize = 30);
116 double EfficiencyCorrection ();
  
```



```

117 double EfficiencyScaleFactor();
118 double IsolationScaleFactor ();
119
120 bool Selection_7TeV_2011 ();
121 bool Selection_8TeV_2012 ();
122 bool Selection_8TeV_2013 ();

```

The class constructor is declared private as memory allocation is handled centrally. Access to instantiation for the user is provided by the `New()` method

```

1 Muon * mu = Muon::New(size_t index,
2                       Algorithm algorithm,
3                       Smearing smear = NoSmearing,
4                       Scale scale = NoScale,
5                       Factor factor = NoFactor);

```

Apart from the index, all settings are implemented as an enum configuration flag to improve readability. Continuing the Muon example:

Listing 3.7: Muon.h

```

29 enum Algorithm { NoAlgorithm, Staco, Muid, Chain3 };
30
31 enum Smearing { NoSmearing, SmearingNominal, SmearingIDUp, SmearingIDDown,
32                SmearingMSUp, SmearingMSDown };
33
34 enum Scale { NoScale, ScaleNominal, ScaleUp, ScaleDown };
35
36 enum Factor { NoFactor, FactorNominal, EfficiencyUp, EfficiencyDown,
37              IsolationUp, IsolationDown };

```

Thus, if the user wants to instantiate the first **STACO** muon in an event with recommended corrections for data or **MC**, he can simply call:

```

1 Muon * mu = Muon::New(0, Staco, SmearingNominal, ScaleNominal,
2                       FactorNominal);

```

Ultimately, the instantiation methods for a Jet or Electron look very similar. Since all analysis objects share some variables and have very similar structure, we derive them from a parent class `AnalysisObject`, the class hierarchy is outlined in [fig. 3.39](#). In this model, class `MuonStaco` inherits commonalities from classes `Muon`, `Lepton` (which shares its properties with `Electron`) and `AnalysisObject`. This make it very straightforward for users to reimplement analysis object to suit their needs by simple exploiting polymorphism. Assuming that users wants to handle the `KinematicCorrection` differently, he implements class `MyMuon` : `MuonStaco`, defines the constructor and a destructor and overloads the `KinematicCorrection` method. All other properties remain intact. Similarly, it is very simple to introduce a new user variable:

```

1 class MyMuon : MuonStaco
2 {
3
4     float mypt;
5 };

```

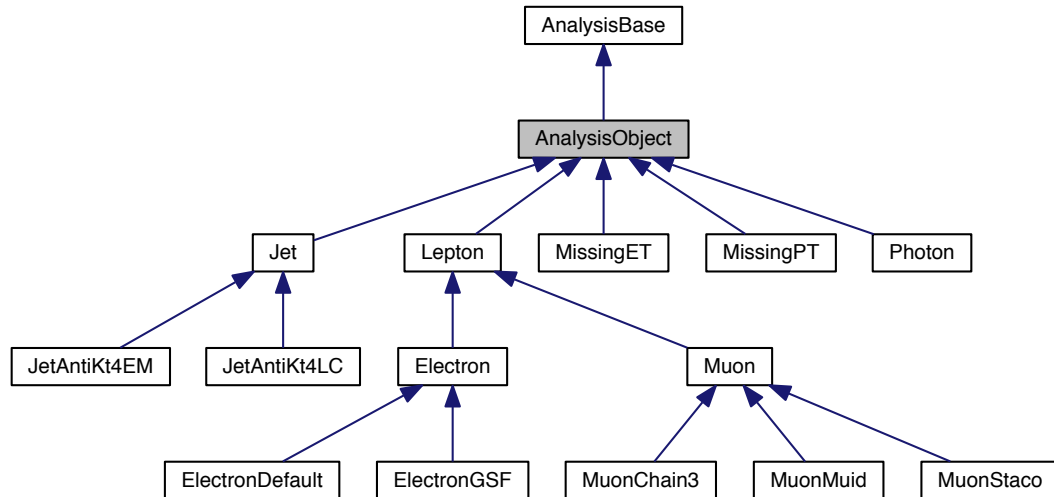


Figure 3.39: Class inheritance graph for implemented physics objects.

Our goal was also to clearly distinguish between user-managed methods and variables with respect to those that are centrally provided in the [D3PD](#) or [RootCore](#) packages. Each analysis objects accesses the [D3PD](#) variables through its corresponding base class `MuonBase` which contains references to the [D3PD](#) variables. This allows us to make clear distinction between the common variables provided in the input [D3PD](#) and any user-defined variables are defined in the object itself.

The base classes access the data through constant references to the `Event` singleton:

Listing 3.8: `MuonBase.h`

```

106 const float & E;
107 const float & pt;
108 const float & eta;
109 const float & phi;
110 const float & theta;

```

and are initialized on construction to the current event and a current object index:

Listing 3.9: `MuonBase.cxx`

```

193 E      ( ev->mu_staco_E      ->at(index) ),
194 pt     ( ev->mu_staco_pt     ->at(index) ),
195 eta    ( ev->mu_staco_eta    ->at(index) ),
196 phi    ( ev->mu_staco_phi    ->at(index) ),
197 theta  ( ev->mu_staco_tracktheta->at(index) ),

```

From the user point of view, accessing the analysis object data members clearly distinguishes between the [D3PD](#) variable and the user variable:

```

1 MyMuon * mymu = MyMuon::New(0, Staco, SmearingNominal, ScaleNominal,
    FactorNominal);
2
3 double pt      = mymu->D3PD->pt;
4 double mypt    = mymu->mypt;

```

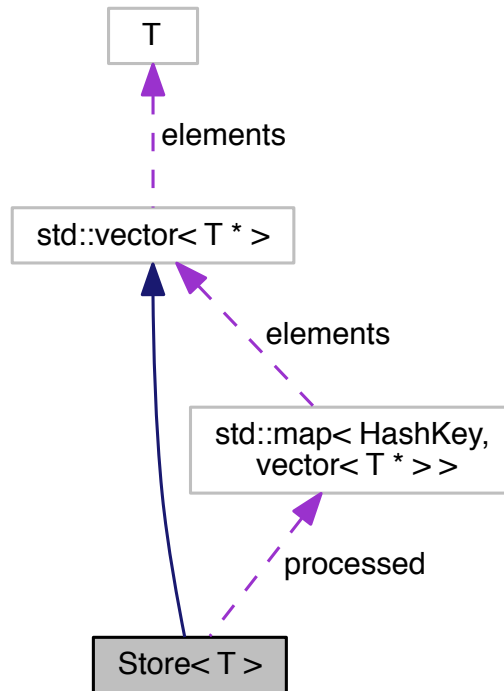


Figure 3.40: Implementation of the Store class.

3.5 References

- [ATL14c] ATLAS Collaboration. *ATLAS Trigger*. 2014. Available at: <https://twiki.cern.ch/twiki/bin/view/Atlas/AtlasTrigger>, visited on 06/13/2014 (cit. on p. 93).
- [ATL08b] ATLAS Collaboration. “The ATLAS Experiment at the CERN Large Hadron Collider”. In: *Journal of Instrumentation* 3.08 (Aug. 2008), S08003–S08003. ISSN: 1748-0221. DOI: [10.1088/1748-0221/3/08/S08003](https://doi.org/10.1088/1748-0221/3/08/S08003) (cit. on pp. 93–97, 111, 112, 115, 117, 118, 123, 125, 136).
- [Col13] T Colombo. “ATLAS TDAQ System Performance in 2012 Data Taking”. In: (Mar. 2013) (cit. on pp. 94, 101).
- [Neg12] A Negri. “Evolution of the Trigger and Data Acquisition System for the ATLAS experiment”. en. In: *Journal of Physics: Conference Series* 396.1 (Dec. 2012), p. 012033. ISSN: 1742-6588. DOI: [10.1088/1742-6596/396/1/012033](https://doi.org/10.1088/1742-6596/396/1/012033) (cit. on pp. 94, 95, 101).
- [Ask+08] S Ask, D Berge, P Borrego-Amaral, D Caracinha, N Ellis, P Farthouat, P Gällnö, S Haas, J Haller, P Klover, A Krasznahorkay, A Messina, C Ohm, T Pauly, M Perantoni, H Pessoa Lima Junior, G Schuler, D Sherman, R Spiwoks, T Wengler, J M de Seixas, and R Torga Teixeira. “The ATLAS central level-1 trigger logic and TTC system”. en.

- In: *Journal of Instrumentation* 3.08 (Aug. 2008), P08002–P08002. ISSN: 1748-0221. DOI: [10.1088/1748-0221/3/08/P08002](https://doi.org/10.1088/1748-0221/3/08/P08002) (cit. on p. 93).
- [ATL11a] ATLAS Collaboration. *ATLAS Fact Sheets*. 2011. Available at: http://www.atlas.ch/fact_sheets.html, visited on 11/08/2013 (cit. on p. 94).
- [ATL12g] ATLAS Collaboration. “Performance of the ATLAS muon trigger in 2011”. In: (July 2012) (cit. on pp. 96, 99).
- [ATL11e] ATLAS Collaboration. “Performance of the ATLAS Trigger System in 2010”. In: (Oct. 2011). arXiv: [1110.1530](https://arxiv.org/abs/1110.1530) (cit. on pp. 96, 99).
- [ATL14r] ATLAS Collaboration. *Trigger Physics Menu*. 2014. Available at: <https://twiki.cern.ch/twiki/bin/view/Atlas/TriggerPhysicsMenu>, visited on 06/13/2014 (cit. on pp. 98, 99).
- [ATL14o] ATLAS Collaboration. *Trigger Menu Glossary*. 2014. Available at: <https://twiki.cern.ch/twiki/bin/viewauth/Atlas/TriggerMenuGlossary>, visited on 06/12/2014 (cit. on pp. 98, 99).
- [But12] Will Buttinger. “The ATLAS Level-1 Trigger System”. en. In: *Journal of Physics: Conference Series* 396.1 (Dec. 2012), p. 012010. ISSN: 1742-6588. DOI: [10.1088/1742-6596/396/1/012010](https://doi.org/10.1088/1742-6596/396/1/012010) (cit. on p. 99).
- [ATL12f] ATLAS Collaboration. “Performance of the ATLAS Electron and Photon Trigger in p-p Collisions at $\sqrt{s} = 7$ TeV in 2011”. In: (May 2012) (cit. on p. 99).
- [ATL12h] ATLAS Collaboration. *Trigger Menu Convention*. 2012. Available at: <https://twiki.cern.ch/twiki/bin/viewauth/Atlas/TriggerMenuConvention>, visited on 06/14/2014 (cit. on p. 99).
- [IP11] O Igonkina and B Petersen. “Proposal and Motivations for 2011 Trigger Menu”. In: (Jan. 2011) (cit. on p. 99).
- [ATL14j] ATLAS Collaboration. *Lowest un-prescaled triggers per data-taking period*. 2014. Available at: <https://twiki.cern.ch/twiki/bin/viewauth/Atlas/LowestUnprescaled>, visited on 06/14/2014 (cit. on p. 99).
- [ATL14p] ATLAS Collaboration. *Trigger Menu Log Book 2012*. 2014. Available at: <https://twiki.cern.ch/twiki/bin/view/Atlas/TriggerMenuLogBook2012>, visited on 06/14/2014 (cit. on p. 99).
- [ATL10a] ATLAS Collaboration. *ATLAS Glossary*. <<http://www.atlas.ch/glossary/glossary.html>>. May 2010. Available at: <http://www.atlas.ch/glossary/glossary.html>, visited on 06/05/2014 (cit. on p. 100).
- [BC13] E C Brost and J T Cummings. “ATLAS Trigger Monitoring in 2012”. In: (Apr. 2013) (cit. on p. 100).
- [CG10] Ilektra A Christidi and the Atlas Muon Offline Dqa Group. “The offline Data Quality Monitoring system of the ATLAS Muon Spectrometer”. In: *Journal of Physics: Conference Series* 219.4 (Apr. 2010), p. 042035. ISSN: 1742-6596. DOI: [10.1088/1742-6596/219/4/042035](https://doi.org/10.1088/1742-6596/219/4/042035) (cit. on p. 100).

- [Oli13] Denis Oliveira Damazio. “Data Quality Monitoring for the ATLAS trigger System during the first data taking period of the Large Hadron Collider”. In: (Sept. 2013) (cit. on p. 100).
- [ATLi] ATLAS Collaboration. *Muon and B-physics HLT expert on-call*. Available at: <https://twiki.cern.ch/twiki/bin/viewauth/Atlas/MuonBPhysHLTONCallExpert>, visited on 06/15/2014 (cit. on p. 101).
- [ATL14q] ATLAS Collaboration. *Trigger Operation Public Results*. 2014. Available at: <https://twiki.cern.ch/twiki/bin/view/AtlasPublic/TriggerOperationPublicResults>, visited on 06/11/2014 (cit. on p. 102).
- [ATL96] ATLAS Collaboration. “ATLAS Computing Technical Proposal”. In: (1996) (cit. on p. 101).
- [ATL05] ATLAS Collaboration. “ATLAS Computing Technical Design Report”. In: (2005) (cit. on pp. 102, 104, 105, 107).
- [ATLj] ATLAS Collaboration. *Physics Analysis Work Book (Release 17)*. Available at: <https://twiki.cern.ch/twiki/bin/view/AtlasProtected/PhysicsAnalysisWorkBookRel17>, visited on 06/16/2014 (cit. on pp. 102, 104).
- [ATL12b] ATLAS Collaboration. *GoodRunsLists*. 2012. Available at: <https://twiki.cern.ch/twiki/bin/view/Atlas/GoodRunsLists>, visited on 06/22/2014 (cit. on p. 103).
- [Ago+03] S. Agostinelli et al. “Geant4—a simulation toolkit”. In: *Nuclear Instruments and Methods in Physics Research Section A: Accelerators, Spectrometers, Detectors and Associated Equipment* 506.3 (July 2003), pp. 250–303. ISSN: 01689002. DOI: [10.1016/S0168-9002\(03\)01368-8](https://doi.org/10.1016/S0168-9002(03)01368-8) (cit. on p. 103).
- [Gea] Geant4 Collaboration. *Geant4: A toolkit for the simulation of the passage of particles through matter*. Available at: <http://geant4.cern.ch/>, visited on 06/16/2014 (cit. on p. 103).
- [RPF98] Elzbieta Richter-Was, Luc Poggioli, and D Froidevaux. “ATLFAST 2.0 a fast simulation package for ATLAS”. In: (Nov. 1998) (cit. on p. 104).
- [She] Peter Sherwood. *Atlfast Website*. Available at: <http://www.hep.ucl.ac.uk/atlas/atlfast/>, visited on 06/16/2014 (cit. on p. 104).
- [ATL14l] ATLAS Collaboration. *Physics Analysis Work Book (Release 17): Introduction to data formats*. 2014. Available at: <https://twiki.cern.ch/twiki/bin/view/AtlasProtected/PhysicsAnalysisWorkBookFormatsIntroduction>, visited on 06/15/2014 (cit. on pp. 104, 105).
- [ATL13g] ATLAS Collaboration. *Update of the Computing Models of the WLCG and the LHC Experiments*. Tech. rep. 2013 (cit. on p. 104).
- [Dob+] Matt Dobbs, Jørgen Beck Hansen, Lynn Garren, and Lars Sonnenschein. *HepMC2 User Manual 2.06*. Available at: http://lcgapp.cern.ch/project/simu/HepMC/206/HepMC2_user_manual.pdf, visited on 06/16/2014 (cit. on p. 104).

- [CERb] CERN. *Pool Of persistent Objects for LHC (POOL) - Persistency Framework*. Available at: <http://pool.cern.ch/>, visited on 06/16/2014 (cit. on p. 105).
- [Bir+14] I Bird, F Carminati, R Mount, B Panzer-Steindel, J Harvey, I Fisk, B Kersevan, P Clarke, M Girone, P Buncic, M Cattaneo, and P Mato. “Update of the Computing Models of the WLCG and the LHC Experiments”. In: (Apr. 2014) (cit. on p. 105).
- [Sch+05] U Schwickerath, R Jones, J Shiers, N Brook, C Grandi, Christoph Eck, I Fisk, Y Schutz, I Bird, B Panzer-Steindel, B Gibbard, H Marten, J Knobloch, A Heiss, L Perini, M Lamanna, D Foster, F Grey, P Mato-Vila, D Düllmann, K Bos, S Jarp, J Harvey, Leslie Robertson, D Kelsey, F Hemmer, T Wenaus, and F Ould-Saada. “LHC computing Grid”. In: (2005) (cit. on p. 105).
- [WLC] WLCG Collaboration. *WLCG Document Repository*. Available at: <https://espace2013.cern.ch/WLCG-document-repository/>, visited on 06/16/2014 (cit. on pp. 105, 106).
- [CER14] CERN Computing Resource Scrutiny Group. *CRSG Report 2013*. Tech. rep. 2014 (cit. on p. 105).
- [CERa] CERN. *CERN Advanced Storage Manager (CASTOR)*. Available at: <http://castor.web.cern.ch/>, visited on 06/16/2014 (cit. on p. 106).
- [Ryb13] G Rybkin. “ATLAS software configuration and build tool optimisation”. In: (Oct. 2013) (cit. on p. 107).
- [ATL14a] ATLAS Collaboration. *ATLAS Computing TWiki*. 2014. Available at: <https://twiki.cern.ch/twiki/bin/view/AtlasComputing>, visited on 05/07/2014 (cit. on p. 107).
- [ROOa] ROOT Development Team. *ROOT: A Data Analysis Framework*. Available at: <http://root.cern.ch/>, visited on 06/16/2014 (cit. on p. 107).
- [ROOb] ROOT Development Team. *ROOT User Guide*. Available at: <http://root.cern.ch/root/html/doc/guides/users-guide/ROOTUsersGuideA4.pdf>, visited on 06/16/2014 (cit. on p. 107).
- [ATLl] ATLAS Collaboration. *RootCore*. Available at: <https://twiki.cern.ch/twiki/bin/view/AtlasComputing/RootCore#CMake>, visited on 06/16/2014 (cit. on pp. 107, 139).
- [ATLa] ATLAS Collaboration. *Atlantis - Event display for ATLAS*. Available at: <http://atlantis.web.cern.ch/atlantis/>, visited on 06/16/2014 (cit. on p. 107).
- [ATLc] ATLAS Collaboration. *ATLAS VPI - The interactive 3D event display for the ATLAS experiment at CERN*. Available at: <http://atlas-vp1.web.cern.ch/atlas-vp1/home/>, visited on 06/16/2014 (cit. on p. 107).
- [EW] Johannes Ebke and Peter Weller. *a4*. Available at: <https://github.com/a4/> (cit. on p. 108).
- [KHB] Attila Krasznahorkay, Johannes Haller, and David Berge. *SFrame - A ROOT Analysis Framework*. Available at: http://sframe.sourceforge.net/SFrame/SFrame_-_A_ROOT_analysis_framework.html%20http://sourceforge.net/projects/sframe/, visited on 06/16/2014 (cit. on pp. 108, 139).

- [ATLe] ATLAS Collaboration. *DPD Naming Convention*. Available at: <https://twiki.cern.ch/twiki/bin/viewauth/AtlasProtected/DPDNamingConvention>, visited on 06/16/2014 (cit. on p. 108).
- [Lay+13] P Laycock, R Henderson, L Zhou, O Ozturk, and M Beckingham. “Derived Physics Data Production in ATLAS: Experience with Run 1 and Looking Ahead (proceedings)”. In: (Oct. 2013) (cit. on p. 108).
- [ATL14n] ATLAS Collaboration. “Recommendations of the Physics Objects and Analysis Harmonisation Study Groups 2014”. In: (May 2014) (cit. on p. 108).
- [ATL10b] ATLAS Collaboration. *ATLAS Public Website*. <<http://www.atlas.ch>>. May 2010. Available at: <http://www.atlas.ch>, visited on 05/06/2014 (cit. on p. 109).
- [Cor+07] T Cornelissen, M Elsing, W Liebig, S Fleischmann, and E Moyse. “Concepts, Design and Implementation of the ATLAS New Tracking (NEWT)”. In: (Mar. 2007) (cit. on pp. 109–112).
- [Was12] Christoph Wasicki. “Track and vertex reconstruction of the ATLAS Inner Detector in the high multiplicity LHC environment”. In: *Journal of Physics: Conference Series* 396.2 (Dec. 2012), p. 022056. ISSN: 1742-6588. DOI: [10.1088/1742-6596/396/2/022056](https://doi.org/10.1088/1742-6596/396/2/022056) (cit. on pp. 111–115).
- [AEH10] Jean-Francois Arguin, Markus Elsing, and Beate Heinemann. “ATLAS Tracking Performance in the Presence of Pile-up”. In: (2010), pp. 1–18 (cit. on p. 112).
- [ATL08a] ATLAS Collaboration. “Expected Performance of the ATLAS Experiment - Detector, Trigger and Physics”. In: (Dec. 2008). arXiv: [0901.0512](https://arxiv.org/abs/0901.0512) (cit. on pp. 112, 117, 118).
- [ATL10c] ATLAS Collaboration. “Performance of primary vertex reconstruction in proton-proton collisions at $\sqrt{s}=7$ TeV in the ATLAS experiment”. In: (July 2010) (cit. on p. 114).
- [Pag+12a] S Pagan Griso, E Guido, F Meloni, A Wildauer, K Grimm, M Rudolph, K Prokofiev, A Andreazza, and A Salzburger. “Vertex reconstruction plots : Collision performance plots for approval 2011”. In: (May 2012) (cit. on pp. 114–116).
- [Pag+12b] S Pagan Griso, E Guido, F Meloni, A Wildauer, K Grimm, M Rudolph, K Prokofiev, A Andreazza, and A Salzburger. “Vertex reconstruction plots : Collision performance plots for approval 2012”. In: (Apr. 2012) (cit. on p. 114).
- [Mel+11] F Meloni, K Prokofiev, S Pagan-Griso, A Milov, and A Wildauer. “Vertexing Performance Data vs MC comparison for LPCC”. In: (Sept. 2011) (cit. on pp. 114, 116).
- [ATL14h] ATLAS Collaboration. *Inner Detector Tracking Performance Approved Plots*. 2014. Available at: <https://twiki.cern.ch/twiki/bin/view/AtlasPublic/InDetTrackingPerformanceApprovedPlots> (cit. on p. 116).
- [Nic+10] R Nicolaidou, L Chevalier, S Hassani, J F Laporte, E Le Menedeu, and A Ouraou. “Muon identification procedure for the ATLAS detector at the LHC using Muonboy reconstruction package and tests of its performance using cosmic rays and single beam data”. en. In: *Journal of Physics: Conference Series* 219.3 (Apr. 2010), p. 032052. ISSN: 1742-6596. DOI: [10.1088/1742-6596/219/3/032052](https://doi.org/10.1088/1742-6596/219/3/032052) (cit. on p. 115).

- [Has+07] S. Hassani, L. Chevalier, E. Lançon, J.-F. Laporte, R. Nicolaidou, and A. Ouraou. “A muon identification and combined reconstruction procedure for the ATLAS detector at the LHC using the (MUONBOY, STACO, MuTag) reconstruction packages”. In: *Nuclear Instruments and Methods in Physics Research Section A: Accelerators, Spectrometers, Detectors and Associated Equipment* 572.1 (Mar. 2007), pp. 77–79. ISSN: 01689002. DOI: [10.1016/j.nima.2006.10.340](https://doi.org/10.1016/j.nima.2006.10.340) (cit. on p. 115).
- [Ada+03] D Adams, J T Shank, G Cataldi, S Spagnolo, L Merola, A Poppleton, S Goldfarb, Ketevi A Assamagan, G Carlino, A Nairz, M Biglietti, F Conventi, L Spogli, G D Stavropoulos, Yu Fisyak, K Mair, T Wenaus, E Gorini, T Lagouri, M Verducci, S Rosati, A Farilla, and M Primavera. “Track reconstruction in the ATLAS Muon Spectrometer with MOORE 007”. In: (May 2003) (cit. on p. 115).
- [ATL13e] ATLAS Collaboration. *Preliminary results on the muon reconstruction efficiency, momentum resolution, and momentum scale in ATLAS 2012 pp collision data*. English. Tech. rep. Aug. 2013 (cit. on pp. 117, 119, 120).
- [Mar13] Marilyn D. Marx. “Standard Model and Exotic Diboson Production with the ATLAS Detector”. PhD thesis. 2013 (cit. on p. 118).
- [ATL11c] ATLAS Collaboration. “Muon Momentum Resolution in First Pass Reconstruction of pp Collision Data Recorded by ATLAS in 2010”. In: (Mar. 2011) (cit. on p. 118).
- [ATL11d] ATLAS Collaboration. “Muon reconstruction efficiency in reprocessed 2010 LHC proton-proton collision data recorded with the ATLAS detector”. In: (Apr. 2011) (cit. on pp. 119, 122).
- [ATL14k] ATLAS Collaboration. *Muon Calorimeter Corrections*. 2014. Available at: <https://twiki.cern.ch/twiki/bin/viewauth/AtlasProtected/MuonCalorimeterCorrections> (cit. on pp. 121, 122).
- [ATL13c] ATLAS Collaboration. “Object Selections and Background estimates in the $H \rightarrow WW$ analysis with 20.7 fb^{-1} of data collected with the ATLAS detector at $\sqrt{s} = 8 \text{ TeV}$ ”. In: (Nov. 2013) (cit. on p. 121).
- [ATL14b] ATLAS Collaboration. *ATLAS Muon Combined Performance Guidelines for Analyses of 2012 Data*. 2014. Available at: <https://twiki.cern.ch/twiki/bin/viewauth/AtlasProtected/MCPAnalysisGuidelinesData2012>, visited on 06/16/2014 (cit. on p. 121).
- [ATL14m] ATLAS Collaboration. *Quality Definition Staco*. 2014. Available at: <https://twiki.cern.ch/twiki/bin/viewauth/AtlasProtected/QualityDefinitionStaco>, visited on 06/05/2014 (cit. on p. 121).
- [Lam+08] W Lampl, P Loch, S Menke, S Rajagopalan, S Laplace, G Unal, H Ma, S Snyder, D Lelas, and D Rousseau. *Calorimeter Clustering Algorithms*. Tech. rep. Apr. 2008 (cit. on p. 123).
- [ATL14f] ATLAS Collaboration. *Electron Efficiency Measurements for 2012 and 2011 Data*. Tech. rep. 2014 (cit. on p. 124).
- [ATL12c] ATLAS Collaboration. “Improved electron reconstruction in ATLAS using the Gaussian Sum Filter-based model for bremsstrahlung”. In: (May 2012) (cit. on p. 124).

- [ATL11b] ATLAS Collaboration. “Electron performance measurements with the ATLAS detector using the 2010 LHC proton-proton collision data”. In: (Oct. 2011), p. 34. DOI: [10.1140/epjc/s10052-012-1909-1](#). arXiv: [1110.3174](#) (cit. on pp. [124](#), [125](#), [137](#)).
- [ATL14d] ATLAS Collaboration. *Calibration recommendations for 2011 and 2012 analyses using GEO-20 MC samples and Calibration-Hits-based calibration*. 2014. Available at: <https://twiki.cern.ch/twiki/bin/viewauth/AtlasProtected/EGammaCalibrationGEO20>, visited on 06/07/2014 (cit. on pp. [124](#), [125](#)).
- [ATL13f] ATLAS Collaboration. “Supporting document on electron efficiency measurements using the 2012 LHC proton-proton collision data”. In: (Sept. 2013) (cit. on pp. [125](#), [127](#)).
- [ATLf] ATLAS Collaboration. *Electron Identification Menu*. Available at: <https://twiki.cern.ch/twiki/bin/viewauth/AtlasProtected/TechnicalitiesForMedium1>, visited on 06/05/2014 (cit. on p. [125](#)).
- [Ali+13] J Alison, C M Lester, K Brendlinger, J Kroll, and S Heim. “Description and Performance of the Electron Likelihood Tool at ATLAS using 2012 LHC Data”. In: (Apr. 2013) (cit. on p. [126](#)).
- [ATL14e] ATLAS Collaboration. *Egamma Isolation*. 2014. Available at: <https://twiki.cern.ch/twiki/bin/viewauth/AtlasProtected/Egammalsolation>, visited on 06/10/2014 (cit. on pp. [127–129](#)).
- [LdV12] S Laplace and JB de Vivie. “Calorimeter isolation and pile-up”. In: (May 2012) (cit. on pp. [127–129](#)).
- [ATLd] ATLAS Collaboration. *Calorimeter isolation with TopoClusters versus pileup*. Available at: <https://atlas.web.cern.ch/Atlas/GROUPS/PHYSICS/EGAMMA/PublicPlots/20120404/Topolsolation/ATL-COM-PHYS-2012-362/index.html>, visited on 06/20/2014 (cit. on p. [128](#)).
- [ATL12a] ATLAS Collaboration. *Egamma Calorimeter Isolation Corrections*. 2012. Available at: <https://twiki.cern.ch/twiki/bin/viewauth/AtlasProtected/CalolsolationCorrections>, visited on 06/16/2014 (cit. on p. [129](#)).
- [Ell93] Stephen D. Ellis. “Successive combination jet algorithm for hadron collisions”. In: *Physical Review D* 48.7 (Oct. 1993), pp. 3160–3166. ISSN: 0556-2821. DOI: [10.1103/PhysRevD.48.3160](#). arXiv: [9305266](#) [[hep-ph](#)] (cit. on p. [129](#)).
- [Dok+97] Yu.L Dokshitzer, G.D Leder, S Moretti, and B.R Webber. “Better jet clustering algorithms”. In: *Journal of High Energy Physics* 1997.08 (Aug. 1997), pp. 001–001. ISSN: 1029-8479. DOI: [10.1088/1126-6708/1997/08/001](#). arXiv: [9707323](#) [[hep-ph](#)] (cit. on p. [129](#)).
- [WW99] M. Wobisch and T. Wengler. “Hadronization Corrections to Jet Cross Sections in Deep-Inelastic Scattering”. In: (July 1999), p. 10. arXiv: [9907280](#) [[hep-ph](#)] (cit. on p. [129](#)).

- [CSS08] Matteo Cacciari, Gavin P Salam, and Gregory Soyez. “The anti- k_t jet clustering algorithm”. In: *Journal of High Energy Physics* 2008.04 (Apr. 2008), pp. 063–063. ISSN: 1029-8479. DOI: [10.1088/1126-6708/2008/04/063](https://doi.org/10.1088/1126-6708/2008/04/063). arXiv: [0802.1189](https://arxiv.org/abs/0802.1189) (cit. on pp. [129](#), [130](#)).
- [ATL12d] ATLAS Collaboration. “Performance of large-R jets and jet substructure reconstruction with the ATLAS detector”. In: (July 2012) (cit. on p. [130](#)).
- [ATL13b] ATLAS Collaboration. “Jet energy scale and its systematic uncertainty in proton-proton collisions at $\sqrt{s}=7$ TeV with ATLAS 2011 data”. In: (Jan. 2013) (cit. on pp. [130](#)–[132](#), [134](#), [135](#)).
- [ATL13a] ATLAS Collaboration. “Jet energy measurement with the ATLAS detector in proton-proton collisions at $\sqrt{s} = 7$ TeV”. In: *The European Physical Journal C* 73.3 (Mar. 2013), p. 2304. ISSN: 1434-6044. DOI: [10.1140/epjc/s10052-013-2304-2](https://doi.org/10.1140/epjc/s10052-013-2304-2). arXiv: [1112.6426](https://arxiv.org/abs/1112.6426) (cit. on pp. [131](#)–[133](#)).
- [SBS14] Maximilian Swiatlowski, Fabrice Balli, and Carlos Sandoval. *Update on Jet Calibrations*. 2014. Available at: <https://indico.cern.ch/event/161252/contribution/0/material/slides/0.pdf>, visited on 06/18/2014 (cit. on pp. [132](#), [133](#)).
- [LG] D Lopez Mateos and Dag Gillberg. *Plans and technicalities for 2012 JES analyses*. Available at: <https://indico.cern.ch/event/191816/material/slides/0?contribId=0>, visited on 06/18/2014 (cit. on p. [134](#)).
- [ATL14i] ATLAS Collaboration. *Jet Uncertainties 2012*. 2014. Available at: <https://twiki.cern.ch/twiki/bin/viewauth/AtlasProtected/JetUncertainties2012Final>, visited on 06/18/2014 (cit. on p. [135](#)).
- [ATLg] ATLAS Collaboration. *Jet Uncertainties 2011*. Available at: <https://twiki.cern.ch/twiki/bin/viewauth/AtlasProtected/JetUncertainties2011>, visited on 06/19/2014 (cit. on p. [135](#)).
- [ATLh] ATLAS Collaboration. *JetEtmis Recommendations 2012*. Available at: <https://twiki.cern.ch/twiki/bin/viewauth/AtlasProtected/JetEtmisRecommendations2012>, visited on 06/19/2014 (cit. on p. [135](#)).
- [Sac+] Sabrina Sacerdoti, Dag Gillberg, Bogdan Malaescu, and Ricardo Piegaia. *Jet Energy Resolution 2012 (Moriond 2013 recommendation)*. Available at: <https://indico.cern.ch/event/223335/contribution/0/material/slides/0.pdf>, visited on 06/19/2014 (cit. on p. [136](#)).
- [ATLk] ATLAS Collaboration. *Recommendations for jet cleaning for data 2012*. Available at: <https://twiki.cern.ch/twiki/bin/view/AtlasProtected/HowToCleanJets2012>, visited on 06/20/2014 (cit. on p. [136](#)).
- [ATL14g] ATLAS Collaboration. *How To Clean Jets 2011*. 2014. Available at: <https://twiki.cern.ch/twiki/bin/viewauth/AtlasProtected/HowToCleanJets2011>, visited on 06/20/2014 (cit. on p. [136](#)).

- [ATL13d] ATLAS Collaboration. “Performance of Missing Transverse Momentum Reconstruction in ATLAS studied in Proton-Proton Collisions recorded in 2012 at 8 TeV”. In: (Aug. 2013) (cit. on pp. 136, 137).
- [ATL12e] ATLAS Collaboration. “Performance of missing transverse momentum reconstruction in proton-proton collisions at $\sqrt{s} = 7 \sim \text{TeV}$ with ATLAS”. In: *The European Physical Journal C* 72.1 (Jan. 2012), p. 1844. ISSN: 1434-6044. DOI: [10.1140/epjc/s10052-011-1844-6](https://doi.org/10.1140/epjc/s10052-011-1844-6). arXiv: [1108.5602](https://arxiv.org/abs/1108.5602) (cit. on pp. 137, 138).
- [13b] “Identification of the Hadronic Decays of Tau Leptons in 2012 Data with the ATLAS Detector”. In: (July 2013) (cit. on p. 137).
- [13a] “Determination of the tau energy scale and the associated systematic uncertainty in proton-proton collisions at $\sqrt{s} = 8 \text{ TeV}$ with the ATLAS detector at the LHC in 2012”. In: (Apr. 2013) (cit. on p. 137).
- [ATLb] ATLAS Collaboration. *Atlas CAT ElectroweakBosons*. Available at: <https://twiki.cern.ch/twiki/bin/view/Main/AtlasCATElectroweakBosons>, visited on 06/17/2014 (cit. on pp. 138, 139).

MEASUREMENT OF THE STANDARD MODEL WW CROSS-SECTION

Contents

4.1	Analysis overview	158
4.1.1	Cross-section extraction	159
4.1.2	Efficiencies and weights	161
4.2	Event selection	162
4.2.1	Differences between the 7 TeV and 8 TeV analysis	167
4.2.2	Final selection	167
4.2.3	Event selection cut-flow	170
4.3	Signal and background modelling	172
4.3.1	Signal samples	172
4.3.2	Background samples	174
4.3.3	Pileup re-weighting	176
4.3.4	PDF re-weighting	180
4.4	Trigger decision	180
4.4.1	Trigger matching	183
4.4.2	Trigger efficiency	185
4.5	Object definitions	186
4.5.1	Muon definition	186
4.5.2	Electron definition	193
4.5.3	Jet definition	198
4.5.4	Missing transverse energy definition	199
4.5.5	Stream overlap removal	202
4.5.6	Object overlap removal	202
4.6	Datasets	203
4.6.1	Derived datasets	203
4.6.2	Data cleaning	204
4.7	Acceptance	205
4.7.1	Cut optimization	206
4.7.2	Selection acceptance	212
4.7.3	Jet veto uncertainties	212
4.7.4	Fiducial region	215

4.8	Systematic uncertainties	216
4.8.1	Lepton systematics	217
4.8.2	Jet systematics	222
4.8.3	Missing transverse energy systematics	224
4.8.4	Missing transverse momentum systematics	224
4.9	Background estimates	226
4.9.1	Simultaneous fit method	226
4.9.2	Z+jets background: Transfer factor method	228
4.9.3	Top background: Jet veto survival probability	229
4.9.4	Top background: Transfer factor method	232
4.9.5	W+jets and multijet background: Matrix method	234
4.9.6	Other diboson production	237
4.10	Cross-section results	238
4.10.1	Candidates and backgrounds	238
4.10.2	Cross-section extraction	244
4.10.3	Cross-section uncertainties	245
4.11	Unfolding	246
4.11.1	Efficiency and background	250
4.11.2	Unfolding methodology	250
4.11.3	Implementation	252
4.11.4	Unfolded distributions	254
4.12	References	257

ELECTROWEAK BOSON PAIR MEASUREMENTS are an important part of the [ATLAS](#) physics programme. At the [LHC](#), di-boson measurements are used to probe the electroweak sector of the [Standard Model](#) at the TeV energy scale and provide new measurements of the production [cross-sections](#). Vector bosons decay channels could also indicate the existence of new particles and probe beyond the [Standard Model](#) physics. The processes involved in the production of vector bosons are sensitive to anomalous *triple gauge couplings* (TGC's) and also present an irreducible background to [Higgs boson](#) searches using the same final state. Additionally, WW measurements can be also used to probe *quartic gauge couplings* (QGC's).

The [SM](#) describes three main diboson production processes: *s*-channel, *t*-channel and *u*-channel. The corresponding Feynman diagrams are shown in [fig. 4.1](#). These processes are common to the WW, WZ and ZZ analyses. In this chapter, we report on the measurement of the WW production cross section in pp collisions at $\sqrt{s} = 7$ TeV and 8 TeV using the [ATLAS](#) detector. The corresponding 4.64 fb^{-1} and 20.28 fb^{-1} of data collected by the [ATLAS](#) detector in years 2011 and 2012 at the [LHC](#) are searched for WW leptonic decay candidates.

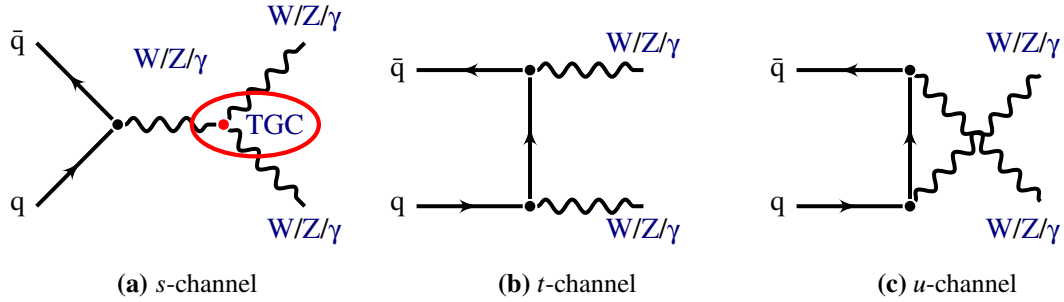


Figure 4.1: [Standard Model](#) tree-level leading-order Feynman diagrams for diboson production. The *s*-channel diagram on the left contains [triple gauge coupling](#) vertex. In case of WW production, the TGC vertex corresponds to WWZ or WW γ coupling.

The $q\bar{q}$ initial states shown in [fig. 4.2](#) are specific to hadron colliders. These are the dominant production mechanism of WW boson pairs at the [LHC](#), while the gluon fusion production mechanisms shown in [fig. 4.3](#) contribute at a 3 % level at $\sqrt{s} = 7$ TeV and 8 TeV. Following the recent discovery of the [Higgs boson](#) [[ATL12d](#)] the WW events coming from the [Higgs boson](#) decay are included in the signal samples and contribute an additional 7 % (given the [Standard Model Higgs boson](#) mass of 125 GeV). *Vector boson fusion* (VBF) and *double parton scattering* (DPS) processes are not included as they only contribute at the permille level according to the [SM](#), see [M. Billoni et al. \[Bil+13\]](#) and [Anastasiya Bierweiler et al. \[Bie+12\]](#). The goal of this analysis is not to optimise the selection of [Higgs boson](#) events, rather we approach the measurement in a more generic way. We include the $H \rightarrow W^+W^-$ in our signal, then cut and count the total WW event yield in data and extract the total WW production cross-section. Additional WW events produced indirectly through top quark decays are considered as background.

This chapter is organized as follows: in the following section we provide a general overview of the analysis and outline our strategy for the measurement. We start with discussing the analysis event selection in [section 4.2](#). Following with [section 4.3](#) we focus on the theoretical predictions and [MC](#) modelling. [Sections 4.4](#) and [4.6](#) focus on technical details of its implementation. Acceptance, background estimates and corresponding systematic uncertainties are discussed in [section 4.7–4.9](#).

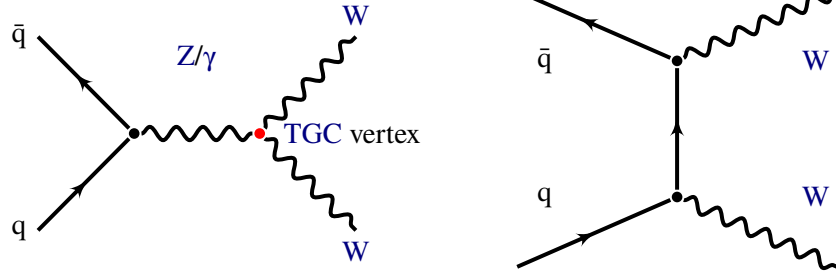


Figure 4.2: Standard Model tree-level leading-order Feynman diagrams for WW production through the $q\bar{q}$ initial state. The s-channel diagram on the left contains the TGC vertex.

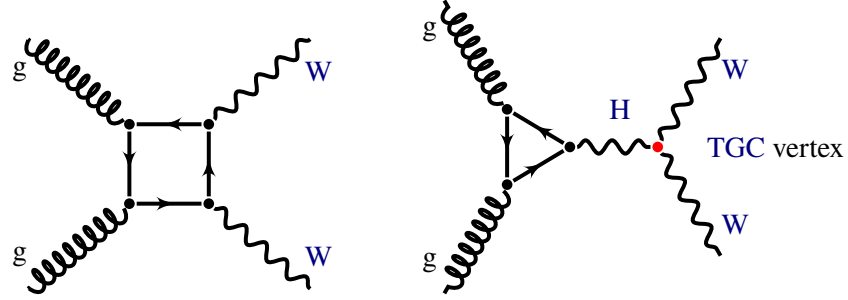


Figure 4.3: Standard Model leading-order Feynman diagrams for WW through gluon-gluon fusion. The box diagram on the left shows the NNLO contribution to WW production, the right diagram occurs through the Higgs boson.

Throughout the text, we describe both the 7 TeV and 8 TeV analyses to give a more complete picture, the differences are highlighted when appropriate. As a PhD student, I have joined the analysis for the second part of 2011 and later I became one of the major contributors to the analysis on the full 2012 dataset of at $\sqrt{s} = 8$ TeV.

4.1 Analysis overview

The W boson is a massive vector boson and thus it only has a very short lifetime. In ATLAS we do not observe the W bosons directly as they decay before they reach the detector, so instead they are identified by their decay products. W bosons decay into two fermions, W^+ can decay into a lepton and anti-neutrino or a quark anti-quark pair. As we have shown in table 1.5, the relevant SM branching ratios are known experimentally to be [Par12]:

$$\text{BR}(W \rightarrow e^+ \nu_e) = (10.75 \pm 0.13) \% \quad (4.1)$$

$$\text{BR}(W \rightarrow \mu^+ \nu_\mu) = (10.57 \pm 0.15) \% \quad (4.2)$$

$$\text{BR}(W \rightarrow \tau^+ \nu_\tau) = (11.25 \pm 0.20) \% \quad (4.3)$$

$$\text{BR}(W \rightarrow q\bar{q}) = (67.60 \pm 0.27) \% \quad (4.4)$$

The lepton decay branching fraction is theoretically predicted by the Standard Model to be equal for all three flavours and the current experimental results are at the limit of compatibility. The jet final states are not considered in this analysis because of the poor *signal over background ratio* (S/B) as the WW production cross-section is orders of magnitude smaller than W + jets and

QCD processes. The WW pair coming from the $t\bar{t}$ process is not considered as signal and we aim to suppress it by vetoing jets in the event (a cut we refer to as jet veto later in the text). The $\tau^+\nu_\tau$ final state decays into electrons or muons, so the experimental signature of the $\ell^+\ell^-\nu\bar{\nu}$ final state consists of two oppositely charged electrons (e^+e^-), muons ($\mu^+\mu^-$) or an electron and a muon ($e^\pm\mu^\mp$). This way we consider τ^\pm decay channels as a part of our signal only indirectly (see [section 4.7](#)). When referring to same flavour channels, we indicate both the e^+e^- and $\mu^+\mu^-$ channel. Likewise, we refer to the $e^\pm\mu^\mp$ channel as combined flavour.

Four separate analyses of leptonic WW decay modes have been published so far. First the analysis on the 2010 dataset at 7 TeV (first **LHC** data) was published only as an internal note [[ATL11b](#)] due to very limited statistics (34 pb^{-1}). The following year two analyses have been published, one on 1.02 fb^{-1} [[ATL12c](#)] and the other on the full 2011 dataset 4.64 fb^{-1} [[ATL13c](#)]. The results of the 8 TeV analysis were published as a conference note [[ATL14i](#)].

4.1.1 Cross-section extraction

The strategy of the measurement is similar for all di-boson analyses. All diboson production processes share relatively small production cross-sections ranging from 1 pb (for ZZ) to 100 pb (for WW) with respect to other **Standard Model** processes as shown in [fig. 4.4](#). The common approach is to consider only the leptonic decay modes because of their **signal over background ratio**. The analysis is performed by simply doing “cut and count” and the total **cross-section** is calculated from the event yield:

$$\sigma_{\text{WW}} = \frac{N_{\text{obs}} - N_{\text{bkg}}}{\epsilon \mathcal{A} \cdot \text{BR} \cdot \int \mathcal{L} dt} \quad (4.5)$$

where N_{obs} represents the number of observed events passing the event selection in data and N_{bkg} refers to the number of estimated background events. In the denominator, ϵ is the reconstruction efficiency, **BR** is the **branching ratio** and \mathcal{L} is the **luminosity**. The **acceptance** \mathcal{A} describes the phase space region where collision products can be measured by the detector. Reconstruction efficiency times **acceptance** $\epsilon \mathcal{A}$ is usually treated as one number as it directly corresponds to the expected number of reconstructed WW events for a given integrated **luminosity** (4.64 fb^{-1} for the 7 TeV analysis and 20.28 fb^{-1} for the 8 TeV).

It is worth noting that the visible **cross-section** is extrapolated to the full space from the kinematic selection applied for a given measurement. This effectively means that uncertainties inherent to the experimental apparatus are included in the total uncertainty. We can however introduce a different definition of the **cross-section** encompassing only the detector phase space. This is referred to as the fiducial **cross-section** and can be obtained simply by replacing $\epsilon \mathcal{A}$ by an overall correction factor C_{WW} .

$$\sigma_{\text{WW}}^{\text{fid}} = \frac{N_{\text{obs}} - N_{\text{bkg}}}{C_{\text{WW}} \cdot \int \mathcal{L} dt} \quad (4.6)$$

where the newly introduced correction factor C_{WW} represents the efficiency correction from **MC** that accounts for detector smearing effects and cut inefficiencies and is defined simply as the ratio of reconstructed events that pass the analysis selection over the number of events that pass the selection

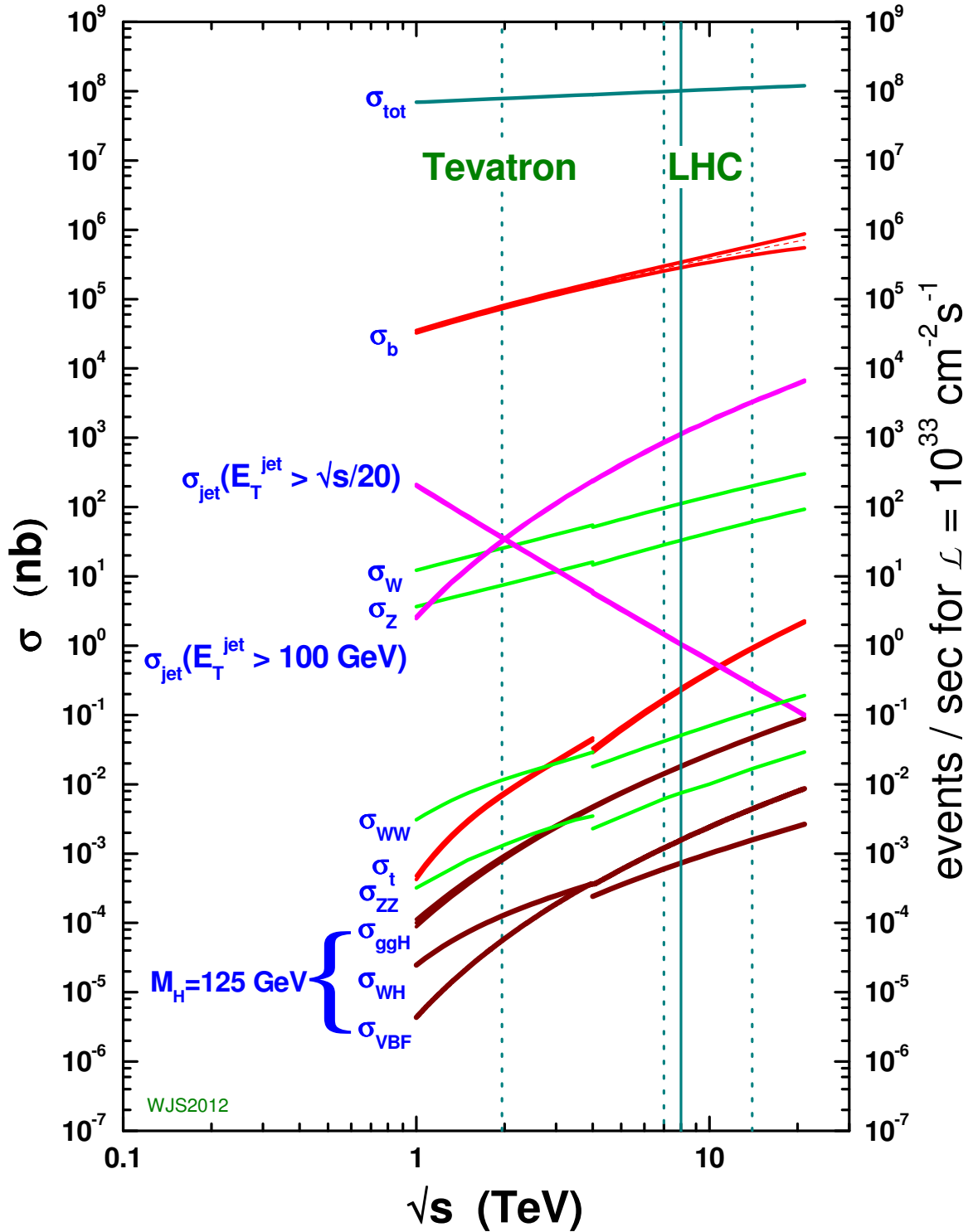


Figure 4.4: Standard Model proton-(anti)proton cross sections as a function of collider energy including the 125 GeV Higgs boson. The cross sections are calculated with NLO or NNLO perturbative QCD, using MSTW2008 parton distributions, with the exception of the total hadronic cross section which is based on a parametrisation of the Particle Data Group. The discontinuity in some of the cross sections at 4 TeV is due to the switch from proton-antiproton (Tevatron) to proton-proton collisions (LHC) at that energy. Figure from [Sti13].

emulated at the truth level

$$C_{\text{WW}} = \frac{N_{\text{WW}} (\text{passed event selection})}{N_{\text{WW}} (\text{passed fiducial selection})}. \quad (4.7)$$

To obtain this ratio we attempt to emulate the event selection at the truth level to match the instrumented region of the detector as closely as possible. Notation wise, the truth level yields are referred to as being measured in the fiducial region of the detector. This reduced phase space is dictated by the detector geometry and kinematic acceptance, [trigger](#) efficiencies etc. and it allows to effectively separate the experimental uncertainties C_{WW} from the theoretical ones. Four different regions were defined to accommodate all three channels plus the inclusive measurement, see [section 4.7](#). This approach is common to both 8 TeV and 7 TeV analyses.

The theoretical correction factor A_{WW} is defined as the number of truth events that pass the fiducial selection over the total number of generated events:

$$A_{\text{WW}} = \frac{N_{\text{WW}} (\text{passed fiducial selection})}{N_{\text{WW}} (\text{total generated signal events})} \quad (4.8)$$

where the event yields are derived from signal [MC](#) samples. These factors are all connected by the following relation:

$$\epsilon_{\mathcal{A}} = A_{\text{WW}} \cdot C_{\text{WW}} = \frac{N_{\text{WW}} (\text{passed event selection})}{N_{\text{WW}} (\text{total generated signal events})} \quad (4.9)$$

which effectively encapsulates the extrapolation from the fiducial region, where the measurement is performed, to the full phase space. A clear advantage of this approach is that fiducial [cross-sections](#) are less dependent on the [MC](#) correction factors and give overall smaller uncertainties. This is especially helpful since the signal and background modelling is specifically tailored to the particular experiment anyway. However, results not extrapolated from the fiducial phase space can only be used for direct comparison within the same experiment.

4.1.2 Efficiencies and weights

The raw [MC](#) description does not correspond to the measured data exactly as it does not inherently contain a perfect description of the detector. These [MC](#) corrections are implemented for all [ATLAS](#) analyses through centrally provided performance packages developed to address specific aspects of data/[MC](#) disagreements. These usually take form of some sort of event re-weighting that is applied on [MC](#) samples. The total [MC](#) event weight is combined together from:

$$w_{\text{event}} = w_{\text{generator}} \cdot w_{\text{pileup}} \cdot w_{\text{PDF}} \cdot w_{\text{trigger}} \cdot w_{\text{electrons}} \cdot w_{\text{muons}} \cdot w_{\text{jets}} \quad (4.10)$$

where each weight matches with a specific source:

- $w_{\text{generator}}$ corresponds to [Monte Carlo](#) generator weights produced by some generators, e.g. [MC@NLO](#),
- w_{PDF} represents the weights assigned when re-weighting between the generator PDF sets in the analysis. In the $\sqrt{s} = 8$ TeV analysis we perform PDF re-weighting on Z + jets samples as described in [section 4.3.4](#),

- ▶ w_{pileup} represents event weights that are used to re-weight MC distributions to the actual pile-up conditions in data (section 4.3.3),
- ▶ w_{trigger} accounts for the differences in trigger efficiencies modelled in data and MC (section 4.4)
- ▶ w_{muons} weights given by the reconstruction and isolation efficiency of muons in the event (section 4.5.1),
- ▶ $w_{\text{electrons}}$ weights given by the reconstruction and isolation efficiency of electrons in the event (section 4.5.2),
- ▶ w_{jets} weight given by the reconstruction and isolation efficiency of jets (section 4.5.3). These weights are not used in the nominal selection in our analysis, only in background estimates using flavour tagging.

The generator, PDF and pile-up weights are generally referred to as cross-section weights and are determined as a part of the MC modelling and will be discussed in a separate section 4.3. The vast majority of detector related weights are determined via dedicated studies using the tag-and-probe method. We are going to discuss the detector in section 4.5.

4.2 Event selection

This section presents the selection criteria (i.e. *cuts*) used in both 7 TeV and 8 TeV analyses, along with the event yields for data and MC for each cut (commonly referred to as *cut-flow*). The cut effects are also presented graphically at different selection stages for relevant kinematic distributions.

The analysis includes three final states: $e^+e^- \cancel{E}_T$, $\mu^+\mu^- \cancel{E}_T$ and $e^\pm\mu^\mp \cancel{E}_T$ with the event selection cuts optimised by maximising the signal to background ratio for WW detection in each channel, see below. The event selection criteria differs between the same flavour (e^+e^- , $\mu^+\mu^-$) and combined flavour ($e^\pm\mu^\mp$) channels in cut values and specifically in the application of Z-veto cut which is required only for same flavour events. The dataset is obtained using both Muons and Egamma data streams where duplicate events are removed, see section 4.5.5.

The preselection of $WW \rightarrow \ell^+ \nu \ell^- \bar{\nu}$ candidate events follows from standard recommendation by data quality and performance groups for all di-boson analyses in ATLAS. A significant part of the thesis is dedicated to the discussion of this selection, see sections 4.4 to 4.6. In summary, these requirements are:

1. **Data quality:** Events must be flagged as good for physics in the `GoodRunsList`, reflecting luminosity blocks with fully functional sub-detectors during data taking (commonly referred to as `AllGood GRL`)
2. **Event cleaning:** Removal of problematic events in data and MC as detailed in section 4.6.2. This step includes the removal of events affected by noise bursts and data corruption or containing incomplete jets.
3. **Primary vertex selection:** The primary vertex (vertex with largest $\sum p_T^2$) is required to be reconstructed with at least 3 good associated tracks (vertex reconstruction is discussed in section 3.3.2)
4. **Trigger selection:** Accept events selected by the combination of lowest unprescaled electron and muon triggers. For 7 TeV only single-lepton triggers were used. The 8 TeV analysis

implements dilepton [triggers](#) in the same flavour channels and a logical OR of dilepton and single lepton [triggers](#) in the combined channel ($e^\pm\mu^\mp$). [Trigger](#) selection is described in [section 4.4](#) in more detail (see also the overview [tables 4.8](#) and [4.9](#)).

5. **Object overlap removal:** Overlapping objects are removed as described in [section 4.5.6](#), for short summary see [table 4.1](#).

Overlap	Analysis at 7 TeV	Analysis at 8 TeV
e^\pm/e^\pm	$\Delta R < 0.1$, drop lower p_T	—— ——(implemented at reconstruction)
μ^\pm/e^\pm	$\Delta R < 0.1$, drop electron	—— ——
e^\pm/jet	$\Delta R < 0.3$, drop jet	—— ——
μ^\pm/jet	not considered	$\Delta R < 0.3$, drop muon

Table 4.1: Object overlap removal considered in each analysis

6. **Dilepton selection:** An event is selected if it has exactly two isolated, oppositely charged leptons with $p_T > 25$ (20) GeV for leading (trailing) leptons respectively. The leptons need to be well defined using the criteria described in [sections 4.5.1](#) and [4.5.2](#). These requirements ensure that the considered lepton is on or close enough to the [trigger](#) plateau and enables the use of the official [trigger](#) scale factors. It also strongly reduces the W + jets and [QCD](#) backgrounds due to the p_T dependence of the muon fake rate.
7. **Trigger matching:** The selected leptons have to be matched to the [trigger](#) that fired the event. At 7 TeV, at least one lepton has to be matched to a single-lepton [trigger](#). In 8 TeV analysis, both leptons have to be matched to the dilepton [trigger](#) in the same flavour channels. In the $e^\pm\mu^\mp$ channel the leptons have to be matched to either of the available [triggers](#), i.e. at least one of the leptons with $p_T > 25$ GeV has to be matched to any of the single lepton [triggers](#) or both have to be matched to the dilepton [trigger](#).

After the preselection, the dominant contribution $>99\%$ in the same flavour channels comes from the inclusive $Z/\gamma^* \rightarrow \ell\ell$ process. The WW signal only contributes $\approx 0.14\%$ (resp. $\approx 0.07\%$) of the selected events at 8 TeV (resp. 7 TeV). For the $e^\pm\mu^\mp$ final state, the WW signal contributes already 11.70% (10.40%), where the major background contributions of 60.70% (50.30%) come from $t\bar{t}$ /single-top, 22.60% (35.40%) from $Z \rightarrow \tau^+\tau^-$ and [QCD](#) background from W + jets and di-jets contribute additional 5% (2.70% at 7 TeV). These numbers are based on [MC](#) studies.

The following figures show the kinematic distributions at the preselection level detailed above. The [MC](#) has been normalised to the integrated luminosity of the dataset (20.28 fb^{-1} at 8 TeV, 4.64 fb^{-1} at 7 TeV) using NLO [SM cross-sections](#) as outlined given in [tables 4.6](#) and [4.7](#) and [tables in appendix A](#). [Figure 4.5](#) shows transverse momentum of the dilepton system $p_T(\ell\ell)$, the leading and sub-leading lepton p_T distributions along with dilepton invariant mass $m_{\ell\ell}$ and the transverse mass m_T at 8 TeV. Data and [MC](#) agree well in all these distributions for preselected dilepton events, illustrating good understanding of our backgrounds. More distributions at preselection level for [missing transverse energy](#) and jet multiplicity are shown in [fig. 4.6](#), lepton [pseudorapidity](#) and azimuthal angle are shown in [fig. 4.7](#).

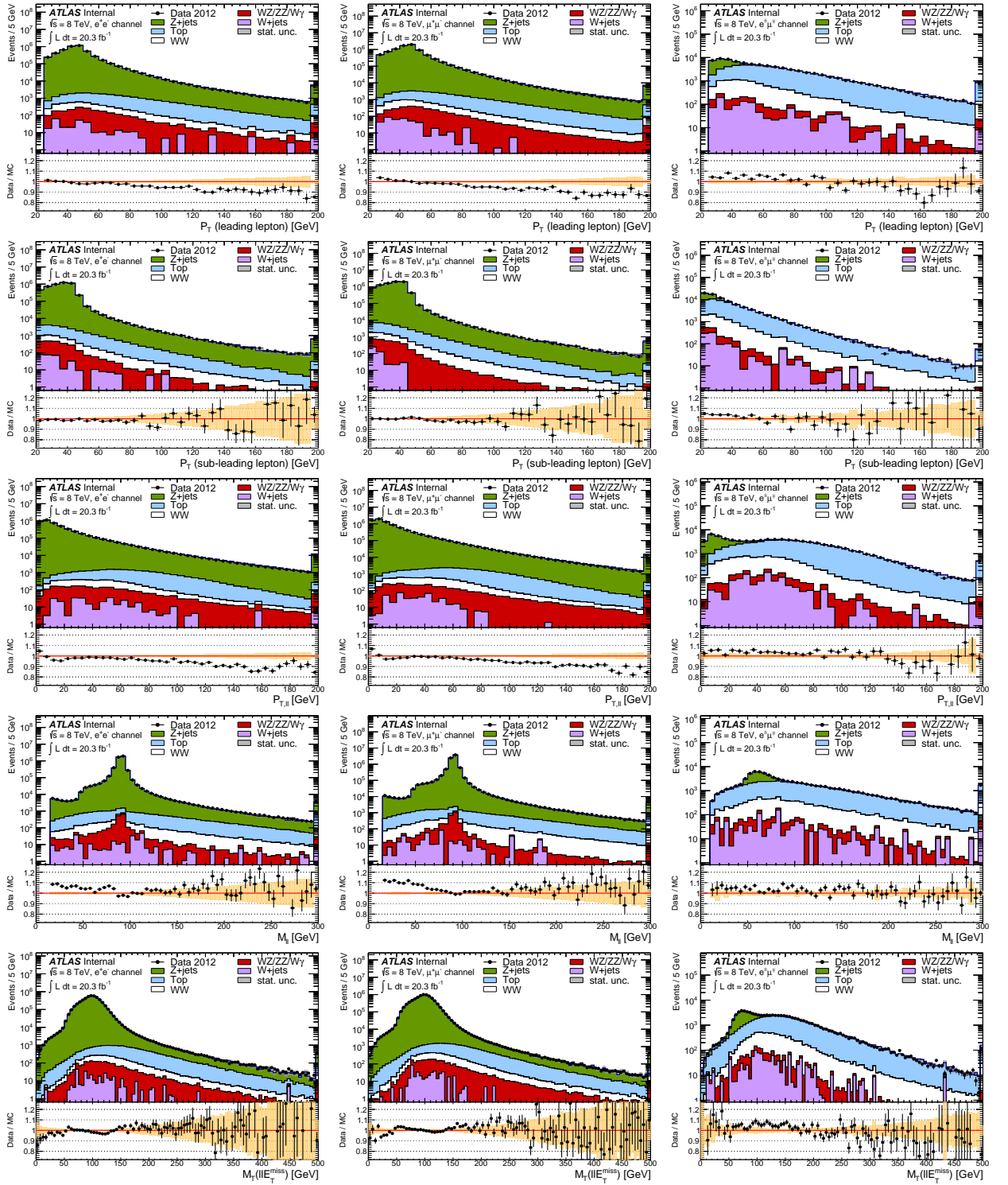


Figure 4.5: Kinematic distributions of the selected events at 8 TeV after preselection stages and after the cut on the invariant mass to account for the low mass spectrum not described by MC. Data are shown on top the signal and background processes as predicted by Monte-Carlo and scaled to 20.28 fb^{-1} . The plots correspond to the e^+e^- , $\mu^+\mu^-$ and $e^\pm\mu^\mp$ channels from left to right. The top row shows invariant mass $m_{\ell\ell}$ of the selected leptons, the second (resp. third) row the transverse momentum p_T of the leading (resp. trailing) lepton. The forth row shows the transverse momentum of the di-lepton system $p_T(\ell\ell)$ followed by the transverse mass m_T .

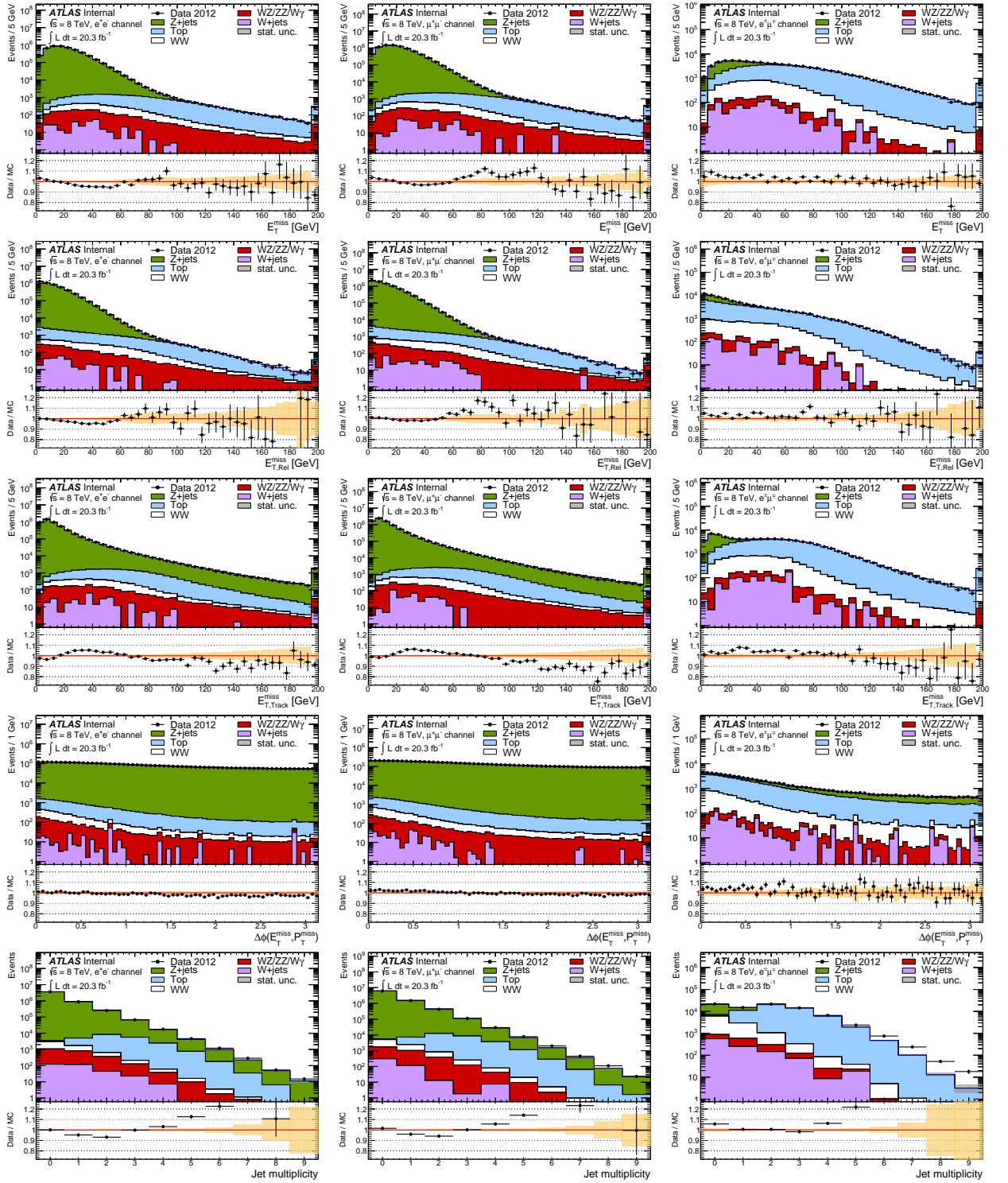


Figure 4.6: Kinematic distributions of the selected events at 8 TeV after preselection stages and after the cut on the invariant mass to account for the low mass spectrum not described by MC. Data are shown on top the signal and background processes as predicted by Monte-Carlo and scaled to 20.28 fb^{-1} . The plots correspond to the e^+e^- , $\mu^+\mu^-$ and $e^\pm\mu^\mp$ channels from left to right. The top row shows the missing transverse energy E_T followed by its projection $E_{T,\text{Rel}}$. The third row shows the track-based p_T . The forth row shows the azimuthal angle difference $\Delta\phi(E_T, p_T)$ and the last row shows the jet multiplicity.

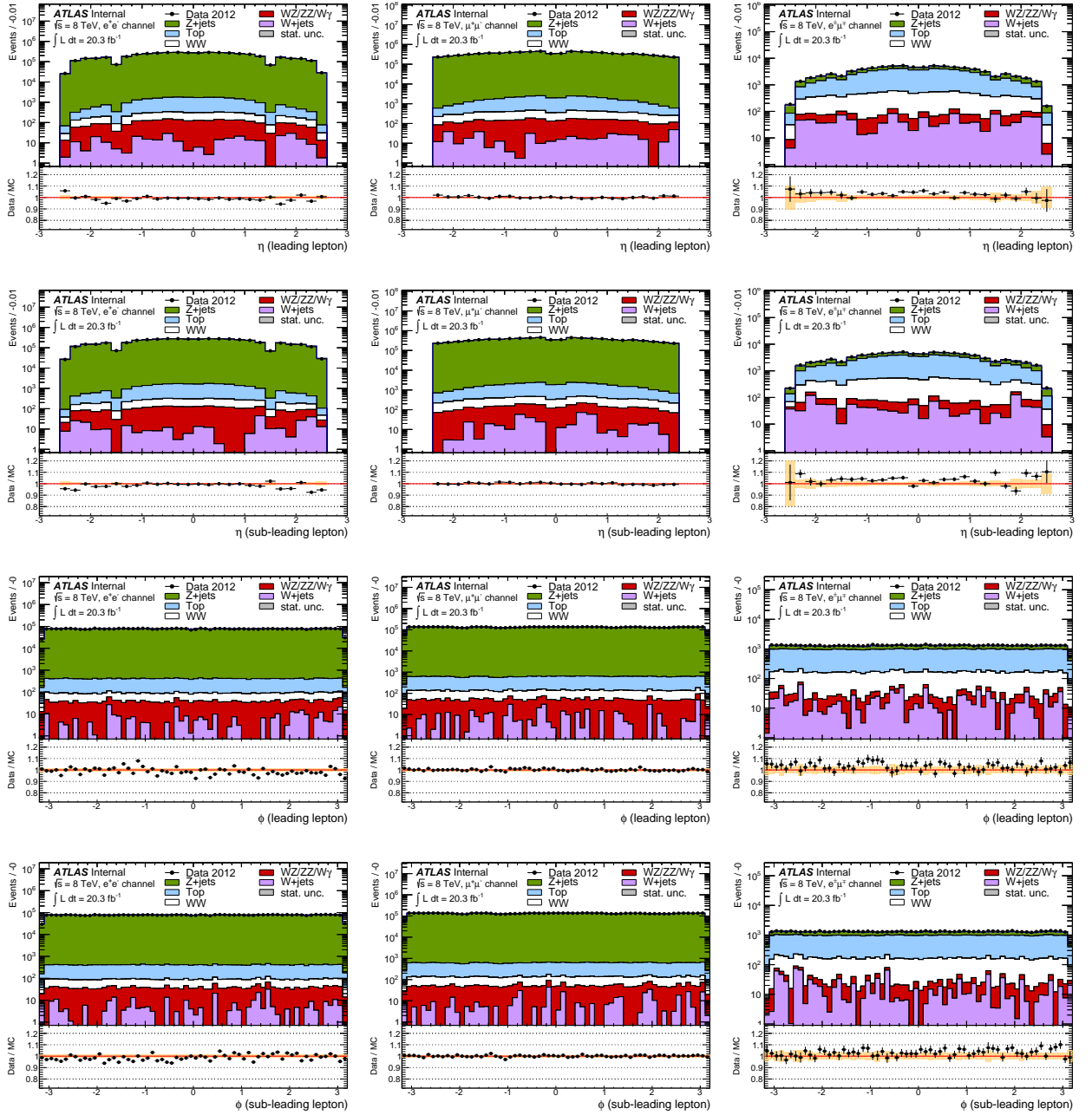


Figure 4.7: Kinematic distributions of the selected events at 8 TeV after preselection stages and after the cut on the invariant mass to account for the low mass spectrum not described by MC. Data are shown on top the signal and background processes as predicted by Monte-Carlo and scaled to 20.28 fb^{-1} . The plots correspond to the e^+e^- , $\mu^+\mu^-$ and $e^\pm\mu^\mp$ channels from left to right. In case of the e^+e^- and $\mu^+\mu^-$ channels the first row shows the pseudorapidity η of the leading lepton, the second the pseudorapidity of the trailing lepton. Third and bottom row show the corresponding ϕ distributions. For the $e^\pm\mu^\mp/\mu^\pm e^\mp$ channels the electron and the muon are shown instead of the leading and sub-leading lepton, respectively. These plots were showing the most difference between before and after PDF reweighting.

4.2.1 Differences between the 7 TeV and 8 TeV analysis

Throughout the text the $\sqrt{s} = 7$ TeV and 8 TeV analyses are going to be presented side-by-side as the analysis procedure is largely similar. However, the event selection for 8 TeV has changed to address the new data-taking conditions, especially the increase in [pile-up](#) (see [section 4.3.3](#)). We implemented new cuts on kinematic variables previously unused at 7 TeV. Specific differences will be clearly noted when referred to. A short summary follows:

1. The signal model was switched from [MC@NLO](#) to [POWHEG](#) at 8 TeV as it gives better description of data, see discussion in [section 4.3](#). The $H \rightarrow W^+W^-$ sample with a 125 GeV [Higgs boson](#) sample was included into the signal model (see [tables 4.6](#) and [4.6](#)).
2. The $\sqrt{s} = 7$ TeV analysis used single-lepton [triggers](#) while the 8 TeV analysis switched to di-lepton [triggers](#) for the same flavour channels and the logical OR of single-lepton and di-lepton [triggers](#) in the combined flavour channel to recover efficiency lost due to 2012 run conditions (see [section 4.4](#)).
3. The lepton definition has been altered in the 8 TeV to match that of the $H \rightarrow W^+W^-$ group mainly, see [sections 4.5.1](#) and [4.5.2](#). This also allows us to share efficiency studies and scale factors across groups.
4. Good jets are defined using two jet algorithms in the 7 TeV analysis: [AntiKt4EM](#) collection is used for physics objects selection while the [AntiKt4LC](#) collection is used in \cancel{E}_T reconstruction. This is the recommended way to handle jets in 7 TeV in 2011. In 2012 the recommendation changed to use only the [AntiKt4LC](#) jets collection for both the object selection and the \cancel{E}_T reconstruction. Following the recommendations from the jet and \cancel{E}_T performance groups, a cut on the jet vertex fraction $|JVF| > 0.5$ has been introduced. As recommended, the JVF cut is only applied to jets with $E_T < 50$ GeV and $|\eta| < 2.4$.
5. The $p_T(\ell\ell)$ cut has been dropped in favour of missing transverse momentum in the barrel region \cancel{p}_T in order to further suppress Z + jets contamination. The azimuthal angle difference between the original \cancel{E}_T and \cancel{p}_T vectors is used: $\Delta\phi(\cancel{E}_T, \cancel{p}_T)$ is additionally used in the same flavour channels (e^+e^- , $\mu^+\mu^-$) since they required further cleaning.

Both analyses follow the recommendations of [ATLAS](#) performance groups and use the centrally provided set of corrections. These will now be described in detail in the following section.

4.2.2 Final selection

The final WW event selection cuts were chosen based on the cut optimisation and the past understanding of the cut values used at $\sqrt{s} = 7$ TeV. In summary, the selection looks as follows:

8 TeV selection

- 1) Invariant mass of the dilepton pair: $m_{\ell\ell} > 15$ (10) GeV for $e^+e^-/\mu^+\mu^-$ ($e^\pm\mu^\mp$) events to further remove dijet events and the low mass spectrum not modelled by [MC](#).
- 2) Z-veto: $|m_{\ell\ell} - m_Z| > 15$ GeV for the e^+e^- and $\mu^+\mu^-$ channels to remove events from $Z \rightarrow \ell\ell$.

- 3) Relative missing transverse energy: $\cancel{E}_{T,\text{Rel}} > 45$ (15) GeV for the $e^+e^-/\mu^+\mu^-$ ($e^\pm\mu^\mp$) channels, respectively. The variable is defined in section 4.5.4.1. Figure 4.9 shows the $\cancel{E}_{T,\text{Rel}}$ distributions for ee , $\mu\mu$ and $e\mu$ channels just before the $\cancel{E}_{T,\text{Rel}}$ cut is applied.
- 4) Missing transverse momentum: $\cancel{p}_T > 45$ (25) GeV for $e^+e^-/\mu^+\mu^-$ ($e^\pm\mu^\mp$) channels to further suppress the Z + jets contributions. This variable is more pileup robust than $p_T(\ell\ell)$, more details in section 4.7.1.2 above.
- 5) Azimuthal angle between missing transverse energy and missing transverse momentum: $|\Delta\phi(\cancel{E}_T, \cancel{p}_T)| < 0.3$ (0.6) for $e^+e^-/\mu^+\mu^-$ ($e^\pm\mu^\mp$) channels. This variable is another powerful discriminant against Z + jets contamination, more so than the cut on $p_T(\ell\ell)$ previously used in the analysis before (see below). Figure 4.12 shows the distribution in the 0 jet bin just before the final cut stage.
- 6) Jet-veto: The number of good jets ($E_T > 25$ GeV, $|\eta| < 4.5$ and $|JVF| > 0.5$) is required to be zero. Jet vertex fraction is only applied to jets with $E_T < 50$ GeV and $|\eta| < 2.4$. Figure 4.8 shows the jet multiplicity distributions before the jet veto cut is applied to the selected WW candidate events. This cut removes very effectively inclusive top events with leptonic decay modes.

7 TeV selection

The original selection for the analysis at $\sqrt{s} = 7$ TeV follows from a series of studies on smaller datasets [ATL12c] [ATL11c] [ATL11b]:

- 1) The invariant mass of the dilepton pair: $m_{\ell\ell} > 15$ (10) GeV for $e^+e^-/\mu^+\mu^-$ ($e^\pm\mu^\mp$) for identical reasons as above.
- 2) Z-veto: $|m_{\ell\ell} - m_Z| > 15$ GeV for the e^+e^- and $\mu^+\mu^-$ as above.
- 3) $\cancel{E}_{T,\text{Rel}} > 45$ (25) GeV for the $e^+e^-/\mu^+\mu^-$ ($e^\pm\mu^\mp$) channels, respectively. The cut in the combined flavour channel is harder than at 8 TeV.
- 4) Jet veto: The number of good jets ($E_T > 25$ GeV, $|\eta| < 4.5$) is required to be zero.
- 5) $p_T(\ell\ell) > 30$ GeV for all three channels. This cut helps to reduce Z + jets background significantly in the 2011 data taking conditions. Higher threshold in the same-flavour channels is required to effectively suppress contamination.

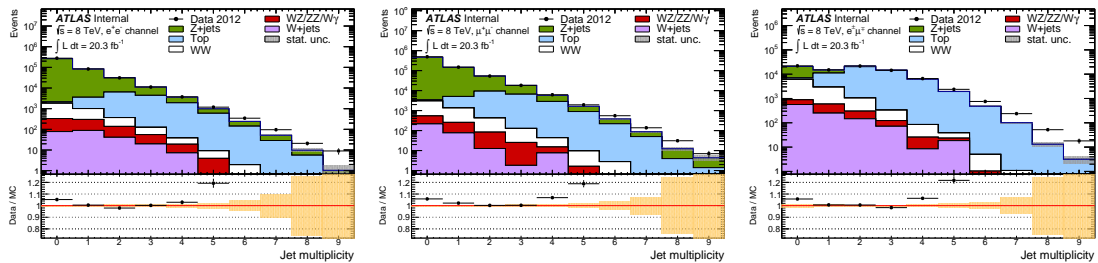


Figure 4.8: Jet multiplicity distribution after Z veto for the e^+e^- (left) and $\mu^+\mu^-$ (middle) and $e^\pm\mu^\mp$ channels. Data are shown together with the processes predicted by Monte-Carlo and scaled to 20.3 fb^{-1} . Statistical uncertainties are shown as grey bands in the main plot or as orange bands on the ratio plot.

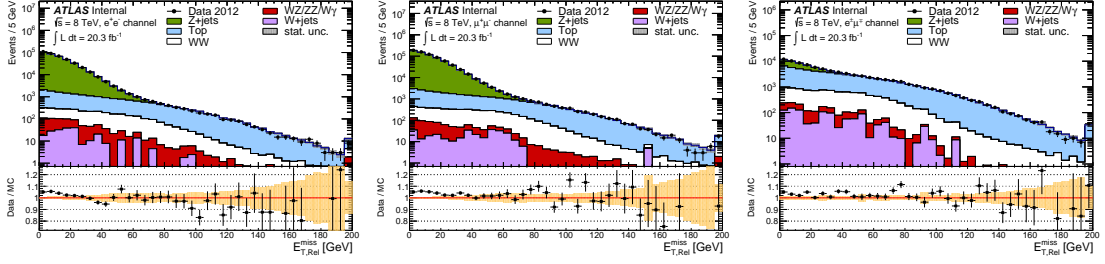


Figure 4.9: Relative missing transverse energy $\vec{E}_{T,\text{Rel}}$ distribution after Z veto for the e^+e^- (left) and $\mu^+\mu^-$ (middle) and $e^\pm\mu^\mp$ (right) channels. Data are shown together with the processes predicted by Monte-Carlo and scaled to 20.3 fb^{-1} . Statistical uncertainties are shown as grey bands in the main plot or as orange bands on the ratio plot.

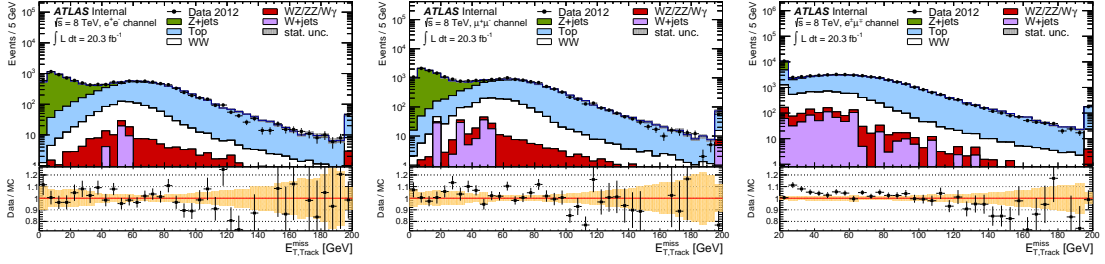


Figure 4.10: Missing transverse momentum \vec{p}_T distribution after $\vec{E}_{T,\text{Rel}}$ cut for the e^+e^- (left) and $\mu^+\mu^-$ (middle) and $e^\pm\mu^\mp$ (right) channels. Data are shown together with the processes predicted by Monte-Carlo and scaled to 20.3 fb^{-1} . Statistical uncertainties are shown as grey bands in the main plot or as orange bands on the ratio plot.

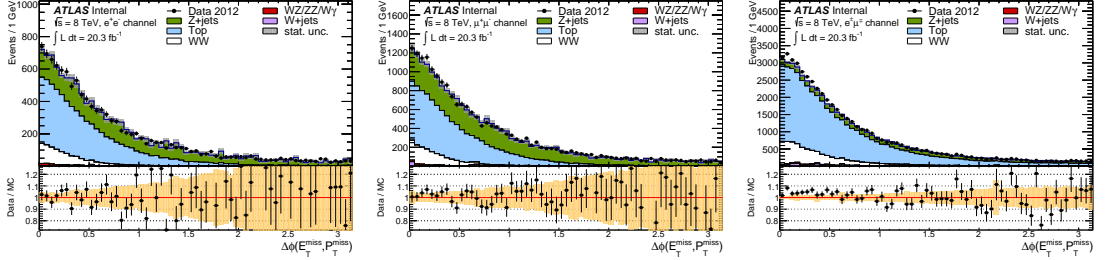


Figure 4.11: Azimuth angle between missing transverse energy and momentum $\Delta\phi(\vec{E}_T, \vec{p}_T)$ distribution after $\vec{E}_{T,\text{Rel}}$ cut and in the zero jet bin. The channels follow from ee (left), $\mu\mu$ (middle) to $e\mu$ channel on the right. Data are shown together with the processes predicted by Monte-Carlo and scaled to 20.3 fb^{-1} . Statistical uncertainties are shown as gray bands in the main plot or as orange bands on the ratio plot.

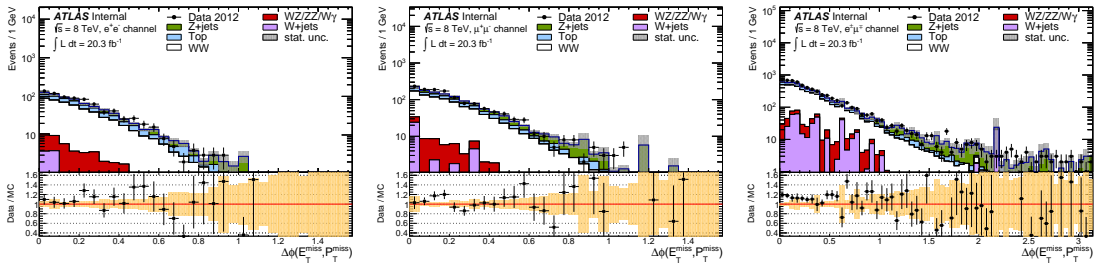


Figure 4.12: Azimuthal angle between missing transverse energy and momentum $\Delta\phi(\vec{E}_T, \vec{p}_T)$ distribution after \vec{p}_T cut and in the zero jet bin. The channels follow from e^+e^- (left), $\mu^+\mu^-$ (middle) to $e^\pm\mu^\mp$ channel on the right. Data are shown together with the processes predicted by Monte-Carlo and scaled to 20.3 fb^{-1} . Statistical uncertainties are shown as gray bands in the main plot or as orange bands on the ratio plot.

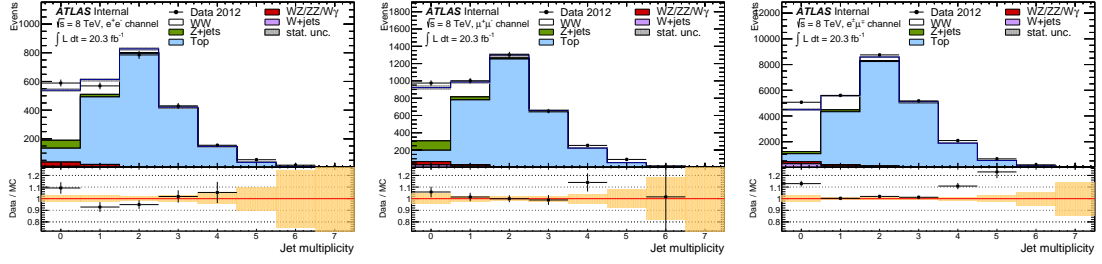


Figure 4.13: Jet multiplicity distribution before the jet veto for the e^+e^- (left) and $\mu^+\mu^-$ (middle) and $e^\pm\mu^\mp$ (right) channels. Data are shown together with the processes predicted by Monte-Carlo and scaled to 20.3 fb^{-1} . Statistical uncertainties are shown as gray bands in the main plot or as orange bands on the ratio plot.

The kinematic distribution for WW candidate events after all selection cuts are shown in [figs. 4.20](#) and [4.21](#). [Figure 4.20](#) shows the **transverse momenta** of the leading and trailing leptons as well as the **transverse momentum** of the di-lepton system $p_T(\ell\ell)$ and **invariant mass**-NoValue- and **transverse mass** of the system. [Figure 4.21](#) shows the distributions of the missing energy expressed as \cancel{E}_T , $\cancel{E}_{T,\text{Rel}}$ and \cancel{p}_T . The azimuthal angle between **missing transverse energy** and **missing transverse momentum** \cancel{p}_T $\Delta\phi(\cancel{E}_T, \cancel{p}_T)$ is also shown. Black points represent the recorded data and stacked histograms are from **Monte Carlo** predictions for signal and backgrounds.

4.2.3 Event selection cut-flow

The WW event selection cut-flow for data is shown in [tables 4.2](#) and [4.3](#) provides the number of observed WW candidates in data per each channel and inclusively, compared to the **MC** expectations for WW signal and backgrounds from different sources. We observed 6636 candidate events after final selection in 20.28 fb^{-1} of data while we expect 5884.9 ± 37.5 events from the **Monte Carlo** prediction, including 4218.8 ± 11.7 expected signal events.

At 7 TeV in 4.64 fb^{-1} we observed 1325 candidate events after the final selection which is again consistent with the expected 1181.60 events in **MC**, including 823.60 expected **SM** WW events and 358.00 estimated background events.

Cuts	e^+e^-	$\mu^+\mu^-$	$e^\pm\mu^\mp$	Inclusive
2 leptons	6 011 503	10 414 698	167 682	16 593 883
opposite-sign	5 996 645	10 410 426	157 280	16 564 351
ℓp_T , trigger-match	4 945 211	8 406 743	84 698	13 436 652
$m_{\ell\ell} > 15$ (10) GeV	4 918 726	8 357 583	83 042	13 359 351
$ m_{\ell\ell} - m_Z > 15$ GeV	412 853	721 978	–	1 217 873
$\cancel{E}_{T,\text{Rel}} > 45$ (15) GeV	11 594	19 887	52 142	83 623
$\cancel{p}_T > 45$ (20) GeV	5762	9152	43 718	58 632
$\Delta\phi(\cancel{E}_T, \cancel{p}_T) < 0.3$ (0.6)	2613	4291	27 591	34 495
Jet veto	594	975	5067	6636

Table 4.2: Event selection cut-flow for data collected in 2012 at 8 TeV for 20.28 fb^{-1} split in channels. For the $m_{\ell\ell}$, $\cancel{E}_{T,\text{Rel}}$, \cancel{p}_T and $\Delta\phi(\cancel{E}_T, \cancel{p}_T)$ cuts, two cut values are presented in first column, with the first one for same flavour channel and the second one for $e^\pm\mu^\mp$ channel.

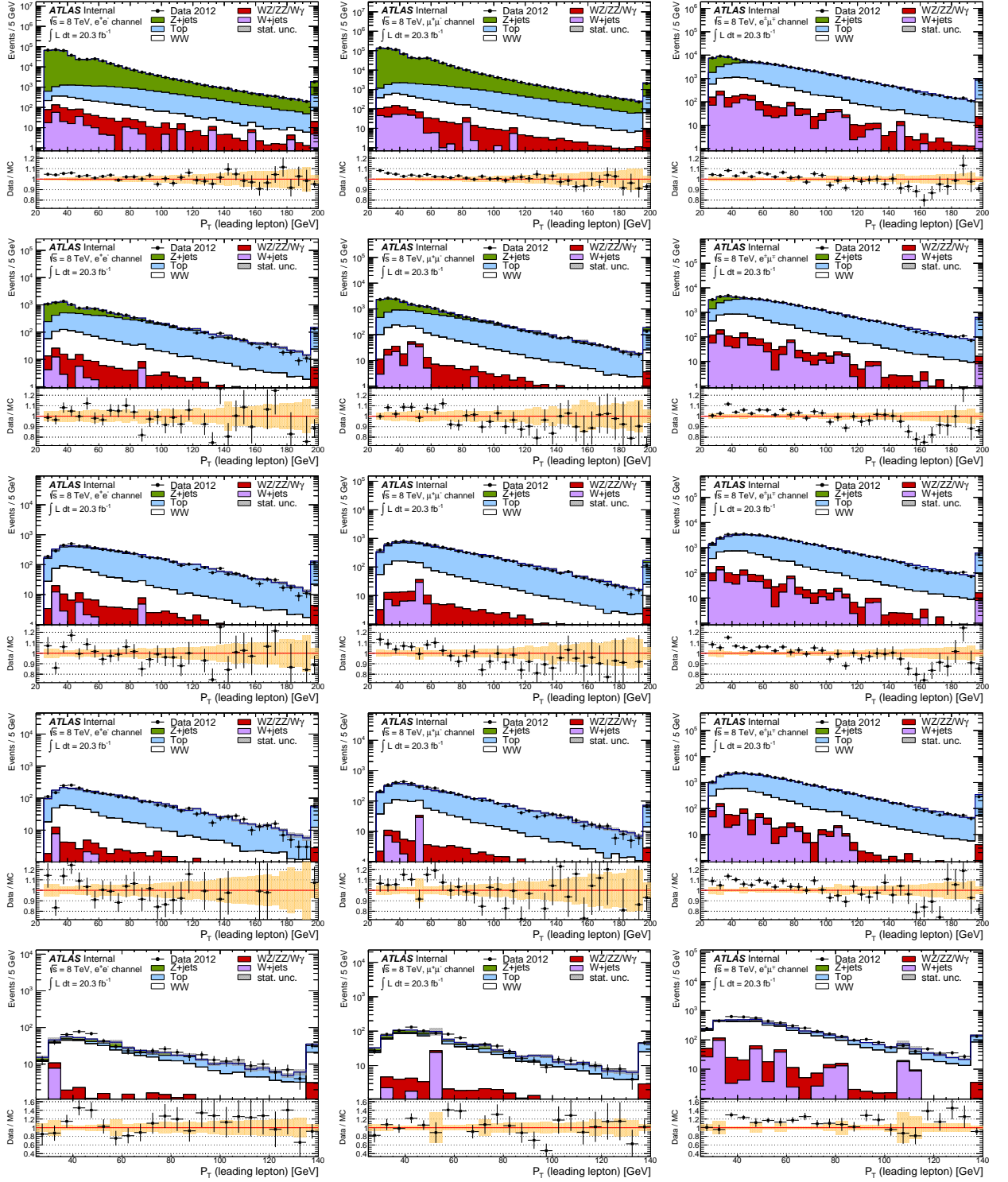


Figure 4.14: Invariant mass of the selected events at 8 TeV after various stages of the cut flow. The top row shows invariant mass $m_{\ell\ell}$ after removing the Z mass window. The second row shows it after the cut on missing transverse energy projection $\cancel{E}_{T,Rel}$, the third row shows after the cut on p_T . The fourth row shows the $m_{\ell\ell}$ distribution after the cut on the azimuthal angle difference $\Delta\phi(\cancel{E}_T, p_T)$ and the last shows the distribution after the jet veto cut, i.e. the final stage. Starting from the third stage, the bin-by-bin systematic error on the signal sample is included. The MC is scaled to 20.28 fb^{-1} .

Final State	e^+e^- channel	$\mu^+\mu^-$ channel	$e^\pm\mu^\mp$ channel	inclusive
Observed Events	594	975	5067	6636
Total MC prediction (S+B)	553.2 ± 13.0	903.9 ± 11.3	4427.9 ± 33.3	5884.9 ± 37.5
MC WW signal	349.6 ± 3.3	614.4 ± 4.5	3254.8 ± 10.3	4218.8 ± 11.7
Top	96.9 ± 4.8	131.4 ± 6.1	625.9 ± 12.5	854.2 ± 14.7
Z + jets	55.3 ± 6.3	106.0 ± 7.0	164.6 ± 15.4	326.0 ± 18.1
W + jets	21.6 ± 9.7	13.6 ± 4.3	225.3 ± 24.4	260.5 ± 26.6
Dibosons	29.8 ± 1.6	38.5 ± 1.3	157.3 ± 4.1	225.6 ± 4.6
Total Background	203.6 ± 12.6	289.5 ± 10.3	1173.1 ± 31.7	1666.1 ± 35.6

Table 4.3: Summary of observed data events and expected signal and background contributions as predicted by MC in the three channels and their combined results at $\sqrt{s} = 8$ TeV. The Monte Carlo yields are normalized to an integrated luminosity of 20.28 fb^{-1} . Only statistical uncertainties are shown. All calculations are precise to two decimal places, while the tables are rounded to one.

4.3 Signal and background modelling

The full list of samples including their cross-sections and corresponding generator information are listed in appendix A. In this section we are going to focus on signal and background Monte Carlo modelling, associated data driven methods employed for background estimates are discussed in section 4.9. The sample description follows closely the details provided in the respective support notes [ATL13c] [ATL14i].

4.3.1 Signal samples

For signal, the major contribution comes from the $q\bar{q} \rightarrow WW \rightarrow \ell^+\nu\ell^-\bar{\nu}$ process. The $q\bar{q}$ initial state and the subsequent combination of final states is modelled by:

- 7 TeV analysis: MC@NLO [FW02] [Fri+14] with parton showering interfaced through Jimmy/Herwig [Cor+00]
- 8 TeV analysis: POWHEG [Nas04; FNO07] with parton showering interfacing Pythia [Sjö+00] as it provided a better description of data.

Both generators incorporate the NLO QCD matrix elements and CT10 parton density function (PDF). The production via gluon-gluon fusion $gg \rightarrow WW \rightarrow \ell^+\nu\ell^-\bar{\nu}$ with the resulting W bosons decaying leptonically is modelled by the MC generator gg2ww [Bin+06] and the CT10 PDF set, interfaced to Herwig/Jimmy [Cor+00] for parton showering and underlying event modelling.

The gauge-boson decays into τ leptons are included in the MC event generator and these leptons decay to all the possible final states. There is a difference between the $\sqrt{s} = 7$ TeV and 8 TeV analyses in the treatment of the final states with respect to the detector fiducial volume, see section 4.7.4.

In the 7 TeV analysis we compared the CT10 cross-section with the MSTW2008 [Mar+09] prediction. The resulting difference was $\approx 0.05\%$ for the $q\bar{q} \rightarrow WW \rightarrow \ell^+\nu\ell^-\bar{\nu}$ process which is a negligible effect. No change was observed for the $gg \rightarrow WW \rightarrow \ell^+\nu\ell^-\bar{\nu}$ process. We extended the study for the 8 TeV analysis to incorporate predictions from NNPDF 2.3 [Bal+10]

and ATLAS-epWZ12 [ATL12b] and found uncertainties to the cross-section as high as 5 % which exceeds the quoted uncertainties estimated by CT10.

The signal combination and normalization is derived using MCFM and CT10 PDFs in order to remain consistent with other di-boson analyses in ATLAS and prepare for future combinations with cross-section measurements from CMS. The re-normalisation (μ_R) and factorisation (μ_F) scales are set dynamically to the invariant mass of the WW system: $m_{WW}/2$. The signal yields:

$$\sigma_{q\bar{q}/gg}(7 \text{ TeV}) = 44.7^{+2.1}_{-1.9} \text{ pb}, \quad (4.11)$$

$$\sigma_{q\bar{q}/gg}(8 \text{ TeV}) = 54.6^{+2.5}_{-2.2} \text{ pb}, \quad (4.12)$$

where uncertainties are derived from the variation of re-normalisation (μ_R) and factorisation (μ_F) scales by a factor of two with the CT10 PDF uncertainties added in quadrature, see table 4.4.

\sqrt{s}	Scale uncertainty	PDF uncertainty	Total uncertainty
7 TeV	$\begin{pmatrix} +3.6\% \\ -2.5\% \end{pmatrix}$	$\begin{pmatrix} +3.1\% \\ -3.4\% \end{pmatrix}$	$\begin{pmatrix} +4.8\% \\ -4.2\% \end{pmatrix}$
8 TeV	$\begin{pmatrix} +3.3\% \\ -2.4\% \end{pmatrix}$	$\begin{pmatrix} +3.0\% \\ -3.2\% \end{pmatrix}$	$\begin{pmatrix} +4.5\% \\ -4.0\% \end{pmatrix}$

Table 4.4: Theoretical uncertainties on the signal cross-section. The PDF uncertainties are quoted at 68 % confidence level.

Given the fact that the experimental evidence for the Higgs boson has been presented in 2011 [ATL12e] [CMS12], the 8 TeV analysis includes the $H \rightarrow W^+W^-$ decay mode into the signal model. The SM Higgs boson is produced via the gluon-gluon fusion process, $gg \rightarrow H \rightarrow WW$, more commonly referred to as *resonant production* of the WW pair. The calculation is performed using MSTW2008 PDF at NNLO assuming $m_H = 125 \text{ GeV}$. [The13] Uncertainties on the PDF, scale and branching fraction are included.

Some higher order contributions to the WW production cross-section are not included in the model. The contribution from $\gamma\gamma$ -induced WW production is expected to be small, as are the contributions from Double parton scattering and Vector boson fusion due to small production rate. For the 7 TeV analysis are below 0.10 % and as such are not considered. The effect of electroweak corrections on the WW production cross-section is found to be about -1% , see Bie+12. Table 4.5 gives the summary of all contributions investigated in the 8 TeV analysis along with the neglected processes. Nota bene, there is an ongoing effort to provide an NNLO-based calculation of the $q\bar{q} \rightarrow WW \rightarrow \ell^+ \nu \ell^- \bar{\nu}$ process as shown by S. Dawson, Ian M. Lewis, and Mao Zeng [DLZ13] and is expected to provide an increase of up to $\approx 3 \%$ with respect to the NLO prediction.

Tables 4.6 and 4.7 summarize all the WW MC signal samples for the 7 TeV and 8 TeV case with their corresponding cross-sections, the generator names, generator level filter efficiencies and total number of events. The resulting NLO theoretical cross-section at the given energies is: $\sigma_{\text{NLO}}(8 \text{ TeV}) = 58.7^{+3.0}_{-2.7} \text{ pb}$ Separate contributions to the 8 TeV cross-section are summarized in table 4.5 including neglected contributions coming from various sources.

Predicted contributions to the WW production cross-section		
Process	Contribution to the σ [pb]	Calculation
$q\bar{q} \rightarrow WW \rightarrow \ell^+ \nu \ell^- \bar{\nu}$	$53.2^{+2.2}_{-2.2}$	NLO MCFM [CEW14]
$gg \rightarrow WW \rightarrow \ell^+ \nu \ell^- \bar{\nu}$	$1.4^{+0.3}_{-0.2}$	LO MCFM [CEW14]
$gg \rightarrow H \rightarrow WW$	4.1 ± 0.5	NNLO QCD [The13]
Neglected contributions to the WW production cross-section		
$gg \rightarrow WW$	$< +2.8$	see [Bon+13]
WW	-0.5	see [Bie+12]
$\gamma\gamma \rightarrow WW$	$+0.5$	see [Bil+13]
DPS	$< +0.5$	see [Blo+13]
VBF	$+0.04$	see [JOZ06]

Table 4.5: Summary of possible contributions to the WW final state considered for the analysis at $\sqrt{s} = 8$ TeV.

4.3.2 Background samples

The following [Standard Model](#) processes effectively mimic the diboson final states: The [cross-section](#) σ , filter efficiencies ϵ_{filter} , total number of events N_{MC} and generator names are provided in the [appendix A](#). For LO generators the [cross-sections](#) are corrected to NLO or NNLO using the k-factors listed in the tables.

W + jets / Z + jets: Denotes [W/Z](#) production in association with jets, where the jet is misidentified as lepton and the apparent \cancel{E}_T arises from [pile-up](#). Both backgrounds have large cross sections, however requiring the presence of more than one lepton in the event is very effective in removing the W + jets contributions. The [Z](#) decays into two leptons which coupled with large fake [missing transverse energy](#) results in a significant background. In the $e^\pm \mu^\mp$ final state, the main contribution comes from the $Z/\gamma^* \rightarrow \tau\tau$, where the tau lepton decays to electron or muon while producing genuine \cancel{E}_T through the escaping neutrino. Samples from the [Alpgen](#) generator are used with the [Pythia](#) parton shower model for the [MC](#) model. These backgrounds are not well modelled by [MC](#), thus data driven methods are used to estimate fake leptons (pion, kaon, b-quark decay). The Z + jets samples are generated with [Alpgen](#) [Man+03] which implements the matrix elements at LO for both [QCD](#) and electroweak interactions.

Top-antitop ($t\bar{t} \rightarrow WbWb$) and **single-top** ($Wt \rightarrow WbW$) processes where the [W boson](#) from the top cascade decays along with jets. The decay products from both top-pair and single-top processes contain WW final states. These processes effectively mimics the prompt WW production in events where the jets fail to be reconstructed. The 8 TeV samples were generated by [MC@NLO](#), while for 7 TeV the [AcerMC](#) [KR13] generator was used to model the top process and all single top process while the [MC@NLO](#) [FW02] [Fri+14] generator was used to model the $t\bar{t}$ process. [Pythia](#) and [Herwig/Jimmy](#) are used for parton showering, respectively. At 8 TeV all samples are modelled by [MC@NLO](#) with the exception of t -channel single top events that are modelled using [AcerMC](#). Similarly to W + jets and Z + jets, this background is estimated using data driven methods.

Process	cross-section [fb]	ϵ_{filter}	N_{MC}	Generator
$q\bar{q} \rightarrow WW \rightarrow e^+ \nu e^- \nu$	510.48	1.0	141 723	MC@NLO
$q\bar{q} \rightarrow WW \rightarrow \mu^+ \nu \mu^- \nu$	510.48	1.0	140 628	MC@NLO
$q\bar{q} \rightarrow WW \rightarrow e^+ \nu \mu^- \nu$	510.48	1.0	141 486	MC@NLO
$q\bar{q} \rightarrow WW \rightarrow \mu^+ \nu e^- \nu$	510.48	1.0	141 365	MC@NLO
$q\bar{q} \rightarrow WW \rightarrow e^+ \nu \tau^- \nu$	510.48	1.0	141 466	MC@NLO
$q\bar{q} \rightarrow WW \rightarrow \mu^+ \nu \tau^- \nu$	510.48	1.0	141 502	MC@NLO
$q\bar{q} \rightarrow WW \rightarrow \tau^+ \nu \mu^- \nu$	510.48	1.0	141 488	MC@NLO
$q\bar{q} \rightarrow WW \rightarrow \tau^+ \nu e^- \nu$	510.48	1.0	141 372	MC@NLO
$q\bar{q} \rightarrow WW \rightarrow \tau^+ \nu \tau^- \nu$	510.48	1.0	141 406	MC@NLO
$gg \rightarrow WW \rightarrow e^+ \nu e^- \nu$	15.24	0.9895	10 000	gg2ww
$gg \rightarrow WW \rightarrow \mu^+ \nu \mu^- \nu$	15.24	0.9890	9999	gg2ww
$gg \rightarrow WW \rightarrow e^+ \nu \mu^- \nu$	15.24	0.9899	10 000	gg2ww
$gg \rightarrow WW \rightarrow \mu^+ \nu e^- \nu$	15.24	0.9869	10 000	gg2ww
$gg \rightarrow WW \rightarrow e^+ \nu \tau^- \nu$	15.24	0.9232	10 000	gg2ww
$gg \rightarrow WW \rightarrow \mu^+ \nu \tau^- \nu$	15.24	0.9288	10 000	gg2ww
$gg \rightarrow WW \rightarrow \tau^+ \nu \mu^- \nu$	15.24	0.9289	10 000	gg2ww
$gg \rightarrow WW \rightarrow \tau^+ \nu e^- \nu$	15.24	0.9219	10 000	gg2ww
$gg \rightarrow WW \rightarrow \tau^+ \nu \tau^- \nu$	15.24	0.3269	10 000	gg2ww

Table 4.6: WW signal production processes used for signal modelling in the 7 TeV analysis. The corresponding cross-section, total number of events, filter efficiency and MC generator is listed for each sample.

Process	cross-section [pb]	ϵ_{filter}	N_{MC}	Generator
$q\bar{q} \rightarrow WW \rightarrow e^+ \nu e^- \nu$	0.62	1.0	299 700	POWHEG
$q\bar{q} \rightarrow WW \rightarrow \mu^+ \nu \mu^- \nu$	0.62	1.0	300 000	POWHEG
$q\bar{q} \rightarrow WW \rightarrow e^+ \nu \mu^- \nu$	0.62	1.0	299 999	POWHEG
$q\bar{q} \rightarrow WW \rightarrow \mu^+ \nu e^- \nu$	0.62	1.0	300 000	POWHEG
$q\bar{q} \rightarrow WW \rightarrow e^+ \nu \tau^- \nu$	0.62	1.0	299 996	POWHEG
$q\bar{q} \rightarrow WW \rightarrow \mu^+ \nu \tau^- \nu$	0.62	1.0	299 999	POWHEG
$q\bar{q} \rightarrow WW \rightarrow \tau^+ \nu \mu^- \nu$	0.62	1.0	300 000	POWHEG
$q\bar{q} \rightarrow WW \rightarrow \tau^+ \nu e^- \nu$	0.62	1.0	299 999	POWHEG
$q\bar{q} \rightarrow WW \rightarrow \tau^+ \nu \tau^- \nu$	0.62	1.0	299 999	POWHEG
$gg \rightarrow WW \rightarrow e^+ \nu e^- \nu$	0.017	1.0	30 000	gg2ww
$gg \rightarrow WW \rightarrow \mu^+ \nu \mu^- \nu$	0.017	1.0	30 000	gg2ww
$gg \rightarrow WW \rightarrow e^+ \nu \mu^- \nu$	0.017	1.0	30 000	gg2ww
$gg \rightarrow WW \rightarrow \mu^+ \nu e^- \nu$	0.017	1.0	30 000	gg2ww
$gg \rightarrow WW \rightarrow e^+ \nu \tau^- \nu$	0.017	1.0	30 000	gg2ww
$gg \rightarrow WW \rightarrow \mu^+ \nu \tau^- \nu$	0.017	1.0	30 000	gg2ww
$gg \rightarrow WW \rightarrow \tau^+ \nu \mu^- \nu$	0.017	1.0	30 000	gg2ww
$gg \rightarrow WW \rightarrow \tau^+ \nu e^- \nu$	0.017	1.0	30 000	gg2ww
$gg \rightarrow WW \rightarrow \tau^+ \nu \tau^- \nu$	0.017	1.0	30 000	gg2ww
$gg \rightarrow H \rightarrow WW \rightarrow \ell \nu \ell \nu$	0.440563	0.49105	500 000	POWHEG

Table 4.7: WW signal production processes including the 125 GeV Higgs used for signal modelling in the 8 TeV analysis. The corresponding cross-section, total number of events, filter efficiency and MC generator is listed for each sample. At 8 TeV we switched to $q\bar{q} \rightarrow WW \rightarrow \ell^+ \nu \ell^- \bar{\nu}$ samples generated by POWHEG as it provided a better description of the observed data.

Dibosons background refers to other diboson production, in our case WZ where one of the final state leptons is not detected and ZZ where the dilepton invariant mass is not reconstructed near the Z mass due to mis-measurements. Thanks to its good MC description this background can be fully estimated from MC. The WZ, ZZ processes are modelled using *Herwig/Jimmy* at $\sqrt{s} = 7$ TeV and using *POWHEG* at 8 TeV.

Other minor backgrounds : $Z\gamma$, $W\gamma$, ZZZ, ZWW and QCD multi-jet production backgrounds are also fully estimated from MC. $W\gamma$ background is generated with *Alpgen* interfaced with *Herwig/Jimmy* and $W\gamma^*$ contributions with $1 \text{ MeV} < m_{\gamma^*} < 7 \text{ GeV}$ are modelled using *Sherpa* with pre-built parton shower (although originally *MadGraph* samples were used in the 8 TeV analysis as well as in the 7 TeV analysis). To remove the overlap between WZ and $W\gamma^*$ samples, we limit the gauge boson mass of 7 GeV in the $W\gamma^*$ samples while simultaneously applying a lower limit of 7 GeV on the WZ samples. To contribution from these backgrounds was found to be negligible, as shown in section 4.2.

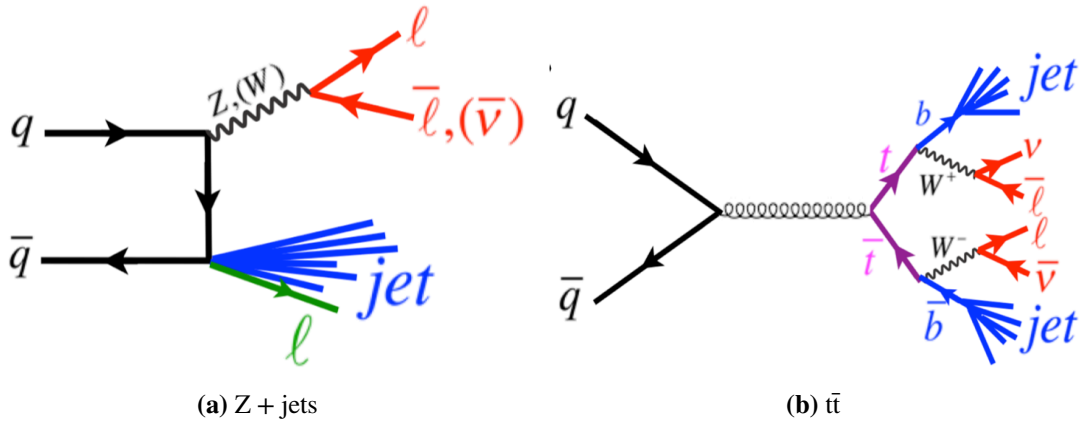


Figure 4.15: Standard Model tree-level leading-order Feynman diagrams for Z + jets and $t\bar{t}$ backgrounds.

Several backgrounds are corrected with data-driven measurements (either in form of a *scale factor* (SF) or a total shape refit). For example the W + jets background shape needs to be fully data-driven, because the modelling of the fragmentation that causes jet/lepton misidentification is not expected to be reliably simulated by MC and because the statistics at final selection for this background is so limited that the binned shape is very “spiky”, i.e. introduces large statistical errors. See section 4.9 for a complete overview of data-driven methods used in this analysis.

4.3.3 Pileup re-weighting

A common ATLAS event records multiple inelastic collisions per *bunch crossing*. Obviously, the true *pile-up* conditions are unknown until the data taking has finished, so the events are simulated with predetermined values of $\langle\mu\rangle$. Consequently, in the analysis the simulated events have to be re-weighted to match the *mean number of interactions per bunch crossing* in the given dataset while keeping the normalization unchanged. Schematically, the re-weighting procedure can be described as follows (see also fig. 4.17):

1. Obtain the data to MC ratio as a function of $\langle\mu\rangle$ to determine correction

2. Fit the ratio to determine the weights in each bin
3. Apply the appropriate weight on each MC event with a given $\langle\mu\rangle$

In data, the [mean number of interactions per bunch crossing](#) is calculated using eq. (2.58), the distributions are shown in fig. 2.47 for 2011 and 2012 dataset. The centrally provided `PileupRe-weighting` tool [ATL14j] [ATL14e] is a general purpose re-weighting software package that is used to compute event-by-event weights to match the simulated $\langle\mu\rangle$ distribution to data. The tool obtains the correct weight for the given event from a given [run number](#) MC channel number and $\langle\mu\rangle$.

In order to ensure the MC describes a wide enough range of the distributions to encompass the actual [mean number of interactions per bunch crossing](#) in observed data, the MC events are simulated in a wide range of $\langle\mu\rangle$. Since only a subset of these events can be eventually used, this leads to a significant loss of MC statistics (certain pileup weights become zero). [ATL14h] [Mor12] On occasion, there can be some amount of data recorded at a [mean number of interactions per bunch crossing](#) value that has not been simulated anywhere in the MC (e.g. when the [mean number of interactions per bunch crossing](#) was unusually low or unusually high). In the 8 TeV analysis we discard any unrepresented data by setting any unrepresented bins of the data distribution to 0 using the tool option: `SetUnrepresentedDataAction(1)`. This effectively removes approx. 1 % of our data set. We then work with the [pile-up](#) weights normally. This effectively reduces the total integrated luminosity of our data but the tool is able to return the corrected total by calling `GetIntegratedLumi()`.

The distribution of the [mean number of interactions per bunch crossing](#) (fig. 2.47) does correspond directly to the measured vertex multiplicity (fig. 4.16). In order to obtain a good description of vertex multiplicity with ≥ 2 tracks the $\langle\mu\rangle$ distribution must be scaled by 1.09 ± 0.04 in MC12a and by 1.14 ± 0.02 for MC11b, i.e. events with a given $\langle\mu\rangle$ have a number of primary vertices comparable with data at $1/1.09 \cdot \langle\mu\rangle$ at 8 TeV. The assigned uncertainty for 2012 is validated within the ID acceptance, but since the WW analysis is largely dependent on the calorimeter based [missing transverse energy](#) measurement and [combined](#) muons, we are evaluating the systematic by varying this scaling by 7 % to test the sensitivity, see section 4.8). [ATLd]

The package release `PileupReweighting-00-02-03` was used for pileup re-weighting at $\sqrt{s} = 7$ TeV and `PileupReweighting-00-02-09` was used at 8 TeV. Applying data quality cuts (see section 3.2.1) does further reduce the total integrated luminosity, however the tool conveniently accepts the output file of the `iLumiCalc` service generated directly from the users' GRL. The tool also provides a mechanism to generate random run numbers according to their luminosity distributions which is required for other corrections. As MC input, a merge of the common mc12a configuration file and the file provided for the Electroweak subgroups is used (`MC12_SMEW_prw_v04.root`). For data, the corresponding [mean number of interactions per bunch crossing](#) histograms for the total integrated luminosity in the full 8 TeV dataset are provided in the `iLumiCalc` file. Also, the fix to the [mean number of interactions per bunch crossing](#) variable saved in input D3PD has been applied. See [ATL13j] [ATL12h] [ATL11f] for implementation details.

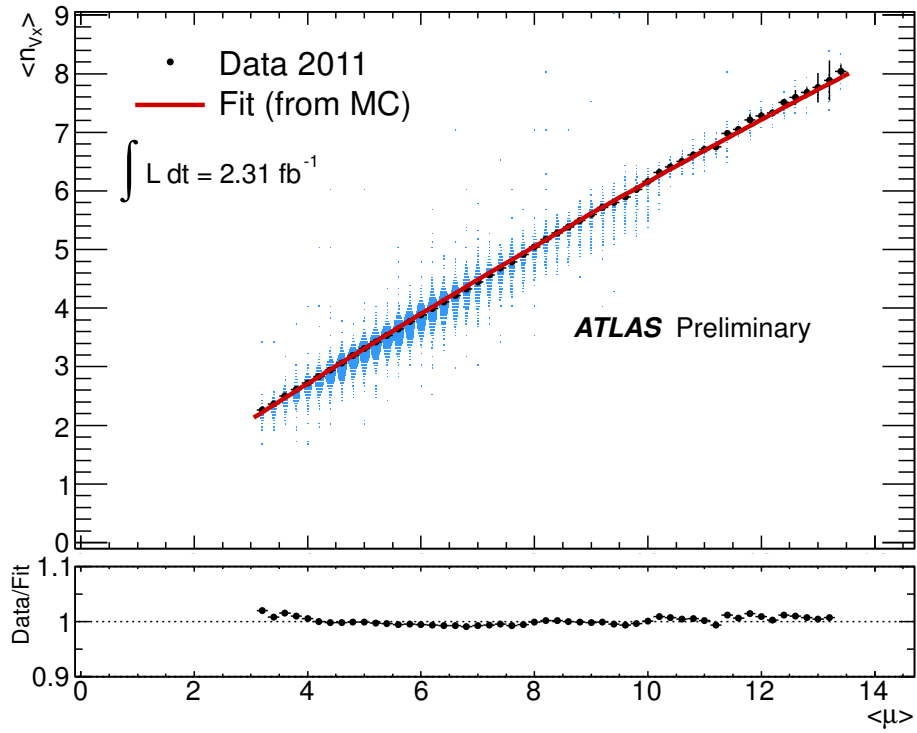


Figure 4.16: Distribution of the average number of reconstructed vertices as function of the **mean number of interactions per bunch crossing** from the LUCID detector. The red curve is taken from a fit on minimum bias MC and superimposed on data. The azure boxes show the mean number of reconstructed vertices per minute of data taking. The data agrees with the fitted MC expectation. It is reasonable to assume that the applicability of this procedure is limited in high **pile-up** ($\langle \mu \rangle \approx 100$). Figure from [ATL14h].

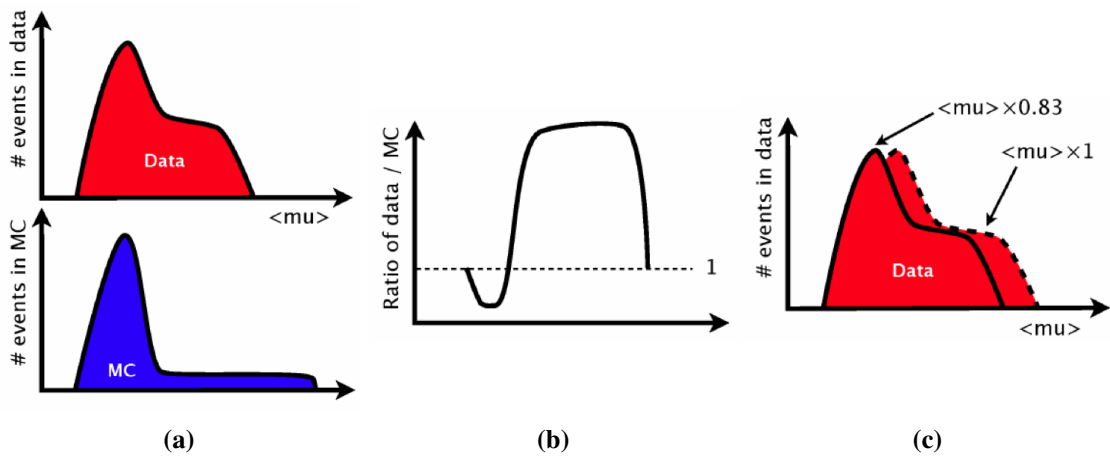


Figure 4.17: **Pile-up** re-weighting procedure schematically. It is common to re-weight events to match the MC vertex multiplicity or the p_T spectrum to data. Figures from [Mor12].

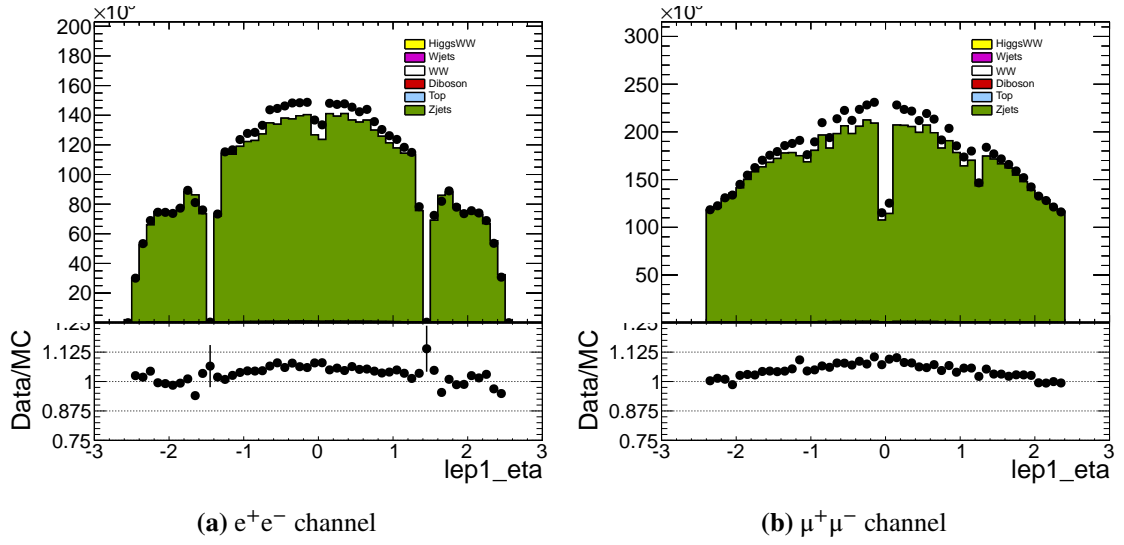


Figure 4.18: Leading and sub-leading lepton $|\eta|$ distribution at pre-selection level before applying the PDF re-weighting. These are the default distributions available from reconstruction after all event cleaning is applied. Courtesy of Karen Chen.

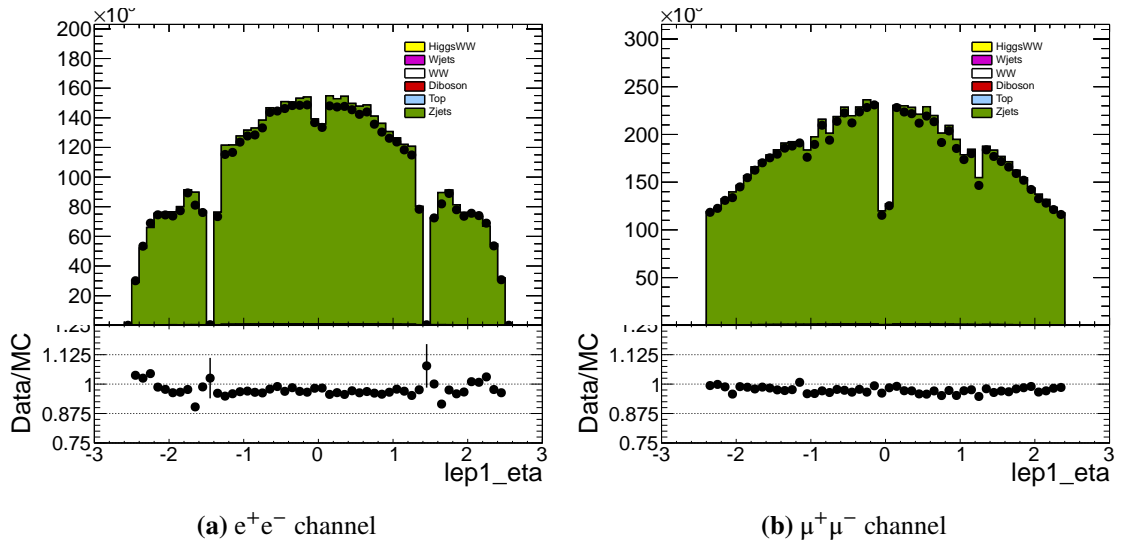


Figure 4.19: The leading and sub-leading lepton $|\eta|$ distribution at pre-selection level after applying the PDF re-weighting. The data/MC agreement has improved, especially in the barrel region the shape is now flat and the ratio stays within 5 %. Courtesy of Karen Chen.

4.3.4 PDF re-weighting

The `Alpgen` generator models $Z + \text{jets}$ events using LO PDF CTEQ66L1. As is evident from [fig. 4.18](#), this model does not perform well in lepton [pseudorapidity](#) distributions already at the pre-selection level, especially around the barrel region. One possible explanation for this is that LO modelling is not sufficient at [LHC](#) energies and some refining of the implemented PDF is required. Since the [Tevatron](#) the high-energy physics community has developed various sets of tools that allow us to re-weight the already generated samples to different PDFs. The re-weighting package centrally used at [CERN](#) is referred to as [LHAPDF](#) since it was conceived at the Les Houches meeting in 2001. It provides a multitude of options for different PDFs, for details see [\[WBG05\]](#) for a brief introduction into the functionalities and history of the project. The package is available from LHAPDF website [\[WB13\]](#).

To address the issue we described earlier, we re-weight the $Z + \text{jets}$ samples generated with the LO PDF to the CT10 NLO PDF using [LHAPDF](#) package. [Figure 4.19](#) shows the same distribution after applying the re-weighting. This has indeed helped us to achieve better modelling of these distributions and as we have verified, overall measurement kinematics were not affected.

4.4 Trigger decision

To select WW candidates we use a combination of lowest [unprescaled](#) electron and muon triggers. The analysis at $\sqrt{s} = 7 \text{ TeV}$ uses a combination of single lepton triggers depending on the channel and different data period, as the evolution of the trigger menu progressed rapidly throughout the year. The triggers require an electron with $p_T > 20 \text{ GeV}$ (later pushed to 22 GeV) or a muon with $p_T > 18 \text{ GeV}$. A summary is given in [table 4.8](#). The [L1](#) trigger seeds are `L1_MU10` and `L1_MU11` for muon chains and `L1_EM14`, `L1_EM16` and `L1_EM16VH` for the electron chains (see [fig. 3.5](#)). The late 2011 trigger `EF_e22vh_medium1` introduced optimized threshold (`v`) and a hadronic leakage veto (`h`). We have dedicated considerable space to the explanation of [ATLAS](#) trigger menu conventions and the [TDAQ](#) system in general in [section 3.1](#)

The 8 TeV analysis originally started with a combination of single lepton triggers, but eventually switched to a combination of single-lepton triggers and di-lepton triggers in the $e^\pm\mu^\mp$ channel and exclusively di-lepton triggers in the same flavour channels, see [table 4.9](#). The reasoning behind this strategy is as follows:

- Large part of events have a sub-leading lepton with $20 < p_T < 25 \text{ GeV}$, so in a purely single-lepton scenario a majority of events were triggered on one lepton only (`e24` or `mu24` threshold at 24 GeV).
- The single-lepton triggers are inefficient below the plateau, [MC](#) relies heavily on efficiency [scale factors](#).
- The newly introduced electron likelihood identification (see [section 3.3.4.3](#)) is not a subset of the standard trigger working points. Given a `looseLLH` electron, the `medium1` trigger is less efficient than a `loose1` trigger. The lowest [unprescaled](#) multi-electron trigger in 2012 fires on two `loose1` leptons (`EF_2e12Tvh_loose1`). [\[ATL14g\]](#)
- Loosening the trigger criterion in same flavour channels is helpful to dedicated background studies which require much looser lepton selection, like $W + \text{jets}$. This is related to the lowest

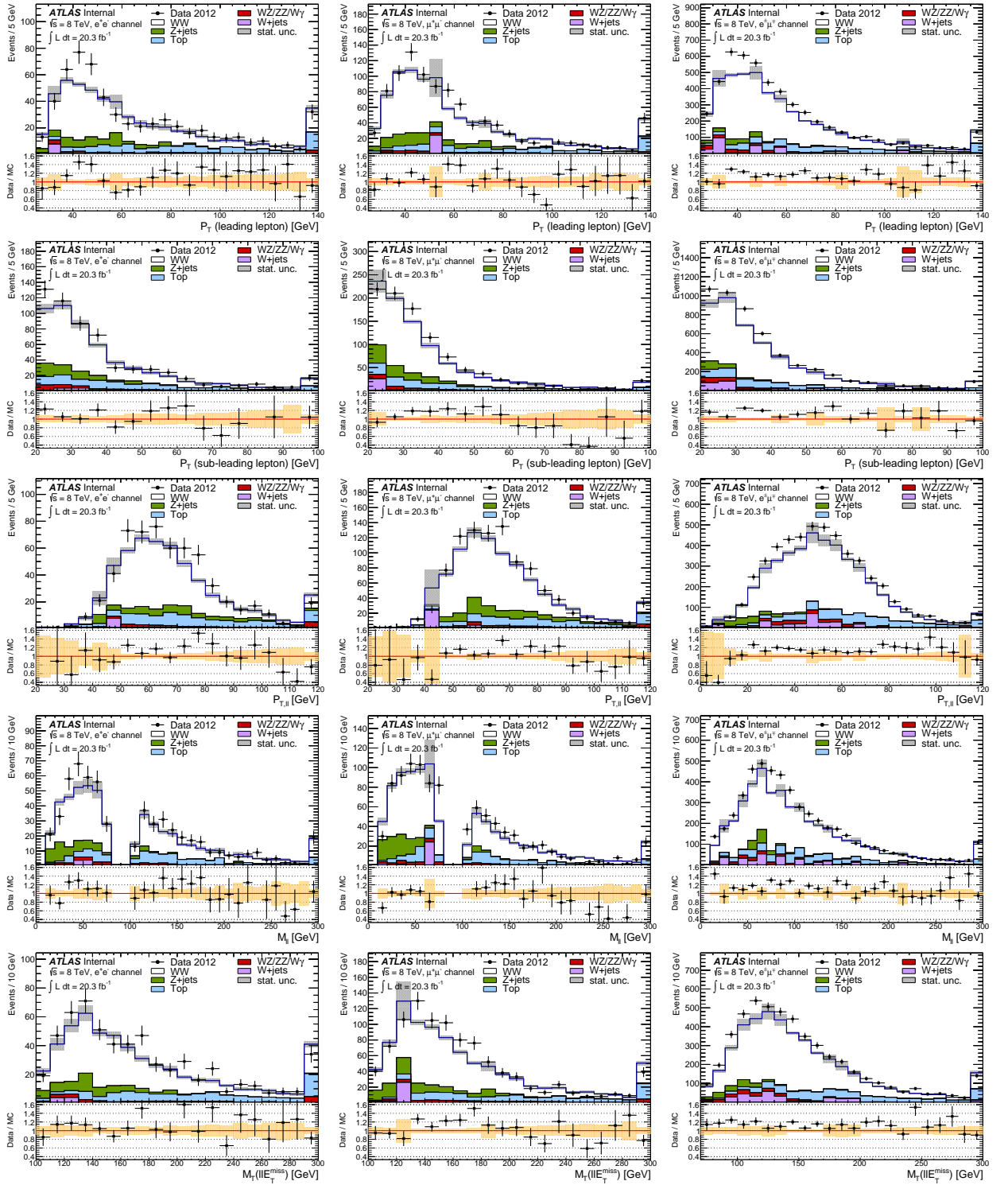


Figure 4.20: Kinematic distributions of the selected events at 8 TeV at final cut stage. Data are shown on top the signal and background processes as predicted by MC and scaled to 20.28 fb^{-1} . The plots correspond to the e^+e^- , $\mu^+\mu^-$ and $e^\pm\mu^\mp$ channels from left to right. The first (resp. second) row shows the transverse momentum p_T of the leading (resp. trailing) lepton. The third row shows missing transverse energy projection $E_{T,\text{Rel}}$ followed by track-based p_T in the fourth row. The last row shows the transverse mass m_T . Bin-by-bin systematic error on the signal sample is included (in blue).

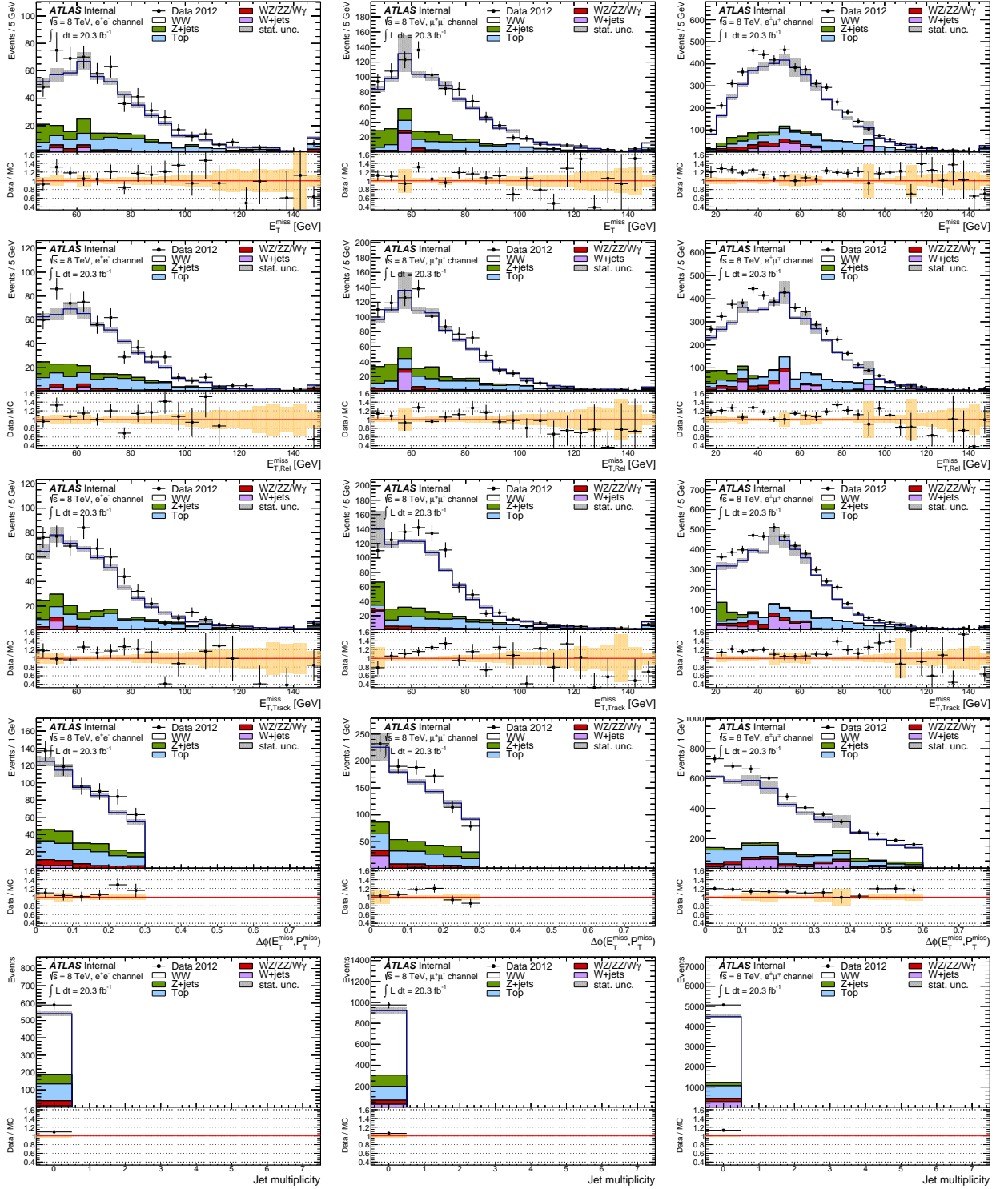


Figure 4.21: Kinematic distributions of the selected events at 8 TeV at final cut stage. Data are shown on top the signal and background processes as predicted by MC and scaled to 20.28 fb^{-1} . The plots correspond to the e^+e^- , $\mu^+\mu^-$ and $e^\pm\mu^\mp$ channels from left to right. The top row shows the missing transverse energy E_T followed by its projection $E_{T,\text{Rel}}$. The third row shows the track-based p_T . The forth row shows the azimuthal angle difference $\Delta\phi(E_T, p_T)$ and the last row shows the jet multiplicity. Bin-by-bin systematic error on the signal sample is included (in blue).

unprescaled trigger available in 2012 data taking, as mentioned above.

The only disadvantage to the introduction of di-lepton triggers is that both leptons have to be matched to the trigger, whereas for single-lepton triggers, matching a single lepton is sufficient. The single-lepton triggers fire on an isolated lepton with $p_T > 24$ GeV; or a muon (resp. electron) with $p_T > 36$ GeV (resp. $p_T > 60$ GeV) with no isolation requirement. Di-lepton triggers have no isolation requirements and fire either on two electrons of $p_T > 12$ GeV, two muons with $p_T > 8$ GeV and 18 GeV, or a combination of electron and a muon with p_T greater than 12 GeV and 8 GeV respectively. The isolation requirement implemented in the trigger is looser than that applied in the analysis. Double-counted events from the `Egamma` and `Muons` are removed, see [section 4.5.5](#)

Channel	Period	Trigger
e^+e^-	D-J	EF_e20_medium
e^+e^-	K	EF_e22_medium
e^+e^-	L-M	EF_e22vh_medium1
$\mu^+\mu^-$	D-I	EF_mu18_MG
$\mu^+\mu^-$	J-M	EF_mu18_MG_medium
$\mu^+\mu^-$	Logical OR of e^+e^- and $\mu^+\mu^-$	

Table 4.8: Trigger chains used in 7 TeV analysis. Due to the rapid development of [TDAQ](#) in the 2011 data taking, triggers were redefined on a per-period basis. Integrated luminosities of 1.80 fb^{-1} , 0.60 fb^{-1} and 2.50 fb^{-1} were recorded by `EF_e20_medium`, `EF_e22_medium` and `EF_e22vh_medium1` respectively.

Channel	Period	Single lepton triggers	Di-lepton triggers
e^+e^-	run \geq 207490	none	EF_2e12Tvh_loose1
e^+e^-		none	EF_2e12Tvh_loose1_L2StarB
$\mu^+\mu^-$	all	none	EF_mu18_tight_mu8_EFFS
$e^\pm\mu^\mp$	all	EF_e24vhi_medium1	EF_e12Tvh_medium1_mu8
$e^\pm\mu^\mp$	all	EF_e60_medium1	
$e^\pm\mu^\mp$	all	EF_mu24i_tight	
$e^\pm\mu^\mp$	all	EF_mu36_tight	

Table 4.9: Trigger chains used in 8 TeV analysis. In the combined flavour channel any combination of the single-lepton or the combined $e^\pm\mu^\mp$ trigger is required. In the same-flavour channels only one di-lepton trigger is used, n.b.: `EF_2e12Tvh_loose1` and `EF_2e12Tvh_loose1_L2StarB` are identical apart from improved tracking efficiency in `L2StarB` deployed from period D on (run 207490).

4.4.1 Trigger matching

Trigger decisions effectively set the first selection criteria on the physics objects corresponding to the physical final states. Analysers take great care in defining the objects of interest for a particular process, yet this definition does not necessarily coincide with what is implemented in the trigger decision. The goal of *trigger matching* ([TDAQ](#)) is to establish whether a particular object driving the candidate selection did actually fire the trigger. Otherwise a selection bias could be introduced. We outline the procedure in three steps:

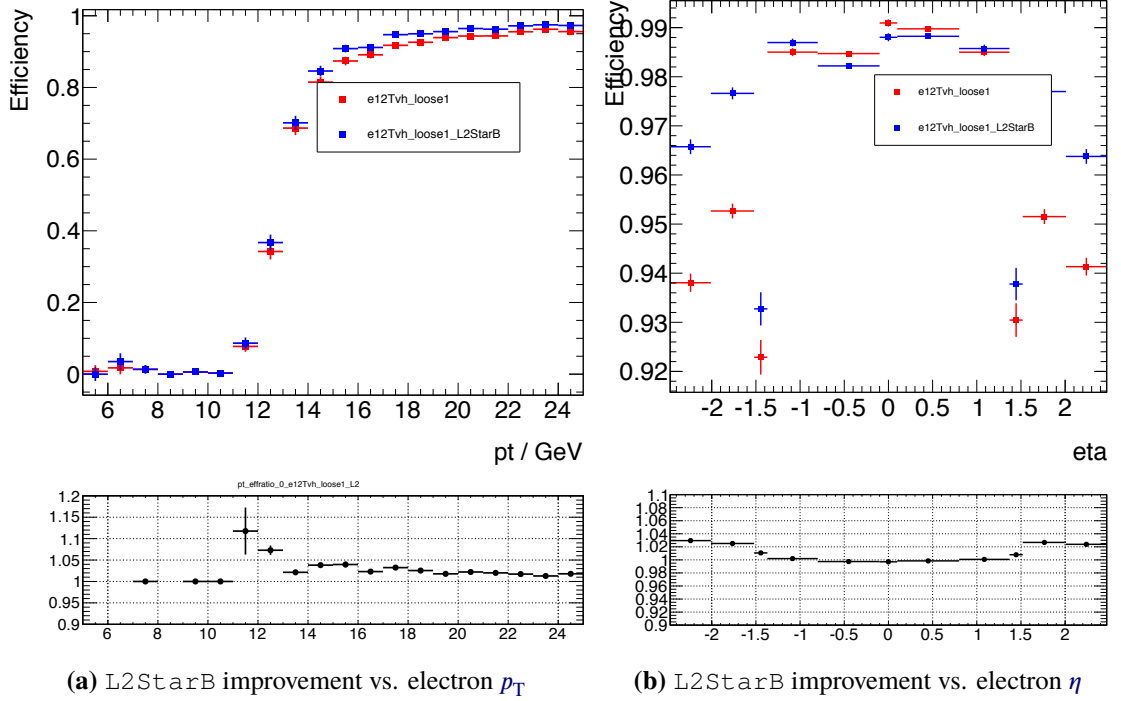


Figure 4.22: Comparison of `EF_2e12Tvh_loose1` and `EF_2e12Tvh_loose1_L2StarB` di-electron trigger performance as a function of electron p_T (left) and η (right). The efficiency ratio in the sub-plot clearly shows improvement of up to 3% in the end-cap region and a steeper turn-on curve in p_T . Figure from [ATLe].

1. Start with the offline object defined for a particular analysis (e.g. a muon preselected for our analysis, see section 4.5.1)
2. Loop on the trigger object passing a given trigger (e.g. `EF_mu24i_tight`).
3. Match the trigger object to the physics object. The matching succeeds if the ΔR between the two objects is close to zero.

To perform the ΔR match, the η and ϕ coordinates for both the offline and online object must be provided (including corrections). The proposed matching radius is $\Delta R < 0.1$ (looser for electrons in 2011) as it ensures a very high matching efficiency and it's very robust for EF. [ATLa] [ATL14m].

To minimize the dependence of the trigger matching on the lepton p_T , low- p_T triggers are matched to leptons only in the trigger efficiency plateau (i.e. a cut on lepton p_T is introduced). The choice of the threshold is motivated by the shape of the trigger turn-on curve and reflects the requirements for the trigger efficiency measurement (see below). To summarize:

- 7 TeV: matching radius $\Delta R < 0.1$ for muons, $\Delta R < 0.15$ for electrons, match to `EF_mu18_MG` only if muon $p_T > 20$ GeV, match to `EF_e20_medium` (`EF_e22*_medium`) only if electron $p_T > 21$ GeV ($p_T > 23$ GeV).
- 8 TeV: matching radius $\Delta R < 0.1$, match to `EF_e24vhi_medium1`, `EF_mu24i_tight` only if lepton $p_T > 25$ GeV

Trigger matching can be applied on multi-object triggers (e.g. `EF_2e12Tvh_loose1`). The procedure is implemented as part of `TrigMuonEfficiency` and `egammaAnalysisUtils` performance packages.

4.4.2 Trigger efficiency

Lepton trigger efficiencies are determined using [tag-and-probe](#) method on $Z/\gamma^* \rightarrow \ell\ell$ candidates. The tag leptons are defined with analysis-specific quality criteria and are required to pass trigger matching. No trigger requirements are placed on the corresponding probe lepton produced in the Z decay. The efficiency of a trigger chain with respect to offline object is defined as $\epsilon = N_{\text{matched}}/N_{\text{probes}}$, where N_{matched} is the number of probes successfully matched to a trigger object following the tag and probe selection. In a two lepton event, each is considered as a tag or probe to the other.

The efficiencies are measured double-differentially as a function of lepton p_T and η . Fixed p_T threshold are applied so that the considered lepton is on or close enough to the trigger plateau [ATLg]. An efficiency of zero (i.e. a SF of 1) is assigned if the lepton is below this threshold. Electrons with $|\eta| \geq 2.47$ also have assigned efficiency of 0. The per-event [scale factors](#) for single or multi-lepton triggers is computed as follows:

$$\text{SF} = \frac{1 - \prod_j (1 - \epsilon_j^{\text{data}})}{1 - \prod_j (1 - \epsilon_j^{\text{MC}})} \quad (4.13)$$

where ϵ_j^{data} for lepton j in data, ϵ_i^{MC} for lepton i in MC. The efficiency multiplied for each lepton in the event. In both analyses, the [scale factors](#) are applied on MC candidates with two well-defined leptons (see below, [sections 4.5.1](#) and [4.5.2](#)).

4.4.2.1 Trigger efficiency in 2011

The definitions of the tags and probes are summarized in [tables 4.10](#) and [4.11](#). Using MC samples, the fraction of probes that are not coming from Z decays was estimated to be less than 1 % in the p_T range of interest. [ATL12g] For muons with $p_T > 20$ GeV, the single muon trigger efficiency for the entire dataset is close to 80 % in the [barrel](#) region and close to 90 % in the [end-caps](#). For electrons with $E_T > 25$ GeV, the single electron trigger efficiency is close to 99 % in the plateau region. The efficiencies determined in the 2011 dataset are shown in [fig. 4.23a](#) for muons and in [fig. 4.23b](#) for electrons.

The systematic uncertainties are estimated by varying the selection: in case of electrons the size of the invariant mass window by 5 GeV and the offline identification for the tag is changed from medium to tight if triggering with e20_medium or e22_medium, and from medium++ to tight++ if triggering with e22vh_medium1. [ATL12f, p. 11] The [scale factors](#) are provided via TrigMuonEfficiency-00-01-01 performance package.

4.4.2.2 Trigger efficiency in 2012

In 2012, the lowest [unprescaled](#) single-lepton trigger threshold has increased to 24 GeV. Consequently, the tag muon p_T threshold was increased to 25 GeV. Tag and probe definition for electrons remain the same, including the jet/electron overlap. [ATL13a] [ATL13f] A comparison of events triggered by single-lepton or di-lepton triggers is shown in [figs. 4.24](#) to [4.26](#).

The efficiency of the di-electron trigger EF_2e12Tvh_loose1 (including L2StarB) is typically higher than 98 % in the [barrel](#) and higher than 95 % in the [end-cap](#) region. The EF_

Muon trigger efficiency measurement at 7 TeV		
Requirements	Tag	Probe
Reconstruction flags:	Reconstructed combined STACO muon	
Geometric acceptance:	$ \eta < 2.4$	$ \eta < 2.5$
	$p_T^{\text{corr}} > 20 \text{ GeV}$	—
Kinematic acceptance:	tag and probe are oppositely charged	
	tag and probe azimuthal separation $\Delta\phi > 2.0$	
	$ m_{\mu\mu} - m_Z < 10 \text{ GeV}$	
Track quality:	Standard MCP 2011 hit requirements, see table 4.12	
Track isolation:	$\sum_{\Delta R < 0.2} p_T(i) < 0.1 \cdot p_T^{\text{corr}}(\mu)$	
Trigger matching radius:	$\Delta R < 0.1$	—

Table 4.10: Muon tag and probe definition for 7 TeV trigger efficiency measurement corresponding to the [scale factors](#) presented in [\[ATL12g, p. 8\]](#)

mul8_tight_mu8_EFFS is seeded by identical [L1](#) trigger as EF_mu24i_tight. The seed efficiency for EF_mul8_tight is 60–90 % in the [barrel](#) and 80–95 % in the [end-cap](#) region. Requiring the second lepton increases the efficiency to 98 % in the [barrel](#) region and higher 95 % in the [end-caps](#). Due to the p_T cut on signal leptons, the efficiency stays in the plateau and the overall effect of the [scale factors](#) is very small.

The combined $e^\pm\mu^\mp$ trigger EF_e12Tvh_medium1_mu8 efficiency is much lower, $\approx 80\%$ for a di-lepton event. To compensate, we use a logical OR of the di-lepton triggers with the combination of lowest [unprescaled](#) single-lepton triggers: EF_e24vhi_medium1, EF_e60_medium1, EF_mu24i_tight, EF_mu36_tight. This results in an increase in efficiency of nearly 20 % and smooths the turn-on curve. Consequently, about 1 in 5 events trigger on muons or electron with track-isolation applied.

The [scale factors](#) are centrally provided with the TrigMuonEfficiency-00-02-42 performance package. The [scale factors](#) also provide the extrapolation from EF_2e12Tvh_loose1 to EF_2e12Tvh_loose1_L2StarB since the latter is not simulated in [MC](#).

4.5 Object definitions

Throughout this section we are going to define the physics objects considered in this analysis. We have discussed the detector data pattern recognition and reconstruction algorithms in [section 3.3](#) along with the correction applied to recorded data and [MC](#).

4.5.1 Muon definition

Both analyses use the muons reconstructed from the combined measurement in [ID](#) and [MS](#). As we have discussed in [section 3.3.3](#), these muons are referred to as [combined](#) in the [STACO](#) algorithm family. The [combined](#) muon momentum is built from a statistical combination of separate [ID](#)

Electron trigger efficiency measurement at 7 TeV		
Requirements	Tag	Probe
Reconstruction flags:	Reconstructed cluster electron candidate OR combined track+cluster electron candidate	
Geometrical acceptance:	$ \eta < 2.47$, excluding “crack” region $1.37 \leq \eta \leq 1.52$ $E_T^{\text{corr}} > 25 \text{ GeV}$	–
Kinematic acceptance:	tag and probe are oppositely charged electrons rejected if overlapping with jet in $\Delta R > 0.4$ $ m_{\text{eeee}} - m_Z < 20 \text{ GeV}$	
Identification criteria:	medium or medium++	–
Track isolation:	$\sum_{\Delta R < 0.2} p_T(i) < 0.1 \cdot p_T^{\text{corr}}(\mu)$	
Trigger matching radius:	$\Delta R < 0.15$	–

Table 4.11: Electron tag and probe definition for 7 TeV trigger efficiency measurement corresponding to the [scale factors](#) presented in [\[ATL12f, p. 9\]](#).

and **MS** momenta. The two measurements are treated as uncorrelated since the **ID** and **MS** are separated by a large volume of calorimeter material that effectively screens any cross-interaction. The correction of the **combined** muon momentum is computed as the linear combination of the **MS** and **ID** contributions weighted by the **MS** and **ID** resolutions [\[ATL11d\]](#):

$$p_{\text{T,CB}}^{\text{corr}} = p_{\text{T,CB}} \cdot \left(\frac{\frac{\Delta_{\text{MS}}}{\sigma_{\text{MS}}^2} + \frac{\Delta_{\text{ID}}}{\sigma_{\text{ID}}^2}}{\frac{1}{\sigma_{\text{MS}}^2} + \frac{1}{\sigma_{\text{ID}}^2}} \right) \quad (4.14)$$

The muon selection criteria differ for $\sqrt{s} = 7 \text{ TeV}$ and 8 TeV analysis as the tracking, reconstruction and isolation recommendations from the Muon Combined Performance Group (MCP) have changed. The selected muons are required to be within the **pseudorapidity** range $|\eta| < 2.4$ and have $p_T > 20 \text{ GeV}$. This requirement was later changed to $p_T > 7 \text{ GeV}$ for the 8 TeV analysis as this reduces the contribution to the total background from other diboson processes by $\approx 10\%$, see [section 4.7.1](#). To ensure that the candidates are compatible with the **PV**, cuts on the absolute distance in the “unbiased” z direction and the “unbiased” transverse impact parameter significance with respect to the primary vertex are introduced. Impact parameter significance is defined as the ratio between the impact parameter value and its uncertainty. **Inner Detector** tracks are required to have a minimum number of hits in **Pixel**, **SCT**. The **TRT** requirements are defined separately for **barrel** and **end-cap** regions.* In addition, we ensure that the muon tracks are isolated from any surrounding tracks in order to reject secondary muons coming from hadronic jets (like the leptonic decay of a quark). Isolation is enforced by requiring the fraction of a scalar sum of the surrounding **ID** tracks within a cone $\Delta R = 0.3$ around the muon to be less than a specified threshold. [\[ATL14i,](#)

* As mentioned in [section 3.3.1](#), a track passing through a known dead module does not count towards the number of holes

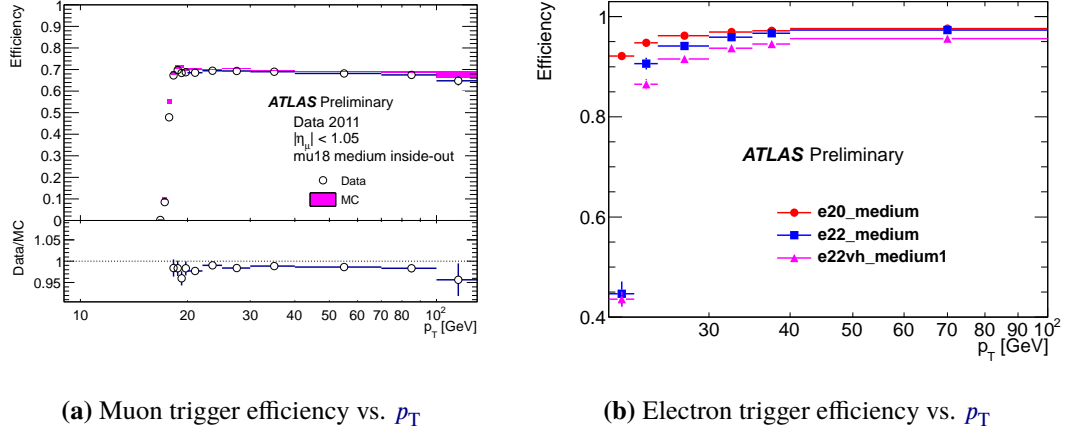


Figure 4.23: Trigger efficiencies and [scale factors](#) at 7 TeV for muon triggers (top row) and electron triggers (bottom row) as a function of online object p_T (left) and the corresponding [scale factors](#) (right). The vertical bars represent statistical and total systematic uncertainties. Figures from [ATL12g, pp. 15,17] [ATL12f, p. 11].

p. 22]. At 7 TeV, the total calorimeter energy, resp. track momentum inside the cone must be less than 14 %, resp. 15 % of the muon corrected momentum. For 8 TeV analysis the isolation efficiency was modelled differentially in 5 GeV bins, which allowed us to refine the isolation requirement to maximize the efficiency. The calorimeter isolation is corrected for [pile-up](#) effects as described in [section 3.3.3.3](#). The requirements are summarized in full detail in [tables 4.12](#) and [4.13](#) for each analysis separately.

As recommended by the MCP [ATL14a] we smear the p_T of simulated muons in the nominal analysis using the following performance packages: MuonMomentumCorrections-00-05-00 at 7 TeV and MuonMomentumCorrections-00-09-23 at 8 TeV, see [section 3.3.3.2](#). Muon momenta are rescaled only as a systematic study, see [section 4.8](#).

4.5.1.1 Muon reconstruction efficiency

Because the [combined](#) muon tracks are stapled together from the [ID](#) and [MS](#) measurements, their reconstruction efficiency is treated as the product of the reconstruction efficiencies for each component and the matching efficiency between [ID](#) and [MS](#). The efficiency is measured using a [tag-and-probe](#) method on $Z \rightarrow \mu^+ \mu^-$ as described in [ATL13h, pp. 3–7]. The events are selected by requiring two oppositely charged being high- p_T ($p_T > 20$ GeV) muons within 10 GeV of the Z mass and inside the acceptance of the [ID](#) ($|\eta| < 2.5$). The [tag](#) muon is required to be a [CB](#) muon that has triggered the event. The probe is required to be a [MS](#)-built track (i.e. a [SA](#) or [CB](#) muon) when measuring the [ID](#) efficiency or [calo-tagged](#) muon when measuring the [MS](#) efficiency. [ATL13h, p. 3]

After selecting all [tag-and-probe](#) pairs, the reconstructed muons in the event are sequentially matched to the probe. The matching is successful within $\Delta R < 0.01$ for [ID](#) probes and $\Delta R < 0.05$ for [MS](#) probes if the muon has the same charge as the probe. The [combined](#) muon efficiency is defined for each [tag-and-probe](#) pair:

$$\epsilon(\text{CB}) = \epsilon(\text{CB}|\text{ID}) \cdot \epsilon(\text{ID}) \quad (4.15)$$

The level of agreement is determined by a ratio of the efficiencies measured in data $\epsilon(\text{data})$ and

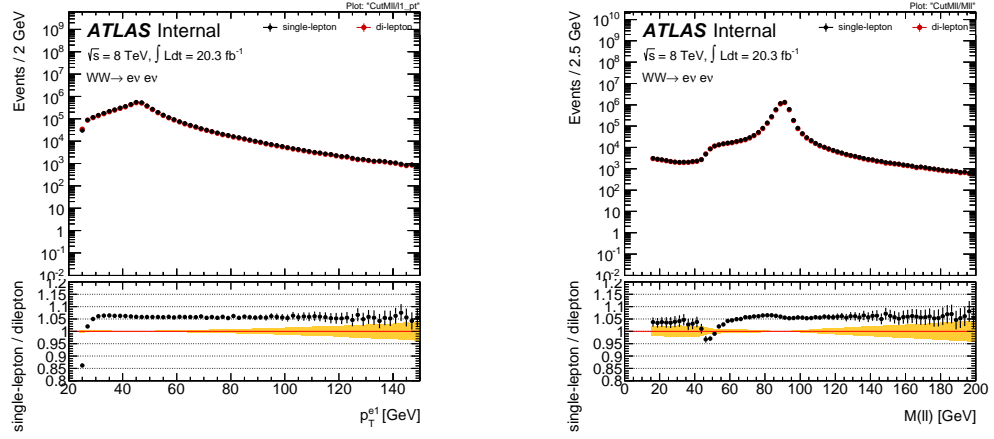


Figure 4.24: Single-lepton and di-lepton trigger comparison in e^+e^- channel as a function of lepton p_T (left) and $m_{\ell\ell}$ (right). The efficiency ratio is shown in the sub-plot. The poor single lepton efficiency at low- p_T is clearly visible. Di-lepton triggers are $\approx 5\%$ less efficient to trigger events at high mass and high- p_T .

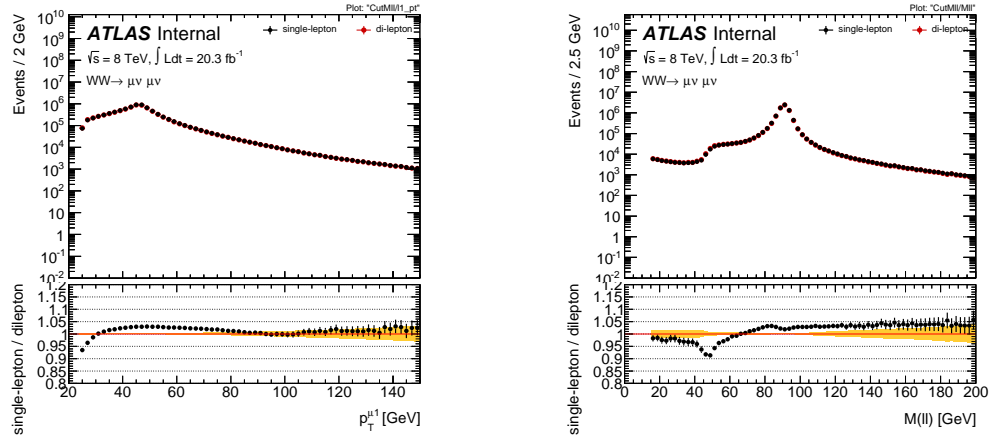


Figure 4.25: Single-lepton and di-lepton trigger comparison in $\mu^+\mu^-$ channel as a function of lepton p_T (left) and $m_{\ell\ell}$ (right). The efficiency ratio is shown in the sub-plot. The poor single lepton efficiency at low- p_T is clearly visible. Di-lepton triggers are $\approx 5\%$ less efficient to trigger events at high mass and high- p_T .

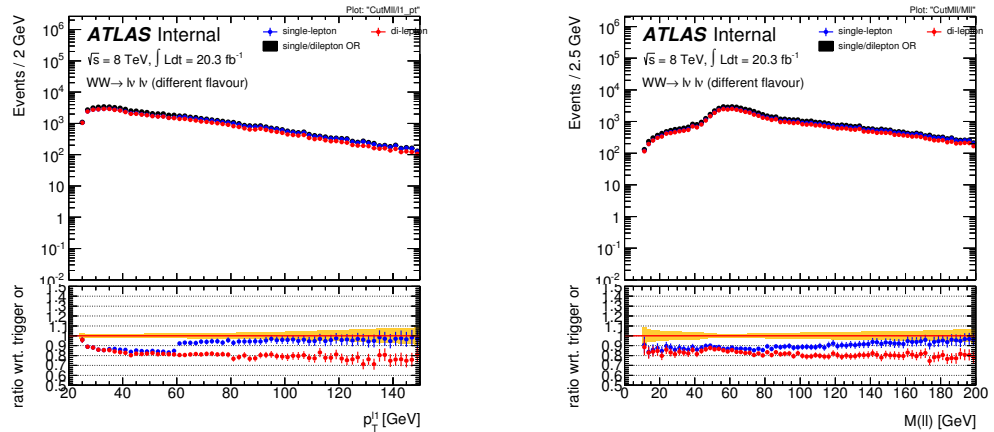


Figure 4.26: Single-lepton and di-lepton trigger comparison in $e^\pm\mu^\mp$ channel as a function of lepton p_T (left) and $m_{\ell\ell}$ (right). The poor efficiency of the combined $e^\pm\mu^\mp$ trigger EF_e12Tvh_medium1_mu8 (red) over the whole momentum as mass range is compensated by combining the trigger decision with single-lepton triggers (blue).

Muon definition in 7 TeV

Reconstruction flags:	Reconstructed combined STACO muon
Geometric acceptance:	$ \eta < 2.4$
Kinematic acceptance:	$p_{\text{T}}^{\text{corr}} > 20 \text{ GeV}$
Longitudinal impact parameter:	$ z_0(\mu) < 1 \text{ mm}$
Transverse impact parameter:	$\frac{d_0}{\sigma_{d_0}} < 3$
Track quality:	$n\text{BLayerHits} > 0$ if BLayerHits are expected $n\text{PixHits} + n\text{PixelDeadSensors} > 1$ $n\text{SCTHits} + n\text{SCTDeadSensors} \geq 6$ $n\text{PixHoles} + n\text{SCTHoles} < 3$ for $ \eta < 1.9$: $(n\text{TRTOutliers} + n\text{TRTHits}) > 5$ for $ \eta < 1.9$: $\frac{n\text{TRTOutliers}}{(n\text{TRTOutliers} + n\text{TRTHits})} < 0.9$ for $ \eta > 1.9$: if $(n\text{TRTOutliers} + n\text{TRTHits}) > 5$ $\frac{n\text{TRTOutliers}}{(n\text{TRTOutliers} + n\text{TRTHits})} < 0.9$
Calorimeter Isolation Requirement:	$\sum_{\Delta R < 0.3} E_{\text{Tcorr}}(i) < 0.14 \cdot p_{\text{Tcorr}}(\mu)$
Track Isolation Requirement:	$\sum_{\Delta R < 0.3} p_{\text{T}}(i) < 0.15 \cdot p_{\text{Tcorr}}(\mu)$

Table 4.12: Muon definition used in 7 TeV analysis**Muon definition in 8 TeV**

Reconstruction flags:	Reconstructed combined STACO muon
Geometric acceptance:	$ \eta < 2.4$
Kinematic acceptance:	$p_{\text{Tcorr}} > 7 \text{ GeV}$
Longitudinal impact parameter:	$ z_0 \cdot \sin \theta < 1 \text{ mm}$
Transverse impact parameter:	$\frac{d_0}{\sigma_{d_0}} < 3$
Track quality:	$n\text{PixHits} + n\text{PixelDeadSensors} > 0$ $n\text{SCTHits} + n\text{SCTDeadSensors} \geq 5$ $n\text{PixHoles} + n\text{SCTHoles} < 3$ for $0.1 < \eta < 1.9$: $(n\text{TRTOutliers} + n\text{TRTHits}) > 5$ $\frac{n\text{TRTOutliers}}{(n\text{TRTOutliers} + n\text{TRTHits})} < 0.9$
Calorimeter isolation:	for $p_{\text{Tcorr}} < 15 \text{ GeV}$: $\sum_{\Delta R < 0.3} E_{\text{Tcorr}}(i) < 0.06 \cdot p_{\text{Tcorr}}(\mu)$ for $15 < p_{\text{Tcorr}} < 20 \text{ GeV}$: $\sum_{\Delta R < 0.3} E_{\text{Tcorr}}(i) < 0.12 \cdot p_{\text{Tcorr}}(\mu)$ for $20 < p_{\text{Tcorr}} < 25 \text{ GeV}$: $\sum_{\Delta R < 0.3} E_{\text{Tcorr}}(i) < 0.18 \cdot p_{\text{Tcorr}}(\mu)$ for $p_{\text{Tcorr}} > 25 \text{ GeV}$: $\sum_{\Delta R < 0.3} E_{\text{Tcorr}}(i) < 0.30 \cdot p_{\text{Tcorr}}(\mu)$
Track isolation:	for $p_{\text{Tcorr}} < 15 \text{ GeV}$: $\sum_{\Delta R < 0.4} p_{\text{T}}(i) < 0.06 \cdot p_{\text{Tcorr}}(\mu)$ for $15 < p_{\text{Tcorr}} < 20 \text{ GeV}$: $\sum_{\Delta R < 0.3} p_{\text{T}}(i) < 0.08 \cdot p_{\text{Tcorr}}(\mu)$ for $p_{\text{Tcorr}} > 20 \text{ GeV}$: $\sum_{\Delta R < 0.3} p_{\text{T}}(i) < 0.12 \cdot p_{\text{Tcorr}}(\mu)$

Table 4.13: Muon definition used in 8 TeV analysis

those predicted by MC:

$$\text{SF}(\mu) = \frac{\epsilon(\text{data})}{\epsilon(\text{MC})} \quad (4.16)$$

The reconstruction efficiencies and derived [scale factors](#) are shown in [figs. 4.27](#) and [4.28](#) as a function of p_T and [pseudorapidity](#). The mean value of the η dependent [scale factors](#) curve is 0.989 ± 0.003 for STACO in the 2011 dataset, the uncertainty is statistical. The CB efficiencies are significantly higher than 0.95 with the exception of the partially instrumented regions of the MS in η . The reconstruction efficiency of the MC event is the product of the single efficiencies of all selected muons.

$$w_{\text{muons}} = \prod_i^{N_\mu} w_i \quad (4.17)$$

The systematic uncertainties associated with the reconstruction efficiency are taken correctly into account, see [section 4.8](#). These systematics come mainly from three sources:

- Background contamination of the [tag-and-probe](#) sample. The systematic uncertainty of 0.20 % on the efficiency SF has been evaluated by varying the selections cuts. The dominant contributions come from the change in mass window to 8 GeV, tag $p_T > 22$ GeV and reduction probe isolation, the full breakdown is given in [\[ATL11a\]](#).
- Low- p_T muons where a deviation of up to 2 % was found. The uncertainty was estimated in 2010 on $J/\psi \rightarrow \mu^- \mu^+$ sample, as shown in [\[ATL12a, p. 5\]](#) by varying the parameters of the signal and background fit. The width and mean of the Gaussian models in the fit were allowed to vary independently, the background shape was fitted with a linear and quadratic function in a reduced mass range. Alternative approaches to the fitted distributions were also implemented. [\[ATL12a, p. 5\]](#) To be conservative, the $Z \rightarrow \mu^+ \mu^-$ decay uncertainties are used, but a systematic uncertainty of 1 % is assigned for $7 < p_T < 10$ GeV and 2 % for $p_T < 7$ GeV.
- Hard muons outside the range of the efficiency measured ($p_T > 100$ GeV). An uncertainty of $1 \% \cdot p$ [TeV] is assigned in this kinematic region, based on a dedicated MC simulation for muon momentum up to 1 TeV.

The [scale factors](#) for each [combined](#) muon are provided by the performance package Muon-EfficiencyCorrections-01-01-00 for 2011 and the updated version MuonEfficiencyCorrections-02-01-17 for the 2012 dataset. All event weights from the MC samples are multiplied by the weight for each selected muon.

4.5.1.2 Muon isolation efficiency

Isolation efficiency quantifies whether a given muon passes the isolation criteria. In our case, the muon isolation efficiency is defined as the probability that a simulated [combined](#) muon passes both the calorimeter and track isolation requirements. The efficiency is determined using [tag-and-probe](#) method tailored to the default selection cuts except the isolation requirements. The selection cuts for this analysis are summarized in [tables 4.12](#) and [4.13](#).

The isolation efficiency is calculated as the fraction of probe muons passing the given set of isolation cuts. The measured isolation efficiencies at $\sqrt{s} = 7$ TeV dataset are studied in $Z \rightarrow \mu^+ \mu^-$ using the same selection as was used for reconstruction efficiency apart from the definition of

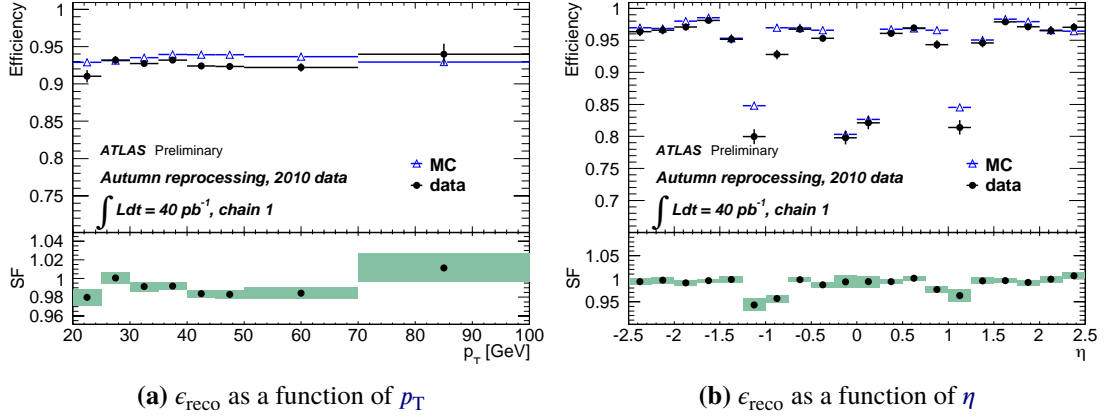


Figure 4.27: Muon reconstruction efficiency for **STACO combined** only muons at $\sqrt{s} = 7$ TeV as a function of p_T and pseudorapidity for muons with $p_T > 20$ GeV. The sub-plot shows the ratio between the measured and predicted efficiencies which defines the **scale factors**. The **CB** efficiencies are significantly lower than 0.95 in the partially instrumented regions of the **MS** at $\eta \approx 0$ and in the poorly instrumented **MS** instrumented regions of the **MS** at $\eta \approx 1.2$. Figures from [ATL11e, p. 13]

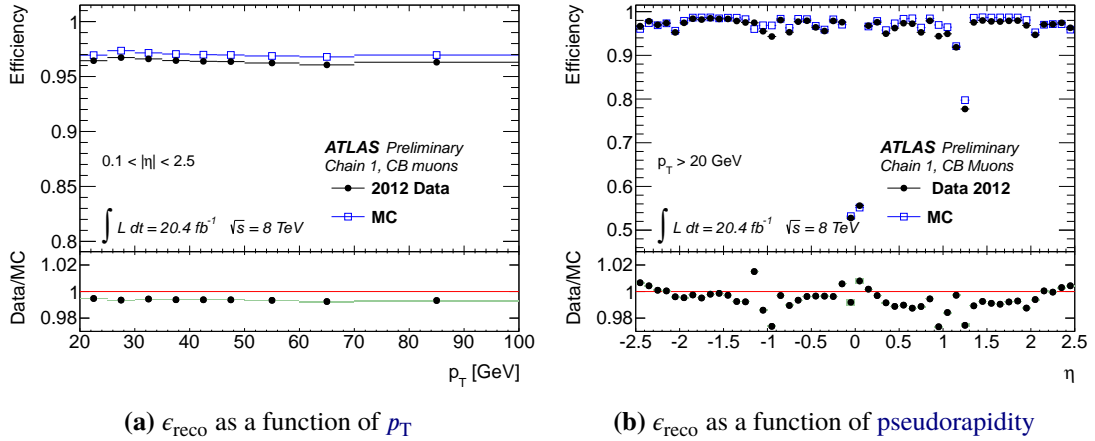


Figure 4.28: Muon reconstruction efficiency ϵ_{reco} for **STACO combined** muons at $\sqrt{s} = 8$ TeV as a function of p_T and pseudorapidity for muons with $p_T > 20$ GeV. The sub-plot shows the ratio between the measured and predicted efficiencies which defines the **scale factors**. The **CB** efficiencies are significantly lower than 0.95 in the partially instrumented regions of the **MS** at $\eta \approx 0$ and in the poorly instrumented regions of the **MS** at $\eta \approx 1.2$. Figures from [ATL13h, p. 6].

the **tag** muon, which is defined as an isolated **CB** muon with $p_T > 20$ GeV that fulfils the common tracking requirements. The resulting efficiencies for track and calorimeter isolation in $\Delta R < 0.3$ are shown in fig. 4.29 as a function of p_T . The efficiency drops at low- p_T because the energy fraction rises with decreasing muon p_T and due to the background in the low- p_T region. [ATL11e, p. 8].

At 8 TeV the official set of isolation **scale factors** is provided by the $H \rightarrow W^+W^-$ group as their analysis has a similar selection. The optimisation was performed on the $Z \rightarrow \mu^+\mu^-$ sample, the **scale factors** is calculated in 5 GeV steps from $10 < p_T < 25$ GeV and for $p_T > 25$ GeV. The total background contamination is around 1 %, although it increases in the low- p_T region. Systematics are assigned based on variations of the Z mass range used and the mass range used for backgrounds. An additional systematic is assigned for the **pile-up** dependence of the **scale factors**. [ATL13g, p. 35]. Both central values and uncertainties have been approved by the MCP [ATL14a]. The resulting efficiency and **scale factors** for the isolation requirements specified in table 4.13 are shown in fig. 4.30.

The [scale factors](#) are applied using the distributed performance packages `IsoIPSF-00-00-07` at $\sqrt{s} = 7$ TeV and `HWIIsolationScaleFactors-00-00-01` at 8 TeV.

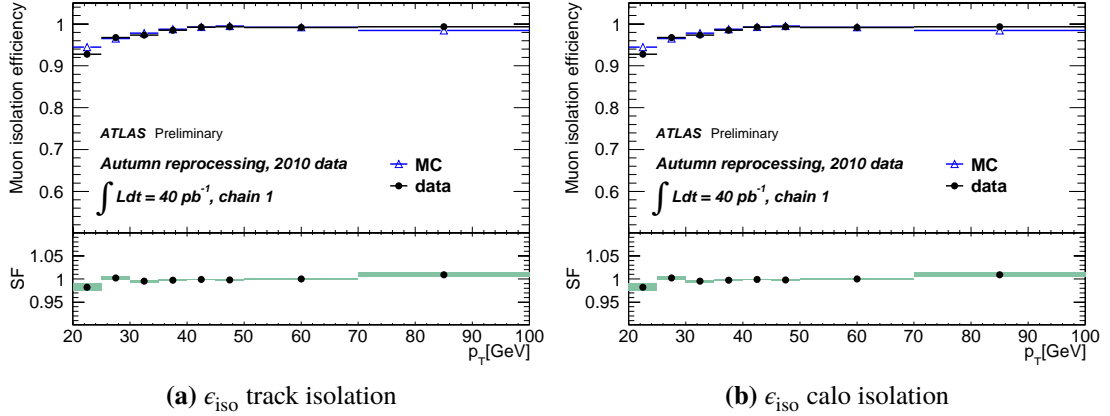


Figure 4.29: Muon track isolation efficiency (left) and calorimeter isolation efficiency (right) for [STACO](#) muons at $\sqrt{s} = 7$ TeV given the isolation cuts as specified in [table 4.12](#) as a function of the muon p_T . The sub-plot shows the ratio between the measured and predicted efficiencies which defines the [scale factors](#). Figures from [\[ATL11e, p. 17\]](#)

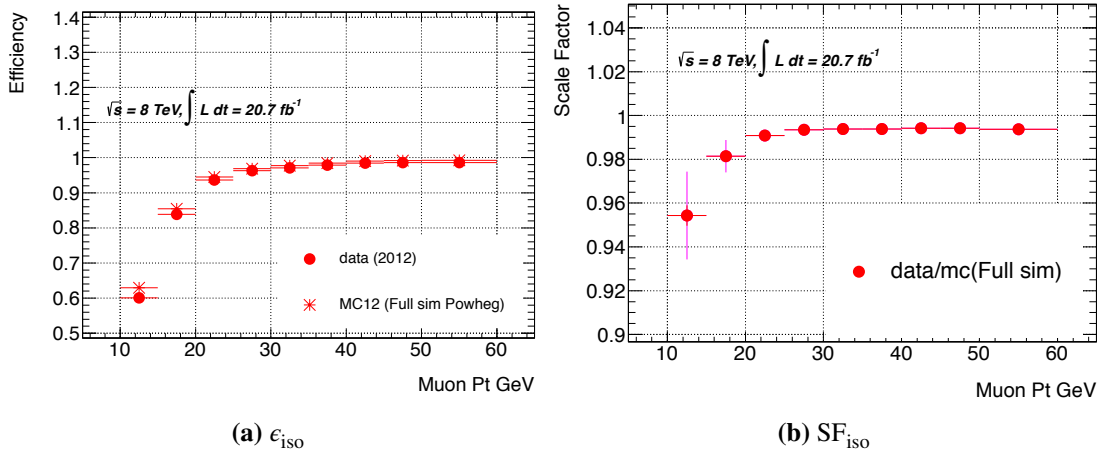


Figure 4.30: Muon isolation efficiency (left) and derived [scale factors](#) (right) at $\sqrt{s} = 8$ TeV for the isolation cuts as specified in [table 4.13](#) as a function of the muon p_T . Figures from [\[ATL13g, p. 40\]](#)

4.5.2 Electron definition

In our analysis, an electron candidate may be found using the cluster based (`AuthorElectron`, flagged as 1 in terms of integer in `D3PD`) or track based (`AuthorSoftE`, flagged as 3 in terms of integer in `D3PD`). If a track is common to the track and calorimeter algorithm, then the objects are considered to be the same [\[ATLc\]](#). Electrons reconstructed this way are largely contaminated by hadronic jets, heavy flavour hadron decays and photon conversions.

To refine object quality, we set requirements on the electron identification level, as described in [section 3.3.4.2](#). The $\sqrt{s} = 7$ TeV selection menu is purely cut-based and is made globally available to all analyses using a C macro configured either for 2011 or 2012 menu. This also includes the re-optimized working points `loose++`, `medium++` and `tight++`, each a subset of the more loose operating points as we described in [section 3.3.4](#), see also [\[ATLb\]](#) for implementation summary. In the 8 TeV analysis we take advantage of a multivariate technique using electron likelihood at

VeryTightLLH operating point (section 3.3.4.3).

We apply additional requirements on top of the predefined quality levels. The electrons are required to be within the pseudorapidity range of the calorimeter $|\eta| < 2.47$ and have $p_T > 20$ GeV. As was in the case of muons, this requirement was later changed to $p_T > 7$ GeV for the 8 TeV analysis, see section 4.7.1. The calorimeter isolation and track isolation are defined in cone $\Delta R = 0.3$ around the electron candidate. At 7 TeV the total calorimeter energy, resp. track momentum must be less than 14 %, resp. 15 % of the electron. In the latter analysis, the isolation efficiency was modelled differentially in 5 GeV bins, the requirements are summarized in tables 4.14 and 4.15. The calorimeter isolation is corrected for lateral leakage of the electron shower and also for pile-up effects as described in section 3.3.4.4.

The electron energy resolution is smeared in MC as described in section 3.3.4.1, re-scaling is applied as a systematic study. The electron energy scale is corrected also in data using the results of the calibration measurements in $W \rightarrow e\nu$. [ATL14c]

4.5.2.1 Electron reconstruction efficiency

Electron efficiency is divided into three different components that correspond to the individual steps of triggering, identification and reconstructing the object. The full efficiency of an electron is given as product of these components:

$$\epsilon_{\text{total}} = \epsilon_{\text{reconstruction}} \cdot \epsilon_{\text{identification}} \cdot \epsilon_{\text{trigger}} \quad (4.18)$$

where $\epsilon_{\text{reconstruction}}$ is measured with respect to clusters reconstructed in the electromagnetic calorimeter using $Z \rightarrow e^+e^-$ tag-and-probe. The identification efficiency is determined with respect to the reconstructed electrons. Trigger efficiencies $\epsilon_{\text{trigger}}$ are calculated as a fraction over reconstructed electrons passing specific identification criteria [ATL13i, p. 14].

To assess the systematic uncertainties, the efficiency measurement vary the tag-and-probe selection, the size of the mass window around the Z peak, the fit conditions and the background models. The total uncertainty on the measurement is <0.50 % with the dominant uncertainty coming from the background estimate in the tag-and-probe samples. [Lam+08] [ATL13i]

The efficiencies are plotted in fig. 4.32 as a function of electron E_T . Figure 4.31 shows the total electron efficiency at 7 TeV and 8 TeV. The overall selection efficiency ranges from 70–90 % in the central region ($|\eta| < 1.37$) and 5–10 % less in the forward region at 8 TeV. The resulting scale factors are provided in 5 GeV bins and 20 η -bins ($-2.47 < \eta < 2.47$). The scale factor values are between 0.90–1.00 depending on electron p_T and η . This correction is distributed centrally through the combined performance package EGAMMAANALYSISUTILS-00-04-55.

4.5.2.2 Electron isolation efficiency

As we already discussed for muons, the isolation efficiency is very dependent on the specific object selection and must be determined for each analysis individually. The electron isolation scale factors for the isolation and impact parameter (Iso/Ip) requirements are measured in $Z \rightarrow e^+e^-$ events using a tag-and-probe technique with the following selection:

Electron definition in 7 TeV

Reconstruction flags:	Reconstructed cluster electron candidate OR combined track+cluster electron candidate
Geometrical acceptance:	$ \eta < 2.47$, excluding “crack” region $1.37 \leq \eta \leq 1.52$
Object quality:	outside of the regions with LAr readout problems
Kinematic acceptance:	$E_T > 20 \text{ GeV}$
Identification Criteria:	Tight++
Longitudinal impact parameter:	$ z_0 < 1 \text{ mm}$
Transverse impact parameter:	$\frac{d_0}{\sigma_{d_0}} < 10$
Calorimeter isolation:	$\sum_{\Delta R < 0.3} E_T(i) < 0.14 \cdot E_T(e)$
Track isolation:	$\sum_{\Delta R < 0.3} p_T(i) < 0.13 \cdot E_T(e)$

Table 4.14: Electron definition used in 7 TeV analysis**Electron definition in 8 TeV**

Reconstruction flags:	Reconstructed cluster electron candidate OR combined track+cluster electron candidate
Geometrical Acceptance:	$ \eta < 2.47$ excluding “crack” region $1.37 \leq \eta \leq 1.52$
Object Quality:	outside of the regions with LAr readout problems
Kinematic Acceptance:	$E_T > 7 \text{ GeV}$
Identification criteria:	VeryTight _{LLH} (likelihood fit)
Longitudinal impact parameter:	$ z_0 \cdot \sin(\theta_{\text{trk}}) < 0.4 \text{ mm}$
Transverse impact parameter:	$\frac{d_0}{\sigma_{d_0}} < 3$
Calorimeter isolation:	for $p_T < 15 \text{ GeV}$: $\sum_{\Delta R < 0.3} E_T^{\text{corr}}(i) < 0.20 \cdot E_T^{\text{corr}}(e)$ for $15 < p_T < 20 \text{ GeV}$: $\sum_{\Delta R < 0.3} E_T^{\text{corr}}(i) < 0.24 \cdot E_T^{\text{corr}}(e)$ for $p_T > 20 \text{ GeV}$: $\sum_{\Delta R < 0.3} E_T^{\text{corr}}(i) < 0.28 \cdot E_T^{\text{corr}}(e)$
Track isolation:	for $p_T < 15 \text{ GeV}$: $\sum_{\Delta R < 0.4} p_T(i) < 0.06 \cdot p_T^{\text{corr}}(e)$ for $15 < p_T < 20 \text{ GeV}$: $\sum_{\Delta R < 0.3} p_T(i) < 0.08 \cdot p_T^{\text{corr}}(e)$ for $p_T > 20 \text{ GeV}$: $\sum_{\Delta R < 0.3} p_T(i) < 0.10 \cdot p_T^{\text{corr}}(e)$

Table 4.15: Electron definition used in 8 TeV analysis

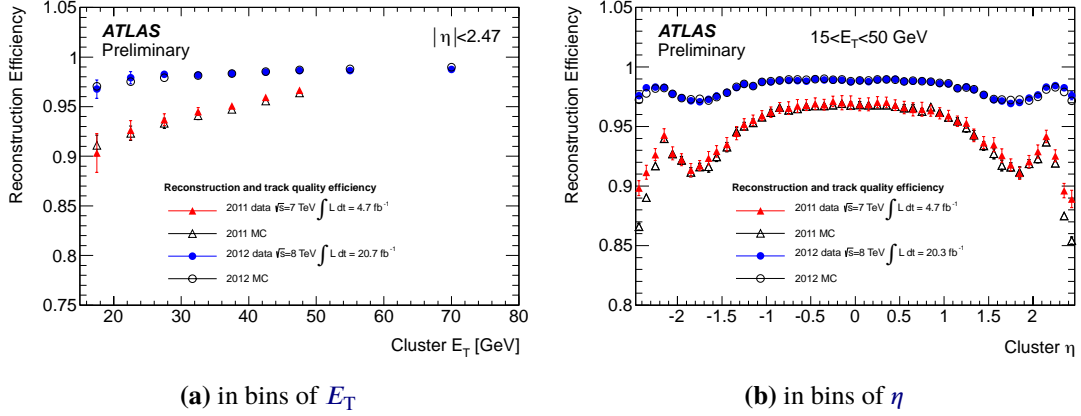


Figure 4.31: Electron reconstruction efficiency for 2011 (triangles) and 2012 (circles) dataset compared with MC. The reconstruction efficiency of electrons is defined with respect to electromagnetic clusters built using a sliding window algorithm, the performance is measured using tag-and-probe in $Z \rightarrow e^+e^-$ events including criteria on track quality. The total statistical and systematic uncertainty is displayed. The absolute increase in reconstruction efficiency in 2012 as compared to 2011 (for both data and MC) is $\approx 2\%$ in the barrel region of the calorimeter and up to $\approx 8\%$ at high $|\eta|$ in the end-caps (where there is more material in front of the calorimeter, hence more electrons undergo bremsstrahlung emissions). Figures from [ATL14d].

- The tag electron is required to have $p_T > 25$ GeV and $|\eta| < 2.47$ excluding the un-instrumented region. Additionally it must match to a single electron trigger EF_e24vhi_medium1 and pass the TIGHT++ electron identification criteria.
- The tag and the probe electrons must have opposite charges and their invariant mass should be consistent with Z mass within 10 GeV.
- The probe electron is selected by applying all the nominal electron selection criteria except the isolation and impact parameter cuts.

A template method has been used to estimate the background contribution in Z events, the background template for $m_{\ell\ell}$ distribution is derived in a QCD enriched region by reverting identification and isolation requirements [ATL13i]. The template distribution is then scaled to match the selected data events in the high mass tails of the distribution (i.e. the side-band region) and subtracted from under the Z peak to obtain the number of electrons yield. The situation is depicted in the denominator plots in fig. 4.35. Trigger scale factors are used to correct for possible mis-modelling, see section 4.4.2.

The Iso/Ip scale factors are computed double differentially from the ratio of data and MC efficiencies in 8 bins of p_T and 20 bins of η . The systematic uncertainties of the scale factors are calculated using the following variations in the model:

- tag electron criterion (e.g. choices of eID or imposing additional isolation cuts)
- Z mass window (invariant mass of tag and probe electron must consistent with Z mass within 5 GeV, 10 GeV and 15 GeV)
- template selection (varying the ID veto or isolation veto criteria)
- threshold for side-band region definition (e.g. $m_{\ell\ell} > 150$ or 170 GeV)

The values of the the Iso/Ip scale factors with their systematic uncertainties are shown in table 4.16. The difference between the Iso/Ip scale factors for triggered and un-triggered electrons is

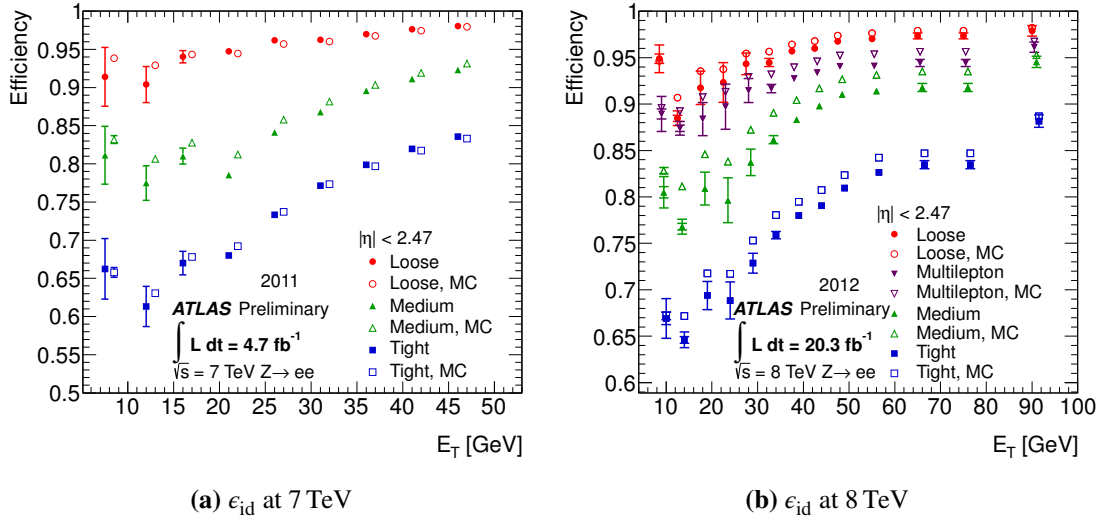


Figure 4.32: Electron identification efficiency for 2011 (left) and 2012 (right) dataset compared with MC shown as a function of E_T within $|\eta| < 2.47$ range. The identification efficiency is computed from the $Z \rightarrow e^+e^-$ using tag-and-probe method decay for the Loose, Multilepton, Medium and Tight operating points. Both data and MC efficiencies are shown. The data efficiencies were derived from the simulated efficiencies scaled by data/MC scale factors. Systematic uncertainties arise dominantly from the background estimation and the probe definition. They are estimated by varying the tag-and-probe selection, the fit conditions and the mass window for signal counting. Figures from [ATL14d].

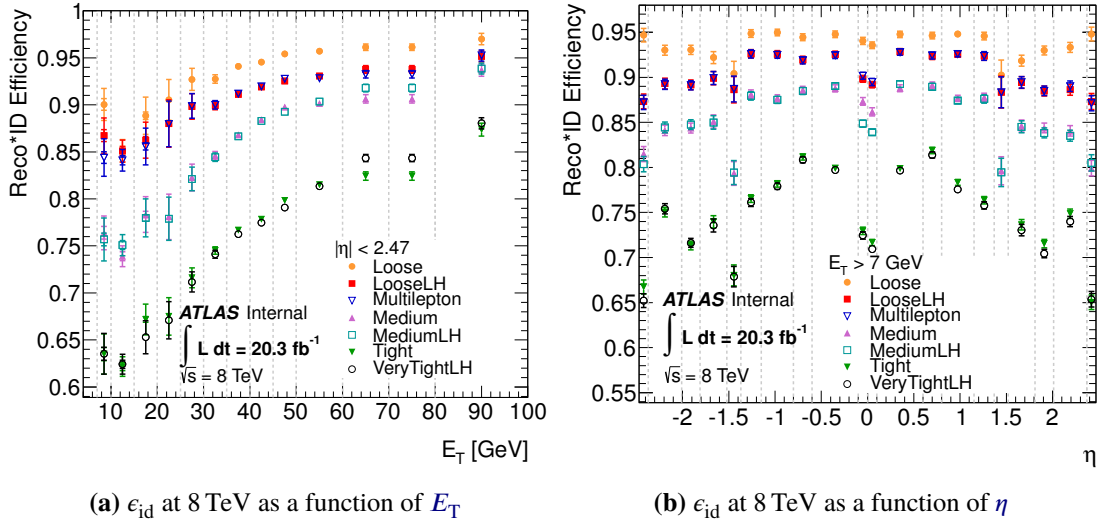


Figure 4.33: Comparison of reconstruction and identification efficiency for the various cut-based and likelihood menus as a function of E_T (left) and η (right) for electrons. The data efficiency is derived from the measured data/MC efficiency ratios. The MC predictions are made the simulated $Z \rightarrow e^+e^-$ decays. The Loose (Very Tight) likelihood was designed to have the same (similar) efficiency as the Multilepton (Tight) cut-based menus, but higher rejection (almost a factor of 2 for hadronic jets). Both data and MC efficiencies are shown. The data efficiencies were derived from the simulated efficiencies scaled by data/MC scale factors. The shown uncertainties are statistical (inner error bars) and statistical \oplus systematic (outer error bars). Systematic uncertainties arise dominantly from the background estimation and the probe definition. They are estimated by varying the tag-and-probe selection, the fit conditions and the mass window for signal counting. The last E_T bin includes the overflow. The dashed lines indicate the bins in which the efficiencies are calculated. Figures from [LdV12, p. 45].

indicated in [fig. 4.34](#). The difference is added as a systematic uncertainty to avoid correcting for the same effect twice, in the trigger [scale factors](#) and the isolation/impact-parameter [scale factors](#). These [scale factors](#) are tailored specifically to our 8 TeV analysis. In the 7 TeV analysis, the distributed performance packages `IsoIPSF-00-00-07` was used to obtain the [scale factors](#).

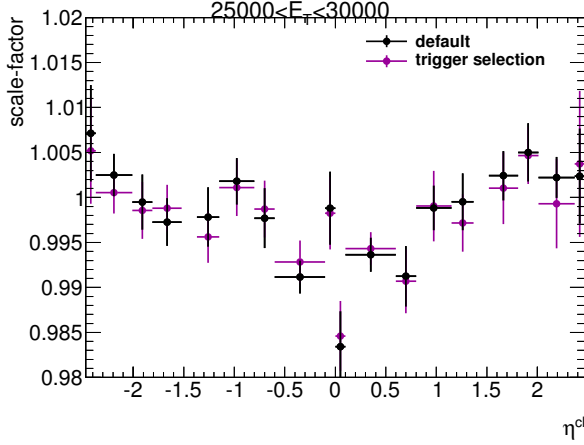


Figure 4.34: Scale-factors for the isolation and impact parameter requirements for $25 < p_T < 30$ GeV electrons. Electrons triggered by `EF_e24vhi_medium1` have a track isolation cut applied on trigger level and thus have a different [scale factors](#). Courtesy of Philip Sommer.

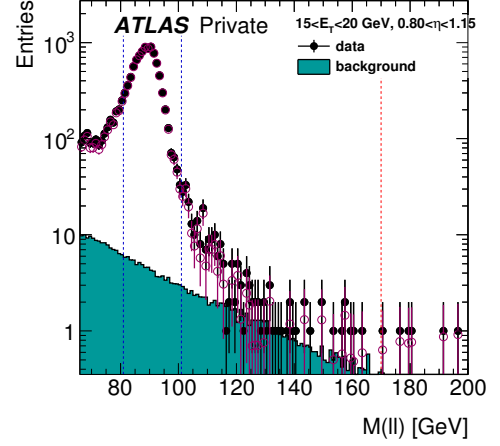


Figure 4.35: Background subtraction in the denominator plot. Black markers show data, open violet markers show background-subtracted data and the green histogram shows one of the background templates, normalized in the high invariant mass side-band. Courtesy of Philip Sommer.

η	15–20 GeV	20–25 GeV	25–30 GeV	30–35 GeV	35–40 GeV	40–45 GeV	45–50 GeV	>50 GeV
[−2.47, −2.37]	1.004 ± 0.014	0.992 ± 0.008	1.007 ± 0.006	1.004 ± 0.004	1.003 ± 0.004	1.005 ± 0.003	1.001 ± 0.004	1.004 ± 0.005
[−2.37, −2.01]	1.006 ± 0.006	1.000 ± 0.003	1.003 ± 0.003	0.997 ± 0.002	0.996 ± 0.002	0.995 ± 0.001	0.994 ± 0.002	0.993 ± 0.002
[−2.01, −1.81]	1.024 ± 0.010	1.002 ± 0.005	0.999 ± 0.003	0.996 ± 0.002	1.000 ± 0.002	0.994 ± 0.002	0.997 ± 0.002	0.996 ± 0.002
[−1.81, −1.52]	0.995 ± 0.007	1.003 ± 0.004	0.997 ± 0.003	1.001 ± 0.002	0.998 ± 0.002	0.998 ± 0.002	0.998 ± 0.002	0.995 ± 0.002
[−1.37, −1.15]	1.015 ± 0.010	1.008 ± 0.006	0.998 ± 0.004	0.999 ± 0.002	0.997 ± 0.002	0.996 ± 0.001	0.998 ± 0.002	0.997 ± 0.002
[−1.15, −0.8]	0.994 ± 0.009	0.995 ± 0.004	1.002 ± 0.003	0.997 ± 0.002	0.997 ± 0.001	0.998 ± 0.001	0.996 ± 0.001	1.001 ± 0.001
[−0.8, −0.6]	0.995 ± 0.009	1.012 ± 0.006	0.998 ± 0.003	0.997 ± 0.002	0.997 ± 0.002	0.996 ± 0.001	0.996 ± 0.002	0.997 ± 0.002
[−0.6, −0.1]	0.990 ± 0.007	0.996 ± 0.004	0.991 ± 0.002	0.995 ± 0.001	0.996 ± 0.001	0.994 ± 0.001	0.994 ± 0.001	0.994 ± 0.001
[−0.1, 0]	0.978 ± 0.013	0.997 ± 0.007	0.999 ± 0.004	0.994 ± 0.003	0.995 ± 0.003	0.994 ± 0.002	0.989 ± 0.002	0.993 ± 0.002
[0, 0.1]	1.052 ± 0.056	0.996 ± 0.007	0.983 ± 0.004	0.998 ± 0.003	0.996 ± 0.002	0.992 ± 0.002	0.997 ± 0.003	0.992 ± 0.003
[0.1, 0.6]	0.986 ± 0.006	0.994 ± 0.004	0.994 ± 0.002	0.993 ± 0.001	0.993 ± 0.001	0.994 ± 0.001	0.995 ± 0.001	0.994 ± 0.001
[0.6, 0.8]	0.992 ± 0.009	0.997 ± 0.006	0.991 ± 0.003	0.997 ± 0.002	0.995 ± 0.002	0.996 ± 0.002	0.995 ± 0.002	0.997 ± 0.002
[0.8, 1.15]	1.003 ± 0.010	1.014 ± 0.005	0.999 ± 0.002	0.997 ± 0.002	0.996 ± 0.001	0.998 ± 0.001	0.997 ± 0.001	0.994 ± 0.001
[1.15, 1.37]	0.998 ± 0.010	1.003 ± 0.005	1.000 ± 0.004	1.002 ± 0.003	0.999 ± 0.002	0.998 ± 0.001	0.999 ± 0.002	0.998 ± 0.002
[1.52, 1.81]	1.006 ± 0.007	0.997 ± 0.004	1.002 ± 0.003	1.002 ± 0.002	0.996 ± 0.002	0.994 ± 0.001	0.995 ± 0.002	0.995 ± 0.003
[1.81, 2.01]	1.014 ± 0.009	0.996 ± 0.005	1.005 ± 0.003	0.998 ± 0.003	0.998 ± 0.002	0.997 ± 0.002	0.998 ± 0.002	0.996 ± 0.003
[2.01, 2.37]	1.008 ± 0.006	0.998 ± 0.003	1.002 ± 0.004	0.995 ± 0.002	0.997 ± 0.001	0.996 ± 0.002	0.996 ± 0.002	0.994 ± 0.002
[2.37, 2.47]	1.004 ± 0.013	0.999 ± 0.008	1.002 ± 0.005	1.000 ± 0.004	1.000 ± 0.004	0.999 ± 0.003	1.009 ± 0.004	1.010 ± 0.005

Table 4.16: Electron isolation [scale factors](#) shown double differentially in bins of p_T and η including full uncertainties. The inefficiency caused by electron isolation is very small as the values are very close to 1 with very small uncertainties.

4.5.3 Jet definition

Both our analyses use jets reconstructed from [topo-clusters](#) using the [anti- \$k_t\$](#) algorithm with $R = 0.4$, as described in [fig. 3.31](#). At 7 TeV the jets are calibrated from the electromagnetic scale to

hadronic energy scale using EM+JES correction (`AntiKt4EM`). At 8 TeV we used LCW +JES scale (`AntiKt4LC`) as it is significantly more `pile-up` robust (see [fig. 3.35](#)) and it also simplified the propagation of jets in \cancel{E}_T rebuilding.

The selected jets are required to have $|\eta| < 4.5$ and $p_T > 25$ GeV at the hadronic energy scale. The 8 TeV analysis also introduces a cut on jet vertex fraction (JVF) to be larger than 0.5 for the purpose of suppressing `pile-up` effects on our object selection. Electron jet overlap is also considered, see [section 4.5.6](#).

The energy calibration introduces the JES uncertainties as described in [fig. 3.32](#), the effect of `jet energy resolution` is also considered. At 7 TeV an overall `jet energy scale` uncertainty is propagated to the WW selection by moving the jet p_T “up” and “down” according to total JES uncertainty. For the 8 TeV analysis, we use a reduced set of 14 nuisance parameters that account for `jet energy scale` correction, `pile-up`, close-by jets and jet flavour composition as discussed in [section 3.3.5.2](#). The baseline uncertainties (with over 60 parameters) was not yet finalized at the time of writing this thesis. This has negligible impact as the 14 parameter set contains enough information about composition of the jet energy uncertainties and each component is treated independently in this analysis. Moreover, we apply the data driven jet veto `scale factors` as described in [section 4.7.2](#).

The uncertainty is applied via the `ApplyJetCalibration-00-01-07` and `ApplyJetResolutionSmearing-00-00-03` performance packages at 7 TeV and `ApplyJetResolutionSmearing-00-01-02` and `ApplyJetCalibration-00-03-20` at 8 TeV. The jet calibration corrections are propagated to \cancel{E}_T rebuilding for each jet separately, see below.

4.5.4 Missing transverse energy definition

The `missing transverse energy` \cancel{E}_T is determined in combination from the energy collected by `Electromagnetic Calorimeter` and `Hadron Calorimeter` calibrated topological clusters and the momentum measurements from the `Muon Spectrometer` and the `Inner Detector`. We have discussed the topological clustering algorithm in [section 3.3.4](#) and [fig. 3.27](#) (topo-clusters shown in orange). `Combined` muon measurements are restricted to the `pseudorapidity` range $|\eta| < 2.5$, but the calorimeter topological clustering extends to $|\eta| < 4.9$ allowing a more complete coverage of the transverse energy in the event. This effectively means, that nearly all transverse energy in the event is recorded in the topological clusters.

4.5.4.1 Relative missing transverse energy

In order to reduce the sensitivity to possibly mis-measured leptons or jets, we define a modified `missing transverse energy` variable referred to as *relative* \cancel{E}_T which is defined as

$$\cancel{E}_{T,\text{Rel}} = \begin{cases} \cancel{E}_T \cdot \sin(\Delta\phi_{\ell,j}) & \text{for } \Delta\phi_{\ell,j} < \pi/2 \\ \cancel{E}_T & \text{for } \Delta\phi_{\ell,j} \geq \pi/2, \end{cases} \quad (4.19)$$

where $\Delta\phi_{\ell,j}$ is the distance between the `missing transverse energy` and the nearest lepton or jet. Only leptons and jets satisfying our object definitions summarized in [tables 4.12 to 4.15](#)) are considered. Comparing the difference in shape between \cancel{E}_T and $\cancel{E}_{T,\text{Rel}}$ as shown in [fig. 4.36](#), one can see that the discriminatory power for our signal has improved. This is because high- p_T muons produced

by $Z + \text{jets}$ have a large momentum uncertainty and any mis-measurement propagates directly as a fake [missing transverse energy](#). This modified variable is also less sensitive to the \cancel{E}_T created by $\tau \rightarrow \ell \nu$ decays.

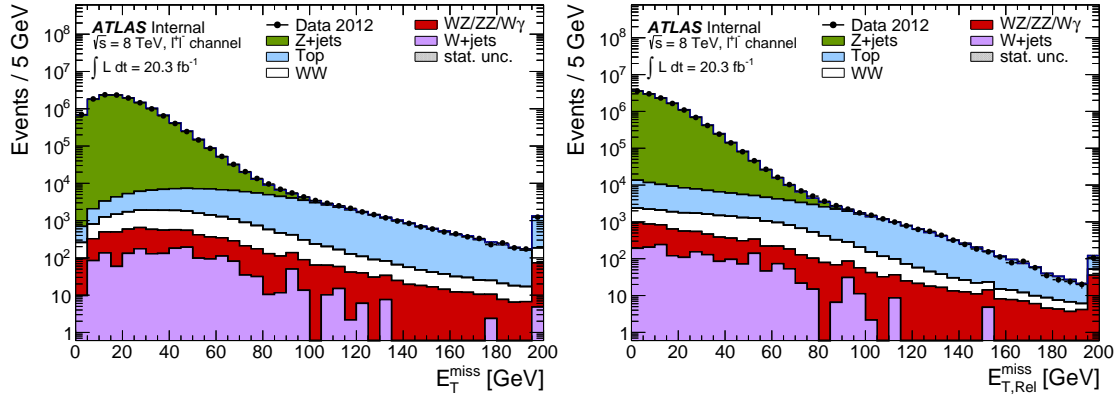


Figure 4.36: Comparison of relative [missing transverse energy](#) (right) with the nominal definition of [missing transverse energy](#) (left). The distributions are shown for the 8 TeV analysis with MC models describing the distribution composition. It is clear from the figure how the introduction of $\cancel{E}_{T,\text{Rel}}$ improves the discriminatory power of \cancel{E}_T variable by moving $Z + \text{jets}$ background to the lower end of the spectrum.

4.5.4.2 Missing energy smearing

The [missing transverse energy](#) reconstructed from the components described in [section 3.3.6](#) is collectively referred to as MET_RefFinal, which is available as a [D3PD](#) branch. However, the correction to physics objects like electron energy scale for data and generally smearing and rescaling of objects in MC to improve the data/MC agreement must be propagated into \cancel{E}_T in a consistent way. The correct procedure is to rebuild the [missing transverse energy](#) completely, seeded by the corrected objects specific to the analysis (electrons, muons and jets with corrected kinematics). As indicated in [table 4.17](#), we rescale electrons and calibrate jets on data. In MC, we apply resolution smearing to muons, electrons and jets. The modified muon p_T is propagated into the muon term $\cancel{E}_{x(y)}^{\text{MS}}$ (MET_MuonBoy), electron \cancel{E}_T is propagated into $\cancel{E}_{x(y)}^{\text{e}^\pm}$ (MET_RefEle) and jets are propagated into $\cancel{E}_{x(y)}^{\text{jets}}$ by vector sum of all objects in a given event. The inputs are handled by the MissingETUtility-01-02-05 performance package. The magnitude of the correction depends on the adjustments made to the input objects, generally keeping under 10 %, yet there are cases where the values are corrected by nearly an order of magnitude. This is a direct consequence of recalibrating the inputs to [missing transverse energy](#) rebuilding which may cause a dramatic change in the soft term contributions not associated with any objects when the total measured \cancel{E}_T is low.

4.5.4.3 Missing transverse momentum

The calorimeter based measurement of [missing transverse energy](#) resolution suffers in high pile-up conditions from the large amount of energy deposited in the detector in each [bunch crossing](#). The run conditions at 8 TeV reduced the discriminatory power of [missing transverse energy](#), notably for the $Z + \text{jets}$ background (see the long tails in [fig. 4.36](#)). The missing energy modelling is enhanced

		Data		MC	
		Smeared	Scaled	Smeared	Scaled
muons	yes	–	–	yes	–
electrons	yes	–	yes	yes	–
jets	yes	–	–	yes	–
\cancel{E}_T	yes	–	–	–	–

Table 4.17: Summary of correction applied to nominal objects. The term *corrected* stands for the application of [scale factors](#) or a correction propagation. Smearing is applied exclusive on [MC](#). Only electrons are scaled in data. Photons are not included in the final state of our analysis, although they are considered in [missing transverse energy](#) rebuilding.

by introducing a track-based measurement of [missing transverse momentum](#) defined as a vectorial sum

$$\cancel{p}_T = - \sum_i \mathbf{p}_T(i) \quad (4.20)$$

of all tracks within the tracker geometrical and kinematic acceptance: $p_T > 500$ MeV, $|\eta| < 2.5$ and compatible with the [PV](#): $|d_0| < 1.50$ mm, $|z_0 \sin(\theta)| < 1.50$ mm. We additionally require the track to be recorded with at least 1 hit in the [Pixel](#) and at least 6 hits in the [SCT](#). Tracks corresponding to the signal leptons in terms of p_T are included regardless of the selection but the [transverse momentum](#) contribution from the muon tracks is replaced by the [combined](#) measurement from the [ID](#) and [MS](#) (see [section 3.3.3](#)) and for electrons the track is replaced by the calibrated calorimeter based measurement.

The systematic uncertainties of the measurement are evaluated independently from the calorimeter based \cancel{E}_T . Most notably, [Missing transverse momentum](#) does not account for photons and neutral hadrons which limits the uncertainty sources. The measurement is expected to be more [pile-up](#) robust, because the selected tracks feeding the missing momentum are compatible with [primary vertex](#) in the given [bunch crossing](#). The uncertainties are estimated from a parametrization of a parallel (longitudinal) and perpendicular (transverse) component as a function of p_T (derived from [Z](#) events), see [section 4.8.4](#). [[ATL14l](#)]

4.5.4.4 Azimuthal angle between missing transverse energy and momentum

Following a definition of track-based missing energy, we further improve the discriminatory power by cross-examining the \cancel{E}_T and \cancel{p}_T measurements using an azimuthal angle between the two vectors:

$$\underbrace{\phi(\cancel{E}_T) = \arctan\left(\frac{\cancel{E}_x}{\cancel{E}_y}\right) \quad \text{and} \quad \phi(\cancel{p}_T) = \arctan\left(\frac{\cancel{p}_x}{\cancel{p}_y}\right)}_{\Delta\phi(\cancel{E}_T, \cancel{p}_T) = |\phi(\cancel{E}_T) - \phi(\cancel{p}_T)|} \quad (4.21)$$

In signal events with large missing energy, the vectors reconstructed by the calorimeter and tracker are more likely to point in the same direction, whereas for events with no missing energy like $Z \rightarrow e^+e^-$ and $Z \rightarrow \mu^+\mu^-$, the measured missing energy is faked by the high detector occupancy caused by [pile-up](#). In this case, the independent measurements from the calorimeter and the tracker are less likely to point in the same direction, as the two systems are not affected by [pile-up](#) in the

same way, so the distribution of $\Delta\phi(\mathbf{E}_T, \mathbf{p}_T)$ is expected to be more uniform. Cutting on higher values in $\Delta\phi(\mathbf{E}_T, \mathbf{p}_T)$ thus allows us to improve our S/B ratio. Figure 4.37 shows the distributions of $\Delta\phi(\mathbf{E}_T, \mathbf{p}_T)$ in the final stages of our selection with signal events shown in white and Z + jets background shown in green.

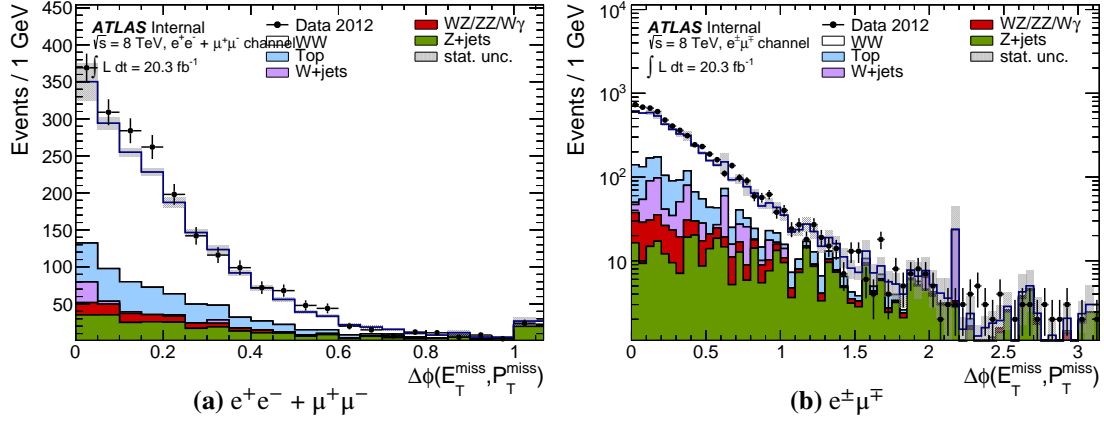


Figure 4.37: Distribution of $\Delta\phi(\mathbf{E}_T, \mathbf{p}_T)$ in the zero jet bin after cutting on \mathbf{p}_T and \mathbf{E}_T as described in section 4.2. Figures show the combination of $e^+e^- + \mu^+\mu^-$ channel (left) and the $e^\pm\mu^\mp$ channel (right). The missing transverse energy and missing transverse momentum vector are less likely to point in similar direction in the presence of fake missing energy, as is the case for Z + jets samples (shown in green).

4.5.5 Stream overlap removal

As described in section 3.1, the ATLAS trigger produces data in separate streams. The muon and electron data streams are used for this analysis in the $\mu^+\mu^-$ and e^+e^- channels, respectively. The inclusive $e^\pm\mu^\mp$ sample is obtained using both streams and duplicate events are removed using the internal `streamDecision_Muons` and `streamDecision_Egamma` data flags.

4.5.6 Object overlap removal

Overlap removal is the final stage of the pre-selection of physics objects. This procedure is designed to remove double counting in cases where two separately reconstructed physics objects could actually represent a single measurement. This situation can occur for example when a calorimeter cluster associated with a high- p_T electron is reconstructed as a part of a jet. The following object overlaps are considered:

e^\pm/jet overlap is the prevalent case of overlapping physics objects. The overlap removal is designed to handle cases where clusters produced by high- p_T electrons overlap with jets reconstructed by the *anti- k_t* algorithm. This common problem is simply handled by removing any jet inside a cone of $\Delta R < 0.3$ in the $(\eta - \phi)$ plane around the pre-selected electrons from the event.

e^\pm/e^\pm overlap removal addresses the issue of electrons that could come from the electron cluster and track reconstruction algorithms as two separate objects. Although this is a rare problem, it is expected to happen if there are multiple low- p_T tracks pointing to the same calorimeter cluster. To remove this possibility, if two electrons have a distance in the $(\eta - \phi)$ plane

$\Delta R < 0.1$, the one with less transverse momentum is dropped. No major effect of this removal has been observed.

This was not an issue in the 8 TeV analysis as the overlap removal between the reconstruction algorithms (track and cluster) is already included inside the reconstruction algorithms. We observed no event in the 2012 dataset where removing this overlap would have an effect on our selection.

μ^\pm/e^\pm **overlap** occurs in rare cases, where the muon traversing through the detector will “fake” and electron cluster (by emitting a bremsstrahlung photon for example). This could in principle lead to the creation of electron pairs very close to the muon. This overlap is removed by removing any electron found within a distance of $\Delta R < 0.1$ in the $(\eta - \phi)$ plane.

μ^\pm/jet **overlap** was only investigated and utilized for the 8 TeV analysis. Muons are not likely to be reconstructed as jets because of the way the measurement is combined from various parts of the detector. The μ^\pm/jet overlap removal concerns those muons coming from heavy-flavour jets (like a semi-leptonic decays of a b-jet). Although this will produce non-isolated muons on most cases, we remove the residual contributions from heavy flavour jets by performing removing any muons that overlap with a jet inside a cone of $\Delta R < 0.3$.

This procedure can also remove genuine, isolated muons that had FSR photon conversions reconstructed as jets. Therefore, the μ^\pm/jet overlap removal negatively affects the efficiency of the muon identification. [ATL14i].

4.6 Datasets

The analysis at centre of mass energy of $\sqrt{s} = 7$ TeV uses the full 2011 dataset with the total integrated [luminosity](#) 5.25 fb^{-1} (starting from period D1, recorded October 2011) while the 8 TeV analysis uses the full 2012 dataset with 23.30 fb^{-1} . The corresponding total integrated [luminosity](#) after the data quality selection applied in this analysis is 4.64 fb^{-1} for 2011 and 20.28 fb^{-1} for 2012 determined from [iLumiCalc](#) tool for the given [GRL](#) (see [section 3.2.1](#)). The uncertainty on the integrated luminosity is obtained using [VMS](#) and reflects the precise understanding of [LHC](#) beam currents, see [section 2.6.2](#).

4.6.1 Derived datasets

Both datasets include a pre-filter at the stage of converting the [AOD](#) events from [Muons](#) and [Egamma](#) data streams made at the [Tier0](#) to a specialized [D3PD](#) format common to all electroweak analyses (the datasets are labelled `NTUP_SMWZ`). This is effectively [NTUP](#) format as described in [section 3.2.3](#) that is produced centrally for [ATLAS](#) electroweak boson analysis group.

While the size of the dataset is limited to hundreds of gigabytes for the 7 TeV analysis, the disk space required in 2012 for the 8 TeV would be over 200 TB. Consequently, a second event filtration stage had to be implemented:

- Removal of variable branches not required for the analysis.
- At least two leptons with $p_T > 10$ GeV. Muons are accepted from the [STACO](#) collection, electrons are accepted at [LOOSE++](#) (standard 2012 menu) [LOOSELLH](#) or [VERYTIGHTLLH](#) (likelihood identification) operating points.

Muon and electron quality definitions have been discussed in [sections 3.3.3.4, 3.3.4.2 and 3.3.4.3](#). The event pre-selection is applied only to data, [MC](#) is filtered only for selected variable branched. This effectively reduces the volume of the dataset by an order of magnitude. The datasets were fully produced by me using the `Skimmer` class described in [section 3.4](#) and are currently used as the official filtered datasets within the Electroweak working group.

Dataset versions with the corresponding integrated [luminosity](#) are listed in the following table:

\sqrt{s}	D3PD version	recorded L	L after GRL
8 TeV	p1328	23.30 fb^{-1}	20.28 fb^{-1}
7 TeV	p1035	5.25 fb^{-1}	4.64 fb^{-1}

Table 4.18: Analysis dataset versions

4.6.2 Data cleaning

The following data quality criteria

- **Data quality flags:** The [GRL](#) specifies the data quality conditions under which events recorded in a given run can be accepted. The data quality flags are assigned per [lumi-block](#) (≈ 1 min). Both our analyses use centrally-provided [GRL](#) which ensure that only events in [lumi-blocks](#) flagged as “good for physics” are processed:
 - ▷ 7 TeV: `data11_7TeV.periodAllYear_DetStatus-v36-pro10_CoolRunQuery-00-04-08_WZjets_allchannels_DtoM.xml`
 - ▷ 8 TeV: `data12_8TeV.periodAllYear_DetStatus-v61-pro14-02_DQDefects-00-01-00_PHYS_StandardGRL_All_Good.xml`
- **LAr hole cleaning:** In 2011 a long-term problem in the LAr calorimeter negatively affected the jet and E_T reconstruction. 6 front-end boards of the calorimeter were not operational). Starting from run 180614 to run 184169, it is recommended that all analyses veto events if a calorimeter jet with $p_T > 25$ GeV falls in the vicinity of the LAr hole: $-0.1 < \eta < 1.5$, $-0.9 < \phi < -0.5$. The veto was provided centrally by the performance group, technical details in [\[ATL14f\]](#).
- **E_T cleaning:** Jets with calibrated $p_T > 20$ GeV that do not overlap with a selected lepton within $\Delta R < 0.3$ are tested to be in `BadLooseMinus` category (see [section 3.3.5.3](#)). Events containing at least one jet that passes these criteria are removed from the analysis to avoid adverse effects to E_T since bad jets are not associated to real energy deposits in the calorimeters. The cleaning is applied to both data and [MC](#). This requirement is common to both analyses. [\[ATL14f\]](#)
- **Hot Tile cell:** In 2012 data taking, periods B1 and B2 were affected by a hot Tile calorimeter cell which has not been marked for correction in reconstruction (commonly referred to

as *masking* the module). This problem can be removed on the jet level with a negligible inefficiency by removing events where a jet points to the region near LBC28 ($\eta = -0.15$, $\phi = 2.7$). It is only necessary to remove the event if the jet has its highest energy fraction in the Tile second layer, provided this fraction is large $E_{\text{layer}}/E_{\text{jet}} > 0.6$. The affected runs are: 202660, 202668, 202712, 202740, 202965, 202987, 202991, 203027, 203169. [ATL1f].

- **TileTrip cleaning:** The Tile calorimeter suffered from frequent module problems during 2012 data taking which resulted in corrupted events. The defect is considered tolerable, as an un-powered module is extrapolated from its neighbours in the offline reconstruction, but it is recommended to veto the events for analyses dependent on jet and E_T quality. The affected events are flagged with *tile trip error* flag `tileTrip == 2`. An additional list of 433 corrupted events was distributed in the `TileTripReader` performance package. [ATL14k]
- **BCH cleaning:** The procedure which was used to correct for masked cells within the tile calorimeter was not able to properly handle entire dead modules in 2012 data set. Studies performed by the jet performance group have shown that medium to high- p_T jets which fall within a masked module are usually under-corrected, while jets in modules adjacent to a masked module are over-corrected. With increasing p_T , the jet become more collimated and as such could be fully contained within masked modules. The `BCHCleaningTool` handles when modules have been masked for a given run and a given **lumi-block**. We veto the event using a combination of geometrical cuts and a p_T efficiency map. If a jet is found falling the core of a masked region for the corresponding event. Jets falling into the edge of a masked region are also removed if they lead to an overestimated jet response, we assign appropriate systematic uncertainties, see [section 4.8](#). Cleaning these events is paramount, as this problem can potentially create large fake E_T . The correction is also applied to **MC** on a random run and **lumi-block** numbers to emulate the right time-dependence of the masking to equalise the data and **MC** and emulate the inefficiency in data in terms of masked modules. [ATL14b]
- **Data corruption:** Events with miscellaneous data corruption are handled using detector flags:
 - ▷ LAr noise burst are removed by vetoing events with `larError == 2`,
 - ▷ corrupted Tile events are rejected (`tileError == 2`),
 - ▷ Clock synchronization in **lumi-blocks** recorded just after the trigger control system resets could potentially result in incomplete events. These are removed if `coreFlags & 0x40000 == 0`, where `&` is a bitwise AND operator.

4.7 Acceptance

In this section it is our goal to investigate the effects of the selection cuts on signal acceptance. The motivation behind the choice of cuts for this analysis has been clearly outlined in [section 4.7.1](#). Defining optimal selection relies on detailed **MC** modelling and precise determination of object and event selection. To summarize, the **MC** description of the event is complemented with the following selection efficiency corrections estimated from data control samples:

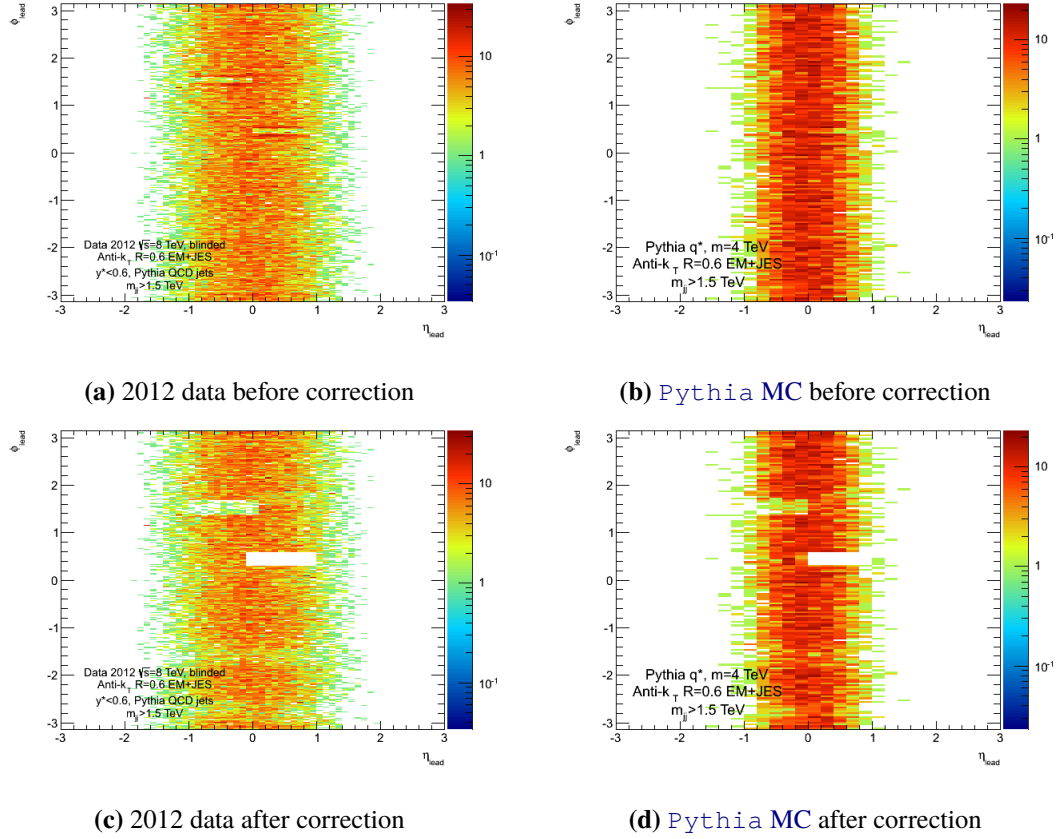


Figure 4.38: $\eta - \phi$ distributions for leading jet in an event $m_{jjjj} > 1.50$ TeV in data (left) and MC (right), before rejecting events (top) and after rejecting events (bottom) flagged by the `BCHCleaningTool`. The events in this plot are required to have at least two central jets reconstructed by `anti- k_t` $R = 0.6$ with $p_T > 50$ GeV at EM+JES scale. The cut demonstrated here is geometrical only. Figures from [ATL14b].

- trigger efficiency
- lepton reconstruction and identification efficiency
- isolation efficiency

We have discussed the relevant [scale factors](#) throughout [section 4.5](#), see also [table 4.17](#). The cut flow for signal MC is shown for the 8 TeV analysis in [table 4.19](#). The event yields are quoted in the three final states and the combined channel for each cut stage following the preselection. We show the prompt electron or muon decays from W bosons and non-prompt decays through τ leptons separately. The MC events are normalized to 20.28 fb^{-1} using the reference NLO SM cross-sections given in [section 4.3.1](#). The signal includes $q\bar{q} \rightarrow WW \rightarrow \ell^+ \nu \ell^- \bar{\nu}$, $gg \rightarrow WW \rightarrow \ell^+ \nu \ell^- \bar{\nu}$ and $gg \rightarrow H \rightarrow WW$ processes which contribute 93 %, 4 %, 3 % and 3 % of the final yield respectively. The τ^\pm decay channels contribute ≈ 8.20 % of the total signal yields after final selection. For completeness, we also show the cut flow for the 7 TeV analysis in [table 4.20](#).

4.7.1 Cut optimization

The selection cuts are applied to maximize the selection of signal events against the backgrounds. The concept of a cut consists of selecting the appropriate cut variable and the cut value. In practice, it is also important that the cut variable is well modelled by MC and not correlated with other cut

Cuts	<i>ee</i> Channel		$\mu\mu$ Channel		<i>eμ</i> Channel	
	<i>evev</i>	$\tau\nu\ell\nu$	$\mu\nu\mu\nu$	$\tau\nu\ell\nu$	<i>evμν</i>	$\tau\nu\ell\nu$
Total events (20.28 fb ⁻¹)	13910.58	5327.42	13910.58	5327.42	27821.14	10654.82
ℓp_T , trigger-match	3052.42	352.69	5019.56	506.55	7977.24	872.12
$m_{\ell\ell} > 15$ (10) GeV	3029.95	350.54	4977.74	502.81	7971.25	871.57
$ m_{\ell\ell} - m_Z > 15$ GeV	2345.37	260.78	3840.29	376.15	7971.25	871.57
$E_{T,Rel} > 45$ (15) GeV	891.61	76.79	1530.75	117.69	6180.39	639.32
$p_T > 45$ (20) GeV	697.89	54.15	1196.00	81.10	5521.67	574.37
$\Delta\phi(E_T, p_T) < 0.3$ (0.6)	453.23	34.49	785.69	52.63	4313.02	439.90
Jet veto	328.03	21.53	578.29	36.10	2968.55	286.26

Table 4.19: WW MC event selection cut flow and overall acceptance. The MC WW signal expectations are normalised to 20.28 fb⁻¹ integrated luminosity, using the NLO SM cross section. For the final WW acceptance, the jet veto SF (0.957/0.954/0.956 for *ee/μμ/eμ*) has already been included.

Cuts	<i>ee</i> Channel		$\mu\mu$ Channel		<i>eμ</i> Channel	
	<i>evev</i>	$\tau\nu\ell\nu$	$\mu\nu\mu\nu$	$\tau\nu\ell\nu$	<i>evμν</i>	$\tau\nu\ell\nu$
Total events (4.64 fb ⁻¹)	2421.1	922.4	2421.1	922.4	4842.2	1844.9
ℓp_T , trigger-match	554.78	68.32	954.58	106.45	1475.24	169.36
$m_{\ell\ell} > 15$ (10) GeV	548.81	67.59	938.84	104.98	1460.10	167.00
$ m_{\ell\ell} - m_Z > 15$ GeV	424.96	49.98	724.75	78.52	1460.10	167.00
$E_{T,Rel} > 45$ (25) GeV	154.42	12.91	286.98	24.21	921.08	94.69
Jet veto	97.60	7.03	180.07	14.56	586.40	57.33
$p_T(\ell\ell) > 30$ GeV	93.57	6.68	171.89	13.66	490.71	47.10

Table 4.20: WW MC event selection cut flow and overall acceptance. The MC WW signal expectations are normalised to 4.64 fb⁻¹ integrated luminosity, using the NLO SM cross section. For the final WW acceptance, the jet veto SF (0.957/0.954/0.956 for *ee/μμ/eμ*) has already been included.

variables used to event selection to avoid potential bias. Another important goal is to keep adequate statistics despite the cuts. It may be that a powerful cut significantly improves the *S/B* ratio, but at the cost of reducing the statistics. It is therefore necessary to balance between these two aspects. To optimize the selection we define the signal significance as:

$$S_{\text{cuts}} = \frac{N_S}{\sqrt{N_S + N_B + \sum_i \Delta N_{B,i}(\text{syst.})^2}} \cdot H(N_S) \quad (4.22)$$

where N_S represents the number of signal events, N_B represents the number of background events and $\Delta N_B(\text{syst.})$ is the systematic uncertainty for the given background and $H(N_S)$ is a unit step function:

$$H(N_S) = \begin{cases} 0 & \text{if } N_S < N_{\text{critical}} \\ 1 & \text{if } N_S \geq N_{\text{critical}} \end{cases} \quad (4.23)$$

where N_{critical} is set to 900 (resp. 2500) for same flavour (resp. combined flavour) channels to ensure that the signal statistics is reasonably large (about 3–4 times of the yields in the 7 TeV analysis). The cut optimization is performed by studying the introduction (or removal) of certain cuts and adjusting the cut values. All critical signal and background samples described in section 4.3 are included in the study and have adequate statistics, with the exception of W + jets in the same flavour

channel, but their contribution is tiny. The fractional background systematic uncertainties are set to fixed values of 30 %, 30 %, 30 % and 10 % for Z + jets, top, W + jets and diboson backgrounds respectively. These numbers are based on our experience with the backgrounds, the full breakdown of systematic uncertainties at nominal selection is shown in [section 4.9](#).

4.7.1.1 Optimization of preselection cuts

A number of scenarios is considered for the preselection stage while the final selection remains fixed. The main optimization issue rests with the choice between single-lepton and di-lepton [triggers](#), however a modification of electron likelihood and 3rd lepton veto requirements are also considered. The results are summarized in [tables 4.21 to 4.23](#) for e^+e^- , $\mu^+\mu^-$ and $e^\pm\mu^\mp$ channels respectively. The electron likelihood identification at [VERYTIGHTLLH](#) operating point has similar efficiency to [TIGHT++](#), we compare them in terms of background rejection power.

We have already discussed in [section 4.4](#) that di-lepton [triggers](#) hold a certain advantage over single-lepton [triggers](#). The results presented here support our strategy to switch to exclusively di-lepton triggers in the same flavour channels. In the combined flavour channel a combination of single-lepton and [triggers](#) is necessary to compensate for the inefficiency of `EF_e12Tvh_medium1_mu8` (see [fig. 4.26](#)). Here, we investigate the scenario of using a combination of single-lepton and di-lepton [triggers](#) for the same flavour channels as well.

Applying the 3rd lepton veto still leaves a large contribution from the diboson backgrounds ($WZ \rightarrow 3\ell$, $ZZ \rightarrow 4\ell$) if the additional leptons lie outside the kinematic or geometric acceptance of the detector. Both the signal leptons in our analysis are required to have $p_T > 20$ GeV including track, identification and isolation requirements as explained in [section 4.5](#). However, lowering the p_T threshold on additional leptons provides better rejection on the diboson backgrounds, reducing it by nearly 10 %. This, with a combination of electron likelihood identification is considered as the optimal scenario.

4.7.1.2 Optimization of final selection

At preselection level, the dominant backgrounds come from Z + jets and top, as clearly indicated in [figs. 4.5 to 4.7](#). Top background is removed by doing the measurement in zero jet bin and as such need not be discussed here. Concerning Z + jets, it is clear that a Z mass veto needs to be applied to cut out a window around the Z mass peak in same flavour channels.

As we already discussed, cutting on [missing transverse energy](#) is a crucial part of analysis. The calorimeter based E_T is considered in its standard form as well as in the relative form $E_{T,Rel}$ (see [section 4.5.4.1](#)) less susceptible to [pile-up](#). As the energy imbalance observed in Z + jets events is faked, we simply need to find the optimal cut value. We also consider additional variables to enhance the Z + jets discriminatory power: $p_T(\ell\ell)$ which was used in the 7 TeV analysis and track-based measurement of [missing transverse momentum](#).

We consider these variables in terms of optimal cut value but also the data/MC agreement and the agreement between the e^+e^- and $\mu^+\mu^-$ channels. Electrons and muons are expected to behave differently in terms of reconstruction and systematic uncertainties. We evaluate the agreement using

Cut case	WW	W + jets	Z + jets	Di-bosons	Top	S_{cuts}
Pre-selection						
Di-lepton trig., LLH eID, > 2ℓ veto at 7 GeV	1	1	1	1	1	–
Single-lepton trig., TIGHT++ eID, > 2 ℓ veto at 7 GeV	1.04	2.78	1.05	1.07	1.03	–
Single or di-lepton trig., LLH eID, > 2 ℓ veto at 7 GeV	1.01	1.16	1.01	1.01	1.01	–
Single-lepton trig., LLH eID, > 2 ℓ veto at 7 GeV	1.00	1.15	1.01	1.00	1.01	–
Di-lepton trig., LLH eID, > 2 ℓ veto at 20 GeV	1.00	1.00	1.00	1.10	1.00	–
Final selection						
Di-lepton trig., LLH eID, > 2ℓ veto at 7 GeV	1	–	1	1	1	9.13
Single-lepton trig., TIGHT++ eID, > 2 ℓ veto at 7 GeV	1.05	–	1.01	1.05	1.05	7.93
Single or di-lepton trig., LLH eID, > 2 ℓ veto at 7 GeV	1.01	–	0.99	1.00	1.04	9.03
Single-lepton trig., LLH eID, > 2 ℓ veto at 7 GeV	1.00	–	0.97	0.99	1.03	9.00
Di-lepton trig., LLH eID, > 2 ℓ veto at 20 GeV	1.00	–	1.00	1.07	1.00	9.10

Table 4.21: The comparison of signal and background yields between different cut cases in e^+e^- channel and signal significance S_{cuts} . The filled numbers are ratios of **MC** yields with respect to the optimal selection in the top row. W + jets are statistically limited in final section (1–2 events), therefore left empty. eID stands for electron identification, LLH stands for likelihood identification (see section 3.3.4.3). Courtesy of Philip Sommer.

Cut case	WW	W + jets	Z + jets	Di-bosons	Top	S_{cuts}
Pre-selection						
Di-lepton trig., > 2ℓ veto 7 GeV	1	1	1	1	1	–
Single or di-lepton trig., > 2 ℓ veto 7 GeV	1.03	1.04	1.03	1.03	1.03	–
Single-lepton trig., > 2 ℓ veto at 7 GeV	1.00	1.00	1.01	1.00	1.01	–
Di-lepton trig., > 2 ℓ veto 20 GeV	1.00	1.00	1.00	1.13	1.00	–
Final selection						
Di-lepton trig., > 2ℓ veto 7 GeV	1	–	1	1	1	11.1
Single or di-lepton trig., > 2 ℓ veto 7 GeV	1.03	–	1.03	1.04	1.04	11.1
Single-lepton trig., > 2 ℓ Veto 7 GeV	0.99	–	0.96	1.00	1.01	11.1
Di-lepton trig., > 2 ℓ Veto 20 GeV	1.00	–	1.00	1.17	1.00	11.0

Table 4.22: The comparison of signal and background yields between different cut cases in $\mu^+\mu^-$ channel and signal significance S_{cuts} . The filled numbers are ratios of **MC** yields with respect to the optimal selection in the top row. W + jets are statistically limited in final section (1–2 events), therefore left empty. Courtesy of Philip Sommer.

Cut case	WW	W + jets	Z + jets	Di-bosons	Top	S_{cuts}
Pre-selection						
Single/di-lep. trig., LLH eID, > 2ℓ veto 7 GeV	1	1	1	1	1	–
Single or di-lepton trig., TIGHT++ eID, > 2 ℓ veto 7 GeV	1.01	1.73	1.03	1.09	1.01	–
Single or di-lepton trig., LH eID, > 2 ℓ veto 20 GeV	1.00	1.00	1.00	1.11	1.00	–
Final selection						
Single/di-lep. trig., LLH eID, > 2ℓ veto 7 GeV	1	1	1	1	1	15.1
Single or di-lepton trig., TIGHT++ eID, > 2 ℓ veto 7 GeV	1.01	1.00	1.94	1.16	1.09	12.8
Single or di-lepton trig., LLH eID, > 2 ℓ veto 20 GeV	1.00	1.00	1.00	1.11	1.00	15.1

Table 4.23: The comparison of signal and background yields between different cut cases in $e^\pm\mu^\mp$ channel and signal significance S_{cuts} . The filled numbers are ratios of **MC** yields with respect to the optimal selection in the top row. eID stands for electron identification, LLH stands for likelihood identification (see section 3.3.4.3). Courtesy of Philip Sommer.

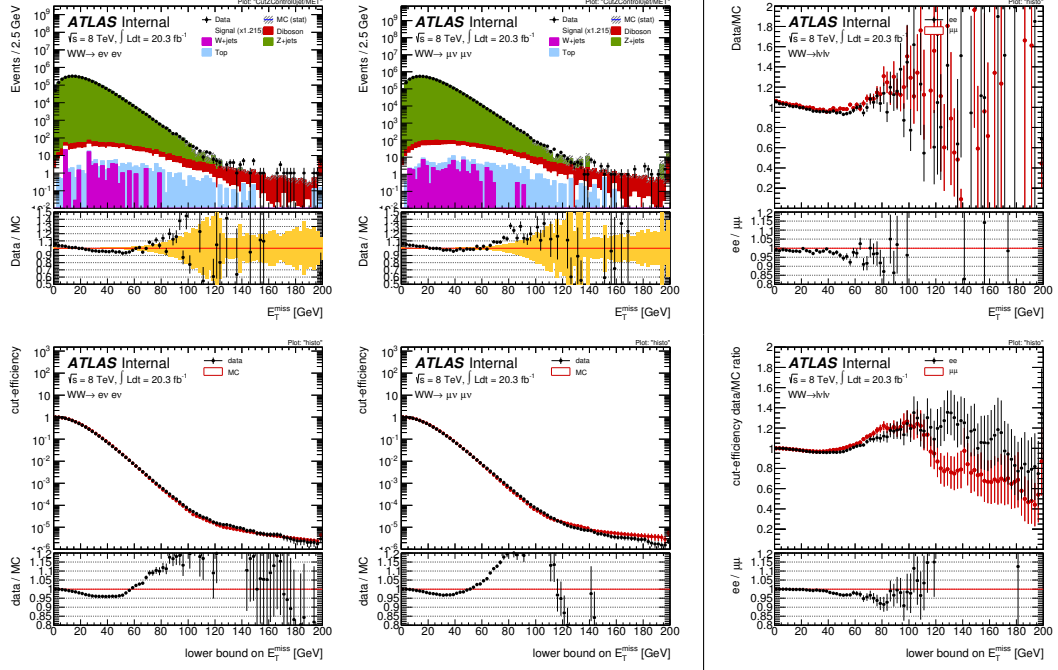


Figure 4.39: Comparison of E_T (RefFinal) in the same flavour channels. Starting from the top left, the two figures show the data/MC comparison for the e^+e^- (leftmost) and $\mu^+\mu^-$ (middle) channels. The bottom left figures show the cut-efficiencies evaluated separately for data and MC in e^+e^- (leftmost) and $\mu^+\mu^-$ (middle) channels. The rightmost side plots show the ratios of the data/MC distribution (top) and the ratios of the cut-efficiencies (bottom). The double-ratios (4.24) correspond to the sub-plot for the figures in the rightmost column. Courtesy of Philip Sommer.

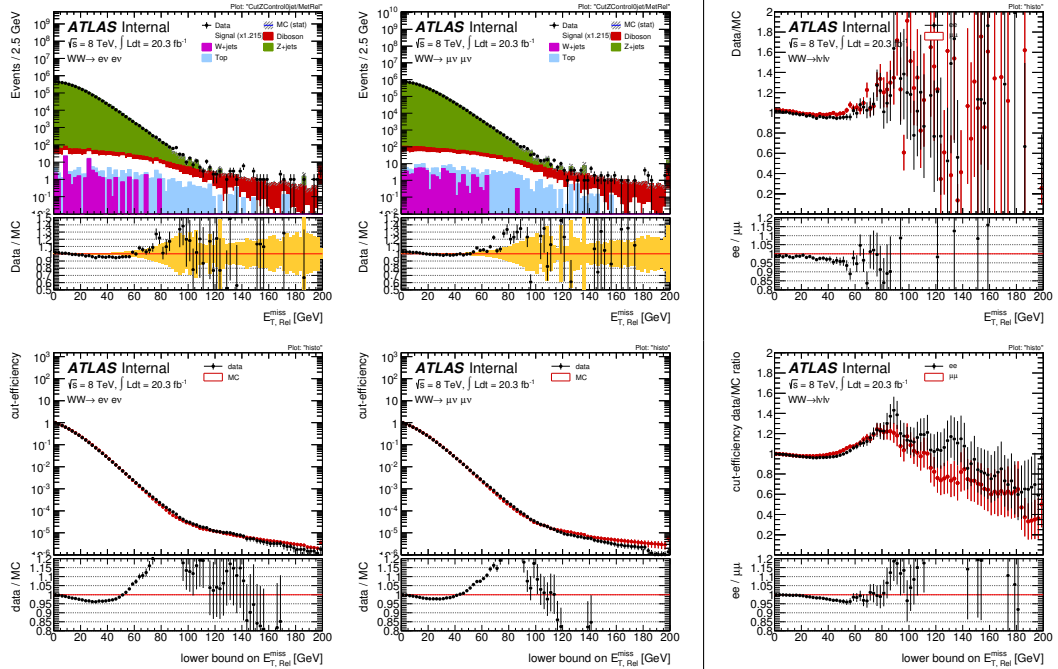


Figure 4.40: Comparison of $E_{T,Rel}$ (RefFinal) in the same flavour channels. Starting from the top left, the two figures show the data/MC comparison for the e^+e^- (leftmost) and $\mu^+\mu^-$ (middle) channels. The bottom left figures show the cut-efficiencies evaluated separately for data and MC in e^+e^- (leftmost) and $\mu^+\mu^-$ (middle) channels. The rightmost side plots show the ratios of the data/MC distribution (top) and the ratios of the cut-efficiencies (bottom). The double-ratios (4.24) correspond to the sub-plot for the figures in the rightmost column. Courtesy of Philip Sommer.

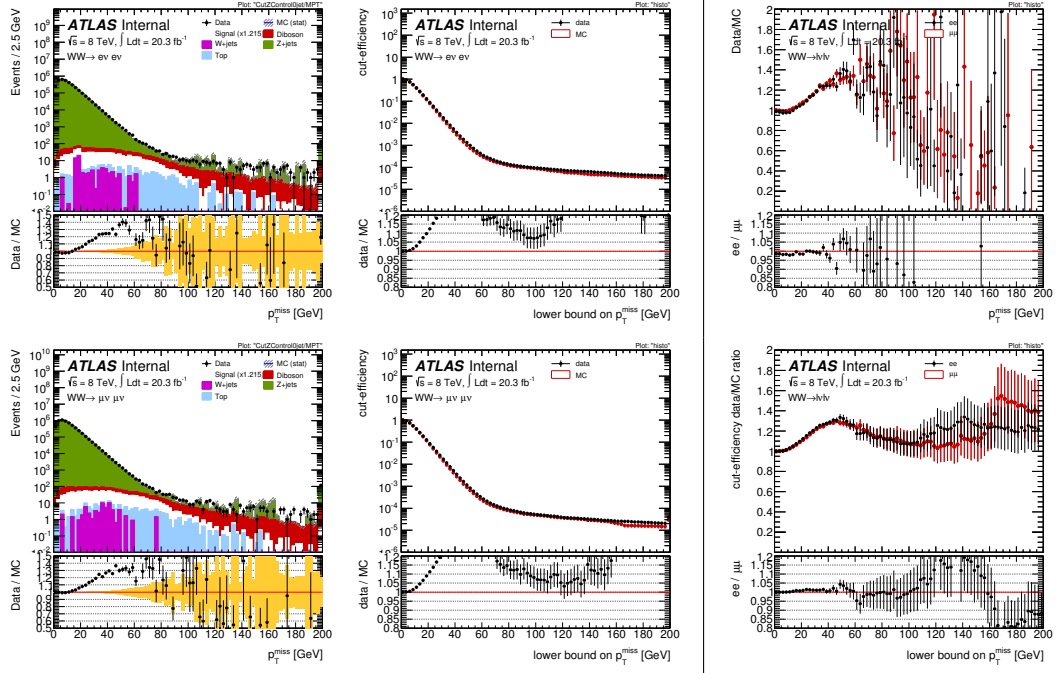


Figure 4.41: Comparison of p_T in the same flavour channels. Starting from the top left, the two figures show the data/MC comparison for the e^+e^- (leftmost) and $\mu^+\mu^-$ (middle) channels. The bottom left figures show the cut-efficiencies evaluated separately for data and MC in e^+e^- (leftmost) and $\mu^+\mu^-$ (middle) channels. The rightmost side plots show the ratios of the data/MC distribution (top) and the ratios of the cut-efficiencies (bottom). The double-ratios (4.24) correspond to the sub-plot for the figures in the rightmost column. Courtesy of Philip Sommer.

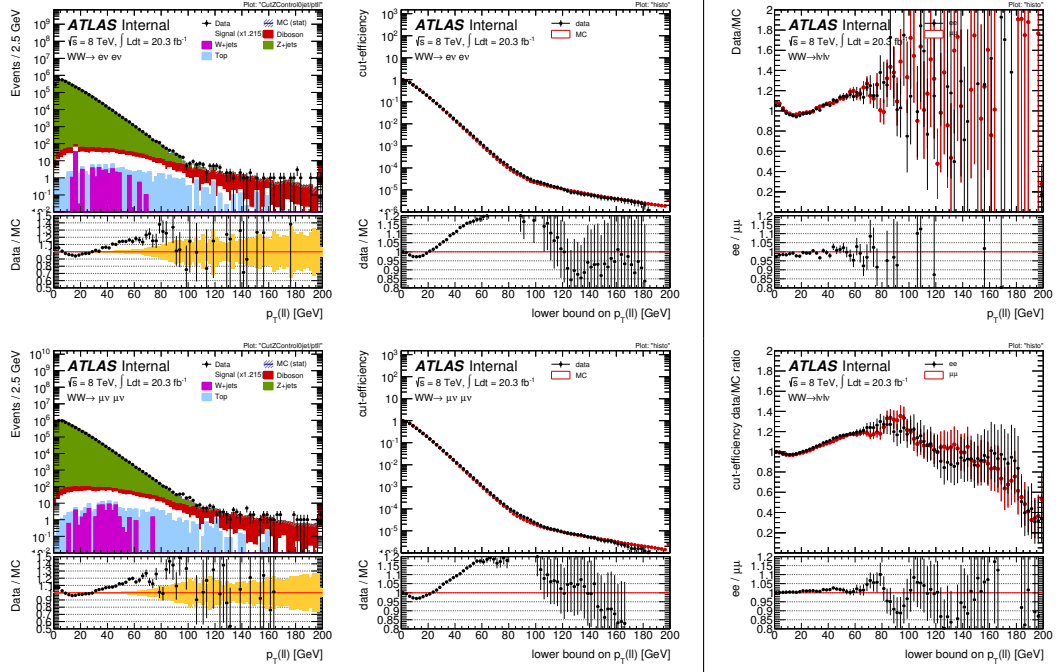


Figure 4.42: Comparison of $p_T(\ell\ell)$ in the same flavour channels. Starting from the top left, the two figures show the data/MC comparison for the e^+e^- (leftmost) and $\mu^+\mu^-$ (middle) channels. The bottom left figures show the cut-efficiencies evaluated separately for data and MC in e^+e^- (leftmost) and $\mu^+\mu^-$ (middle) channels. The rightmost side plots show the ratios of the data/MC distribution (top) and the ratios of the cut-efficiencies (bottom). The double-ratios (4.24) correspond to the sub-plot for the figures in the rightmost column. Courtesy of Philip Sommer.

double-ratios:

$$\frac{\text{data}(e^+e^-)}{\text{MC}(e^+e^-)} \bigg/ \frac{\text{data}(\mu^+\mu^-)}{\text{MC}(\mu^+\mu^-)} \quad \text{or} \quad \frac{\text{data}(e^+e^-)}{\text{data}(\mu^+\mu^-)} \bigg/ \frac{\text{MC}(e^+e^-)}{\text{MC}(\mu^+\mu^-)}. \quad (4.24)$$

shown in figures 4.39 for \cancel{E}_T , fig. 4.40 for $\cancel{E}_{T,\text{Rel}}$, fig. 4.41 for \cancel{p}_T and fig. 4.42 for $p_T(\ell\ell)$ in the Z control region, i.e. after Z veto and in the zero jet bin. As one can see, $\cancel{E}_{T,\text{Rel}}$ is best modelled and thus is the preferred cut variable. The choice of a track based variable remains between \cancel{p}_T and $p_T(\ell\ell)$ which has been used at $\sqrt{s} = 7$ TeV. Comparing between fig. 4.41 and fig. 4.42, \cancel{p}_T shows better rejection power at a lower cut level and is better modelled in MC at 8 TeV than $p_T(\ell\ell)$.

The optimal cut values for the selected variables are identified using a grid scan. The significance plots are shown in fig. 4.43 for same flavour channels and in fig. 4.44 for combined flavour. The optimal cut values are what we refer to as *final selection* from now on.

4.7.2 Selection acceptance

Another important correction to the signal yield is introduced to account for the difference between data and MC in the efficiency of jet veto, since we limit jet multiplicity in our analysis only to the zero jet bin. Due to the fact, that the effects of JES and JER differ between data and MC, we expect that the rate of events passing the jet veto may be predicted incorrectly by the MC model.

To derive the correction, we exploit the similarities between the $q\bar{q} \rightarrow WW \rightarrow \ell^+\nu\ell^-\bar{\nu}$ and $q\bar{q} \rightarrow Z \rightarrow \ell^+\ell^-$ production mechanisms to calibrate the final yield as suggested in [Cam+09]. The Z bosons are selected from the Z mass window using the same preselection as applied to the WW selection, including trigger matching and the cut on lepton p_T . Any remaining cuts on the Z production are omitted with the exception of the jet veto which is used to define the efficiency:

$$\epsilon = \frac{N(0 \text{ jets})}{N(\geq 0 \text{ jets})} \quad (4.25)$$

where N is the number of events under the corresponding conditions. It should be noted here, that we can only apply this method to the $q\bar{q} \rightarrow WW \rightarrow \ell^+\nu\ell^-\bar{\nu}$ process, as the Z production does not come from the gluon source. The Z events are then used to determine the data/MC efficiency correction factor f_Z to the WW signal selection:

$$\epsilon_{\text{WW}}^{\text{data}} = \epsilon_{\text{WW}}^{\text{MC}} \cdot f_Z \quad \text{where} \quad f_Z = \frac{\epsilon_Z^{\text{data}}}{\epsilon_Z^{\text{MC}}} \quad (4.26)$$

The central values of the *jet veto scale factor* f_Z are $f_Z(8 \text{ TeV}) = 0.990$ and $f_Z(7 \text{ TeV}) = 0.957$ with statistical uncertainties at the per mille level, which as such are not quoted here. The e^+e^- and $\mu^+\mu^-$ scale factors are applied to their respective WW channels, the combined flavour channel ($e^\pm\mu^\mp$) uses an average of the two.

4.7.3 Jet veto uncertainties

The systematic uncertainties due to JES, JER and JVF (in case of 8 TeV) are determined independently by studying the effects on the MC efficiencies defined in the above mentioned eq. (4.25). To study the effect of JES for example, we apply $\pm 1\sigma$ variation to the jet energies and consequently obtain a different number of events in the nominator and the denominator (see section 4.8.2 for

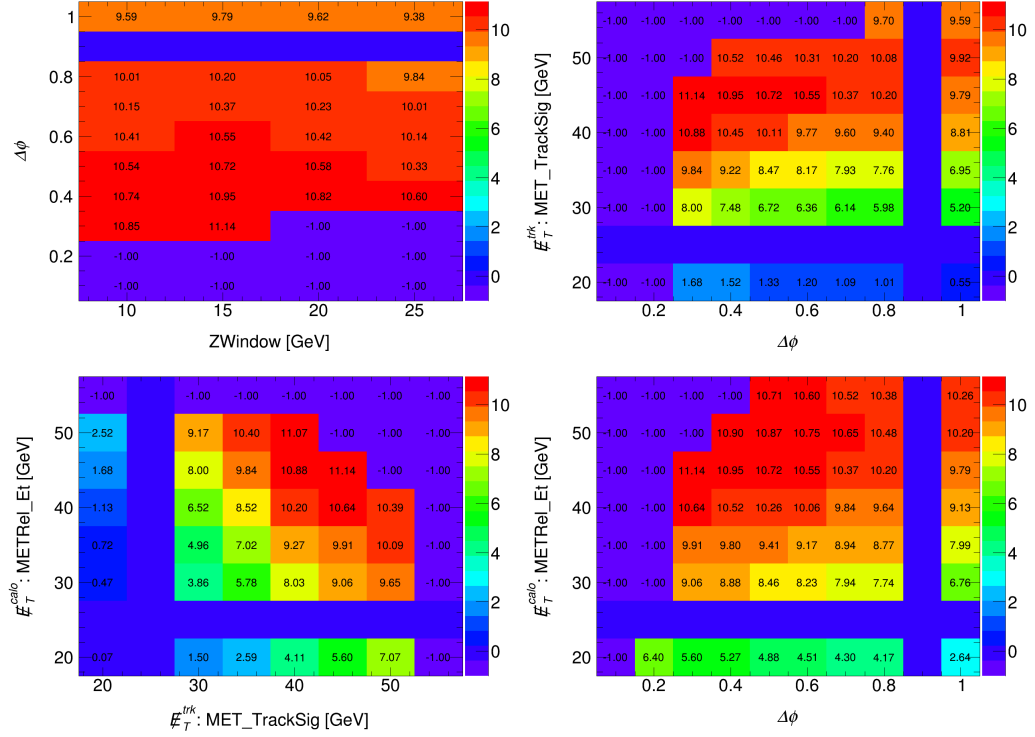


Figure 4.43: The 2D significance plots in same flavour channel for optimization grid scan on cut variable pairs. While one cut variable pair is plotted, other cuts are set to their nominal values. Top left shows $\Delta\phi(\mathbf{E}_T, \mathbf{p}_T)$ and Z veto cuts, top right shows p_T and $\Delta\phi(\mathbf{E}_T, \mathbf{p}_T)$, bottom left shows p_T and $\mathbf{E}_{T,\text{Rel}}$ and bottom right shows $\mathbf{E}_{T,\text{Rel}}$ and $\Delta\phi(\mathbf{E}_T, \mathbf{p}_T)$. Courtesy of Philip Sommer.

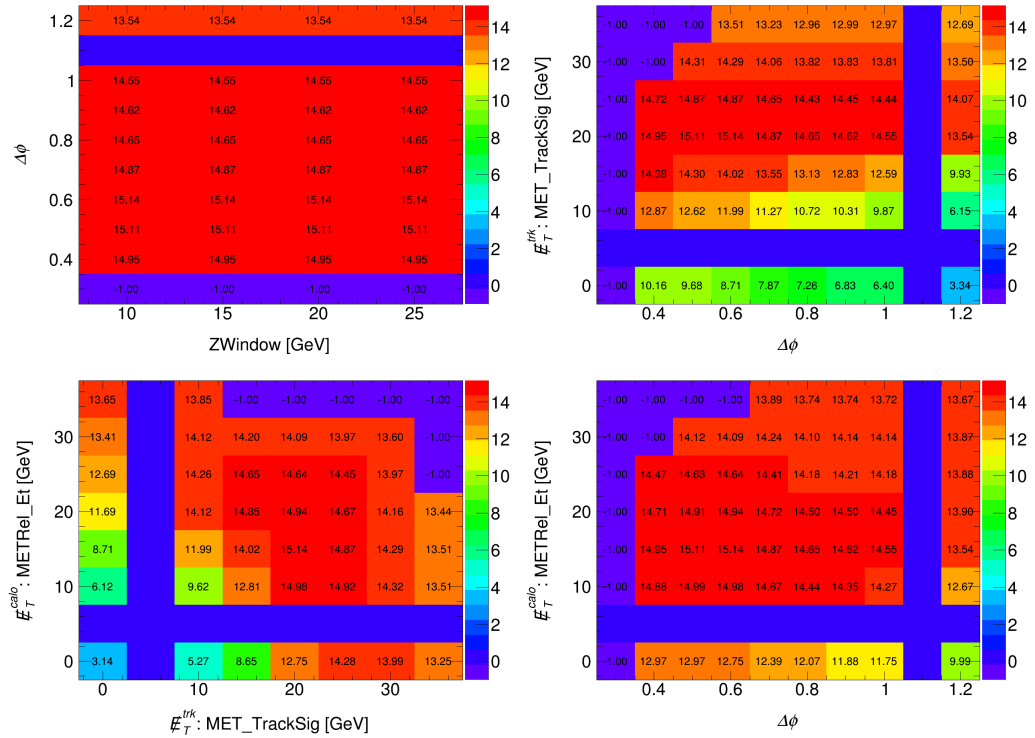


Figure 4.44: The 2D significance plots in the combined flavour channel for optimization grid scan on cut variable pairs. While one cut variable pair is plotted, other cuts are set to their nominal values. Top left shows $\Delta\phi(\mathbf{E}_T, \mathbf{p}_T)$ and Z veto cuts, top right shows p_T and $\Delta\phi(\mathbf{E}_T, \mathbf{p}_T)$, bottom left shows p_T and $\mathbf{E}_{T,\text{Rel}}$ and bottom right shows $\mathbf{E}_{T,\text{Rel}}$ and $\Delta\phi(\mathbf{E}_T, \mathbf{p}_T)$. Courtesy of Philip Sommer.

more details on jet related systematic uncertainties). We should also emphasize that using data to derive the correction factor reduces the uncertainties associated with the jet veto. Writing the eq. (4.25) in the following form:

$$\epsilon_{\text{WW}}^{\text{data}} = \epsilon_{\text{Z}}^{\text{data}} \cdot \frac{\epsilon_{\text{WW}}^{\text{MC}}}{\epsilon_{\text{Z}}^{\text{MC}}} \quad (4.27)$$

we see the experimental systematic uncertainties on the measured efficiency of the jet veto appear in ratio where they partially cancel. This is because the Z data provides an effective calibration of the JES with overall smaller uncertainties, as Z selection does not apply cuts to \vec{E}_{T} or any of its modified forms (\vec{p}_{T} , $\vec{E}_{\text{T,Rel}}$). It is however important to use the same MC generator for Z and WW events so the jets are modelled in a similar way.

Uncertainties due to higher correction of perturbation theory are also accounted for by studying the variations in the factorisation and re-normalization scales at the truth level. The PDF uncertainties on the signal acceptance are taken from the CT10 error sets. To estimate PDF uncertainties due to different PDF parametrizations, we compare the CT10 samples with MSTW2008, NNPDF and ATLAS-epWZ PDF sets. The combined PDF uncertainty in the ratio of jet veto acceptances is found to be 0.68 %. For the parton shower uncertainty, events simulated by *Herwig/Jimmy* are directly compared with events simulated by *Pythia*. For the generator uncertainty, we compare events generated with *POWHEG* and *MC@NLO* generators, both interfaced to *Herwig/Jimmy* parton shower model. The scale uncertainty on the signal acceptance is calculated by varying re-normalisation and factorisation scales by a factor of 2 or 0.5. The factorisation and re-normalisation scale uncertainties for gg-induced events are taken from [ATL13d] and amount to 18 %. The values of f_{Z} and $\epsilon_{\text{WW}}^{\text{data}}$ with full uncertainties are shown in table 4.25 for both the 8 TeV and 7 TeV analyses. The investigation of theoretical uncertainties was performed by Yusheng Wu from the University of Michigan.

$\sqrt{s} = 7 \text{ TeV}$			
e^+e^-	f_{Z}	$0.957 \pm 0.04(\text{JES}) \pm 0.02(\text{JER}) \pm 0.025(\text{theory})$	
$\mu^+\mu^-$	f_{Z}	$0.954 \pm 0.04(\text{JES}) \pm 0.03(\text{JER}) \pm 0.025(\text{theory})$	
$e^\pm\mu^\mp$	f_{Z}	$0.956 \pm 0.04(\text{JES}) \pm 0.02(\text{JER}) \pm 0.025(\text{theory})$	
e^+e^-	$\epsilon_{\text{WW}}^{\text{data}}$	$0.624 \pm 0.007(\text{JES}) \pm 0.0016(\text{JER}) \pm 0.022(\text{theory})$	
$\mu^+\mu^-$	$\epsilon_{\text{WW}}^{\text{data}}$	$0.625 \pm 0.004(\text{JES}) \pm 0.003(\text{JER}) \pm 0.022(\text{theory})$	
$e^\pm\mu^\mp$	$\epsilon_{\text{WW}}^{\text{data}}$	$0.633 \pm 0.004(\text{JES}) \pm 0.002(\text{JER}) \pm 0.022(\text{theory})$	

$\sqrt{s} = 8 \text{ TeV}$			
e^+e^-	f_{Z}	$0.989 \pm 0.002(\text{JVF}) \pm 0.025(\text{JES}) \pm 0.015(\text{JER}) \pm 0.032(\text{theory})$	
$\mu^+\mu^-$	f_{Z}	$0.991 \pm 0.002(\text{JVF}) \pm 0.025(\text{JES}) \pm 0.013(\text{JER}) \pm 0.032(\text{theory})$	
$e^\pm\mu^\mp$	f_{Z}	$0.990 \pm 0.002(\text{JVF}) \pm 0.025(\text{JES}) \pm 0.014(\text{JER}) \pm 0.032(\text{theory})$	
e^+e^-	$\epsilon_{\text{WW}}^{\text{data}}$	$0.710 \pm 0.000(\text{JVF}) \pm 0.008(\text{JES}) \pm 0.008(\text{JER}) \pm 0.024(\text{theory})$	
$\mu^+\mu^-$	$\epsilon_{\text{WW}}^{\text{data}}$	$0.729 \pm 0.000(\text{JVF}) \pm 0.007(\text{JES}) \pm 0.007(\text{JER}) \pm 0.024(\text{theory})$	
$e^\pm\mu^\mp$	$\epsilon_{\text{WW}}^{\text{data}}$	$0.684 \pm 0.000(\text{JVF}) \pm 0.004(\text{JES}) \pm 0.004(\text{JER}) \pm 0.023(\text{theory})$	

Table 4.24: The jet veto *scale factors* f_{Z} and predicted WW jet veto acceptance (including the *scale factor*) for each channel, with accompanying uncertainties. The $e^\pm\mu^\mp$ *scale factor* is calculated as the average of the two same-flavour *scale factor*. The 8 TeV contain an additional systematic uncertainty due to the application of JVF cut. f_{Z} is defined as the ratio $\epsilon_{\text{Z}}^{\text{data}}/\epsilon_{\text{Z}}^{\text{MC}}$, see eq. (4.26).

The resulting contributions to C_{WW} and A_{WW} factors are given by:

$$C_{WW}^{\text{jet}} = \frac{N_{WW}^{\text{MC reco}}(0 \text{ jets})}{N_Z^{\text{MC truth}}(0 \text{ jets})} \cdot \frac{\epsilon_Z^{\text{data}}}{\epsilon_Z^{\text{MC reco}}} \quad \text{and} \quad A_{WW}^{\text{jet}} = \frac{N_{WW}^{\text{MC truth}}(0 \text{ jets})}{N_{WW}^{\text{MC truth}}(\geq 0 \text{ jets})} \quad (4.28)$$

where the quantities labelled “MC reco” are given from the signal MC following the selection at the reconstruction level (including all object and trigger related [scale factors](#)) and quantities labelled “MC truth” correspond to the fiducial selection as described in [section 4.7.4](#). The “MC truth” contain the theoretical uncertainties while “MC reco” contain both the experimental and theoretical uncertainties. The complete list of uncertainties by channel is given [table 4.25](#) and in [table 4.27](#) along with the full the systematic uncertainties summary.

	$\sqrt{s} = 7 \text{ TeV}$			$\sqrt{s} = 8 \text{ TeV}$		
e^+e^- channel	Reco.	Theory	Total	Reco.	Theory	Total
A_{WW}^{jet}	—	5.6%	5.6%	—	3.20%	3.20%
C_{WW}^{jet}	1.1%	2.6%	2.8%	1.54%	4.25%	4.52%
$C_{WW}^{\text{jet}} A_{WW}^{\text{jet}}$	1.1%	3.5%	3.7%	1.54%	3.32%	3.66%
$\mu^+\mu^-$ channel	Reco.	Theory	Total	Reco.	Theory	Total
A_{WW}^{jet}	—	5.6%	5.6%	—	3.20%	3.20%
C_{WW}^{jet}	1.0%	2.6%	2.8%	1.30%	4.25%	4.44%
$C_{WW}^{\text{jet}} A_{WW}^{\text{jet}}$	1.0%	3.5%	3.6%	1.30%	3.32%	3.56%
$e^\pm\mu^\mp$ channel	Reco.	Theory	Total	Reco.	Theory	Total
A_{WW}^{jet}	—	5.6%	5.6%	—	3.20%	3.20%
C_{WW}^{jet}	0.7%	2.6%	2.7%	1.03%	4.25%	4.37%
$C_{WW}^{\text{jet}} A_{WW}^{\text{jet}}$	0.7%	3.5%	3.6%	1.03%	3.32%	3.48%

Table 4.25: The uncertainties in the jet veto contributions to C_{WW}^{jet} and A_{WW}^{jet} .

4.7.4 Fiducial region

To emulate the behaviour of analysis selection applied in a given experiment, we define the detector fiducial volume at the MC truth level. This volume is specific to the analysis channels and the kinematic and geometrical acceptance due to experimental limitations of the detector. For the needs of our measurement, we define four different fiducial regions, each corresponding to the individual final states e^+e^- , $\mu^+\mu^-$, $e^\pm\mu^\mp$ and a region from all three channels combined, as it has the lowest statistical uncertainty. The truth objects are defined to closely resemble the reconstruction level objects we defined in [section 4.5](#). In the signal MC samples we use the following physics objects:

- All leptons stemming directly from one of the [W](#). The truth lepton four-momentum is corrected for radiation losses by adding the four-momenta of all photons inside a cone of a radius $\Delta R = 0.1$. This procedure is referred to as *lepton dressing*.
- MC truth jets are reconstructed from stable truth particles with [anti- \$k_t\$](#) algorithm with jet radius parameter of $R = 0.4$.
- We apply overlap removal on truth jets within $\Delta R = 0.3$ of a truth lepton to keep track only of jets valid for the jet veto.

- For the calculation of the [missing transverse energy](#), we use the four-vector sum of the [transverse momentum](#) of the neutrinos stemming from the [W boson](#) decays.

The selection in the fiducial region is designed to closely mimic the reconstruction level cuts:

- 1) Di-lepton selection: exactly two oppositely charged leptons with $p_T > 25$ (20) GeV for leading (trailing) leptons respectively, $|\eta| < 1.37$ or $1.52 < |\eta| < 2.47$ for electrons and $|\eta| < 2.4$ for muons. Leptons are corrected for [QED](#) radiation losses as mentioned above.
- 2) Invariant mass of the dilepton pair: $m_{\ell\ell} > 15$ (10) GeV for the $e^+e^-/\mu^+\mu^-$ ($e^\pm\mu^\mp$) channels
- 3) Z-veto: $|m_{\ell\ell} - m_Z| > 15$ GeV for the e^+e^- and $\mu^+\mu^-$ channels.
- 4) Neutrino [transverse momentum](#): $p_{T,\text{Rel}}^{\nu+\bar{\nu}} > 45$ (15) GeV for the $e^+e^-/\mu^+\mu^-$ ($e^\pm\mu^\mp$) channels which corresponds to $\vec{E}_{T,\text{Rel}}$ cut and $p_T^{\nu+\bar{\nu}} > 45$ (20) GeV for the $e^+e^-/\mu^+\mu^-$ ($e^\pm\mu^\mp$) channels which corresponds to \vec{p}_T cut.
- 5) Jet-veto: The number of reconstructed [MC](#) truth jets with $p_T > 25$ GeV and $|\eta| < 4.5$ must be exactly zero. Jets within $\Delta R < 0.3$ of a selected lepton are ignored as it is likely reconstructed from the electron shower, this follows from the overlap removal discussed in [section 4.5.6](#).

The definition of A_{WW} and C_{WW} follows from [eqs. \(4.7\) and \(4.8\)](#), with one key difference. At 8 TeV we consider the τ contribution as a background for the fiducial [cross-section](#) measurements. Consequently, the fiducial [cross-sections](#) presented for the 8 TeV analysis include only prompt electrons and muons from [W](#) bosons. The nominator in C_{WW} is determined from the number of events in [MC](#) that passed the selection at reconstruction level while the denominator corresponds to the number of events in [MC](#) satisfying the kinematic cuts implemented in the fiducial phase space. The same applies to the A_{WW} nominator. The A_{WW} is simply the total number of generated events in the signal sample. The results separated by channel are given in [table 4.26](#).

4.8 Systematic uncertainties

This section summarizes the systematic uncertainties on the WW signal acceptance. All individual sources of systematic uncertainties on WW signal are discussed through [sections 4.8.1 and 4.8.4](#). The summary is given in [table 4.27](#) for e^+e^- , $\mu^+\mu^-$ and $e^\pm\mu^\mp$ channels as well as for all channels combined. The uncertainty is calculated as a ratio of event yields at final selection:

$$R[\%] = \frac{N_{\text{syst}} - N_{\text{nominal}}}{N_{\text{nominal}}} \quad (4.29)$$

where N_{nominal} is the number of events at a given cut stage obtained from the nominal analysis, N_{syst} is the number of events at a given cut stage with the individual systematic effect applied. We take this approach since the datasets are identical for nominal and systematic instances of the analysis and thus we avoid artificially inflating the statistical uncertainty. Since the statistical uncertainty is lower than 0.01 % we are not going to show it here to avoid clutter, but limit our systematic uncertainties to two-digit precision here. See extended tables in [appendix B](#) for complete listings.

Additionally, [tables 4.28 and 4.29](#) provide systematic yields as they progress for each cut stage in our analysis. Each number represents shift from the nominal yield at a given cut stage (shown in percent). The cut level starts from the left at pre-selection level and evolves to the final stage, jet

$\sqrt{s} = 8 \text{ TeV}$			
	e^+e^-	$\mu^+\mu^-$	$e^\pm\mu^\mp$
A_{WW}	$0.0856 \pm 0.0003 \pm 0.0029$	$0.0930 \pm 0.0003 \pm 0.0029$	$0.2269 \pm 0.0003 \pm 0.0063$
$\Delta A_{WW}/A_{WW}$	3.34%	3.09%	2.79%
C_{WW}	$0.2907 \pm 0.0018 \pm 0.0204$	$0.4711 \pm 0.0019 \pm 0.0319$	$0.5108 \pm 0.0008 \pm 0.0230$
$\Delta C_{WW}/C_{WW}$	7.01%	6.78%	4.49%
$A_{WW} \cdot C_{WW} = \epsilon \mathcal{A}$	$0.0249 \pm 0.0002 \pm 0.0018$	$0.0438 \pm 0.0002 \pm 0.0030$	$0.1159 \pm 0.0003 \pm 0.0056$
$\Delta \epsilon \mathcal{A}/\epsilon \mathcal{A}$	7.20%	6.94%	4.81%

$\sqrt{s} = 7 \text{ TeV}$			
	e^+e^-	$\mu^+\mu^-$	$e^\pm\mu^\mp$
A_{WW}	$0.075 \pm 0.001 \pm 0.0043$	$0.081 \pm 0.001 \pm 0.0046$	$0.159 \pm 0.001 \pm 0.0091$
$\Delta A_{WW}/A_{WW}$	5.68%	5.69%	5.70%
C_{WW}	$0.403 \pm 0.005 \pm 0.017$	$0.687 \pm 0.005 \pm 0.021$	$0.505 \pm 0.002 \pm 0.016$
$\Delta C_{WW}/C_{WW}$	4.2%	3.1%	3.2%
$A_{WW} \cdot C_{WW} = \epsilon \mathcal{A}$	$0.030 \pm 0.001 \pm 0.001$	$0.056 \pm 0.001 \pm 0.002$	$0.080 \pm 0.001 \pm 0.003$
$\Delta \epsilon \mathcal{A}/\epsilon \mathcal{A}$	4.9%	4.0%	4.1%

Table 4.26: The acceptance factor A_{WW} , correction factor C_{WW} and the WW overall acceptance $A_{WW} \cdot C_{WW}$ with their corresponding uncertainties for 7 TeV and 8 TeV analyses. The first uncertainties are statistical, the second are systematic. The full uncertainties are also shown in percentage below the values. The jet veto [scale factors](#) from [table 4.24](#) are applied on $q\bar{q} \rightarrow WW \rightarrow \ell^+\nu\ell^-\bar{\nu}$ events when deriving the final C_{WW} and $A_{WW} \cdot C_{WW}$.

veto. The colour corresponds to the magnitude of the systematic shift. The up and down component of each systematic uncertainty has been symmetrized. In this section, the cut progression is shown only for the combined channel, please see [appendix B](#) for the per channel breakdown.

The full WW signal uncertainty includes all experimental uncertainties but also the uncertainty of the theoretical prediction of the WW cross-section and can be therefore used to compare the measured and predicted cross-sections in terms of significance. The combined uncertainties are estimated within the full [Monte Carlo](#) signal samples where no distinction between the final states is made. The jet veto uncertainty has theoretical and reconstruction components, and those are separated in the table. For the jet veto uncertainty on the product $A_{WW} C_{WW}$, a reduced uncertainty applies due to cancellation, see [table 4.25](#).

4.8.1 Lepton systematics

Lepton systematic uncertainties are evaluated independently for electrons and muons. The systematics on the electrons selection come from four sources considered separately:

Trigger: The electron and muon trigger uncertainties are derived by varying the selection in the [tag-and-probe](#) measurements, as explained in [section 4.4.2](#).

Energy/momentum scale and resolution: The muon momentum scale and momentum resolution uncertainties are estimated from $Z \rightarrow \mu^+\mu^-$ [tag-and-probe](#) measurements described in [section 4.5.1.1](#), the values are given in [fig. 3.22](#). As a reminder, the correction for [combined](#) muons is computed as a linear combination of the [MS](#) and [ID](#) as shown in [eq. \(4.14\)](#). The

Sources	$e^+e^- \cancel{E}_T$	$\mu^+\mu^- \cancel{E}_T$	$e^\pm\mu^\mp \cancel{E}_T$	Inclusive
A_{WW} uncertainties				
Jet veto SF (theory)	2.78%	2.78%	2.78%	2.78%
PDF	1.00%	0.91%	0.99%	0.98%
Scale	1.88%	1.45%	0.41%	0.67%
$\Delta A_{WW}/A_{WW}$	3.50%	3.26%	2.98%	3.02%
C_{WW} uncertainties				
Pileup	1.87%	1.97%	1.30%	1.44%
e Trigger Efficiency SF	2.52%	0%	0.30%	0.44%
m Trigger Efficiency SF	0%	2.84%	0.27%	0.62%
Muon MS Resolution	0%	0.05%	0.01%	0.01%
Muon ID Resolution	0%	1.53%	0.54%	0.63%
Muon Scale	0%	0.35%	0.10%	0.12%
Muon Efficiency SF	0%	0.77%	0.39%	0.41%
Muon Isolation SF	0%	1.13%	0.56%	0.60%
Electron Resolution	0.18%	0%	0.03%	0.02%
Electron Scale	1.40%	0%	0.37%	0.40%
Electron Efficiency SF	2.00%	0%	0.93%	0.88%
Electron Isolation SF	0.44%	0%	0.21%	0.20%
Jet Vertex Fraction (corrected)	0.08%	0.08%	0.04%	0.05%
Jet Energy Resolution (corrected)	0.74%	0.81%	0.64%	0.67%
Jet Energy Scale (corrected)	1.84%	2.51%	1.78%	1.89%
Missing $\cancel{E}_{T,Rel}$ Reso Soft Terms	0.31%	0.50%	0.29%	0.32%
Missing $\cancel{E}_{T,Rel}$ Scale Soft Terms	4.21%	3.81%	2.34%	2.71%
Missing p_T Reso Soft Terms	0.04%	0.21%	0.05%	0.07%
Missing p_T Scale Soft Terms	0.62%	0.49%	0.31%	0.36%
Jet veto SF (reco)	1.43%	1.21%	0.97%	1.17%
Jet veto SF (theory)	2.39%	2.39%	2.42%	2.41%
PDF	0.59%	0.13%	0.35%	0.31%
Scale	1.68%	0.66%	0.61%	0.59%
$\Delta C_{WW}/C_{WW}$	7.01%	6.78%	4.49%	4.88%
$A_{WW}C_{WW}$ uncertainties				
Jet veto SF (reco)	1.43%	1.21%	0.97%	1.17%
Jet veto SF (theory)	2.60%	2.61%	2.64%	2.63%
PDF	1.58%	0.84%	1.32%	1.28%
Scale	1.54%	0.95%	0.80%	0.85%
$\Delta C_{WW} A_{WW}/C_{WW} A_{WW}$	7.20%	6.94%	4.81%	5.18%
Luminosity	2.8%	2.8%	2.8%	2.8%
$\sigma(WW)$ theoretic uncertainty	5.30%	5.30%	5.30%	5.30%
Full WW signal estimation uncertainty	9.37%	9.17%	7.69%	7.92%

Table 4.27: Uncertainty sources and associated relative uncertainties for WW signal acceptance estimations for e^+e^- , $\mu^+\mu^-$, $e^\pm\mu^\mp$ channels and inclusive. The overall WW signal estimation uncertainties include A_{WW} C_{WW} uncertainties, luminosity (2.8%) and theoretical cross-section (5.3%) uncertainties. If a definitive 0% effect is implied, there is no effect expected in the given channel and it has been measured to be exactly zero. The jet veto [scale factor](#) uncertainties are only evaluated for $q\bar{q} \rightarrow WW \rightarrow \ell^+\nu\ell^-\bar{\nu}$ process in [table 4.25](#), and it is scaled in order to apply on total WW acceptance. For the other jet systematics, the $q\bar{q} \rightarrow WW \rightarrow \ell^+\nu\ell^-\bar{\nu}$ are evaluated before the jet veto cut and $gg \rightarrow WW \rightarrow \ell^+\nu\ell^-\bar{\nu}$ along with $gg \rightarrow H \rightarrow WW$ processes are evaluated after the jet veto and combined together.

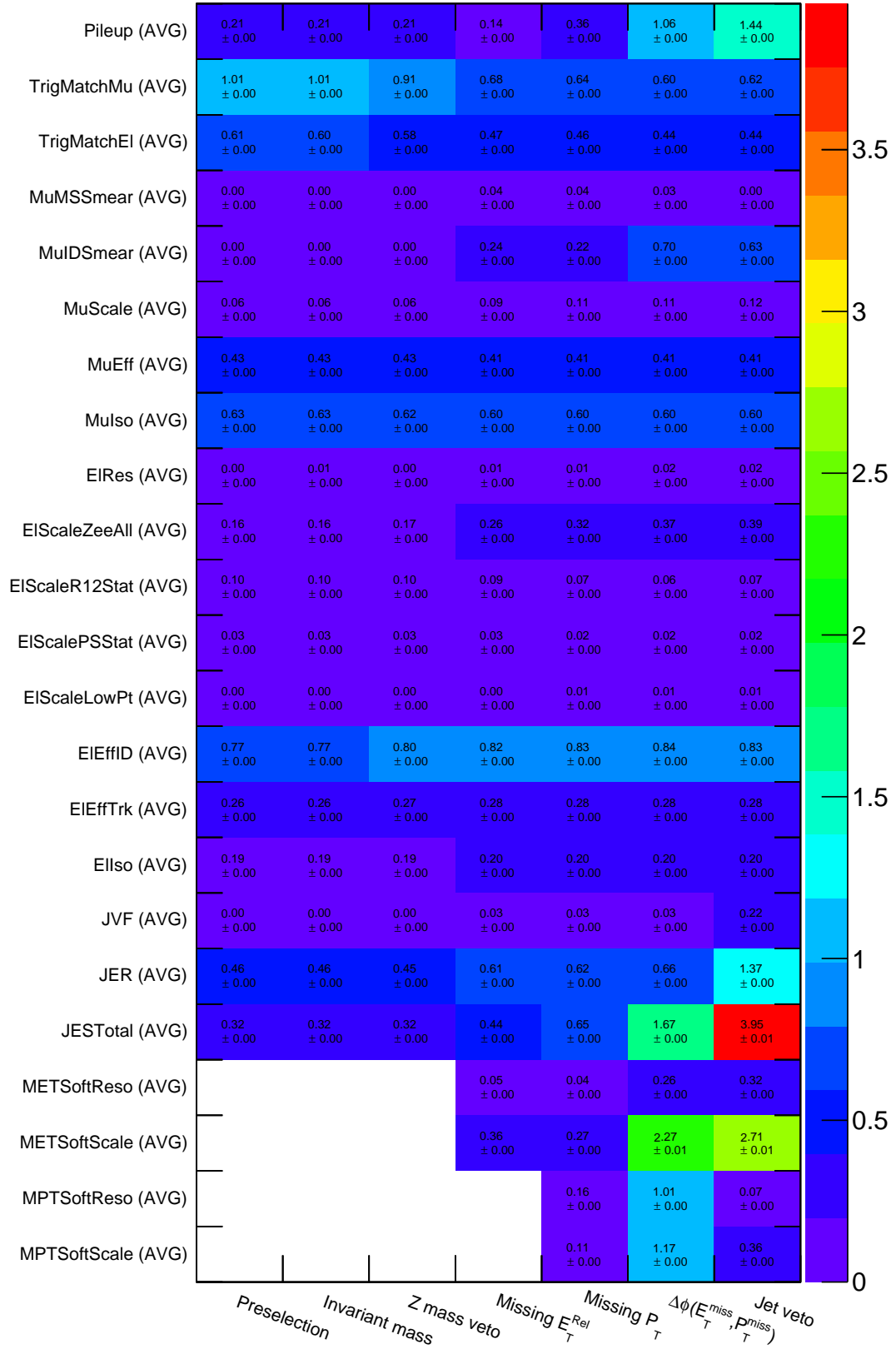


Table 4.28: Cut progression of systematic uncertainties on the signal samples for the inclusive channel ($\ell^+\ell^-$). The table shows the full set of systematics evolving as we introduce analysis cuts (columns left to right). Each number presents a percentage difference with respect to nominal yield at a given cut stage. Statistical uncertainty on each yield is shown. The color corresponds to the magnitude of the systematic shift. The up and down component of each systematic uncertainty has been symmetrized (indicated by the “AVG” label).

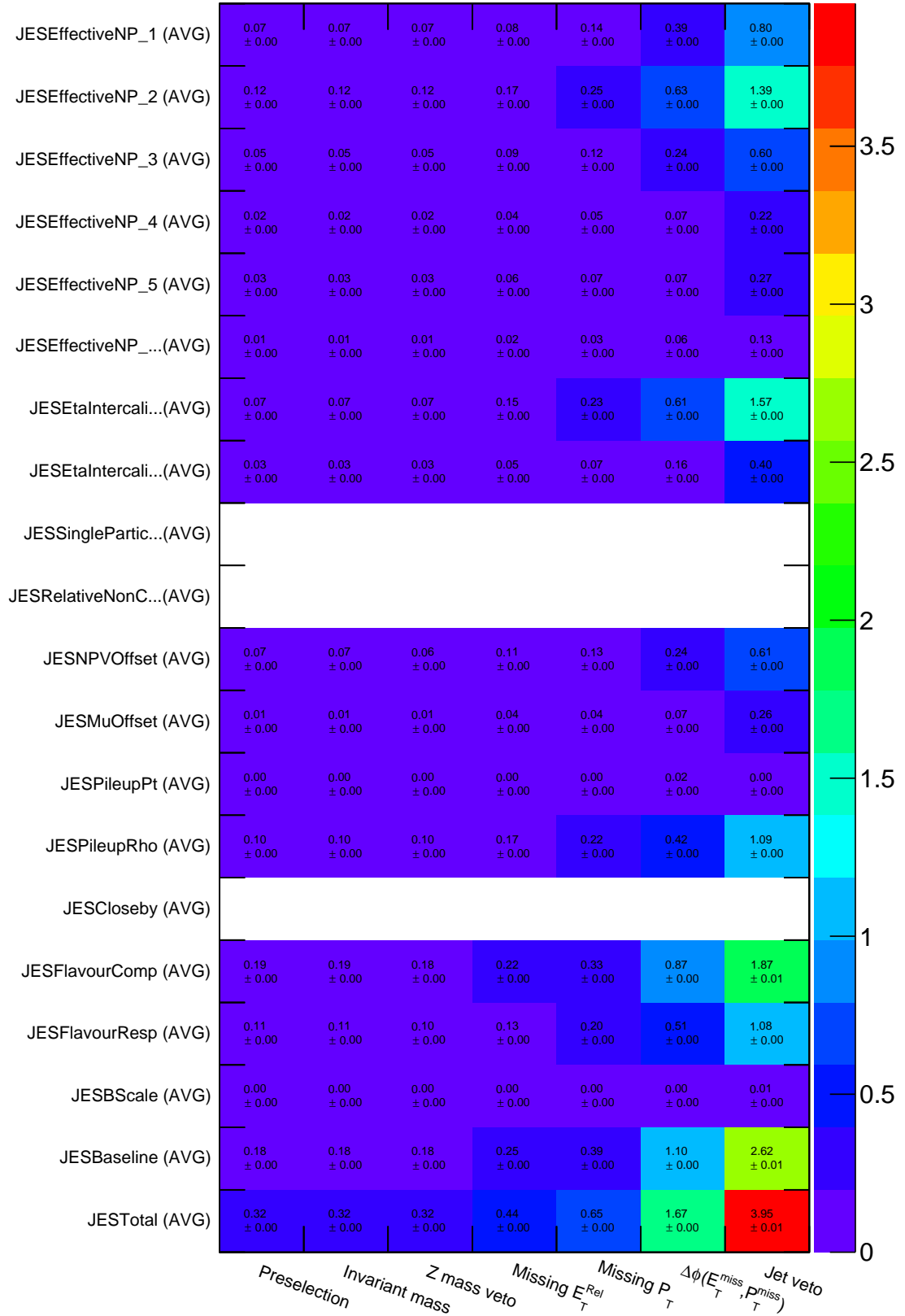


Table 4.29: Cut progression of jet energy scale components systematics on the signal samples for the inclusive channel ($\ell^+\ell^-$). The table shows the full set of systematics evolving as we introduce analysis cuts (columns left to right). Each number presents a percentage difference with respect to nominal yield at a given cut stage. Statistical uncertainty on each yield is shown. The color corresponds to the magnitude of the systematic shift. The up and down component of each systematic uncertainty has been symmetrized (indicated by the “AVG” label). JES Baseline is introduced for comparison between components and indicates the quadratic sum of JES Effective_NP* components and is not included in the total uncertainty to avoid duplication.

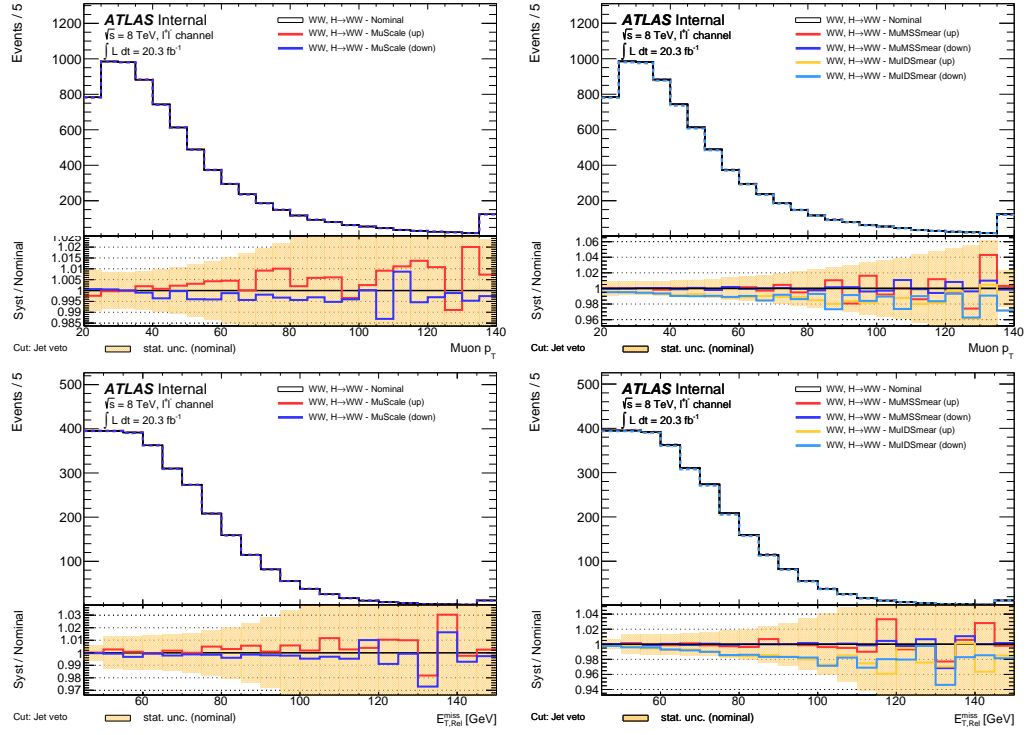


Figure 4.45: Effect of muon smearing and scale systematic uncertainty on muon p_T distribution (shown in top row) and the propagation to E_T (bottom row). The distributions are shown at the final cut stage, relative systematic uncertainties are shown in the subplot. Statistical uncertainty is shown as the orange band.

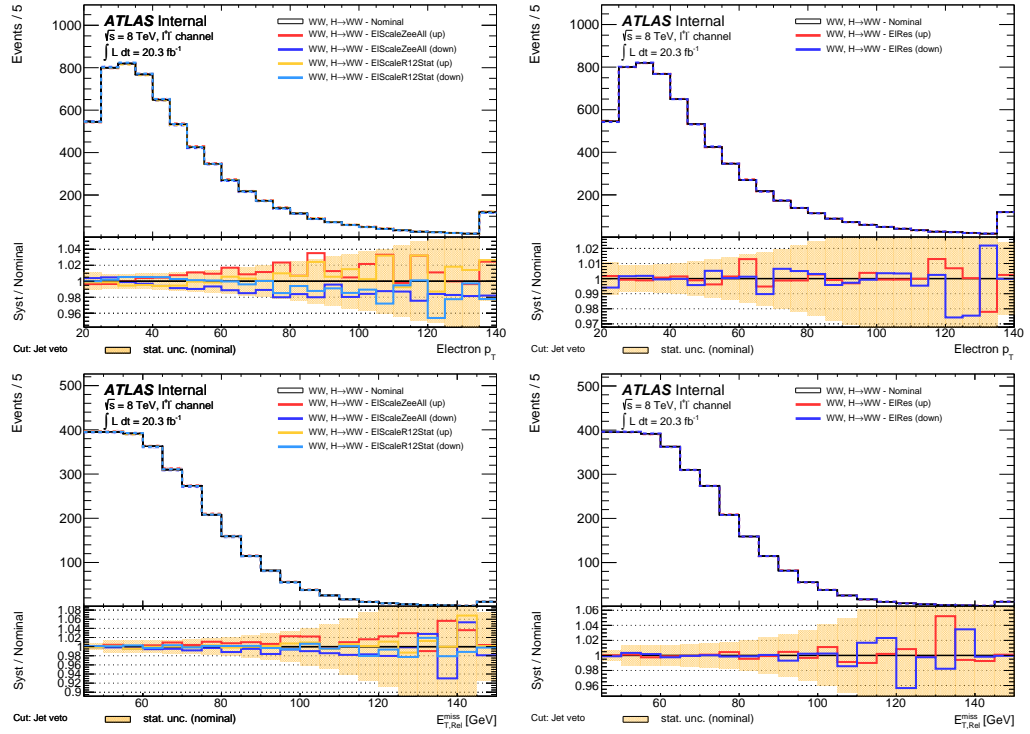


Figure 4.46: Effect of electron smearing and scale systematic uncertainty on electron p_T distribution (shown in top row) and the propagation to E_T (bottom row). The distributions are shown at the final cut stage, relative systematic uncertainties are shown in the subplot. Statistical uncertainty is shown as the orange band.

Sources	$e^+e^- \cancel{E}_T$	$\mu^+\mu^- \cancel{E}_T$	$e^\pm\mu^\mp \cancel{E}_T$	Inclusive
Electron Scale ZeeAll	1.40%	0%	0.36%	0.39%
Electron Scale R12Stat	0.06%	0%	0.09%	0.07%
Electron Scale PSStat	0.06%	0%	0.03%	0.02%
Electron Scale Low p_T	0.02%	0%	0.01%	0.01%
Electron Scale Total	1.41%	0%	0.37%	0.40%

Table 4.30: Electron scale components. As expected, there is no effect of electron scale on the muon channel.

relative change on the selected signal events for muon scaling and smearing systematics are shown in [fig. 4.45](#) as a function of muon p_T and $\cancel{E}_{T,\text{Rel}}$.

Similarly, electron energy scale and resolution uncertainties are derived from $Z \rightarrow e^+e^-$ [tag-and-probe](#) measurements ([section 3.3.4.1](#)). The uncertainty can be broken down into specific components, as shown in [table 4.30](#). The electron scaling and smearing systematics are shown in [fig. 4.46](#) as a function of electron p_T and $\cancel{E}_{T,\text{Rel}}$.

Reconstruction efficiency: Since the analysis uses combined muons, the muon [ID](#) and [MS](#) components are handled separately. Muon reconstruction efficiency uncertainties were fully discussed in [section 4.5.1.1](#). Electron reconstruction and identification uncertainties (e.g. [LOOSE++](#), [VERYTIGHTLLH](#) etc.) are considered together in the full electron efficiency. The uncertainty is estimated by varying the [tag-and-probe](#) selection ([section 4.5.2.1](#)).

Isolation efficiency: The uncertainties due to the isolation cut for electrons and muons are tailored specifically to our analysis: muon uncertainties are shown in [fig. 4.30](#), electron uncertainties are given in [table 4.16](#). The scale factors are very close to 1 with an uncertainty of $\approx 1\%$.

The systematic uncertainty for each individual effect is assumed to be independent from the others. Therefore the full systematic uncertainty can be estimated by varying each correction value by $\pm 1\sigma$ while the whole analysis is recomputed for each systematic source individually. It should be noted that in this way also all object corrections to \cancel{E}_T are correctly forwarded and taken into account, when \cancel{E}_T is being rebuilt.

4.8.2 Jet systematics

The [jet energy scale](#) uncertainty estimation follows the outline of the lepton scale systematic uncertainties, i.e. we varying the nominal scaling parameters by $\pm 1\sigma$. The jet energy smearing is implemented differently: Following the standard procedure of the [SM](#) Electroweak group, the nominal reconstructed [MC](#) jets are not smeared in the analysis. The application of smearing itself is considered as a systematic uncertainty as described in [section 3.3.5.2](#).

The resulting relative uncertainties are shown in [figs. 4.47](#) and [4.48](#) as a function of jet multiplicity distribution, jet p_T and $\cancel{E}_{T,\text{Rel}}$ distributions. Jet energy scale uncertainties have also been separated into its components, as summarized in [table 4.31](#). We are currently using the reduced set of 14 nuisance parameters.

Sources	$e^+e^- \cancel{E}_T$	$\mu^+\mu^- \cancel{E}_T$	$e^\pm\mu^\mp/\mu^\pm e^\mp \cancel{E}_T$	Combined
JES Effective NP1	0.47%	0.57%	0.35%	0.39%
JES Effective NP2	0.68%	0.94%	0.57%	0.63%
JES Effective NP3	0.31%	0.40%	0.21%	0.24%
JES Effective NP4	0.08%	0.13%	0.06%	0.07%
JES Effective NP5	0.09%	0.14%	0.05%	0.07%
JES Effective NP6 rest term	0.07%	0.10%	0.05%	0.06%
JES Eta Intercalibration Modelling	0.22%	0.23%	0.14%	0.16%
JES Eta Intercalibration StatAndMethod	0.65%	0.80%	0.57%	0.61%
JES SingleParticle HighPt	0%	0%	0%	0%
JES Relative Non Closure	0%	0%	0%	0%
JES NPV Offset	0.23%	0.37%	0.22%	0.24%
JES Mu Offset	0.07%	0.09%	0.06%	0.07%
JES Pileup Pt	0.02%	0.01%	0.02%	0.02%
JES Pileup Rho	0.49%	0.69%	0.37%	0.42%
JES Closeby	0%	0%	0%	0%
JES Flavour Composition	0.55%	0.80%	0.46%	0.51%
JES Flavour Response	0.92%	1.25%	0.80%	0.87%
JES B Scale	0%	0.01%	0%	0%
JES Baseline	1.21%	1.52%	1.02%	1.10%
JES Total	1.65%	2.34%	1.56%	1.67%

Table 4.31: jet energy scale uncertainty components for signal samples. **JES Total** refers to the overall estimate of the total uncertainty obtained from the tool (does not include pileup uncertainty for example). **JES Baseline** is a quadratic sum. of effective NP* components. Numbers are shown before the jet veto is applied.

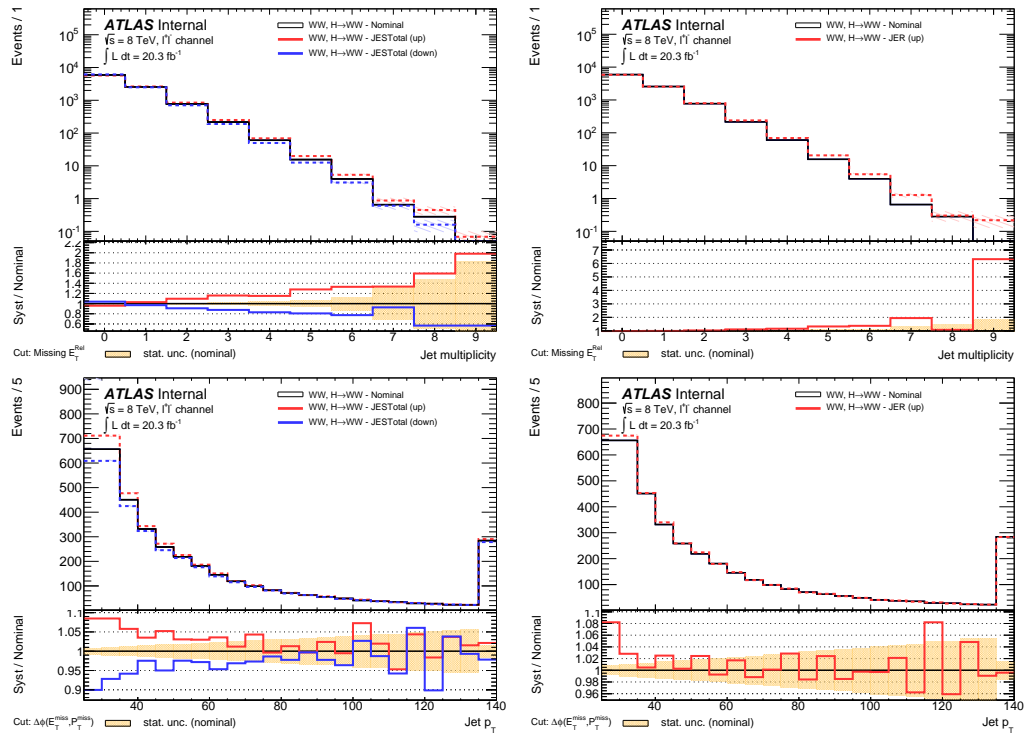


Figure 4.47: Effect of jet smearing and scale systematic uncertainty on jet multiplicity (shown in top row), jet p_T distribution (bottom row). The distributions are shown at the final cut stage, relative systematic uncertainties are shown in the subplot. Statistical uncertainty is shown as the orange band.

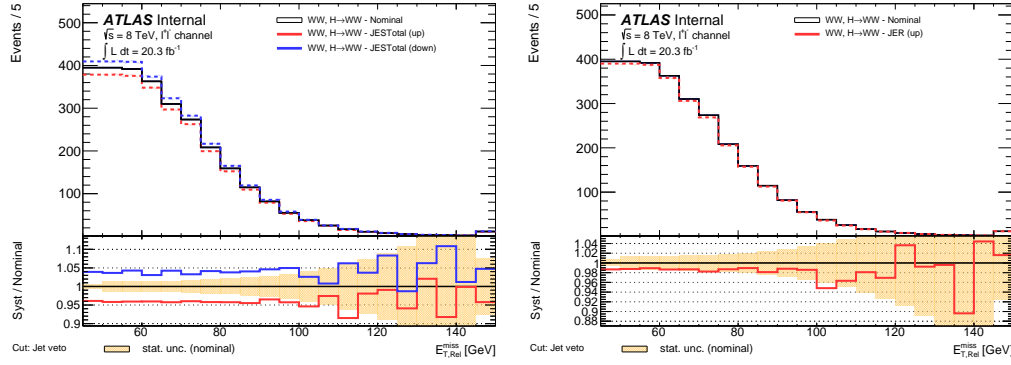


Figure 4.48: Effect of jet smearing and scale systematic uncertainty on E_T . The distributions are shown at the final cut stage, relative systematic uncertainties are shown in the subplot. Statistical uncertainty is shown as the orange band.

4.8.3 Missing transverse energy systematics

The E_T term in this analysis is based on the MET_{REFFINAL} algorithm. As we have shown in section 3.3.6, the calorimeter energy deposits are associated to high- p_T objects such as electrons, photons, muons and jets. The calibrations, scale and resolution uncertainties on electrons, muons and jets have therefore a direct impact on the E_T .

It should be noted that a 100 % correlation between the input objects and E_T is assumed. When shifting the electron energy scale by $+1\sigma$ then this correction affect not only the electron objects themselves but leads affect the recalculation of the E_T quantity. It is therefore necessary that all object-related corrections on energy and momentum described in the previous section are propagated and E_T itself is recalculated (a procedure commonly referred to as E_T rebuilding).

The uncertainties due to pile-up and soft scale and resolution systematic terms are independently estimated. They are denoted in table 4.27 and provided directly by the MISSINGETUTILITY package.

N.B.: While the 8 TeV is consistent with the selected jet collection for calibration and missing transverse energy rebuilding, the 7 TeV analysis used `AntiKt4EM` jets for selection and the `LCW+JES` scale for E_T . It is assumed that the scale and resolution uncertainties for both jet collections are fully correlated: e.g. varying the `JES` by $+1\sigma$ was done for both collections simultaneously, where one is used for the jet related cuts in the analysis and the other is used for the recalculation of E_T .

4.8.4 Missing transverse momentum systematics

Considering the definition of p_T given in section 4.5.4.3, the uncertainties come from the momentum measurement of the selected leptons and the tracks not associated with the leptons. The lepton related uncertainty is simultaneously evaluated when propagating the lepton momentum scale and resolution systematics in the full selection, similarly to E_T rebuilding. The uncertainties on the component coming from soft tracks (commonly referred to as soft p_T or `SoftTrackMET`) is derived from the ratio between data and MC in $Z \rightarrow \mu^+\mu^-$ events with no jets above $p_T > 25$ GeV.

The method exploits the balance between the transverse momenta of the soft tracks p_T^{soft} and the transverse momentum of the hard interaction p_T^{ℓ} , which in the case of the WW signal includes the

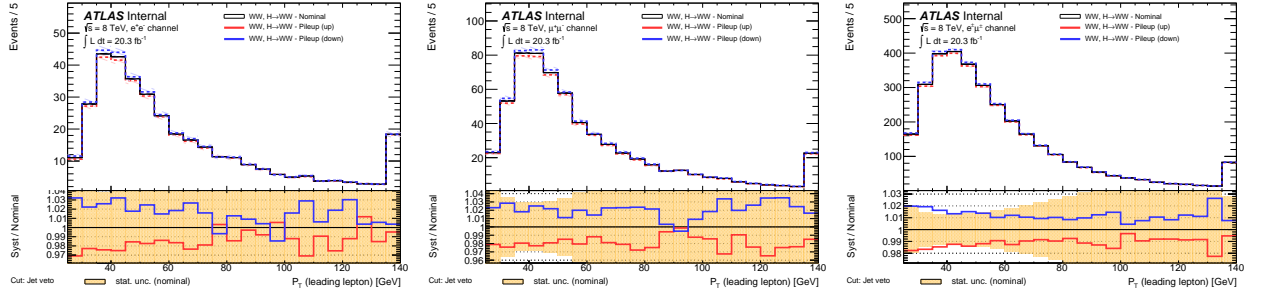


Figure 4.49: Pileup systematic uncertainty as a function of leading p_T distribution. The distributions are shown at the final cut stage, relative systematic uncertainties are shown in the subplot. Statistical uncertainty is shown as the orange band.

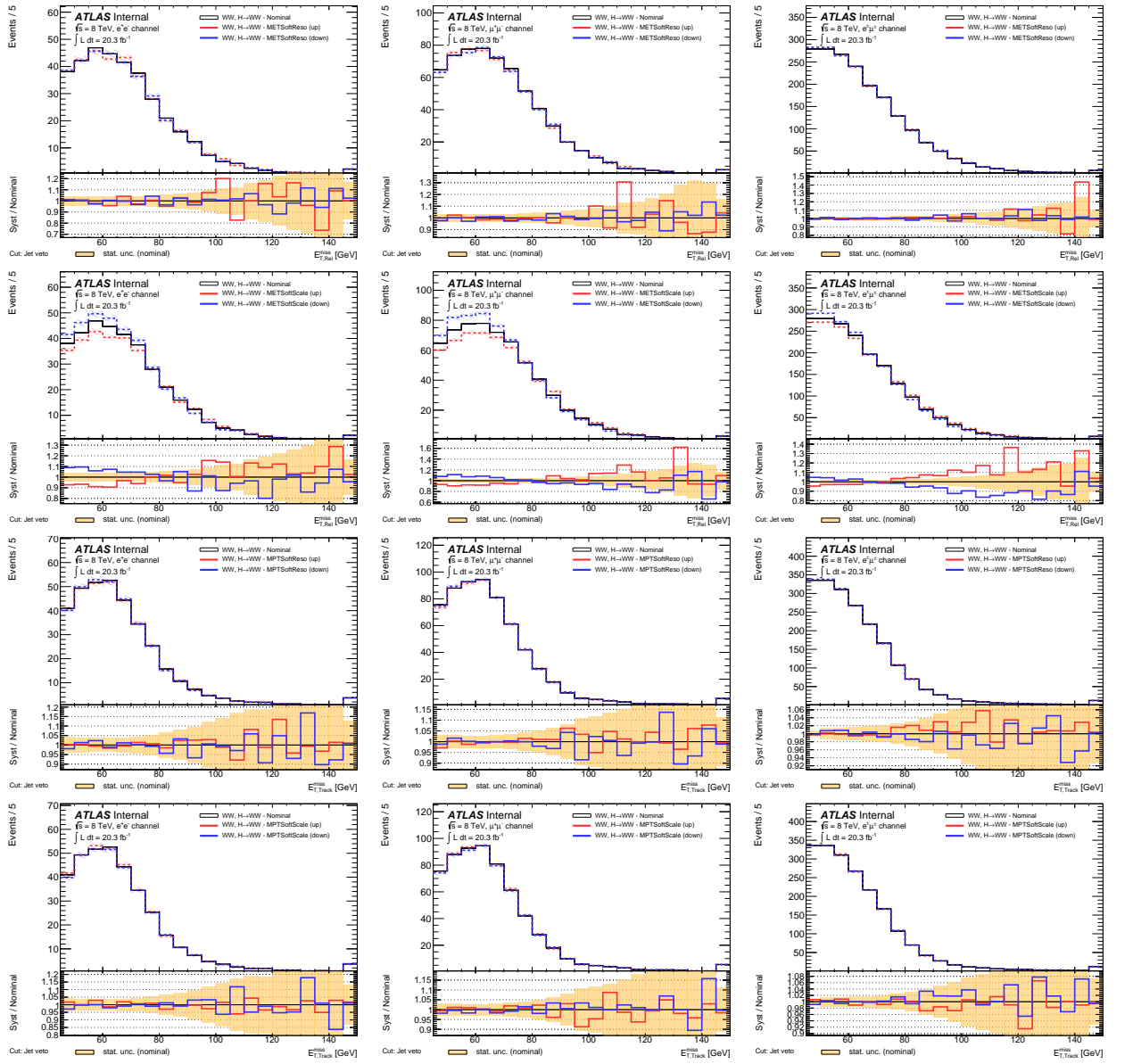


Figure 4.50: missing transverse energy systematic uncertainties on scale and resolution as a function of $E_{T,Rel}$. The distributions are shown at the final cut stage, relative systematic uncertainties are shown in the subplot. Statistical uncertainty is shown as the orange band.

leptons *and* the neutrinos (i.e. the truth \mathbf{E}_T known from MC):

$$\mathbf{p}_T = - \sum \mathbf{p}_T^\ell - \sum \mathbf{p}_T^{\text{soft}} \quad (4.30)$$

where \mathbf{p}_T^ℓ stands for momenta of leptons or neutrinos and $\mathbf{p}_T^{\text{soft}}$ is the residual momentum vector from soft tracks which is obtained by subtracting \mathbf{p}_T^ℓ from \mathbf{p}_T . The symbol p_T^X denotes the magnitude of the vector sum.

The soft track component p_T^{soft} is then decomposed along the transverse and longitudinal direction defined by \mathbf{p}_T^ℓ , yielding $p_T^{\text{soft},\perp}$ and $p_T^{\text{soft},\parallel}$, respectively. By comparing with data, the scale uncertainty is derived based on $p_T^{\text{soft},\parallel}$ and the resolution uncertainties are estimated on both components. Similar decomposition is then conducted in the signal and other background MC events, and the scale and resolution uncertainties are propagated in order to estimate \mathbf{p}_T uncertainty from soft tracks. [ATL141] The resulting uncertainties on \mathbf{p}_T sample are less than 1 %, see table 4.27.

4.9 Background estimates

The background contributions come from events produced by top ($t\bar{t}$ and single top), Z + jets, W + jets and other diboson processes, as we described in section 4.3.2. In this section we report on the data-driven methods developed to estimate the background contributions:

- Top: jet veto survival probability method, simultaneous fit method and transfer factor method,
- Z + jets: simultaneous fit method, ABCD method and transfer factor method,
- W + jets: matrix method and fake factor method

It is not in the scope of this thesis to explain all these methods in their entirety. Instead, we are going to focus on the baseline methods used to determine the final background composition and provide an independent verification using *Transfer factor method* (TF) methods which I implemented with my colleague Jiří Hejbal. Full details concerning the baseline and additional methods are given in the supporting document [ATL13b].

4.9.1 Simultaneous fit method

The main background estimation method used at 8 TeV is a profile likelihood based fit used to estimate signal strength along with top and Z + jets background contributions in the signal region (referred to as *simultaneous fit method* throughout the text). The number of signal and background events is described using a Poisson probability density function with the following parameters:

- **Free parameters**, i.e. the parameters that are fitted for signal and background components. We introduce three free parameters for each background and each channel: e^+e^- , $\mu^+\mu^-$ and $e^\pm\mu^\mp$.
- **Nuisance parameters** represent all the statistical and systematic uncertainties of the analysis as described in section 4.8. This accounts for 4 sources of electron energy scale uncertainties, electron energy resolution, 3 sources of the muon resolution, 16 sources of the jet energy scale, jet energy resolution, \mathbf{E}_T scale and \mathbf{E}_T resolution and 2 corresponding sources on \mathbf{p}_T .

We also include [pile-up](#), muon and electron identification uncertainties and trigger [scale factors](#). The nuisance parameters are constrained by a Gaussian distribution.

The W + jets, multi-jet and diboson backgrounds are estimated independently (see below) and remain fixed in the fit. The input template shapes for signal and $Z/\gamma^* \rightarrow \ell\ell$ events are obtained from [MC](#). As is common to all background estimation method, we start by defining the analysis regions:

Signal region (SR) corresponds exactly to the nominal WW selection introduced in [section 4.2](#).

The region defines the signal selection but also specifies the constraints on the backgrounds.

Z + jets control region (CR) is defined with respect to [SR](#) by inverting the p_T cut and adding a low p_T threshold: $5 < p_T < 45$ (20) GeV for same (combined) flavour channels. The $\Delta\phi(\mathbf{E}_T, \mathbf{p}_T)$ cut is completely omitted.

Top control region is defined using the same criteria as the [SR](#) apart from the jet veto. Instead, we require are least two jets with $p_T > 25$ GeV to accept the event in the top [CR](#).

The [control regions](#) are defined The fit is then performed on the $\Delta\phi(\mathbf{E}_T, \mathbf{p}_T)$ distribution in five equidistant bins within the [CR](#) and the [SR](#) simultaneously. In addition, to cross-check the results of the study we defined two verification regions to cross-check the

The [simultaneous fit](#) method was originally used to fit both top and Z+jets backgrounds, however only the Z + jets normalization is extracted from the fit as the dedicated top estimation method provides more detailed breakdown of systematic uncertainties. The method was implemented by Dimitra Tsionou from CEA Saclay.

e ⁺ e ⁻ channel		
	top	Z + jets
MC prediction	96.9 ± 4.8 (stat.) ± 26.5 (syst.)	55.3 ± 6.3 (stat.) ± 17.1 (syst.)
DD estimation	94.1 ± 2.5 (stat.) ± 24.6 (syst.)	54.5 ± 1.2 (stat.) ± 23.1 (syst.)
Normalisation factor	1.00 ± 0.06	1.03 ± 0.08
μ ⁺ μ ⁻ channel		
	top	Z + jets
MC prediction	131.4 ± 6.1 (stat.) ± 32.8 (syst.)	106.0 ± 7.0 (stat.) ± 27.4 (syst.)
DD estimation	136.9 ± 2.9 (stat.) ± 18.7 (syst.)	95.6 ± 1.5 (stat.) ± 26.5 (syst.)
Normalisation factor	1.02 ± 0.06	1.04 ± 0.11
e [±] μ [∓] channel		
	top	Z + jets
MC prediction	625.9 ± 12.5 (stat.) ± 129.4 (syst.)	164.6 ± 15.4 (stat.) ± 18.5 (syst.)
DD estimation	653.1 ± 5.2 (stat.) ± 122.3 (syst.)	166.1 ± 3.2 (stat.) ± 26.3 (syst.)
Normalisation factor	1.04 ± 0.04	1.02 ± 0.09

Table 4.32: The [MC](#) prediction for the top and the $Z/\gamma^* \rightarrow \ell\ell$ estimation with each statistical uncertainty and the result of the fit with its statistical and systematic uncertainty is shown along with the normalisation factor returned by the fit. The reason why the estimation doesn't scale exactly according to the normalisation factor is due to the fact that there are nuisance parameters fixed away from zero. Courtesy of Dimitra Tsionou.

4.9.2 Z+jets background: Transfer factor method

As an independent verification of the Z + jets background estimate we use a partially data-driven method based on a transfer factor approach. First we estimate Z + jets in the **control region** using data from which we subtract non-Z + jets events based on the **MC** description. To estimate the Z + jets in the **control region** we apply the **transfer factor**, effectively scaling events from the **control region** to the **control region**.

For Z + jets data-driven background estimation we use the following formula:

$$\text{Data-Driven Z + jets : } N_{Z+jets,SR} = \text{TF} \cdot \left(N_{CR}^{\text{data}} - N_{\text{non-Z,CR}}^{\text{MC}} \right) = \text{SF} \cdot N_{Z,SR}^{\text{MC}} \quad (4.31)$$

where N_{CR}^{data} is the total number of events observed in the **control region** in data, $N_{\text{non-Z,CR}}^{\text{MC}}$ is the **MC** predicted number of non-Z + jets events in the **control region**, $N_{Z,SR}^{\text{MC}}$ is the expected number of Z + jets events in the signal region from **MC**. The **TF** and **SF** stand for the transfer factor and **scale factors** respectively, both defined as follows:

$$\text{TF} = \frac{N_{Z,SR}^{\text{MC}}}{N_{Z,CR}^{\text{MC}}}, \quad \text{SF} = \frac{N_{Z,CR}^{\text{data}}}{N_{Z,CR}^{\text{MC}}} = \frac{N_{CR}^{\text{data}} - N_{\text{non-Z,CR}}^{\text{MC}}}{N_{Z,CR}^{\text{MC}}} \quad (4.32)$$

where $N_{Z,CR}^{\text{MC}}$ is the expected number of Z + jets events in the control region estimated from **MC**.

The following selection criteria are defined:

Control region is defined with respect to the nominal analysis:

- $p_T < 45 \text{ GeV}$ for e^+e^- and $\mu^+\mu^-$ channel and $\Delta\phi(\vec{E}_T, \vec{p}_T)$ cut is omitted
- $\Delta\phi(\vec{E}_T, \vec{p}_T) > 0.6$ for $e^\pm\mu^\mp$ channel, p_T cut is omitted

i.e. for the same flavour channels the control region is defined by inverting the p_T cut in the event selection, while in the $e^\pm\mu^\mp$ channel by inverting the $\Delta\phi(\vec{E}_T, \vec{p}_T)$ cut. Both p_T and $\Delta\phi(\vec{E}_T, \vec{p}_T)$ cuts were designed to improve the discrimination of Z + jets events in WW **control region** making them ideal candidates. All the other selection cuts remain the same.

Signal region which corresponds to the signal region of the analysis and contains events passing all cuts defined in [section 4.2.2](#)

[Figure 4.51](#) show the control region distributions of p_T in the same flavour channels and $\Delta\phi(\vec{E}_T, \vec{p}_T)$ in the combined flavour channel. The results are summarized in [table 4.33](#), the **MC** prediction on Z + jets events scale up by 1.04 in e^+e^- , by 1.07 in $\mu^+\mu^-$ and by 1.02 in $e^\pm\mu^\mp$ channel in the signal region. The effect of subtracting the background in the **control region** based on the **MC** prediction was found to be negligible (1 % for e^+e^- and $\mu^+\mu^-$ channel, 2 % for $e^\pm\mu^\mp$ channel).

To evaluate the systematic uncertainties, we calculate the **transfer factors** independently for each systematic source as described in [section 4.8](#). The resulting uncertainties are listed in [table 4.35](#) quoted as the deviation from the nominal estimation. The total systematic uncertainty is calculated as:

$$\sigma_{\text{syst}} = \max \left(\sqrt{\sum_{\text{syst}+} (N_{\text{nominal}} - N_{\text{syst}+})^2}, \sqrt{\sum_{\text{syst}-} (N_{\text{nominal}} - N_{\text{syst}-})^2} \right) \quad (4.33)$$

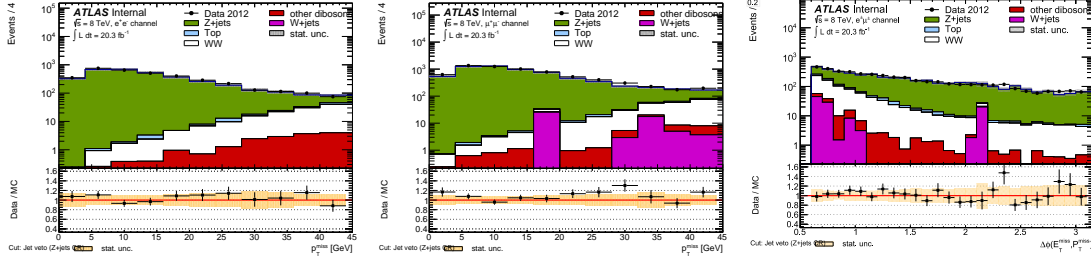


Figure 4.51: The $\Delta\phi(\mathbf{E}_T, \mathbf{p}_T)$ distribution in $e\mu$ channel and \mathbf{p}_T distribution in ee and $\mu\mu$ channel in the Z+jets control region.

chn.	$N_{\text{CR}}^{\text{data}}$	$N_{\text{non-Z,CR}}^{\text{MC}}$	$N_{\text{Z,CR}}^{\text{data}}$	$N_{\text{Z,CR}}^{\text{MC}}$	SF	TF	$N_{\text{Z,SR}}^{\text{MC}}$	$N_{\text{Z,SR}}^{\text{DD}}$
e^+e^-	3602.0 ± 60.0	166.9 ± 3.3	3435.1 ± 60.1	3297.0 ± 93.3	1.042 ± 0.035	0.01702 ± 0.002	55.3 ± 6.3	58.5 ± 7.0
$\mu^+\mu^-$	6876.0 ± 82.9	335.2 ± 30.5	6540.8 ± 88.3	6122.9 ± 127.1	1.068 ± 0.026	0.0186 ± 0.002	106.0 ± 7.0	121.6 ± 10.2
$e^\pm\mu^\mp$	4348.0 ± 65.9	1027.6 ± 50.4	3320.4 ± 83.0	3244.8 ± 69.5	1.023 ± 0.034	0.04866 ± 0.005	164.6 ± 15.4	161.5 ± 16.6

Table 4.33: The event yields in the Z + jets control region. All uncertainties are statistical only. The number of Z + jets events in the signal region are given in the rightmost two columns, for both the MC prediction and the data-driven estimation.

where N_{nominal} is number of events measured in the nominal estimation and $N_{\text{sys}+/ -}$ is number of events corresponding to each positive and negative systematic variation. Theoretical uncertainties on the sample dependence are estimated by replacing the MC@NLO sample with POWHEG.

Total systematic uncertainty of the TF for Z + jets background estimation in e^+e^- , $\mu^+\mu^-$, $e^\pm\mu^\mp$ channels is shown in table 4.34. These uncertainties are then propagated to the final Z + jets estimation obtained by the data-driven method. The final data-driven estimation of Z + jets events and corresponding MC prediction with both statistic and systematic uncertainties are summarized in table 4.36. The dominant systematic uncertainty comes from missing transverse energy soft terms and jet energy resolution.

chn.	Z + jets estimation	MC prediction
e^+e^-	$58.5 \pm 7.0(\text{stat}) \pm 30.9(\text{syst})$	$55.3 \pm 6.3(\text{stat.}) \pm 17.1(\text{syst.})$
$\mu^+\mu^-$	$121.6 \pm 10.2(\text{stat}) \pm 52.3(\text{syst})$	$106.0 \pm 7.0(\text{stat.}) \pm 27.4(\text{syst.})$
$e^\pm\mu^\mp$	$161.5 \pm 16.6(\text{stat}) \pm 26.6(\text{syst})$	$164.6 \pm 15.4(\text{stat.}) \pm 18.5(\text{syst.})$

Table 4.34: Z + jets background yields in the control region for three channels and its comparison to the MC prediction with both statistical and systematic uncertainties

The systematic uncertainties on the estimate are rather large. However, compared to the Scale factor approach defined in formula (4.32) we managed to reduce systematic uncertainties by propagating them via the transfer factor approach instead. This is due to the fact that the systematics coming from the control region and the control region enter the TF in the ratio (ibid).

4.9.3 Top background: Jet veto survival probability

The decay products from both top-pair ($t\bar{t} \rightarrow WbWb$) and single top ($Wt \rightarrow WbW$) processes contain WW final states producing a major background to our measurement. However, top events are distinctly characterized by the presence of jets in the final states. Consequently, the majority of these background events can be removed by applying a jet veto cut on jets with $p_T > 25$ GeV and

Systematic source for top TF	e^+e^-	$\mu^+\mu^-$	$e^\pm\mu^\mp$
Missing $\cancel{E}_{T,Rel}$ Scale Soft Terms	33.17%	26.87%	8.65%
Jet Energy Resolution (corrected)	23.07%	16.07%	0.22%
Missing pT Scale Soft Terms	10.63%	10.63%	1.91%
Missing $\cancel{E}_{T,Rel}$ Reso Soft Terms	10.10%	5.24%	2.48%
Pileup	10.81%	8.39%	2.70%
Missing pT Reso Soft Terms	2.05%	2.77%	10.76%
JES Flavour Composition	5.24%	6.70%	2.11%
JES Effective NP2 rest term	3.58%	4.27%	1.72%
JES Flavour Response	2.77%	3.76%	1.57%
JES Eta Intercalibration Modelling	1.61%	3.59%	1.66%
JES Pileup Rho	2.82%	3.53%	1.12%
JES NPV Offset	2.47%	2.62%	1.23%
Muon MS Resolution	0.24%	4.40%	1.52%
JES Effective NP1 rest term	1.23%	3.22%	1.52%
Electron Scale ZeeAll	3.07%	0.00%	0.29%
JES Effective NP3 rest term	1.57%	2.41%	0.67%
Jet Vertex Fraction (corrected)	1.27%	0.89%	1.06%
Muon ID Resolution	0.24%	1.76%	1.85%
JES Eta Intercalibration StatAndMethod	0.52%	1.21%	0.73%
Electron Resolution	1.51%	0.00%	0.64%
Muon Scale	0.00%	1.74%	0.06%
JES Mu Offset	1.23%	0.83%	0.52%
Jet Efficiency B	0.60%	0.61%	1.10%
Jet Efficiency Light	0.60%	0.61%	1.10%
Jet Efficiency C	0.60%	0.61%	1.10%
JES Effective NP4 rest term	0.83%	0.44%	0.18%
JES Effective NP6 rest term	0.76%	0.34%	0.10%
JES Effective NP5 rest term	0.38%	0.44%	0.33%
Electron Scale R12Stat	0.62%	0.00%	0.35%
JES Pileup Pt	0.32%	0.11%	0.18%
Electron Scale PSStat	0.26%	0.00%	0.16%
JES B Scale	0.24%	0.0%	0.00%
Trigger Matching (Electrons)	0.20%	0.00%	0.12%
Electron Efficiency SF (ID)	0.06%	0.00%	0.05%
Muon Isolation SF	0.00%	0.07%	0.03%
Muon Efficiency SF	0.00%	0.04%	0.01%

Table 4.35: The systematic sources of the data-driven background estimation using [transfer factor](#) method for Z + jets background.

chn	TF	δ_{stat}	δ_{syst}
e^+e^-	$0.017 \pm 0.002(stat) \pm 0.009(syst)$	11.70 %	52.90 %
$\mu^+\mu^-$	$0.018 \pm 0.002(stat) \pm 0.008(syst)$	11.10 %	44.40 %
$e^\pm\mu^\mp$	$0.049 \pm 0.005(stat) \pm 0.008(syst)$	10.20 %	16.30 %

Table 4.36: Statistical and total systematic uncertainties of the [TF](#) for Z + jets background estimation for e^+e^- , $\mu^+\mu^-$ and $e^\pm\mu^\mp$. The two rightmost columns show the relative statistical and systematic uncertainties.

$|\eta| < 4.5$. However, some top events could still mimic the WW final state if they contain jets outside the jet veto acceptance. As the MC predictions of this behaviour might not be accurate, we estimate the background contribution using a data driven method by defining the *Jet veto survival probability method (JVSP)*. This method is based on the techniques of background extraction discussed in [MRZ11]. It uses two control regions:

CR 1 is defined analogously to our signal region with the exception of the jet veto cut. Instead, we introduce a requirement on the scalar sum of the transverse energy of final state leptons and jets to be $H_T > 130$ GeV. This requirement is designed to remove WW signal events from the control region, reducing the contamination below 10 % in the same flavour channels and below 1 % in the $e^\pm\mu^\mp$ channel.

CR 2 is a subset of CR 1 which enhances the top event selection by requiring the presence of at least one τ -jet with $p_T > 25$ GeV and $|\eta| < 2.5$ (tracker information is required for τ -tagging). The jet is tagged using a multivariate technique (MV1 tagger) with 85 % efficiency.

To estimate the number of $t\bar{t}$ and Wt events in the control region, we multiply the number of top events from CR 1 measured in data ($N_{CR1}^{\text{top,data}}$) with the probability that a top event survives the jet veto p_{CR1}^{data} . The number of top events in data is obtained by subtracting all non-top events estimated from MC: $N_{CR1}^{\text{top,data}} = N_{CR1}^{\text{data}} - N_{CR1}^{\text{non-top,MC}}$. The non-top background contributions in CR 1 are summarized in table 4.37. We can express the final data driven yield as:

$$N_{\text{top}}^{\text{DD}} = (N_{CR1}^{\text{data}} - N_{CR1}^{\text{non-top,MC}}) \cdot p_{CR1}^{\text{data}} / \epsilon_{H_T} \quad (4.34)$$

where ϵ_{H_T} is the efficiency of the H_T cut applied in CR 1. This efficiency is better 95 % and the data/MC agreement is better than 1 %.

The jet veto survival probability (p_{CR1}^{data}) is extrapolated from CR 2:

$$p_{CR1}^{\text{data}} = (p_{CR2}^{\text{data}})^2 \cdot \frac{p_{CR1}^{\text{MC}}}{(p_{CR2}^{\text{MC}})^2} \quad (4.35)$$

where p_{CR2}^{data} (resp. p_{CR2}^{MC}) is the probability for a data (resp. MC) event in CR 2 to survive the jet veto, and p_{CR1}^{MC} is the survival probability determined from MC in CR 1.

Final State	e^+e^-	$\mu^+\mu^-$	$e^\pm\mu^\mp$	inclusive
Observed Events	1966	3444	22134	27544
Top	1897.7 ± 18.1	3016.8 ± 23.4	20073.5 ± 59.6	24987.4 ± 66.5
WW	187.7 ± 3.2	341.8 ± 4.2	1847.2 ± 9.7	2376.1 ± 11.1
W + jets	2.67 ± 2.67	4.72 ± 4.72	118.0 ± 23.3	125.4 ± 23.9
Z + jets	10.1 ± 1.5	31.5 ± 8.4	73.8 ± 18.5	115.4 ± 20.4
Other diboson	18.6 ± 1.2	19.4 ± 0.9	99.7 ± 3.1	137.8 ± 3.4
Total non-top background	219.1 ± 4.6	397.6 ± 10.6	2138.76 ± 31.5	2755.5 ± 33.6

Table 4.37: Summary of observed data events in CR 1 and expected top and non-top background contributions derived from MC in CR 1 show per channel and combined. The uncertainties are statistical only.

The total contribution from the $t\bar{t}$ and Wt is estimated to be 836.6 ± 12.3 (stat.) ± 71.1 (syst.), the yields are broken down per channel in [table 4.38](#). The systematic uncertainties are estimated by studying the variations on the $\frac{p_{CR1}^{MC}}{(p_{CR2}^{MC})^2}$ term. These come from various sources:

- Experimental systematics related to jets: [jet energy scale](#) systematics are evaluated by varying the nominal scaling parameters, [jet energy resolution](#) is estimated by applying jet energy smearing (see [section 4.8.2](#)). The resulting symmetrized variations are $\pm 3.90\%$ for [JES](#) and $\pm 1.20\%$ for [JER](#). In comparison to other background estimation methods, this uncertainty is much smaller (see [table 4.41](#) below). This is expected, since the two [control regions](#) are kinematically similar, the systematic uncertainties on the [MC](#) description partially cancel in the ratio as they affect both regions in a similar way.
- Systematics coming from non-top background subtraction are estimated by assigning an overall uncertainty for each [MC](#) driven background: 15 % for WW, 50 % for W + jets and Z + jets, 15 % for other dibosons. These numbers correspond to our [MC](#) systematic estimates apart from WW, where we use an enlarged uncertainty. The relative uncertainty of $N_{\text{non-top}}/N_{\text{non-top}}^{\text{data}}$ is 2.10 %.
- Theoretical uncertainties: We estimate sample dependence by switching from the nominal [MC@NLO + Jimmy](#) sample for [POWHEG + Jimmy](#) and [POWHEG + Pythia](#) yielding an uncertainty of 5.10 %, resp. 3.70 %. The overall uncertainty is 6.30 %. Another source of uncertainty comes from re-weighting the nominal [MC@NLO](#) PDF to CT10, the maximum variation is 1.70 %. To estimate the uncertainties coming from single-top, we vary its cross-section by 30 % giving an uncertainty of 1.10 %.
- Systematics of the method: The exponent used in the [control region](#) ratio has a value of $N = 2$ because we assume that there are 2 b-jets in top events in the [CR 2](#). To test this, we test the method with different exponents $N = 1.5$ and $N = 2.5$, the resulting uncertainty is within 1 %. We also estimate the effect of cut efficiency ϵ_{H_T} based on data/[MC](#) agreement, the resulting uncertainty is 0.87 %.

The [JVSP](#) data driven method is used as the nominal estimate of top background in the 8 TeV analysis. The study was conducted by Jun Gao from CPPM, France.

Channel	p_{CR2}^{MC}	p_{CR2}^{data}	p_2^{MC}	$p_2^{MC}/(p_{CR2}^{MC})^2$	$N_{\text{top}}^{\text{data}}(CR1)$	$N_{\text{top}}^{MC}(CR1)$
e^+e^-	0.229 ± 0.004	0.231 ± 0.010	0.040 ± 0.002	0.762 ± 0.025	$91.8 \pm 7.3 \pm 7.9$	96.9 ± 4.8
$\mu^+\mu^-$	0.186 ± 0.004	0.185 ± 0.009	0.036 ± 0.002	0.937 ± 0.021	$127.2 \pm 9.4 \pm 10.9$	131.4 ± 6.1
$e^\pm\mu^\mp$	0.221 ± 0.001	0.217 ± 0.003	0.029 ± 0.001	0.593 ± 0.012	$608.6 \pm 17.5 \pm 52.3$	625.9 ± 12.5

Table 4.38: Summary of results for the jet veto efficiencies used for the prediction of the number of top background events and final data-driven top yield for each channel. The first is statistical and the second systematic in the last column.

4.9.4 Top background: Transfer factor method

The alternative method for estimating the top background uses a control region defined by the presence of a [b-tagged](#) sub-threshold jet. The [Transfer factor](#) takes advantage of two features that distinguish top production from WW events:

- the larger jet multiplicity at leading order and the presence of quarks from the top decay (see fig. 4.15b).
- The presence of a **b-tagged** jet used for jet counting in the analysis allows the identification of a top-enriched control region.

The **control region** contains events passing the nominal selection up to and including the relative missing energy cut ($E_{T,Rel}$) which in addition have at least one **b-tagged** jet with $p_T > 20$ GeV. In practice, this means that the control events in the “zero jet bin” have at least one **b-tagged** jet, which is below the jet counting threshold of the analysis.

The jet multiplicity distributions for the control region are shown in fig. 4.52 for e^+e^- , $\mu^+\mu^-$ and $e^\pm\mu^\mp$ channels. To determine the total contribution from the top background, we first estimate a number of top events in the **control region** and consequently extrapolate it to the **control region** using a **Transfer factor** defined as:

$$TF = \frac{N_{top,SR}^{MC}}{N_{top,CR}^{MC}} \quad (4.36)$$

where $N_{top,SR}$ ($N_{top,CR}$) is the number of **MC** events in the **SR** (**CR**) including both $t\bar{t}$ and single top.

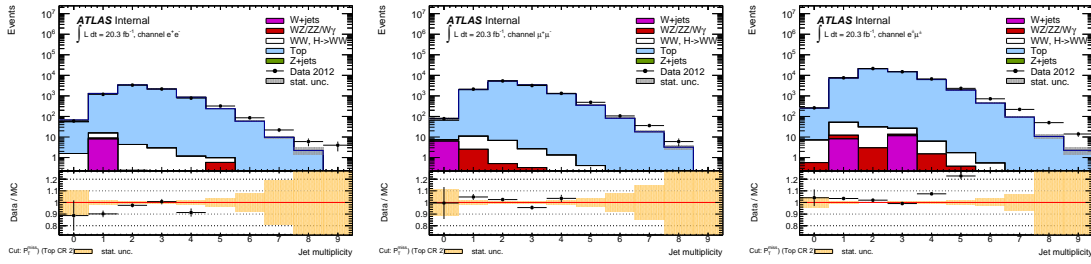


Figure 4.52: Predicted and observed distribution of number of reconstructed jets above the analysis threshold in the control region used for the **TF** method top background estimation in the e^+e^- , $\mu^+\mu^-$ and $e^\pm\mu^\mp$ channel.

To estimate the top background in the signal region we use the the following formula:

$$\text{Data-driven top} : N_{top,SR} = TF \cdot \left(N_{CR}^{data} - N_{non-top,CR}^{MC} \right) \quad (4.37)$$

where $N_{top,SR}^{MC}$ is the expected number of top events in the signal region and $N_{top,CR}^{MC}$ is the expected number of top events in the control region as predicted by the top **MC** model. N_{CR}^{data} is the total number of top events observed in the control region in data and $N_{non-top,CR}^{MC}$ is the background with respect to top events in the control region (e.g. WW). The resulting **transfer factors** and event yields are summarized in table 4.39. The effect of subtracting the backgrounds in the **control region** using the **MC** prediction was found to be negligible (1.50 % for $\mu^+\mu^-$ channel and less than 1 % for e^+e^- and $e^\pm\mu^\mp$ channel).

To evaluate the systematic uncertainties on the top background estimation, we calculate the **transfer factors** independently for each systematic source in a similar way as we do in the Z + jets **transfer factor** method, see eq. (4.33). The uncertainties are summarized in table 4.41 quoted as the deviation from the nominal estimation. Theoretical uncertainties on the sample dependence are estimated by replacing the **MC@NLO** sample with **POWHEG**. The total systematic uncertainty is given in table 4.40 and compared with **MC** predictions in table 4.42. Dominating systematic

chn.	MC Top CR	Data CR	MC non-Top CR	TF	MC Top SR	DD Top SR
e^+e^-	8051.0 ± 36.2	7980.0 ± 89.3	79.5 ± 7.7	0.01232 ± 0.00063	96.9 ± 4.8	97.3 ± 5.1
$\mu^+\mu^-$	12305.8 ± 46.3	12720.0 ± 112.8	117.1 ± 7.8	0.01041 ± 0.00050	131.4 ± 6.1	131.2 ± 6.4
$e^\pm\mu^\mp$	52184.4 ± 93.5	54238.0 ± 232.9	185.5 ± 11.9	0.01187 ± 0.00024	625.9 ± 12.5	641.4 ± 13.6

Table 4.39: The event yields in the top control region. The number of top events in the [control region](#) are given in the rightmost two columns, for both the [MC](#) prediction and the data-driven estimation. The uncertainties listed here are statistical only.

uncertainty was found to be [JER](#), sample dependence and components of [JES](#).

chn.	Top estimation	MC prediction
e^+e^-	$97.3 \pm 5.1(\text{stat}) \pm 22.8(\text{syst})$	$96.9 \pm 4.8 (\text{stat.}) \pm 26.5 (\text{syst.})$
$\mu^+\mu^-$	$131.2 \pm 6.4(\text{stat}) \pm 38.6(\text{syst})$	$131.4 \pm 6.1 (\text{stat.}) \pm 32.8 (\text{syst.})$
$e^\pm\mu^\mp$	$641.4 \pm 13.6(\text{stat}) \pm 145.9(\text{syst})$	$625.9 \pm 12.5 (\text{stat.}) \pm 129.4 (\text{syst.})$

Table 4.40: Top background yields in the [control region](#) for three channels and its comparison to the MC prediction with both statistical and systematic uncertainties

4.9.5 W+jets and multijet background: Matrix method

The single [W](#) production in association with jets can mimic the WW final state when the associated jet is misidentified as lepton during reconstruction. Similarly, the multi-jet [QCD](#) background can pass the signal selection if at least two jets are misidentified as leptons and there is sufficiently large E_T in the event due to [pile-up](#). Thus, both of these backgrounds are largely affected by the detector conditions and might not be accurately described in [MC](#).

The data-driven method relies on comparing the number of events with leptons passing specific selection requirements with the number of *real* (R) and *fake* (F) leptons in the sample. We define two alternative sets of selection criteria: *tight* (T) which corresponds to the nominal analysis object selection (see [sections 4.5.1](#) and [4.5.2](#)) and *loose* (L) which is a superset of the nominal selection chosen to be as loose as possible:

- Loose electrons satisfy the nominal kinematic and object quality criteria, but only pass the MEDIUMLLH operating point (relaxing the racking and calorimeter shower shape criteria). No [Interaction point](#) and isolation criteria are applied.
- Loose muons satisfy the nominal muon identification criteria with the exception of isolation and [Interaction point](#) requirements.

The respective contribution to real or fake leptons from the control groups depend on the probability that a real or a fake lepton pass or fail the given selection. The total number of events with a given combination of real or fake leptons can be expressed as a system of linear equations.

Systematic source for top TF	e^+e^-	$\mu^+\mu^-$	$e^\pm\mu^\mp$
Jet Energy Resolution (corrected)	17.59%	19.78%	16.03%
Jet Efficiency B	5.86%	5.67%	5.50%
Sample dependence	9.40%	5.44%	1.21%
JES Eta Intercalibration Modelling	6.78%	5.76%	5.30%
JES Effective NP2 rest term	5.78%	6.17%	6.19%
Jet Vertex Fraction (corrected)	4.41%	4.90%	4.86%
JES B Scale	4.25%	4.31%	4.25%
JES Pileup Rho	4.09%	4.44%	4.86%
$\cancel{E}_{T,Rel}$ Scale Soft Terms	5.58%	3.58%	1.74%
JES Effective NP1 rest term	3.61%	3.49%	3.64%
Jet Efficiency Light	2.89%	2.99%	3.07%
Jet Efficiency C	2.77%	2.90%	2.91%
JES Effective NP3 rest term	2.45%	2.95%	2.59%
JES Flavour Composition	2.45%	2.81%	2.63%
JES NPV Offset	1.64%	3.27%	2.15%
JES Eta Intercalibration StatAndMethod	1.77%	1.90%	1.70%
JES Flavour Response	1.73%	1.49%	1.53%
Muon ID Resolution	0.28%	3.08%	0.93%
JES Effective NP5 rest term	0.96%	1.36%	1.09%
JES Mu Offset	0.76%	1.18%	0.93%
JES Effective NP4 rest term	0.80%	1.09%	0.97%
$\cancel{E}_{T,Rel}$ Reso Soft Terms	1.12%	0.54%	0.48%
Missing pT Scale Soft Terms	0.68%	1.22%	0.48%
JES Effective NP6 rest term	0.44%	0.68%	0.57%
Missing pT Reso Soft Terms	0.60%	0.18%	0.12%
Pileup	0.32%	0.27%	0.08%
Electron Resolution	0.84%	0.00%	0.04%
Electron Scale PSStat	0.36%	0.00%	0.00%
Electron Scale R12Stat	0.40%	0.00%	0.04%
JES Pileup Pt	0.04%	0.31%	0.00%
Electron Scale ZeeAll	0.40%	0.00%	0.08%
Muon MS Resolution	0.00%	0.36%	0.00%
Trigger Matching (Electrons)	0.24%	0.00%	0.00%
Muon Scale	0.00%	0.13%	0.00%
Electron Efficiency SF (Trk)	0.00%	0.00%	0.00%
Electron Efficiency SF (ID)	0.08%	0.00%	0.00%

Table 4.41: The systematic sources of the data-driven background estimation using [transfer factor](#) method for top background.

chn	TF	δ_{stat}	δ_{syst}
e^+e^-	$0.0123 \pm 0.0006(\text{stat}) \pm 0.0029(\text{syst})$	4.90 %	23.60 %
$\mu^+\mu^-$	$0.0104 \pm 0.0005(\text{stat}) \pm 0.0030(\text{syst})$	4.80 %	28.80 %
$e^\pm\mu^\mp$	$0.0119 \pm 0.0002(\text{stat}) \pm 0.0027(\text{syst})$	1.70 %	22.70 %

Table 4.42: Statistical and total systematic uncertainties of the [TF](#) for top background estimation for e^+e^- , $\mu^+\mu^-$ and $e^\pm\mu^\mp$. The two rightmost columns show the relative statistical and systematic uncertainties.

For a di-lepton analysis this can be written as:

$$(4.38) \quad \begin{pmatrix} N_{TT} \\ N_{TL} \\ N_{LT} \\ N_{LL} \end{pmatrix} = \begin{pmatrix} r_1 r_2 & r_1 f_2 & f_1 r_2 & f_1 f_2 \\ r_1(1-r_2) & r_1(1-f_2) & f_1(1-r_2) & f_1(1-f_2) \\ (1-r_1)r_2 & (1-r_1)f_2 & (1-f_1)r_2 & (1-f_1)f_2 \\ (1-r_1)(1-r_2) & (1-r_1)(1-f_2) & (1-f_1)(1-r_2) & (1-f_1)(1-f_2) \end{pmatrix} \cdot \begin{pmatrix} N_{RR} \\ N_{RF} \\ N_{FR} \\ N_{FF} \end{pmatrix}$$

where we define:

- ▶ N_{TT} as the number of events which have exactly two tight leptons,
- ▶ N_{TL} and N_{LT} are the numbers of events which have one tight and one loose lepton,
- ▶ N_{LL} is the number of events which have exactly two loose leptons,
- ▶ N_{RR} is the number of events which have exactly two real leptons,
- ▶ N_{RF} and N_{FR} are the number of events which have one real and one fake lepton,
- ▶ N_{FF} is the number of events which have exactly two fake leptons.
- ▶ r_1, r_2 are the probabilities for the loose real leptons to pass the tight criteria (referred to as efficiencies),
- ▶ f_1, f_2 are the probabilities for loose fake leptons to pass the tight criteria (referred to as fake rates).

One can subsequently extract the number of events with one real and one fake lepton (N_{RF} corresponding W + jets) or with two fake leptons (N_{FF} corresponding to multijet background) by solving the above mentioned system of equations, provided one knows r and f for both leptons. The number of W + jets and multijet events passing the tight selection can be expressed as:

$$N_{W+jets} = N_{RF}^{LL} \cdot r_1 f_2 + N_{FR}^{LL} \cdot f_1 r_2 \quad (4.39)$$

$$N_{QCD} = N_{FF}^{LL} \cdot f_1 f_2 \quad (4.40)$$

The central piece of the estimation is the determination of the efficiencies r and fake rates f . Both efficiencies and fake rates are determined double differentially as a function of p_T and η and also separately for electrons and muons.

The efficiencies r are measured using MC simulation on Z events in a control region based on our nominal selection but with loosened cuts on $E_{T,Rel}$, p_T and $\Delta\phi(E_T, p_T)$ to regain statistics. In practice, the loose criterion mentioned above is limited by the available triggers and cannot be defined independently of the trigger selection. Consequently, a different set of efficiencies needs to be determined for each trigger used in the selection. The muon efficiencies are above 90 %, reaching peak efficiency above $p_T > 40$ GeV. The electron efficiencies start below 80 % and reach 90 % at $p_T > 80$ GeV. Due to lack of statistically significant sample of W + jets events in the signal region, the fake rates f are measured on di-jet events in a control region enriched with fake leptons. The events are selected using an unbiased lepton trigger with respect to the loose definition of leptons. The resulting fake rates, measured for a loose lepton with respect to an opposing jet (in $\Delta\phi > 2.0$), are below 30 % for electrons and below 60 % for muons.

The main source of systematic uncertainties comes from the different composition of jets in events coming from single W production in association with jets with respect to jets in events

with multijet production. The systematic uncertainty is evaluated using probabilities measured in multijet events and applying them to W + jets events. The uncertainty is determined to be up to 30–50 % depending on lepton flavour and its kinematics. The statistical uncertainties on the measured efficiencies and fake rates are included in the total systematic uncertainty. The final estimate of the W + jets contribution at final signal selection is 236.5 ± 16.8 (stat.) ± 112.3 (syst.)

This method is used as the nominal background estimation of W + jets background in the 8 TeV analysis, mainly because its internal consistency, detailed cross-checks and closure tests. We shall not dive into details here as this method benefited solely from the work of Philip Sommer from the University of Freiburg. An alternative fake factor method was investigated by Jun Gao from CPPM [ATL13b].

4.9.6 Other diboson production

We use the term “other dibosons” when referring to the production processes containing vector bosons other than the WW pairs which we consider as signal. The estimate of diboson background coming from WZ, ZZ, $W\gamma$ and $W\gamma^*$ processes is based purely on the MC model normalized to 20.28 fb^{-1} . The leptonic decays of WZ and ZZ can mimic the WW signal when any of the additional final state leptons are not reconstructed. The WZ processes also contains genuine \cancel{E}_T , in ZZ the missing leptons contribute to \cancel{E}_T instead. These processes were simulated with POWHEG + Pythia.

Concerning the single vector boson processes, the photon produced in the $W\gamma$ process can be misidentified for an electron, hence this background has non-negligible effect only in e^+e^- and $e^\pm\mu^\mp$ channels. The MC model is provided by Alpgen + Jimmy. The $W\gamma^*$ process is simulated with Sherpa. The Z γ process is already included in the Z + jets estimate.

The total diboson background estimate is 225.6 ± 4.6 (stat.) ± 31.6 (syst.) events at 20.28 fb^{-1} including the uncertainties. The results by channel are summarized in table 4.43, where we also quote the estimates separated by independent processes.

Final state	$e^+e^- \cancel{E}_T$	$\mu^+\mu^- \cancel{E}_T$	$e^\pm\mu^\mp \cancel{E}_T$	inclusive
WZ	7.96 ± 0.72	19.48 ± 1.01	66.04 ± 1.78	93.47 ± 2.17
ZZ	10.68 ± 0.43	16.02 ± 0.53	3.56 ± 0.18	30.26 ± 0.71
$W\gamma$	5.84 ± 1.01	0.00 ± 0.00	44.68 ± 2.81	50.52 ± 2.98
$W\gamma^*$	5.35 ± 0.83	2.96 ± 0.60	42.98 ± 2.31	51.28 ± 2.53
Total	$29.8 \pm 1.6 \pm 5.3$	$38.5 \pm 1.3 \pm 5.4$	$157.3 \pm 4.1 \pm 30.7$	$225.6 \pm 4.6 \pm 31.6$

Table 4.43: Other diboson background estimates and their statistical uncertainties as determined from MC for 20.28 fb^{-1} . The systematic uncertainties for total diboson backgrounds are calculated according to table 4.41.

The systematic uncertainties on the diboson background are computed from:

- Theoretical uncertainties on the cross-section coming from the NLO cross-section prediction. The uncertainties are 32 %, 11 %, 8 % and 13 % for $W\gamma$, $W\gamma^*$, WZ and ZZ respectively. The $W\gamma^*$ theoretical uncertainty is due to the scale uncertainty on the k-factor. For $W\gamma$ processes the measured cross-section is reported to be enhanced by more than 30 % than the corresponding NLO prediction at 7 TeV [ATL13e], which we considered as an uncertainty.

The theoretical uncertainties due to jet veto are assumed to be similar to the signal (3 %). Dedicated studies on the theoretical uncertainties of the diboson background were performed by Karen Chen from Stony Brook, US.

- Experimental uncertainties estimated along the same lines as the signal uncertainties described in [section 4.8](#). The main sources are [JES](#), \cancel{E}_T reconstruction and [luminosity](#).

4.10 Cross-section results

In this section we present the results of the WW [cross-section](#) extraction from the observed events and the signal and background estimates. The procedure follows the strategy outlined in [section 4.1.1](#). The final result is compiled from the contributions made by all analysers. My specific input is in the full implementation of experimental uncertainties on the signal and the other diboson background, including alternative data-driven methods for Z + jets and top backgrounds.

4.10.1 Candidates and backgrounds

To compute the [cross-section](#), we extract the number of observed events from the dataset using the selection criteria described in [section 4.2](#). The number of expected signal events is obtained from [MC](#) at the reconstruction level and in the fiducial region described in [section 4.7](#). The background events are estimated using methods described in [section 4.9](#). Finally, the total number of expected events is given as:

$$N_{\text{exp}}^i = N_S^i + N_B^i \quad (4.41)$$

where N_S^i is the number of expected signal events and N_B^i is the number of background events. Index $i = 1, 2, 3$ corresponds to the three channels: e^+e^- , $\mu^+\mu^-$ and $e^\pm\mu^\mp$. The inclusive channel is simply the sum of all three channels.

The final yields are summarized in [table 4.47](#) including both statistical and systematic uncertainties. The top background was estimated using the [JVSP](#) method discussed in [section 4.9.3](#), the Z + jets yields were derived using the [simultaneous fit](#) ([section 4.9.1](#)) and W + jets were estimated using the matrix method ([section 4.9.5](#)). A number of alternative background estimation methods were also considered, for example the [transfer factor](#) method discussed in [sections 4.9.2](#) and [4.9.4](#). The signal yields and contributions from other diboson backgrounds are estimated from [MC](#). For the final result we selected the methods with the lowest systematic uncertainties, provided their description is detailed and complete.

[Figures 4.53](#) and [4.54](#) show the final kinematic distributions with backgrounds estimated from baseline estimation methods. The statistical and total uncertainties (stat \oplus syst) are indicated in the plots with overlays or a coloured band in the ratio plots. The systematic uncertainties include the experimental uncertainties on the signal and total uncertainties of the backgrounds. The WW signal contribution is scaled to match to the measured [cross-section](#). The [scale factors](#) are 1.17 in the e^+e^- channel, 1.18 in the $\mu^+\mu^-$ channel and 1.21 in the $e^\pm\mu^\mp$ channel.

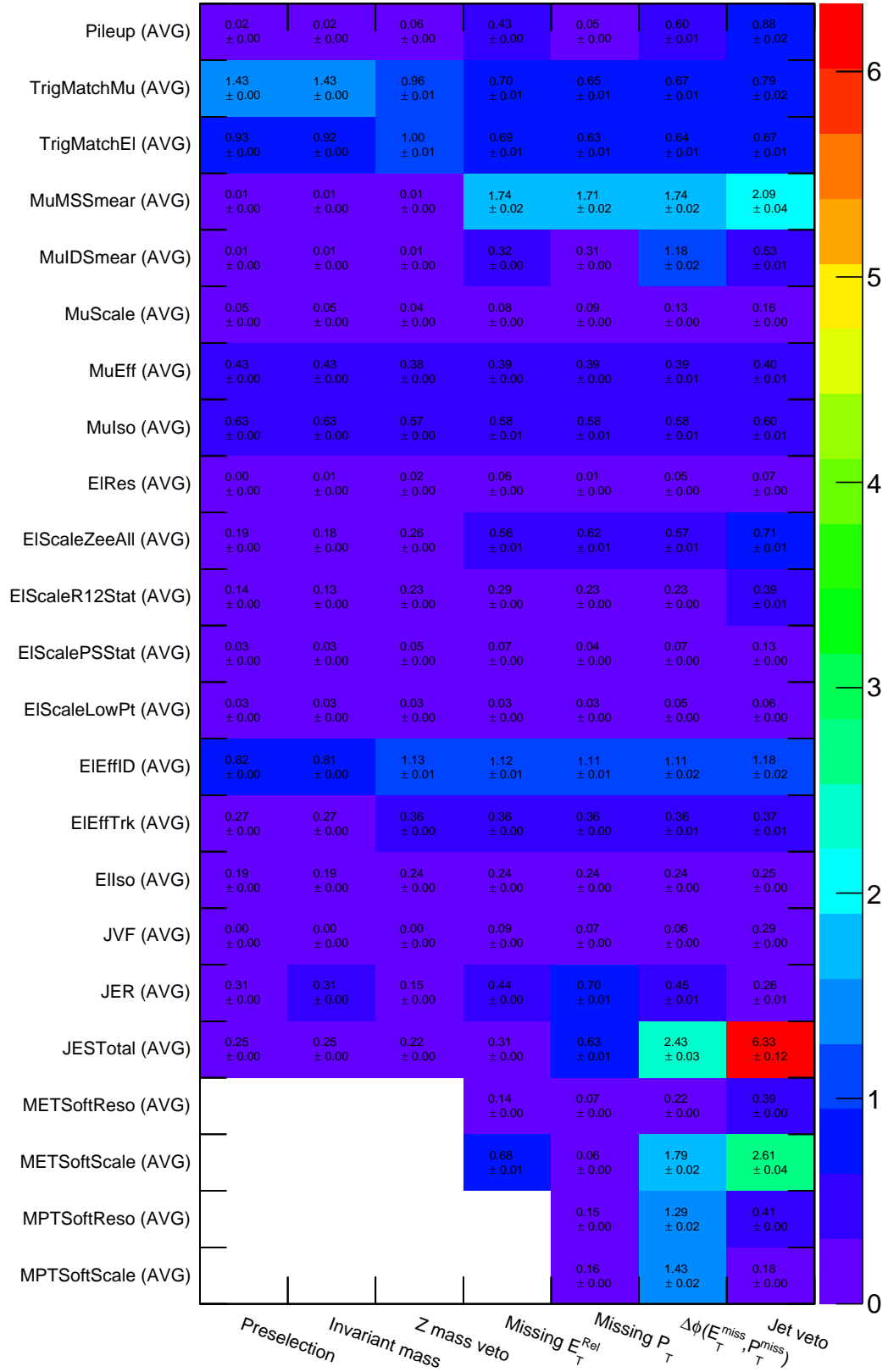


Table 4.44: Cut progression of systematic uncertainties on “other diboson” background processes (WZ , ZZ , $W\gamma$ and $W\gamma^*$) for combined channel. The table shows the full set of systematics evolving as we introduce analysis cuts (columns left to right). Each number presents a percentage difference with respect to nominal yield at a given cut stage. Statistical uncertainty on each yield is shown. The color corresponds to the magnitude of the systematic shift. The up and down component of each systematic uncertainty has been symmetrized (indicated by the “AVG” label).

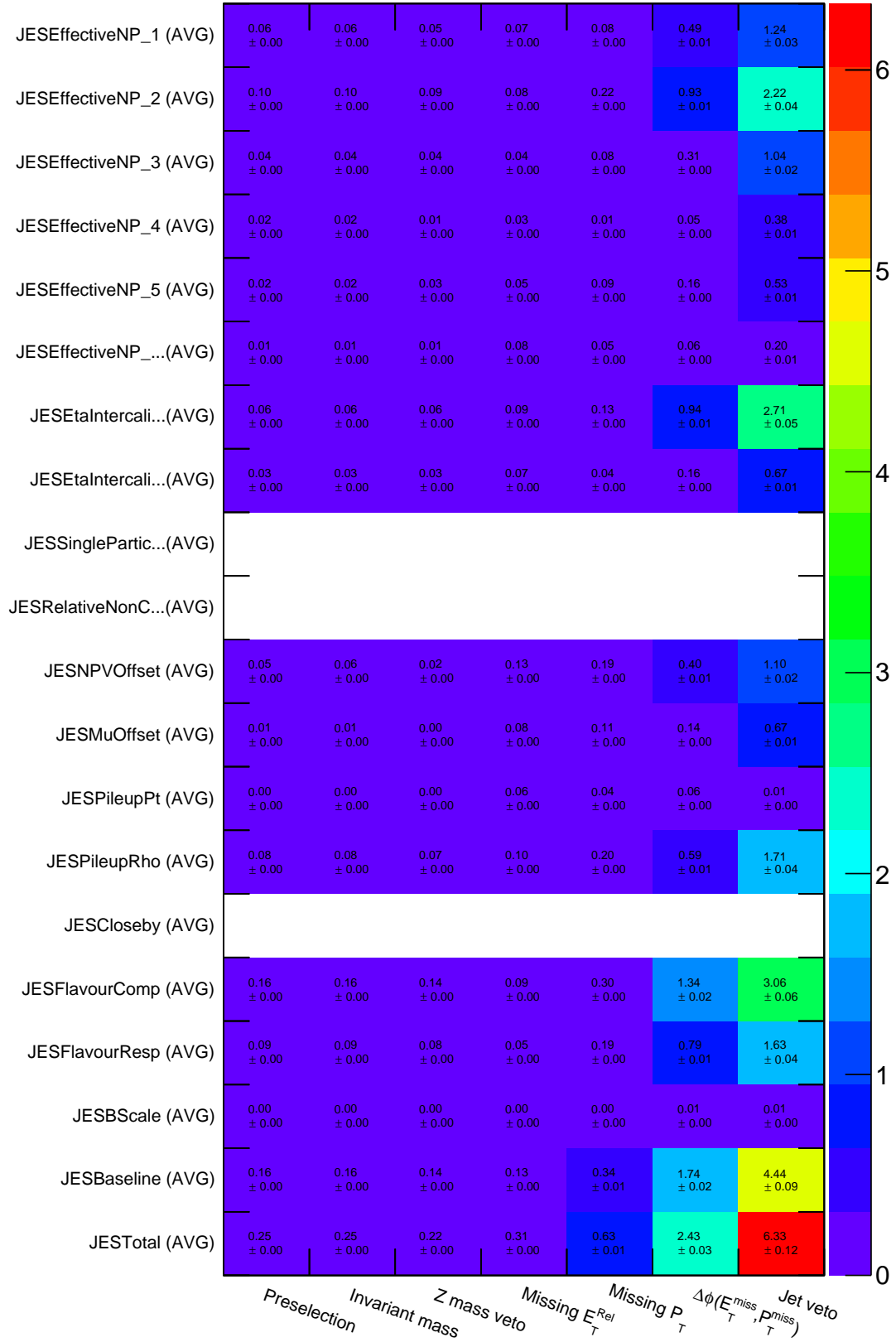


Table 4.45: Cut progression of jet energy scale components systematics on “other diboson” background processes (WZ , ZZ , $W\gamma$ and $W\gamma^*$) for combined channel. The table shows the full set of systematics evolving as we introduce analysis cuts (columns left to right). Each number presents a percentage difference with respect to nominal yield at a given cut stage. Statistical uncertainty on each yield is shown. The color corresponds to the magnitude of the systematic shift. The up and down component of each systematic uncertainty has been symmetrized (indicated by the “AVG” label). JES Baseline is introduced for comparison between components and indicates the quadratic sum of JES Effective_NP* components and is not included in the total uncertainty to avoid duplication.

Sources	$e^+e^-E_T$	$\mu^+\mu^-E_T$	$e^\pm\mu^\mp E_T$	Combined
Luminosity	2.8%	2.8%	2.8%	2.8%
Pileup	1.57%	0.28%	0.92%	0.88%
Trigger Efficiency SF (muons)	0%	2.84%	0.44%	0.79%
Trigger Efficiency SF (electrons)	2.75%	0%	0.44%	0.67%
Muon MS Resolution	0.55%	3.12%	2.14%	2.09%
Muon ID Resolution	0.93%	2.29%	0.38%	0.53%
Muon Scale	0%	0.65%	0.06%	0.16%
Muon Efficiency SF	0%	0.80%	0.38%	0.40%
Muon Isolation SF	0%	1.12%	0.59%	0.60%
Electron Resolution	0.88%	0%	0.11%	0.07%
Electron Scale	0.55%	0%	1.10%	0.82%
Electron Efficiency SF	2.30%	0%	1.33%	1.24%
Electron Isolation SF	0.46%	0%	0.27%	0.25%
Jet Vertex Fraction	0.40%	0.41%	0.23%	0.29%
Jet Energy Resolution	0.58%	2.32%	0.31%	0.26%
Jet Energy Scale	5.59%	5.25%	6.74%	6.33%
$E_{T,Rel}$ Reso Soft Terms	1.10%	0.42%	0.48%	0.39%
$E_{T,Rel}$ Scale Soft Terms	2.52%	3.66%	2.37%	2.61%
p_T Reso Soft Terms	0.51%	0.79%	0.45%	0.41%
p_T Scale Soft Terms	0.34%	1.10%	0.08%	0.18%
Theory	16%	11%	18%	16%
Total	17.85%	14.13%	19.52%	18.19%

Sources	$e^+e^-E_T$	$\mu^+\mu^-E_T$	$e^\pm\mu^\mp E_T$	Combined
JES Effective NP1	0.90%	1.20%	1.31%	1.24%
JES Effective NP2	2.20%	2.13%	2.25%	2.22%
JES Effective NP3	0.70%	0.96%	1.13%	1.04%
JES Effective NP4	0.37%	0.14%	0.45%	0.38%
JES Effective NP5	0.36%	0.47%	0.58%	0.53%
JES Effective NP6 rest term	0.17%	0.08%	0.23%	0.20%
JES Eta Intercalibration Modelling	2.71%	2.11%	2.85%	2.71%
JES Eta Intercalibration StatAndMethod	0.42%	0.72%	0.70%	0.67%
JES SingleParticle HighPt	0%	0%	0%	0%
JES Relative Non Closure	0%	0%	0%	0%
JES NPV Offset	0.44%	1.30%	1.18%	1.10%
JES Mu Offset	0.17%	0.72%	0.79%	0.67%
JES Pileup Pt	0%	0%	0.01%	0.01%
JES Pileup Rho	1.45%	1.59%	1.79%	1.71%
JES Closeby	0%	0%	0%	0%
JES Flavour Composition	2.98%	2.53%	3.21%	3.06%
JES Flavour Response	1.47%	1.71%	1.64%	1.63%
JES B Scale	0.01%	0%	0.02%	0.01%

Table 4.46: Systematic uncertainties for the combined “other diboson” background processes (WZ , ZZ , $W\gamma$ and $W\gamma^*$) including the [jet energy scale](#) components. The total systematic uncertainty includes the theoretical uncertainties estimated for the independent processes. [JES Total](#) refers to the overall estimate of the total uncertainty as explained in [section 3.3.5.2](#).

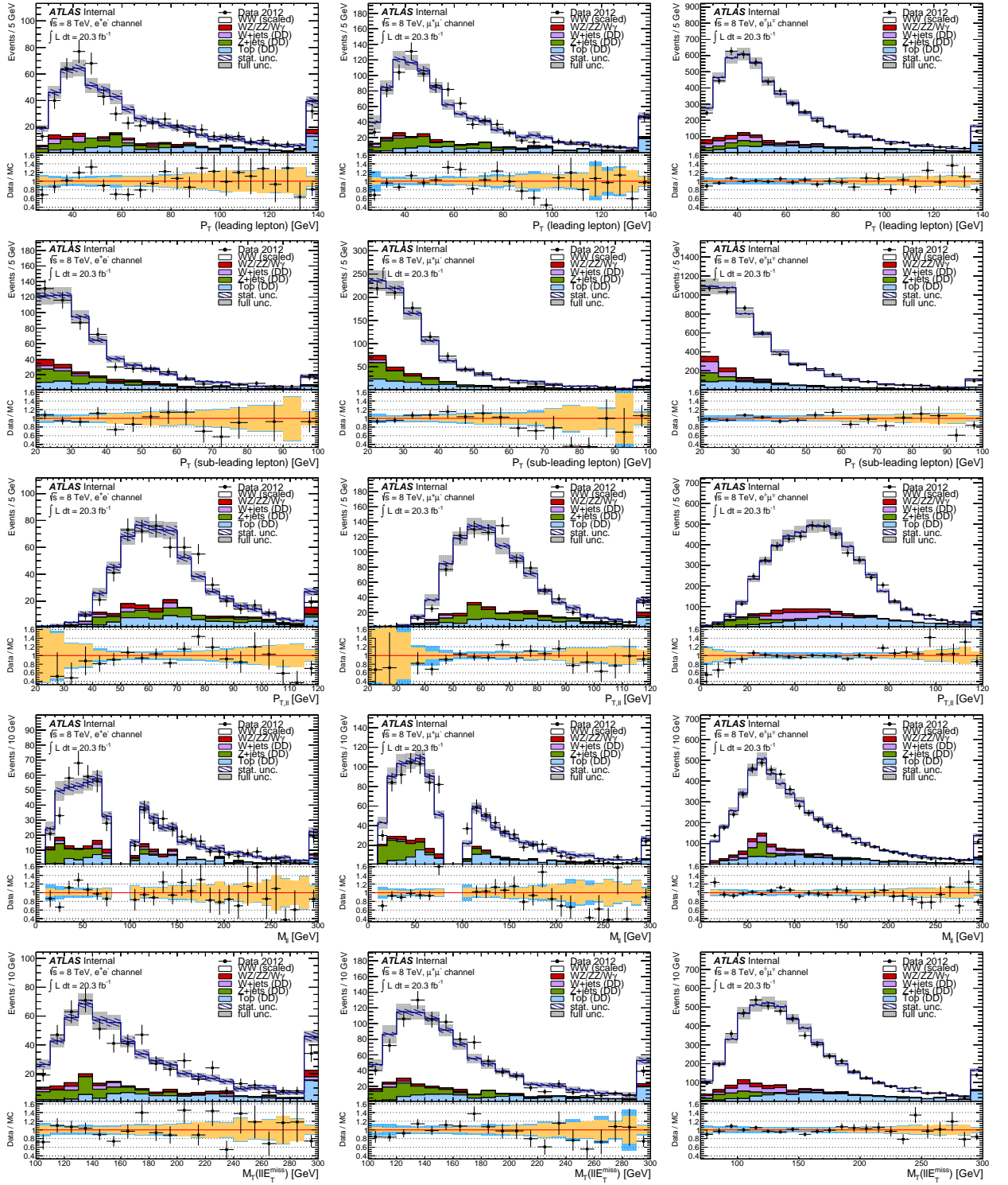


Figure 4.53: Final kinematic distributions of the WW candidates at 8 TeV at final cut stage (1): Data are shown on top the signal and background processes modelled by the data-driven estimates (with the exception of diboson contributions) and scaled to 8TeV.20ifb. The plots correspond to the e^+e^- , $\mu^+\mu^-$ and $e^\pm\mu^\mp$ channels from left to right. The first (resp. second) row shows the transverse momentum p_T of the leading (resp. trailing) lepton. The third row shows **invariant mass-NoValue**- followed by transverse mass m_T in the fourth row. The statistical and total uncertainties (stat \oplus syst) are indicated in the plots with overlays or a coloured band in the ratio plots. The WW signal contribution is scaled to match to the measured **cross-section**.

Final State	$e^+e^- \cancel{E}_T$	$\mu^+\mu^- \cancel{E}_T$	$e^\pm\mu^\mp \cancel{E}_T$
Observed Events	594	975	5067
Total expected events (S+B)	$553.2 \pm 13.0 \pm 77.3$	$903.9 \pm 11.3 \pm 104.9$	$4427.9 \pm 33.3 \pm 469.0$
MC WW signal	$349.6 \pm 3.3 \pm 32.4$	$614.4 \pm 4.5 \pm 55.9$	$3254.8 \pm 10.3 \pm 247.9$
Top(data-driven)	$91.8 \pm 7.3 \pm 7.9$	$127.2 \pm 9.4 \pm 10.9$	$608.6 \pm 17.5 \pm 52.3$
Z+jets (data-driven)	$54.5 \pm 1.2 \pm 23.1$	$95.6 \pm 1.5 \pm 26.5$	$166.1 \pm 3.2 \pm 26.3$
W+jets(data-driven)	$14.2 \pm 4.8 \pm 8.6$	$2.8 \pm 4.6 \pm 6.2$	$219.5 \pm 15.4 \pm 111.8$
Other dibosons (MC)	$29.8 \pm 1.6 \pm 5.3$	$38.5 \pm 1.3 \pm 5.4$	$157.3 \pm 4.1 \pm 30.7$
Total background	$203.6 \pm 12.6 \pm 44.9$	$289.5 \pm 10.3 \pm 49.1$	$1173.1 \pm 31.7 \pm 221.1$

Table 4.47: Summary of observed events and expected signal and background contributions in three dilepton channels. The first uncertainty is statistical, the second is systematic. The systematic uncertainties for total background and total expectation are calculated assuming full correlation among processes. Jet veto scale factors are applied to $q\bar{q} \rightarrow WW \rightarrow \ell^+\nu\ell^-\bar{\nu}$ events to get final signal yields.

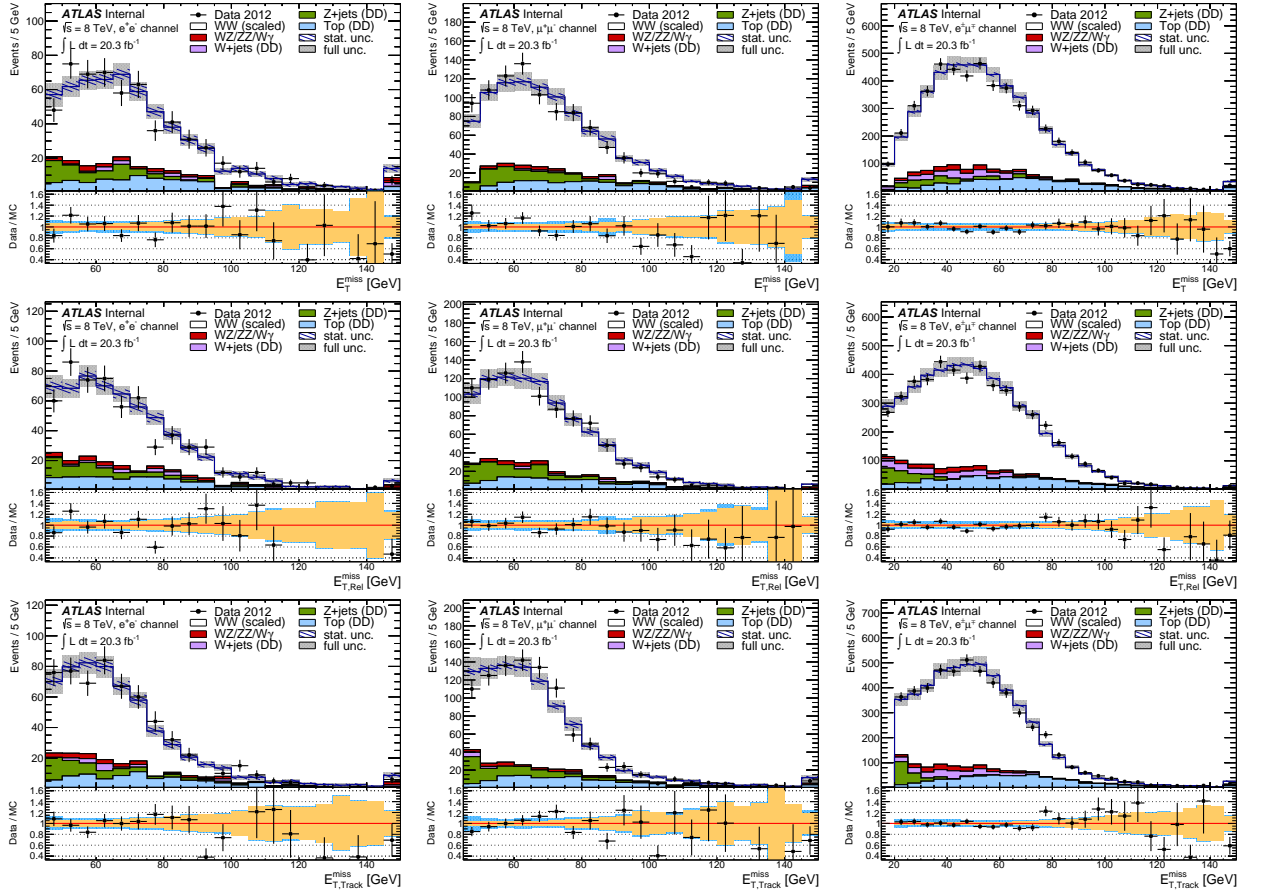


Figure 4.54: Final kinematic distributions of the WW candidates at 8 TeV at final cut stage (2): Data are shown on top the signal and background processes modelled by the data-driven estimates (with the exception of diboson contributions) and scaled to 8TeV.20ifb. The plots correspond to the e^+e^- , $\mu^+\mu^-$ and $e^\pm\mu^\mp$ channels from left to right. The top row shows the missing transverse energy \cancel{E}_T followed by its projection $\cancel{E}_{T,Rel}$. The third row shows the track-based p_T . The statistical and total uncertainties (stat \oplus syst) are indicated in the plots with overlays or a coloured band in the ratio plots. The WW signal contribution is scaled to match to the measured cross-section.

4.10.2 Cross-section extraction

We have outlined the strategy for the [cross-section](#) measurement in [section 4.1.1](#). Following from [eq. \(4.6\)](#), the number of obtained signal events is related to the [cross-section](#) and the total integrated [luminosity](#) as follows:

$$N_S^i(\sigma_{\text{tot}}) = \sigma_{\text{tot}} \cdot \text{BR} \cdot L \cdot A_{\text{WW}} \cdot C_{\text{WW}} \quad (4.42)$$

which in the fiducial region transforms to

$$N_S^i(\sigma_{\text{fid}}) = \sigma_{\text{fid}} \cdot L \cdot C_{\text{WW}}. \quad (4.43)$$

It follows that the relationship between the measured fiducial [cross-section](#) and the total [cross-section](#) can be expressed through the branching fraction of [W](#) bosons decaying to electrons and muons in the fiducial phase space:

$$\sigma_{\text{tot}} = \text{BR} \cdot A_{\text{WW}} \cdot \sigma_{\text{fid}} \quad (4.44)$$

This approach is common to both 8 TeV and 7 TeV analyses. The key difference in our approach used at 8 TeV is in the treatment of τ leptons which are considered as background to the fiducial [cross-section](#) measurements.

Another notable difference at 8 TeV is the treatment of systematic uncertainties. Here we account for the effect of systematic uncertainties as a direct correction to the [cross-section](#) by introducing an additional term. Assuming that each systematic uncertainty on the i -th channel is a standard normal distribution $x_k \sim \mathcal{N}(0, 1)$ we can write the number of signal and background events as follows:

$$N_S^i(\sigma_{\text{tot}}, \{x_k\}) = \sigma_{\text{tot}} \cdot \text{BR} \cdot L \cdot A_{\text{WW}} \cdot C_{\text{WW}} \cdot (1 + \sum_{k=1}^n x_k S_k^i) \quad (4.45)$$

$$N_B^i(\{x_k\}) = N_B^i \cdot (1 + \sum_{k=1}^n x_k B_k^i) \quad (4.46)$$

where parameters S_k^i and B_k^i are standard deviations representing the k -th systematic uncertainty in channel i (e^+e^- , $\mu^+\mu^-$ and $e^\pm\mu^\mp$).

Using statistics, we can express the probability that a given number of events occurs in a given time interval if these events are known to occur with a known average rate. This is expressed in terms of a Poisson distribution. To determine the [cross-section](#), we introduce a log-likelihood function and minimize its negative logarithm (standard maximum/minimum likelihood estimation):

$$-\ln L(\sigma, \{x_k\}) = -\ln \left(\frac{e^{-N_S^i(\sigma, \{x_k\}) - N_B^i(\{x_k\})} \cdot (N_S^i(\sigma, \{x_k\}) + N_B^i(\{x_k\}))^{N_{\text{data}}^i}}{N_{\text{data}}^i!} \right) + \sum_{k=1}^n \frac{x_k^2}{2} \quad (4.47)$$

where the sum runs over $i = 1, 2, 3$ which corresponds to the three channels and x_k are the nuisance parameters as introduced in [eq. \(4.46\)](#). The event yields N_S^i , N_B^i and N_{data}^i represent the expected signal, backgrounds and observed data events in the i -th measurement as listed in [table 4.47](#).

A single random variable x_k is used over all channels for signal and background as the effect of each systematic source is 100 % correlated across channels and between signal and background components. The object systematics are treated as fully correlated when they act on more than one channel. The systematic uncertainties on data-driven background estimates are treated as fully correlated between the channels while the statistical uncertainties of the backgrounds are treated as uncorrelated. An exception is made for the case of the W + jets background where the uncertainty on the efficiency measurement is treated as uncorrelated between the three channels since it is dominated by the statistical uncertainty. The fake rate and the samples dependence uncertainties are treated as fully correlated.

The log-likelihood gives the probability that the expected number of signal and background events $N_S^i(\sigma, \{x_k\}) + N_B^i(\{x_k\})$ will produce the number of events observed in data N_{data}^i in the i -th channel at final selection. The last term introduced Gaussian constraints on the nuisance parameters x_k , the corresponding uncertainty sources on the signal are listed in [table 4.27](#) To obtain the [eq. \(4.47\)](#) combined measurement, we simply multiply the Poisson probability in each channel i (or sum the log-likelihoods). The results are summarized in [tables 4.48](#) and [4.49](#). The fit was performed by Dimitra Tsionou from CEA Saclay using the MINUIT package. [\[JR75\]](#)

Channel	Fiducial $\sigma_{\text{WW}}(8 \text{ TeV})$ [fb]	Fiducial $\sigma_{\text{WW}}(7 \text{ TeV})$ [fb]
e^+e^-	$68.5^{+4.2}_{-4.1} (\text{stat.})^{+7.7}_{-6.6} (\text{syst.})^{+2.1}_{-2.0} (\text{lumi.}) \text{ fb}$	$56.4 \pm 6.8 (\text{stat.}) \pm 9.8 (\text{syst.}) \pm 2.2 (\text{lumi.}) \text{ fb}$
$\mu^+\mu^-$	$74.4^{+3.3}_{-3.2} (\text{stat.})^{+7.0}_{-6.0} (\text{syst.})^{+2.3}_{-2.1} (\text{lumi.}) \text{ fb}$	$73.9 \pm 5.9 (\text{stat.}) \pm 6.9 (\text{syst.}) \pm 2.9 (\text{lumi.}) \text{ fb}$
$e^\pm\mu^\mp$	$377.8^{+6.9}_{-6.8} (\text{stat.})^{+25.1}_{-22.2} (\text{syst.})^{+11.4}_{-10.7} (\text{lumi.}) \text{ fb}$	$262.3 \pm 12.3 (\text{stat.}) \pm 20.7 (\text{syst.}) \pm 10.2 (\text{lumi.}) \text{ fb}$

Table 4.48: Measured total WW [cross-sections](#) per channel.

Channel	Total $\sigma_{\text{WW}}(8 \text{ TeV})$ [pb]	Total $\sigma_{\text{WW}}(7 \text{ TeV})$ [pb]
e^+e^-	$68.6^{+4.2}_{-4.1} (\text{stat.})^{+7.8}_{-6.7} (\text{syst.})^{+2.1}_{-2.0} (\text{lumi.}) \text{ pb}$	$46.85 \pm 5.65 (\text{stat.}) \pm 8.21 (\text{syst.}) \pm 1.8 (\text{lumi.}) \text{ pb}$
$\mu^+\mu^-$	$68.6^{+3.1}_{-3.0} (\text{stat.})^{+6.6}_{-5.6} (\text{syst.})^{+2.1}_{-2.0} (\text{lumi.}) \text{ pb}$	$56.65 \pm 4.52 (\text{stat.}) \pm 5.46 (\text{syst.}) \pm 2.2 (\text{lumi.}) \text{ pb}$
$e^\pm\mu^\mp$	$71.4^{+1.3}_{-1.3} (\text{stat.})^{+5.0}_{-4.4} (\text{syst.})^{+2.1}_{-2.0} (\text{lumi.}) \text{ pb}$	$51.13 \pm 2.41 (\text{stat.}) \pm 4.24 (\text{syst.}) \pm 2.0 (\text{lumi.}) \text{ pb}$
Combined	$71.4^{+1.2}_{-1.2} (\text{stat.})^{+5.0}_{-4.4} (\text{syst.})^{+2.2}_{-2.1} (\text{lumi.}) \text{ pb}$	$51.91 \pm 2.0 (\text{stat.}) \pm 3.92 (\text{syst.}) \pm 2.0 (\text{lumi.}) \text{ pb}$

Table 4.49: Measured total WW [cross-sections](#) per channel and the combined result.

4.10.3 Cross-section uncertainties

The likelihood function is constructed so that it takes into account all the statistical and systematic uncertainties and propagates them into the final uncertainty. The uncertainties can be broken down to individual components: statistical and systematic (which include the theoretical A_{WW} and experimental C_{WW} sources).

- The statistical uncertainty is obtained by running another instance of the fit with all nuisance parameters fixed to their pre-fitted values.

- The **luminosity** uncertainty is determined by fixing the **luminosity** nuisance parameter to $\pm 1\sigma$ while all other parameters remain fixed to their central values.
- The decomposition of all individual sources of systematic uncertainties is handled in the same way. The total systematic uncertainty is determined from the quadratic difference:

$$\Delta_{\text{syst}} = \sqrt{\Delta_{\text{tot}}^2 - \Delta_{\text{stat}}^2 - \Delta_{\text{lumi}}^2}$$

The results of the decomposition are given in [tables 4.50](#) and [4.51](#). The dominant uncertainty on the **cross-section** comes from the experimental sources and ranges between 4–6 %. The background uncertainties account for an additional 3–6 %. Of all the channels the largest uncertainties come from the e^+e^- final state. The theoretical uncertainties contribute around 3 % at the fiducial level and 4 % in the full phase space. This yields a total uncertainty of $\approx 7.50\%$. Combining the per-channel measurements, the resulting **cross-section** is:

$$\sigma_{\text{tot}}(8 \text{ TeV}) = 71.4^{+1.2}_{-1.2} (\text{stat.})^{+5.0}_{-4.4} (\text{syst.})^{+2.2}_{-2.1} (\text{lumi.}) \text{ pb.} \quad (4.48)$$

Additional details concerning the measurement are discussed in the [ATLAS Collaboration \[ATL13c\]](#) internal documentation [\[ATL14i\]](#), including other background estimate methods, independent cross-checks, investigation of data/MC ratio, period A reprocessing and most notably the effect of [Herwig](#) lifetime bug which affects the analysis presented here. The issue concerns the parton shower model which caused particles with lifetime $< 10 \text{ ns}$ to decay in vacuum instead of interacting with the detector. This affects the \cancel{E}_T and **JES** at the $\mathcal{O}(10^3)$. Overall, it is a small effect which will be mitigated in future processing.

4.11 Unfolding

Deconvolution, more commonly referred to as *unfolding* in particle physics, is a mathematical method of correcting distributions for the effects of smearing. When we measure a random variable, like some kinematic observable, we make repeated observations to determine its distribution. In terms of the experiment, we simply measure the quantity in each event and make a histogram with some number of bins (i.e. binned distribution).

To compare experimental results with theory, two scenarios:

- a) A parametric function for the variable $f(y, \theta_i)$ is available as predicted from theory. We simply build the likelihood function and choose the estimated parameters $\hat{\theta}_i$ that maximize the likelihood.
- b) There is no analytical description available for the distribution which is when unfolding comes in. Instead of describing the distribution analytically, we make a histogram with a given number of bins. The goal of the method remains effectively the same: we simply estimate the value of each bin, thus we have one parameter for each bin in the distribution instead of a single parametric function.

To establish this formally, assume we have an observable x distributed according to $f_{\text{true}}(x)$. Because of instrumental limitations, such as detector acceptance, efficiency and finite resolution, the values we measure in the detector differ from the true values. For this reason the measurements

Source	$e^+e^- \cancel{E}_T$	$\mu^+\mu^- \cancel{E}_T$	$e^\pm\mu^\mp \cancel{E}_T$
Pileup	+2.03 -1.95	+2.06 -1.91	+1.35 -1.32
Trigger	+2.80 -2.65	+3.12 -2.88	+0.43 -0.42
e^\pm – Energy scale	+1.46 -1.42	+0.00 -0.00	+0.42 -0.41
e^\pm – Energy resolution	+0.25 -0.24	+0.00 -0.00	+0.04 -0.03
μ^\pm – Scale	+0.00 -0.00	+0.42 -0.35	+0.11 -0.10
μ^\pm – ID resolution	+0.07 -0.07	+1.71 -1.59	+0.56 -0.55
μ^\pm – MS resolution	+0.04 -0.04	+0.25 -0.18	+0.10 -0.09
e^\pm – Id. & rec. efficiency	+2.22 -2.13	+0.00 -0.00	+0.99 -0.97
μ^\pm – Id. & rec. efficiency	+0.00 -0.00	+0.85 -0.77	+0.41 -0.40
e^\pm – Isolation	+0.48 -0.47	+0.00 -0.00	+0.23 -0.22
μ^\pm – Isolation	+0.00 -0.00	+1.24 -1.14	+0.59 -0.58
\cancel{E}_T – Soft Reso	+0.39 -0.39	+0.56 -0.49	+0.31 -0.30
\cancel{E}_T – Soft Scale	+4.59 -4.22	+4.20 -3.83	+2.50 -2.37
\cancel{p}_T – Soft Reso	+0.08 -0.08	+0.29 -0.22	+0.07 -0.06
\cancel{p}_T – Soft Scale	+0.65 -0.64	+0.59 -0.51	+0.32 -0.31
JES	+2.25 -2.17	+2.89 -2.69	+2.04 -2.00
JER	+0.79 -0.78	+0.98 -0.89	+0.66 -0.65
JVF	+0.11 -0.11	+0.14 -0.07	+0.05 -0.04
Jet veto SF (reco)	+1.22 -1.19	+1.24 -1.14	+0.70 -0.68
C_{WW} PDF unc.	+0.59 -0.59	+0.17 -0.09	+0.35 -0.35
C_{WW} scale unc.	+1.71 -1.65	+0.70 -0.62	+0.62 -0.60
C_{WW} jet veto SF (theory)	+2.12 -2.03	+2.15 -1.99	+2.12 -2.06
Dibosons cross-section	+0.59 -0.59	+0.47 -0.40	+0.33 -0.32
Top	+1.91 -1.91	+1.54 -1.47	+1.29 -1.31
W + jets & QCD (efficiency)	+0.62 -0.62	+0.87 -0.79	+0.76 -0.76
W + jets & QCD (fake rate)	+0.92 -0.92	+0.34 -0.27	+1.08 -1.09
W + jets & QCD (sample dependence)	+2.08 -2.08	+0.30 -0.23	+2.81 -2.80
Z + jets	+5.73 -5.70	+3.76 -3.67	+0.67 -0.66
Bkg stat. (Data Driven)	+2.17 -2.16	+1.52 -1.45	+0.61 -0.60
Bkg stat. (MC)	+0.40 -0.40	+0.22 -0.15	+0.11 -0.10
Total (no lumi. unc.)	+10.15 -9.84	+8.59 -8.01	+5.73 -5.62

Table 4.50: Relative systematic uncertainties (in percent) on the fiducial WW production cross-section for each channel. Courtesy of Dimitra Tsionou.

Source	$e^+e^- \cancel{E}_T$	$\mu^+\mu^- \cancel{E}_T$	$e^\pm\mu^\mp \cancel{E}_T$	combined
Pileup	+2.03 -1.95	+2.05 -1.92	+1.36 -1.32	+1.51 -1.46
Trigger	+2.80 -2.65	+3.10 -2.89	+0.43 -0.42	+0.75 -0.74
e^\pm – Energy scale	+1.46 -1.42	+0.00 -0.00	+0.42 -0.41	+0.43 -0.43
e^\pm – Energy resolution	+0.25 -0.24	+0.00 -0.00	+0.04 -0.03	+0.05 -0.04
μ^\pm – Scale	+0.00 -0.00	+0.41 -0.36	+0.11 -0.10	+0.14 -0.13
μ^\pm – ID resolution	+0.07 -0.07	+1.70 -1.61	+0.56 -0.55	+0.67 -0.66
μ^\pm – MS resolution	+0.04 -0.04	+0.24 -0.20	+0.10 -0.09	+0.11 -0.11
e^\pm – Id. & rec. efficiency	+2.22 -2.13	+0.00 -0.00	+0.99 -0.97	+0.93 -0.91
μ^\pm – Id. & rec. efficiency	+0.00 -0.00	+0.84 -0.78	+0.41 -0.40	+0.44 -0.43
e^\pm – Isolation	+0.48 -0.47	+0.00 -0.00	+0.22 -0.22	+0.21 -0.21
μ^\pm – Isolation	+0.00 -0.00	+1.23 -1.15	+0.59 -0.58	+0.63 -0.62
\cancel{E}_T – Soft Reso	+0.39 -0.39	+0.55 -0.50	+0.31 -0.31	+0.35 -0.35
\cancel{E}_T – Soft Scale	+4.59 -4.22	+4.19 -3.84	+2.49 -2.38	+2.80 -2.67
\cancel{p}_T – Soft Reso	+0.08 -0.08	+0.28 -0.23	+0.07 -0.07	+0.10 -0.09
\cancel{p}_T – Soft Scale	+0.65 -0.64	+0.58 -0.52	+0.32 -0.31	+0.38 -0.37
JES	+2.25 -2.17	+2.88 -2.70	+2.06 -1.98	+2.19 -2.11
JER	+0.79 -0.78	+0.97 -0.90	+0.66 -0.65	+0.71 -0.70
JVF	+0.11 -0.11	+0.13 -0.08	+0.05 -0.05	+0.06 -0.06
Jet veto SF (reco)	+1.22 -1.19	+1.23 -1.15	+0.70 -0.68	+0.81 -0.80
C_{WW} PDF unc.	+1.61 -1.55	+0.87 -0.81	+1.34 -1.30	+1.29 -1.26
C_{WW} scale unc.	+1.56 -1.52	+0.98 -0.92	+0.81 -0.79	+0.89 -0.87
C_{WW} jet veto SF (theory)	+2.03 -1.95	+2.05 -1.93	+2.06 -1.98	+2.07 -1.99
Dibosons cross-section	+0.59 -0.59	+0.46 -0.41	+0.32 -0.32	+0.36 -0.35
Top	+1.91 -1.91	+1.53 -1.48	+1.30 -1.30	+1.37 -1.37
W + jets & QCD (efficiency)	+0.62 -0.62	+0.85 -0.81	+0.76 -0.76	+0.61 -0.60
W + jets & QCD (fake rate)	+0.92 -0.92	+0.33 -0.29	+1.08 -1.08	+0.96 -0.96
W + jets & QCD (sample dependence)	+2.08 -2.08	+0.29 -0.24	+2.80 -2.80	+2.27 -2.25
Z + jets	+5.73 -5.70	+3.75 -3.68	+0.67 -0.66	+1.19 -1.16
Bkg stat. (Data Driven)	+2.17 -2.16	+1.51 -1.46	+0.61 -0.60	+0.54 -0.54
Bkg stat. (MC)	+0.40 -0.40	+0.21 -0.16	+0.11 -0.10	+0.09 -0.09
Total (no lumi. unc.)	+10.22 -9.90	+8.60 -8.10	+5.88 -5.75	+6.01 -5.84

Table 4.51: Relative systematic uncertainties (in percent) on the total WW production cross-section for each channel. Courtesy of Dimitra Tsionou.

actually provide a different variable y distributed according to $f_{\text{obs}}(y)$. The relationship between these distributions can be expressed as a convolution:

$$f_{\text{obs}}(y) = \int \mathbb{R}(y|x) f_{\text{true}}(x) dx \quad (4.49)$$

with a kernel $\mathbb{R}(y|x)$, also called the *response function*, which gives the probability of measuring y given x . In case of a binned distribution, we discretise the formula:

$$y_i = \sum_{j=1}^M \mathbb{R}_{ij} x_j \quad (4.50)$$

where \mathbb{R}_{ij} is the response matrix with indices $i = 1 \dots N$, $j = 1 \dots M$ corresponding to the number of bins in distributions \mathbf{x} and \mathbf{y} and x_j , y_i are expectation values. The matrix gives the probability of an event to be observed in bin i given that its true bin is j . This can be interpreted in a sense that when an event is created in nature with a true value corresponding to bin j , the imperfections in measurements cause it to be measured with a different value corresponding to a different bin i .

In particle physics, the response matrix \mathbb{R} is generally referred to as the *detector smearing matrix*. The complex situation means that generally there is no parametrization available, and the effect is modelled using MC simulation instead. Alternatively, one can devise a data-driven method of estimating matrix \mathbb{R} by cleverly implementing various *control regions*. Given the matrix \mathbb{R} , there are two choices when relating the underlying true distributions \mathbf{x} to the measurement \mathbf{y} :

Folding refers to the application of the response matrix on the true distribution \mathbf{x} to obtain the smeared distribution \mathbf{y} which can effectively predict the number of events observed in data. Using vector notation:

$$\mathbf{y} = \mathbb{R}\mathbf{x} \quad (4.51)$$

The distribution \mathbf{x} enters from the MC model. Nota bene: we introduce smearing to MC simulated physics objects at the detector level to improve the description of measured data, as discussed in [section 3.3](#).

Unfolding is an inverse approach which uses the response matrix to strip the smearing effects from the measured distribution \mathbf{y} . The main advantage of this approach is that the unfolding the measured distributions to the truth level allows theoreticians to directly compare their predictions with our measurements without the necessity of running the full detector simulation. The solution takes the form of:

$$\mathbf{x} = \mathbb{R}^{-1}\mathbf{y}. \quad (4.52)$$

Generally speaking, unfolding is the preferred approach in complicated experiments with intricate detectors as it is far less computationally intensive, since the smearing approach would require running the full chain simulation (i.e. generation, detector simulation and event reconstruction) for variation in the model.

4.11.1 Efficiency and background

Knowing the detector matrix \mathbb{R} , we can directly infer on the measurement efficiency and background expectations. In a situation where a true event corresponding to bin j in \mathbf{x} goes undetected, its corresponding contribution to bin i in \mathbf{y} is missing. If we sum over all possible observed bins $i = 1, \dots, N$, we get the probability of the event to be observed in any bin in \mathbf{y} given the true value is in bin j .

$$\begin{aligned} \sum_i \mathbb{R}_{ij} &= \sum_{i=1}^N P(\text{observed in bin } i | \text{true value in bin } j) \\ &= P(\text{observed in any bin} | \text{true value in bin } j) \\ &= \epsilon_j \end{aligned} \quad (4.53)$$

where ϵ_j is the efficiency of detecting event with the true value in bin j .

The situation can also happen in reverse, where the event observed in bin i is due to background process, i.e. there is no true event anywhere in \mathbf{x} corresponding to the value measured in \mathbf{y} . To account for this, the expected number of events in \mathbf{y} is given by

$$y_i = \sum_j R_{ij} x_j + b_i \quad (4.54)$$

where b_i is the expected background contribution to bin i . Since y_i is in fact the expected number of signal events in bin i , it needs to be distinguished from the actual number of events measured in data in bin i . Given the data entries $\mathbf{n} = (n_1, \dots, n_N)$, the probability to observe n_i events in bin i is given by the Poisson distribution and is subject to statistical fluctuations. In this case, the relationship between the expected values and the observation itself is given by [Cow98, p. 155]:

$$P(n_i, y_i) = \frac{y_i^{n_i} e^{-y_i}}{n_i!} \quad (4.55)$$

4.11.2 Unfolding methodology

Having discussed the basic principle of unfolding, we will now discuss the general methodology. First, let us summarize all the ingredients we introduced:

- $\mathbf{n} = (n_1, \dots, n_N)$ is the observed histogram obtained from data with integral $n_{\text{tot}} = \sum_i n_i$
- $\mathbf{x} = (x_1, \dots, x_M)$ is the true histogram with integral $x_{\text{tot}} = \sum_j x_j$
- $\mathbf{y} = (y_1, \dots, y_N)$ are the expectation values of the observed histogram obtained from MC
- \mathbb{R}_{ij} is detector response matrix
- $\epsilon_j = \sum_{i=1}^N \mathbb{R}_{ij}$ are the efficiencies

which are all related by the master equation:

$$E(\mathbf{n}) = \mathbf{y} = \mathbb{R}\mathbf{x} + \mathbf{b} \quad (4.56)$$

The simplest solution to the problem described above would seem to be simply inverting the response matrix \mathbb{R} , provided the matrix is invertible:

$$\mathbf{x} = \mathbb{R}^{-1}(\mathbf{y} - \mathbf{b}) \quad (4.57)$$

where we simply choose the observed data as the estimator of the true distribution $\hat{\mathbf{y}} = \mathbf{n}$ to obtain:

$$\hat{\mathbf{x}} = \mathbb{R}^{-1}(\mathbf{n} - \mathbf{b}) \quad (4.58)$$

and call the job done. However, it has been repeatedly shown that this approach might not necessarily work as it leads to a wildly oscillating solutions with enormous uncertainties. This situation is common in many parameter estimations, as the presence of the large number of parameters inflates the statistical errors of these estimated parameters. Such solutions are of course unacceptable, hence a more sophisticated method is used. One can also show that using maximum-likelihood estimate and the least-squares method are essentially identical to this approach:

$$\ln L(\mathbf{x}) = \sum_i (n_i \ln y_i - y_i), \quad (4.59)$$

An excellent summary of unfolding methods is given by [Glen Cowan \[Cow98\]](#), pp. 153–187 where the revised method using correction factors (bin-by-bin unfolding) is also described.

A more sophisticated approach to solve this problem comes from a set of methods referred to as *regularized unfolding*. The principle behind it is that in order to get reasonable estimators which are not wildly oscillating, one tries solutions other than the one given by the maximum-likelihood:

$$\ln L(\mathbf{x}) \geq \ln L(\mathbf{x})_{\max} - \Delta \ln L(\mathbf{x}) \quad (4.60)$$

and pick the “smoothest” one. The search usually takes form of maximizing a different quantity:

$$\tau \left(\ln L(\mathbf{x}) - \left(\ln L(\mathbf{x})_{\max} - \Delta \ln L(\mathbf{x}) \right) \right) + S(\mathbf{x}) \quad (4.61)$$

with respect to both \mathbf{x} and a newly introduced parameter τ which is a Lagrange multiplier called the *regularization parameter*. The choice of the regularization function $S(\mathbf{x})$ remains a subject of considerable debate and presents the key difference between various regularized unfolding methods. One of the popular methods uses singular value decomposition to minimize the mean squared curvature between bins as described by [Andreas Höcker and Vakhtang Kartvelishvili \[HK96\]](#). It is implemented in [ROOT](#) as a part of the `TSVDUnfold` class. It should be noted that that optimizing the shape and uncertainty on the unfolded distribution with respect to the regularization may in principle introduce bias as one is exploiting the information introduced through the regularization procedure (referred to as “imposed smoothness”).

The alternative to regularized unfolding is to use the *iterative method* as described by [G. D’Agostini \[D’Ag10\]](#), which is a form of an expectation-minimization (EM) algorithm. The goal is to estimate the probability distribution of true events $\mathbf{p} = (p_1, \dots, p_M)$ given the observed data $\mathbf{n} = (n_1, \dots, n_N)$.

1. Start with making an initial guess, e.g. simply suppose the variable has a uniform distribution:

$p_i = 1/M$ where M is the number of bins in \mathbf{p} . This allows us to build the initial estimator of \mathbf{x} :

$$\mathbf{x}(0) = n_{\text{tot}}\mathbf{p}(0) \quad (4.62)$$

where 0 indicates the iteration number.

2. Update the probabilities \mathbf{p} according to rule

$$\hat{x}_i = \frac{1}{\epsilon_i} \sum_{j=1}^N P(\text{true value in bin } i | \text{found in bin } j) n_j = \frac{1}{\epsilon_i} \sum_{j=1}^N \left(\frac{\mathbb{R}_{ij} p_j}{\sum_k \mathbb{R}_{jk} p_k} \right) \quad (4.63)$$

where n_j is the actual number of events in bin j and the sum exploits the law of total probability to give the probability of the event being in bin j .

3. Continue iterating until the solution is stable. The stability criterion is usually determined using a χ^2 test with respect to the result of the previous iteration.

In particle physics, this method is commonly referred to as *Bayesian unfolding* as the Bayes' theorem is used to transform The main advantage of iterative method is that it avoids explicitly setting the regularization parameter or building the regularization function. Instead we simply specify the number of iterations, which is more convenient when searching for stable solutions. It is for these reason that both analysis at 7 TeV and 8 TeV use the iterative method as the baseline.

4.11.3 Implementation

To summarize the theoretical concepts describe above: in order to compute the unfolded distribution the knowledge of detector response matrix \mathbb{R} is required. It accounts for bin-to-bin migrations between the reconstructed \mathbf{y} and the truth distribution \mathbf{x} . Due to the fact that the distribution at the reconstruction level is obtained by applying kinematic cuts, it should be made clear that \mathbb{R} is only defined for events which are selected on the reconstruction level and are also included by the fiducial selection defined on truth level. Apart from the distribution \mathbf{n} measured in data we define the following quantities using the full simulation of MC signal samples:

Correction factors defined for each bin i of the true distribution \mathbf{x} , as the ratio of reconstructed events N_i^{reco} in bin i over the number of truth events N_i^{truth} , where all events are required to pass the fiducial selection defined at the truth level

$$c_i = \left. \frac{N_i^{\text{reco}}}{N_i^{\text{truth}}} \right|_{\text{fid}} \quad (4.64)$$

where index i corresponds to a bin in the true distribution \mathbf{x} of the target variable. This correction factor accounts for acceptance and efficiency losses at the reconstruction level.

Fiducial factors defined for each bin i of the reconstructed distribution \mathbf{y} , as the ratio of events which fall in the fiducial region on the truth level N_i^{fid} over all events N_i that passed the selection at the reconstruction level

$$f_i = \left. \frac{N_i^{\text{fid}}}{N_i} \right|_{\text{reco}} \quad (4.65)$$

where index i corresponds to a bin in the reconstructed distribution \mathbf{y} of the target variable. This efficiency corrects for those reconstructed events that fall outside the fiducial region and hence have no associated truth-value which can be used during the unfolding. Contrary to what is stated in [section 4.11.1](#), these are not background events as the **MC** consists of purely signal events.

These efficiencies are computed on an event-by-event basis. The method then transfers between the observed distribution in data \mathbf{n} and the final unfolded distribution as follows:

$$y_i = (n_i - b_i) \cdot f_i \quad (4.66)$$

$$x_i = (\mathbb{R}_{ij}^{-1} y_j) \cdot c_i \quad (4.67)$$

where c_i and f_i are the factors defined above. The procedure is schematically illustrated in [fig. 4.55](#). This approach is implemented in the unfolding framework `EWUnfolding` which was developed by Matthias Schott. The code provides the interface to the event data, histograms and computes the correction and fiducial factors, the final systematic and statistical uncertainty estimations and the final result calculations. The unfolding numerical kernel, which is responsible for solving the response matrix problem, is based on `RooUnfold` framework which provides access to the iterative methods as well as a number of other methods, including also the regularized unfolding.

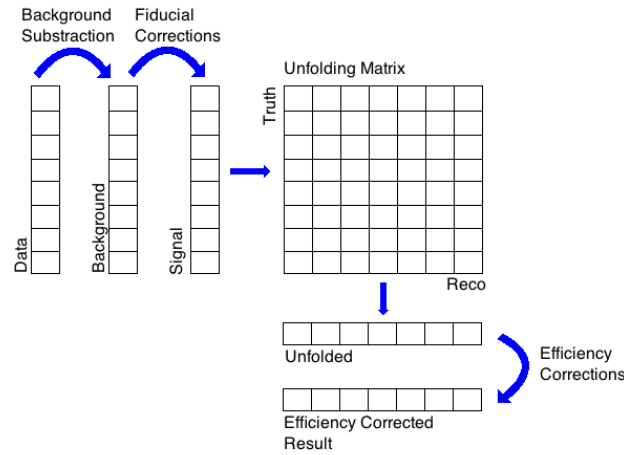


Figure 4.55: Schematic of the unfolding method for a distribution in a fiducial volume. Courtesy of Matthias Schott.

As input to the unfolding framework, the **MC** event information is provided through a dedicated **N-tuple** with the following branches for the given quantity:

- `MCTRUTHVALUE` is the **MC** truth value of the quantity
- `MCTRUTHWEIGHT` is the **MC** truth weight of the quantity, which is unfolded.
- `MCTRUTHISFIDUCIAL` flags whether or not the event falls within the fiducial region defined on **MC** truth level.
- `RECOVALUE` is the reconstructed value of the quantity, which is unfolded.
- `RECOWEIGHT` is the event weight at reconstruction level, i.e. it contains in addition to the

MCTrUTHWEIGHT also all reconstruction efficiencies applied in the analysis (i.e. trigger, isolation efficiency, correction factors etc., see [section 4.5](#)).

- RECOIsRECONSTRUCTED flags whether or not this event passes the full signal selection at reconstruction level

Observed data and background expectations are provided as histograms.

The central value of the unfolded distribution is computed using the nominal MC simulation of the signal samples, including all reconstruction level corrections as described in [section 4.5](#). The statistical uncertainty of the unfolded distribution is determined via toy Monte Carlo tests. Each measured entry in the data histogram \mathbf{n} is fluctuated using a Poisson distribution and the full nominal unfolding procedure is applied. This is repeated 200 times and the RMS of the resulting unfolded values x_i is taken as the statistical uncertainty.

A new set of branches (or a new N-tuple) is provided for each systematic uncertainty on the signal with the corresponding systematic variation applied (object systematics, pile-up uncertainties etc. see [section 4.8](#). The detector matrix \mathbb{R} is recomputed for each systematic uncertainty, including the c_i and f_i factors and the data distribution \mathbf{n} is then unfolded for each systematic separately. The differences in the unfolded distribution \mathbf{x} are then evaluated for each systematic in each bin:

$$\Delta_i^{\text{sys}} = x_i - x_i^{\text{sys}} \quad (4.68)$$

and quoted as the systematic uncertainty on the unfolded values on each bin x_i . As most systematic uncertainties are provided asymmetrically (e.g. JES $+1\sigma$, -1σ), we take the larger value of Δ_i^{sys} from both variations as the symmetrized uncertainty.

The systematic uncertainties on backgrounds are also treated independently, the values of $\Delta_i^{\text{bkg}} = x_i - x_i^{\text{bkg}}$ are defined as systematic uncertainties. We assume that all symmetrized signal and background variations can be treated as uncorrelated.

The stability of the unfolding procedure is tested by comparing the iterative unfolding algorithm with different number of iterations. The difference of both results is taken as systematic uncertainty due to the unfolding method itself.

4.11.4 Unfolded distributions

In this analysis, we apply the above-mentioned method to unfold the distribution of the leading lepton transverse momentum: p_T^{lead} . The choice of binning is mostly limited by statistics:

$$p_T^{\text{lead}}(7 \text{ TeV}) = \{25, 40, 60, 80, 100, 120, 140, 350\} \text{ GeV} \quad (4.69)$$

$$p_T^{\text{lead}}(8 \text{ TeV}) = \{25, 30, 35, 40, 50, 60, 70, 80, 100, 120, 140, 500\} \text{ GeV} \quad (4.70)$$

Given the fact, that the 8 TeV dataset is about 4 times larger than the 7 TeV datasets, we were able to improve on the resolution and unfold the distribution with finer binning, especially in the lower part of the spectrum. For the 8 TeV case, we investigate the limitations of the detector resolution by constructing a resolution matrix from the estimated signal events simulated by MC. The resolution profile is shown in [fig. 4.61](#). It clearly shows that the choice of bin size is limited to 5 GeV under $p_T < 100 \text{ GeV}$, provided there is enough statistics. Finer binning is not desired in the tails due to

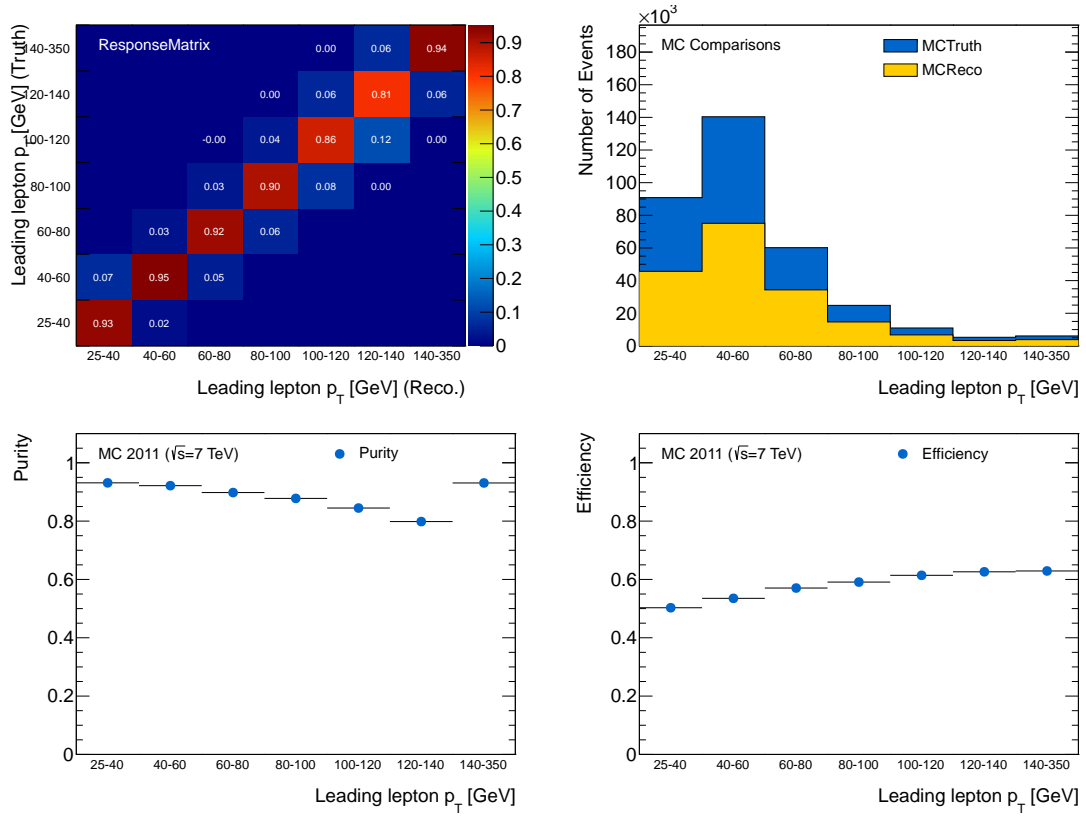


Figure 4.56: Ingredients to unfolding of the leading lepton p_T at 7 TeV. The top row shows the response matrix (left) and the truth and reconstruction level MC distributions (left). The bottom row shows the purity distribution (left) and the efficiency correction factors c_i (right).

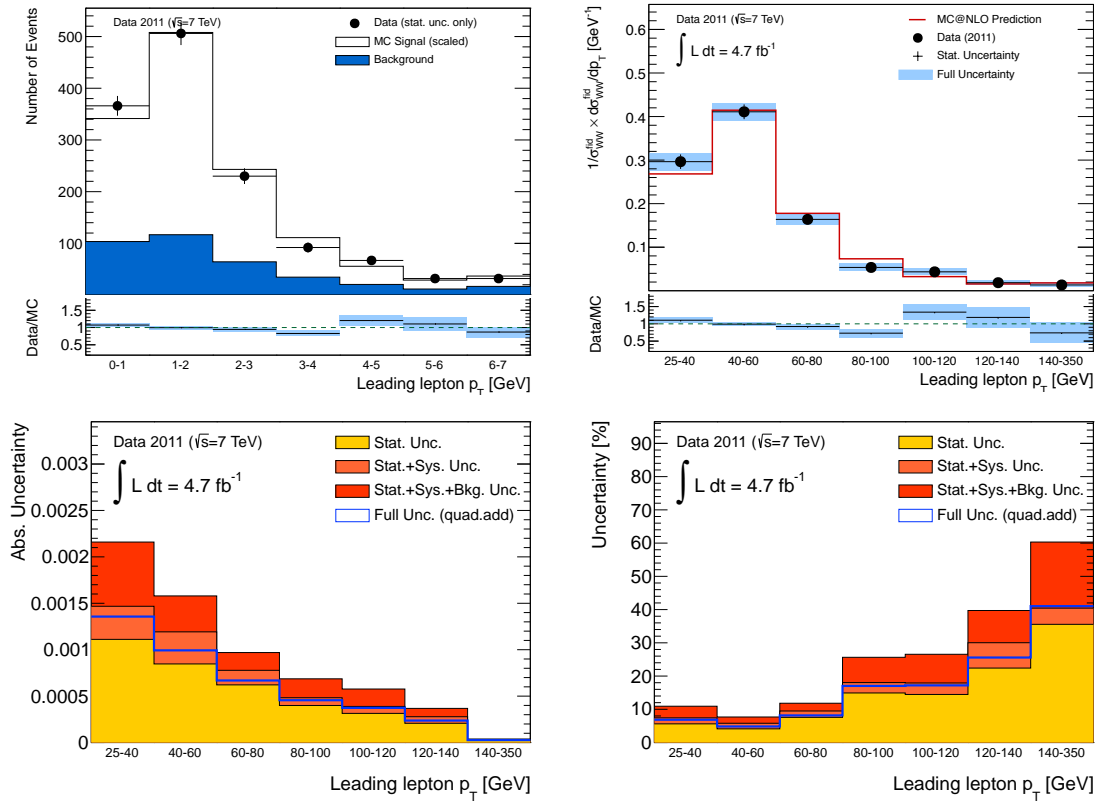


Figure 4.57: Data, signal and background distributions which are unfolded (top left), unfolded distribution and comparison with MC prediction (top right), absolute errors (bottom left) and relative errors (bottom right) for the leading lepton p_T distribution.

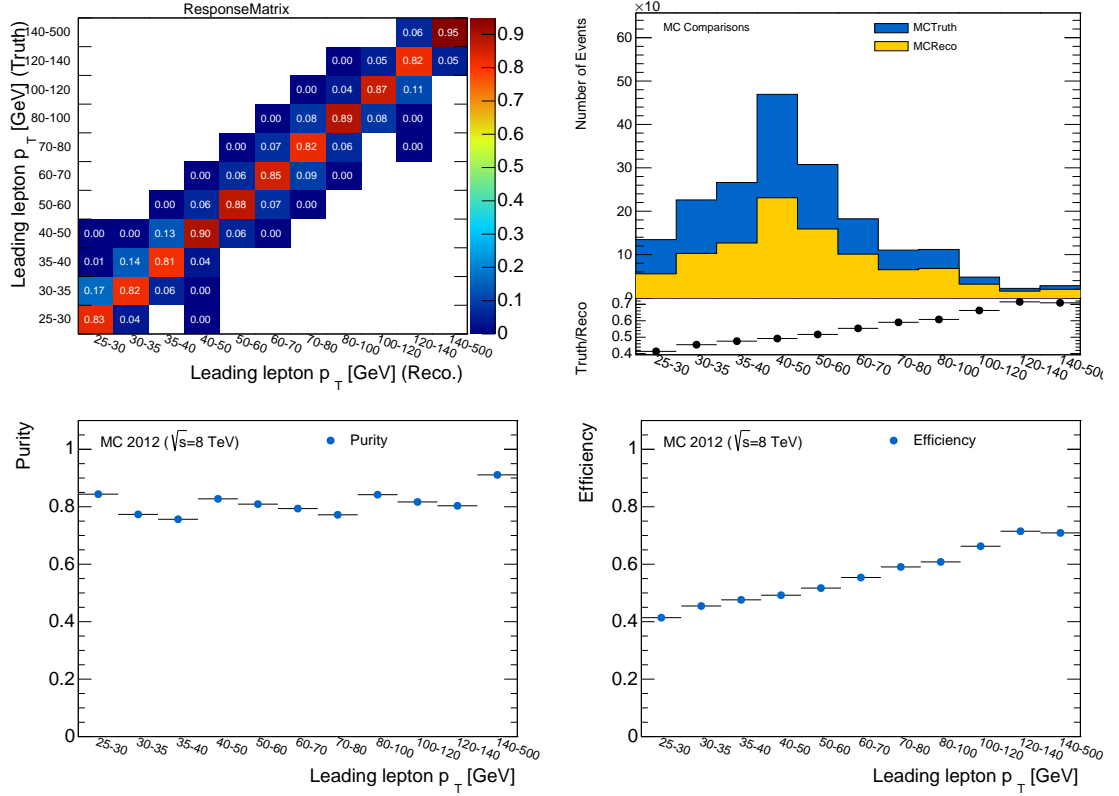


Figure 4.58: Ingredients to unfolding of the leading lepton p_T at 8 TeV. The top row shows the response matrix (left) and the truth and reconstruction level MC distributions (left). The bottom row shows the purity distribution (left) and the efficiency correction factors c_i (right).

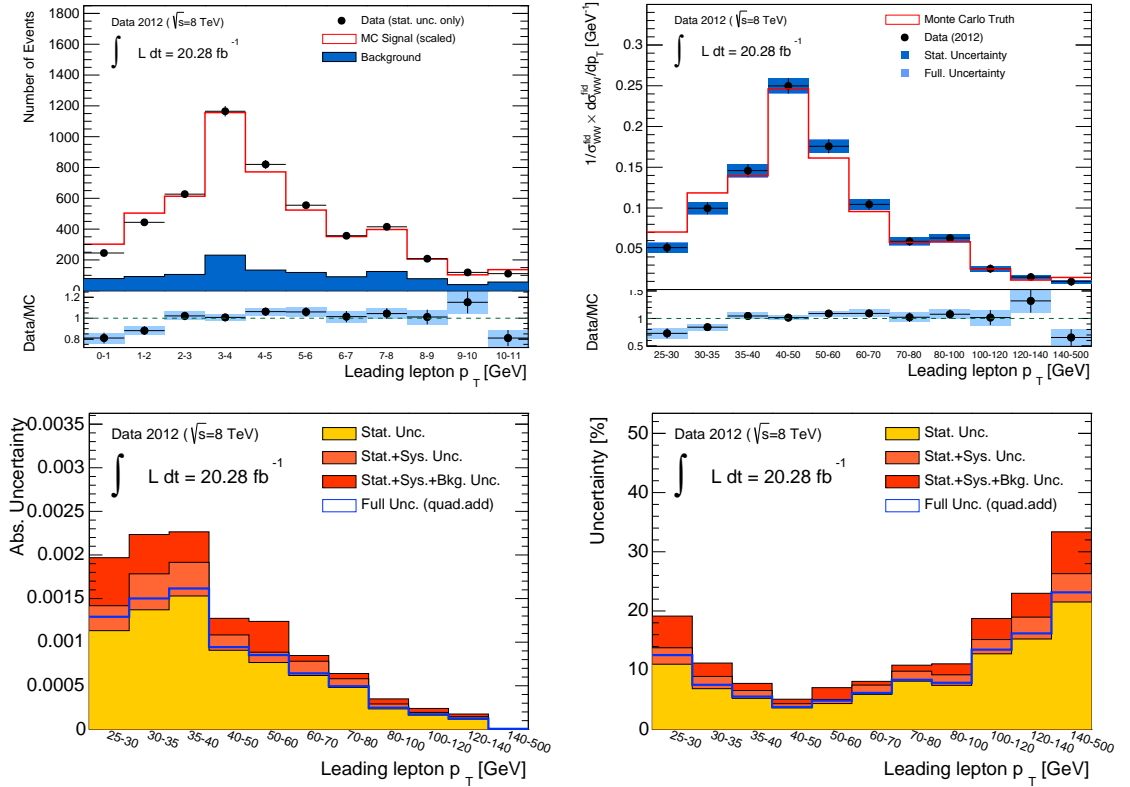


Figure 4.59: Data, signal and background distributions which are unfolded (top left), unfolded distribution and comparison with MC prediction (top right), absolute errors (bottom left) and relative errors (bottom right) for the leading lepton p_T distribution.

statistical uncertainties. The upper-bound of 500 GeV (resp. 350 GeV) includes all measured data at $\sqrt{s} = 8$ TeV (resp. 7 TeV).

As a sanity check, we tested the unfolding procedure using a MC closure test. We take the expected signal events from MC and use them as the observed distribution \mathbf{n} . In such case, a perfect agreement to the corresponding truth distribution is expected. The resulting distribution shown in fig. 4.60 confirms this expectation.

Figures figs. 4.56 and 4.58 show the response matrix \mathbb{R} and the associated purity and efficiency correction factors for the nominal distribution. In both cases the purity of all bins is close to 80 % which implies only small bin-to-bin migrations. The efficiency correction factors c_i are in the range of 0.40–0.60 and tend to increase with increasing leading lepton p_T .

The unfolded differential cross-sections of leading lepton p_T are summarized in figures figs. 4.57 and 4.59 along with the input distributions and associated binned uncertainties (absolute and relative). The unfolded distributions are normalized to unity within the given kinematic range. A comparison between the MC distribution and the unfolded distribution is also provided. In addition, we also provide the corresponding numerical values in tables tables 4.52 and 4.53. The tables contain the full list of systematic uncertainties and their independent contributions to the final measurement.

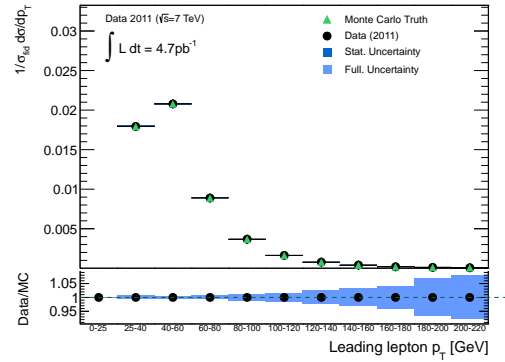


Figure 4.60: Result of closure test with nominal MC used as observed data in the p_T^{lead} distribution.

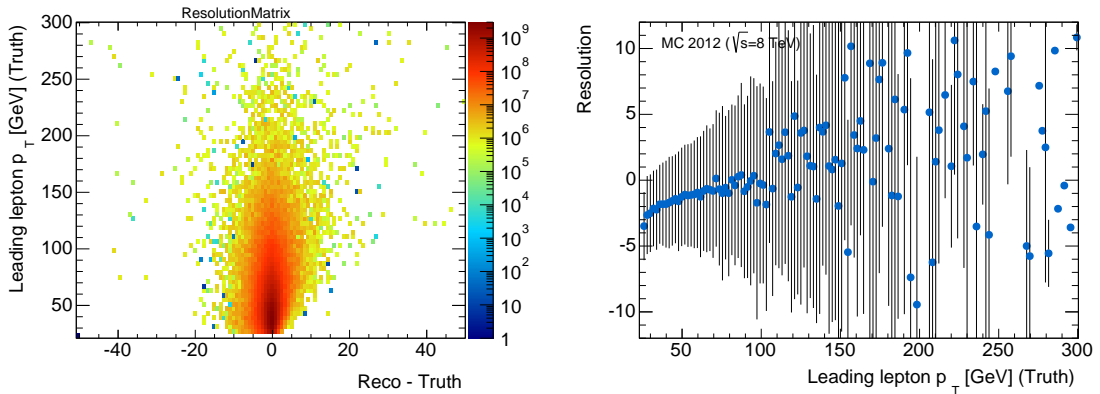


Figure 4.61: Resolution of the leading lepton p_T at $\sqrt{s} = 8$ TeV. The figure on the left shows the resolution matrix filled with the MC events passing both the reconstruction and fiducial selection. The resolution profile is shown on the right.

4.12 References

- [ATL12d] ATLAS Collaboration. “Observation of a new particle in the search for the Standard Model Higgs boson with the ATLAS detector at the LHC”. In: *Physics Letters B* 716.1 (July 2012), p. 24. ISSN: 03702693. DOI: [10.1016/j.physletb.2012.08.020](https://doi.org/10.1016/j.physletb.2012.08.020). arXiv: [1207.7214](https://arxiv.org/abs/1207.7214) (cit. on p. 157).

Leading p_T bin [GeV]	25 - 40	40 - 60	60 - 80	80 - 100	100 - 120	120 - 140	140 - 350
Results	0.2964	0.4109	0.163907	0.0535292	0.0434283	0.0185259	0.0133096
Comb. Unc.	0.0200014 (6.74%)	0.0198614 (4.83%)	0.0133735 (8.15%)	0.0091188 (17.0%)	0.0074693 (17.1%)	0.0047380 (25.5%)	0.0054611 (41.0%)
Stat. Unc.	0.0146713 (5.62%)	0.0169354 (4.12%)	0.0124248 (7.58%)	0.0079859 (14.9%)	0.0062833 (14.4%)	0.0041506 (22.4%)	0.0047335 (35.5%)
Sys. Unc.	0.0053454 (1.80%)	0.0069102 (1.68%)	0.0031346 (1.91%)	0.0016672 (3.11%)	0.0014981 (3.44%)	0.0014128 (7.62%)	0.0006490 (4.87%)
Bkg. Unc.	0.0103765 (3.50%)	0.0077405 (1.88%)	0.0038272 (2.33%)	0.0040741 (7.61%)	0.0037504 (8.63%)	0.0017959 (9.69%)	0.0026451 (19.8%)
Stat. Unc. (MC)	0.40%	0.29%	0.50%	0.87%	1.13%	1.80%	1.75%
AlternativeUnfolding	0.11%	0.08%	0.31%	2.15%	1.92%	0.19%	1.08%
UniformPrior	1.14%	1.45%	1.06%	1.08%	1.45%	6.58%	2.50%
JES	0.41%	0.10%	0.64%	0.88%	0.28%	0.17%	0.20%
EScale	0.71%	0.06%	0.60%	0.44%	0.96%	1.99%	2.75%
ERes	0.07%	0.00%	0.39%	0.42%	1.02%	1.92%	0.55%
MEff	0.00%	0.00%	0.00%	0.00%	0.00%	0.00%	0.05%
MSSmear	0.00%	0.08%	0.40%	0.37%	0.58%	0.55%	1.30%
IDSmeas	0.00%	0.06%	0.32%	0.32%	0.47%	0.42%	1.27%
METCluster	0.95%	0.74%	0.51%	0.78%	0.85%	1.68%	0.23%
JER	0.16%	0.07%	0.39%	0.63%	0.38%	0.16%	0.00%
METTool	0.00%	0.00%	0.29%	0.28%	0.54%	0.30%	0.91%
EEff	0.09%	0.00%	0.00%	0.08%	0.06%	0.11%	0.11%
EEffTkID	0.00%	0.00%	0.00%	0.00%	0.05%	0.00%	0.06%
Trigger	0.00%	0.00%	0.00%	0.00%	0.00%	0.00%	0.00%
Eliso	0.07%	0.00%	0.10%	0.12%	0.16%	0.15%	0.17%
METPileUp	0.22%	0.14%	0.34%	0.36%	0.63%	0.47%	0.54%
ResSoftTerms	0.09%	0.00%	0.43%	0.60%	0.28%	0.11%	0.70%
ScaleSoftTerms	0.23%	0.11%	0.37%	0.23%	0.67%	0.32%	0.49%
BkgTop	2.27%	1.09%	1.19%	6.09%	4.78%	7.62%	19.0%
BkgWJets	2.44%	0.84%	0.90%	0.48%	2.70%	1.93%	3.77%
BkgDrellYan	0.81%	0.11%	0.50%	0.33%	1.18%	1.49%	1.05%
Bkg	0.23%	0.28%	0.00%	0.44%	0.22%	0.17%	2.36%
BkgElectronScale	0.11%	0.38%	0.11%	1.80%	1.47%	2.48%	2.00%
BkgElectronRes	0.20%	0.43%	1.47%	2.96%	0.57%	1.40%	2.59%
BkgElectronEff	0.06%	0.00%	0.00%	0.10%	0.00%	0.14%	0.23%
BkgMuonScale	0.47%	0.39%	0.27%	0.00%	0.74%	3.02%	0.00%
BkgMuonRes	0.00%	0.06%	0.00%	1.09%	0.96%	0.22%	0.00%
BkgMuonEff	0.00%	0.00%	0.00%	0.00%	0.00%	0.00%	0.00%
BkgOthers	0.28%	1.01%	0.82%	2.63%	6.23%	3.52%	0.50%
Bayesian3	0.11%	0.08%	0.31%	2.15%	1.92%	0.19%	1.08%

Table 4.52: Unfolded results including uncertainties for the leading lepton p_T distribution at 7 TeV. The table shows the central unfolded values and statistical, systematic and background uncertainties. Also shown are uncertainties from applying the Bayesian unfolding algorithm with an additional iteration and the uncertainties from a closure test.

Leading p_T bin	25 - 30	30 - 35	35 - 40	40 - 50	50 - 60	60 - 70	70 - 80	80 - 100	100 - 120	120 - 140	140 - 500
Results											
Comb. Unc.	0.0514378 0.0064550 (12.5%) 0.0056605 (11.0%) 0.004296 (2.77%) 0.0027534 (5.55%)	0.0997412 0.0075062 (7.52%) 0.0068564 (6.87%) 0.0020613 (2.06%) 0.0022549 (2.26%)	0.1458712 0.0080786 (5.53%) 0.0076472 (5.24%) 0.0019295 (1.32%) 0.0017492 (1.19%)	0.2498332 0.0094337 (3.77%) 0.0090709 (3.63%) 0.0017593 (0.70%) 0.0019020 (0.76%)	0.1757292 0.0085244 (4.85%) 0.0076669 (4.36%) 0.0011807 (0.67%) 0.0035341 (2.01%)	0.1044717 0.0064266 (6.15%) 0.0061804 (5.91%) 0.0016348 (1.56%) 0.0006567 (0.62%)	0.0591066 0.0049506 (8.37%) 0.0048120 (8.14%) 0.0009966 (1.68%) 0.0006001 (1.01%)	0.0631668 0.0049696 (7.86%) 0.0046971 (7.43%) 0.0011243 (1.78%) 0.0011706 (1.85%)	0.0256221 0.0034504 (13.4%) 0.0032702 (12.7%) 0.0006168 (2.40%) 0.0009112 (3.55%)	0.0153081 0.0023369 (16.2%) 0.0023369 (16.2%) 0.0005655 (3.69%) 0.0006162 (4.02%)	0.0097115 0.0022478 (23.1%) 0.0020895 (21.5%) 0.0004650 (4.78%) 0.0006859 (7.06%)
Stat. Unc. (MC)	0.095%	0.64%	0.48%	0.33%	0.42%	0.54%	0.62%	0.65%	0.87%	0.94%	1.10%
AlternativeUnfolding	0.47%	0.66%	0.96%	0.30%	0.16%	0.17%	0.52%	0.31%	1.15%	2.54%	1.85%
Pileup	0.89%	0.49%	0.29%	0.00%	0.15%	0.40%	0.26%	0.37%	0.46%	0.15%	0.43%
TrigMatchMu	0.35%	0.14%	0.06%	0.00%	0.00%	0.09%	0.12%	0.14%	0.16%	0.18%	0.18%
TrigMatchEl	0.55%	0.09%	0.00%	0.08%	0.00%	0.00%	0.06%	0.07%	0.08%	0.00%	0.00%
MuMSmear	0.14%	0.00%	0.11%	0.00%	0.06%	0.12%	0.35%	0.06%	0.57%	0.35%	1.26%
MuMSmear	1.03%	0.00%	0.19%	0.00%	0.05%	0.25%	0.18%	0.23%	0.50%	0.83%	0.99%
MuScale	0.36%	0.13%	0.00%	0.00%	0.00%	0.11%	0.05%	0.11%	0.18%	0.19%	0.00%
MuEff	0.00%	0.00%	0.00%	0.00%	0.00%	0.00%	0.00%	0.00%	0.00%	0.00%	0.07%
MuIso	0.15%	0.08%	0.00%	0.00%	0.00%	0.00%	0.00%	0.00%	0.05%	0.05%	0.06%
ElRes	0.66%	0.66%	0.24%	0.00%	0.26%	0.91%	0.95%	0.14%	0.23%	0.20%	0.85%
ElScaleZeeAll	1.11%	1.45%	0.12%	0.05%	0.23%	0.81%	0.76%	0.39%	0.53%	1.08%	1.03%
ElScaleR12Stat	0.48%	0.16%	0.29%	0.20%	0.11%	0.21%	0.34%	0.97%	0.20%	1.80%	2.52%
ElScalePSSStat	0.15%	0.00%	0.11%	0.06%	0.07%	0.24%	0.24%	0.19%	0.22%	0.26%	0.49%
ElScaleLowPt	0.00%	0.00%	0.00%	0.00%	0.00%	0.00%	0.00%	0.00%	0.00%	0.00%	0.00%
ElEffID	1.07%	0.30%	0.00%	0.17%	0.19%	0.12%	0.16%	0.14%	0.16%	0.16%	0.16%
ElEffTrk	0.19%	0.05%	0.00%	0.06%	0.05%	0.00%	0.00%	0.14%	0.16%	0.17%	0.18%
ElIso	0.14%	0.05%	0.00%	0.00%	0.00%	0.00%	0.00%	0.00%	0.00%	0.00%	0.00%
METSoftReso	0.86%	0.31%	0.05%	0.18%	0.08%	0.13%	0.05%	0.00%	0.38%	0.20%	0.00%
METSoftScale	0.27%	0.31%	0.28%	0.09%	0.00%	0.07%	0.31%	0.42%	0.99%	0.68%	0.00%
MPTSoftReso	0.31%	0.09%	0.00%	0.00%	0.00%	0.19%	0.00%	0.06%	0.38%	0.08%	0.27%
MPTSoftScale	0.26%	0.17%	0.10%	0.00%	0.07%	0.00%	0.11%	0.08%	0.95%	0.19%	0.10%
JVF	0.00%	0.07%	0.06%	0.00%	0.00%	0.18%	0.07%	0.00%	0.15%	0.14%	0.00%
JES	0.23%	0.32%	0.28%	0.34%	0.07%	0.38%	0.22%	1.06%	0.96%	0.20%	1.84%
JER	0.29%	0.31%	0.27%	0.14%	0.08%	0.00%	0.17%	0.15%	0.08%	0.36%	1.58%
Pileup(BKG)	0.24%	0.00%	0.00%	0.00%	0.00%	0.00%	0.08%	0.00%	0.06%	0.15%	0.40%
TrigMatchMu(BKG)	0.10%	0.00%	0.00%	0.00%	0.00%	0.00%	0.00%	0.00%	0.00%	0.00%	0.00%
TrigMatchEl(BKG)	0.15%	0.00%	0.00%	0.00%	0.00%	0.00%	0.00%	0.00%	0.00%	0.00%	0.00%
MuMSmear(BKG)	0.35%	0.08%	0.00%	0.00%	0.10%	0.08%	0.00%	0.07%	0.10%	0.05%	0.06%
MuMSmear(BKG)	0.19%	0.00%	0.00%	0.00%	0.08%	0.00%	0.10%	0.00%	0.00%	0.00%	0.11%
MuScale(BKG)	0.00%	0.00%	0.00%	0.00%	0.00%	0.00%	0.00%	0.00%	0.00%	0.00%	0.00%
MuEff(BKG)	0.05%	0.00%	0.00%	0.00%	0.00%	0.00%	0.00%	0.00%	0.00%	0.00%	0.00%
MuIso(BKG)	0.09%	0.00%	0.00%	0.00%	0.00%	0.00%	0.00%	0.00%	0.00%	0.00%	0.00%
ElRes(BKG)	0.14%	0.08%	0.00%	0.00%	0.00%	0.00%	0.00%	0.00%	0.09%	0.11%	0.41%
ElScaleZeeAll(BKG)	0.50%	0.18%	0.00%	0.00%	0.00%	0.06%	0.00%	0.08%	0.12%	0.18%	0.35%
ElScaleR12Stat(BKG)	0.60%	0.00%	0.00%	0.00%	0.07%	0.00%	0.12%	0.00%	0.16%	0.14%	0.41%
ElScalePSSStat(BKG)	0.23%	0.00%	0.00%	0.00%	0.00%	0.00%	0.00%	0.00%	0.00%	0.21%	0.27%
ElScaleLowPt(BKG)	0.20%	0.00%	0.00%	0.00%	0.00%	0.00%	0.00%	0.00%	0.00%	0.00%	0.00%
ElEffID(BKG)	0.31%	0.00%	0.00%	0.00%	0.00%	0.00%	0.00%	0.00%	0.00%	0.00%	0.00%
ElEffTrk(BKG)	0.06%	0.00%	0.00%	0.00%	0.00%	0.00%	0.00%	0.00%	0.00%	0.00%	0.00%
ElIso(BKG)	0.05%	0.00%	0.00%	0.00%	0.00%	0.00%	0.00%	0.00%	0.00%	0.00%	0.00%
METSoftReso(BKG)	0.50%	0.13%	0.06%	0.00%	0.08%	0.00%	0.16%	0.16%	0.00%	0.10%	0.62%
METSoftScale(BKG)	0.74%	0.05%	0.00%	0.00%	0.00%	0.05%	0.05%	0.27%	0.06%	0.32%	0.56%
MPTSoftReso(BKG)	0.15%	0.08%	0.05%	0.06%	0.09%	0.10%	0.00%	0.06%	0.10%	0.10%	0.22%
MPTSoftScale(BKG)	0.15%	0.09%	0.00%	0.00%	0.00%	0.00%	0.05%	0.05%	0.13%	0.08%	0.00%
JVF(BKG)	0.09%	0.00%	0.00%	0.00%	0.00%	0.00%	0.00%	0.00%	0.00%	0.00%	0.00%
JES(BKG)	0.50%	0.16%	0.00%	0.00%	0.05%	0.13%	0.05%	0.06%	0.00%	0.21%	0.30%
JER(BKG)	0.77%	0.00%	0.06%	0.00%	0.00%	0.16%	0.18%	0.12%	0.15%	0.00%	0.57%
Z-jet(BKG)	1.26%	0.28%	0.25%	0.40%	0.58%	0.50%	0.32%	0.63%	0.23%	0.45%	0.34%
W-jet(BKG)	4.87%	2.07%	0.84%	0.37%	1.90%	0.05%	0.38%	0.13%	1.31%	2.99%	0.67%
Top(BKG)	0.54%	0.76%	0.79%	0.50%	0.13%	0.23%	0.81%	1.69%	3.27%	2.59%	6.88%
Bayesian2	0.47%	0.96%	0.96%	0.30%	0.16%	0.17%	0.52%	0.31%	1.15%	2.54%	1.85%
Bayesian4	2.56%	2.17%	1.14%	0.00%	0.57%	0.67%	0.46%	0.56%	0.81%	4.80%	4.08%

Table 4.53: Unfolded results including uncertainties for the leading lepton p_T distribution at 8 TeV. The table shows the central unfolded values and statistical, systematic and background uncertainties. Also shown are uncertainties from a closure test and from applying the Bayesian unfolding algorithm with one more and one less iteration (Bayesian2, Bayesian4)

- [Bil+13] M. Billoni, S. Dittmaier, B. Jäger, and C. Speckner. “Next-to-leading-order electroweak corrections to $pp \rightarrow WW \rightarrow 4$ leptons in double-pole approximation at the LHC”. In: (Nov. 2013). arXiv: [1311.5491](#) (cit. on pp. [157](#), [174](#)).
- [Bie+12] Anastasiya Bierweiler, Tobias Kasprzik, Johann H. Kühn, and Sandro Uccirati. “Electroweak corrections to W-boson pair production at the LHC”. In: (Aug. 2012). arXiv: [1208.3147](#) (cit. on pp. [157](#), [173](#), [174](#)).
- [Par12] Particle Data Group. “Review of Particle Physics”. In: *Physical Review D* 86.1 (July 2012), p. 010001. ISSN: 1550-7998. DOI: [10.1103/PhysRevD.86.010001](#) (cit. on p. [158](#)).
- [ATL11b] ATLAS Collaboration. “Measurement of the WW cross section in $\sqrt{s} = 7$ TeV pp collisions with ATLAS”. In: *Physical Review Letters* 107.4 (Apr. 2011), p. 041802. ISSN: 0031-9007. DOI: [10.1103/PhysRevLett.107.041802](#). arXiv: [1104.5225v1](#) (cit. on pp. [159](#), [168](#)).
- [ATL12c] ATLAS Collaboration. “Measurement of the WW cross section in $\sqrt{s} = 7$ TeV pp collisions with the ATLAS detector and limits on anomalous gauge couplings”. In: *Physics Letters B* 712.4-5 (Mar. 2012), p. 11. ISSN: 03702693. DOI: [10.1016/j.physletb.2012.05.003](#). arXiv: [1203.6232](#) (cit. on pp. [159](#), [168](#)).
- [ATL13c] ATLAS Collaboration. “Measurement of W^+W^- production in pp collisions at $\sqrt{s}=7$ TeV with the ATLAS detector and limits on anomalous WWZ and WW_γ couplings”. In: *Physical Review D* 87.11 (June 2013), p. 112001. ISSN: 1550-7998. DOI: [10.1103/PhysRevD.87.112001](#). arXiv: [1210.2979v2](#) (cit. on pp. [159](#), [172](#), [246](#)).
- [ATL14i] ATLAS Collaboration. “Measurement of the W^+W^- production cross section in proton-proton collisions at $\sqrt{s} = 8$ TeV with the ATLAS detector”. In: *Conference Note of SM WW analysis for ICHEP 2014*. June 2014 (cit. on pp. [159](#), [172](#), [187](#), [203](#), [246](#)).
- [Sti13] James Stirling. *Parton luminosity and cross section plots*. 2013. Available at: [http://www.hep.ph.ic.ac.uk/~%5Csim\\$wstirlin/plots/plots.html](http://www.hep.ph.ic.ac.uk/~%5Csim$wstirlin/plots/plots.html), visited on 12/23/2013 (cit. on p. [160](#)).
- [ATL11c] ATLAS Collaboration. *Measurement of the WW production cross section in proton-proton collisions at $\sqrt{s} = 7$ TeV with the ATLAS detector*. Tech. rep. 15. Geneva: CERN, Mar. 2011 (cit. on p. [168](#)).
- [FW02] Stefano Frixione and Bryan R Webber. “Matching NLO QCD computations and parton shower simulations”. en. In: *Journal of High Energy Physics* 2002.06 (June 2002), pp. 029–029. ISSN: 1029-8479. DOI: [10.1088/1126-6708/2002/06/029](#) (cit. on pp. [172](#), [174](#)).
- [Fri+14] Stefano Frixione, Fabian Stoeckli, Paolo Torrielli, Bryan Webber, and Chris White. *The MC@NLO Package*. 2014. Available at: <http://www.hep.phy.cam.ac.uk/theory/webber/MCatNLO/>, visited on 06/24/2014 (cit. on pp. [172](#), [174](#)).

- [Cor+00] Gennaro Corcella, Ian G Knowles, Giuseppe Marchesini, Stefano Moretti, Kosuke Odagiri, Peter Richardson, Michael H Seymour, and Bryan R Webber. “HERWIG 6.5: an event generator for Hadron Emission Reactions With Interfering Gluons (including supersymmetric processes)”. In: *Journal of High Energy Physics* 2001.01 (Nov. 2000), p. 112. ISSN: 1029-8479. DOI: [10.1088/1126-6708/2001/01/010](https://doi.org/10.1088/1126-6708/2001/01/010). arXiv: [0011363 \[hep-ph\]](https://arxiv.org/abs/hep-ph/0011363) (cit. on p. 172).
- [Nas04] Paolo Nason. “A New Method for Combining NLO QCD with Shower Monte Carlo Algorithms”. In: *Journal of High Energy Physics* 2004.11 (Nov. 2004), pp. 040–040. ISSN: 1029-8479. DOI: [10.1088/1126-6708/2004/11/040](https://doi.org/10.1088/1126-6708/2004/11/040). arXiv: [0409146 \[hep-ph\]](https://arxiv.org/abs/hep-ph/0409146) (cit. on p. 172).
- [FNO07] Stefano Frixione, Paolo Nason, and Carlo Oleari. “Matching NLO QCD computations with Parton Shower simulations: the POWHEG method”. In: *Journal of High Energy Physics* 2007.11 (Sept. 2007), p. 91. ISSN: 1029-8479. DOI: [10.1088/1126-6708/2007/11/070](https://doi.org/10.1088/1126-6708/2007/11/070). arXiv: [0709.2092](https://arxiv.org/abs/hep-ph/0709209) (cit. on p. 172).
- [Sjö+00] Torbjörn Sjöstrand, Patrik Edén, Christer Friberg, Leif Lönnblad, Gabriela Miu, Stephen Mrenna, and Emanuel Norrbin. “High-Energy-Physics Event Generation with PYTHIA 6.1”. In: *Computer Physics Communications* 135.2 (Oct. 2000), p. 27. ISSN: 00104655. DOI: [10.1016/S0010-4655\(00\)00236-8](https://doi.org/10.1016/S0010-4655(00)00236-8). arXiv: [0010017 \[hep-ph\]](https://arxiv.org/abs/hep-ph/0010017) (cit. on p. 172).
- [Bin+06] Thomas Binoth, Mariano Ciccolini, Nikolas Kauer, and Michael Krämer. “Gluon-induced W-boson pair production at the LHC”. en. In: *Journal of High Energy Physics* 2006.12 (Dec. 2006), pp. 046–046. ISSN: 1029-8479. DOI: [10.1088/1126-6708/2006/12/046](https://doi.org/10.1088/1126-6708/2006/12/046). arXiv: [0611170](https://arxiv.org/abs/hep-ph/0611170) (cit. on p. 172).
- [Mar+09] A. D. Martin, W. J. Stirling, R. S. Thorne, and G. Watt. “Parton distributions for the LHC”. In: *The European Physical Journal C* 63.2 (July 2009), pp. 189–285. ISSN: 1434-6044. DOI: [10.1140/epjc/s10052-009-1072-5](https://doi.org/10.1140/epjc/s10052-009-1072-5). arXiv: [0901.0002](https://arxiv.org/abs/hep-ph/0901002) (cit. on p. 172).
- [Bal+10] Richard D. Ball, Luigi Del Debbio, Stefano Forte, Alberto Guffanti, Jose I. Latorre, Juan Rojo, and Maria Ubiali. “A first unbiased global NLO determination of parton distributions and their uncertainties”. In: (Feb. 2010), p. 86. arXiv: [1002.4407](https://arxiv.org/abs/hep-ph/1002440) (cit. on p. 172).
- [ATL12b] ATLAS Collaboration. “Determination of the Strange-Quark Density of the Proton from ATLAS Measurements of the $W \rightarrow \ell\nu$ and $Z \rightarrow \ell\ell$ Cross Sections”. In: *Physical Review Letters* 109.1 (July 2012), p. 012001. ISSN: 0031-9007. DOI: [10.1103/PhysRevLett.109.012001](https://doi.org/10.1103/PhysRevLett.109.012001). arXiv: [1203.4051](https://arxiv.org/abs/hep-ex/1203.4051) (cit. on p. 173).
- [ATL12e] ATLAS Collaboration. “Observation of a new particle in the search for the Standard Model Higgs boson with the ATLAS detector at the LHC”. In: *Physics Letters B* 716.1 (Sept. 2012), pp. 1–29. ISSN: 03702693. DOI: [10.1016/j.physletb.2012.08.020](https://doi.org/10.1016/j.physletb.2012.08.020). arXiv: [1207.7214](https://arxiv.org/abs/hep-ex/1207.7214) (cit. on p. 173).

- [CMS12] CMS Collaboration. “Observation of a new boson at a mass of 125 GeV with the CMS experiment at the LHC”. In: *Physics Letters B* 716.1 (Sept. 2012), pp. 30–61. ISSN: 03702693. DOI: [10.1016/j.physletb.2012.08.021](https://doi.org/10.1016/j.physletb.2012.08.021). arXiv: [1207.7235](https://arxiv.org/abs/1207.7235) (cit. on p. 173).
- [The13] The LHC Higgs Cross Section Working Group. “Handbook of LHC Higgs Cross Sections: 3. Higgs Properties”. In: (July 2013), p. 404. DOI: [10.5170/CERN-2013-004](https://doi.org/10.5170/CERN-2013-004). arXiv: [1307.1347](https://arxiv.org/abs/1307.1347) (cit. on pp. 173, 174).
- [DLZ13] S. Dawson, Ian M. Lewis, and Mao Zeng. “Threshold resummed and approximate next-to-next-to-leading order results for W^+W^- pair production at the LHC”. In: *Physical Review D* 88.5 (Sept. 2013), p. 054028. ISSN: 1550-7998. DOI: [10.1103/PhysRevD.88.054028](https://doi.org/10.1103/PhysRevD.88.054028). arXiv: [1307.3249](https://arxiv.org/abs/1307.3249) (cit. on p. 173).
- [CEW14] John Campbell, Keith Ellis, and Ciaran Williams. *MCFM - Monte Carlo for FeMtobarn processes*. 2014. Available at: <http://mcfm.fnal.gov/>, visited on 05/10/2014 (cit. on p. 174).
- [Bon+13] Marco Bonvini, Fabrizio Caola, Stefano Forte, Kirill Melnikov, and Giovanni Ridolfi. “Signal-background interference effects for $gg \rightarrow H \rightarrow W^+W^-$ beyond leading order”. In: *Physical Review D* 88.3 (Aug. 2013), p. 034032. ISSN: 1550-7998. DOI: [10.1103/PhysRevD.88.034032](https://doi.org/10.1103/PhysRevD.88.034032). arXiv: [1304.3053](https://arxiv.org/abs/1304.3053) (cit. on p. 174).
- [Blo+13] B. Blok, Yu. Dokshitzer, L. Frankfurt, and M. Strikman. “Perturbative QCD correlations in multi-parton collisions”. In: (June 2013), p. 16. arXiv: [1306.3763](https://arxiv.org/abs/1306.3763) (cit. on p. 174).
- [JOZ06] Barbara Jäger, Carlo Oleari, and Dieter Zeppenfeld. “Next-to-leading order QCD corrections to $W+W^-$ production via vector-boson fusion”. In: *Journal of High Energy Physics* 2006.07 (July 2006), pp. 015–015. ISSN: 1029-8479. DOI: [10.1088/1126-6708/2006/07/015](https://doi.org/10.1088/1126-6708/2006/07/015). arXiv: [0603177](https://arxiv.org/abs/hep-ph/0603177) [hep-ph] (cit. on p. 174).
- [Man+03] Michelangelo L Mangano, Fulvio Piccinini, Antonio D Polosa, Mauro Moretti, and Roberto Pittau. “ALPGEN, a generator for hard multiparton processes in hadronic collisions”. In: *Journal of High Energy Physics* 2003.07 (July 2003), pp. 001–001. ISSN: 1029-8479. DOI: [10.1088/1126-6708/2003/07/001](https://doi.org/10.1088/1126-6708/2003/07/001) (cit. on p. 174).
- [KR13] Borut Paul Kersevan and Elzbieta Richter-Was. “The Monte Carlo event generator AcerMC versions 2.0 to 3.8 with interfaces to PYTHIA 6.4, HERWIG 6.5 and ARIADNE 4.1”. In: *Computer Physics Communications* 184.3 (Mar. 2013), pp. 919–985. ISSN: 00104655. DOI: [10.1016/j.cpc.2012.10.032](https://doi.org/10.1016/j.cpc.2012.10.032). arXiv: [0405247](https://arxiv.org/abs/0405247) [hep-ph] (cit. on p. 174).
- [ATL14j] ATLAS Collaboration. *Pileup Reweighting*. 2014. Available at: <https://twiki.cern.ch/twiki/bin/viewauth/AtlasProtected/PileupReweighting>, visited on 01/06/2013 (cit. on p. 177).
- [ATL14e] ATLAS Collaboration. *Extended Pileup Reweighting*. 2014. Available at: <https://twiki.cern.ch/twiki/bin/viewauth/AtlasProtected/ExtendedPileupReweighting>, visited on 01/06/2013 (cit. on p. 177).

- [ATL14h] ATLAS Collaboration. *Luminosity Public Results*. 2014. Available at: <https://twiki.cern.ch/twiki/bin/view/AtlasPublic/LuminosityPublicResults>, visited on 05/06/2014 (cit. on pp. 177, 178).
- [Mor12] John Morris. *HEP Analysis*. London, 2012. Available at: [http://www.hep.ucl.ac.uk/\\$%5Csim\\$campanel/Post_Grads/2013-2014/JMorris_HEPAnalysis.pdf](http://www.hep.ucl.ac.uk/$%5Csim$campanel/Post_Grads/2013-2014/JMorris_HEPAnalysis.pdf) (cit. on pp. 177, 178).
- [ATLd] ATLAS Collaboration. *Innner Detector Tracking Performance Guidelines*. Available at: <https://twiki.cern.ch/twiki/bin/viewauth/AtlasProtected/InDetTrackingPerformanceGuidelines>, visited on 06/09/2014 (cit. on p. 177).
- [ATL13j] ATLAS Collaboration. *WZ Electroweak Common Topics 2013*. 2013. Available at: <https://twiki.cern.ch/twiki/bin/viewauth/AtlasProtected/WZElectroweakCommonTopics2013> (cit. on p. 177).
- [ATL12h] ATLAS Collaboration. *WZ Electroweak Common Topics 2012*. 2012. Available at: <https://twiki.cern.ch/twiki/bin/viewauth/AtlasProtected/WZElectroweakCommonTopics2012>, visited on 06/09/2014 (cit. on p. 177).
- [ATL11f] ATLAS Collaboration. *WZ Electroweak Common Topics 2011*. 2011. Available at: <https://twiki.cern.ch/twiki/bin/viewauth/AtlasProtected/WZElectroweakCommonTopics2011> (cit. on p. 177).
- [WBG05] M. R. Whalley, D. Bourilkov, and R. C. Group. “The Les Houches Accord PDFs (LHAPDF) and Lhaglu”. In: (Aug. 2005), p. 8. arXiv: [0508110](https://arxiv.org/abs/0508110) [[hep-ph](https://arxiv.org/archive/hep)] (cit. on p. 180).
- [WB13] Mike Whalley and Andy Buckley. *The Les Houches Accord PDF Interface (LHAPDF) website*. 2013. Available at: <https://lhpdf.hepforge.org/>, visited on 01/13/2014 (cit. on p. 180).
- [ATL14g] ATLAS Collaboration. *Lowest un-prescaled triggers per data-taking period*. 2014. Available at: <https://twiki.cern.ch/twiki/bin/viewauth/Atlas/LowestUnprescaled>, visited on 06/14/2014 (cit. on p. 180).
- [ATLe] ATLAS Collaboration. *L2StarB electron efficiencies*. English. Tech. rep. (cit. on p. 184).
- [ATLa] ATLAS Collaboration. *Egamma Trigger Matching*. Available at: <https://twiki.cern.ch/twiki/bin/view/AtlasProtected/EgammaTriggerMatching>, visited on 06/22/2014 (cit. on p. 184).
- [ATL14m] ATLAS Collaboration. *Trigger Object Matching*. 2014. Available at: <https://twiki.cern.ch/twiki/bin/view/Atlas/TriggerObjectMatching>, visited on 06/22/2014 (cit. on p. 184).
- [ATLg] ATLAS Collaboration. *TrigMuonEfficiency Documentation*. Available at: <https://twiki.cern.ch/twiki/bin/view/Atlas/TrigMuonEfficiency>, visited on 06/22/2014 (cit. on p. 185).
- [ATL12g] ATLAS Collaboration. “Performance of the ATLAS muon trigger in 2011”. In: (July 2012) (cit. on pp. 185, 186, 188).

- [ATL12f] ATLAS Collaboration. “Performance of the ATLAS Electron and Photon Trigger in p-p Collisions at $\sqrt{s} = 7$ TeV in 2011”. In: (May 2012) (cit. on pp. 185, 187, 188).
- [ATL13a] ATLAS Collaboration. *EGamma: Recommended Triggers in 2012*. 2013. Available at: <https://twiki.cern.ch/twiki/bin/view/Atlas/TrigEgammaRecommendedTriggers2012>, visited on 10/03/2013 (cit. on p. 185).
- [ATL13f] ATLAS Collaboration. *Muons: Recommended triggers in 2012*. 2013. Available at: <https://twiki.cern.ch/twiki/bin/viewauth/Atlas/MuonTriggerPhysicsTriggerRecommendations2012>, visited on 06/22/2014 (cit. on p. 185).
- [ATL11d] ATLAS Collaboration. “Muon Momentum Resolution in First Pass Reconstruction of pp Collision Data Recorded by ATLAS in 2010”. In: (Mar. 2011) (cit. on p. 187).
- [ATL14a] ATLAS Collaboration. *ATLAS Muon Combined Performance Guidelines for Analyses of 2012 Data*. 2014. Available at: <https://twiki.cern.ch/twiki/bin/viewauth/AtlasProtected/MCPAnalysisGuidelinesData2012>, visited on 06/16/2014 (cit. on pp. 188, 192).
- [ATL13h] ATLAS Collaboration. *Preliminary results on the muon reconstruction efficiency, momentum resolution, and momentum scale in ATLAS 2012 pp collision data*. English. Tech. rep. Aug. 2013 (cit. on pp. 188, 192).
- [ATL11a] ATLAS Collaboration. “Determination of the muon reconstruction efficiency in ATLAS at the Z resonance in proton-proton collisions at $\sqrt{s}=7$ TeV”. In: (Feb. 2011) (cit. on p. 191).
- [ATL12a] ATLAS Collaboration. *A measurement of the muon reconstruction efficiency in 2010 ATLAS data using jpsi decays*. English. Tech. rep. Aug. 2012 (cit. on p. 191).
- [ATL11e] ATLAS Collaboration. “Muon reconstruction efficiency in reprocessed 2010 LHC proton-proton collision data recorded with the ATLAS detector”. In: (Apr. 2011) (cit. on pp. 192, 193).
- [ATL13g] ATLAS Collaboration. “Object Selections and Background estimates in the $H \rightarrow WW$ analysis with 20.7 fb^{-1} of data collected with the ATLAS detector at $\sqrt{s} = 8$ TeV”. In: (Nov. 2013) (cit. on pp. 192, 193).
- [ATLc] ATLAS Collaboration. *Electron Reconstruction*. Available at: <https://twiki.cern.ch/twiki/bin/view/AtlasProtected/ElectronReconstruction>, visited on 06/07/2014 (cit. on p. 193).
- [ATLb] ATLAS Collaboration. *Electron Identification Menu*. Available at: <https://twiki.cern.ch/twiki/bin/viewauth/AtlasProtected/TechnicalitiesForMedium1>, visited on 06/05/2014 (cit. on p. 193).
- [ATL14c] ATLAS Collaboration. *Calibration recommendations for 2011 and 2012 analyses using GEO-20 MC samples and Calibration-Hits-based calibration*. 2014. Available at: <https://twiki.cern.ch/twiki/bin/viewauth/AtlasProtected/EGammaCalibrationGEO20>, visited on 06/07/2014 (cit. on p. 194).

- [ATL13i] ATLAS Collaboration. “Supporting document on electron efficiency measurements using the 2012 LHC proton-proton collision data”. In: (Sept. 2013) (cit. on pp. 194, 196).
- [Lam+08] W Lampl, P Loch, S Menke, S Rajagopalan, S Laplace, G Unal, H Ma, S Snyder, D Lelas, and D Rousseau. *Calorimeter Clustering Algorithms*. Tech. rep. Apr. 2008 (cit. on p. 194).
- [ATL14d] ATLAS Collaboration. *Electron Efficiency Measurements for 2012 and 2011 Data*. Tech. rep. 2014 (cit. on pp. 196, 197).
- [LdV12] S Laplace and JB de Vivie. “Calorimeter isolation and pile-up”. In: (May 2012) (cit. on p. 197).
- [ATL14i] ATLAS Collaboration. *TrackMET 2011/2012*. 2014. Available at: <https://twiki.cern.ch/twiki/bin/viewauth/AtlasProtected/TrackMET>, visited on 06/28/2014 (cit. on pp. 201, 226).
- [ATL14f] ATLAS Collaboration. *How To Clean Jets 2011*. 2014. Available at: <https://twiki.cern.ch/twiki/bin/viewauth/AtlasProtected/HowToCleanJets2011>, visited on 06/20/2014 (cit. on p. 204).
- [ATLf] ATLAS Collaboration. *Recommendations for jet cleaning for data 2012*. Available at: <https://twiki.cern.ch/twiki/bin/view/AtlasProtected/HowToCleanJets2012>, visited on 06/20/2014 (cit. on p. 205).
- [ATL14k] ATLAS Collaboration. *Tile Trip Reader*. 2014. Available at: <https://twiki.cern.ch/twiki/bin/viewauth/Atlas/TileTripReader>, visited on 06/20/2014 (cit. on p. 205).
- [ATL14b] ATLAS Collaboration. *BCH Cleaning Tool*. 2014. Available at: <https://twiki.cern.ch/twiki/bin/viewauth/AtlasProtected/BCHCleaningTool>, visited on 06/20/2014 (cit. on pp. 205, 206).
- [Cam+09] J. Campbell, E. Castaneda-Miranda, Y. Fang, N. Kauer, B. Mellado, and Sau Wu. “Normalizing weak boson pair production at the Large Hadron Collider”. In: *Physical Review D* 80.5 (Sept. 2009), p. 054023. ISSN: 1550-7998. DOI: [10.1103/PhysRevD.80.054023](https://doi.org/10.1103/PhysRevD.80.054023). arXiv: [0906.2500](https://arxiv.org/abs/0906.2500) (cit. on p. 212).
- [ATL13d] ATLAS Collaboration. “Measurements of Higgs boson production and couplings in diboson final states with the ATLAS detector at the LHC”. In: *Physics Letters B* 726.1-3 (Oct. 2013), pp. 88–119. ISSN: 03702693. DOI: [10.1016/j.physletb.2013.08.010](https://doi.org/10.1016/j.physletb.2013.08.010). arXiv: [1307.1427](https://arxiv.org/abs/1307.1427) (cit. on p. 214).
- [ATL13b] ATLAS Collaboration. “Measurement of the WW Production Cross Section in Proton-Proton Collisions at $\sqrt{s} = 8$ TeV with the ATLAS Detector”. In: (Oct. 2013) (cit. on pp. 226, 237).
- [MRZ11] Bruce Mellado, Xifeng Ruan, and Zhiqing Zhang. “Extraction of Top Backgrounds in the Higgs Boson Search with the $H \rightarrow WW^* \rightarrow \ell\ell + \cancel{E}_T$ Decay with a Full-Jet Veto at the LHC”. In: (Jan. 2011). arXiv: [1101.1383](https://arxiv.org/abs/1101.1383) (cit. on p. 231).

- [ATL13e] ATLAS Collaboration. “Measurements of $W\gamma$ and $Z\gamma$ production in pp collisions at $\sqrt{s}=7$ TeV with the ATLAS detector at the LHC”. In: (Feb. 2013). arXiv: [1302.1283](#) (cit. on p. [237](#)).
- [JR75] F. James and M. Roos. “Minuit - a system for function minimization and analysis of the parameter errors and correlations”. en. In: *Computer Physics Communications* 10.6 (Dec. 1975), pp. 343–367. ISSN: 00104655. DOI: [10.1016/0010-4655\(75\)90039-9](#) (cit. on p. [245](#)).
- [Cow98] Glen Cowan. *Statistical Data Analysis*. Cowan1998: Oxford University Press, 1998, p. 216. ISBN: 0198501552 (cit. on pp. [250](#), [251](#)).
- [HK96] Andreas Höcker and Vakhtang Kartvelishvili. “SVD approach to data unfolding”. In: *Nuclear Instruments and Methods in Physics Research Section A: Accelerators, Spectrometers, Detectors and Associated Equipment* 372.3 (Apr. 1996), pp. 469–481. ISSN: 01689002. DOI: [10.1016/0168-9002\(95\)01478-0](#). arXiv: [9509307 \[hep-ph\]](#) (cit. on p. [251](#)).
- [DAg10] G. D’Agostini. “Improved iterative Bayesian unfolding”. In: (Oct. 2010), p. 31. arXiv: [1010.0632](#) (cit. on p. [251](#)).

DISCUSSION AND CONCLUSIONS

THE STANDARD MODEL is the most successful theory of elementary particles and fundamental interactions available to date. The theory describes the electromagnetic, weak and strong nuclear interactions which mediate the dynamics of elementary particles. It was developed as a collaborative effort driven by theoretical and experimental particle physicists alike. The success of the theory is attributed mainly to its ability to predict the existence of elementary particles.

The theoretical foundations are introduced in [chapter 1](#). Among the essentials discussed in this chapter is the role of symmetries and conservation laws, the principle of gauge invariance which gives rise to interaction fields and the definition of production [cross-sections](#). The electroweak unification requires that gauge bosons have no mass, which is in direct violation with the observed [W](#) and [Z boson](#) masses. Therefore, a crucial part of the model is provided by mechanism of spontaneous symmetry breaking which can be symbolised by $SU(3)_C \otimes SU(2)_L \otimes U(1)_Y \rightarrow SU(3)_C \otimes U(1)$. When a symmetrical system ends up in a ground state that does not possess all of the original symmetries, we get at least one massive scalar boson for each symmetry breaking. This is the basis of the Higgs mechanism, particles obtain their masses through the interaction with the Higgs field. The prediction of the [Higgs boson](#) was experimentally verified by the measurements simultaneously published by [ATLAS Collaboration \[ATL12\]](#) and [CMS Collaboration \[CMS12\]](#) in 2012.

Despite its success, the [Standard Model](#) only describes physics to a limited energy scale. Super-symmetry (SUSY) is a promising theoretical framework for physics beyond the [Standard Model](#). In its minimal version (MSSM), super-symmetry predicts the existence of two Higgs doubles (one charged) and one singlet. The discovery of additional Higgs fields would bring irrefutable evidence of new physics. The current observation of the neutral [Higgs boson](#) is consistent with both theories.

The [Large Hadron Collider](#) at [CERN](#) is the world's most powerful particle accelerator to date. For the analysis, the data from proton-proton collisions produced throughout the years 2011 and 2012 at the centre-of-mass energy of $\sqrt{s} = 7 \text{ TeV}$ and $\sqrt{s} = 8 \text{ TeV}$ are used. For [Run-II](#) (2014 onwards) the [LHC](#) is expected to reach its design energy of $\sqrt{s} = 14 \text{ TeV}$ upon conclusion of the upgrade phase. A sizeable part of the [LHC](#) programme is also dedicated to Pb – Pb and Pb – p collisions.

There are a total of seven experiments at the [LHC](#). Having multiple independent experiments is required to adhere to the principles of scientific method. Out of the main four experiments, [ATLAS](#) and [CMS](#) are general-purpose detectors designed to record a wide range of signals. The other two large experiments: [ALICE](#) and [LHCb](#) are highly specialized detectors designed to precisely

measure interactions from heavy ion collisions (when the LHC runs in that mode) and b-physics respectively. The additional experiments: TOTEM and LHCf are dedicated to forward physics while MoEDAL is designed specifically for exotic physics like the search for a magnetic monopole. The thesis provides an overview of the experiments at the LHC in section 2.4.

The results presented in this thesis were measured using the ATLAS detector. A detailed description of the experiment is provided in section 2.5. The detector system is composed of numerous subsystems each contributing to the measurement of collision products. At the inner-most radii is a high-resolution tracker (the Inner Detector, see section 2.5.4) while the calorimeter system and muon spectrometer are stacked in layers at the outer radii. The detector is submerged in a magnetic field which allows the measurement of charged particle momenta.

The data recorded with the ATLAS detector are pre-filtered using the trigger system which streams only a portion of data with interesting physics content. The reconstruction of physics objects from the detector signals is thoroughly discussed through section 3.3 including the discussion of experimental conditions affecting the measurement. The fully reconstructed data are then redistributed to the Worldwide LHC Computing Grid and analysed by the collaboration. The analysis software tools are discussed in detail in section 3.2.5, as they were essential for the practical part of this thesis.

Following the theoretical introduction into the problem, this thesis reports the results of the measurement of the WW production cross-section in pp collisions at centre-of-mass energy of 8 TeV with 20.28 fb^{-1} and 7 TeV with 4.64 fb^{-1} of data collected using the ATLAS detector. All diboson analyses deal with relatively small production cross-sections ranging from 1 pb (for ZZ) to 100 pb (for WW) in comparison with other SM processes shown in fig. 4.4. Coincidentally, the common strategy for the measurement is to consider only the leptonic decay modes since the resulting final states involve high- p_T isolated leptons (electrons or muons) providing a much higher signal over background ratio. In the analysis presented in this thesis, we measure the WW production cross-section in the three leptonic final states: $e^+e^- \cancel{E}_T$, $\mu^+\mu^- \cancel{E}_T$ and $e^\pm\mu^\mp \cancel{E}_T$. It should be noted that the measurement of the missing energy coming from the neutrino is challenging in high pile-up conditions.

To obtain the final result a number of inputs from our analysis team has been used. This involves mainly the dedicated studies of background estimates and cut optimization studies, the respective analysers are credited in the text. My individual contributions to the measurement are:

- Complete implementation of the selection at reconstruction level and experimental systematic uncertainties on the signal MC samples.
- Transfer factor method for top and Z + jets background including full systematics estimation as discussed in sections 4.9.2 and 4.9.4.
- Complete implementation of the fiducial selection (see section 4.7.4).
- Unfolding the differential cross-section measurement of the leading lepton p_T distribution, see section 4.11.
- Production of derived datasets, see section 4.6.1.
- Development of analysis framework as discussed in section 3.4.

The analysis cuts are optimized in order to select WW pairs in their leptonic final states and discriminate them from backgrounds. Section 4.4 provides a comprehensive discussion of the

triggers. Analysis-specific definitions of physics objects are given in [section 4.5](#) and selection criteria including kinematic distributions and their evolution between the $\sqrt{s} = 7$ TeV and 8 TeV analyses are shown in [section 4.2](#). Conceptually, the selection can be summarized as follows:

- Use single or di-lepton **triggers** (single electron, single muon, di-electron, di-muon or electron-muon **triggers**), see [section 4.4](#).
- Accept only events with exactly two isolated high- p_T leptons with opposite charge in order to select the WW final state and eliminate W + jets background. The hard cut is set to $p_T > 25$ (20) GeV for e^+e^- or $\mu^+\mu^-$ ($e^\pm\mu^\mp$ respectively), see [section 4.7.1](#).
- Require di-lepton mass $m_{\ell\ell} > 15$ (10) GeV in the e^+e^- , $\mu^+\mu^-$ ($e^\pm\mu^\mp$) channels to suppress the multi-jet backgrounds and remove the low mass spectrum that is not modelled by MC.
- Reject events in the same flavour channels (e^+e^- or $\mu^+\mu^-$) where the di-lepton mass $m_{\ell\ell}$ is close to the Z mass. This is handled in the simplest way possible: by cutting out a window around the Z peak: $|m_{\ell\ell} - m_Z| > 15$ GeV.
- Reject events with low E_T in order to account for the neutrinos coming from the WW decay and eliminate Z + jets background. The cut can be more relaxed in the combined flavour channels since there is no contamination from Z + jets. Various modified E_T variables are used, like the missing energy projection $E_{T,Rel}$, see [section 4.5.4.1](#).
- Reject events with (good) jets in order to eliminate $t\bar{t}$ and single-top backgrounds. This step is referred to as “jet veto” throughout the text.

In contrast to low- p_T analyses, diboson production measurements have the advantage of fairly low backgrounds. However, this advantage dissipates in high detector occupancy conditions caused by **pile-up**. The list of relevant backgrounds has been mentioned in the analysis overview, [section 4.3.2](#). The major backgrounds come from the production of W and Z in association with jets, where the jet is misidentified as lepton and the apparent E_T arises from **pile-up**. Additionally, the decay products from both $t\bar{t}$ and single-top processes contain the same final state signature as WW, which we consider as background. The remaining background contributions from the remaining di-bosons arises when in WZ events one of the final state leptons is not detected and in ZZ events if the di-lepton invariant mass is not reconstructed near the Z mass due to mis-measurements. Data-driven estimates for W + jets, Z + jets and $t\bar{t}$ backgrounds are discussed in [section 4.9](#). The contribution from other minor backgrounds: $Z\gamma$, $W\gamma$, ZWW and QCD multi-jet production backgrounds was found to be negligible. These backgrounds are fully estimated from MC.

We should note, that simply cutting on E_T fails to reliably remove Z + jets contamination in the same flavour channels as a large number of Z + jets events is reconstructed with high values of fake missing energy. To address this, the 7 TeV strategy uses an additional cut on the transverse momentum of the di-lepton system $p_T(\ell\ell)$. This strategy has proved to be ineffective in the 8 TeV analysis. Instead, a cut on a track-based measurement of **missing transverse energy** referred to as \cancel{p}_T in the text (defined in [section 4.5.4.3](#)) and the azimuthal angle difference between the original **missing transverse energy** and the **missing transverse momentum** vectors is used: $\Delta\phi(\cancel{E}_T, \cancel{p}_T)$, see also [section 4.5.4.4](#). Fiducial region had to be adjusted accordingly.

We have observed 6636 events in the $\sqrt{s} = 8$ TeV dataset and 1325 in the 7 TeV dataset. At $\sqrt{s} = 8$ TeV, the number of estimated signal events is 4218.80 and the number of estimated

background events 1666.10. At 7 TeV, we estimated 823.60 signal events and 358.00 background events. The combined production [cross-section](#) extrapolated to the total phase space is:

$$\sigma_{\text{tot}}(8 \text{ TeV}) = 71.4^{+1.2}_{-1.2} (\text{stat.})^{+5.0}_{-4.4} (\text{syst.})^{+2.2}_{-2.1} (\text{lumi.}) \text{ pb}, \quad (5.1)$$

$$\sigma_{\text{tot}}(7 \text{ TeV}) = 51.91 \pm 2.0 (\text{stat.}) \pm 3.92 (\text{syst.}) \pm 2.0 (\text{lumi.}) \text{ pb}. \quad (5.2)$$

The overall systematic uncertainty is 9 % and 7 % respectively. A comparison with $\sqrt{s} = 7 \text{ TeV}$ analysis were made throughout the text with detailed discussion of methods. The theoretical prediction derived using [MCFM](#) and CT10 PDFs is:

$$\sigma_{q\bar{q}/gg}(8 \text{ TeV}) = 58.7^{+3.0}_{-2.7} \text{ pb}, \quad (5.3)$$

$$\sigma_{q\bar{q}/gg}(7 \text{ TeV}) = 44.7^{+2.1}_{-1.9} \text{ pb}. \quad (5.4)$$

As shown in [fig. 5.1](#), all our measurements are above the [Standard Model](#) prediction. With respect to the $\sqrt{s} = 8 \text{ TeV}$ prediction, the statistical significance of the excess is $\pm 1.1\sigma$ in the e^+e^- channel, $\pm 1.3\sigma$ in the $\mu^+\mu^-$ channel and most significantly $\pm 2.1\sigma$ in the $e^\pm\mu^\mp$ channel (and the combined [cross-section](#) as well). The predicted [cross-section](#) differs in 0.70–5 % compared to the CT10 values quoted in [section 4.3.1](#).

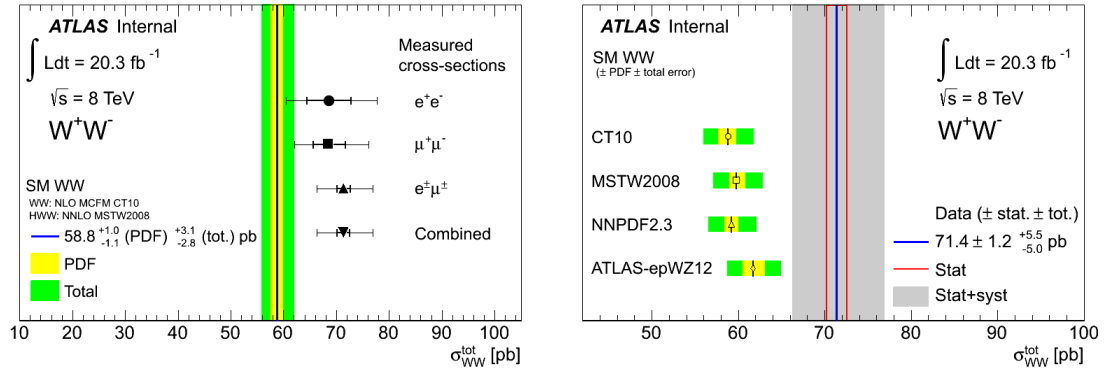


Figure 5.1: Comparison between the theoretical WW production [cross-sections](#) and the measurement at $\sqrt{s} = 8 \text{ TeV}$. The figure on the left shows the comparison with the CT10 PDF for e^+e^- , $\mu^+\mu^-$, $e^\pm\mu^\mp$ channels and the combined measurement. The yellow band represents the PDF uncertainty, the green band represents the theoretical uncertainties. The figure on the right shows the comparison between the measured combined WW production [cross-section](#) with theoretical predictions from different PDF sets. The red line signifies the statistical uncertainty on the measurement, the grey band shows the total uncertainty. The meaning of yellow and green bands for the PDF sets remains the same as in the left figure. Courtesy of Kristin Lohwasser.

As we have discussed in [section 4.3](#), several contributions to the [cross-section](#) have been neglected in this analysis and could potentially increase the prediction by as much as 5 % percent (2.90 pb). Investigating these effects is a potential goal for future analyses. Additional effects can also be attributed to the WW pairs produced through the $gg \rightarrow H \rightarrow WW$ process. Furthermore, there is currently no NNLO calculation of the $q\bar{q} \rightarrow WW \rightarrow \ell^+\nu\ell^-\bar{\nu}$ process available, an effect of a few percent is expected. Finally, the effect of electroweak corrections is expected to be of the order of $\approx 1\%$ on WW production.

Unfolded differential distributions were obtained for the leading lepton p_T , the final result is

shown in [fig. 5.2](#). The unfolded distributions are normalized to unity within the given kinematic range: i.e. the measured quantities is:

$$\mu = \frac{1}{\sigma_{\text{fid}}} \frac{d\sigma_{\text{fid}}}{dp_T^{\text{lead}}} \quad (5.5)$$

This normalization implies that the detector efficiency corrections, have no impact on the final result. This is intentional, as the efficiency corrections are in principle independent from the unfolded variable, leaving only the shape-dependent systematic effects. The resulting distributions are in reasonable agreement with the observations. The signal model is provided by [MC@NLO](#) at 7 TeV and by [POWHEG](#) at 8 TeV.

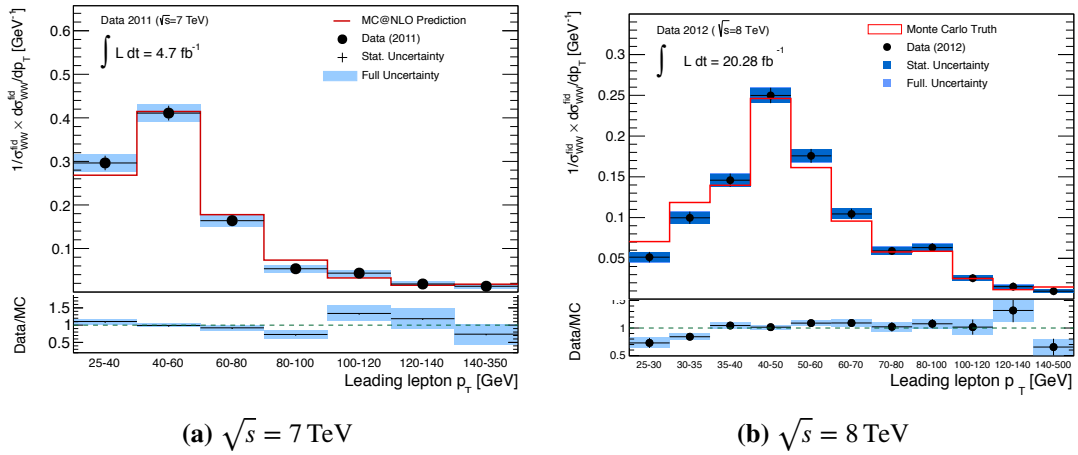


Figure 5.2: Unfolded distributions of leading lepton [transverse momentum](#) (p_T^{lead}).

The $\sqrt{s} = 8 \text{ TeV}$ results summarised in this thesis were published in by the [ATLAS Collaboration](#) [[ATL14](#)] and the 7 TeV baseline in [[ATL13](#)]. The group continues the work on the 8 TeV analysis with a goal of publishing paper later this year with the main goal being unfolded differential distributions and investigation of anomalous [triple gauge couplings](#).

Appendices

MONTÉ CARLO SAMPLES

This appendix provides the full list of samples used for background and signal modelling in the 7 TeV and 8 TeV analyses, as described in [section 4.3](#). The tables quote the [cross-sections](#), filter efficiencies ϵ_{filter} , numbers of events N_{MC} for each process and the respective [MC](#) generator.

A.1 Analysis at $\sqrt{s} = 7$ TeV

Process	σ [fb]	ϵ_{filter}	N_{MC}	Generator
$q\bar{q} \rightarrow WW \rightarrow e^+ \nu e^- \nu$	510.48	1.0	141 723	MC@NLO
$q\bar{q} \rightarrow WW \rightarrow \mu^+ \nu \mu^- \nu$	510.48	1.0	140 628	MC@NLO
$q\bar{q} \rightarrow WW \rightarrow e^+ \nu \mu^- \nu$	510.48	1.0	141 486	MC@NLO
$q\bar{q} \rightarrow WW \rightarrow \mu^+ \nu e^- \nu$	510.48	1.0	141 365	MC@NLO
$q\bar{q} \rightarrow WW \rightarrow e^+ \nu \tau^- \nu$	510.48	1.0	141 466	MC@NLO
$q\bar{q} \rightarrow WW \rightarrow \mu^+ \nu \tau^- \nu$	510.48	1.0	141 502	MC@NLO
$q\bar{q} \rightarrow WW \rightarrow \tau^+ \nu \mu^- \nu$	510.48	1.0	141 488	MC@NLO
$q\bar{q} \rightarrow WW \rightarrow \tau^+ \nu e^- \nu$	510.48	1.0	141 372	MC@NLO
$q\bar{q} \rightarrow WW \rightarrow \tau^+ \nu \tau^- \nu$	510.48	1.0	141 406	MC@NLO
$gg \rightarrow WW \rightarrow e^+ \nu e^- \nu$	15.24	0.9895	10 000	gg2ww
$gg \rightarrow WW \rightarrow \mu^+ \nu \mu^- \nu$	15.24	0.9890	9999	gg2ww
$gg \rightarrow WW \rightarrow e^+ \nu \mu^- \nu$	15.24	0.9899	10 000	gg2ww
$gg \rightarrow WW \rightarrow \mu^+ \nu e^- \nu$	15.24	0.9869	10 000	gg2ww
$gg \rightarrow WW \rightarrow e^+ \nu \tau^- \nu$	15.24	0.9232	10 000	gg2ww
$gg \rightarrow WW \rightarrow \mu^+ \nu \tau^- \nu$	15.24	0.9288	10 000	gg2ww
$gg \rightarrow WW \rightarrow \tau^+ \nu \mu^- \nu$	15.24	0.9289	10 000	gg2ww
$gg \rightarrow WW \rightarrow \tau^+ \nu e^- \nu$	15.24	0.9219	10 000	gg2ww
$gg \rightarrow WW \rightarrow \tau^+ \nu \tau^- \nu$	15.24	0.3269	10 000	gg2ww

Table A.1: WW signal production processes used for signal modelling for the 7 TeV analysis. The corresponding [cross-section](#), total number of events, filter efficiency and [MC](#) generator is listed for each sample.

Process	σ [pb]	k-factor	ϵ_{filter}	N_{MC}	Generator
ZnunuNp0	3533.76	1.25	0.01	54 949	Alpgen
ZnunuNp1	732.31	1.25	0.61	909 848	Alpgen
ZnunuNp2	222.34	1.25	0.88	169 899	Alpgen
ZnunuNp3	61.96	1.25	0.97	144 999	Alpgen
ZnunuNp4	15.77	1.25	0.99	309 849	Alpgen
ZnunuNp5	4.42	1.25	1.00	84 999	Alpgen
ZeeNp0($M > 40$ GeV)	668.32	1.25	1.00	6 618 284	Alpgen
ZeeNp1($M > 40$ GeV)	134.36	1.25	1.00	1 334 897	Alpgen
ZeeNp2($M > 40$ GeV)	40.54	1.25	1.00	909 999	Alpgen
ZeeNp3($M > 40$ GeV)	11.16	1.25	1.00	220 000	Alpgen
ZeeNp4($M > 40$ GeV)	2.88	1.25	1.00	60 000	Alpgen
ZeeNp5($M > 40$ GeV)	0.83	1.25	1.00	20 000	Alpgen
ZmumuNp0($M > 40$ GeV)	668.7	1.25	1.00	6 615 230	Alpgen
ZmumuNp1($M > 40$ GeV)	134.1	1.25	1.00	1 334 296	Alpgen
ZmumuNp2($M > 40$ GeV)	40.3	1.25	1.00	404 947	Alpgen
ZmumuNp3($M > 40$ GeV)	11.2	1.25	1.00	110 000	Alpgen
ZmumuNp4($M > 40$ GeV)	2.8	1.25	1.00	30 000	Alpgen
ZmumuNp5($M > 40$ GeV)	0.77	1.25	1.00	10 000	Alpgen
ZtautauNp0($M > 40$ GeV)	668.4	1.25	1.00	10 613 179	Alpgen
ZtautauNp1($M > 40$ GeV)	134.8	1.25	1.00	1 999 491	Alpgen
ZtautauNp2($M > 40$ GeV)	40.4	1.25	1.00	404 950	Alpgen
ZtautauNp3($M > 40$ GeV)	11.3	1.25	1.00	509 847	Alpgen
ZtautauNp4($M > 40$ GeV)	2.8	1.25	1.00	29 999	Alpgen
ZtautauNp5($M > 40$ GeV)	0.77	1.25	1.00	45 000	Alpgen
ZeeNp0($10 < M < 40$ GeV)	3051.62	1.22	1.00	994 949	Alpgen
ZeeNp1($10 < M < 40$ GeV)	87.87	1.22	1.00	299 998	Alpgen
ZeeNp2($10 < M < 40$ GeV)	41.40	1.22	1.00	499 997	Alpgen
ZeeNp3($10 < M < 40$ GeV)	8.38	1.22	1.00	149 998	Alpgen
ZeeNp4($10 < M < 40$ GeV)	1.85	1.22	1.00	40 000	Alpgen
ZeeNp5($10 < M < 40$ GeV)	0.46	1.22	1.00	10 000	Alpgen
ZmumuNp0($10 < M < 40$ GeV)	3051.62	1.22	1.00	999 849	Alpgen
ZmumuNp1($10 < M < 40$ GeV)	87.87	1.22	1.00	300 000	Alpgen
ZmumuNp2($10 < M < 40$ GeV)	41.45	1.22	1.00	999 995	Alpgen
ZmumuNp3($10 < M < 40$ GeV)	8.38	1.22	1.00	150 000	Alpgen
ZmumuNp4($10 < M < 40$ GeV)	1.85	1.22	1.00	39 999	Alpgen
ZmumuNp5($10 < M < 40$ GeV)	0.46	1.22	1.00	10 000	Alpgen
ZtautauNp0($10 < M < 40$ GeV)	3055.1	1.22	1.00	999 649	Alpgen
ZtautauNp1($10 < M < 40$ GeV)	84.93	1.22	1.00	299 999	Alpgen
ZtautauNp2($10 < M < 40$ GeV)	41.47	1.22	1.00	498 899	Alpgen
ZtautauNp3($10 < M < 40$ GeV)	8.36	1.22	1.00	150 000	Alpgen
ZtautauNp4($10 < M < 40$ GeV)	1.85	1.22	1.00	39 999	Alpgen
ZtautauNp5($10 < M < 40$ GeV)	0.46	1.22	1.00	10 000	Alpgen

Table A.2: Samples used to model Z + jets backgrounds for the 7 TeV analysis. The corresponding [cross-section](#), generator names, generator level filter efficiencies and total numbers of events are shown in the table. NpX ($X = 0 \dots 5$) in the process name refers to the number of additional partons in the final state. The k-factor of 1.0* indicate the value quoted from the generator, while a k-factor of 1.432 was applied in the analysis, see [section 4.3.2](#).

Process	σ [pb]	k-factor	ϵ_{filter}	N_{MC}	Generator
$t\bar{t}$	166.8	1.0	0.543	1 499 991	MC@NLO
Wt	15.74	1.0	1.0	994 897	AcerMC
t -channel – e^\pm	6.97	1.0	1.0	99 999	AcerMC
t -channel – μ^\pm	6.97	1.0	1.0	999 948	AcerMC
t -channel – τ^\pm	6.97	1.0	1.0	199 999	AcerMC
s -channel – e^\pm	0.5	1.0	1.0	199 899	AcerMC
s -channel – μ^\pm	0.5	1.0	1.0	199 850	AcerMC
s -channel – τ^\pm	0.5	1.0	1.0	190 000	AcerMC
bbcc_mu10mu10X	2830.0	1.0	1.0	296 599	PythiaB
bbcc_mu10e10X	4017.0	1.0	1.0	795 695	PythiaB
bbcc_e10e10X	1693.0	1.0	1.0	290 995	PythiaB

Table A.3: Samples used to model top backgrounds ($t\bar{t}$ and single top) for the 7 TeV analysis. The corresponding cross-section, total number of events, k-factor, filter efficiency and MC generator name is listed for each sample.

Process	σ [pb]	k-factor	ϵ_{filter}	N_{MC}	Generator
WenuNp0	6921.6	1.2	1	3358884	Alpgen
WenuNp1	1304.3	1.2	1	2499645	Alpgen
WenuNp2	378.3	1.2	1	3768632	Alpgen
WenuNp3	101.4	1.2	1	1008947	Alpgen
WenuNp4	25.9	1.2	1	250000	Alpgen
WenuNp5	7.0	1.2	1	69999	Alpgen
WmunuNp0	6919.6	1.2	1	3462942	Alpgen
WmunuNp1	1304.2	1.2	1	2498592	Alpgen
WmunuNp2	377.8	1.2	1	3768737	Alpgen
WmunuNp3	101.9	1.2	1	1008446	Alpgen
WmunuNp4	25.8	1.2	1	254950	Alpgen
WmunuNp5	6.9	1.2	1	70000	Alpgen
WtaunuNp0	6918.60	1.2	1	3418296	Alpgen
WtaunuNp1	1303.20	1.2	1	2499194	Alpgen
WtaunuNp2	378.18	1.2	1	3750986	Alpgen
WtaunuNp3	101.51	1.2	1	1009946	Alpgen
WtaunuNp4	25.64	1.2	1	249998	Alpgen
WtaunuNp5	7.04	1.2	1	65000	Alpgen

Table A.4: Samples used to model W + jets backgrounds for the 7 TeV analysis. The corresponding cross-sections, generator names, generator level filter efficiencies and total numbers of events are shown in this table. NpX ($X = 0 \dots 5$) in the process name refers to the number of additional partons in the final state.

Process	σ [pb]	k-factor	ϵ_{filter}	N_{MC}	Generator
ZeebbNp0	6.57	1.25	1.0	150 000	Alpgen
ZeebbNp1	2.48	1.25	1.0	100 000	Alpgen
ZeebbNp2	0.89	1.25	1.0	40 000	Alpgen
ZeebbNp3	0.39	1.25	1.0	10 000	Alpgen
ZmmbbNp0	6.56	1.25	1.0	149 950	Alpgen
ZmmbbNp1	2.47	1.25	1.0	100 000	Alpgen
ZmmbbNp2	0.89	1.25	1.0	40 000	Alpgen
ZmmbbNp3	0.39	1.25	1.0	9999	Alpgen
WcNp0	650.0	1.2	1.0	6 498 837	Alpgen
WcNp1	205.0	1.2	1.0	2 069 646	Alpgen
WcNp2	50.8	1.2	1.0	519 998	Alpgen
WcNp3	11.4	1.2	1.0	115 000	Alpgen
WcNp4	2.8	1.2	1.0	30 000	Alpgen
WbbNp0	47.32	1.2	1.0	474 997	Alpgen
WbbNp1	35.77	1.2	1.0	205 000	Alpgen
WbbNp2	17.34	1.2	1.0	174 499	Alpgen
WbbNp3	6.63	1.2	1.0	69 999	Alpgen
WccNp0	127.53	1.2	1.0	1 264 846	Alpgen
WccNp1	104.68	1.2	1.0	1 049 847	Alpgen
WccNp2	52.08	1.2	1.0	524 947	Alpgen
WccNp3	16.96	1.2	1.0	170 000	Alpgen

Table A.5: Samples used to model W + jets and Z + jets backgrounds with heavy quark flavour (b and c) backgrounds for the 7 TeV analysis. The corresponding cross-sections, generator names, generator level filter efficiencies and total numbers of events are shown in this table. NpX ($X = 0 \dots 5$) in the process name refers to the number of additional partons in the final state.

Process	σ [pb]	k-factor	ϵ_{filter}	N_{MC}	Generator
WZ	11.076	1.857	0.30986	999896	Herwig
ZZ	4.5964	1.847	0.21152	249998	Herwig
$W\gamma$ (Np0)	198.876	1.50	0.323	3198694	Alpgen
$W\gamma$ (Np1)	48.944	1.50	0.457	999998	Alpgen
$W\gamma$ (Np2)	17.183	1.50	0.551	499699	Alpgen
$W\gamma$ (Np3)	5.2981	1.50	0.632	199899	Alpgen
$W\gamma^* \rightarrow \ell \nu e^+ e^-$	4.80130	1.0*	1.0	294999	MadGraph
$W\gamma^* \rightarrow \ell \nu \mu^+ \mu^-$	1.45360	1.0*	1.0	149900	MadGraph
$W\gamma^* \rightarrow \ell \nu \tau^+ \tau^-$	0.21330	1.0*	1.0	50000	MadGraph

Table A.6: Samples used to model the di-boson backgrounds WZ, ZZ, $W\gamma$, $W\gamma^*$ for the 7 TeV analysis. The corresponding cross-sections, total number of events, k-factor, filter efficiency and MC generator name is listed for each sample. NpX ($X = 0 \dots 3$) in the sample name refers to the number of additional partons simulated in the final state. The k-factors of 1.0* indicate the value quoted from the generator, while a non-unity k-factor was applied in the analysis, see section 4.3.2.

A.2 Analysis at $\sqrt{s} = 8 \text{ TeV}$

Process	σ [pb]	ϵ_{filter}	N_{MC}	Generator
$q\bar{q} \rightarrow WW \rightarrow e^+ \nu e^- \nu$	0.62	1.0	299 700	POWHEG
$q\bar{q} \rightarrow WW \rightarrow \mu^+ \nu \mu^- \nu$	0.62	1.0	300 000	POWHEG
$q\bar{q} \rightarrow WW \rightarrow e^+ \nu \mu^- \nu$	0.62	1.0	299 999	POWHEG
$q\bar{q} \rightarrow WW \rightarrow \mu^+ \nu e^- \nu$	0.62	1.0	300 000	POWHEG
$q\bar{q} \rightarrow WW \rightarrow e^+ \nu \tau^- \nu$	0.62	1.0	299 996	POWHEG
$q\bar{q} \rightarrow WW \rightarrow \mu^+ \nu \tau^- \nu$	0.62	1.0	299 999	POWHEG
$q\bar{q} \rightarrow WW \rightarrow \tau^+ \nu \mu^- \nu$	0.62	1.0	300 000	POWHEG
$q\bar{q} \rightarrow WW \rightarrow \tau^+ \nu e^- \nu$	0.62	1.0	299 999	POWHEG
$q\bar{q} \rightarrow WW \rightarrow \tau^+ \nu \tau^- \nu$	0.62	1.0	299 999	POWHEG
$gg \rightarrow WW \rightarrow e^+ \nu e^- \nu$	0.017	1.0	30 000	gg2ww
$gg \rightarrow WW \rightarrow \mu^+ \nu \mu^- \nu$	0.017	1.0	30 000	gg2ww
$gg \rightarrow WW \rightarrow e^+ \nu \mu^- \nu$	0.017	1.0	30 000	gg2ww
$gg \rightarrow WW \rightarrow \mu^+ \nu e^- \nu$	0.017	1.0	30 000	gg2ww
$gg \rightarrow WW \rightarrow e^+ \nu \tau^- \nu$	0.017	1.0	30 000	gg2ww
$gg \rightarrow WW \rightarrow \mu^+ \nu \tau^- \nu$	0.017	1.0	30 000	gg2ww
$gg \rightarrow WW \rightarrow \tau^+ \nu \mu^- \nu$	0.017	1.0	30 000	gg2ww
$gg \rightarrow WW \rightarrow \tau^+ \nu e^- \nu$	0.017	1.0	30 000	gg2ww
$gg \rightarrow WW \rightarrow \tau^+ \nu \tau^- \nu$	0.017	1.0	30 000	gg2ww
$gg \rightarrow H \rightarrow WW \rightarrow \ell^+ \nu \ell^- \nu$	0.440563	0.49105	500 000	POWHEG

Table A.7: WW signal production processes including the 125 GeV Higgs used for signal modelling in the 8 TeV analysis. The corresponding [cross-section](#), total number of events, filter efficiency and [MC](#) generator is listed for each sample. At 8 TeV we switched to $q\bar{q} \rightarrow WW \rightarrow \ell^+ \nu \ell^- \bar{\nu}$ samples generated by [POWHEG](#) as it provided a better description of the observed data.

Process	σ [pb]	k-factor	ϵ_{filter}	N_{MC}	Generator
$t\bar{t}$	21.806	1.2177	1.0	9 977 338	MC@NLO
Wt	20.67	1.082	1.0	1 999 194	MC@NLO
t -channel – e^\pm	9.48	1.0	1.0	299 899	AcerMC
t -channel – μ^\pm	9.48	1.0	1.0	300 000	AcerMC
t -channel – τ^\pm	9.48	1.0	1.0	293 499	AcerMC
s -channel – e^\pm	0.606	1.0	1.0	199 899	MC@NLO
s -channel – μ^\pm	0.606	1.0	1.0	199 899	MC@NLO
s -channel – τ^\pm	0.606	1.0	1.0	199 799	MC@NLO

Table A.8: Processes used to model top backgrounds ($t\bar{t}$ and single top) for the 8 TeV analysis. The corresponding [cross-sections](#), total number of events, k-factor, filter efficiency and [MC](#) generator name is listed for each sample.

Process	σ [pb]	k-factor	ϵ_{filter}	N_{MC}	Generator
ZeeNp0($M > 60$ GeV)	718.89	1.18	1.0	6 619 984	Alpgen
ZeeNp1($M > 60$ GeV)	175.6	1.18	1.0	1 329 498	Alpgen
ZeeNp2($M > 60$ GeV)	58.849	1.18	1.0	404 998	Alpgen
ZeeNp3($M > 60$ GeV)	15.56	1.18	1.0	109 999	Alpgen
ZeeNp4($M > 60$ GeV)	3.9322	1.18	1.0	30 000	Alpgen
ZeeNp5($M > 60$ GeV)	1.1994	1.18	1.0	10 000	Alpgen
ZmumuNp0($M > 60$ GeV)	718.91	1.18	1.0	6 608 490	Alpgen
ZmumuNp1($M > 60$ GeV)	175.81	1.18	1.0	1 334 697	Alpgen
ZmumuNp2($M > 60$ GeV)	58.805	1.18	1.0	404 995	Alpgen
ZmumuNp3($M > 60$ GeV)	15.589	1.18	1.0	110 000	Alpgen
ZmumuNp4($M > 60$ GeV)	3.9072	1.18	1.0	30 000	Alpgen
ZmumuNp5($M > 60$ GeV)	1.1933	1.18	1.0	10 000	Alpgen
ZtautauNp0($M > 60$ GeV)	718.85	1.18	1.0	6 615 490	Alpgen
ZtautauNp1($M > 60$ GeV)	175.83	1.18	1.0	1 334 998	Alpgen
ZtautauNp2($M > 60$ GeV)	58.63	1.18	1.0	405 000	Alpgen
ZtautauNp3($M > 60$ GeV)	15.508	1.18	1.0	108 999	Alpgen
ZtautauNp4($M > 60$ GeV)	3.9526	1.18	1.0	30 000	Alpgen
ZtautauNp5($M > 60$ GeV)	1.1805	1.18	1.0	10 000	Alpgen
ZeeNp0($10 < M < 60$ GeV)	3477.9	1.19	0.01045	6 994 180	Alpgen
ZeeNp1($10 < M < 60$ GeV)	108.72	1.19	0.20383	4 497 280	Alpgen
ZeeNp2($10 < M < 60$ GeV)	52.837	1.19	0.13841	1 468 393	Alpgen
ZeeNp3($10 < M < 60$ GeV)	11.291	1.19	0.20806	438 397	Alpgen
ZeeNp4($10 < M < 60$ GeV)	2.5852	1.19	0.25262	108 930	Alpgen
ZeeNp5($10 < M < 60$ GeV)	0.6937	1.19	1.0	112 180	Alpgen
ZmumuNp0($10 < M < 60$ GeV)	3477.7	1.19	0.01086	6 984 686	Alpgen
ZmumuNp1($10 < M < 60$ GeV)	108.74	1.19	0.21096	4 491 587	Alpgen
ZmumuNp2($10 < M < 60$ GeV)	52.814	1.19	0.14253	1 503 397	Alpgen
ZmumuNp3($10 < M < 60$ GeV)	11.299	1.19	0.21385	439 699	Alpgen
ZmumuNp4($10 < M < 60$ GeV)	2.5793	1.19	0.25869	108 890	Alpgen
ZmumuNp5($10 < M < 60$ GeV)	0.69373	1.19	0.69373	115 000	Alpgen
ZtautauNp0($10 < M < 60$ GeV)	3477.9	1.19	0.00002	27 969	Alpgen
ZtautauNp1($10 < M < 60$ GeV)	108.71	1.19	0.00136	30 000	Alpgen
ZtautauNp2($10 < M < 60$ GeV)	52.827	1.19	0.00174	27 610	Alpgen
ZtautauNp3($10 < M < 60$ GeV)	11.311	1.19	0.00387	29 600	Alpgen
ZtautauNp4($10 < M < 60$ GeV)	2.592	1.19	1.0	365 497	Alpgen
ZtautauNp5($10 < M < 60$ GeV)	0.6929	1.19	1.0	114 420	Alpgen

Table A.9: Samples used to model Z + jets backgrounds for the 8 TeV analysis. The corresponding cross-sections, generator names, generator level filter efficiencies and total numbers of events are shown in this table. NpX ($X = 0 \dots 5$) in the process name refers to the number of additional partons in the final state.

Process	σ [pb]	k-factor	ϵ_{filter}	N_{MC}	Generator
WenuNp0	8037.1	1.19	1.0	3 459 894	Alpgen
WenuNp1	1579.2	1.19	1.0	2 499 491	Alpgen
WenuNp2	477.2	1.19	1.0	3 769 487	Alpgen
WenuNp3	133.93	1.19	1.0	1 009 997	Alpgen
WenuNp4	35.622	1.19	1.0	249 999	Alpgen
WenuNp5	10.533	1.19	1.0	70 000	Alpgen
WmunuNp0	8040	1.19	1.0	3 469 692	Alpgen
WmunuNp1	1580.3	1.19	1.0	2 499 694	Alpgen
WmunuNp2	477.5	1.19	1.0	3 769 886	Alpgen
WmunuNp3	133.94	1.19	1.0	1 006 698	Alpgen
WmunuNp4	35.636	1.19	1.0	254 999	Alpgen
WmunuNp5	10.571	1.19	1.0	69 900	Alpgen
WtaunuNp0	8035.8	1.19	1.0	3 419 992	Alpgen
WtaunuNp1	1579.8	1.19	1.0	2 499 793	Alpgen
WtaunuNp2	477.55	1.19	1.0	3 765 989	Alpgen
WtaunuNp3	133.79	1.19	1.0	1 009 998	Alpgen
WtaunuNp4	35.583	1.19	1.0	249 998	Alpgen
WtaunuNp5	10.54	1.19	1.0	65 000	Alpgen

Table A.10: Samples used to model Z + jets backgrounds for the 8 TeV analysis. The corresponding cross-sections, generator names, generator level filter efficiencies and total numbers of events are shown in this table. NpX ($X = 0 \dots 5$) in the process name refers to the number of additional partons in the final state.

Process	σ [pb]	k-factor	ϵ_{filter}	N_{MC}	Generator
WcNp0	807.89	1.19	1.0	6 499 580	Alpgen
WcNp1	267.61	1.19	1.0	2 069 796	Alpgen
WcNp2	69.823	1.19	1.0	519 998	Alpgen
WcNp3	20.547	1.19	1.0	110 000	Alpgen
WcNp4	4.3069	1.19	1.0	19 900	Alpgen
WbbNp0	55.682	1.19	1.0	474 997	Alpgen
WbbNp1	45.243	1.19	1.0	359 500	Alpgen
WbbNp2	23.246	1.19	1.0	174 898	Alpgen
WbbNp3	11.144	1.19	1.0	50 000	Alpgen
WccNp0	150.19	1.19	1.0	1 274 900	Alpgen
WccNp1	132.68	1.19	1.0	1 049 994	Alpgen
WccNp2	71.807	1.19	1.0	524 900	Alpgen
WccNp3	30.264	1.19	1.0	169 500	Alpgen

Table A.11: Samples used to model W + jets backgrounds with heavy quark flavour (b and c) backgrounds for the 8 TeV analysis. The corresponding cross-sections, generator names, generator level filter efficiencies and total numbers of events are shown in this table. NpX ($X = 0 \dots 5$) in the process name refers to the number of additional partons in the final state.

Process	σ [pb]	k-factor	ϵ_{filter}	N_{MC}	Generator
$W^+Z \rightarrow e^+ \nu e^+ e^-$	1.407	1.0	0.29456	190 000	POWHEG
$W^+Z \rightarrow e^+ \nu \mu^+ \mu^-$	0.9328	1.0	0.35211	190 000	POWHEG
$W^+Z \rightarrow e^+ \nu \tau^+ \tau^-$	0.1746	1.0	0.16682	76 000	POWHEG
$W^+Z \rightarrow \mu^+ \nu e^+ e^-$	1.399	1.0	0.29351	189 999	POWHEG
$W^+Z \rightarrow \mu^+ \nu \mu^+ \mu^-$	0.9537	1.0	0.35132	190 000	POWHEG
$W^+Z \rightarrow \mu^+ \nu \tau^+ \tau^-$	0.1746	1.0	0.16863	76 000	POWHEG
$W^+Z \rightarrow \tau^+ \nu e^+ e^-$	1.399	1.0	0.14289	75 400	POWHEG
$W^+Z \rightarrow \tau^+ \nu \mu^+ \mu^-$	0.9382	1.0	0.18256	76 000	POWHEG
$W^+Z \rightarrow \tau^+ \nu \tau^+ \tau^-$	0.1719	1.0	0.058517	19 000	POWHEG
$W^-Z \rightarrow e^- \nu e^+ e^-$	0.9795	1.0	0.29694	189 899	POWHEG
$W^-Z \rightarrow e^- \nu \mu^+ \mu^-$	0.639	1.0	0.35302	190 000	POWHEG
$W^-Z \rightarrow e^- \nu \tau^+ \tau^-$	0.1125	1.0	0.15969	76 000	POWHEG
$W^-Z \rightarrow \mu^- \nu e^+ e^-$	0.9359	1.0	0.29766	76 000	POWHEG
$W^-Z \rightarrow \mu^- \nu \mu^+ \mu^-$	0.6488	1.0	0.35414	190 000	POWHEG
$W^-Z \rightarrow \mu^- \nu \tau^+ \tau^-$	0.1125	1.0	0.16023	190 000	POWHEG
$W^-Z \rightarrow \tau^- \nu e^+ e^-$	0.9359	1.0	0.14803	76 000	POWHEG
$W^-Z \rightarrow \tau^- \nu \mu^+ \mu^-$	0.638	1.0	0.18657	76 000	POWHEG
$W^-Z \rightarrow \tau^- \nu \tau^+ \tau^-$	0.1107	1.0	0.056651	19 000	POWHEG
$ZZ \rightarrow 4e$	0.0735	1.0	0.90765	1 099 997	POWHEG
$ZZ \rightarrow 2e2\mu$	0.1708	1.0	0.82724	1 599 696	POWHEG
$ZZ \rightarrow 2e2\tau$	0.1708	1.0	0.58278	599 899	POWHEG
$ZZ \rightarrow 4\mu$	0.0735	1.0	0.91241	1 099 798	POWHEG
$ZZ \rightarrow 2\mu2\tau$	0.1708	1.0	0.58725	600 000	POWHEG
$ZZ \rightarrow 4\tau$	0.0735	1.0	0.10604	300 000	POWHEG
$ZZ \rightarrow 2e2\nu$	0.168	1.0	1.0	299 400	POWHEG
$ZZ \rightarrow 2\mu2\nu$	0.168	1.0	1.0	300 000	POWHEG
$ZZ \rightarrow 2\tau2\nu$	0.168	1.0	1.0	299 999	POWHEG
$W\gamma$ (Np0)	229.88	1.15	0.31372	14 296 258	Alpgen
$W\gamma$ (Np1)	59.518	1.15	0.44871	5 393 984	Alpgen
$W\gamma$ (Np2)	21.39	1.15	0.54461	2 899 389	Alpgen
$W\gamma$ (Np3)	7.1203	1.15	0.62974	859 697	Alpgen
$W\gamma$ (Np4)	2.1224	1.15	1.0	364 999	Alpgen
$W\gamma$ (Np5)	0.46612	1.15	1.0	60 000	Alpgen
$W\gamma^* \rightarrow \ell \nu e^+ e^-$ ($M_{\gamma^*} < 7 \text{ GeV}$)	5.6	1.3	1.0	399 699	MadGraph
$W\gamma^* \rightarrow \ell \nu \mu^+ \mu^-$ ($M_{\gamma^*} < 7 \text{ GeV}$)	1.3777	1.3	1.0	299 800	MadGraph
$W\gamma^* \rightarrow \ell \nu \tau^+ \tau^-$ ($M_{\gamma^*} < 7 \text{ GeV}$)	0.14717	1.3	1.0	30 000	MadGraph

Table A.12: Processes used to model di-boson backgrounds WZ, ZZ, $W\gamma$, and $W\gamma^*$ in the 8 TeV analysis. The corresponding cross-sections, generator names, generator level filter efficiencies and total numbers of events are shown in the table. NpX ($X = 0 \dots 3$) in the process name refers to the number of additional partons in the final state.

SYSTEMATICS CUT-FLOW PROGRESSION

This appendix complements the [section 4.8](#) by providing more detailed numbers for [MC](#) driven systematic uncertainties. [Table B.1](#) show systematic yields for signal and all background models estimated by [MC](#). Each number presents a percentage difference with respect to nominal yields at the final cut stage (jet veto). The following line for each systematic source shows the statistical uncertainty. These [JES](#) components are listed in [table B.2](#).

The progress of systematic uncertainties with each cut stage are shown in the following tables:

Table	Channel	Comment
Table B.3	e^+e^-	individual systematics
Table B.4	e^+e^-	jet energy scale components
Table B.5	$\mu^+\mu^-$	individual systematics
Table B.6	$\mu^+\mu^-$	jet energy scale components
Table B.7	$e^\pm\mu^\mp$	individual systematics
Table B.8	$e^\pm\mu^\mp$	jet energy scale components
Table B.9	$\ell^+\ell^-$	individual systematics
Table B.10	$\ell^+\ell^-$	jet energy scale components

Systematic	e^+e^- [%]				$\mu^+\mu^-$ [%]				$e^+e^-\mu^+$ [%]				$e^+e^-\mu^-$ [%]			
	Signal	Z+jets	Top	Dibosons	W+jets	Signal	Z+jets	Top	Dibosons	W+jets	Signal	Z+jets	Top	Dibosons	W+jets	Signal
Pileup avg	1.87	1.92	0.22	1.4	55.38	1.97	4.1	0.17	0.28	11.93	1.3	1.32	0.31	0.91	1.85	1.44
stats	0.02	0.2	0.01	0.07	39.16	0.01	0.33	0.01	0.28	0.0	0.0	0.28	0.01	0.03	0.5	0.0
MuMisSmear avg	0.0	0.62	0.12	0.55	0.0	0.05	0.47	0.23	3.12	0.0	0.01	0.0	0.23	2.15	0.01	0.14
stats	0.0	0.06	0.01	0.03	0.0	0.0	0.03	0.01	0.11	0.0	0.0	0.0	0.01	0.06	0.0	0.0
MuIDSmear avg	0.02	0.38	0.89	0.87	0.0	1.53	5.45	4.04	2.31	0.0	0.54	2.33	1.06	0.39	1.29	0.64
stats	0.0	0.04	0.04	0.04	0.0	0.0	0.43	0.19	0.08	0.0	0.0	0.49	0.02	0.01	0.34	0.0
MuScale avg	0.0	0.0	0.0	0.0	0.0	0.35	1.76	0.48	0.66	0.0	0.1	0.0	0.07	0.07	0.01	0.12
stats	0.0	0.0	0.0	0.0	0.0	0.0	0.14	0.02	0.02	0.0	0.0	0.0	0.0	0.0	0.0	0.0
ElRes avg	0.18	2.93	0.78	0.81	0.0	0.0	0.0	0.0	0.0	0.0	0.03	6.3	0.08	0.12	0.11	0.02
stats	0.0	0.3	0.04	0.04	0.0	0.0	0.0	0.0	0.0	0.0	0.0	1.33	0.0	0.0	0.03	0.0
ElScaleZeeAll avg	1.4	7.44	1.01	0.5	0.32	0.0	0.0	0.0	0.0	0.0	0.36	5.8	0.24	0.96	0.11	0.39
stats	0.01	0.76	0.05	0.03	0.23	0.0	0.0	0.0	0.0	0.0	0.0	1.22	0.01	0.03	0.03	0.0
ElScaleR12Stat avg	0.06	0.17	0.31	0.25	0.0	0.0	0.0	0.0	0.0	0.0	0.09	2.26	0.07	0.61	0.09	0.07
stats	0.0	0.02	0.01	0.01	0.0	0.0	0.0	0.0	0.0	0.0	0.0	0.48	0.0	0.02	0.03	0.0
ElScalePSSStat avg	0.06	0.21	0.31	0.03	0.0	0.0	0.0	0.0	0.0	0.0	0.03	0.0	0.06	0.18	0.09	0.02
stats	0.0	0.02	0.02	0.0	0.0	0.0	0.0	0.0	0.0	0.0	0.0	0.0	0.0	0.01	0.03	0.0
ElScaleLowPt avg	0.02	0.0	0.0	0.02	0.0	0.0	0.0	0.02	0.0	0.0	0.01	0.0	0.0	0.1	0.0	0.01
stats	0.0	0.0	0.0	0.0	0.0	0.0	0.0	0.0	0.0	0.0	0.0	0.0	0.0	0.0	0.0	0.0
METSoftReso avg	0.31	5.12	1.09	1.17	0.0	0.5	3.53	0.34	0.45	0.0	0.29	7.29	0.34	0.5	8.0	0.32
stats	0.0	0.52	0.05	0.06	0.0	0.0	0.28	0.02	0.02	0.0	0.0	1.53	0.01	0.01	2.13	0.0
METSoftScale avg	4.21	6.53	5.57	2.46	0.0	3.81	4.36	3.13	3.7	8.06	2.34	5.19	1.79	2.37	8.03	2.71
stats	0.04	0.67	0.27	0.13	0.0	0.03	0.35	0.15	0.12	6.95	0.01	1.09	0.04	0.06	2.14	0.01
MPTSoftReso avg	0.04	2.18	0.72	0.53	0.0	0.21	1.77	0.14	0.78	42.77	0.05	10.52	0.05	0.45	1.53	0.08
stats	0.0	0.22	0.04	0.03	0.0	0.0	0.14	0.01	0.03	36.85	0.0	2.22	0.0	0.01	0.41	0.0
MPTSoftScale avg	0.62	6.42	0.67	0.35	0.0	0.49	9.44	1.73	1.1	42.77	0.31	13.83	0.45	0.07	0.01	0.36
stats	0.01	0.65	0.04	0.02	0.0	0.0	0.75	0.08	0.03	36.85	0.0	2.91	0.01	0.0	0.0	0.0
EEHFD avg	1.88	2.42	1.69	2.18	1.8	0.0	0.0	0.0	0.0	0.0	0.88	1.31	0.83	1.27	1.0	0.83
stats	0.02	0.25	0.08	0.11	1.27	0.0	0.0	0.0	0.0	0.0	0.0	0.28	0.02	0.03	0.27	0.0
EEHFTK avg	0.63	0.75	0.68	0.74	0.51	0.0	0.0	0.0	0.0	0.0	0.29	0.37	0.32	0.38	0.29	0.28
stats	0.01	0.08	0.03	0.04	0.36	0.0	0.0	0.0	0.0	0.0	0.0	0.08	0.01	0.01	0.08	0.0
MuEff avg	0.0	0.0	0.0	0.0	0.0	0.77	0.75	0.81	0.8	0.72	0.39	0.41	0.4	0.38	0.38	0.41
stats	0.0	0.0	0.0	0.0	0.0	0.01	0.06	0.04	0.03	0.62	0.0	0.09	0.01	0.01	0.1	0.0
ElIso avg	0.44	0.53	0.38	0.46	0.41	0.0	0.0	0.0	0.0	0.0	0.21	0.26	0.2	0.27	0.24	0.2
stats	0.0	0.05	0.02	0.02	0.29	0.0	0.0	0.0	0.0	0.0	0.0	0.06	0.0	0.01	0.06	0.0
MuIso avg	0.0	0.0	0.0	0.0	0.0	1.13	1.17	1.1	1.13	1.21	0.56	0.59	0.55	0.59	0.64	0.6
stats	0.0	0.0	0.0	0.0	0.0	0.0	0.09	0.05	0.04	1.05	0.0	0.12	0.01	0.01	0.17	0.0
TrigMatchMu avg	0.0	0.0	0.0	0.0	0.0	2.84	2.89	2.8	2.83	2.96	0.27	0.57	0.2	0.44	0.21	0.62
stats	0.0	0.0	0.0	0.0	0.0	0.02	0.23	0.13	0.09	2.55	0.0	0.12	0.0	0.01	0.06	0.0
TrigMatchEl avg	2.52	3.32	2.07	2.75	1.72	0.0	0.0	0.0	0.0	0.0	0.3	0.34	0.27	0.44	0.46	0.44
stats	0.02	0.34	0.1	0.14	1.22	0.0	0.0	0.0	0.0	0.0	0.0	0.07	0.01	0.01	0.12	0.0
JER avg	1.29	13.54	16.79	0.6	0.0	1.22	37.29	18.42	2.35	0.0	1.4	16.35	15.07	0.14	2.19	1.37
stats	0.01	1.38	0.82	0.03	0.0	0.01	2.96	0.86	0.08	0.0	0.0	3.44	0.3	0.0	0.58	0.0
JVF avg	0.24	1.23	1.57	0.4	0.0	0.23	1.28	1.05	0.41	0.0	0.22	0.03	1.79	0.24	0.0	0.22
stats	0.0	0.13	0.08	0.02	0.0	0.0	0.11	0.05	0.02	0.0	0.0	0.01	0.04	0.01	0.0	0.0
JetEffB avg	0.0	0.0	0.0	0.0	0.0	0.0	0.0	0.0	0.0	0.0	0.0	0.0	0.0	0.0	0.0	0.0
stats	0.0	0.0	0.0	0.0	0.0	0.0	0.0	0.0	0.0	0.0	0.0	0.0	0.0	0.0	0.0	0.0
JetEffC avg	0.0	0.0	0.0	0.0	0.0	0.0	0.0	0.0	0.0	0.0	0.0	0.0	0.0	0.0	0.0	0.0
stats	0.0	0.0	0.0	0.0	0.0	0.0	0.0	0.0	0.0	0.0	0.0	0.0	0.0	0.0	0.0	0.0
JetEffLight avg	0.0	0.0	0.0	0.0	0.0	0.0	0.0	0.0	0.0	0.0	0.0	0.0	0.0	0.0	0.0	0.0
stats	0.0	0.0	0.0	0.0	0.0	0.0	0.0	0.0	0.0	0.0	0.0	0.0	0.0	0.0	0.0	0.0

Table B.1: Systematic uncertainties including stat. errors. The numbers are shown for each channel separately and for the combined channel. The up and down component of each systematic uncertainty has been symmetrized (indicated by the “avg” label).

Systematic	e^+e^- [%]				$\mu^+\mu^-$ [%]				$e^+\mu^-$ [%]				$e^+\mu^+$ [%]			
	Signal	Z+jets	W+jets	Dibosons	Signal	Z+jets	W+jets	Dibosons	Signal	Z+jets	W+jets	Dibosons	Signal	Z+jets	W+jets	Dibosons
JES EffectiveNP_1 avg	0.7	2.15	3.9	3.14	0.92	5.38	1.19	3.76	0.79	0.78	1.42	1.31	0.8	2.11	3.65	1.23
stats	0.01	0.22	0.16	0.05	0.01	0.43	0.18	0.04	0.0	0.17	0.08	0.03	0.0	0.21	0.06	0.03
JES EffectiveNP_2 avg	1.25	4.88	2.19	5.29	1.57	7.49	6.74	2.13	1.38	5.14	6.24	2.24	1.39	6.0	6.21	2.22
stats	0.01	0.5	0.11	0.26	0.01	0.6	0.32	0.07	0.0	1.08	0.13	0.06	0.0	0.59	0.11	0.05
JES EffectiveNP_3 avg	0.53	1.59	2.41	2.41	0.7	4.96	3.28	0.96	0.6	0.78	2.75	1.11	0.61	1.85	2.79	1.03
stats	0.01	0.16	0.12	0.04	0.01	0.4	0.16	0.03	0.0	0.17	0.06	0.03	0.0	0.18	0.05	0.02
JES EffectiveNP_4 avg	0.21	1.09	0.83	0.37	0.27	0.56	1.21	0.14	0.22	0.3	1.0	0.45	0.22	0.54	1.01	0.38
stats	0.0	0.11	0.04	0.02	0.0	0.05	0.06	0.0	0.0	0.07	0.02	0.01	0.0	0.06	0.02	0.01
JES EffectiveNP_5 avg	0.26	1.01	1.02	0.36	0.32	0.42	1.67	0.47	0.27	0.3	1.14	0.57	0.28	0.47	1.21	0.53
stats	0.0	0.1	0.05	0.02	0.0	0.03	0.08	0.02	0.0	0.07	0.02	0.01	0.0	0.05	0.02	0.01
JES NPVOffset avg	0.51	3.32	1.63	0.44	0.71	4.07	3.7	1.3	0.61	1.84	2.2	1.19	0.62	2.96	2.36	1.11
stats	0.01	0.34	0.08	0.03	0.01	0.32	0.17	0.05	0.0	0.39	0.05	0.03	0.0	0.3	0.04	0.02
JES MuOffset avg	0.22	0.05	0.82	0.17	0.24	1.16	1.14	0.72	0.27	5.76	0.92	0.8	0.26	2.97	0.95	0.68
stats	0.0	0.01	0.04	0.01	0.0	0.09	0.05	0.03	0.0	1.21	0.02	0.02	0.0	0.3	0.02	0.01
JES PileupPt avg	0.02	0.37	0.07	0.0	0.02	0.71	0.03	0.0	0.0	0.0	0.02	0.01	0.0	0.34	0.02	0.01
stats	0.0	0.04	0.0	0.0	0.0	0.06	0.0	0.0	0.0	0.0	0.0	0.0	0.0	0.04	0.0	0.0
JES PileupRho avg	0.96	3.29	3.97	1.47	1.27	6.19	5.18	1.59	1.07	3.61	5.09	1.78	1.09	4.55	4.97	1.71
stats	0.01	0.34	0.2	0.08	0.01	0.49	0.24	0.06	0.0	0.76	0.1	0.05	0.0	0.45	0.09	0.04
JES Closeby avg	0.0	0.0	0.0	0.0	0.0	0.0	0.0	0.0	0.0	0.0	0.0	0.0	0.0	0.0	0.0	0.0
stats	0.0	0.0	0.0	0.0	0.0	0.0	0.0	0.0	0.0	0.0	0.0	0.0	0.0	0.0	0.0	0.0
JES FlavourComp avg	1.78	6.02	2.52	2.98	2.08	12.16	3.75	2.53	1.85	6.35	2.86	3.19	1.88	8.53	2.96	3.05
stats	0.02	0.62	0.13	0.16	0.02	0.97	0.18	0.09	0.01	1.34	0.06	0.08	0.01	0.84	0.05	0.06
JES FlavourResp avg	0.9	3.32	1.73	1.48	1.27	5.68	1.98	1.7	1.07	0.78	1.75	1.64	1.08	2.43	1.78	1.63
stats	0.01	0.34	0.09	0.08	0.01	0.45	0.1	0.06	0.0	0.17	0.04	0.04	0.0	0.24	0.03	0.04
JES BScale avg	0.01	0.29	3.71	0.01	0.01	0.0	4.22	0.0	0.01	0.0	4.14	0.02	0.01	0.05	4.1	0.01
stats	0.0	0.03	0.19	0.0	0.0	0.0	0.2	0.0	0.0	0.0	0.09	0.0	0.0	0.01	0.07	0.0
JES Baseline avg	2.44	8.05	10.62	4.09	2.8	12.73	11.99	3.79	2.61	8.96	10.22	4.65	2.62	10.25	10.53	4.43
stats	0.02	0.82	0.52	0.21	0.02	1.01	0.56	0.13	0.01	1.89	0.21	0.12	0.01	1.01	0.19	0.09
JES Total avg	3.62	12.58	15.75	5.6	4.22	19.56	15.97	5.26	3.94	13.46	15.02	6.72	3.95	15.66	15.25	6.32
stats	0.03	1.28	0.77	0.29	0.03	1.55	0.75	0.18	0.01	2.84	0.3	0.18	0.01	1.55	0.26	0.13

Table B.2: Jet energy scale components systematics including stat. errors. The numbers are shown for each channel separately and for the combined channel. The up and down component of each systematic uncertainty has been symmetrized (indicated by the “avg” label). JES Baseline is introduced for comparison between components and indicates the quadratic sum of JES Effective_NP* components and is not included in the total uncertainty to avoid duplication.

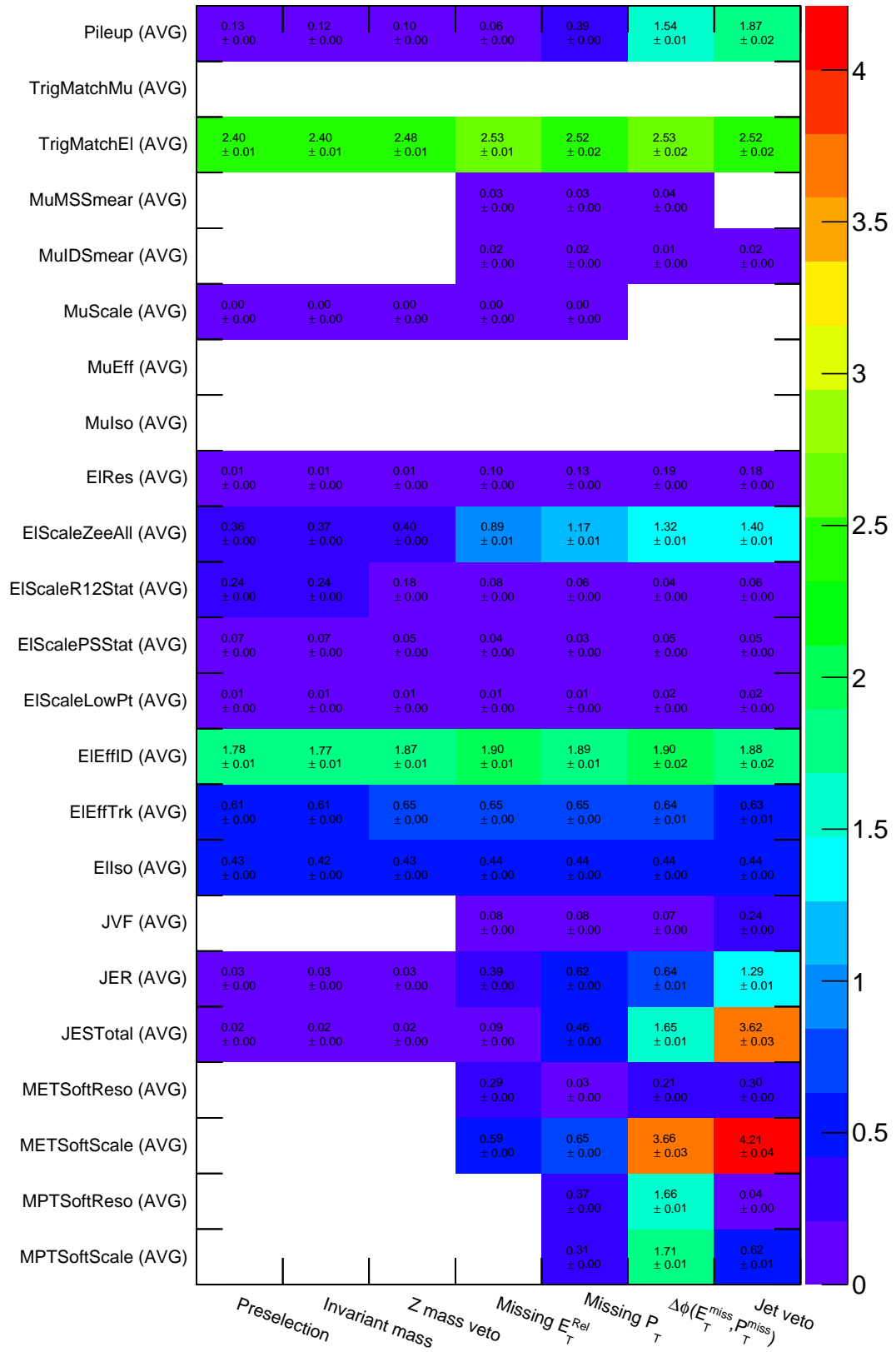


Table B.3: Cut progression of systematic uncertainties on the signal samples for e^+e^- channel. The table shows the full set of systematics evolving as we introduce analysis cuts (columns left to right). Each number presents a percentage difference with respect to nominal yield at a given cut stage. Statistical uncertainty on each yield is shown. The up and down component of each systematic uncertainty has been symmetrized (indicated by the “AVG” label).

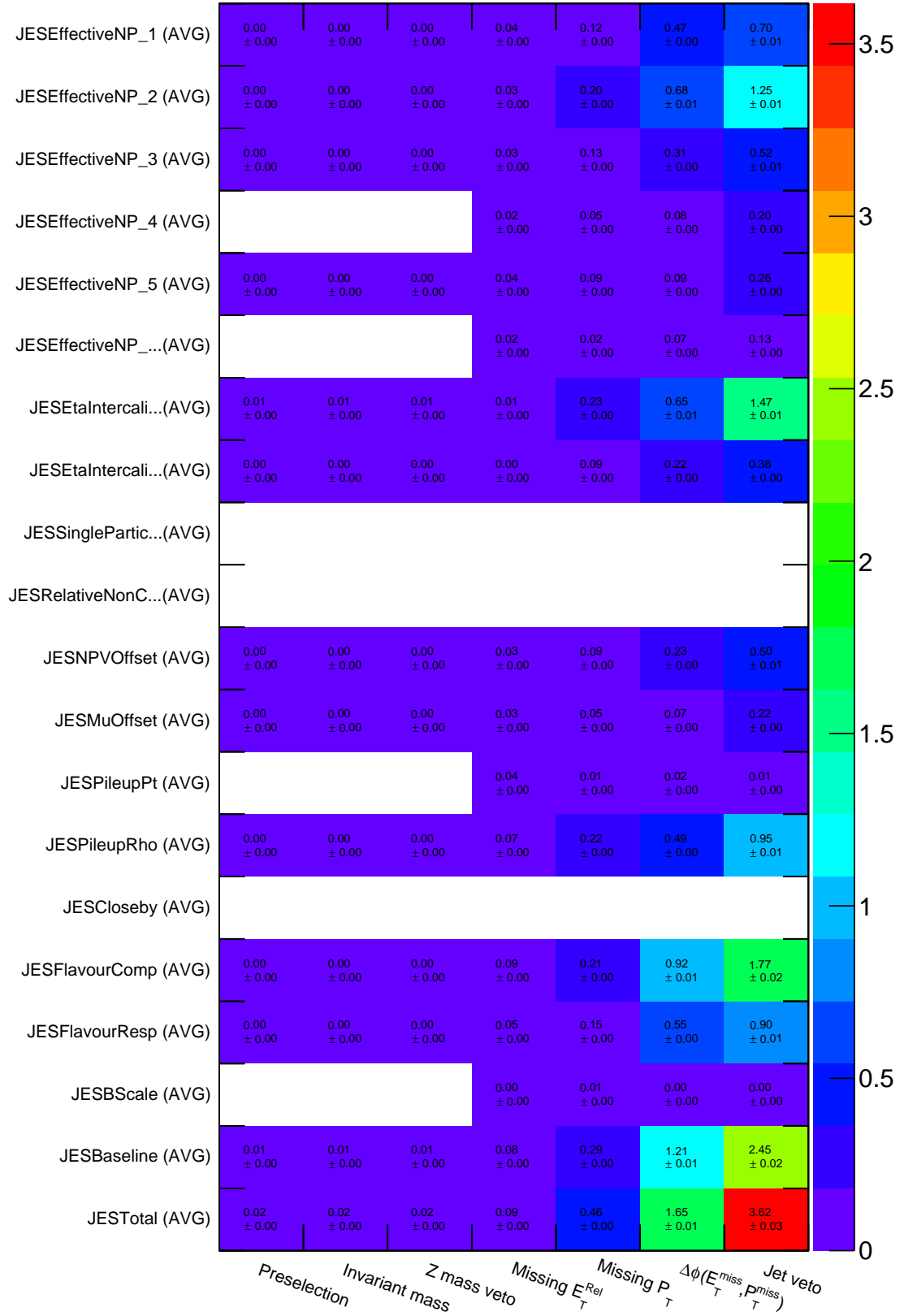


Table B.4: Cut progression of jet energy scale components systematics on the signal samples for e^+e^- channel. The table shows the full set of systematics evolving as we introduce analysis cuts (columns left to right). Each number presents a percentage difference with respect to nominal yield at a given cut stage. Statistical uncertainty on each yield is shown. The up and down component of each systematic uncertainty has been symmetrized (indicated by the “AVG” label). JES Baseline is introduced for comparison between components and indicates the quadratic sum of JES Effective_NP* components and is not included in the total uncertainty to avoid duplication.

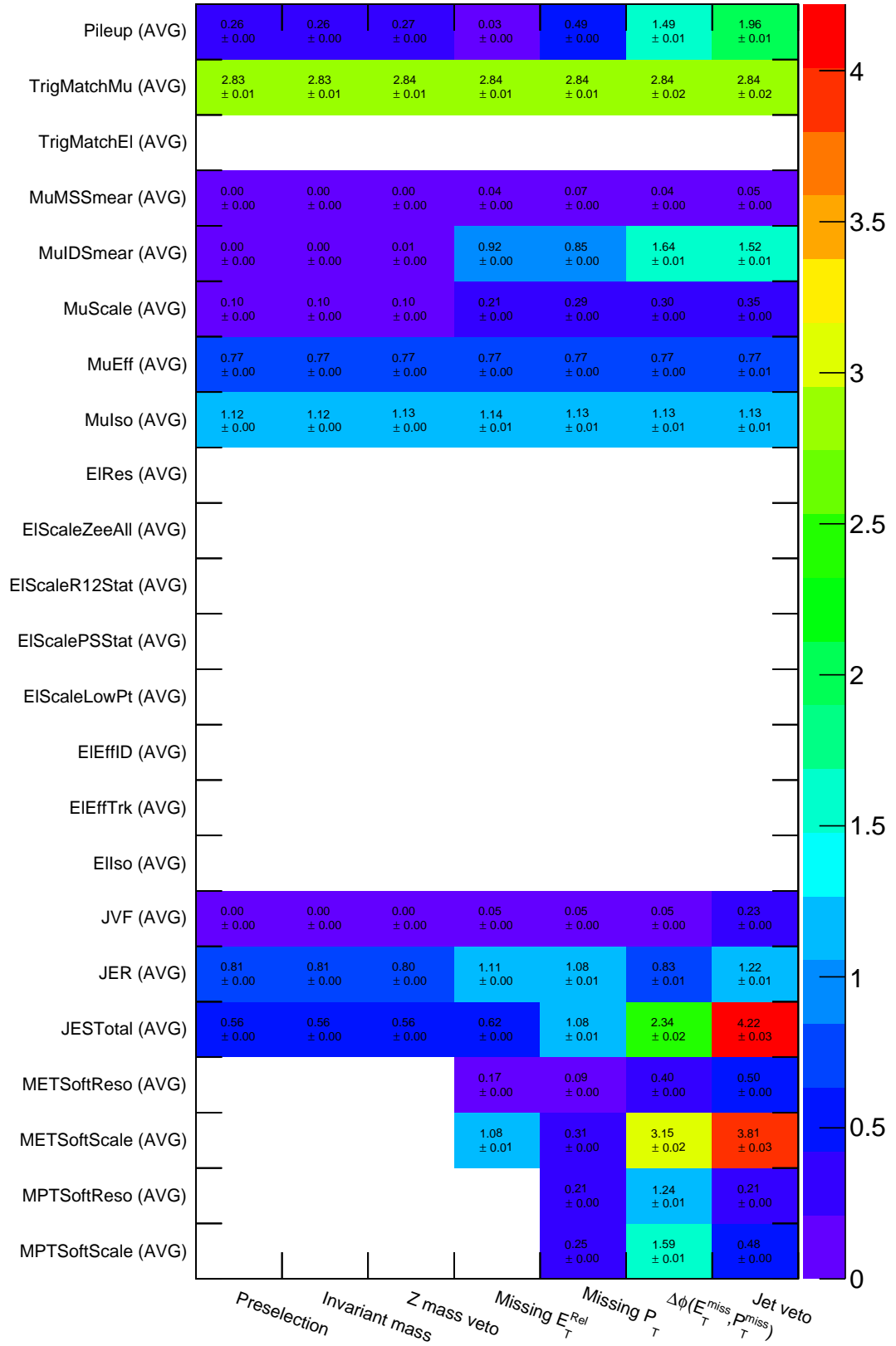


Table B.5: Cut progression of systematic uncertainties on the signal samples for $\mu^+\mu^-$ channel. The table shows the full set of systematics evolving as we introduce analysis cuts (columns left to right). Each number presents a percentage difference with respect to nominal yield at a given cut stage. Statistical uncertainty on each yield is shown. The up and down component of each systematic uncertainty has been symmetrized (indicated by “AVG” label).

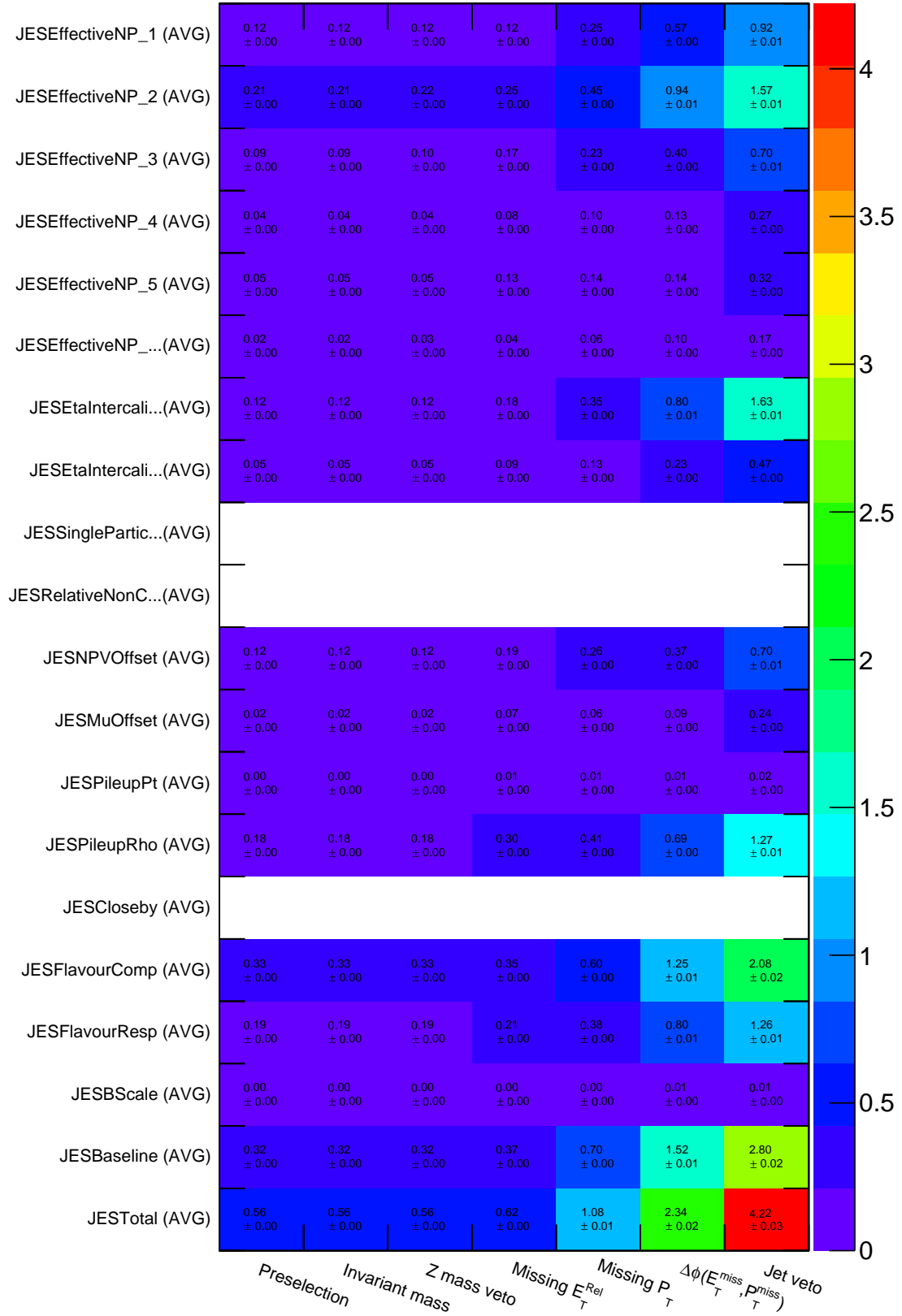


Table B.6: Cut progression of jet energy scale components systematics on the signal samples for $\mu^+\mu^-$ channel. The table shows the full set of systematics evolving as we introduce analysis cuts (columns left to right). Each number presents a percentage difference with respect to nominal yield at a given cut stage. Statistical uncertainty on each yield is shown. The up and down component of each systematic uncertainty has been symmetrized (indicated by the “AVG” label). JES Baseline is introduced for comparison between components and indicates the quadratic sum of JES Effective_NP* components and is not included in the total uncertainty to avoid duplication.

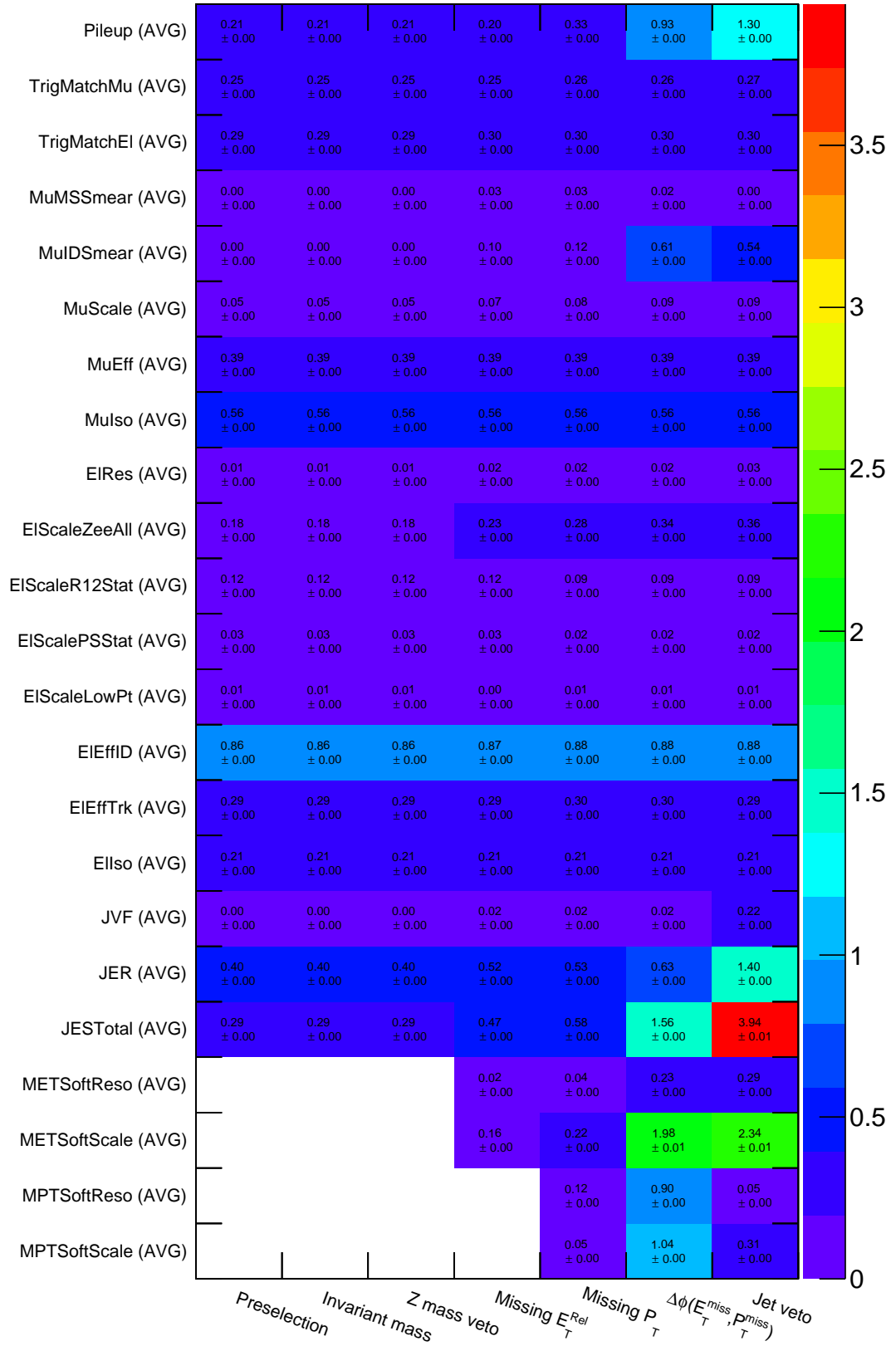


Table B.7: Cut progression of systematic uncertainties on the signal samples for $e^\pm\mu^\mp$ channel. The table shows the full set of systematics evolving as we introduce analysis cuts (columns left to right). Each number presents a percentage difference with respect to nominal yield at a given cut stage. Statistical uncertainty on each yield is shown. The up and down component of each systematic uncertainty has been symmetrized (indicated by the “AVG” label).

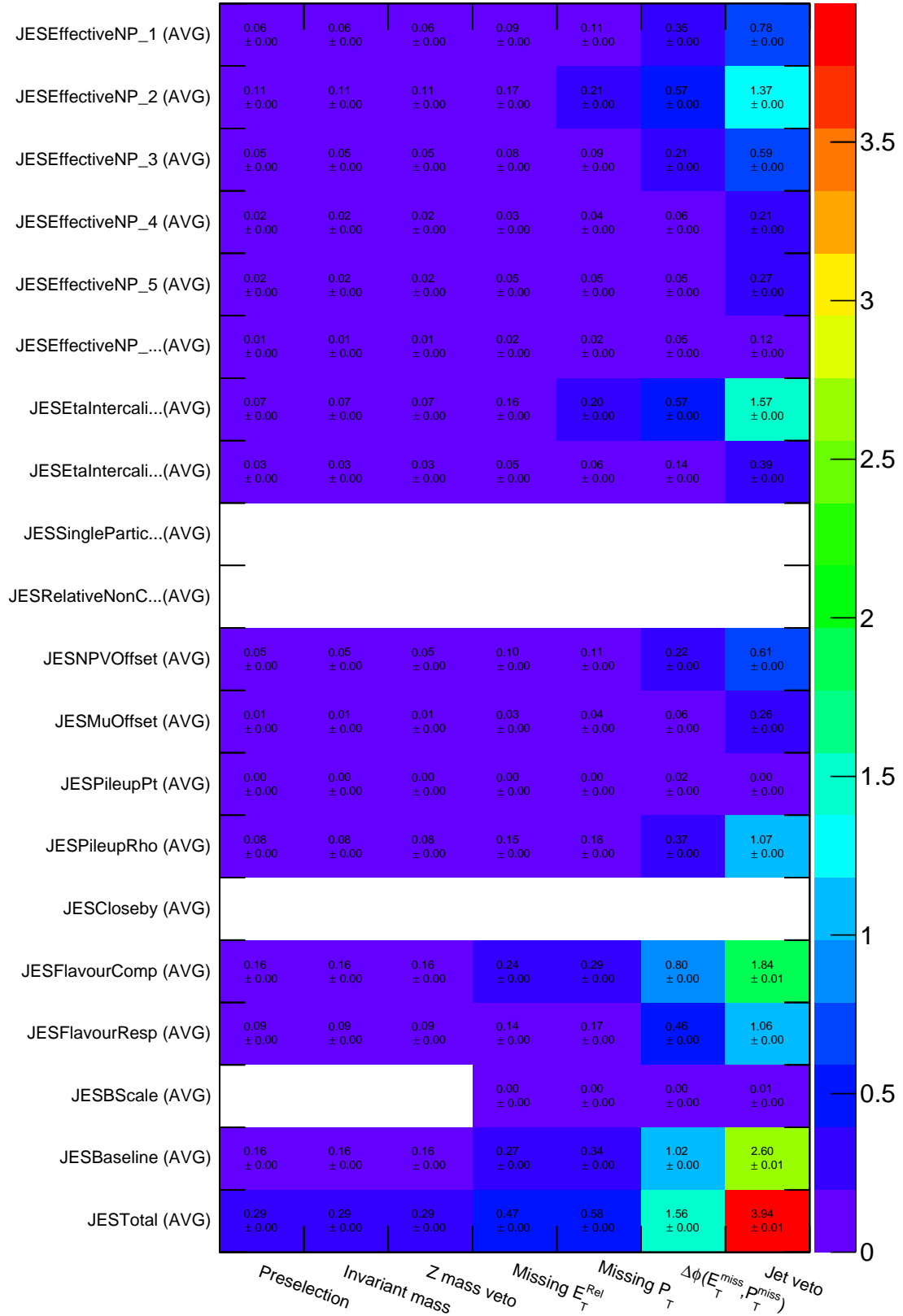


Table B.8: Cut progression of jet energy scale components systematics on the signal samples for $e^\pm\mu^\mp$ channel. The table shows the full set of systematics evolving as we introduce analysis cuts (columns left to right). Each number presents a percentage difference with respect to nominal yield at a given cut stage. Statistical uncertainty on each yield is shown. The up and down component of each systematic uncertainty has been symmetrized (indicated by the “AVG” label). JES Baseline is introduced for comparison between components and indicates the quadratic sum of JES Effective_NP* components and is not included in the total uncertainty to avoid duplication.

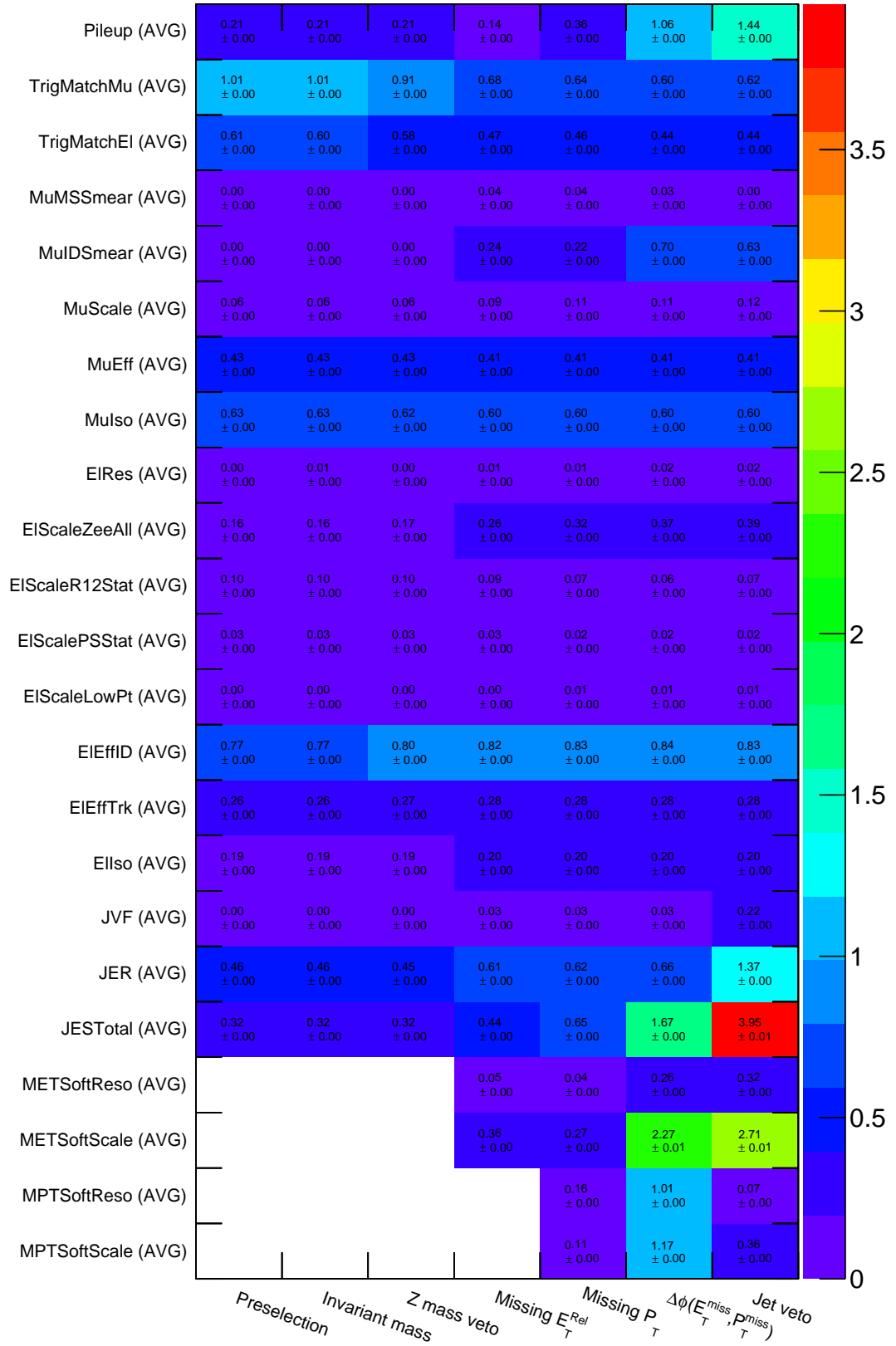


Table B.9: Cut progression of systematic uncertainties on the signal samples for $\ell^+\ell^-$ channel. The table shows the full set of systematics evolving as we introduce analysis cuts (columns left to right). Each number presents a percentage difference with respect to nominal yield at a given cut stage. Statistical uncertainty on each yield is shown. The up and down component of each systematic uncertainty has been symmetrized (indicated by the “AVG” label).

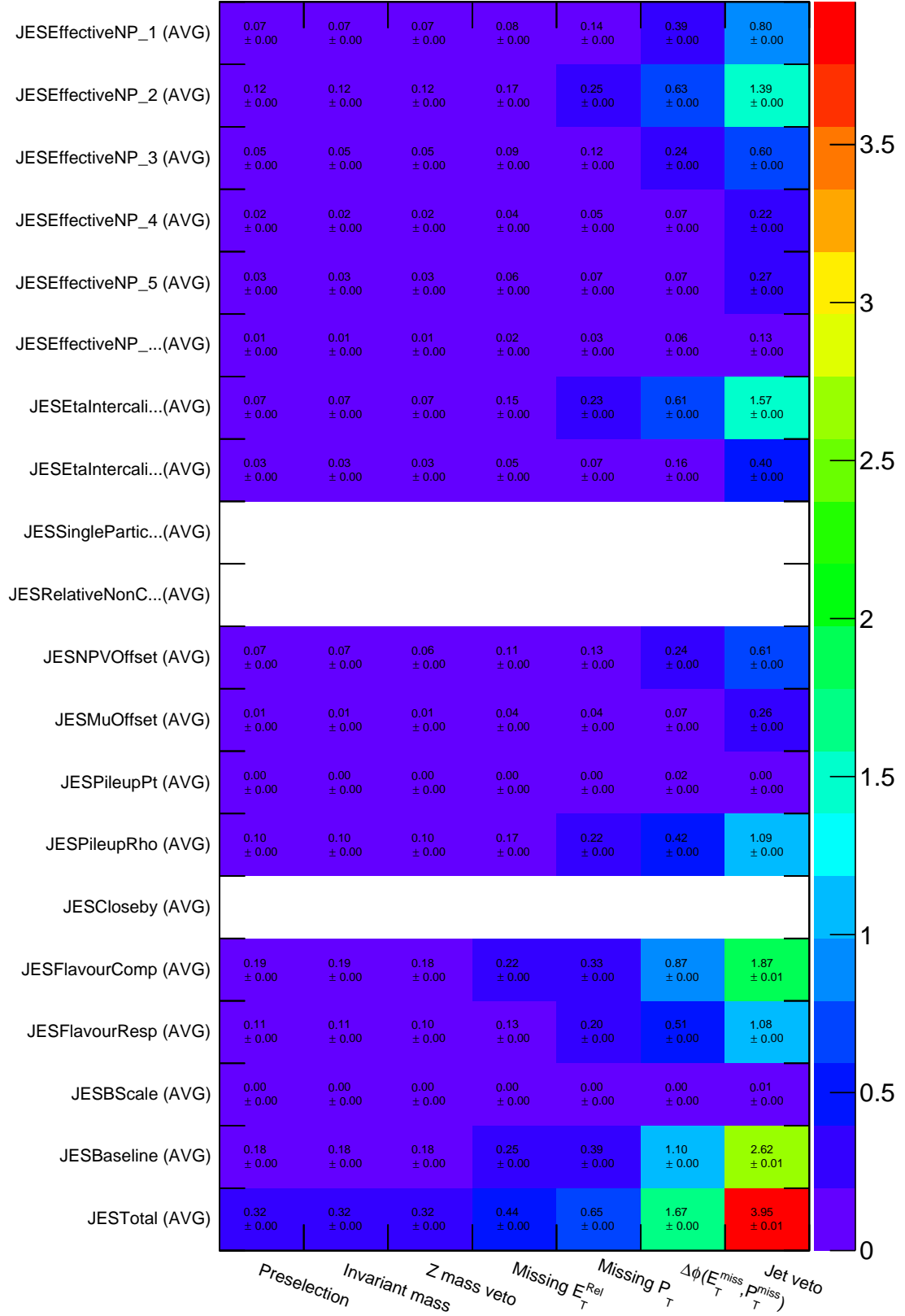


Table B.10: Cut progression of jet energy scale components systematics on the signal samples for $\ell^+\ell^-$ channel. The table shows the full set of systematics evolving as we introduce analysis cuts (columns left to right). Each number presents a percentage difference with respect to nominal yield at a given cut stage. Statistical uncertainty on each yield is shown. The up and down component of each systematic uncertainty has been symmetrized (indicated by the “AVG” label). JES Baseline is introduced for comparison between components and indicates the quadratic sum of JES Effective_NP* components and is not included in the total uncertainty to avoid duplication.

References

A

ABCD method ([ABCD](#)) is a data-driven background estimation method used in the WW [cross-section](#) measurement at $\sqrt{s} = 8$ TeV to estimate the composition of Z + jets background. This method is used for independent verification and as such is only described in the [ATLAS](#) internal documentation [[ATL13](#)]. Ref on pp. [226](#)

Absolute Luminosity for ATLAS ([ALFA](#)) is a detector system designed to measure particles emitted at very large η . It is installed inside specialized retractable devices called *Roman pots* mounted at ± 240 m from the [Interaction point](#). Ref on pp. [80](#), [102](#)

Acceptance (\mathcal{A}) describes the phase space region where collision products can be measured by a given experiment. The detector can measure only a subset of these products due to mechanical or technological limitations. In principle, detectors only measure the electrical signals of produced by particles interacting with the active material (i.e. neutrinos escape undetected). The geometrical acceptance describes the limited [pseudorapidity](#) and azimuthal angle range of the detector (hence the importance of forward detectors). The detector acceptance also depends on the type and momentum of the particle, see [fig. 3.10](#). Ref on pp. [159](#), [161](#), [217](#), see [acceptance factor](#)

Acceptance factor (A_{WW}) is defined as the ratio of the number of [MC](#) signal events passing the fiducial selection at the truth level to the total number of events generated in the signal sample. The factor encapsulates the extrapolation from the fiducial region to the full phase space and incorporates most of the uncertainties related to the theoretical modelling. Ref on pp. [161](#), [215–218](#), [244–245](#)

AcerMC is a [MC](#) event generator dedicated for generation of the [Standard Model](#) background processes in p – p collisions at the [LHC](#). The matrix elements have been coded by [Mad-Graph](#) package. The hard process events generated by [AcerMC](#) can be interfaced with [Pythia](#) or [Herwig](#). Ref on pp. [174](#), [275](#), [277](#)

ALICE experiment ([ALICE](#)) is an experiment at [LHC](#) optimised to the study of heavy ion collisions and the quark-gluon plasma. The [ALICE](#) collaboration aims to study the quark-gluon plasma phase-transitions leading to re-hadronisation. [[ALI10](#)]. Ref on pp. [45](#), [55](#), [57–58](#), [267](#), [293](#)

Alignment is the procedure of correcting for the effect of detector [mis-alignment](#) (assembly imprecision etc.), see [section 2.6.1](#). Ref on pp. [82](#), see [mis-alignment](#)

Alpgen is a leading order matrix-element [MC](#) generator which includes predictions up to six additional partons in the final state. Thus, it allows to include tree-level diagrams corresponding to higher jet multiplicities. Ref on pp. [174](#), [176](#), [180](#), [237](#), [274–276](#), [278–280](#)

Analysis Object Data ([AOD](#)) is a reduced data format that contains a summary of the reconstructed event derived from [ESD](#). [AOD](#) contains sufficient information for common physics analyses using reconstructed physics objects (electrons, muons, jets etc.) as discussed in [section 3.2.3](#). Ref on pp. [104–105](#), [108](#), [203](#), [293](#), [297](#), see [Event Summary Data](#)

- anti- k_t** is a jet reconstruction algorithm used in the [ATLAS](#) experiment which was developed by [Matteo Cacciari](#), [Gavin P Salam](#), and [Gregory Soyez](#) [CSS08]. In [ATLAS](#), jets are measured as groups of topologically-related energy deposits in the calorimeters (*calorimeter jets*) associated to tracks of charged particles measured in the [Inner Detector](#) (*track jets*). Jet reconstruction algorithms used in [ATLAS](#) implement some sort of sequential recombination to build jets. See [section 3.3.5](#) for more details. Ref on pp. 129–130, 135, 137, 198, 202, 206, 215, 294
- AntiKt4EM** refers to the collection of jets reconstructed using the [anti- \$k_t\$](#) jet clustering algorithm from $R = 4.0$ topological clusters calibrated using the EM+JES calibration scheme. JES refers to jet energy scale. Ref on pp. 130, 133, 167, 199, 224, *see anti- k_t*
- AntiKt4LC** refers to the collection of jets reconstructed using the [anti- \$k_t\$](#) jet clustering algorithm from $R = 4.0$ topological clusters calibrated using the LCW +JES calibration scheme. LCW refers to clusters being locally calibrated, JES refers to jet energy scale. Ref on pp. 130, 167, 199, *see anti- k_t*
- Athena framework** is an [ATLAS](#) offline software framework that connect all MC and data processing stages. See [section 3.2.5](#). Ref on pp. 107–108, 138, 306
- ATLAS Electromagnetic Calorimeter (ECAL)** part of the [ATLAS](#) calorimeter system which measures the energy deposits from electrons or photons, see [section 2.5.5](#). The ECAL is divided into a [barrel](#) part ($|\eta| < 1.475$) and two [end-caps](#) ($1.375 < |\eta| < 3.2$) located at a radius $2.8 < R < 4$ m. Ref on pp. 60, 70–73, 76, 96, 123–125, 127, 133, 136, 199, 294, *see ATLAS*
- ATLAS experiment (ATLAS) (A Toroidal LHC ApparatuS)** is one of the five particle detectors developed for the Large Hadron Collider at [CERN](#). The experiment is described in detail in [chapter 2](#), [section 2.5](#). Ref on pp. 30, 42, 44–45, 48, 52, 54–56, 59–85, 93–94, 100–105, 107–111, 115, 117–118, 123, 129, 131, 136–137, 139, 157–158, 161–162, 167, 173, 176, 180, 202–203, 267–268, 293–297, 299, 301–303, 305, 307, 309
- ATLAS Hadron Calorimeter (HCAL)** is part of the [ATLAS](#) calorimeter system designed to measure energy deposits from hadronic jets. It is placed directly outside the ECAL and is separated into a large [barrel](#) in the range $|\eta| < 1.0$ and two extended barrel cylinders on either side ranging $0.8 < |\eta| < 1.7$, see [section 2.5.5](#). Ref on pp. 60, 70, 72, 74, 96, 127, 199, *see ATLAS*
- ATLAS Inner Detector (ID)** is the centre-most sub-system of the [ATLAS](#) detector designed as a tracking system discussed in [section 2.5.4](#). It uses high-resolution semiconductor-based detectors made from layers of silicon pixel sensors and pairs of silicon micro-strips with increasing granularity around towards the vertex region, see [PIX](#) and [SCT](#). Continuous tracking detectors made of multiple layers of gaseous straw tubes with the capability to generate and detect transition radiation are placed at outer radii, see [TRT](#). Ref on pp. 60–66, 68, 70, 81, 84–85, 93–94, 99, 109–112, 114–115, 117–120, 123, 129, 137, 177, 186–188, 199, 201, 217, 222, 268, 294–296, 300, 306, *see ATLAS*
- ATLAS Muon Spectrometer (MS)** is an [ATLAS](#) detector subsystem which identifies and measures muons and complements the trigger system, see [section 2.5.6](#). In [ATLAS](#) four different methods of muon detection are implemented. Two of them ([CSC](#) and [MDT](#)) are designed

for precision measurement and the other two ([RPC](#) and [TGC](#)) are designed for triggering. Ref on pp. [60](#), [62](#), [71](#), [77–79](#), [94–95](#), [115](#), [117–120](#), [136–138](#), [186–188](#), [191–192](#), [199–201](#), [217](#), [222](#), [296](#), [303](#), [306–307](#), see [ATLAS](#)

ATLAS Pixel Detector (PIX) is a high-granularity high-precision semiconductor tracker installed at the very heart of [ATLAS](#), discussed in [section 2.5.4.1](#). The detector is designed so that it provides at least three measured points for track reconstruction within $|\eta| < 2.50$. The innermost layer is referred to as the [b-layer](#) and is situated just 5 cm from the beam pipe. Ref on pp. [63–68](#), [81](#), [84](#), [109–112](#), [114](#), [117](#), [126](#), [187](#), [201](#), [294–295](#), see [Inner Detector](#)

ATLAS Semiconductor Tracker (SCT) is part of the [ATLAS ID](#) designed for tracking at larger radii is handled by the [SCT](#) subsystem. The main difference between [SCT](#) and [PIX](#) is in the implementation of the modules as they are required to cover a much larger area for reasonable cost. Ref on pp. [63–66](#), [68–70](#), [81](#), [84](#), [109–112](#), [114](#), [117](#), [123](#), [126](#), [187](#), [201](#), [294–295](#), see [Inner Detector](#)

ATLAS Transition Radiation Tracker (TRT) is the outer-most part of the [ATLAS ID](#). It is a continuous tracking detectors made of multiple layers of gaseous straw tubes with the capability to generate and detect transition radiation. In addition to tracking, it introduces a pattern recognition system allowing for electron identification complementary to the calorimeter system Ref on pp. [63–66](#), [68](#), [81](#), [84](#), [110–111](#), [117](#), [123](#), [187](#), [294](#), [297](#), see [Inner Detector](#)

ATLFAST framework is a fast simulation package for [ATLAS](#) that provides an alternative to the full detector simulation and reconstruction. [[She](#)] The version currently used by [ATLAS](#) is ATLFAST II. Ref on pp. [104](#), see [Athena](#)

B

Barrel region is a region of the detector where the components (tracker layers, calorimeter, magnets etc.) are mounted atop of the other in the direction parallel to the beam. Ref on pp. [60–65](#), [67–75](#), [95–96](#), [109–112](#), [117](#), [121](#), [123–124](#), [185–187](#), [196](#), [294](#), [306](#)

b-layer is the innermost layer in the [ATLAS Pixel Detector](#) situated just 5 cm from the beam pipe. This close proximity allows the detection of short-track particles such as B hadrons and τ^\pm leptons by providing the resolution necessary for precise measurement of impact parameters. These particles decay before reaching the detector and the [secondary vertex](#) has to be reconstructed from their decay products. Ref on pp. [64](#), [126](#), [295](#), see [Pixel Detector](#)

Branching ratio (BR) or the *branching fraction* is the likelihood that a particle will decay to a particular mode. Ref on pp. [20](#), [158–159](#), [244](#)

Bremsstrahlung (braking radiation) refers to the electromagnetic radiation produced when a fast charged particle undergoes deceleration through interaction with another charged particle. Ref on pp. [71](#), [124](#)

Bunch crossing (BC) generally refers to two machine channels crossing at experimental insertion regions ([interaction points](#)). Bunches are collections of particles confined in a region defined by the accelerator longitudinal focusing. At nominal conditions the [LHC](#) proton-proton bunches cross every 25 ns producing over 600 million collisions per second. Ref on pp. [43](#), [83–85](#), [93](#), [101](#), [114](#), [132](#), [176](#), [200–201](#), [309](#)

C

Calo-tagged muons is a muon identification label for muon reconstructed from an energy deposit in the [ATLAS](#) calorimeter. This method is used mainly for specialized analyses requiring deeper understanding of low- p_T muons. The average muon energy deposit in the calorimeter is small compared to low- p_T hadrons and electrons. Muon reconstruction is discussed in [section 3.3.3](#). Ref on pp. 117, 188

Cathode Strip Chambers (CSC) are multi-wire proportional chambers with segmented cathode plates used at large pseudorapidities $2.0 < |\eta| < 2.7$ of the [ATLAS Muon Spectrometer](#). Ref on pp. 77, 117, 294, *see* [Muon Spectrometer](#)

Central Trigger Processor (CTP) combines the information from the [L1](#) calorimeter and muon trigger processor (and other sources like calibration triggers) and makes the final [L1](#) decision. It also synchronizes the trigger inputs from different sources to the internal clock. Ref on pp. 95

charge-parity invariance ($\hat{C}\hat{P}$) states, that all interactions are invariant after the application of two transformations: charge conjugation \hat{C} and parity inversion \hat{P} . Parity and charge conjugation are conserved in strong and electromagnetic interaction but is violated in weak interaction. Ref on pp. 17, 57, *see* [charge-parity-time](#)

Chi-squared distribution (χ^2) (chi-square) is a statistical distribution used in the χ^2 test. The distribution is defined as

$$f(z) = \frac{1}{2^{n/2}\Gamma(n/2)} z^{n/2-1} \exp\left(\frac{-z}{2}\right) \quad \text{where } n = 1, 2, \dots \quad (\text{B.1})$$

is the *number of degrees of freedom* and the gamma function is defined as:

$$\Gamma(z) = \int_0^\infty \exp(-t) t^{z-1} dt. \quad (\text{B.2})$$

The importance of the χ^2 distribution lies in its relation to the sum of squares of Gaussian variables. The χ^2 test is used to determine whether there is a difference between the expected frequencies and the observed frequencies of a certain phenomenon. [\[Cow98, pp. 35–36\]](#) Ref on pp. 110, 112, 114, 117–118, 252, 296

CMS experiment (CMS) is the second largest experiment at the [LHC](#) (see [section 2.4.2](#)). It has similar physics goals as [ATLAS](#), but uses different technological approach and detector design to accomplish them. Ref on pp. 45, 48, 54–57, 105, 173, 267

Combined muons (CB), often referred to as STACOMUONS in the [STACO](#) collection, are reconstructed from combination of full [ID](#) tracks matched to [MS](#) tracks. Both of the muon combination algorithms, [STACO](#) and [MUID](#), pair the [MS](#) with [ID](#) tracks by minimizing the χ^2 defined as the difference between the outer and the inner track vectors weighted by their combined covariance matrix. Muon reconstruction is discussed in [section 3.3.3](#). Ref on pp. 117–118, 120–121, 137, 177, 186–188, 190–192, 199, 201, 217

Control region (CR) is defined for [MC](#) modelling studies usually by inverting some of the signal selection cuts in a given analysis. Ref on pp. 227–229, 231–234, 236, 249

Correction factor (C_{WW}) is defined as the ratio of the number of reconstructed events in the fiducial

region over the number of WW events generated in the fiducial region. The factor also corrects for inefficiencies of the trigger selection, identification and isolation requirements applied in the analysis and the detector resolution, kinematic and geometric acceptance. Ref on pp. [159](#), [161](#), [215–218](#), [244–245](#), [247–248](#)

Cross-section (σ) in particle physics is used to express the likelihood of interaction between colliding particles. From a purely classical standpoint the cross section is a hypothetical area corresponding to the target, if the incoming particle crosses this surface an interaction occurs, see [section 1.1.9](#) Ref on pp. [9–10](#), [21](#), [25](#), [30](#), [40](#), [42–43](#), [82–84](#), [157](#), [159](#), [161–163](#), [172–175](#), [206](#), [216](#), [237–238](#), [242–248](#), [257](#), [267–268](#), [270–271](#), [273–280](#), [293](#), [298](#), [300–301](#), [303](#), [306](#), [308](#)

Crystal Ball function (CB) is a continuous probability density function (named after the Crystal Ball Collaboration) that consists of a Gaussian and an exponential tail, below a certain threshold. It is commonly used to model decay processes in [HEP](#). Ref on pp. [124](#), [127–128](#)

D

Data acquisition (DAQ) commonly refers to the data collection systems of the [TDAQ](#). Ref on pp. [97](#), [101](#), *see* [trigger](#)

Data quality (DQ) is a process of pre-analysing and maintaining the recorded data. Monitoring of data quality is essential to maintain consistent physics object reconstruction across the large dataset. The [data quality](#) monitoring information is concentrated into *DQ status flags* that reflect the overall status of relevant [ATLAS](#) subsystems, see [section 3.2.1](#). Ref on pp. [102–103](#), [297](#), [299](#)

Data Quality Monitoring Framework (DQMF) involves automated analysis and monitoring tool relaying the summary information to monitoring experts while the data is being processed. Ref on pp. [100–101](#), [103](#)

Decay width (Γ) allows for the identification of particles through their decay products. It is related to particle lifetime as a reciprocal sum of all its decay rates: $\tau = \Gamma_{\text{TOT}}^{-1}$, see [section 1.1.9](#) Ref on pp. [10](#), [297](#)

Derived Physics Data (D3PD) is general format derived from the other formats discussed in [section 3.2.3](#) (usually [AOD](#)). Ref on pp. [104–105](#), [108](#), [121–122](#), [139–143](#), [145](#), [177](#), [193](#), [200](#), [203–204](#), [303](#), *see* [Analysis Object Data](#)

Deutsches Elektronen-Synchrotron (DESY) or the German Electron-Synchrotron is a research centre in Hamburg, Germany that specializes in high-energy physics, particle accelerators and nano-materials. The laboratory is a host to a large number of experiments, chief among them was the HERA synchrotron Ref on pp. [35](#)

Double parton scattering (DPS) is a processes where two partons in one hadron collide with two partons from the other hadron. Ref on pp. [157](#), [173–174](#)

Drift circle is the distance of closest approach of a charged particle to each wire in the [TRT](#). Ref on pp. [68](#), [110–111](#), [117](#), *see* [Transition Radiation Tracker](#)

E

End-cap region is a region of the detector where the components (tracker wheels, calorimeter systems, magnets etc.) are mounted next to the other in the longitudinal direction perpen-

dicular to the beam. Ref on pp. 60–65, 67–68, 70–72, 74–77, 95, 109, 117, 121, 123–124, 129, 184–187, 196, 294, 306–307

European Organization for Nuclear Research (CERN) or the European Organization for Nuclear Research, is the world’s largest particle physics laboratory situated near Genève on the border between France and Switzerland. CERN is run by 20 European Member States, but many non-European countries are also involved^{*}. [Chapter 2](#) of this thesis concerns the devices currently built at CERN site. The acronym comes from the French Conseil Européen de la Recherche Nucleaire. Ref on pp. 2, 32, 35, 43, 47, 49, 54–55, 57, 60, 100, 105–107, 138, 180, 267, 294, 300, 304, 307, 309

Event Filter (EF) is effectively the last level of the trigger system. It has access the full event information with full granularity and additionally uses reconstruction algorithms that are the same or similar to those used in the offline reconstruction. In addition, the EF classifies the selected events into pre-determined set of event streams, see [section 3.1.2](#) Ref on pp. 94, 97, 99, 101–102, 104, 184, 298–299, 305, *see trigger*

Event Summary Data (ESD) represents the full output of the detector reconstruction stored in organized containers (see [POOL](#) format). It contains reconstruction details such as tracks and their hits, calorimeter clusters etc. to allow particle identification, track re-fitting, jet calibration as discussed in [section 3.2.3](#). Ref on pp. 104–105, 108, 293, *see Raw Data Objects*

F

Fake factor method (FF) is a data-driven background estimation method used in the WW [cross-section](#) measurement at $\sqrt{s} = 8$ TeV to estimate the composition of W + jets backgrounds. This method is used for independent verification and for this reason is not described in this thesis [[ATL13](#)]. Ref on pp. 226

Fermi National Accelerator Laboratory (FNAL) in Illinois, United States of America is the second largest particle physics laboratory in the world and a home to the [Tevatron](#) accelerator. Ref on pp. 13, 35, 307

Flavour tagging is a statistical method of identifying flavour of jets. Ability to tag jets is an important aspect of the experiment. It is used to classify many physics channels and it is also very important in searches for new physics (theoretically predicted decay chains etc.) b-tagging, the most common form of flavour tagging, is used distinguish between b-jets and jets from hadronisation of lighter quarks (called *light jets*). Ref on pp. 81, 162, 231–233

G

Gaussian Sum Filter algorithm (GSF) is an electron reconstruction algorithm which uses a weighted Gaussian function to correct for radiative losses of electrons passing through the material and refit the track. This algorithm is not studied in this thesis, see [[ATL12](#)] for more details. Ref on pp. 124, 142

^{*}The current CERN Member States are: Austria, Belgium, Bulgaria, the Czech Republic, Denmark, Finland, France, Germany, Greece, Hungary, Italy, the Netherlands, Norway, Poland, Portugal, the Slovak Republic, Spain, Sweden, Switzerland and the United Kingdom

gg2ww MC generator that implements the pair production of **W** bosons from gluon-fusion process in NNLO. The generator includes all background and signal contributions, full spin correlations, off-shell and interference effects, as well as finite top and bottom quark mass effects. Parton distribution functions are included via the **LHAPDF** package. [Bin+06] Ref on pp. 172, 175, 273, 277

GoodRunsList (GRL) is a list of **lumi-blocks** flagged for physics use. The list configuration is defined by a query of detector and combined performance **DQ** flags in a given run range. The actual integrated **luminosity** for a given **GRL** can be obtained using the **iLumiCalc** service, which is a standard **ATLAS** tool for luminosity calculations. Ref on pp. 100, 103, 162, 177, 203–204, 299

H

Herwig (Hadron Emission Reactions With Interfering Gluons) is a general-purpose **MC** generator which includes the simulation of hard lepton-lepton, lepton-hadron and hadron-hadron scattering and soft hadron-hadron collisions in one package. It uses the parton-shower approach for initial and final-state **QCD** radiation, including colour coherence effects and azimuthal correlations both within and between jets. The original **Herwig** was developed in **FORTAN**, **HERWIG++** is written in **C++**. [Cor+00] Ref on pp. 104, 130, 172, 174, 176, 214, 246, 276, 293, 300

Higgs boson (H) is an elementary particle predicted by **Peter Higgs** [Hig64], **F. Englert** and **R. Brout** [EB64] as a necessary component of the **SM** to explain the masses of elementary particles and the mechanism behind the electroweak symmetry breaking. Ref on pp. 2, 47, 59, 157–158, 160, 167, 173–175, 192, 206, 218, 267, 270, 277

High Level Trigger (HLT) is a distribute software system designed as a part of the **TDAQ** system. It consists of Level-2 (L2) trigger and the **Event Filter**, see section 3.1. Ref on pp. 94, 97–98, 100–101, 103, 105, 107, see trigger

High-energy physics (HEP), also known as *particle physics*, is a field of physics studying phenomena in high-energy particle interaction. Ref on pp. 30, 129, 138, 297

I

iLumiCalc service otherwise known as **ATLAS** luminosity calculator is an official **ATLAS** tool used for computation of the total integrated **luminosity** for a user-provided **GRL**. Ref on pp. 103, 177, 203, 299

Transverse impact parameter (d_0) is defined as the distance of closest approach to the beam-line in the transverse plane. See section 2.3.2. Ref on pp. 53–54, 114, 126, 201, 301

Interaction point (IP) a point on the accelerator where the particle beams collide and around which the experiments are installed. Ref on pp. 39–40, 42, 45, 47–48, 51–54, 57, 59–60, 63, 67, 80, 82–84, 95–96, 110, 113, 117, 123, 234, 293, 295, 301, 309

Invariant mass (m) In a system of N particles with four-momenta $p = p_1 + p_2 + \dots + p_N$ the invariant mass of the system m is defined as: $p_\mu p^\mu = m^2$ or $E^2 = p^2 + m^2$. The mass m is Lorentz invariant and thus has the same value in any reference frame. Ref on pp. 121, 170, 173, 186–187, 206, 242

J

Jet energy resolution (JER) is an additional experimental uncertainty on the jet reconstruction caused by detector smearing. In [MC](#), the “truth resolution” derives from the width of the distribution of jet response. The parametrization of the resolution function is given in [section 3.3.5.2](#). Ref on pp. [135–136](#), [199](#), [212](#), [214](#), [229](#), [232](#), [234](#), [247–248](#)

Jet energy scale (JES) is the the calibration scale of jets reconstructed in the calorimeter. The jet energy measured in the calorimeter does correspond to the energy of final state at the particle level. The goal of jet energy calibration is to correctly relate the calorimeter response to the true jet energy independent of [pile-up](#). The factor is derived as a function of reconstructed jet η and p_T using [MC](#) truth jets with two calibration schemes: EM+JES or LCW +JES, see [section 3.3.5.2](#). Ref on pp. [131–133](#), [135–137](#), [199](#), [206](#), [212](#), [214](#), [222–224](#), [226](#), [232](#), [234](#), [238](#), [241](#), [246–248](#), [254](#), [281](#), [283](#), [285](#), [287](#), [289](#), [294](#), [300](#)

Jet veto survival probability method (JVSP) is a data-driven background estimation method used in the WW [cross-section](#) measurement at $\sqrt{s} = 8$ TeV to estimate the composition of the top background, see [section 4.9.3](#). This method is used as a baseline. Ref on pp. [226](#), [231–232](#), [238](#)

Jimmy is a library of routines which designed to link with the [Herwig MC](#) event generator. It allows to generate multiple parton scattering events in hadron-hadron, photon-photon or photon-hadron events. [[BFS96](#)] [[But+](#)] Ref on pp. [172](#), [174](#), [176](#), [214](#), [232](#), [237](#), see [Herwig](#)

L

Lagrangian function (\mathcal{L}) is a functional that represents the dynamics of the system. It is used in Euler-Lagrange equations to find the path of a particle through Hamilton’s principle of least action. In simple mechanical systems, the function is given by the difference of kinetic and potential energy: $L = E_{\text{kinetic}} - E_{\text{potential}}$. The specific situation in field theories is discussed in [section 1.1.1](#). Ref on pp. [3–5](#), [7–8](#), [13–16](#), [301](#)

Large Electron-Positron Collider (LEP) at [CERN](#) was one of the largest colliders ever constructed. It started operation in 1989 with a nominal centre-of-mass energy of 100 GeV each to enable production of the [Z](#) and [W](#) bosons. It was eventually superseded by the [LHC](#), which was installed in the same tunnel. Ref on pp. [35](#), [37](#), [43](#), [48](#), see [Large Hadron Collider](#)

Large Hadron Collider (LHC) is the largest particle accelerator installed at [CERN](#). A significant portion of this thesis is dedicated to the [LHC](#), starting [section 2.2](#). Ref on pp. [30](#), [32](#), [35](#), [37](#), [43–52](#), [54–55](#), [57](#), [59–61](#), [63](#), [80](#), [83](#), [85](#), [93](#), [100–103](#), [105](#), [108](#), [115](#), [123](#), [129](#), [157](#), [159–160](#), [180](#), [203](#), [267–268](#), [293](#), [295–296](#), [300–301](#), [303–309](#), see [CERN](#)

Level-1 Trigger (L1) is a hardware-based system which uses a reduced granularity information from the calorimeter and the muon system to search for signatures of high- p_T muons, electrons, photons, jets and τ leptons. There is no tracking information from the [ID](#) because the simultaneous readout is not fast enough. Only events accepted at this level are used to seed the subsequent levels. Ref on pp. [93–99](#), [103](#), [180](#), [186](#), [296](#)

LHAPDF is a general purpose C++ interpolator and reweighting tool for evaluating PDFs. It is designed to work not only with individual PDF sets but also with the more recent multiple

“error” sets. [WB13] Ref on pp. 180, 299, 304

LHCb experiment (LHCb) is an experiment at LHC dedicated to the study of heavy flavour physics. The experiment consists of a single arm forward detector 10 m high and 13 m wide. For details, see section 2.4.4. Ref on pp. 45, 57–59, 105, 107, 267

LHCf experiment (LHCf) is an experiment at LHC designed to detect forward particles coming from the collisions at large $|\eta|$. The detector consists of two different calorimeters, each placed approximately 140 m away from Point 1 site. See section 2.4.6. Ref on pp. 268

Local cluster weighting (LCW) provides an alternative calibration method that applies corrections to calorimeter *topo-clusters* independent of any jet context. The corrections are based on the response from electromagnetic and hadronic *topo-clusters* as discussed in section 3.3.5.2. Ref on pp. 133–137, 199, 224, 294, 300, *see jet energy scale*

Longitudinal impact parameter (z_0) is defined as the value of the longitudinal coordinate z of the point on the track that determines the *transverse impact parameter*. See section 2.3.2. Ref on pp. 53–54, 114, 201

LOOSELLH is a electron likelihood identification operating point that implements MVA techniques discriminate between real and fake electrons, *see section 3.3.4.3* Ref on pp. 204

LOOSE++ is a loose set of cuts used in electron identification to discriminate between real and fake electrons, *see section 3.3.4.2*. Ref on pp. 204, 222

Lumi-block (LB) is a fundamental unit of time for the luminosity measurement. It is defined as a period during which all trigger *prescales* do not change. A lumi-block and was approximately 120 seconds long in 2010 data taking. [ATL14b] Ref on pp. 87, 100, 102–103, 204–205, 299

Luminosity (\mathcal{L}) is a critical parameter of an accelerator. It provides a measure of the number of collisions produced per surface area and per second. The number of events N_{tot} produced by the accelerator is a product of the total probability of interaction expressed in terms of the total interaction *cross-section*, *see section 2.1.4*. Ref on pp. 10, 37–43, 45, 47, 80, 82–85, 100–103, 159, 177, 203–204, 238, 244, 246, 299, 301, 309

Luminosity measurement using Cherenkov integrating detector (LUCID) is made out of an array of Cherenkov tubes placed at distance ± 17 m (in both directions) from the ATLAS Interaction point. Its main and key function is the measurement of *luminosity* using the products of inelastic pp scattering escaping at large *pseudorapidities*, *see section 2.5.7*. Ref on pp. 80, 84, 178

M

MadGraph (more technically MadGraph5_aMC@NLO) is a framework that aims at providing all the elements necessary for *Standard Model* and beyond the *Standard Model* phenomenology: computations of cross sections, generation of hard events and matching with event generators, and the use of a variety of tools relevant to event manipulation and analysis. Processes can be simulated to LO accuracy for any user-defined \mathcal{L} , and the NLO accuracy in the case of QCD corrections to SM processes. [Alw+14] Ref on pp. 176, 276, 280, 293

Matrix method is a data-driven background estimation method used in the WW *cross-section* measurement at $\sqrt{s} = 8$ TeV to estimate the composition of W + jets backgrounds, *see section 4.9.5*. This method is used as a baseline. Ref on pp. 226

MC@NLO is a [MC](#) generator developed for matching the NLO calculations of a given [QCD](#) process with a parton shower [MC](#) simulation. The method has the following features: fully exclusive events are generated, with hadronization according to the [MC](#) model; total exclusive rates are accurate to NLO, hard emissions are treated as in NLO computations while soft/collinear emissions are handled by the [MC](#) simulation, with the same logarithmic accuracy as the [MC](#). The matching between the hard- and soft/collinear-emission regions is smooth. A fraction of events with negative weight is generated, but unweighting remains possible with reasonable efficiency. [[FW02](#)] [[Fri+14](#)] Ref on pp. 103, 161, 167, 172, 174–175, 214, 229, 232–233, 271, 273, 275, 277

Mean number of interactions per bunch crossing ($\langle\mu\rangle$) represents the number of interactions averaged over all bunch crossings and averaged over the dataset. In data, $\langle\mu\rangle$ is calculated using the formula [eq. \(2.58\)](#). The [mean number of interactions per bunch crossing](#) for 7 TeV and 8 TeV is shown in [fig. 2.47](#). Ref on pp. 82–85, 87, 101, 113–116, 126, 132, 135, 176–178, 302

Minimum Bias Trigger Scintillators (MBTS) are a part of the [ATLAS TDAQ](#) designed to function only at low luminosities during initial data-taking. The system is essential for triggering minimum-bias events at $\langle\mu\rangle < 0.05$ which is essential for soft-[QCD](#) analyses. [[ATL14a](#)] Ref on pp. 84, *see* [ATLAS](#)

Mis-alignment a situation that occurs after assembly of the detector, where the actual position of the detector modules does not exactly correspond to the simulation model, *see* [section 2.6.1](#). Ref on pp. 81–82, 103, 112, 119, 293, *see* [alignment](#)

Missing transverse energy (E_T) denotes the amount of missing energy in the detector due neutrinos or other invisible particles. Due to geometrical arrangement of the detector, the conservation of momentum can only be reliably constrained in the transverse plane, as the p_T of the initial state is in ideal case zero:

$$E_T \equiv - \sum_i \left(\sqrt{p_x^2 + p_y^2} \right)$$

where the sum runs over all visible final state particles. [[Par13](#), p. 425] See detector nomenclature in [section 2.3.2](#). Ref on pp. 20, 53, 70–71, 98, 136–138, 162–163, 165, 167–171, 174, 177, 182, 199–202, 204–205, 207–208, 210, 212–214, 216, 218, 221–229, 234, 236–238, 241, 243, 246–248, 265, 268–269, 302, 335

Missing transverse momentum (\not{p}_T) denotes the amount of missing energy measured using the tracking system, defined as a vectorial sum

$$\not{p}_T = - \sum_i \mathbf{p}_T(i)$$

of all tracks within the tracker geometrical and kinematic acceptance and compatible with the [PV](#). This alternative definition is used to enhance the calorimeter based measurement of [missing transverse energy](#) which is significantly affected by high [pile-up](#) conditions. See [section 4.5.4.3](#). Ref on pp. 165, 167–171, 181–182, 201–202, 207–208, 211–214, 216, 224, 226–229, 236, 241, 243, 247–248, 269, 302

MoEDAL experiment (MoEDAL) is a newest addition to the [LHC](#) experiments. Its main goal is the search for the magnetic monopole, see [section 2.4.7](#). Ref on pp. 268

Monitored Drift Tubes (MDT) are a part of the the [ATLAS Muon Spectrometer](#). The sensors provide precision track measurement over the largest η -range ($|\eta| < 2.7$). Ref on pp. 77, 117, 294, 306, *see* [Muon Spectrometer](#)

Monte Carlo (MC) is a computational algorithm that uses random number generators in order to calculate a numerical solution to a given problem. Typically this means running MC simulations many times in order to obtain a probabilistic distribution of a given measure. In particle physics, the term MC is sometimes interchanged with the word “model”. Hence the term indicates that a whole set of samples has been used in a given analysis for signal and background modelling. Ref on pp. 98, 103–105, 107–108, 112–116, 118–120, 122, 124, 128, 131–136, 144, 157, 159, 161–163, 167, 170–182, 185–186, 191, 194, 196–197, 200–201, 204–206, 208–212, 214–217, 222, 224, 226–229, 231–234, 236–238, 246, 249–250, 252–257, 268–269, 273–281, 293–294, 296, 299–300, 302, 304–307

Monte Carlo for Femtobarn processes (MCFM) is program designed to calculate [cross-sections](#) for various femtobarn-level processes at hadron-hadron colliders. For most processes, matrix elements are included at NLO and incorporate full spin correlations. For more details, including a list of available processes, see [\[CEW14\]](#) Ref on pp. 173–174, 270

MUID algorithm is muon reconstruction algorithm (sometimes referred to as Chain 2) described in [\[Ada+03\]](#). This algorithm is not used for the definition of muon physics objects in this thesis. Muon reconstruction is discussed in [section 3.3.3](#). Ref on pp. 115, 117–118, 142, 296, *see* [STACO](#)

N

n-tuple (NTUP) is a generic data format arranged as an event-by-event table. See [section 3.2.3](#). Ref on pp. 105, 139, 141–142, 203, 253–254

P

Photon (γ) is an elementary quantum of light and an intermediate boson in quantum electrodynamics. Ref on pp. 8, 16, 51, 135, 137, 157–158, 173–174, 176, 269

Pile-up (PU) is a situation that occurs when multiple particles collide inside the detector within very short intervals so that the detector electronics reads them out as simultaneous interactions. There are various methods of addressing pileup, the simplest solution being faster data taking. ATLAS implements a simple strategy where the vertex with the largest $\sum p_T$ is considered as the primary vertex for the given event. Pileup also introduces a significant systematic errors into the measurement. Pile-up can be in-time or out-of-time. Ref on pp. 84–85, 87, 101, 112–114, 119, 122–129, 131–135, 137, 162, 167, 174, 176–178, 188, 192, 194, 199–201, 208, 224, 227, 234, 254, 268–269, 300, 302, 308

Pixel cluster is defined as a group of neighbouring pixel hits. The pixel commissioning [D3PD](#) contain approximately 1.30 (1.23) million clusters with field off (on). Both the field off and on cosmic ray simulation samples contain 2.1 million clusters each. Ref on pp. 109–110

POOL ([POOL](#)) is a hybrid technology store for C++ objects, using a mixture of streaming and relational technologies to implement both object persistency and object metadata catalogs and collections. It provides generic components that can be used by the experiments to store both their event data and their conditions data. [\[CER\]](#) Ref on pp. 104–105, 298

POWHEG (**P**ositive **W**eight **H**ardest **E**mission **G**enerator) is a general computer framework for implementing NLO calculations in shower [MC](#) programs. It provides a library of a multitude of processes and can be interfaced with all modern shower [MC](#) programs that support the [LHAPDF](#) interface for user generated processes. [\[FNO07\]](#) Ref on pp. 103, 120, 167, 172, 175–176, 214, 229, 232–233, 237, 271, 277, 280

Prescale of a trigger setting by a factor X means that the given trigger chain will only accept every X th event passing the trigger requirements. Ref on pp. 99–100, 162, 180, 183, 185–186, 301

Proton Synchrotron (**PS**) is particle accelerator at [CERN](#) which is currently a part of the [LHC](#) injection chain as discussed in [table 2.4](#). It accelerates either protons delivered by the Proton Synchrotron Booster or heavy ions from the Low Energy Ion Ring (LEIR). The PS accelerated its first protons on November 24, 1959.[\[CER14\]](#) Ref on pp. 35, 47–48, *see Large Hadron Collider*

Pseudorapidity (η) is a spatial coordinate describing the angle of a particle relative to the beam axis. It is defined as:

$$\eta = \ln \left[\tan \left(\frac{\theta}{2} \right) \right]$$

where θ is the angle relative to the beam axis. Ref on pp. 52, 55, 57, 59–61, 63–65,

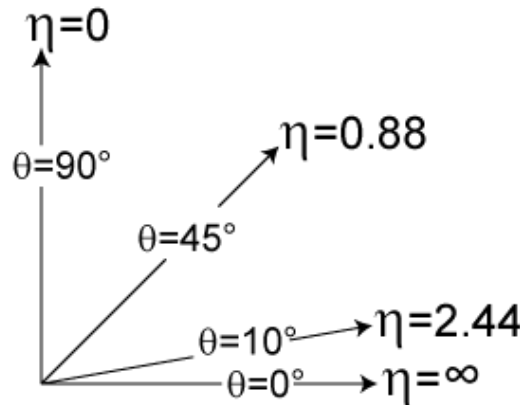


Figure B.1: As angle increases from zero, pseudorapidity decreases from infinity. In particle physics, an angle of zero is usually along the beam axis. Figure from Wikipedia.

68, 70–75, 77–78, 80, 84, 96, 98–99, 109, 112–115, 117, 119, 121, 123–129, 131–137, 163, 166–168, 179–180, 184–188, 190–192, 194–199, 201–206, 216, 231, 236, 293–296, 300–301, 303, 306–307

Pythia is a program for generation of high-energy-physics events that provides a combination of analytical results and various models based on experimental observations. Since [Pythia 6](#), the framework integrates the [PYTHIA 5](#), [JETSET 7](#) and [SPYTHIA](#) programs. With the release of [Physics@Pythia 8.1](#), this new C++ version series takes over from the older Fortran 77-based [PYTHIA 6.4](#) one as the current standard, which is a standard for

LHC analyses. [Sjö+00] Ref on pp. 104, 172, 174, 206, 214, 232, 237, 293, 305

PythiaB is an **ATLAS** modification of the **Pythia MC** generator for the generation of \bar{b} events. Ref on pp. 275, see **Pythia**

Q

Quantum chromodynamics (QCD) is a non-Abelian gauge theory of the strong force describing interactions between quarks and gluons as discussed in section 1.2. Ref on pp. 2, 13–16, 159–160, 163, 172, 174, 176, 196, 234, 236, 247–248, 269, 299, 301–302

Quantum electrodynamics (QED) created by **R. Feynman** [Fey49] [Fey50], **Julian Schwinger** [Sch48] and **S. Tomonaga** [Tom49] was the first quantum field theory that provided a consistent relativistic quantum mechanical description of electromagnetism. Quantum electrodynamics provides the means to describe particle interaction through the means of perturbation theory. Mathematically, it is an Abelian gauge theory with internal symmetry group $U(1)$. See section 1.1.7 for a short discussion about the subject. Ref on pp. 2, 8–10, 14–16, 18–19, 216

Quartic gauge coupling (QGC) self-coupling of four gauge bosons at a given vertex. If lower-case letter “a” is present in front of the abbreviation, it indicates anomalous QGC. Ref on pp. 157

R

Radiation length (m_T) is a energy-loss characteristic of a material. A single charged particle of momentum p and velocity v , with the product pv measured in MeV, suffers a quadratic mean deflection of $\frac{21}{pv}$ radians [Per00, p. 353]. Ref on pp. 61, 71–72

Rapidity (y) is a measure allowing relativistic description of motion. Rapidity is defined as the hyperbolic angle between two frames of reference in relative motion. Rapidity is defined as a hyperbolic rotation of spacetime coordinates. This allows us to rewrite the Lorentz transform to a form similar to spatial rotation:

$$\begin{pmatrix} t' \\ x' \end{pmatrix} = \begin{pmatrix} \cosh(u) & -\sinh(u) \\ -\sinh(u) & \cosh(u) \end{pmatrix} \begin{pmatrix} t \\ x \end{pmatrix} \quad (\text{B.3})$$

$$\text{and from that we write } \gamma = \cosh(u), \gamma\beta = \sinh(u) \quad (\text{B.4})$$

$$\implies \beta = \tanh(u) \implies u = \operatorname{arctanh}(\beta) \quad (\text{B.5})$$

For parallel movement at low speeds, rapidity is proportional to speed. Ref on pp. 52, 130

Raw Data Objects (RDO) are the direct output of **Event Filter**, sometimes referred to as *byte-stream* to indicate the persistent flow through the **trigger** system. The format is a direct input of reconstruction step in the full chain and is stored only until the reconstruction is finished, see section 3.2.3. Ref on pp. 104–105

Region of Interest (RoI) is a geometrical region of the **ATLAS** detector used by the trigger to define regions of the event data to be further investigated at higher trigger levels. Ref on pp. 94, 97–98

Resistive Plate Chambers (RPC) provide muon trigger capabilities and complement the other [Muon Spectrometer](#) systems. RPC stations are installed on both sides of an [MDT](#). Ref on pp. 77, 95, 117, 295, 307, *see* [Monitored Drift Tubes](#)

ROOT framework ([ROOT](#)) is an object oriented framework for large scale data analysis written in a C++. It includes a C++ interpreter (formerly `CINT`, now `CLING`) so that the package can be used in interactive, scripted or compiled modes as is common for high-end commercial products like `MATLAB`. [[ROO](#)]. Ref on pp. 105, 107–108, 138–139, 142, 251, 306

RootCore package is a software package that helps developers build packages that work standalone (outside [Athena](#)). Ref on pp. 107, 138–139, 141, 145, *see* [Athena](#)

run number is a unique identifier assigned for a single particle accelerator fill. At the [LHC](#) these run numbers take form of a six digit number. Ref on pp. 177

Run-I denotes the first long run of data-taking on the [LHC](#) between 2010 and 2012. See [[Lam14](#)] for exact dates for each data-taking period. Ref on pp. xiii, 108

Run-II denotes a [LHC](#) data-taking period starting after the long shutdown from 2014 onwards [[Lam14](#)]. Ref on pp. 108, 267

S

Scale factor (SF) generally refers to a correction factor for some quantity, usually computed as a ratio between event yields or efficiencies at particular conditions. Ref on pp. 176, 180, 185–188, 191–194, 196–199, 201, 206, 212, 214–215, 217–218, 227–229, 238

Segment-tagged muons (ST), also called `MuTAG` in the [STACO](#) collection, are reconstructed from the track segment in the [ID](#) in the [pseudorapidity](#) range $|\eta| < 2.5$. This method is an important extension to the [standalone](#) measurement mainly because the middle stations are missing in the [barrel/end-cap](#) transition region $1.1 < |\eta| < 1.7$ and muons with momenta below 6 GeV do not always reach the [Muon Spectrometer](#). Muon reconstruction is discussed in [section 3.3.3](#). Ref on pp. 117, 121, 137

SFrame framework is a C++ framework built around the [ROOT](#) libraries for analysing particle physics data. It gives a very high performance for processing data, by allowing the user to run the code on a distributed farm of machines. [[KHB](#)] Ref on pp. 108, 138–141, *see* [ROOT framework](#)

Sherpa is a [MC](#) event generator for the Simulation of **H**igh-Energy **R**eactions of **P**articles in lepton-lepton, lepton-photon, photon-photon, lepton-hadron and hadron-hadron collisions. [[She14](#)] Ref on pp. 176, 237

Signal over background ratio (S/B) is the fraction of signal events over the background events, signifying the signal strength. Ref on pp. 158–159, 202, 207, 268, 306

Signal region (SR) maximizes the [signal over background ratio](#) defined by selection criteria tailored to a specific analysis. Ref on pp. 227–229, 233–234

Simultaneous fit method is a data-driven background estimation method used in the WW [cross-section](#) measurement at $\sqrt{s} = 8$ TeV to estimate the composition of top and Z + jets backgrounds, *see* [section 4.9.1](#). This method is used as a baseline. Ref on pp. 226–227, 238

SLAC National Accelerator Laboratory (SLAC), originally named the Stanford Linear Accelerator Center, was founded in 1962 in Menlo Park, California. It has been instrumental in

the investigation of deep inelastic scattering phenomena. The research at SLAC produced three Nobel Prizes in Physics for the discovery of the quark structure of nucleons, the discovery of the c and the tau lepton. Ref on pp. 12–13, 35

STACO algorithm is muon reconstruction algorithm (sometimes referred to as Chain 1) described in [Nic+10] [Has+07]. Muon reconstruction is discussed in section 3.3.3. Ref on pp. 115, 117–121, 142, 144, 186, 190–193, 204, 296, 306, *see* MUID

Standalone muons (SA) Muon reconstruction is discussed in section 3.3.3. Ref on pp. 117, 137, 188, 306

Standard Model (SM) of particle physics is a gauge quantum field theory with an internal group $SU(3)_C \otimes SU(2)_L \otimes U(1)_Y$ formulated in 1970s. Its theoretical implications are discussed in chapter 1. Ref on pp. 2, 11, 13, 16, 21–22, 30, 45, 51, 55, 59, 157–160, 163, 170, 173–174, 176, 206, 222, 267–268, 270, 293, 299, 301

Super Proton Synchrotron (SPS) is a particle accelerator at CERN It is 6.90 km in circumference and accelerates protons up to 450 GeV. It is the last part of the LHC injection chain as described in section 2.2.3. Ref on pp. 2, 35, 47–48, 55, 309, *see* Large Hadron Collider

Symmetry group correspond to the internal symmetries of a particular theory under which the laws of physics are invariant, a property exploited in designing gauge theories. In particle physics, the most common internal symmetry groups are denoted: S (*special*), U (*unitary*). The mathematical properties are given by the Lie algebra of the group (e.g. $U(1)$ corresponds to the circle group of all complex numbers in the unit circle). Ref on pp. 2, 13–16, 18–19, 21, 267, 305, 307

T

Tag-and-probe A standard method to study physics objects, trigger and reconstruction efficiencies in order to resolve data/MC discrepancies. The method uses some sort of “standard candle” processes like decays of well known particles with low backgrounds (e.g. $Z \rightarrow e^+e^-$, $Z \rightarrow \mu^+\mu^-$) and use the products to determine the detector response. Ref on pp. 99, 117, 121, 124, 126, 162, 185, 188, 191–192, 194, 196–197, 217, 222

Tevatron was a particle accelerator at FNAL and second highest energy accelerator after the LHC. The main achievement of the Tevatron physics programme was the discovery of the top quark in 1995 by CDF Collaboration [CDF95] and D0 Collaboration [D0 95]. Ref on pp. 35, 45, 53, 160, 180, 298, 307

Thin Gap Chambers (TGC) are multi-wire proportional chambers wire-to-cathode distance of 1.40 mm that cover the end-cap region of the ATLAS MS ($1.05 < |\eta| < 2.7$). Similarly to RPC, they contribute to the measurement of the azimuthal angle ϕ and muon triggering. Ref on pp. 77, 95, 117, 121, 295, *see* Muon Spectrometer

Tier0 sites is a category of data storage sites. The main task of Tier-0s is the safe-keeping and distribution of raw data. It includes the CERN Data Centre in Geneva, Switzerland and the Wigner Research Centre for Physics in Budapest, Hungary connected by 100 Gbit s⁻¹ links. See section 3.2.4. Ref on pp. 100, 203, *see* Worldwide LHC Computing Grid

TIGHT++ is a tight set of cuts used in electron identification to discriminate between real and fake electrons, *see* section 3.3.4.2. Ref on pp. 196, 208–209

Topological cluster are objects used in electron reconstruction. The topological clustering algorithm is efficient at suppressing noise in clusters and is recommended to be used for 8 TeV run conditions as it is more **pile-up** robust, see [section 3.3.4](#). Ref on pp. [123](#), [127–128](#), [130](#), [133](#), [198](#), [301](#)

TOTEM experiment (TOTEM) is an experiment at the **LHC** focused on the measurement of total **cross-section**, elastic scattering and diffraction dissociation, see [section 2.4.5](#). Ref on pp. [45](#), [57](#), [268](#)

Transfer factor method (TF) is a data-driven background estimation method used in the WW **cross-section** measurement at $\sqrt{s} = 8$ TeV to estimate the composition of top and Z + jets backgrounds, see [sections 4.9.2](#) and [4.9.4](#). This method is used for independent verification. Ref on pp. [226](#), [228–230](#), [232–235](#), [238](#)

Transverse energy (E_T) is defined in the transverse plane (x - y) of the detector, i.e. perpendicular to the beam axis:

$$E_T = E \sin(\theta)$$

Because of the nature of the experiment constraints on the conservation of momentum or energy can only be set in the plane perpendicular to the beam axis, i.e. (x - y). See detector nomenclature in [section 2.3.2](#). Ref on pp. [52–53](#), [96](#), [98–99](#), [119](#), [121–122](#), [124–125](#), [127–128](#), [132](#), [167–168](#), [185](#), [187](#), [190](#), [194–197](#), [200](#), [308](#)

Transverse mass (m_T) is a quantity that puts a maximum constraint on the parent particle in terms of its mass. It is defined as follows

$$m_T^2 \equiv (E_{T1} + E_{T2})^2 - (p_{T1} + p_{T2})^2.$$

The transverse direction is again preferable due to resolution limitations in the longitudinal directions since the z component of a neutrino is effectively unknown, see [section 2.3.2](#). Ref on pp. [53](#), [163–164](#), [170](#), [181](#), [242](#), [308](#)

Transverse momentum (p_T) is defined in the transverse plane ($x - y$) of the detector, i.e. perpendicular to the beam axis:

$$p_T = \sqrt{p_x^2 + p_y^2} = |p| \sin(\theta)$$

Because of the nature of the experiment constraints on the conservation of momentum or energy can only be set in the plane perpendicular to the beam axis, i.e. (x - y). See detector nomenclature in [section 2.3.2](#). Ref on pp. [20](#), [52–53](#), [64–65](#), [68](#), [77](#), [81–82](#), [86](#), [93](#), [95–96](#), [98–99](#), [109](#), [111–115](#), [117–125](#), [127–133](#), [135–138](#), [163–164](#), [167–168](#), [170](#), [178](#), [180–181](#), [183–196](#), [198–202](#), [204–208](#), [211–212](#), [216](#), [218](#), [221–227](#), [229](#), [231](#), [233](#), [236](#), [242](#), [254–259](#), [268–271](#), [296](#), [300](#), [302–303](#), [308–309](#)

Trigger and data acquisition system (TDAQ) is a term used to collectively describe the data collection and filtering system. See [section 3.1](#) for a comprehensive description of its functions and subsystems. Ref on pp. [93–95](#), [97–98](#), [100–101](#), [103–104](#), [161–163](#), [167](#), [180](#), [183](#), [208](#), [236](#), [268–269](#), [297](#), [299](#), [302](#), [305](#)

Trigger matching is a procedure used to establish whether a particular object driving the candidate selection did actually fire the trigger. The trigger matching procedure used for the analysis presented in this thesis is described in [section 4.4.1](#). Ref on pp. [183–184](#)

Triple gauge coupling (TGC) self-coupling of three gauge bosons at a given vertex. If lower-case letter “a” is present in front of the abbreviation, it indicates anomalous TGC. Ref on pp. 157–158, 271

V

Van der Meer scan (VMS) is method by which absolute [luminosity](#) can be measured in an accelerator by sweeping beams transversely across each other, see [section 2.1.4](#). Ref on pp. 41, 83–85, 102, 203, *see* [luminosity](#)

Vector boson fusion (VBF) is a process vector boson production process, e.g. two [W](#) bosons fusing together to make a [Z](#). A significant fraction of Higgs bosons are produced by vector boson fusion according to the Standard Model. Ref on pp. 157, 173–174

Vertex is a more general name given to an [Interaction point](#), i.e. a point where the momenta of interacting particles have changed. There are primary, secondary, tertiary etc. vertices, which relates to the origin of particles in question. In [ATLAS](#), the primary vertex is defined as the vertex with at least 3 tracks that have the highest $\sum p_T$ of all vertices in the given [bunch crossing](#). In Feynman diagrams this term is used for any three or four lines coming together. Ref on pp. 111, 113–115, 121, 129, 132, 201, 295, 311–312

VERYTIGHTLLH is a electron likelihood identification operating point that implements MVA techniques discriminate between real and fake electrons, see [section 3.3.4.3](#) Ref on pp. 204, 208, 222

W

W boson (W) is an electrically charged intermediate boson that mediates the weak interaction. The W^+ has a positive charge of 1 e, W^- is its antiparticle with a negative charge. The existence of weak bosons was predicted by the electroweak theory by [Sheldon L. Glashow \[Gla61\]](#), [Steven Weinberg \[Wei67\]](#), [Abdus Salam \[Sal68\]](#) and experimentally verified at [CERN](#) in 1983 on the UA1 and UA2 experiments at [SPS](#). Ref on pp. 2, 10–11, 16, 19–20, 22, 53, 59, 81, 98, 115, 136, 157–158, 162, 172–176, 194, 206, 212, 215–218, 229, 234, 236–237, 243–244, 267, 269–270, 276–277, 280, 299–300, 309

Worldwide LHC Computing Grid (WLCG) provides the computing for the [LHC](#) experiments including distributions and storage of data sets. [[Sch+05](#)] [[WLC](#)] See [section 3.2.4](#). Ref on pp. 105–106, 268

Z

Z boson (Z) is an electrically neutral intermediate boson that mediates the weak interaction. It was predicted by the electroweak theory by [Sheldon L. Glashow \[Gla61\]](#), [Steven Weinberg \[Wei67\]](#), [Abdus Salam \[Sal68\]](#) and experimentally observed at [CERN](#) in 1983 on the UA1 and UA2 experiments at [SPS](#). Ref on pp. 2, 16, 20, 22, 59, 86, 99, 115, 117–121, 124–126, 131, 135, 157–158, 162–163, 167–169, 171, 174, 176, 185–188, 191–192, 194, 196–197, 201, 208, 212–215, 217, 222, 224, 227–229, 236–237, 267, 269, 280, 300, 307, 309

Zero-Degree Calorimeter (ZDC) is a forward calorimeter located at ± 140 m from the [interaction point](#). was designed mainly to complement the measurement of heavy ion collisions inside [ATLAS](#). Ref on pp. 80

Notation	Description
ABCD	ABCD method
ALFA	Absolute Luminosity for ATLAS
ALICE	ALICE experiment
AOD	Analysis Object Data
ATLAS	ATLAS experiment
BC	Bunch crossing
BR	Branching ratio
CB	Combined muons
CERN	European Organization for Nuclear Research
CMS	CMS experiment
$\hat{C}\hat{P}$	charge–parity invariance
CR	Control region
CSC	Cathode Strip Chambers
CTP	Central Trigger Processor
D3PD	Derived Physics Data
DAQ	Data acquisition
DESY	Deutsches Elektronen-Synchrotron
DPS	Double parton scattering
DQ	Data quality
DQMF	Data Quality Monitoring Framework
ECAL	ATLAS Electromagnetic Calorimeter
EF	Event Filter
ESD	Event Summary Data
FF	Fake factor method
FNAL	Fermi National Accelerator Laboratory
GRL	GoodRunsList
GSF	Gaussian Sum Filter algorithm
HCAL	ATLAS Hadron Calorimeter
HEP	High-energy physics
HLT	High Level Trigger

Notation	Description
ID	ATLAS Inner Detector
IP	Interaction point
JER	Jet energy resolution
JES	Jet energy scale
JVSP	Jet veto survival probability method
L1	Level-1 Trigger
LB	Lumi-block
LCW	Local cluster weighting
LEP	Large Electron-Positron Collider
LHC	Large Hadron Collider
LHCb	LHCb experiment
LHCf	LHCf experiment
LUCID	Luminosity measurement using Cherenkov integrating detector
MBTS	Minimum Bias Trigger Scintillators
MC	Monte Carlo
MCFM	Monte Carlo for FeMtobarn processes
MDT	Monitored Drift Tubes
MoEDAL	MoEDAL experiment
MS	ATLAS Muon Spectrometer
NTUP	n-tuple
PIX	ATLAS Pixel Detector
POOL	POOL
PS	Proton Synchrotron
PU	Pile-up
PV	primary vertex
QCD	Quantum chromodynamics
QED	Quantum electrodynamics
QGC	Quartic gauge coupling
RDO	Raw Data Objects
RoI	Region of Interest
ROOT	ROOT framework
RPC	Resistive Plate Chambers

Notation	Description
S/B	Signal over background ratio
SA	Standalone muons
SCT	ATLAS Semiconductor Tracker
SF	Scale factor
SLAC	SLAC National Accelerator Laboratory
SM	Standard Model
SPS	Super Proton Synchrotron
SR	Signal region
ST	Segment-tagged muons
SV	secondary vertex
TDAQ	Trigger and data acquisition system
TF	Transfer factor method
TGC	Triple gauge coupling
TGC	Thin Gap Chambers
TOTEM	TOTEM experiment
TRT	ATLAS Transition Radiation Tracker
VBF	Vector boson fusion
VMS	Van der Meer scan
WLCG	Worldwide LHC Computing Grid
ZDC	Zero-Degree Calorimeter

Notation	Description
A_{WW}	Acceptance factor
\mathcal{A}	Acceptance
BR	Branching ratio
C_{WW}	Correction factor
CB	Crystal Ball function
χ^2	Chi-squared distribution
d_0	Transverse impact parameter
E_{T}	Transverse energy
η	Pseudorapidity
γ	Photon
H	Higgs boson
\mathcal{L}	Lagrangian function
\mathfrak{L}	Luminosity
m	Invariant mass
\cancel{E}_{T}	Missing transverse energy
\cancel{p}_{T}	Missing transverse momentum
m_{T}	Transverse mass
$\langle \mu \rangle$	Mean number of interactions per bunch crossing
p_{T}	Transverse momentum
σ	Cross-section
SU(2)	Symmetry group
SU(3)	Symmetry group
U(1)	Symmetry group
W	W boson
X_0	Radiation length
y	Rapidity
Z	Z boson
z_0	Longitudinal impact parameter

Introduction

- [Zem10] Martin Zeman. “b-tagging in ATLAS experiment”. English. Master thesis. Prague: Czech Technical University in Prague, 2010 (cit. on p. [xix](#)).

Notation

- [Par13] Particle Data Group. “Review of Particle Physics”. In: *Physical Review D* (2013) (cit. on p. [xx](#)).

Theoretical framework

- [ATL12] ATLAS Collaboration. “Observation of a new particle in the search for the Standard Model Higgs boson with the ATLAS detector at the LHC”. In: *Physics Letters B* 716.1 (Sept. 2012), pp. 1–29. ISSN: 03702693. DOI: [10.1016/j.physletb.2012.08.020](#). arXiv: [1207.7214](#) (cit. on p. [2](#)).
- [Aub+74] J. Aubert, U. Becker, P. Biggs, J. Burger, M. Chen, G. Everhart, P. Goldhagen, J. Leong, T. McCarriston, T. Rhoades, M. Rohde, Samuel Ting, Sau Wu, and Y. Lee. “Experimental Observation of a Heavy Particle J”. In: *Physical Review Letters* 33.23 (Dec. 1974), pp. 1404–1406. ISSN: 0031-9007. DOI: [10.1103/PhysRevLett.33.1404](#) (cit. on pp. [11](#), [13](#), [17](#)).
- [Aug+74] J. Augustin, A. Boyarski, M. Breidenbach, F. Bulos, J. Dakin, G. Feldman, G. Fischer, D. Fryberger, G. Hanson, B. Jean-Marie, R. Larsen, V. Lüth, H. Lynch, D. Lyon, C. Morehouse, J. Paterson, M. Perl, B. Richter, P. Rapidis, R. Schwitters, W. Tanenbaum, F. Vannucci, G. Abrams, D. Briggs, W. Chinowsky, C. Friedberg, G. Goldhaber, R. Hollebeek, J. Kadyk, B. Lulu, F. Pierre, G. Trilling, J. Whitaker, J. Wiss, and J. Zipse. “Discovery of a Narrow Resonance in e+e- Annihilation”. In: *Physical Review Letters* 33.23 (Dec. 1974), pp. 1406–1408. ISSN: 0031-9007. DOI: [10.1103/PhysRevLett.33.1406](#) (cit. on p. [13](#)).
- [CDF95] CDF Collaboration. “Observation of Top Quark Production in p̄p Collisions with the Collider Detector at Fermilab”. In: *Physical Review Letters* 74.14 (Apr. 1995), pp. 2626–2631. ISSN: 0031-9007. DOI: [10.1103/PhysRevLett.74.2626](#) (cit. on p. [13](#)).
- [CMS12] CMS Collaboration. “Observation of a new boson at a mass of 125 GeV with the CMS experiment at the LHC”. In: *Physics Letters B* 716.1 (Sept. 2012), pp. 30–61. ISSN: 03702693. DOI: [10.1016/j.physletb.2012.08.021](#). arXiv: [1207.7235](#) (cit. on p. [2](#)).

- [Cow98] Glen Cowan. *Statistical Data Analysis*. Cowan1998: Oxford University Press, 1998, p. 216. ISBN: 0198501552 (cit. on pp. 23–25).
- [Cur94] Pierre Curie. “Sur la symétrie dans les phénomènes physiques, symétrie d’un champ électrique et d’un champ magnétique”. fr. In: *Journal de Physique Théorique et Appliquée* 3.1 (1894), pp. 393–415. DOI: [10.1051/jphystap:018940030039300](https://doi.org/10.1051/jphystap:018940030039300) (cit. on p. 2).
- [Fey49] R. Feynman. “Space-Time Approach to Quantum Electrodynamics”. In: *Physical Review* 76.6 (Sept. 1949), pp. 769–789. ISSN: 0031-899X. DOI: [10.1103/PhysRev.76.769](https://doi.org/10.1103/PhysRev.76.769) (cit. on p. 9).
- [Fey50] R. Feynman. “Mathematical Formulation of the Quantum Theory of Electromagnetic Interaction”. In: *Physical Review* 80.3 (Nov. 1950), pp. 440–457. ISSN: 0031-899X. DOI: [10.1103/PhysRev.80.440](https://doi.org/10.1103/PhysRev.80.440) (cit. on p. 9).
- [Gel64] Murray Gell-Mann. “A schematic model of baryons and mesons”. In: *Physics Letters* 8.3 (Feb. 1964), pp. 214–215. ISSN: 00319163. DOI: [10.1016/S0031-9163\(64\)92001-3](https://doi.org/10.1016/S0031-9163(64)92001-3) (cit. on p. 11).
- [Gla61] Sheldon L. Glashow. “Partial-symmetries of weak interactions”. In: *Nuclear Physics* 22.4 (Feb. 1961), pp. 579–588. ISSN: 00295582. DOI: [10.1016/0029-5582\(61\)90469-2](https://doi.org/10.1016/0029-5582(61)90469-2) (cit. on p. 2).
- [Gre64] O. Greenberg. “Spin and Unitary-Spin Independence in a Paraquark Model of Baryons and Mesons”. In: *Physical Review Letters* 13.20 (Nov. 1964), pp. 598–602. ISSN: 0031-9007. DOI: [10.1103/PhysRevLett.13.598](https://doi.org/10.1103/PhysRevLett.13.598) (cit. on pp. 12, 13).
- [GS22] Walther Gerlach and Otto Stern. “Das magnetische Moment des Silberatoms”. In: *Zeitschrift für Physik* 9.1 (Dec. 1922), pp. 353–355. ISSN: 1434-6001. DOI: [10.1007/BF01326984](https://doi.org/10.1007/BF01326984) (cit. on p. 6).
- [GW73] David Gross and Frank Wilczek. “Ultraviolet Behavior of Non-Abelian Gauge Theories”. In: *Physical Review Letters* 30.26 (June 1973), pp. 1343–1346. ISSN: 0031-9007. DOI: [10.1103/PhysRevLett.30.1343](https://doi.org/10.1103/PhysRevLett.30.1343) (cit. on p. 15).
- [HFG08] D. Hanneke, S. Fogwell, and G. Gabrielse. “New Measurement of the Electron Magnetic Moment and the Fine Structure Constant”. In: *Physical Review Letters* 100.12 (Mar. 2008), p. 120801. ISSN: 0031-9007. DOI: [10.1103/PhysRevLett.100.120801](https://doi.org/10.1103/PhysRevLett.100.120801). arXiv: [0801.1134](https://arxiv.org/abs/0801.1134) (cit. on p. 2).
- [HM85] Francis Halzen and Alan D. Martin. *Quarks and Leptons: An Introductory Course in Modern Particle Physics*. 1985. DOI: [10.1119/1.14146](https://doi.org/10.1119/1.14146) (cit. on pp. 9, 10).
- [HN65] M. Y. Han and Y. Nambu. “Three-Triplet Model with Double SU(3) Symmetry”. In: *Physical Review* 139.4B (Aug. 1965), B1006–B1010. ISSN: 0031-899X. DOI: [10.1103/PhysRev.139.B1006](https://doi.org/10.1103/PhysRev.139.B1006) (cit. on p. 13).
- [Kan93] Gordon Kane. *Modern Elementary Particle Physics: Updated Edition*. Upd Sub (A. Westview Press, 1993, p. 352. ISBN: 0201624605 (cit. on p. 5).
- [Kul14] Petr Kulháněk. *Aldebaran Group for Astrophysics webpage*. 2014. Available at: <http://www.aldebaran.cz/>, visited on 07/20/2014 (cit. on p. 12).

- [LB14] Tom Lancaster and Stephen J. Blundell. *Quantum Field Theory for the Gifted Amateur*. 2014. ISBN: 0191510939 (cit. on p. 9).
- [Led79] Leon M Lederman. “Resonant and Continuum Dilepton Production”. en. In: *Physica Scripta* 20.2 (Aug. 1979), pp. 227–234. ISSN: 0031-8949. DOI: [10.1088/0031-8949/20/2/016](https://doi.org/10.1088/0031-8949/20/2/016) (cit. on pp. 13, 17).
- [MLM02] T. Morii, C. S. Lim, and S. N. Mukherjee. *The Physics of the Standard Model and Beyond*. World Scientific Pub Co Inc, 2002, p. 312. ISBN: 9810245718 (cit. on pp. 7, 8, 11, 13–15, 17–19, 22, 23).
- [Noe18] Emmy Noether. “Invariante Variationsprobleme”. In: *Gött. Nachr.* (1918), pp. 235–257 (cit. on p. 3).
- [Par12] Particle Data Group. “Review of Particle Physics”. In: *Physical Review D* 86.1 (July 2012), p. 010001. ISSN: 1550-7998. DOI: [10.1103/PhysRevD.86.010001](https://doi.org/10.1103/PhysRevD.86.010001) (cit. on pp. 19, 20, 23–25).
- [Par13] Particle Data Group. “Review of Particle Physics”. In: *Physical Review D* (2013) (cit. on p. 13).
- [Pau25] W. Pauli. “Über den Zusammenhang des Abschlusses der Elektronengruppen im Atom mit der Komplexstruktur der Spektren”. In: *Zeitschrift für Physik* 31.1 (Feb. 1925), pp. 765–783. ISSN: 0044-3328. DOI: [10.1007/BF02980631](https://doi.org/10.1007/BF02980631) (cit. on p. 5).
- [Per00] Donald H. Perkins. *Introduction to High Energy Physics*. 4th. Cambridge University Press, 2000, p. 426. ISBN: 0521621968 (cit. on pp. 6, 11–13, 15–21).
- [Pic07] Antonio Pich. “The Standard Model of Electroweak Interactions”. In: (May 2007), p. 50. arXiv: [0705.4264](https://arxiv.org/abs/0705.4264) (cit. on pp. 3–5, 7, 9).
- [Pol73] H. Politzer. “Reliable Perturbative Results for Strong Interactions?” In: *Physical Review Letters* 30.26 (June 1973), pp. 1346–1349. ISSN: 0031-9007. DOI: [10.1103/PhysRevLett.30.1346](https://doi.org/10.1103/PhysRevLett.30.1346) (cit. on p. 15).
- [PS95] Michael E. Peskin and Dan V. Schroeder. *An Introduction To Quantum Field Theory*. Westview Press; First Edition edition, 1995, p. 864. ISBN: 0201503972 (cit. on pp. 3, 4, 9, 10, 16).
- [Sal68] Abdus Salam. “Weak and Electromagnetic Interactions”. In: *Conf.Proc.* C680519 (1968), pp. 367–377 (cit. on p. 2).
- [Sch48] Julian Schwinger. “On Quantum-Electrodynamics and the Magnetic Moment of the Electron”. In: *Physical Review* 73.4 (Feb. 1948), pp. 416–417. ISSN: 0031-899X. DOI: [10.1103/PhysRev.73.416](https://doi.org/10.1103/PhysRev.73.416) (cit. on p. 9).
- [Tom49] S. Tomonaga. “On a Relativistically Invariant Formulation of the Quantum Theory of Wave Fields”. In: *Progress of Theoretical Physics* 1.2 (Feb. 1949), pp. 27–42. ISSN: 0033-068X. DOI: [10.1143/PTP.1.27](https://doi.org/10.1143/PTP.1.27) (cit. on p. 9).

- [UA183] UA1 Collaboration. “Experimental observation of isolated large transverse energy electrons with associated missing energy at”. In: *Physics Letters B* 122.1 (Feb. 1983), pp. 103–116. ISSN: 03702693. DOI: [10.1016/0370-2693\(83\)91177-2](https://doi.org/10.1016/0370-2693(83)91177-2) (cit. on pp. 11, 19).
- [UA283] UA2 Collaboration. “Observation of single isolated electrons of high transverse momentum in events with missing transverse energy at the CERN p collider”. In: *Physics Letters B* 122.5-6 (Mar. 1983), pp. 476–485. ISSN: 03702693. DOI: [10.1016/0370-2693\(83\)91605-2](https://doi.org/10.1016/0370-2693(83)91605-2) (cit. on p. 19).
- [Wei67] Steven Weinberg. “A Model of Leptons”. In: *Physical Review Letters* 19.21 (Nov. 1967), pp. 1264–1266. ISSN: 0031-9007. DOI: [10.1103/PhysRevLett.19.1264](https://doi.org/10.1103/PhysRevLett.19.1264) (cit. on p. 2).
- [Zwe64a] George Zweig. “An SU_3 model for strong interaction symmetry and its breaking”. In: (Jan. 1964) (cit. on p. 11).
- [Zwe64b] George Zweig. “An SU_3 model for strong interaction symmetry and its breaking”. In: (Feb. 1964) (cit. on p. 11).

Experimental background

- [ALI09] ALICE Collaboration. *ALICE Technical Design Reports*. Mar. 2009 (cit. on p. 57).
- [ALI10] ALICE Collaboration. *ALICE Public Website*. <<http://aliceinfo.cern.ch/Public/>>. Apr. 2010. Available at: <http://aliceinfo.cern.ch/Public/>, visited on 05/07/2014 (cit. on pp. 57, 58).
- [ATL08a] ATLAS Collaboration. *ATLAS Pixel Detector group homepage*. <http://atlas.web.cern.ch/Atlas/GROUPS/INNER_DETECTOR/PIXELS/pixel.html>. 2008. Available at: http://atlas.web.cern.ch/Atlas/GROUPS/INNER_DETECTOR/PIXELS/pixel.html, visited on 05/07/2014 (cit. on pp. 63, 64, 67).
- [ATL08b] ATLAS Collaboration. “Expected Performance of the ATLAS Experiment - Detector, Trigger and Physics”. In: (Dec. 2008). arXiv: [0901.0512](https://arxiv.org/abs/0901.0512) (cit. on p. 60).
- [ATL08c] ATLAS Collaboration. “The ATLAS Experiment at the CERN Large Hadron Collider”. In: *Journal of Instrumentation* 3.08 (Aug. 2008), S08003–S08003. ISSN: 1748-0221. DOI: [10.1088/1748-0221/3/08/S08003](https://doi.org/10.1088/1748-0221/3/08/S08003) (cit. on pp. 52, 56, 60–82).
- [ATL10a] ATLAS Collaboration. *ATLAS Magnet System*. <<http://atlas-magnet.web.cern.ch/atlas-magnet/>>. 2010. Available at: <http://atlas-magnet.web.cern.ch/atlas-magnet/>, visited on 05/07/2014 (cit. on p. 61).
- [ATL10b] ATLAS Collaboration. *ATLAS Public Website*. <<http://www.atlas.ch>>. May 2010. Available at: <http://www.atlas.ch>, visited on 05/06/2014 (cit. on pp. 56, 59, 63–65, 67, 68, 71, 78).
- [ATL11a] ATLAS Collaboration. *ATLAS Fact Sheets*. 2011. Available at: http://www.atlas.ch/fact_sheets.html, visited on 11/08/2013 (cit. on pp. 59–62, 66–68, 72, 77).

- [ATL11b] ATLAS Collaboration. “Luminosity determination in pp collisions at $\sqrt{s} = 7$ TeV using the ATLAS detector at the LHC”. In: *The European Physical Journal C* 71.4 (Apr. 2011), p. 1630. ISSN: 1434-6044. DOI: [10.1140/epjc/s10052-011-1630-5](https://doi.org/10.1140/epjc/s10052-011-1630-5). arXiv: [1101.2185](https://arxiv.org/abs/1101.2185) (cit. on pp. 82, 84).
- [ATL11c] ATLAS Collaboration. “Luminosity Determination in pp Collisions at $\sqrt{s} = 7$ TeV using the ATLAS Detector in 2011”. In: (Aug. 2011) (cit. on pp. 82, 85).
- [ATL11d] ATLAS Collaboration. “Updated Luminosity Determination in pp Collisions at $\sqrt{s} = 7$ TeV using the ATLAS Detector”. In: (Mar. 2011) (cit. on p. 82).
- [ATL12] ATLAS Collaboration. “Observation of a new particle in the search for the Standard Model Higgs boson with the ATLAS detector at the LHC”. In: *Physics Letters B* 716.1 (Sept. 2012), pp. 1–29. ISSN: 03702693. DOI: [10.1016/j.physletb.2012.08.020](https://doi.org/10.1016/j.physletb.2012.08.020). arXiv: [1207.7214](https://arxiv.org/abs/1207.7214) (cit. on pp. 55, 59).
- [ATL13] ATLAS Collaboration. “Improved luminosity determination in pp collisions at $\sqrt{s} = 7$ TeV using the ATLAS detector at the LHC”. In: (Feb. 2013), p. 27. arXiv: [1302.4393](https://arxiv.org/abs/1302.4393) (cit. on pp. 40, 80, 82–85).
- [ATL14a] ATLAS Collaboration. *ATLAS Computing TWiki*. 2014. Available at: <https://twiki.cern.ch/twiki/bin/view/AtlasComputing>, visited on 05/07/2014 (cit. on pp. 53, 54).
- [ATL14b] ATLAS Collaboration. *ATLAS Data Summary*. 2014. Available at: <https://atlas.web.cern.ch/Atlas/GROUPS/DATAPREPARATION/DataSummary/2012/records.html>, visited on 05/25/2014 (cit. on pp. 45, 47).
- [ATL14c] ATLAS Collaboration. *ATLAS Public Event Displays*. Available from: <https://twiki.cern.ch/twiki/bin/view/Atlas/EventDisplayPublicResults>. May 2014. Available at: <https://twiki.cern.ch/twiki/bin/view/AtlasPublic/EventDisplayPublicResults>, visited on 06/03/2014 (cit. on p. 86).
- [ATL14d] ATLAS Collaboration. *Luminosity Public Results*. 2014. Available at: <https://twiki.cern.ch/twiki/bin/view/AtlasPublic/LuminosityPublicResults>, visited on 05/06/2014 (cit. on pp. 44, 45, 82, 86, 87).
- [ATL94] ATLAS Collaboration. *ATLAS Technical Proposal for a General-purpose Pp Experiment at the Large Hadron Collider at CERN*. Ed. by LHC Experiment Committee. Geneva: CERN, Dec. 1994, p. 272. ISBN: 9290830670, 9789290830672 (cit. on pp. 60, 66, 68).
- [ATL99a] ATLAS Collaboration. *ATLAS detector and physics performance: Technical Design Report, 1*. Technical Design Report ATLAS. Geneva: CERN, 1999 (cit. on p. 60).
- [ATL99b] ATLAS Collaboration. *ATLAS detector and physics performance: Technical Design Report, 2*. Technical Design Report ATLAS. Geneva: CERN, 1999 (cit. on p. 60).
- [Bai07] S Baird. “Accelerators for pedestrians”. In: (Feb. 2007) (cit. on pp. 30, 33, 34, 36, 37).
- [Bai14] R Bailey. “An Application for Research: the Large Hadron Collider”. In: (Apr. 2014), p. 10. DOI: [10.5170/CERN-2013-007.565](https://doi.org/10.5170/CERN-2013-007.565). arXiv: [1404.0966](https://arxiv.org/abs/1404.0966) (cit. on pp. 47–49).

- [Bra+97] Enrico Bravin, Peter Galbraith, M A Geitz, Bernd Dehning, G Brun, A Drees, K N Henrichsen, M Koratzinos, and G Mugnai. “The Influence of Train Leakage Currents on the LEP Dipole Field”. In: *Nucl. Instrum. Methods Phys. Res., A* 417 (Sept. 1997), pp. 9–15 (cit. on p. 37).
- [CER] CERN. *CERN Public Website*. Available at: <http://www.cern.ch/>, visited on 05/27/2014 (cit. on p. 54).
- [CER04] CERN. “LHC Design Report”. In: (2004). DOI: [10.5170/CERN-2004-003-V-1](https://doi.org/10.5170/CERN-2004-003-V-1) (cit. on pp. 43, 50).
- [CER06] CERN. “CAS - CERN Accelerator School: Intermediate Course on Accelerator Physics - CERN Document Server”. In: (2006). DOI: [10.5170/CERN-2006-002](https://doi.org/10.5170/CERN-2006-002) (cit. on pp. 33, 36–38, 41).
- [CER08] CERN. “LHC Machine”. en. In: *Journal of Instrumentation* 3.08 (Aug. 2008), S08001–S08001. ISSN: 1748-0221. DOI: [10.1088/1748-0221/3/08/S08001](https://doi.org/10.1088/1748-0221/3/08/S08001) (cit. on pp. 37, 40, 42, 43, 45, 47–50).
- [CER13] CERN. *LHC Machine Outreach*. 2013. Available at: <http://lhc-machine-outreach.web.cern.ch/>, visited on 05/19/2014 (cit. on pp. 40, 43, 46, 49).
- [CER14a] CERN. *LHC Online Status Display*. 2014. Available at: <http://op-webtools.web.cern.ch/op-webtools/vistar/vistars.php?usr=LHC1>, visited on 05/24/2014 (cit. on p. 45).
- [CER14b] CERN. *LHC Performance and Statistics*. 2014. Available at: <http://lhc-statistics.web.cern.ch/LHC-Statistics/>, visited on 05/22/2014 (cit. on p. 47).
- [CMS06] CMS Collaboration. *CMS Technical Design Report (post 2005)*. Technical Design Report CMS. Geneva: CERN, 2006 (cit. on p. 55).
- [CMS10] CMS Collaboration. *CMS Public Website*. <<http://cms.web.cern.ch/cms/>>. Apr. 2010. Available at: <http://cms.web.cern.ch>, visited on 05/07/2014 (cit. on p. 55).
- [CMS12] CMS Collaboration. “Observation of a new boson at a mass of 125 GeV with the CMS experiment at the LHC”. In: *Physics Letters B* 716.1 (Sept. 2012), pp. 30–61. ISSN: 03702693. DOI: [10.1016/j.physletb.2012.08.021](https://doi.org/10.1016/j.physletb.2012.08.021). arXiv: [1207.7235](https://arxiv.org/abs/1207.7235) (cit. on p. 55).
- [CS00] E.D. Courant and H.S. Snyder. “Theory of the Alternating-Gradient Synchrotron”. In: *Annals of Physics* 281.1-2 (Apr. 2000), pp. 360–408. ISSN: 00034916. DOI: [10.1006/aphy.2000.6012](https://doi.org/10.1006/aphy.2000.6012) (cit. on pp. 30, 37).
- [CW32] John Douglas Cockcroft and Ernest Thomas Sinton Walton. “Artificial Production of Fast Protons”. In: *Nature* 129 (1932), pp. 242, 649 (cit. on p. 31).
- [Fer14] Fermi National Accelerator Laboratory. *Muon Accelerator Program (MAP) homepage*. 2014. Available at: <http://map.fnal.gov/>, visited on 05/19/2014 (cit. on p. 31).
- [Gil13] Simone Gilardoni. “Introduction to Accelerators (1/2)”. In: *Italian Teachers Programme* (Sept. 2013) (cit. on pp. 31, 39).
- [Her06] Werner Herr. “Beam-beam interactions”. In: (2006). DOI: [10.5170/CERN-2006-002.379](https://doi.org/10.5170/CERN-2006-002.379) (cit. on pp. 47–49).

- [HM06] Werner Herr and B Muratori. “Concept of luminosity”. In: (2006). doi: [10.5170/CERN-2006-002.361](#) (cit. on pp. [34](#), [39](#), [42](#)).
- [Hol13] Bernhard J. Holzer. “Beam optics and lattice design for particle accelerators”. In: (Mar. 2013), p. 36. doi: [10.5170/CERN-2013-001.171](#). arXiv: [1303.6514](#) (cit. on p. [36](#)).
- [Hol14] B. J. Holzer. “Introduction to Transverse Beam Dynamics”. In: (Apr. 2014), p. 19. doi: [10.5170/CERN-2013-007.27](#). arXiv: [1404.0923](#) (cit. on pp. [32](#), [34](#), [36–38](#)).
- [Hug06] F. Hugging. “The ATLAS pixel detector”. In: *IEEE Transactions on Nuclear Science* 53.3 (June 2006), pp. 1732–1736. ISSN: 0018-9499. doi: [10.1109/TNS.2006.871506](#). arXiv: [0401068 \[physics\]](#) (cit. on p. [64](#)).
- [Lam13] Mike Lamont. “Status of the LHC”. en. In: *Journal of Physics: Conference Series* 455.1 (Aug. 2013), p. 012001. ISSN: 1742-6596. doi: [10.1088/1742-6596/455/1/012001](#) (cit. on pp. [45](#), [47](#)).
- [Let13] Alan Letchford. “Beam dynamics in linacs”. In: (2013). doi: [10.5170/CERN-2013-001.1](#) (cit. on p. [36](#)).
- [LHC10] LHCf Collaboration. *LHCf Public Website*. <<http://www.stelab.nagoya-u.ac.jp/LHCf/>>. Apr. 2010. Available at: <http://www.stelab.nagoya-u.ac.jp/LHCf/>, visited on 05/07/2014 (cit. on p. [59](#)).
- [LHC14] LHCb Collaboration. *LHCb Public Website*. <<http://lhcb-public.web.cern.ch/lhcb-public/>>. Apr. 2014. Available at: <http://lhcb-public.web.cern.ch/>, visited on 05/07/2014 (cit. on pp. [57](#), [58](#)).
- [Lum12] The Luminosity Group. “Preliminary Luminosity Determination in pp Collisions at $\sqrt{s} = 8$ TeV using the ATLAS Detector in 2012”. In: (Nov. 2012) (cit. on p. [83](#)).
- [MoE14] MoEDAL Collaboration. *The Monopole & Exotics Detector at the LHC*. 2014. Available at: <http://moedal.web.cern.ch>, visited on 07/18/2014 (cit. on p. [59](#)).
- [Mos11] J. Moss. “Commissioning and operation of the ATLAS pixel detector”. In: *Nuclear Instruments and Methods in Physics Research Section A: Accelerators, Spectrometers, Detectors and Associated Equipment* 650.1 (Sept. 2011), pp. 1–5. ISSN: 01689002. doi: [10.1016/j.nima.2010.11.190](#) (cit. on pp. [64](#), [66](#), [67](#)).
- [Nav14] Rod Nave. *HyperPhysics*. 2014. Available at: <http://hyperphysics.phy-astr.gsu.edu/hbase/hph.html>, visited on 05/19/2014 (cit. on p. [33](#)).
- [Pap11] Vaia Papadimitriou. “Luminosity determination at the Tevatron”. In: (June 2011). arXiv: [1106.5182](#) (cit. on p. [45](#)).
- [Par12] Particle Data Group. “Review of Particle Physics”. In: *Physical Review D* 86.1 (July 2012), p. 010001. ISSN: 1550-7998. doi: [10.1103/PhysRevD.86.010001](#) (cit. on pp. [30](#), [36–38](#), [41](#), [53](#)).
- [Par13] Particle Data Group. “Review of Particle Physics”. In: *Physical Review D* (2013) (cit. on pp. [40](#), [53](#), [62](#), [68](#), [70](#), [77](#)).

- [Par97] Particle Physics Department at the Rutherford Appleton Laboratory. *Technology for Particle Physics*. 1997. Available at: http://hepwww.rl.ac.uk/OpenDays97/Atlas_SCT_sidetector.htm, visited on 05/09/2014 (cit. on p. 69).
- [Per00] Donald H. Perkins. *Introduction to High Energy Physics*. 4th. Cambridge University Press, 2000, p. 426. ISBN: 0521621968 (cit. on pp. 31–35, 41, 51, 52, 68, 70–72).
- [Pik+14] O. J. Pike, F. Mackenroth, E. G. Hill, and S. J. Rose. “A photon–photon collider in a vacuum hohlraum”. In: *Nature Photonics* advance on (May 2014). ISSN: 1749-4885. DOI: [10.1038/nphoton.2014.95](https://doi.org/10.1038/nphoton.2014.95) (cit. on p. 31).
- [SLA] SLAC. *The Stanford Linear Accelerator Center*. Available at: <http://www.slac.stanford.edu/gen/grad/GradHandbook/slac.html>, visited on 05/23/2014 (cit. on p. 32).
- [SM13] Tai Sakuma and Thomas McCauley. “Detector and event visualization with SketchUp at the CMS experiment”. In: (Oct. 2013) (cit. on p. 56).
- [TOT10] TOTEM Collaboration. *TOTEM Public website*. <<http://totem-experiment.web.cern.ch/totem-experiment/>>. Apr. 2010. Available at: <http://totem-experiment.web.cern.ch/totem-experiment/>, visited on 05/07/2014 (cit. on p. 57).
- [VC] Xabier Cid Vidal and Ramon Cid. *Taking a closer look at LHC*. Available at: <http://www.lhc-closer.es/>, visited on 05/19/2014 (cit. on p. 37).
- [vMee68] S van der Meer. “Calibration of the effective beam height in the ISR”. In: (1968) (cit. on p. 41).
- [Was12] Christoph Wasicki. “Track and vertex reconstruction of the ATLAS Inner Detector in the high multiplicity LHC environment”. In: *Journal of Physics: Conference Series* 396.2 (Dec. 2012), p. 022056. ISSN: 1742-6588. DOI: [10.1088/1742-6596/396/2/022056](https://doi.org/10.1088/1742-6596/396/2/022056) (cit. on p. 85).
- [Wei] Eric W. Weisstein. *Wolfram MathWorld: The Web’s Most Extensive Mathematics Resource*. en. Available at: <http://mathworld.wolfram.com/>, visited on 05/08/2014 (cit. on p. 60).
- [Wid28] Rolf Wideröe. “Über ein neues Prinzip zur Herstellung hoher Spannungen”. In: *Archiv für Elektrotechnik* 21.4 (July 1928), pp. 387–406. ISSN: 0003-9039. DOI: [10.1007/BF01656341](https://doi.org/10.1007/BF01656341) (cit. on p. 31).
- [WM01] Klaus Wille and Jason McFall. *The Physics of Particle Accelerators: An Introduction*. 2001. ISBN: 978-0198505495 (cit. on p. 30).

Computational and reconstruction tools

- [13a] “Determination of the tau energy scale and the associated systematic uncertainty in proton-proton collisions at $\sqrt{s} = 8$ TeV with the ATLAS detector at the LHC in 2012”. In: (Apr. 2013) (cit. on p. 137).
- [13b] “Identification of the Hadronic Decays of Tau Leptons in 2012 Data with the ATLAS Detector”. In: (July 2013) (cit. on p. 137).

- [Ada+03] D Adams, J T Shank, G Cataldi, S Spagnolo, L Merola, A Poppleton, S Goldfarb, Ketevi A Assamagan, G Carlino, A Nairz, M Biglietti, F Conventi, L Spogli, G D Stavropoulos, Yu Fisyak, K Mair, T Wenaus, E Gorini, T Lagouri, M Verducci, S Rosati, A Farilla, and M Primavera. “Track reconstruction in the ATLAS Muon Spectrometer with MOORE 007”. In: (May 2003) (cit. on p. 115).
- [AEH10] Jean-Francois Arguin, Markus Elsing, and Beate Heinemann. “ATLAS Tracking Performance in the Presence of Pile-up”. In: (2010), pp. 1–18 (cit. on p. 112).
- [Ago+03] S. Agostinelli et al. “Geant4—a simulation toolkit”. In: *Nuclear Instruments and Methods in Physics Research Section A: Accelerators, Spectrometers, Detectors and Associated Equipment* 506.3 (July 2003), pp. 250–303. ISSN: 01689002. DOI: [10.1016/S0168-9002\(03\)01368-8](https://doi.org/10.1016/S0168-9002(03)01368-8) (cit. on p. 103).
- [Ali+13] J Alison, C M Lester, K Brendlinger, J Kroll, and S Heim. “Description and Performance of the Electron Likelihood Tool at ATLAS using 2012 LHC Data”. In: (Apr. 2013) (cit. on p. 126).
- [Ask+08] S Ask, D Berge, P Borrego-Amaral, D Caracinha, N Ellis, P Farthouat, P Gällnö, S Haas, J Haller, P Klover, A Krasznahorkay, A Messina, C Ohm, T Pauly, M Perantoni, H Pessoa Lima Junior, G Schuler, D Sherman, R Spiwoks, T Wengler, J M de Seixas, and R Torga Teixeira. “The ATLAS central level-1 trigger logic and TTC system”. en. In: *Journal of Instrumentation* 3.08 (Aug. 2008), P08002–P08002. ISSN: 1748-0221. DOI: [10.1088/1748-0221/3/08/P08002](https://doi.org/10.1088/1748-0221/3/08/P08002) (cit. on p. 93).
- [ATLa] ATLAS Collaboration. *Atlantis - Event display for ATLAS*. Available at: <http://atlantis.web.cern.ch/atlantis/>, visited on 06/16/2014 (cit. on p. 107).
- [ATLb] ATLAS Collaboration. *Atlas CAT ElectroweakBosons*. Available at: <https://twiki.cern.ch/twiki/bin/view/Main/AtlasCATElectroweakBosons>, visited on 06/17/2014 (cit. on pp. 138, 139).
- [ATLc] ATLAS Collaboration. *ATLAS VP1 - The interactive 3D event display for the ATLAS experiment at CERN*. Available at: <http://atlas-vp1.web.cern.ch/atlas-vp1/home/>, visited on 06/16/2014 (cit. on p. 107).
- [ATLd] ATLAS Collaboration. *Calorimeter isolation with TopoClusters versus pileup*. Available at: <https://atlas.web.cern.ch/Atlas/GROUPS/PHYSICS/EGAMMA/PublicPlots/20120404/TopoIsolation/ATL-COM-PHYS-2012-362/index.html>, visited on 06/20/2014 (cit. on p. 128).
- [ATLe] ATLAS Collaboration. *DPD Naming Convention*. Available at: <https://twiki.cern.ch/twiki/bin/viewauth/AtlasProtected/DPDNamingConvention>, visited on 06/16/2014 (cit. on p. 108).
- [ATLf] ATLAS Collaboration. *Electron Identification Menu*. Available at: <https://twiki.cern.ch/twiki/bin/viewauth/AtlasProtected/TechnicalitiesForMedium1>, visited on 06/05/2014 (cit. on p. 125).

- [ATLg] ATLAS Collaboration. *Jet Uncertainties 2011*. Available at: <https://twiki.cern.ch/twiki/bin/viewauth/AtlasProtected/JetUncertainties2011>, visited on 06/19/2014 (cit. on p. 135).
- [ATLh] ATLAS Collaboration. *JetEtmis Recommendations 2012*. Available at: <https://twiki.cern.ch/twiki/bin/viewauth/AtlasProtected/JetEtmisRecommendations2012>, visited on 06/19/2014 (cit. on p. 135).
- [ATLi] ATLAS Collaboration. *Muon and B-physics HLT expert on-call*. Available at: <https://twiki.cern.ch/twiki/bin/viewauth/Atlas/MuonBPhysHLTONCallExpert>, visited on 06/15/2014 (cit. on p. 101).
- [ATLj] ATLAS Collaboration. *Physics Analysis Work Book (Release 17)*. Available at: <https://twiki.cern.ch/twiki/bin/view/AtlasProtected/PhysicsAnalysisWorkBookRel17>, visited on 06/16/2014 (cit. on pp. 102, 104).
- [ATLk] ATLAS Collaboration. *Recommendations for jet cleaning for data 2012*. Available at: <https://twiki.cern.ch/twiki/bin/view/AtlasProtected/HowToCleanJets2012>, visited on 06/20/2014 (cit. on p. 136).
- [ATLl] ATLAS Collaboration. *RootCore*. Available at: <https://twiki.cern.ch/twiki/bin/view/AtlasComputing/RootCore#CMake>, visited on 06/16/2014 (cit. on pp. 107, 139).
- [ATL05] ATLAS Collaboration. “ATLAS Computing Technical Design Report”. In: (2005) (cit. on pp. 102, 104, 105, 107).
- [ATL08a] ATLAS Collaboration. “Expected Performance of the ATLAS Experiment - Detector, Trigger and Physics”. In: (Dec. 2008). arXiv: 0901.0512 (cit. on pp. 112, 117, 118).
- [ATL08b] ATLAS Collaboration. “The ATLAS Experiment at the CERN Large Hadron Collider”. In: *Journal of Instrumentation* 3.08 (Aug. 2008), S08003–S08003. ISSN: 1748-0221. DOI: 10.1088/1748-0221/3/08/S08003 (cit. on pp. 93–97, 111, 112, 115, 117, 118, 123, 125, 136).
- [ATL10a] ATLAS Collaboration. *ATLAS Glossary*. <<http://www.atlas.ch/glossary/glossary.html>>. May 2010. Available at: <http://www.atlas.ch/glossary/glossary.html>, visited on 06/05/2014 (cit. on p. 100).
- [ATL10b] ATLAS Collaboration. *ATLAS Public Website*. <<http://www.atlas.ch>>. May 2010. Available at: <http://www.atlas.ch>, visited on 05/06/2014 (cit. on p. 109).
- [ATL10c] ATLAS Collaboration. “Performance of primary vertex reconstruction in proton-proton collisions at $\sqrt{s}=7$ TeV in the ATLAS experiment”. In: (July 2010) (cit. on p. 114).
- [ATL11a] ATLAS Collaboration. *ATLAS Fact Sheets*. 2011. Available at: http://www.atlas.ch/fact_sheets.html, visited on 11/08/2013 (cit. on p. 94).
- [ATL11b] ATLAS Collaboration. “Electron performance measurements with the ATLAS detector using the 2010 LHC proton-proton collision data”. In: (Oct. 2011), p. 34. DOI: 10.1140/epjc/s10052-012-1909-1. arXiv: 1110.3174 (cit. on pp. 124, 125, 137).

- [ATL11c] ATLAS Collaboration. “Muon Momentum Resolution in First Pass Reconstruction of pp Collision Data Recorded by ATLAS in 2010”. In: (Mar. 2011) (cit. on p. 118).
- [ATL11d] ATLAS Collaboration. “Muon reconstruction efficiency in reprocessed 2010 LHC proton-proton collision data recorded with the ATLAS detector”. In: (Apr. 2011) (cit. on pp. 119, 122).
- [ATL11e] ATLAS Collaboration. “Performance of the ATLAS Trigger System in 2010”. In: (Oct. 2011). arXiv: [1110.1530](#) (cit. on pp. 96, 99).
- [ATL12a] ATLAS Collaboration. *Egamma Calorimeter Isolation Corrections*. 2012. Available at: <https://twiki.cern.ch/twiki/bin/viewauth/AtlasProtected/CalIsolationCorrections>, visited on 06/16/2014 (cit. on p. 129).
- [ATL12b] ATLAS Collaboration. *GoodRunsLists*. 2012. Available at: <https://twiki.cern.ch/twiki/bin/view/Atlas/GoodRunsLists>, visited on 06/22/2014 (cit. on p. 103).
- [ATL12c] ATLAS Collaboration. “Improved electron reconstruction in ATLAS using the Gaussian Sum Filter-based model for bremsstrahlung”. In: (May 2012) (cit. on p. 124).
- [ATL12d] ATLAS Collaboration. “Performance of large-R jets and jet substructure reconstruction with the ATLAS detector”. In: (July 2012) (cit. on p. 130).
- [ATL12e] ATLAS Collaboration. “Performance of missing transverse momentum reconstruction in proton-proton collisions at $\sqrt{s} = 7 \sim \text{TeV}$ with ATLAS”. In: *The European Physical Journal C* 72.1 (Jan. 2012), p. 1844. ISSN: 1434-6044. DOI: [10.1140/epjc/s10052-011-1844-6](#). arXiv: [1108.5602](#) (cit. on pp. 137, 138).
- [ATL12f] ATLAS Collaboration. “Performance of the ATLAS Electron and Photon Trigger in p-p Collisions at $\sqrt{s} = 7 \text{ TeV}$ in 2011”. In: (May 2012) (cit. on p. 99).
- [ATL12g] ATLAS Collaboration. “Performance of the ATLAS muon trigger in 2011”. In: (July 2012) (cit. on pp. 96, 99).
- [ATL12h] ATLAS Collaboration. *Trigger Menu Convention*. 2012. Available at: <https://twiki.cern.ch/twiki/bin/viewauth/Atlas/TriggerMenuConvention>, visited on 06/14/2014 (cit. on p. 99).
- [ATL13a] ATLAS Collaboration. “Jet energy measurement with the ATLAS detector in proton-proton collisions at $\sqrt{s} = 7 \text{ TeV}$ ”. In: *The European Physical Journal C* 73.3 (Mar. 2013), p. 2304. ISSN: 1434-6044. DOI: [10.1140/epjc/s10052-013-2304-2](#). arXiv: [1112.6426](#) (cit. on pp. 131–133).
- [ATL13b] ATLAS Collaboration. “Jet energy scale and its systematic uncertainty in proton-proton collisions at $\sqrt{s}=7 \text{ TeV}$ with ATLAS 2011 data”. In: (Jan. 2013) (cit. on pp. 130–132, 134, 135).
- [ATL13c] ATLAS Collaboration. “Object Selections and Background estimates in the $H \rightarrow WW$ analysis with 20.7 fb^{-1} of data collected with the ATLAS detector at $\sqrt{s} = 8 \text{ TeV}$ ”. In: (Nov. 2013) (cit. on p. 121).

- [ATL13d] ATLAS Collaboration. “Performance of Missing Transverse Momentum Reconstruction in ATLAS studied in Proton-Proton Collisions recorded in 2012 at 8 TeV”. In: (Aug. 2013) (cit. on pp. 136, 137).
- [ATL13e] ATLAS Collaboration. *Preliminary results on the muon reconstruction efficiency, momentum resolution, and momentum scale in ATLAS 2012 pp collision data*. English. Tech. rep. Aug. 2013 (cit. on pp. 117, 119, 120).
- [ATL13f] ATLAS Collaboration. “Supporting document on electron efficiency measurements using the 2012 LHC proton-proton collision data”. In: (Sept. 2013) (cit. on pp. 125, 127).
- [ATL13g] ATLAS Collaboration. *Update of the Computing Models of the WLCG and the LHC Experiments*. Tech. rep. 2013 (cit. on p. 104).
- [ATL14a] ATLAS Collaboration. *ATLAS Computing TWiki*. 2014. Available at: <https://twiki.cern.ch/twiki/bin/view/AtlasComputing>, visited on 05/07/2014 (cit. on p. 107).
- [ATL14b] ATLAS Collaboration. *ATLAS Muon Combined Performance Guidelines for Analyses of 2012 Data*. 2014. Available at: <https://twiki.cern.ch/twiki/bin/viewauth/AtlasProtected/MCPAnalysisGuidelinesData2012>, visited on 06/16/2014 (cit. on p. 121).
- [ATL14c] ATLAS Collaboration. *ATLAS Trigger*. 2014. Available at: <https://twiki.cern.ch/twiki/bin/view/Atlas/AtlasTrigger>, visited on 06/13/2014 (cit. on p. 93).
- [ATL14d] ATLAS Collaboration. *Calibration recommendations for 2011 and 2012 analyses using GEO-20 MC samples and Calibration-Hits-based calibration*. 2014. Available at: <https://twiki.cern.ch/twiki/bin/viewauth/AtlasProtected/EGammaCalibrationGEO20>, visited on 06/07/2014 (cit. on pp. 124, 125).
- [ATL14e] ATLAS Collaboration. *Egamma Isolation*. 2014. Available at: <https://twiki.cern.ch/twiki/bin/viewauth/AtlasProtected/EGammaIsolation>, visited on 06/10/2014 (cit. on pp. 127–129).
- [ATL14f] ATLAS Collaboration. *Electron Efficiency Measurements for 2012 and 2011 Data*. Tech. rep. 2014 (cit. on p. 124).
- [ATL14g] ATLAS Collaboration. *How To Clean Jets 2011*. 2014. Available at: <https://twiki.cern.ch/twiki/bin/viewauth/AtlasProtected/HowToCleanJets2011>, visited on 06/20/2014 (cit. on p. 136).
- [ATL14h] ATLAS Collaboration. *Inner Detector Tracking Performance Approved Plots*. 2014. Available at: <https://twiki.cern.ch/twiki/bin/view/AtlasPublic/InDetTrackingPerformanceApprovedPlots> (cit. on p. 116).
- [ATL14i] ATLAS Collaboration. *Jet Uncertainties 2012*. 2014. Available at: <https://twiki.cern.ch/twiki/bin/viewauth/AtlasProtected/JetUncertainties2012Final>, visited on 06/18/2014 (cit. on p. 135).
- [ATL14j] ATLAS Collaboration. *Lowest un-prescaled triggers per data-taking period*. 2014. Available at: <https://twiki.cern.ch/twiki/bin/viewauth/Atlas/LowestUnprescaled>, visited on 06/14/2014 (cit. on p. 99).

- [ATL14k] ATLAS Collaboration. *Muon Calorimeter Corrections*. 2014. Available at: <https://twiki.cern.ch/twiki/bin/viewauth/AtlasProtected/MuonCalorimeterCorrections> (cit. on pp. 121, 122).
- [ATL14l] ATLAS Collaboration. *Physics Analysis Work Book (Release 17): Introduction to data formats*. 2014. Available at: <https://twiki.cern.ch/twiki/bin/view/AtlasProtected/PhysicsAnalysisWorkBookFormatsIntroduction>, visited on 06/15/2014 (cit. on pp. 104, 105).
- [ATL14m] ATLAS Collaboration. *Quality Definition Staco*. 2014. Available at: <https://twiki.cern.ch/twiki/bin/viewauth/AtlasProtected/QualityDefinitionStaco>, visited on 06/05/2014 (cit. on p. 121).
- [ATL14n] ATLAS Collaboration. “Recommendations of the Physics Objects and Analysis Harmonisation Study Groups 2014”. In: (May 2014) (cit. on p. 108).
- [ATL14o] ATLAS Collaboration. *Trigger Menu Glossary*. 2014. Available at: <https://twiki.cern.ch/twiki/bin/viewauth/Atlas/TriggerMenuGlossary>, visited on 06/12/2014 (cit. on pp. 98, 99).
- [ATL14p] ATLAS Collaboration. *Trigger Menu Log Book 2012*. 2014. Available at: <https://twiki.cern.ch/twiki/bin/view/Atlas/TriggerMenuLogBook2012>, visited on 06/14/2014 (cit. on p. 99).
- [ATL14q] ATLAS Collaboration. *Trigger Operation Public Results*. 2014. Available at: <https://twiki.cern.ch/twiki/bin/view/AtlasPublic/TriggerOperationPublicResults>, visited on 06/11/2014 (cit. on p. 102).
- [ATL14r] ATLAS Collaboration. *Trigger Physics Menu*. 2014. Available at: <https://twiki.cern.ch/twiki/bin/view/Atlas/TriggerPhysicsMenu>, visited on 06/13/2014 (cit. on pp. 98, 99).
- [ATL96] ATLAS Collaboration. “ATLAS Computing Technical Proposal”. In: (1996) (cit. on p. 101).
- [BC13] E C Brost and J T Cummings. “ATLAS Trigger Monitoring in 2012”. In: (Apr. 2013) (cit. on p. 100).
- [Bir+14] I Bird, F Carminati, R Mount, B Panzer-Steindel, J Harvey, I Fisk, B Kersevan, P Clarke, M Girone, P Buncic, M Cattaneo, and P Mato. “Update of the Computing Models of the WLCG and the LHC Experiments”. In: (Apr. 2014) (cit. on p. 105).
- [But12] Will Buttinger. “The ATLAS Level-1 Trigger System”. en. In: *Journal of Physics: Conference Series* 396.1 (Dec. 2012), p. 012010. ISSN: 1742-6588. DOI: [10.1088/1742-6596/396/1/012010](https://doi.org/10.1088/1742-6596/396/1/012010) (cit. on p. 99).
- [CERa] CERN. *CERN Advanced Storage Manager (CASTOR)*. Available at: <http://castor.web.cern.ch/>, visited on 06/16/2014 (cit. on p. 106).
- [CERb] CERN. *Pool Of persistent Objects for LHC (POOL) - Persistency Framework*. Available at: <http://pool.cern.ch/>, visited on 06/16/2014 (cit. on p. 105).
- [CER14] CERN Computing Resource Scrutiny Group. *CRSG Report 2013*. Tech. rep. 2014 (cit. on p. 105).

- [CG10] Ilektra A Christidi and the Atlas Muon Offline Dqa Group. “The offline Data Quality Monitoring system of the ATLAS Muon Spectrometer”. In: *Journal of Physics: Conference Series* 219.4 (Apr. 2010), p. 042035. ISSN: 1742-6596. DOI: [10.1088/1742-6596/219/4/042035](https://doi.org/10.1088/1742-6596/219/4/042035) (cit. on p. 100).
- [Col13] T Colombo. “ATLAS TDAQ System Performance in 2012 Data Taking”. In: (Mar. 2013) (cit. on pp. 94, 101).
- [Cor+07] T Cornelissen, M Elsing, W Liebig, S Fleischmann, and E Moyse. “Concepts, Design and Implementation of the ATLAS New Tracking (NEWT)”. In: (Mar. 2007) (cit. on pp. 109–112).
- [CSS08] Matteo Cacciari, Gavin P Salam, and Gregory Soyez. “The anti- k_t jet clustering algorithm”. In: *Journal of High Energy Physics* 2008.04 (Apr. 2008), pp. 063–063. ISSN: 1029-8479. DOI: [10.1088/1126-6708/2008/04/063](https://doi.org/10.1088/1126-6708/2008/04/063). arXiv: [0802.1189](https://arxiv.org/abs/0802.1189) (cit. on pp. 129, 130).
- [Dob+] Matt Dobbs, Jørgen Beck Hansen, Lynn Garren, and Lars Sonnenschein. *HepMC2 User Manual 2.06*. Available at: http://lcgapp.cern.ch/project/simu/HepMC/206/HepMC2_user_manual.pdf, visited on 06/16/2014 (cit. on p. 104).
- [Dok+97] Yu.L Dokshitzer, G.D Leder, S Moretti, and B.R Webber. “Better jet clustering algorithms”. In: *Journal of High Energy Physics* 1997.08 (Aug. 1997), pp. 001–001. ISSN: 1029-8479. DOI: [10.1088/1126-6708/1997/08/001](https://doi.org/10.1088/1126-6708/1997/08/001). arXiv: [9707323](https://arxiv.org/abs/9707323) [hep-ph] (cit. on p. 129).
- [Ell93] Stephen D. Ellis. “Successive combination jet algorithm for hadron collisions”. In: *Physical Review D* 48.7 (Oct. 1993), pp. 3160–3166. ISSN: 0556-2821. DOI: [10.1103/PhysRevD.48.3160](https://doi.org/10.1103/PhysRevD.48.3160). arXiv: [9305266](https://arxiv.org/abs/9305266) [hep-ph] (cit. on p. 129).
- [EW] Johannes Ebke and Peter Weller. *a4*. Available at: <https://github.com/a4/> (cit. on p. 108).
- [Gea] Geant4 Collaboration. *Geant4: A toolkit for the simulation of the passage of particles through matter*. Available at: <http://geant4.cern.ch/>, visited on 06/16/2014 (cit. on p. 103).
- [Has+07] S. Hassani, L. Chevalier, E. Lançon, J.-F. Laporte, R. Nicolaidou, and A. Ouraou. “A muon identification and combined reconstruction procedure for the ATLAS detector at the LHC using the (MUONBOY, STACO, MuTag) reconstruction packages”. In: *Nuclear Instruments and Methods in Physics Research Section A: Accelerators, Spectrometers, Detectors and Associated Equipment* 572.1 (Mar. 2007), pp. 77–79. ISSN: 01689002. DOI: [10.1016/j.nima.2006.10.340](https://doi.org/10.1016/j.nima.2006.10.340) (cit. on p. 115).
- [IP11] O Igonkina and B Petersen. “Proposal and Motivations for 2011 Trigger Menu”. In: (Jan. 2011) (cit. on p. 99).
- [KHB] Attila Krasznahorkay, Johannes Haller, and David Berge. *SFrame - A ROOT Analysis Framework*. Available at: http://sframe.sourceforge.net/SFrame/SFrame_-_A_ROOT_analysis_framework.html%20http://sourceforge.net/projects/sframe/, visited on 06/16/2014 (cit. on pp. 108, 139).

- [Lam+08] W Lampl, P Loch, S Menke, S Rajagopalan, S Laplace, G Unal, H Ma, S Snyder, D Lelas, and D Rousseau. *Calorimeter Clustering Algorithms*. Tech. rep. Apr. 2008 (cit. on p. 123).
- [Lay+13] P Laycock, R Henderson, L Zhou, O Ozturk, and M Beckingham. “Derived Physics Data Production in ATLAS: Experience with Run 1 and Looking Ahead (proceedings)”. In: (Oct. 2013) (cit. on p. 108).
- [LdV12] S Laplace and JB de Vivie. “Calorimeter isolation and pile-up”. In: (May 2012) (cit. on pp. 127–129).
- [LG] D Lopez Mateos and Dag Gillberg. *Plans and technicalities for 2012 JES analyses*. Available at: <https://indico.cern.ch/event/191816/material/slides/0?contribId=0>, visited on 06/18/2014 (cit. on p. 134).
- [Mar13] Marilyn D. Marx. “Standard Model and Exotic Diboson Production with the ATLAS Detector”. PhD thesis. 2013 (cit. on p. 118).
- [Mel+11] F Meloni, K Prokofiev, S Pagan-Griso, A Milov, and A Wildauer. “Vertexing Performance Data vs MC comparison for LPCC”. In: (Sept. 2011) (cit. on pp. 114, 116).
- [Neg12] A Negri. “Evolution of the Trigger and Data Acquisition System for the ATLAS experiment”. en. In: *Journal of Physics: Conference Series* 396.1 (Dec. 2012), p. 012033. ISSN: 1742-6588. DOI: [10.1088/1742-6596/396/1/012033](https://doi.org/10.1088/1742-6596/396/1/012033) (cit. on pp. 94, 95, 101).
- [Nic+10] R Nicolaidou, L Chevalier, S Hassani, J F Laporte, E Le Menedeu, and A Ouraou. “Muon identification procedure for the ATLAS detector at the LHC using Muonboy reconstruction package and tests of its performance using cosmic rays and single beam data”. en. In: *Journal of Physics: Conference Series* 219.3 (Apr. 2010), p. 032052. ISSN: 1742-6596. DOI: [10.1088/1742-6596/219/3/032052](https://doi.org/10.1088/1742-6596/219/3/032052) (cit. on p. 115).
- [Oli13] Denis Oliveira Damazio. “Data Quality Monitoring for the ATLAS trigger System during the first data taking period of the Large Hadron Collider”. In: (Sept. 2013) (cit. on p. 100).
- [Pag+12a] S Pagan Griso, E Guido, F Meloni, A Wildauer, K Grimm, M Rudolph, K Prokofiev, A Andreazza, and A Salzburger. “Vertex reconstruction plots : Collision performance plots for approval 2011”. In: (May 2012) (cit. on pp. 114–116).
- [Pag+12b] S Pagan Griso, E Guido, F Meloni, A Wildauer, K Grimm, M Rudolph, K Prokofiev, A Andreazza, and A Salzburger. “Vertex reconstruction plots : Collision performance plots for approval 2012”. In: (Apr. 2012) (cit. on p. 114).
- [ROOa] ROOT Development Team. *ROOT: A Data Analysis Framework*. Available at: <http://root.cern.ch/>, visited on 06/16/2014 (cit. on p. 107).
- [ROOb] ROOT Development Team. *ROOT User Guide*. Available at: <http://root.cern.ch/root/html/doc/guides/users-guide/ROOTUsersGuideA4.pdf>, visited on 06/16/2014 (cit. on p. 107).
- [RPF98] Elzbieta Richter-Was, Luc Poggioli, and D Froidevaux. “ATLFAST 2.0 a fast simulation package for ATLAS”. In: (Nov. 1998) (cit. on p. 104).

- [Ryb13] G Rybkin. “ATLAS software configuration and build tool optimisation”. In: (Oct. 2013) (cit. on p. 107).
- [Sac+] Sabrina Sacerdoti, Dag Gillberg, Bogdan Malaescu, and Ricardo Piegaia. *Jet Energy Resolution 2012 (Moriond 2013 recommendation)*. Available at: <https://indico.cern.ch/event/223335/contribution/0/material/slides/0.pdf>, visited on 06/19/2014 (cit. on p. 136).
- [SBS14] Maximilian Swiatlowski, Fabrice Balli, and Carlos Sandoval. *Update on Jet Calibrations*. 2014. Available at: <https://indico.cern.ch/event/161252/contribution/0/material/slides/0.pdf>, visited on 06/18/2014 (cit. on pp. 132, 133).
- [Sch+05] U Schwickerath, R Jones, J Shiers, N Brook, C Grandi, Christoph Eck, I Fisk, Y Schutz, I Bird, B Panzer-Steindel, B Gibbard, H Marten, J Knobloch, A Heiss, L Perini, M Lamanna, D Foster, F Grey, P Mato-Vila, D Düllmann, K Bos, S Jarp, J Harvey, Leslie Robertson, D Kelsey, F Hemmer, T Wenaus, and F Ould-Saada. “LHC computing Grid”. In: (2005) (cit. on p. 105).
- [She] Peter Sherwood. *Atlfast Website*. Available at: <http://www.hep.ucl.ac.uk/atlas/atlfast/>, visited on 06/16/2014 (cit. on p. 104).
- [Was12] Christoph Wasicki. “Track and vertex reconstruction of the ATLAS Inner Detector in the high multiplicity LHC environment”. In: *Journal of Physics: Conference Series* 396.2 (Dec. 2012), p. 022056. ISSN: 1742-6588. DOI: [10.1088/1742-6596/396/2/022056](https://doi.org/10.1088/1742-6596/396/2/022056) (cit. on pp. 111–115).
- [WLC] WLCG Collaboration. *WLCG Document Repository*. Available at: <https://espace2013.cern.ch/WLCG-document-repository/>, visited on 06/16/2014 (cit. on pp. 105, 106).
- [WW99] M. Wobisch and T. Wengler. “Hadronization Corrections to Jet Cross Sections in Deep-Inelastic Scattering”. In: (July 1999), p. 10. arXiv: [9907280](https://arxiv.org/abs/9907280) [[hep-ph](#)] (cit. on p. 129).

Measurement of the Standard Model WW cross-section

- [ATLa] ATLAS Collaboration. *Egamma Trigger Matching*. Available at: <https://twiki.cern.ch/twiki/bin/view/AtlasProtected/EgammaTriggerMatching>, visited on 06/22/2014 (cit. on p. 184).
- [ATLb] ATLAS Collaboration. *Electron Identification Menu*. Available at: <https://twiki.cern.ch/twiki/bin/viewauth/AtlasProtected/TechnicalitiesForMedium1>, visited on 06/05/2014 (cit. on p. 193).
- [ATLc] ATLAS Collaboration. *Electron Reconstruction*. Available at: <https://twiki.cern.ch/twiki/bin/view/AtlasProtected/ElectronReconstruction>, visited on 06/07/2014 (cit. on p. 193).
- [ATLd] ATLAS Collaboration. *Innner Detector Tracking Performance Guidelines*. Available at: <https://twiki.cern.ch/twiki/bin/viewauth/AtlasProtected/InDetTrackingPerformanceGuidelines>, visited on 06/09/2014 (cit. on p. 177).

- [ATLe] ATLAS Collaboration. *L2StarB electron efficiencies*. English. Tech. rep. (cit. on p. 184).
- [ATLf] ATLAS Collaboration. *Recommendations for jet cleaning for data 2012*. Available at: <https://twiki.cern.ch/twiki/bin/view/AtlasProtected/HowToCleanJets2012>, visited on 06/20/2014 (cit. on p. 205).
- [ATLg] ATLAS Collaboration. *TrigMuonEfficiency Documentation*. Available at: <https://twiki.cern.ch/twiki/bin/view/Atlas/TrigMuonEfficiency>, visited on 06/22/2014 (cit. on p. 185).
- [ATL11a] ATLAS Collaboration. “Determination of the muon reconstruction efficiency in ATLAS at the Z resonance in proton-proton collisions at $\sqrt{s}=7$ TeV”. In: (Feb. 2011) (cit. on p. 191).
- [ATL11b] ATLAS Collaboration. “Measurement of the WW cross section in $\sqrt{s} = 7$ TeV pp collisions with ATLAS”. In: *Physical Review Letters* 107.4 (Apr. 2011), p. 041802. ISSN: 0031-9007. DOI: [10.1103/PhysRevLett.107.041802](https://doi.org/10.1103/PhysRevLett.107.041802). arXiv: [1104.5225v1](https://arxiv.org/abs/1104.5225v1) (cit. on pp. 159, 168).
- [ATL11c] ATLAS Collaboration. *Measurement of the WW production cross section in proton-proton collisions at $\sqrt{s} = 7$ TeV with the ATLAS detector*. Tech. rep. 15. Geneva: CERN, Mar. 2011 (cit. on p. 168).
- [ATL11d] ATLAS Collaboration. “Muon Momentum Resolution in First Pass Reconstruction of pp Collision Data Recorded by ATLAS in 2010”. In: (Mar. 2011) (cit. on p. 187).
- [ATL11e] ATLAS Collaboration. “Muon reconstruction efficiency in reprocessed 2010 LHC proton-proton collision data recorded with the ATLAS detector”. In: (Apr. 2011) (cit. on pp. 192, 193).
- [ATL11f] ATLAS Collaboration. *WZ Electroweak Common Topics 2011*. 2011. Available at: <https://twiki.cern.ch/twiki/bin/viewauth/AtlasProtected/WZElectroweakCommonTopics2011> (cit. on p. 177).
- [ATL12a] ATLAS Collaboration. *A measurement of the muon reconstruction efficiency in 2010 ATLAS data using jpsi decays*. English. Tech. rep. Aug. 2012 (cit. on p. 191).
- [ATL12b] ATLAS Collaboration. “Determination of the Strange-Quark Density of the Proton from ATLAS Measurements of the $W \rightarrow \ell \nu$ and $Z \rightarrow \ell \ell$ Cross Sections”. In: *Physical Review Letters* 109.1 (July 2012), p. 012001. ISSN: 0031-9007. DOI: [10.1103/PhysRevLett.109.012001](https://doi.org/10.1103/PhysRevLett.109.012001). arXiv: [1203.4051](https://arxiv.org/abs/1203.4051) (cit. on p. 173).
- [ATL12c] ATLAS Collaboration. “Measurement of the WW cross section in $\sqrt{s} = 7$ TeV pp collisions with the ATLAS detector and limits on anomalous gauge couplings”. In: *Physics Letters B* 712.4-5 (Mar. 2012), p. 11. ISSN: 03702693. DOI: [10.1016/j.physletb.2012.05.003](https://doi.org/10.1016/j.physletb.2012.05.003). arXiv: [1203.6232](https://arxiv.org/abs/1203.6232) (cit. on pp. 159, 168).
- [ATL12d] ATLAS Collaboration. “Observation of a new particle in the search for the Standard Model Higgs boson with the ATLAS detector at the LHC”. In: *Physics Letters B* 716.1 (July 2012), p. 24. ISSN: 03702693. DOI: [10.1016/j.physletb.2012.08.020](https://doi.org/10.1016/j.physletb.2012.08.020). arXiv: [1207.7214](https://arxiv.org/abs/1207.7214) (cit. on p. 157).

- [ATL12e] ATLAS Collaboration. “Observation of a new particle in the search for the Standard Model Higgs boson with the ATLAS detector at the LHC”. In: *Physics Letters B* 716.1 (Sept. 2012), pp. 1–29. ISSN: 03702693. DOI: [10.1016/j.physletb.2012.08.020](https://doi.org/10.1016/j.physletb.2012.08.020). arXiv: [1207.7214](https://arxiv.org/abs/1207.7214) (cit. on p. 173).
- [ATL12f] ATLAS Collaboration. “Performance of the ATLAS Electron and Photon Trigger in p-p Collisions at $\sqrt{s} = 7$ TeV in 2011”. In: (May 2012) (cit. on pp. 185, 187, 188).
- [ATL12g] ATLAS Collaboration. “Performance of the ATLAS muon trigger in 2011”. In: (July 2012) (cit. on pp. 185, 186, 188).
- [ATL12h] ATLAS Collaboration. *WZ Electroweak Common Topics 2012*. 2012. Available at: <https://twiki.cern.ch/twiki/bin/viewauth/AtlasProtected/WZElectroweakCommonTopics2012>, visited on 06/09/2014 (cit. on p. 177).
- [ATL13a] ATLAS Collaboration. *EGamma: Recommended Triggers in 2012*. 2013. Available at: <https://twiki.cern.ch/twiki/bin/view/Atlas/TrigEgammaRecommendedTriggers2012>, visited on 10/03/2013 (cit. on p. 185).
- [ATL13b] ATLAS Collaboration. “Measurement of the WW Production Cross Section in Proton-Proton Collisions at $\sqrt{s} = 8$ TeV with the ATLAS Detector”. In: (Oct. 2013) (cit. on pp. 226, 237).
- [ATL13c] ATLAS Collaboration. “Measurement of W^+W^- production in pp collisions at $\sqrt{s}=7$ TeV with the ATLAS detector and limits on anomalous WWZ and WW_γ couplings”. In: *Physical Review D* 87.11 (June 2013), p. 112001. ISSN: 1550-7998. DOI: [10.1103/PhysRevD.87.112001](https://doi.org/10.1103/PhysRevD.87.112001). arXiv: [1210.2979v2](https://arxiv.org/abs/1210.2979v2) (cit. on pp. 159, 172, 246).
- [ATL13d] ATLAS Collaboration. “Measurements of Higgs boson production and couplings in diboson final states with the ATLAS detector at the LHC”. In: *Physics Letters B* 726.1-3 (Oct. 2013), pp. 88–119. ISSN: 03702693. DOI: [10.1016/j.physletb.2013.08.010](https://doi.org/10.1016/j.physletb.2013.08.010). arXiv: [1307.1427](https://arxiv.org/abs/1307.1427) (cit. on p. 214).
- [ATL13e] ATLAS Collaboration. “Measurements of W gamma and Z gamma production in pp collisions at $\sqrt{s}=7$ TeV with the ATLAS detector at the LHC”. In: (Feb. 2013). arXiv: [1302.1283](https://arxiv.org/abs/1302.1283) (cit. on p. 237).
- [ATL13f] ATLAS Collaboration. *Muons: Recommended triggers in 2012*. 2013. Available at: <https://twiki.cern.ch/twiki/bin/viewauth/Atlas/MuonTriggerPhysicsTriggerRecommendations2012>, visited on 06/22/2014 (cit. on p. 185).
- [ATL13g] ATLAS Collaboration. “Object Selections and Background estimates in the $H \rightarrow WW$ analysis with 20.7 fb^{-1} of data collected with the ATLAS detector at $\sqrt{s} = 8$ TeV”. In: (Nov. 2013) (cit. on pp. 192, 193).
- [ATL13h] ATLAS Collaboration. *Preliminary results on the muon reconstruction efficiency, momentum resolution, and momentum scale in ATLAS 2012 pp collision data*. English. Tech. rep. Aug. 2013 (cit. on pp. 188, 192).
- [ATL13i] ATLAS Collaboration. “Supporting document on electron efficiency measurements using the 2012 LHC proton-proton collision data”. In: (Sept. 2013) (cit. on pp. 194, 196).

- [ATL13j] ATLAS Collaboration. *WZ Electroweak Common Topics 2013*. 2013. Available at: <https://twiki.cern.ch/twiki/bin/viewauth/AtlasProtected/WZElectroweakCommonTopics2013> (cit. on p. 177).
- [ATL14a] ATLAS Collaboration. *ATLAS Muon Combined Performance Guidelines for Analyses of 2012 Data*. 2014. Available at: <https://twiki.cern.ch/twiki/bin/viewauth/AtlasProtected/MCPAnalysisGuidelinesData2012>, visited on 06/16/2014 (cit. on pp. 188, 192).
- [ATL14b] ATLAS Collaboration. *BCH Cleaning Tool*. 2014. Available at: <https://twiki.cern.ch/twiki/bin/viewauth/AtlasProtected/BCHCleaningTool>, visited on 06/20/2014 (cit. on pp. 205, 206).
- [ATL14c] ATLAS Collaboration. *Calibration recommendations for 2011 and 2012 analyses using GEO-20 MC samples and Calibration-Hits-based calibration*. 2014. Available at: <https://twiki.cern.ch/twiki/bin/viewauth/AtlasProtected/EGammaCalibrationGEO20>, visited on 06/07/2014 (cit. on p. 194).
- [ATL14d] ATLAS Collaboration. *Electron Efficiency Measurements for 2012 and 2011 Data*. Tech. rep. 2014 (cit. on pp. 196, 197).
- [ATL14e] ATLAS Collaboration. *Extended Pileup Reweighting*. 2014. Available at: <https://twiki.cern.ch/twiki/bin/viewauth/AtlasProtected/ExtendedPileupReweighting>, visited on 01/06/2013 (cit. on p. 177).
- [ATL14f] ATLAS Collaboration. *How To Clean Jets 2011*. 2014. Available at: <https://twiki.cern.ch/twiki/bin/viewauth/AtlasProtected/HowToCleanJets2011>, visited on 06/20/2014 (cit. on p. 204).
- [ATL14g] ATLAS Collaboration. *Lowest un-prescaled triggers per data-taking period*. 2014. Available at: <https://twiki.cern.ch/twiki/bin/viewauth/Atlas/LowestUnprescaled>, visited on 06/14/2014 (cit. on p. 180).
- [ATL14h] ATLAS Collaboration. *Luminosity Public Results*. 2014. Available at: <https://twiki.cern.ch/twiki/bin/view/AtlasPublic/LuminosityPublicResults>, visited on 05/06/2014 (cit. on pp. 177, 178).
- [ATL14i] ATLAS Collaboration. “Measurement of the W^+W^- production cross section in proton-proton collisions at $\sqrt{s} = 8$ TeV with the ATLAS detector”. In: *Conference Note of SM WW analysis for ICHEP 2014*. June 2014 (cit. on pp. 159, 172, 187, 203, 246).
- [ATL14j] ATLAS Collaboration. *Pileup Reweighting*. 2014. Available at: <https://twiki.cern.ch/twiki/bin/viewauth/AtlasProtected/PileupReweighting>, visited on 01/06/2013 (cit. on p. 177).
- [ATL14k] ATLAS Collaboration. *Tile Trip Reader*. 2014. Available at: <https://twiki.cern.ch/twiki/bin/viewauth/Atlas/TileTripReader>, visited on 06/20/2014 (cit. on p. 205).
- [ATL14l] ATLAS Collaboration. *TrackMET 2011/2012*. 2014. Available at: <https://twiki.cern.ch/twiki/bin/viewauth/AtlasProtected/TrackMET>, visited on 06/28/2014 (cit. on pp. 201, 226).

- [ATL14m] ATLAS Collaboration. *Trigger Object Matching*. 2014. Available at: <https://twiki.cern.ch/twiki/bin/view/Atlas/TriggerObjectMatching>, visited on 06/22/2014 (cit. on p. 184).
- [Bal+10] Richard D. Ball, Luigi Del Debbio, Stefano Forte, Alberto Guffanti, Jose I. Latorre, Juan Rojo, and Maria Ubiali. “A first unbiased global NLO determination of parton distributions and their uncertainties”. In: (Feb. 2010), p. 86. arXiv: [1002.4407](#) (cit. on p. 172).
- [Bie+12] Anastasiya Bierweiler, Tobias Kasprzik, Johann H. Kühn, and Sandro Uccirati. “Electroweak corrections to W-boson pair production at the LHC”. In: (Aug. 2012). arXiv: [1208.3147](#) (cit. on pp. 157, 173, 174).
- [Bil+13] M. Billoni, S. Dittmaier, B. Jäger, and C. Speckner. “Next-to-leading-order electroweak corrections to $pp \rightarrow WW \rightarrow 4$ leptons in double-pole approximation at the LHC”. In: (Nov. 2013). arXiv: [1311.5491](#) (cit. on pp. 157, 174).
- [Bin+06] Thomas Binoth, Mariano Ciccolini, Nikolas Kauer, and Michael Krämer. “Gluon-induced W-boson pair production at the LHC”. en. In: *Journal of High Energy Physics* 2006.12 (Dec. 2006), pp. 046–046. ISSN: 1029-8479. DOI: [10.1088/1126-6708/2006/12/046](#). arXiv: [0611170](#) (cit. on p. 172).
- [Blo+13] B. Blok, Yu. Dokshitzer, L. Frankfurt, and M. Strikman. “Perturbative QCD correlations in multi-parton collisions”. In: (June 2013), p. 16. arXiv: [1306.3763](#) (cit. on p. 174).
- [Bon+13] Marco Bonvini, Fabrizio Caola, Stefano Forte, Kirill Melnikov, and Giovanni Ridolfi. “Signal-background interference effects for $gg \rightarrow H \rightarrow W^+W^-$ beyond leading order”. In: *Physical Review D* 88.3 (Aug. 2013), p. 034032. ISSN: 1550-7998. DOI: [10.1103/PhysRevD.88.034032](#). arXiv: [1304.3053](#) (cit. on p. 174).
- [Cam+09] J. Campbell, E. Castaneda-Miranda, Y. Fang, N. Kauer, B. Mellado, and Sau Wu. “Normalizing weak boson pair production at the Large Hadron Collider”. In: *Physical Review D* 80.5 (Sept. 2009), p. 054023. ISSN: 1550-7998. DOI: [10.1103/PhysRevD.80.054023](#). arXiv: [0906.2500](#) (cit. on p. 212).
- [CEW14] John Campbell, Keith Ellis, and Ciaran Williams. *MCFM - Monte Carlo for FeMtobarn processes*. 2014. Available at: <http://mcfm.fnal.gov/>, visited on 05/10/2014 (cit. on p. 174).
- [CMS12] CMS Collaboration. “Observation of a new boson at a mass of 125 GeV with the CMS experiment at the LHC”. In: *Physics Letters B* 716.1 (Sept. 2012), pp. 30–61. ISSN: 03702693. DOI: [10.1016/j.physletb.2012.08.021](#). arXiv: [1207.7235](#) (cit. on p. 173).
- [Cor+00] Gennaro Corcella, Ian G Knowles, Giuseppe Marchesini, Stefano Moretti, Kosuke Odagiri, Peter Richardson, Michael H Seymour, and Bryan R Webber. “HERWIG 6.5: an event generator for Hadron Emission Reactions With Interfering Gluons (including supersymmetric processes)”. In: *Journal of High Energy Physics* 2001.01 (Nov. 2000), p. 112. ISSN: 1029-8479. DOI: [10.1088/1126-6708/2001/01/010](#). arXiv: [0011363](#) [[hep-ph](#)] (cit. on p. 172).

- [Cow98] Glen Cowan. *Statistical Data Analysis*. Cowan1998: Oxford University Press, 1998, p. 216. ISBN: 0198501552 (cit. on pp. 250, 251).
- [DAg10] G. D’Agostini. “Improved iterative Bayesian unfolding”. In: (Oct. 2010), p. 31. arXiv: [1010.0632](#) (cit. on p. 251).
- [DLZ13] S. Dawson, Ian M. Lewis, and Mao Zeng. “Threshold resummed and approximate next-to-next-to-leading order results for W^+W^- pair production at the LHC”. In: *Physical Review D* 88.5 (Sept. 2013), p. 054028. ISSN: 1550-7998. DOI: [10.1103/PhysRevD.88.054028](#). arXiv: [1307.3249](#) (cit. on p. 173).
- [FNO07] Stefano Frixione, Paolo Nason, and Carlo Oleari. “Matching NLO QCD computations with Parton Shower simulations: the POWHEG method”. In: *Journal of High Energy Physics* 2007.11 (Sept. 2007), p. 91. ISSN: 1029-8479. DOI: [10.1088/1126-6708/2007/11/070](#). arXiv: [0709.2092](#) (cit. on p. 172).
- [Fri+14] Stefano Frixione, Fabian Stoeckli, Paolo Torrielli, Bryan Webber, and Chris White. *The MC@NLO Package*. 2014. Available at: <http://www.hep.phy.cam.ac.uk/theory/webber/MCatNLO/>, visited on 06/24/2014 (cit. on pp. 172, 174).
- [FW02] Stefano Frixione and Bryan R Webber. “Matching NLO QCD computations and parton shower simulations”. en. In: *Journal of High Energy Physics* 2002.06 (June 2002), pp. 029–029. ISSN: 1029-8479. DOI: [10.1088/1126-6708/2002/06/029](#) (cit. on pp. 172, 174).
- [HK96] Andreas Höcker and Vakhtang Kartvelishvili. “SVD approach to data unfolding”. In: *Nuclear Instruments and Methods in Physics Research Section A: Accelerators, Spectrometers, Detectors and Associated Equipment* 372.3 (Apr. 1996), pp. 469–481. ISSN: 01689002. DOI: [10.1016/0168-9002\(95\)01478-0](#). arXiv: [9509307 \[hep-ph\]](#) (cit. on p. 251).
- [JOZ06] Barbara Jäger, Carlo Oleari, and Dieter Zeppenfeld. “Next-to-leading order QCD corrections to $W+W^-$ production via vector-boson fusion”. In: *Journal of High Energy Physics* 2006.07 (July 2006), pp. 015–015. ISSN: 1029-8479. DOI: [10.1088/1126-6708/2006/07/015](#). arXiv: [0603177 \[hep-ph\]](#) (cit. on p. 174).
- [JR75] F. James and M. Roos. “Minuit - a system for function minimization and analysis of the parameter errors and correlations”. en. In: *Computer Physics Communications* 10.6 (Dec. 1975), pp. 343–367. ISSN: 00104655. DOI: [10.1016/0010-4655\(75\)90039-9](#) (cit. on p. 245).
- [KR13] Borut Paul Kersevan and Elzbieta Richter-Was. “The Monte Carlo event generator AcerMC versions 2.0 to 3.8 with interfaces to PYTHIA 6.4, HERWIG 6.5 and ARIADNE 4.1”. In: *Computer Physics Communications* 184.3 (Mar. 2013), pp. 919–985. ISSN: 00104655. DOI: [10.1016/j.cpc.2012.10.032](#). arXiv: [0405247 \[hep-ph\]](#) (cit. on p. 174).
- [Lam+08] W Lampl, P Loch, S Menke, S Rajagopalan, S Laplace, G Unal, H Ma, S Snyder, D Lelas, and D Rousseau. *Calorimeter Clustering Algorithms*. Tech. rep. Apr. 2008 (cit. on p. 194).

- [LdV12] S Laplace and JB de Vivie. “Calorimeter isolation and pile-up”. In: (May 2012) (cit. on p. 197).
- [Man+03] Michelangelo L Mangano, Fulvio Piccinini, Antonio D Polosa, Mauro Moretti, and Roberto Pittau. “ALPGEN, a generator for hard multiparton processes in hadronic collisions”. In: *Journal of High Energy Physics* 2003.07 (July 2003), pp. 001–001. ISSN: 1029-8479. DOI: [10.1088/1126-6708/2003/07/001](https://doi.org/10.1088/1126-6708/2003/07/001) (cit. on p. 174).
- [Mar+09] A. D. Martin, W. J. Stirling, R. S. Thorne, and G. Watt. “Parton distributions for the LHC”. In: *The European Physical Journal C* 63.2 (July 2009), pp. 189–285. ISSN: 1434-6044. DOI: [10.1140/epjc/s10052-009-1072-5](https://doi.org/10.1140/epjc/s10052-009-1072-5). arXiv: [0901.0002](https://arxiv.org/abs/0901.0002) (cit. on p. 172).
- [Mor12] John Morris. *HEP Analysis*. London, 2012. Available at: [http://www.hep.ucl.ac.uk/\\$%5Csim\\$campanel/Post_Grads/2013-2014/JMorris_HEPAnalysis.pdf](http://www.hep.ucl.ac.uk/$%5Csim$campanel/Post_Grads/2013-2014/JMorris_HEPAnalysis.pdf) (cit. on pp. 177, 178).
- [MRZ11] Bruce Mellado, Xifeng Ruan, and Zhiqing Zhang. “Extraction of Top Backgrounds in the Higgs Boson Search with the $H \rightarrow WW^* \rightarrow \ell\ell + \cancel{E}_T$ Decay with a Full-Jet Veto at the LHC”. In: (Jan. 2011). arXiv: [1101.1383](https://arxiv.org/abs/1101.1383) (cit. on p. 231).
- [Nas04] Paolo Nason. “A New Method for Combining NLO QCD with Shower Monte Carlo Algorithms”. In: *Journal of High Energy Physics* 2004.11 (Nov. 2004), pp. 040–040. ISSN: 1029-8479. DOI: [10.1088/1126-6708/2004/11/040](https://doi.org/10.1088/1126-6708/2004/11/040). arXiv: [0409146](https://arxiv.org/abs/0409146) [[hep-ph](https://arxiv.org/archive/hep)] (cit. on p. 172).
- [Par12] Particle Data Group. “Review of Particle Physics”. In: *Physical Review D* 86.1 (July 2012), p. 010001. ISSN: 1550-7998. DOI: [10.1103/PhysRevD.86.010001](https://doi.org/10.1103/PhysRevD.86.010001) (cit. on p. 158).
- [Sjö+00] Torbjörn Sjöstrand, Patrik Edén, Christer Friberg, Leif Lönnblad, Gabriela Miu, Stephen Mrenna, and Emanuel Norrbin. “High-Energy-Physics Event Generation with PYTHIA 6.1”. In: *Computer Physics Communications* 135.2 (Oct. 2000), p. 27. ISSN: 00104655. DOI: [10.1016/S0010-4655\(00\)00236-8](https://doi.org/10.1016/S0010-4655(00)00236-8). arXiv: [0010017](https://arxiv.org/abs/0010017) [[hep-ph](https://arxiv.org/archive/hep)] (cit. on p. 172).
- [Sti13] James Stirling. *Parton luminosity and cross section plots*. 2013. Available at: [http://www.hep.ph.ic.ac.uk/\\$%5Csim\\$wstirlin/plots/plots.html](http://www.hep.ph.ic.ac.uk/$%5Csim$wstirlin/plots/plots.html), visited on 12/23/2013 (cit. on p. 160).
- [The13] The LHC Higgs Cross Section Working Group. “Handbook of LHC Higgs Cross Sections: 3. Higgs Properties”. In: (July 2013), p. 404. DOI: [10.5170/CERN-2013-004](https://doi.org/10.5170/CERN-2013-004). arXiv: [1307.1347](https://arxiv.org/abs/1307.1347) (cit. on pp. 173, 174).
- [WB13] Mike Whalley and Andy Buckley. *The Les Houches Accord PDF Interface (LHAPDF) website*. 2013. Available at: <https://lhapdf.hepforge.org/>, visited on 01/13/2014 (cit. on p. 180).
- [WBG05] M. R. Whalley, D. Bourilkov, and R. C. Group. “The Les Houches Accord PDFs (LHAPDF) and Lhaglu”. In: (Aug. 2005), p. 8. arXiv: [0508110](https://arxiv.org/abs/0508110) [[hep-ph](https://arxiv.org/archive/hep)] (cit. on p. 180).

Discussion and conclusions

- [ATL12] ATLAS Collaboration. “Observation of a new particle in the search for the Standard Model Higgs boson with the ATLAS detector at the LHC”. In: *Physics Letters B* 716.1 (Sept. 2012), pp. 1–29. ISSN: 03702693. DOI: [10.1016/j.physletb.2012.08.020](https://doi.org/10.1016/j.physletb.2012.08.020). arXiv: [1207.7214](https://arxiv.org/abs/1207.7214) (cit. on p. 267).
- [ATL13] ATLAS Collaboration. “Measurements of $W\gamma$ and $Z\gamma$ production in pp collisions at $\sqrt{s} = 7$ TeV with the ATLAS detector at the LHC”. In: (Feb. 2013). arXiv: [1302.1283](https://arxiv.org/abs/1302.1283) (cit. on p. 271).
- [ATL14] ATLAS Collaboration. “Measurement of the W^+W^- production cross section in proton-proton collisions at $\sqrt{s} = 8$ TeV with the ATLAS detector”. In: *Conference Note of SM WW analysis for ICHEP 2014*. June 2014 (cit. on p. 271).
- [CMS12] CMS Collaboration. “Observation of a new boson at a mass of 125 GeV with the CMS experiment at the LHC”. In: *Physics Letters B* 716.1 (Sept. 2012), pp. 30–61. ISSN: 03702693. DOI: [10.1016/j.physletb.2012.08.021](https://doi.org/10.1016/j.physletb.2012.08.021). arXiv: [1207.7235](https://arxiv.org/abs/1207.7235) (cit. on p. 267).

Glossary

- [Ada+03] D Adams, J T Shank, G Cataldi, S Spagnolo, L Merola, A Poppleton, S Goldfarb, Ketevi A Assamagan, G Carlino, A Nairz, M Biglietti, F Conventi, L Spogli, G D Stavropoulos, Yu Fisyak, K Mair, T Wenaus, E Gorini, T Lagouri, M Verducci, S Rosati, A Farilla, and M Primavera. “Track reconstruction in the ATLAS Muon Spectrometer with MOORE 007”. In: (May 2003) (cit. on p. 303).
- [ALI10] ALICE Collaboration. *ALICE Public Website*. <<http://aliceinfo.cern.ch/Public/>>. Apr. 2010. Available at: <http://aliceinfo.cern.ch/Public/>, visited on 05/07/2014 (cit. on p. 293).
- [Alw+14] J. Alwall, R. Frederix, S. Frixione, V. Hirschi, F. Maltoni, O. Mattelaer, H. -S. Shao, T. Stelzer, P. Torrielli, and M. Zaro. “The automated computation of tree-level and next-to-leading order differential cross sections, and their matching to parton shower simulations”. In: (May 2014), p. 158. arXiv: [1405.0301](https://arxiv.org/abs/1405.0301) (cit. on p. 301).
- [ATL12] ATLAS Collaboration. “Improved electron reconstruction in ATLAS using the Gaussian Sum Filter-based model for bremsstrahlung”. In: (May 2012) (cit. on p. 298).
- [ATL13] ATLAS Collaboration. “Measurement of the WW Production Cross Section in Proton-Proton Collisions at $\sqrt{s} = 8$ TeV with the ATLAS Detector”. In: (Oct. 2013) (cit. on pp. 293, 298).
- [ATL14a] ATLAS Collaboration. *MBTS Trigger*. 2014. Available at: <https://twiki.cern.ch/twiki/bin/view/Atlas/MbtsTrigger>, visited on 06/09/2014 (cit. on p. 302).
- [ATL14b] ATLAS Collaboration. *Trigger Menu Glossary*. 2014. Available at: <https://twiki.cern.ch/twiki/bin/viewauth/Atlas/TriggerMenuGlossary>, visited on 06/12/2014 (cit. on p. 301).

- [BFS96] J. M. Butterworth, J. R. Forshaw, and M. H. Seymour. “Multiparton interactions in photoproduction at HERA”. In: *Zeitschrift für Physik C: Particles and Fields* 72.4 (Dec. 1996), pp. 637–646. ISSN: 0170-9739. DOI: [10.1007/s002880050286](https://doi.org/10.1007/s002880050286). arXiv: [9601371](https://arxiv.org/abs/9601371) [[hep-ph](#)] (cit. on p. 300).
- [Bin+06] Thomas Binoth, Mariano Ciccolini, Nikolas Kauer, and Michael Krämer. “Gluon-induced W-boson pair production at the LHC”. en. In: *Journal of High Energy Physics* 2006.12 (Dec. 2006), pp. 046–046. ISSN: 1029-8479. DOI: [10.1088/1126-6708/2006/12/046](https://doi.org/10.1088/1126-6708/2006/12/046). arXiv: [0611170](https://arxiv.org/abs/0611170) (cit. on p. 299).
- [But+] Jon Butterworth, Jeff Forshaw, Mike Seymour, and Rod Walker. *JIMMY Generator - Multiparton Interactions in HERWIG*. Available at: <http://jimmy.hepforge.org/>, visited on 06/29/2014 (cit. on p. 300).
- [CDF95] CDF Collaboration. “Observation of Top Quark Production in $p\bar{p}$ Collisions with the Collider Detector at Fermilab”. In: *Physical Review Letters* 74.14 (Apr. 1995), pp. 2626–2631. ISSN: 0031-9007. DOI: [10.1103/PhysRevLett.74.2626](https://doi.org/10.1103/PhysRevLett.74.2626) (cit. on p. 307).
- [CER] CERN. *Persistency Framework Webpage*. Available at: <https://twiki.cern.ch/twiki/bin/view/Persistency>, visited on 06/16/2014 (cit. on p. 304).
- [CER14] CERN. *The Proton Synchrotron*. 2014. Available at: <http://home.web.cern.ch/about/accelerators/proton-synchrotron>, visited on 06/28/2014 (cit. on p. 304).
- [CEW14] John Campbell, Keith Ellis, and Ciaran Williams. *MCFM - Monte Carlo for FeMtobarn processes*. 2014. Available at: <http://mcfm.fnal.gov/>, visited on 05/10/2014 (cit. on p. 303).
- [Cor+00] Gennaro Corcella, Ian G Knowles, Giuseppe Marchesini, Stefano Moretti, Kosuke Odagiri, Peter Richardson, Michael H Seymour, and Bryan R Webber. “HERWIG 6.5: an event generator for Hadron Emission Reactions With Interfering Gluons (including supersymmetric processes)”. In: *Journal of High Energy Physics* 2001.01 (Nov. 2000), p. 112. ISSN: 1029-8479. DOI: [10.1088/1126-6708/2001/01/010](https://doi.org/10.1088/1126-6708/2001/01/010). arXiv: [0011363](https://arxiv.org/abs/0011363) [[hep-ph](#)] (cit. on p. 299).
- [Cow98] Glen Cowan. *Statistical Data Analysis*. Cowan1998: Oxford University Press, 1998, p. 216. ISBN: 0198501552 (cit. on p. 296).
- [CSS08] Matteo Cacciari, Gavin P Salam, and Gregory Soyez. “The anti- k_t jet clustering algorithm”. In: *Journal of High Energy Physics* 2008.04 (Apr. 2008), pp. 063–063. ISSN: 1029-8479. DOI: [10.1088/1126-6708/2008/04/063](https://doi.org/10.1088/1126-6708/2008/04/063). arXiv: [0802.1189](https://arxiv.org/abs/0802.1189) (cit. on p. 294).
- [D0 95] D0 Collaboration. “Search for High Mass Top Quark Production in $pp\bar{p}$ Collisions at $s = 1.8$ TeV”. In: *Physical Review Letters* 74.13 (Mar. 1995), pp. 2422–2426. ISSN: 0031-9007. DOI: [10.1103/PhysRevLett.74.2422](https://doi.org/10.1103/PhysRevLett.74.2422) (cit. on p. 307).
- [EB64] F. Englert and R. Brout. “Broken Symmetry and the Mass of Gauge Vector Mesons”. In: *Physical Review Letters* 13.9 (Aug. 1964), pp. 321–323. ISSN: 0031-9007. DOI: [10.1103/PhysRevLett.13.321](https://doi.org/10.1103/PhysRevLett.13.321) (cit. on p. 299).

- [Fey49] R. Feynman. “Space-Time Approach to Quantum Electrodynamics”. In: *Physical Review* 76.6 (Sept. 1949), pp. 769–789. ISSN: 0031-899X. DOI: [10.1103/PhysRev.76.769](https://doi.org/10.1103/PhysRev.76.769) (cit. on p. 305).
- [Fey50] R. Feynman. “Mathematical Formulation of the Quantum Theory of Electromagnetic Interaction”. In: *Physical Review* 80.3 (Nov. 1950), pp. 440–457. ISSN: 0031-899X. DOI: [10.1103/PhysRev.80.440](https://doi.org/10.1103/PhysRev.80.440) (cit. on p. 305).
- [FNO07] Stefano Frixione, Paolo Nason, and Carlo Oleari. “Matching NLO QCD computations with Parton Shower simulations: the POWHEG method”. In: *Journal of High Energy Physics* 2007.11 (Sept. 2007), p. 91. ISSN: 1029-8479. DOI: [10.1088/1126-6708/2007/11/070](https://doi.org/10.1088/1126-6708/2007/11/070). arXiv: [0709.2092](https://arxiv.org/abs/0709.2092) (cit. on p. 304).
- [Fri+14] Stefano Frixione, Fabian Stoeckli, Paolo Torrielli, Bryan Webber, and Chris White. *The MC@NLO Package*. 2014. Available at: <http://www.hep.phy.cam.ac.uk/theory/webber/MCatNLO/>, visited on 06/24/2014 (cit. on p. 302).
- [FW02] Stefano Frixione and Bryan R Webber. “Matching NLO QCD computations and parton shower simulations”. en. In: *Journal of High Energy Physics* 2002.06 (June 2002), pp. 029–029. ISSN: 1029-8479. DOI: [10.1088/1126-6708/2002/06/029](https://doi.org/10.1088/1126-6708/2002/06/029) (cit. on p. 302).
- [Gla61] Sheldon L. Glashow. “Partial-symmetries of weak interactions”. In: *Nuclear Physics* 22.4 (Feb. 1961), pp. 579–588. ISSN: 00295582. DOI: [10.1016/0029-5582\(61\)90469-2](https://doi.org/10.1016/0029-5582(61)90469-2) (cit. on p. 309).
- [Has+07] S. Hassani, L. Chevalier, E. Lançon, J.-F. Laporte, R. Nicolaidou, and A. Ouraou. “A muon identification and combined reconstruction procedure for the ATLAS detector at the LHC using the (MUONBOY, STACO, MuTag) reconstruction packages”. In: *Nuclear Instruments and Methods in Physics Research Section A: Accelerators, Spectrometers, Detectors and Associated Equipment* 572.1 (Mar. 2007), pp. 77–79. ISSN: 01689002. DOI: [10.1016/j.nima.2006.10.340](https://doi.org/10.1016/j.nima.2006.10.340) (cit. on p. 307).
- [Hig64] Peter Higgs. “Broken Symmetries and the Masses of Gauge Bosons”. In: *Physical Review Letters* 13.16 (Oct. 1964), pp. 508–509. ISSN: 0031-9007. DOI: [10.1103/PhysRevLett.13.508](https://doi.org/10.1103/PhysRevLett.13.508) (cit. on p. 299).
- [KHB] Attila Krasznahorkay, Johannes Haller, and David Berge. *SFrame - A ROOT Analysis Framework*. Available at: http://sframe.sourceforge.net/SFrame/SFrame_-_A_ROOT_analysis_framework.html%20http://sourceforge.net/projects/sframe/, visited on 06/16/2014 (cit. on p. 306).
- [Lam14] Mike Lamont. *LHC Commissioning*. 2014. Available at: <http://lhc-commissioning.web.cern.ch/lhc-commissioning/>, visited on 06/25/2014 (cit. on p. 306).
- [Nic+10] R Nicolaidou, L Chevalier, S Hassani, J F Laporte, E Le Menedeu, and A Ouraou. “Muon identification procedure for the ATLAS detector at the LHC using Muonboy reconstruction package and tests of its performance using cosmic rays and single beam data”. en. In: *Journal of Physics: Conference Series* 219.3 (Apr. 2010), p. 032052. ISSN: 1742-6596. DOI: [10.1088/1742-6596/219/3/032052](https://doi.org/10.1088/1742-6596/219/3/032052) (cit. on p. 307).

- [Par13] Particle Data Group. “Review of Particle Physics”. In: *Physical Review D* (2013) (cit. on p. 302).
- [Per00] Donald H. Perkins. *Introduction to High Energy Physics*. 4th. Cambridge University Press, 2000, p. 426. ISBN: 0521621968 (cit. on p. 305).
- [ROO] ROOT Development Team. *ROOT: A Data Analysis Framework*. Available at: <http://root.cern.ch/>, visited on 06/16/2014 (cit. on p. 306).
- [Sal68] Abdus Salam. “Weak and Electromagnetic Interactions”. In: *Conf.Proc.* C680519 (1968), pp. 367–377 (cit. on p. 309).
- [Sch+05] U Schwickerath, R Jones, J Shiers, N Brook, C Grandi, Christoph Eck, I Fisk, Y Schutz, I Bird, B Panzer-Steindel, B Gibbard, H Marten, J Knobloch, A Heiss, L Perini, M Lamanna, D Foster, F Grey, P Mato-Vila, D Düllmann, K Bos, S Jarp, J Harvey, Leslie Robertson, D Kelsey, F Hemmer, T Wenaus, and F Ould-Saada. “LHC computing Grid”. In: (2005) (cit. on p. 309).
- [Sch48] Julian Schwinger. “On Quantum-Electrodynamics and the Magnetic Moment of the Electron”. In: *Physical Review* 73.4 (Feb. 1948), pp. 416–417. ISSN: 0031-899X. DOI: [10.1103/PhysRev.73.416](https://doi.org/10.1103/PhysRev.73.416) (cit. on p. 305).
- [She] Peter Sherwood. *Atlfast Website*. Available at: <http://www.hep.ucl.ac.uk/atlas/atlfast/>, visited on 06/16/2014 (cit. on p. 295).
- [She14] Sherpa Team. *Sherpa website*. 2014. Available at: <https://sherpa.hepforge.org/trac/wiki>, visited on 06/07/2014 (cit. on p. 306).
- [Sjö+00] Torbjörn Sjöstrand, Patrik Edén, Christer Friberg, Leif Lönnblad, Gabriela Miu, Stephen Mrenna, and Emanuel Norrbin. “High-Energy-Physics Event Generation with PYTHIA 6.1”. In: *Computer Physics Communications* 135.2 (Oct. 2000), p. 27. ISSN: 00104655. DOI: [10.1016/S0010-4655\(00\)00236-8](https://doi.org/10.1016/S0010-4655(00)00236-8). arXiv: [0010017 \[hep-ph\]](https://arxiv.org/abs/hep-ph/0010017) (cit. on p. 305).
- [Tom49] S. Tomonaga. “On a Relativistically Invariant Formulation of the Quantum Theory of Wave Fields”. In: *Progress of Theoretical Physics* 1.2 (Feb. 1949), pp. 27–42. ISSN: 0033-068X. DOI: [10.1143/PTP.1.27](https://doi.org/10.1143/PTP.1.27) (cit. on p. 305).
- [WB13] Mike Whalley and Andy Buckley. *The Les Houches Accord PDF Interface (LHAPDF) website*. 2013. Available at: <https://lhapdf.hepforge.org/>, visited on 01/13/2014 (cit. on p. 301).
- [Wei67] Steven Weinberg. “A Model of Leptons”. In: *Physical Review Letters* 19.21 (Nov. 1967), pp. 1264–1266. ISSN: 0031-9007. DOI: [10.1103/PhysRevLett.19.1264](https://doi.org/10.1103/PhysRevLett.19.1264) (cit. on p. 309).
- [WLC] WLCG Collaboration. *WLCG Document Repository*. Available at: <https://espace2013.cern.ch/WLCG-document-repository/>, visited on 06/16/2014 (cit. on p. 309).

A

acceptance, 159, 161, 217, 293
 ALICE, 45, 55, 57, 58, 267, 293
 alignment, 82, 293
 ATLAS, 30, 42, 44, 45, 48, 52, 54–56, 59–67,
 69–75, 77–85, 93, 94, 100–105,
 107–111, 115, 117, 118, 123, 129,
 131, 136, 137, 139, 157, 158, 161,
 162, 167, 173, 176, 180, 202, 203,
 267, 268, 293–297, 299, 301–303,
 305, 307, 309
 ALFA, 80, 102, 293
 b-layer, 64, 126, 295
 Cathode Strip Chambers, 77, 117, 294,
 296
 Electromagnetic Calorimeter, 70, 124,
 133, 199, 294
 Hadron Calorimeter, 60, 70, 72, 74, 96,
 127, 199, 294
 Inner Detector, 60–66, 68, 70, 81, 84, 85,
 93, 94, 99, 109–112, 114, 115,
 117–120, 123, 129, 137, 177,
 186–188, 199, 201, 217, 222, 268,
 294–296, 300, 306
 Minimum Bias Trigger Scintillators, 84,
 302
 Monitored Drift Tubes, 77, 117, 294,
 303, 306
 Muon Spectrometer, 60, 62, 71, 77–79,
 94, 95, 115, 117–120, 136–138,
 186–188, 191, 192, 199–201, 217,
 222, 294, 296, 303, 306, 307
 Pixel Detector, 63–68, 81, 84, 109–112,
 114, 117, 126, 187, 201, 294, 295
 Resistive Plate Chambers, 77, 95, 117,
 295, 306, 307
 Semiconductor Tracker, 63–66, 68–70,

81, 84, 109–112, 114, 117, 123,
 126, 187, 201, 294, 295

Thin Gap Chambers, 77, 95, 117, 121,
 295, 307

Transition Radiation Tracker, 63, 84, 295
 ZDC, 80, 309

B

barrel, 60–65, 67–75, 95, 96, 109–112, 117,
 121, 123, 124, 185–187, 196, 294,
 295, 306
 branching ratio, 20, 158, 159, 244, 295
 bremsstrahlung, 71, 124, 295
 bunch crossing, 43, 83–85, 93, 101, 114, 132,
 176, 200, 201, 295, 309
 mean number of interactions per bunch
 crossing, 82–85, 87, 101, 113–116,
 126, 132, 135, 176–178, 302

C

CERN, 2, 32, 35, 43, 47, 49, 54, 55, 57, 60,
 100, 105–107, 138, 180, 267, 294,
 298, 300, 304, 307, 309
 χ^2 distribution, 110, 112, 114, 117, 118, 252,
 296
 CMS, 45, 48, 54–57, 105, 173, 267, 296
 charge–parity, 17, 57, 296
 cross-section, 9, 10, 21, 25, 30, 40, 42, 43,
 82–84, 157, 159, 161–163,
 172–175, 206, 216, 237, 238,
 242–248, 257, 267, 268, 270, 271,
 273–280, 293, 297, 298, 300, 301,
 303, 306, 308
 acceptance factor, 161, 215–218, 244,
 245, 293
 correction factor, 159, 161, 215–218,
 244, 245, 247, 248, 296
 Crystal Ball, 124, 127, 128, 297

D

data acquisition , 101, 297
data driven methods
 ABCD, 293
 fake factor, 298
 jet veto survival probability, 231, 232,
 238, 300
 matrix method, 301
 simultaneous fit, 226, 227, 238, 306
 transfer factor, 226, 228–230, 232–235,
 238, 308
data formats
 Analysis Object Data, 104, 105, 108,
 203, 293, 297
 Event Summary Data, 104, 105, 108,
 293, 298
 POOL, 104, 105, 298, 304
 Raw Data Objects, 104, 105, 305
decay width, 10, 297
DESY, 35, 297
Derived Physics Data, 297
double parton scattering, 157, 173, 174, 297
data quality, 102, 103, 297, 299
Data Quality Monitoring Framework, 100,
 101, 103, 297
drift circle, 68, 110, 111, 117, 297

E

electron
 Gaussian Sum Filter, 124, 142, 298
 LOOSELLH, 204, 301
 LOOSE++, 204, 222, 301
 TIGHT++, 196, 208, 209, 307
 VERYTIGHTLLH, 204, 208, 222, 309
end-cap, 60–65, 67, 68, 70–72, 74–77, 95,
 109, 117, 121, 123, 124, 129,
 184–187, 196, 294, 297, 306, 307
energy
 transverse energy, 52, 53, 96, 98, 99,
 119, 121, 122, 124, 125, 127, 128,
 132, 167, 168, 185, 187, 190,
 194–197, 200, 308
 missing transverse energy, 20, 53, 70,

71, 98, 136–138, 162, 163, 165,
167–171, 174, 177, 182, 199–202,
204, 205, 207, 208, 210, 212–214,
216, 218, 221–229, 234, 236–238,
241, 243, 246–248, 265, 268, 269,
302, 335

F

flavour tagging, 81, 162, 231–233, 298
FNAL, 13, 35, 298, 307

G

GoodRunsList, 100, 103, 162, 177, 203,
 204, 299
symmetry group, 2, 13–16, 18, 19, 21, 267,
 305, 307

H

high-energy physics, 30, 129, 138, 297, 299

I

impact parameter
 transverse impact parameter, 53, 54, 114,
 126, 201, 299, 301
 longitudinal impact parameter, 53, 54,
 114, 201, 301
interaction point, 39, 40, 42, 45, 47, 48,
 51–54, 57, 59, 60, 63, 67, 80,
 82–84, 95, 96, 110, 113, 117, 123,
 234, 293, 295, 299, 301, 309

J

jet
 anti- k_t , 129, 130, 135, 137, 198, 202,
 206, 215, 294
 AntiKt4EM, 130, 133, 167, 199, 224,
 294
 AntiKt4LC, 130, 167, 199, 294
 jet energy resolution, 135, 136, 199, 212,
 214, 229, 232, 234, 247, 248, 300
 jet energy scale, 131–133, 135–137, 199,
 206, 212, 214, 222–224, 226, 232,
 234, 238, 241, 246–248, 254, 281,
 283, 285, 287, 289, 294, 300

local cluster weighting, 133–137, 199,
224, 294, 300, 301

L

Lagrangian, 3–5, 7, 8, 13–16, 300, 301

lumi-block, 87, 100, 102, 103, 204, 205, 299,
301

Large Electron-Positron Collider, 35, 37, 43,
48, 300

Large Hadron Collider, 30, 32, 35, 37, 43, 45,
47–52, 54, 55, 57, 59–61, 63, 80,
83, 85, 93, 100–103, 105, 108, 115,
123, 129, 157, 159, 160, 180, 203,
267, 268, 293, 295, 296, 300, 301,
303–309

LHCb, 301

LHCf, 268, 301

LUCID, 80, 84, 178, 301

luminosity, 10, 37–43, 45, 47, 80, 82–85,
100–103, 159, 177, 203, 204, 238,
244, 246, 299, 301, 309

M

invariant mass, 186, 187, 206

invariant mass, 121, 170, 173, 186, 187,
242, 299

transverse mass, 53, 163, 164, 170, 181,
242, 308

Monte Carlo, 98, 103–105, 107, 108,
112–116, 118–120, 122, 124, 128,
131–136, 144, 157, 159, 161–163,
167, 170–182, 185, 186, 191, 194,
196, 197, 200, 201, 204–206,
208–212, 214–217, 222, 224,
226–229, 231–234, 236–238, 246,
249, 250, 252–257, 268, 269,
273–281, 293, 294, 296, 299, 300,
302–307

AcerMC, 174, 275, 277, 293

Alpgen, 174, 176, 180, 237, 274–276,
278–280, 293

gg2ww, 172, 175, 273, 277, 299

Herwig, 104, 130, 172, 174, 176, 214,
246, 276, 293, 299, 300

Jimmy, 172, 174, 176, 214, 232, 237,
300

LHAPDF, 180, 299, 300, 304

MadGraph, 176, 276, 280, 293, 301

MC@NLO, 103, 161, 167, 172, 174, 175,
214, 229, 232, 233, 271, 273, 275,
277, 302

Monte Carlo for FeMtobarn
processes, 173, 174, 270, 303

POWHEG, 103, 120, 167, 172, 175, 176,
214, 229, 232, 233, 237, 271, 277,
280, 304

Pythia, 104, 172, 174, 206, 214, 232,
237, 293, 304, 305

PythiaB, 275, 305

Sherpa, 176, 237, 306

missing transverse energy, 136, 138

mis-alignment, 81, 82, 103, 112, 119, 293,
302

modelling

control region, 227–229, 231–234, 296

signal region, 227–229, 233, 234, 306

MoEDAL, 268, 303

momentum

missing transverse momentum, 165,
167–171, 181, 182, 201, 202, 207,
208, 211–214, 216, 224, 226–229,
236, 241, 243, 247, 248, 269, 302

transverse momentum, 20, 52, 53, 64,
65, 68, 77, 81, 82, 86, 93, 95, 96,
98, 99, 109, 111–115, 117–125,
127–133, 135–138, 163, 164, 167,
168, 170, 178, 180, 181, 183–196,
198–202, 204–208, 211, 212, 216,
218, 221–227, 229, 231, 233, 236,
242, 254–259, 268–271, 296, 300,
302, 303, 308, 309

muon

calo-tagged, 117, 188, 296

combined, 117, 118, 120, 121, 137, 177,
186–188, 190–192, 199, 201, 217,
296

- MUID, 303
 - segment-tagged, 117, 121, 137, 306
 - STACO, 115, 117–121, 142, 144, 186, 190–193, 204, 296, 306, 307
 - standalone, 117, 137, 306, 307
- N**
- n-tuple, 105, 139, 141, 142, 203, 253, 254, 303
- P**
- pile-up, 84, 85, 87, 101, 112–114, 119, 122–129, 131–135, 137, 162, 167, 174, 176–178, 188, 192, 194, 199–201, 208, 224, 227, 234, 254, 268, 269, 300, 302, 303, 308
 - pixel
 - cluster, 109, 110, 303
 - Proton Synchrotron, 35, 47, 48, 304
 - pseudorapidity, 52, 55, 57, 59–61, 63–65, 68, 70–75, 77, 78, 80, 84, 96, 98, 99, 109, 112–115, 117, 119, 121, 123–129, 131–137, 163, 166–168, 179, 180, 184–188, 190–192, 194–199, 201–206, 216, 231, 236, 293–296, 300, 301, 303, 304, 306, 307
- Q**
- quantum chromodynamics, 2, 13–16, 159, 160, 163, 172, 174, 176, 196, 234, 236, 247, 248, 269, 299, 301, 302, 305
 - quantum electrodynamics, 2, 8–10, 14–16, 18, 19, 216, 305
 - quartic gauge coupling, 157, 305
- R**
- radiation length, 61, 71, 72, 305, 313
 - rapidity, 52, 130, 305
- S**
- scale factor, 176, 180, 185–188, 191–194, 196–199, 201, 206, 212, 214, 215, 217, 218, 227–229, 238, 306
 - SLAC, 12, 13, 35, 306
 - Standard Model, 2, 11, 13, 16, 21, 22, 30, 45, 51, 55, 59, 157–160, 163, 170, 173, 174, 176, 206, 222, 267, 268, 270, 293, 299, 301, 307
 - Higgs boson, 2, 47, 59, 157, 158, 160, 167, 173–175, 192, 206, 218, 267, 270, 277, 299
 - photon, 8, 16, 51, 135, 137, 157, 158, 173, 174, 176, 269, 303
 - W boson, 2, 10, 11, 16, 19, 20, 22, 53, 59, 81, 98, 115, 136, 157, 158, 162, 172–176, 194, 206, 212, 215–218, 229, 234, 236, 237, 243, 244, 267, 269, 270, 276, 277, 280, 299, 300, 309
 - Z boson, 2, 16, 20, 22, 59, 86, 99, 115, 117–121, 124–126, 131, 135, 157, 158, 162, 163, 167–169, 171, 174, 176, 185–188, 191, 192, 194, 196, 197, 201, 208, 212–215, 217, 222, 224, 227–229, 236, 237, 267, 269, 280, 300, 307, 309
- software
- Athena, 107, 108, 138, 294, 306
 - ATLFAST, 104, 295
 - iLumiCalc, 103, 177, 203, 299
 - ROOT framework, 105, 107, 108, 138, 139, 142, 251, 306
 - RootCore, 107, 138, 139, 141, 145, 306
 - SFrame, 108, 138–141, 306
- signal over background ratio, 158, 159, 202, 207, 268, 306
 - Super Proton Synchrotron, 2, 35, 47, 48, 55, 307, 309
- T**
- tag-and-probe, 99, 117, 121, 124, 126, 162, 185, 188, 191, 192, 194, 196, 197, 217, 222, 307
 - trigger, 93–95, 97, 98, 100, 101, 103, 104, 161–163, 167, 180, 183, 208, 236,

- 268, 269, 297, 299, 302, 305, 308
 - Central Trigger Processor, 95, 296
 - Event Filter, 94, 97, 99, 101, 102, 104, 184, 298, 299, 305
 - High Level Trigger, 94, 97, 98, 100, 101, 103, 105, 107, 299
 - Level-1 Trigger, 93–99, 103, 180, 186, 296, 300
 - prescale, 99, 100, 162, 180, 183, 185, 186, 301, 304
 - region-of-interest, 94, 97, 98, 305
 - Tevatron, 35, 45, 53, 160, 180, 298, 307
 - triple gauge coupling, 157, 158, 271, 309
 - Tier0, 100, 203, 307
 - topo-cluster, 123, 127, 128, 130, 133, 198, 301, 308
 - TOTEM, 45, 57, 268, 308
 - trigger matching , 183, 184, 308
- V**
- vector boson fusion, 157, 173, 174, 309
 - vertex, 111, 113, 114, 121, 129, 309
 - primary, 113–115, 119, 127, 129, 132, 133, 135, 187, 201, 302
 - secondary, 113, 295
 - van der Meer scan, 41, 83–85, 102, 203, 309
- W**
- Worldwide LHC Computing Grid, 105, 106, 268, 309